Computational Studies into the Rhodium Catalysed Dehydrocoupling of Amine- and Phosphine-Boranes

Nicholas Alastair Beattie

Submitted for the degree of Doctor of Philosophy

Heriot-Watt University

School of Engineering and Physical Sciences

February 2018

Abstract

This thesis details the use of density functional theory to study the mechanisms of dehydrocoupling of amine- and phosphine-boranes using a variety of Rh catalysts in collaboration with the group of Professor Andrew Weller at the University of Oxford.

The dehydrocoupling of phosphine-boranes with pre-catalysts $[\mathrm{Rh(Ph_2P(CH_2)_2(PPh_2)(\eta^6\text{-}C_6H_5F)}]^+$ (**Chapter 3**) and $[\mathrm{Rh(Me)(CH_2Cl_2)(PMe_3)(\eta^5\text{-}Cp^*)}]^+$ (**Chapter 4**) were studied. For $[\mathrm{Rh(Ph_2P(CH_2)_2(PPh_2)(\eta^6\text{-}C_6H_5F)}]^+$ the computed mechanism involves facile P-H activation, B-H activation and a rate-limiting B-P coupling process. A functional and basis set study was conducted to benchmark against experimental activation parameters. Furthermore, the differences in reaction of pre-catalyst $[\mathrm{Rh(Me)(CH_2Cl_2)(PMe_3)(\eta^5\text{-}Cp^*)}]^+$ with $\mathrm{H_3B\text{-}PPh_2H}$ and $\mathrm{H_3B\text{-}P^tBu_2H}$, which yield $[\mathrm{Rh(PMe_3)(\eta^5\text{-}Cp^*)(PPh_2BH_3)}]^+$ and $[\mathrm{Rh(H)(\eta^5\text{-}Cp^*)(P^tBu_2BH_2PMe_3)}]^+$ respectively were rationalised computationally.

The dehydropolymerisation of monomethylamine-borane $\mathrm{H_3B\text{-}NMeH_2}$ using a range of alkyl-Xantphos Rh catalysts: neutral $[\mathrm{Rh(\mathit{mer}\text{-}\kappa^3\text{-}P,O,P\text{-}Xantphos\text{-}^iPr)H}]$, and $[\mathrm{Rh(\mathit{mer}\text{-}\kappa^3\text{-}P,O,P\text{-}Xantphos\text{-}^tBu)H}]$, and cationic $[\mathrm{Rh(\mathit{mer}\text{-}\kappa^3\text{-}P,O,P\text{-}Xantphos\text{-}^iPr)(H)_2(\eta^1\text{-}H_3B\text{-}NMeH_2)}]^+$, and $[\mathrm{Rh(\mathit{mer}\text{-}\kappa^3\text{-}P,O,P\text{-}Xantphos\text{-}^tBu)H_2}]^+$ is discussed in **Chapter 5**. The neutral catalysts were found to proceed *via* different outer-sphere dehydrogenation pathways. $[\mathrm{Rh(\mathit{mer}\text{-}\kappa^3\text{-}P,O,P\text{-}Xantphos\text{-}^iPr)H}]$ forms free $\mathrm{H_2B{=}NMeH}$ and a tri-hydride intermediate while $[\mathrm{Rh(\mathit{mer}\text{-}\kappa^3\text{-}P,O,P\text{-}Xantphos\text{-}^tBu)H}]$ proceeds through a novel process to form free $\mathrm{H_2B{=}NMeH}$, $\mathrm{H_2}$ and regenerate the catalyst in one step. A head-to-tail propagation mechanism would then form polyamino-borane $[\mathrm{H_2BNMeH}]_n$. Dehydropolymerisation mechanisms have also been explored for the cationic catalysts with $[\mathrm{Rh(\mathit{mer}\text{-}\kappa^3\text{-}P,O,P\text{-}Xantphos\text{-}^tBu)H_2}]^+$ being postulated to follow a dehydrogenation mechanism involving the formation of boronium cations $[\mathrm{(NMeH_2)_2BH_2}]^+$.

In **Chapter 6** a study of the electronic structure and bonding of boron-containing Rh-dimers $[\mathrm{\{Rh(dipp)\}_2(H)(BH_2NH_2)}]^+$, $[\mathrm{\{RhH\}_2(\mu\text{-}BNMe_2)(\mu\text{-}dpcm)_2(\mu\text{-}H)}]^+$, and $[\mathrm{\{Rh(\kappa^3\text{-}P,O,P\text{-}Xantphos\text{-}^iPr)\}_2B}]^+$ was conducted. All of these species are formed during amine-borane dehydrocoupling catalysis.

Acknowledgements

I would like to thank to my supervisor, Professor Stuart Macgregor, for the opportunity to work for him and his help and guidance throughout my PhD.

Thank you to close collaborator Professor Andrew Weller and his group at The University of Oxford including Tom, Amit, Annie, Gemma and Anna for fantastic experimental work and advice. Thanks to Professor Holger Braunschweig and Marius Schäfer at the University of Würzburg, Professor Alan Welch and Dr Alasdair Robertson at Heriot-Watt University, and Professor Michael Whittlesey at the University of Bath for their collaboration. Also, I am grateful to Dr Christophe Raynaud for accommodating me during my 6 week visit at the University of Montpellier.

Further thanks to the "Computational Inorganic Chemistry" group members both past and present: Dave M, Claire M, Dave J, Tobi, Kevin, Nasir, and Sam for the support, discussion, and coffee breaks. Thanks also to lunch club.

Thanks to my family, especially my parents, Norma and Neil, and my brother Chris. I am always appreciative of their love and support.

Finally, a thank you to my partner, Claire, who is a constant source of advice and encouragement, and my best friend. Without her I would not have been able to submit this thesis.

Table of Contents

Publication List

T. N. Hooper, A. S. Weller, N. A. Beattie, S. A. Macgregor, "Dehydrocoupling of Phosphine-Boranes using the $[RhCp^*Me(PMe_3)(CH_2Cl_2)][BAr^F_4]$ Precatalyst: Stoichiometric and Catalytic Studies", *Chem. Sci.*, **2016**, *7*, 2414-2426,
DOI: 10.1039/C5SC04150C

M. Schäfer, N. A. Beattie, K. Geetharani, J. Schafer, W. C. Ewing, M. Krahfuss, C. Horl, R. D. Dewhurst, S. A. Macgregor, C. Lambert, H. Braunschweig, "Synthesis of Functionalized 1,4-Azaborinines by the Cyclization of Di-*tert*-butyliminoborane and Alkynes", *J. Am. Chem. Soc.,* **2016**, *138*, 8212-8220,
DOI: 10.1021/jacs.6b04128

A. Kumar, N. A. Beattie, S. D. Pike, S. A. Macgregor, A. S. Weller, "The Simplest Amino-Borane $H_2B{=}NH_2$ Trapped on a Rhodium Dimer: Pre-Catalysts for Amine-Borane Dehydropolymerisation", *Angew. Chem. Int. Ed.,* **2016**, *23*, 6651-6656,
DOI: 10.1002/anie.201600898

A. P. M. Robertson, N. A. Beattie, G. Scott, W. Y. Man, J. J. Jones, S. A. Macgregor, G. M. Rosair, A. J. Welch, "14-Vertex Heteroboranes with 14 Skeletal Electron Pairs: An Experimental and Computational Study", *Angew. Chem. Int. Ed.,* **2016**, *30*, 8706-8710,
DOI: 10.1002/anie.201602440

A. L. Colebatch, A. I. McKay, N. A. Beattie, S. A. Macgregor, A. S. Weller, "Fluoroarene Complexes with Small Bite Angle Bisphosphines: Routes to Amine-Borane and Aminoborylene Complexes", *Eur. J. Inorg. Chem.*, **2017**, *38*, 4533-4540,
DOI: 10.1002/ejic.201700600

G. M. Adams, A. L. Colebatch, J. T. Skornia, A. I. McKay, H. C. Johnson, G. C. Lloyd-Jones, S. A. Macgregor, N. A. Beattie, A. S. Weller, "The Dehydropolymerisation of $H_3B\text{-}NMeH_2$ to form Polyaminoboranes using [Rh(Xantphos-alkyl)] Catalysts", *J. Am. Chem. Soc.*, **2018**, *140*, 1481-1495,
DOI: 10.1021/jacs.7b11975

Chapter 1: Introduction

1.1 – Background into the Dehydrocoupling of Amine-Boranes

Amine-boranes, R_3B-NR_3, which are isoelectronic with alkanes, R_3C-CR_3, are of scientific interest due to their potential to be used for H_2 storage.[1, 2] This arises from the simplest amine-borane, ammonia-borane H_3B-NH_3, being an air-stable solid and having 19.6 % weight percentage with respect to H_2.[3] The release of H_2 from ammonia-borane can be easily achieved to the point where H_3B-NH_3 is used as a source of H_2 in hydrogenation reactions.[4-8] However, recharging the system with H_2 remains a challenge due to the process being thermodynamically unfavourable.[9] There is also interest in the formation of polyamino-boranes, **1-1** (**Figure 1-1**), which are isoelectronic with polyolefins, through the process of amine-borane dehydrocoupling. [1] There have been relatively few studies on the properties of polyamino-boranes.[1, 10-12], however, they have demonstrated the potential to be piezoelectric materials and precursors for BN-based materials such as white graphene (which is an anti-pollutant).[13, 14] The synthesis of polyamino-boranes is also less explored relative to polyolefins. The aim, as always when synthesising polymeric materials, is to produce long polymer chains with a high average mass (M_n) as well as having a polydisperity index (PDI) close to 1.0 which indicates that all polymers being produced by the reaction are the same length.

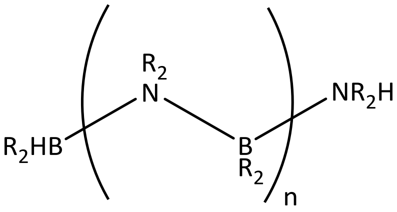

1-1

Figure 1-1: *General structure of polyamino-borane*

In the synthesis of polyolefins such as polyethylene, ethene can be used as a feedstock as it is stable in ambient conditions.[15] The isoelectronic amino-borane equivalent, $H_2B{=}NH_2$, is not stable as it oligomerises at 123 K meaning that polyamino-boranes cannot be formed through the same process as polyolefins. Therefore, to form polyamino-boranes, amine-boranes are used as the starting material. This means a dehydrogenation has to take place in order to generate the amino-borane *in situ* before propagation to form the polymer can occur.[16]

A generalised scheme for the catalytic dehydrogenation and dehydropolymerisation of amine-boranes is shown below in **Scheme 1-1**. The dehydrogenation of secondary amine-boranes, such as H_3B-NMe_2H, leads to the formation of common intermediates such as the amino-borane $H_2B{=}NMe_2$ and the linear dimer H_3B-NMe_2BH_2-NMe_2H which both rapidly cyclise, and lose H_2 in the case of the linear dimer, to form the cyclic dimer $[H_2BNMe_2]_2$, **I**. Primary amine-boranes, such as H_3B-$NMeH_2$, can form polyamino-boranes $[H_2BNMeH]_n$, **II**, when 1 equivalent of H_2 is lost or borazines $[HBNMe]_3$, **III**, when 2 equivalents of H_2 are lost. The parent H_3B-NH_3 can also form polyamino-boranes $[H_2BNH_2]_n$, **II**, and borazines $[HBNH]_3$, **III**, but can also lose a further equivalent of H_2 to form polyborazine, **IV**, as well as other oligomeric and polymeric materials which form when less than 2 equivalents of H_2 are lost. However, in principle up to 3 equivalents of H_2 can be lost from H_3B-NH_3 and some catalysts have been shown to produce 2.7 equivalents of H_2.[17]

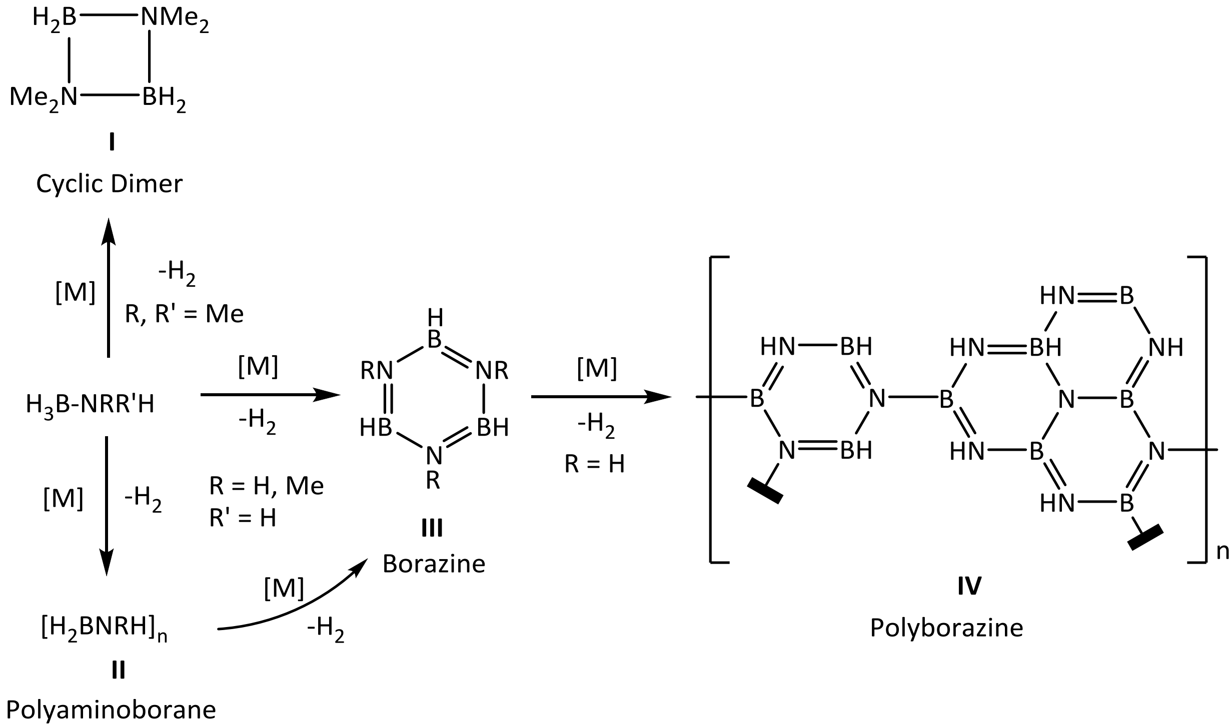

Scheme 1-1: *Simplified dehydrocoupling pathways for H_3B-NMe_2H, H_3B-$NMeH_2$, H_3B-NH_3. Adapted from reference No. 18.*

It is possible to dehydrocouple H_3B-NH_3 without the presence of catalyst upon heating to 393 K.[18-20] Recent work by Alcaraz *et al.*[21] have shown high molecular weight polyamino-boranes can be formed without the need for solvent or catalyst by reacting diisopropylamino-borane and primary amines. However, this requires low temperature conditions (233 K). There is interest in the catalytic formation of polyamino-boranes as catalysts can provide greater control and efficiency to a reaction with the first example published by Roberts *et al.* in 1989.[22] Various dehydrogenation and dehydrocoupling catalysts including group 1 and 2 metal complexes[23-27], lanthanides[28-32], and frustrated Lewis pairs[33, 34] [19] are present in the literature. However, transition metal catalysis shows the greatest potential for controlling the rate and amount of H_2 release whilst maintaining high catalyst activities.[17, 35] Studying the mechanism of these dehydrogenation and dehydropolymerisation reactions is important as a greater understanding of the mechanism will allow for greater control of the reaction. This would allow for greater H_2 release, more efficient polymer formation and the ability to extend the polymer library which is currently limited when compared to polyolefins.

Studying the mechanism of amine-borane dehydrocoupling through experimental and computational investigation is currently an active field. Recent reviews by Weller *et al.*[35], Paul *et al.*[9], and Rossin and Peruzzini[36] discuss the published work on amine-borane dehydrocoupling thoroughly. Therefore, this chapter will focus on specific studies in order to give a general view on what is known about the dehydrogenation and propagation mechanisms of the catalytic dehydrocoupling of amine-boranes using transition-metal catalysts. Both heterogeneous and homogenous catalysts have been developed for the dehydrocoupling of amine-boranes.

1.1.1 – Heterogenous Catalysis

Heterogeneous catalyst systems are some of the most active amine-borane dehydrocoupling catalysts reported in the literature. For example Morris *et al.*[37] found that Fe nanoparticles formed *in situ* from $[Fe(NCMe_2)(PNNP)][BF_4]/KO^tBu$ [$(PNNP = Ph_2PC_6H_4CH{=}NCH_2)_2$] exhibit a TOF (turn over frequency) of 2400 h^{-1} which is one of the fastest in the literature. Mechanistic insight into the formation of polyamino-boranes *via* heterogeneous catalysis was published by Manners *et al.*[38] Reaction of $H_3B\text{-}NMe_2H$ with a Ni catalyst produced from a Ni/Al alloy yields $[H_2NBMe_2]_2$ with a TOF of 3 h^{-1}. The proposed mechanism in **Scheme 1-2(A)** involves a major pathway where $H_3B\text{-}NMe_2H$ loses H_2 on-metal and then rapidly dimerises off-metal to form $[H_2BNMe_2]_2$. A minor pathway is also thought to exist where there is on-metal formation of linear dimer $H_3B\text{-}NMe_2BH_2\text{-}NMe_2H$ before on-metal dehydrocyclisation occurs to form the cyclic dimer. Investigations into the dehydrocoupling of $H_3B\text{-}NMeH_2$ were also carried out (**Scheme 1-2(B)**). It was found that reaction of $H_3B\text{-}NMeH_2$ in the presence of a 5 mol% loading of Ni saw the formation of cyclic borazine $[H_2BNMeH]_3$. However, repeating the reaction at a 100 mol% loading of Ni saw the formation of $[H_2BNMeH]_n$ (M_n = 51300 $gmol^{-1}$, PDI = 1.5). The catalyst loading is thought to have such an effect because it alters the concentration of $H_2B{=}NMeH$, formed from the major pathway that is present in the reaction. The amino-borane will be formed at higher concentrations at higher catalyst loadings in which case polymerisation will be favoured over cyclisation as it is the kinetically favourable process. It was found that $H_3B\text{-}NH_3$ reacts in a similar manner.

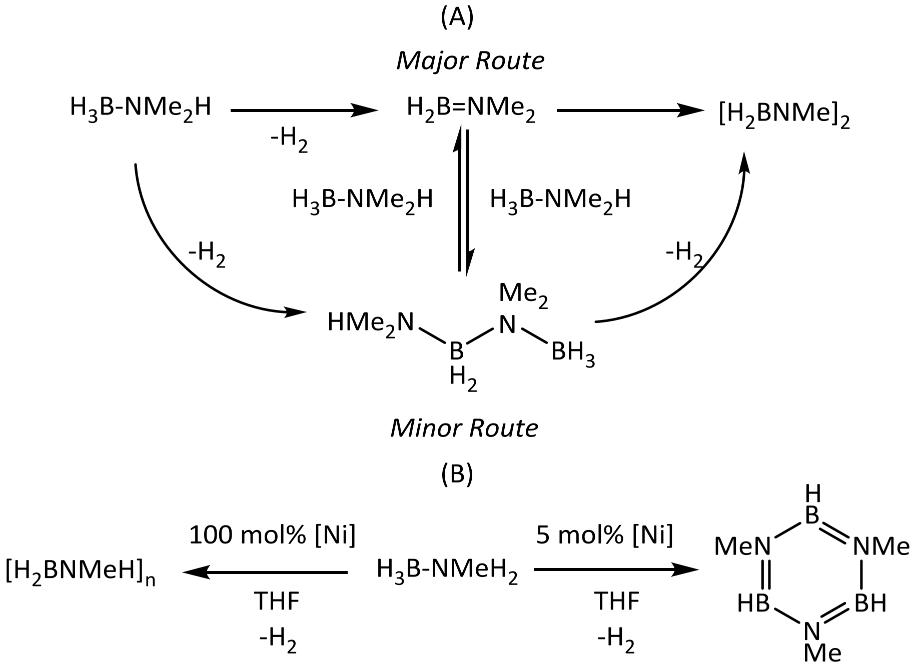

Scheme 1-2: ***(A)*** *Proposed mechanism for the dehydrocoupling of H_3B-NMe_2H using Ni nanoparticles.* ***(B)*** *Dehydrocoupling of H_3B-$NMeH_2$ using Ni nanoparticles. Adapted from reference No. 38.*

Other heterogeneous catalysts for the dehydrogenation or dehydrocoupling of amine-boranes include Fe complexes developed by Manners *et al.*[39] and Liu *et al.*[40] which react as Fe nanoparticles in the catalytic solution. Co, Mn, Ru, Rh, Pt and Pd nanoparticles have also been discovered to dehydrocouple amine-boranes.[41-51] Sneddon *et al.* demonstrated an increase in the rate of H_2 produced when conducting heterogeneous amine-borane dehydrocoupling using ionic liquids as a solvent which complemented their work on the non-catalysed dehydrogenation of amine-boranes.[52, 53] It was also discovered that different products were observed depending on the ionic liquid used (**Scheme 1-3**). For example, using Ru nanoparticles (produced from $[RuCl_2(PMe_3)_4]$) as a catalyst, the ionic liquid $[emim][O_3SOEt]$ (emim = 1-ethyl-3-methylimidazole) saw a mixture of borazine and polyborazine form, while reaction with [bmim][Cl] (bmim = 1-butyl-3-methylimidazole) would form polyamino-borane. This allowed for greater control in heterogeneous catalysis and was exploited by Baker *et al.*[54] when developing liquid fuel cell mixtures.

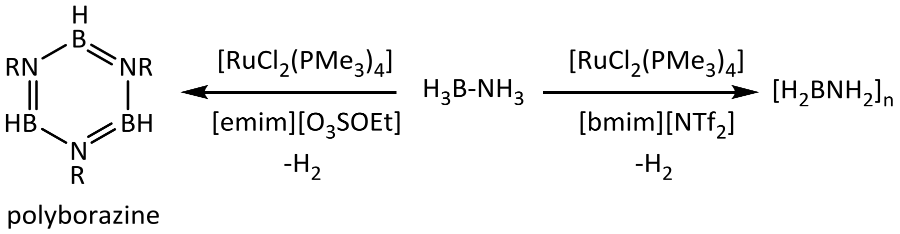

Scheme 1-3: *The dehydrogenation of H_3B-NH_3 in different ionic liquids. Adapted from reference No. 53.*

1.1.2 – Homogeneous Catalysis

As discussed previously, the transition-metal catalysed dehydrocoupling of amine-boranes must involve the dehydrogenation of the amine-borane to form amino-borane *in situ* prior to propagation to form polymer. In general, the dehydrogenation of amine-boranes using homogeneous catalysis follows three main pathways shown in **Scheme 1-4**. Firstly, the reaction can proceed through an initial B-H activation mechanism (**Section 1.1.2.1**). Here, the amine-borane binds to the metal centre to form an amine-borane σ-complex, **V**, before proceeding through a B-H activation to form a base-stabilised boryl intermediate, **VI**. An N-H activation then produces free amino-borane and a di-hydride intermediate, **VII**, which loses H_2 to regenerate the active catalyst. The dehydrogenation of amine-borane can also occur *via* an initial N-H activation from intermediate **V** (**Section 1.1.2.2**) to form an amido-borate intermediate, **VIII**, before B-H activation completes the dehydrogenation. Finally, the dehydrogenation could advance through a concerted mechanism where the B-H and N-H activation steps occur at the same time to directly form di-hydride intermediate **VII** (**Section 1.1.2.3**).

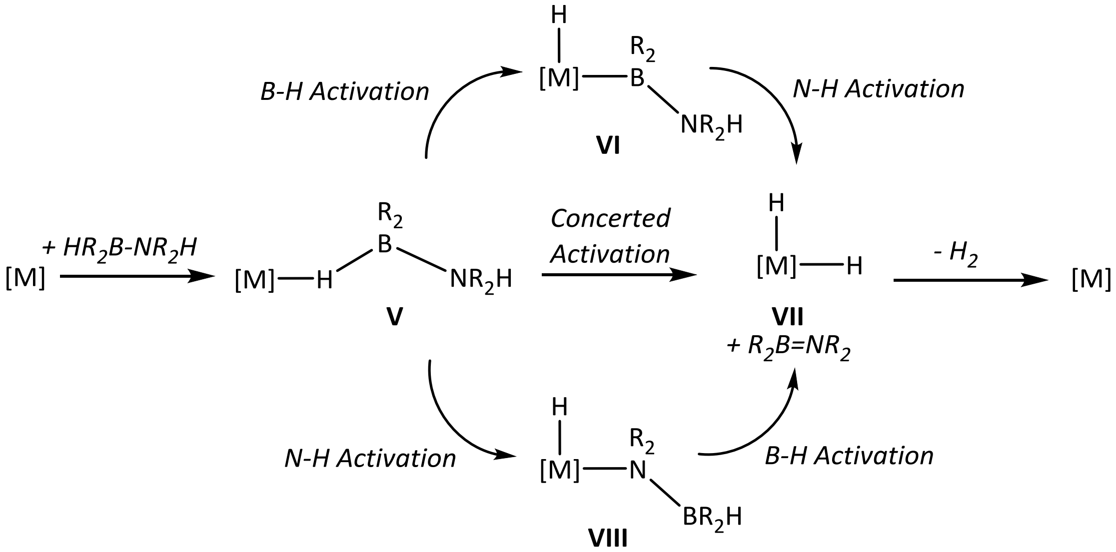

Scheme 1-4: *General scheme for the transition-metal catalysed dehydrogenation of amine-boranes*

The following sections discuss mechanistic studies into the dehydrogenation and propagation processes with a particular focus on studies where experimental and computational techniques have been used together to investigate the dehydrocoupling process.

1.1.2.1 – Dehydrogenation Mechanisms initiated by B-H Activation

Weller, Macgregor *et al.*[55] published a study where 10-20 mol% catalyst loadings of $[Ir(PCy_3)_2(H)_2(H_2)_2][BAr^F_4]$ **1-2** was used to dehydrocouple H_3BNMe_2H, H_3BNMeH_2 and H_3BNH_3 with TOF ~0.1 h^{-1}. The low TOF proved useful as it allowed for reaction intermediates to be observed and compared between different amine-boranes. Reaction with $H_3B\text{-}NMe_2H$ yields $[H_2BNMe_2]_2$ with the major reaction intermediate isolated involving a metal-bound amino-borane $[Ir(PCy_3)_2(H)_2(\eta^2\text{-}H_2B{=}NMe_2)][BAr^F_4]$. Primary amine-borane $H_3B\text{-}NMeH_2$ undergoes on-metal oligomerisation to form the linear dimer $H_3B\text{-}NMeHBH_2\text{-}NMeH_2$ with the major reaction intermediate isolated involving the metal-bound dimer $[Ir(PCy_3)_2(H)_2(\eta^2\text{-}H_3B\text{-}NMeHBH_2\text{-}NMeH_2)][BAr^F_4]$. Furthermore, $H_3B\text{-}NH_3$ proceeds through more oligomerisation steps to produce $[H_3B\text{-}(H_2BNH_2)_n\text{-}NH_3]$ with various reaction intermediates of $[Ir(PCy_3)_2(H)_2(\eta^2\text{-}H_3B\text{-}(NH_2BH_2)_n\text{-}NH_3)][BAr^F_4]$ ($n = 0 – 4$) characterised using ESI-MS (electron-spray ionisation mass spectrometry). Computational studies into the mechanism utilised DFT calculations on a model system $[Ir(PMe_3)_2(H)_2]^+$ with the BP86-(D3)(C_6H_5F)/6-31g**,SDDALL(Ir,P) level of theory. This study allowed the authors to propose pathways for the dehydrogenation (seen in **Scheme 1-5**) and propagation (discussed in **Section 1.1.2.5**) mechanisms. The dehydrogenation pathway for $H_3B\text{-}NH_3$ starting from complex **1-3**, proceeds *via* the initial binding of a second $H_3B\text{-}NH_3$ unit to form intermediate **1-4** which is more stable by 5 kcal mol^{-1}. B-H activation then occurs through hydride transfer to form a dihydrogen ligand on the metal and a base-stabilised boryl moiety **1-5**. Loss of H_2 and then rate-limiting N-H activation with a free energy barrier of 26.7 kcal mol^{-1} then occur to afford amino-borane, amine-borane complex **1-7**. The dehydrogenation of $H_3B\text{-}NMeH_2$ and $H_3B\text{-}NMe_2H$ were found to have free energy barriers of 25.2 and 26.2 kcal mol^{-1} respectively.

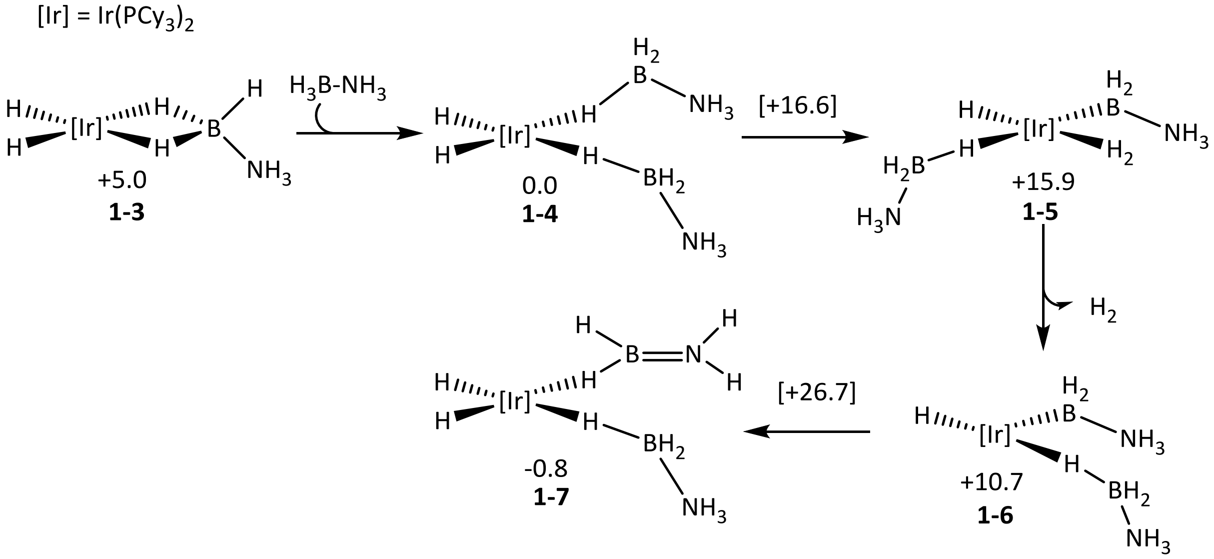

Scheme 1-5: *Proposed dehydrogenation mechanism for reaction of H_3B-NH_3 with catalyst **1-2.** Free energies in kcal mol^{-1}. Adapted from reference No. 55.*

Other examples of homogeneous catalytic systems proposed to proceed by an initial B-H activation pathway are shown in **Figure 1-2**. They include Chirik's Ti^{II} complex [(Ti(η^5-$C_5H_3(SiMe_3)_2)_2\mu$-N_2], **1-8**[56], and [CpFe$(CO)_2$I], **1-9**, which acts under photoirradiation published by Manners *et al.*[39] Manganese complexes such as [Mn(2,6-$Xyl_2C_6H_3)_2$] (Xyl = 2,6-$Me_2C_6H_3$), **1-10** also dehydrocouple amine-boranes under photoirradiation.[49] Furthermore, Peruzzini *et al.*[57] conducted a theoretical study on [Ir$(dppm)_2$][OTf] (dppm = $Ph_2PCH_2PPh_2$), **1-11** at the MPW1K/6-31g+** level on a truncated model. It was found that co-ordinating H_3B-NH_3 to the metal centre *via* an Ir-BH_3 interaction was favoured as the Ir-NH_3 interaction was repulsive and no Ir-N bond would form. Furthermore, B-H oxidative addition was then calculated to have a very low barrier of 4.3 kcal mol^{-1} which confirmed that B-H activation was more favoured than N-H activation. An initial B-H activation mechanism was one of the pathways postulated by Berke *et al.*[7] for their range of rhenium catalysts such as [Re$(PCy_3)_2$(Br)(NO)(H_2)(H)] **1-12**.

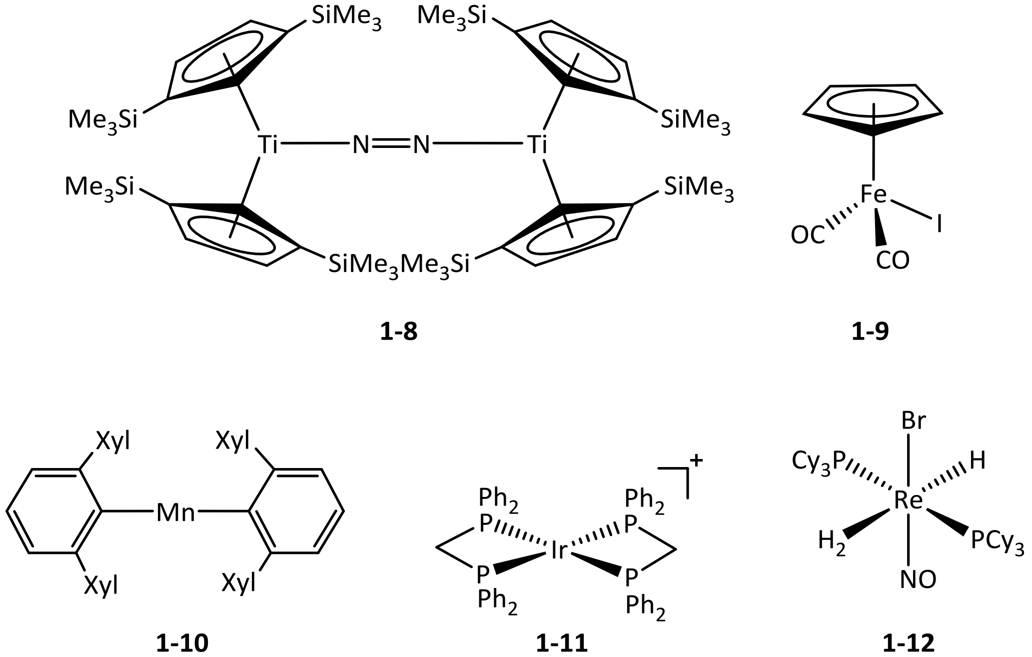

Figure 1-2: *Catalysts proposed to proceed via mechanisms involving initial B-H activation*

1.1.2.2 – Dehydrogenation Mechanisms initiated by N-H activation

N-H activation pathways are generally observed for early transition-metal complexes such as [Cp_2TiCl_2], **1-13**, as published by Manners *et al.*[58] in what was the first example of well-defined dehydrocoupling of amine-boranes by a homogeneous catalyst. The formation of [H_2BNMe_2]$_2$ from H_3B-NMe_2H was achieved by reacting **1-13** with ^{n}BuLi to generate {Cp_2Ti} fragment **1-14** *in situ*. No reaction was observed with H_3B-$NMeH_2$. In later studies by Manners, Lloyd-Jones *et al.*[59], H_3B-NMe_2BH_2-NMe_2H was thought to be the sole reaction intermediate. To prove this, independently synthesised H_3B-NMe_2BH_2-NMe_2H was reacted with the catalyst which resulted in complete consumption of the linear dimer and formation of [H_2BNMe_2]$_2$. This led to the mechanism in **Scheme 1-6** being proposed which begins with the formation of [$Cp_2Ti(\eta^2$-H_3B-$NMe_2H)$], **1-15** through initial coordination of the H_3B-NMe_2H to the Ti^{II} centre. This is followed by NH-activation to form the metal-bound amido-borate [$Cp_2Ti(H)(NMe_2$-$BH_3)$], **1-16**. Addition of a second H_3B-NMe_2H results in B-N bond formation to generate the linear dimer H_3B-NMe_2BH_2-NMe_2H and [Cp_2TiH_2] **1-17** (which loses H_2 to regenerate the active catalyst). The mechanism then goes through a second cycle where the linear dimer binds to the metal centre to form **1-18** before undergoing an on-metal dehydrocyclisation to form [H_2BNMe_2]$_2$ and **1-17** which again loses H_2 to regenerate the active catalyst.

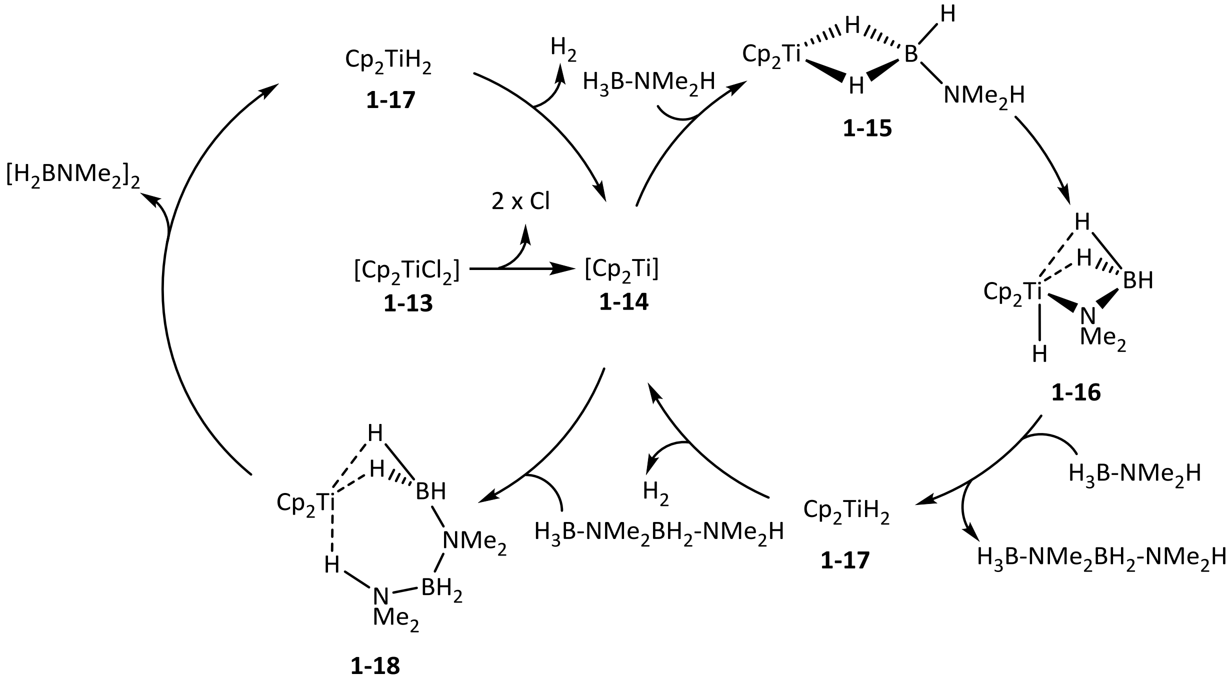

Scheme 1-6: *Proposed dehydrocoupling pathway of H_3B-NMe_2H by the {Cp_2Ti} fragment. Adapted from reference No. 58.*

Further work into dehydrogenation of amine-boranes using [Cp_2Ti] fragments has been published.*[60-62]* Paramagnetic Ti^{III} complexes [$Cp_2Ti(NMe_2$-$BH_3)$], **1-19** (**Figure 1-3**), and [$Cp_2Ti(PPh_2$-$BH_3)$], **1-20** were synthesised before using them as catalysts under the same reaction conditions Manners and co-workers had used above. Both complexes proved to be effective catalysts for the dehydrogenation of H_3B-NMe_2H with similar activity to the $Cp_2TiCl_2/{}^nBuLi$ system. Furthermore, H_3B-NMe_2BH_2-NMe_2H was again seen as an intermediate indicating that it follows the same mechanism outlined in **Scheme 1-6**. However the equivalent complexes where Cp* was used showed no dehydrocoupling activity. The zirconocene analogues, **1-21**, were also synthesised and proved to be a much less active catalysts. Metallocene complexes have also been investigated by Rosenthal *et al.*[63] who were able to increase catalytic activity by using [$(\eta^5$-$C_5H_4{}^iPr)_2Ti(\eta^2$-$Me_3SiCCSiMe_3)$] **1-22** as a pre-catalyst. Other catalytic systems proposed to proceed through initial N-H activation mechanisms include a Fe β-diketiminate catalyst **1-23** developed by Webster *et al.*[64], rhenium catalysts such as **1-12** developed by Berke *et al.*[7] and the heterobimetallic complex [$ZrMe(\mu$-η^5:η^1-$C_5H_4PEt_2)_2RuCp^*$] **1-24** from Nishibayashi *et al.*[65] where the N-H activation occurs on the Zr centre and B-H activation on the Ru centre. Further examples include a range of group VI carbonyl complexes such as [$Cr(CO)_6$] **1-25** published by Shimoi *et al.* where calculations postulate the active species is a [$M(CO)_4$] complex[66, 67] and [$Mo(\eta^6$:η^1:η^1-$C_6H_4(C_6H_4(P^iPr_2))_2(NCMe)_2$] **1-26** developed by Agapie *et al.*[68] Furthermore, Rossin and Peruzzini *et al.*[69] developed a Pd^{II} complex, [$({}^{tBu}PCP)Pd(H_2O)$][PF_6] (${}^{tBu}PCP$ = $P^tBu_2CH_2(C_6H_3)CH_2P^tBu_2$) **1-27** which was proposed to procced *via* an unconventional mechanism where initial B-N coupling occurs between a metal-bound H_3B-NH_3 molecule and a second outer-sphere H_3B-NH_3 to form free H_2 and the metal-bound linear dimer. N-H and B-H activation then occur to form the cyclic dimer $[H_2BNH_2]_2$.

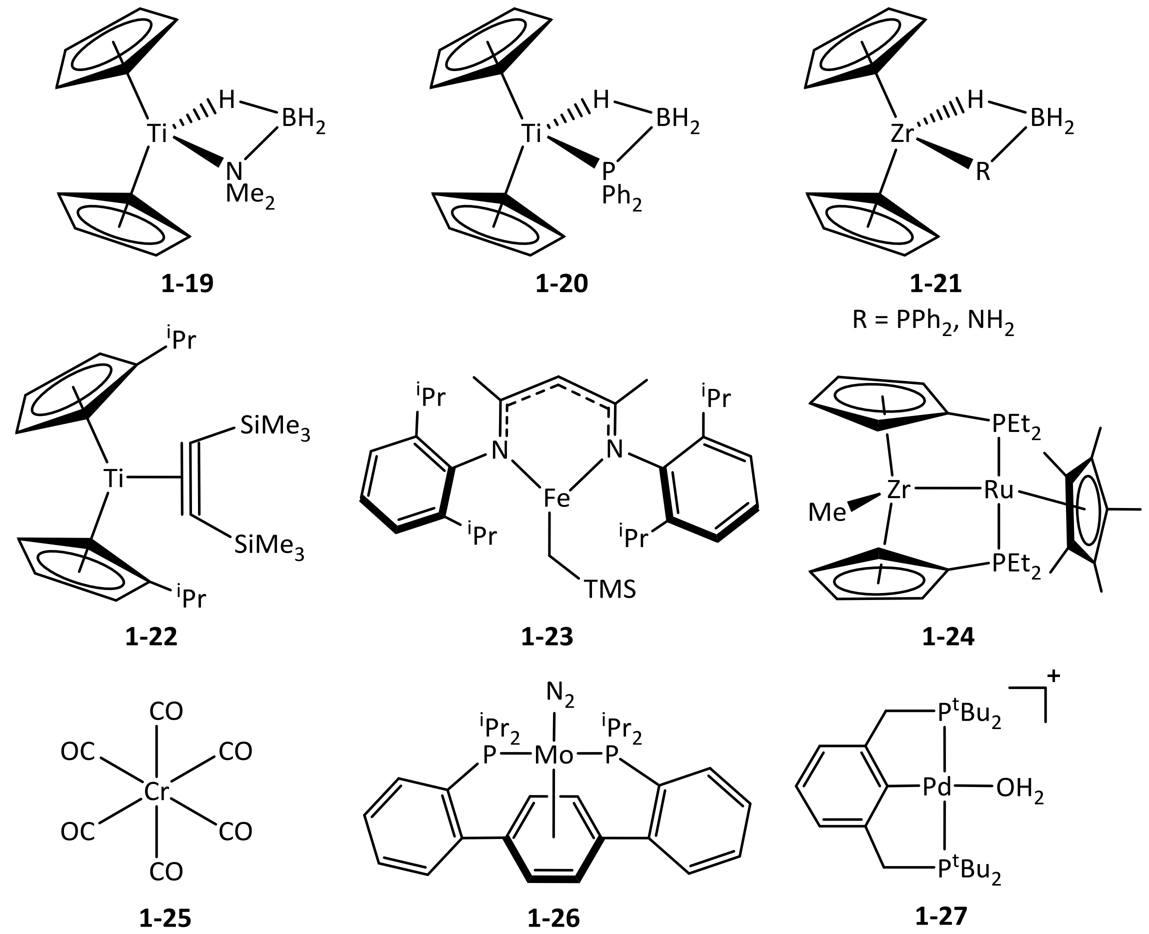

1-19 **1-20** **1-21**

R = PPh_2, NH_2

1-22 **1-23** **1-24**

1-25 **1-26** **1-27**

Figure 1-3: *Catalysts proposed to proceed via N-H activation first mechanisms*

Initial N-H activation pathways also occur during mechanisms which involve ligand cooperativity. A variety of $Ni(NHC)_2$ (NHC = N-Heterocyclic Carbene) systems **1-28** were reported by Baker *et al.*[70] to be capable of dehydrocoupling $H_3B\text{-}NH_3$ to form polyborazine at 333 K for 4 h with the most active NHC ligand being based on Enders' carbene (1,3,4-triphenyl-4,5-dihydro-1H-1,2,3-triazol-5-ylidene), **1-29**. It was determined through kinetic isotope effect (KIE) experiments that both B-H activation and N-H activation occur in the rate limiting step. Several computational mechanistic studies have been published on this system.[71-75] Hall *et al.* [72, 73]proposed a mechanism using the TPSS functional and cc-pVDZ basis set (**Scheme 1-7**). The NHC facilitates a proton transfer from the NH_3 of a σ-bound $H_3B\text{-}NH_3$ molecule in intermediate **1-30** to form **1-31** with a free energy barrier of 9.1 kcal mol^{-1} making it the rate-limiting step. The newly formed C-H bond would then proceed through oxidative addition with a barrier of 8.7 kcal mol^{-1} to form a Ni-H bond as seen in **1-32**. Facile B-H activation then occurs to form a metal-bound amino-borane and an H_2 ligand, **1-33**. Both ligands would then dissociate to complete the cycle and reform complex **1-30**.

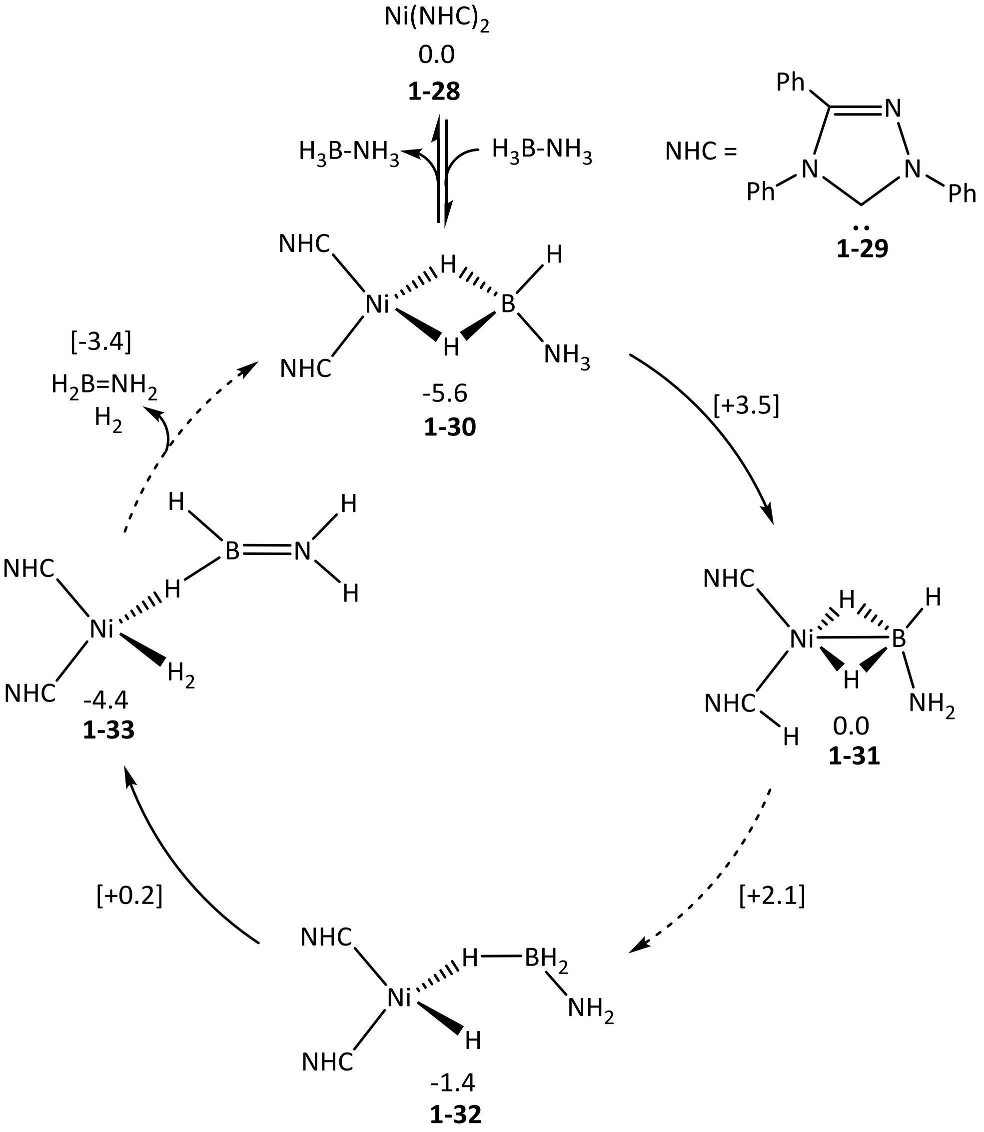

Scheme 1-7: *Proposed mechanism for dehydrocoupling of H_3B-NH_3 using $Ni(NHC)_2$ by Hall et al. Dashed lines represent multiple steps taking place. The energy quoted is from the highest energy transition state of those multiple steps. Free energies in kcal mol^{-1}. Adapted from reference No. 73.*

A second mechanism was proposed by Zimmerman *et al.* where the active catalyst is a mono-carbene nickel complex, **1-34a** (**Scheme 1-8**).[74, 75] The calculations used in this study were run with the B3LYP functional and a combination of the 6-31g++** and 6-31g* basis sets. The authors calculated Hall's mechanism to have a free energy barrier of 12.8 kcal mol^{-1}. Losing an NHC ligand was calculated to have a lower barrier of 11.5 kcal mol^{-1} and therefore it was thought the dehydrogenation would proceed by the following mechanism (**Scheme 1-8**). The dehydrogenation follows the pathway of the Hall mechanism up to the formation of **1-32** before NHC dissociation yields **1-34a.** B-H activation and the loss of H_2 then forms intermediate **1-35** with a free energy barrier of 25.4 kcal mol^{-1}. Another molecule of H_3B-NH_3 would then coordinate to the Ni centre and transfer a proton to the NHC ligand to form intermediate **1-36.** This process has a free energy activation of 20.1 kcal mol^{-1}. A combination of facile C-H and B-H activation steps is then proposed to occur to form free H_2 and $H_2B=NH_2$ as well as **1-34b** which would isomerise to **1-34a** to complete the cycle.

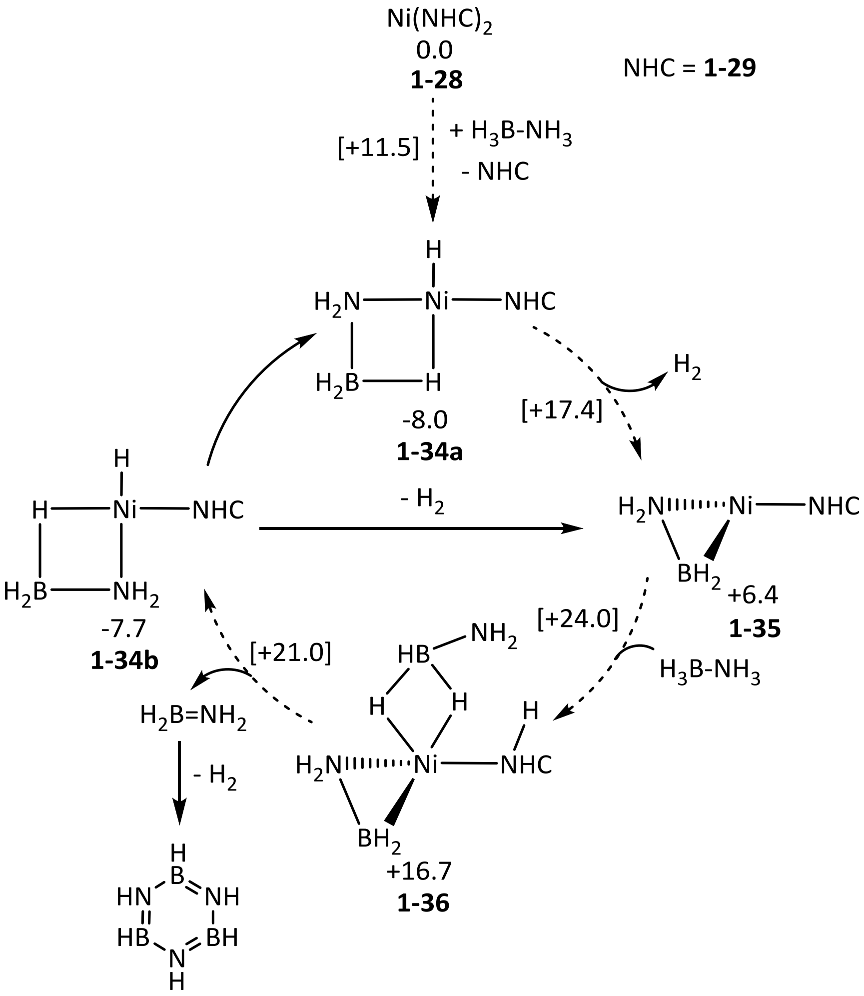

Scheme 1-8: *Proposed mechanism for dehydrocoupling of H_3B-NH_3 using $Ni(NHC)_2$ by Zimmerman et al. Free energies in kcal mol^{-1}. Adapted from reference No. 74.*

Ligand cooperativity mechanisms are also postulated for other catalytic systems in the literature with the common theme of a basic ligand being protonated *via* an N-H activation process. For example, this is postulated to occur for the $[Zr(\eta^5\text{-}Cp)_2(OC_6H_4P^tBu_2)][BAr^F_4]$ **1-37** (**Figure 1-4**) catalyst published by Wass *et al.*[76, 77] which acts like a frustrated Lewis pair with a δ+ Zr and δ- phosphine. Fe catalyst $[Fe(PCy_2CH_2CH_2PCy_2)(NPhCH_2CH_2NPh)]$ **1-38** developed by Gordon, Baker *et al.*[78] is also proposed to follow a ligand cooperativity mechanism and is discussed further in **Section 1.1.2.4**. Furthermore, there are a range of ruthenium catalysts such as $[Ru(^iPr_2PCH_2CH_2NH_2)_2Cl_2]$ **1-39** published by Fagnou *et al.*[79]

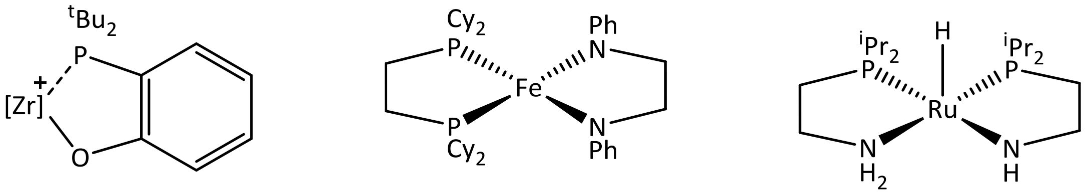
1-37 **1-38** **1-39**

Figure 1-4: *Catalysts proposed to proceed via mechanisms involving initial B-H activation*

The majority of catalytic systems that proceed *via* ligand cooperativity mechanisms make use of ligands that act like Lewis Bases. However, a catalyst developed by Peters *et al.*[80] makes use of a ligand acting as a Lewis Acid. Reacting diamagnetic complex **1-40** with H_3B-NMe_2H in stoichiometric quantities produced a dihydridoborato-cobalt dihydride complex, **1-41**. When both complexes were reacted with H_3B-NMe_2H under N_2 in C_6D_6 for 6 hrs at 273 K, the catalytic formation of $[H_2BNMe_2]_2$ and H_2 was observed. Computational studies carried out by Paul *et al.*[81] investigated the mechanism of this dehydrogenation (see **Scheme 1-9**). The calculations were run using the B3PW91-D(C_6D_6)/SDDALL(Co)/6-31g** level of theory. It was found that complex **1-40** was a pre-catalyst that would form active catalyst **1-41** *via* an initial N-H activation initiation mechanism. First, the N_2 ligand dissociates before one equivalent of H_3B-NMe_2H binds to the metal in an η^2-fashion in **1-43**. N-H activation then occurs with a free energy barrier of 25.0 kcal mol^{-1} to form **1-44** where the transferred hydride is bridging between the metal and the Lewis acidic boron on the ligand. A more facile B-H activation with a free energy barrier of 10.5 kcal mol^{-1} then results in the loss of $H_2B{=}NMe_2$ and formation of **1-41**. The catalytic dehydrogenation was found to proceed *via* a concerted activation mechanism and is discussed in **Section 1.1.2.3**.

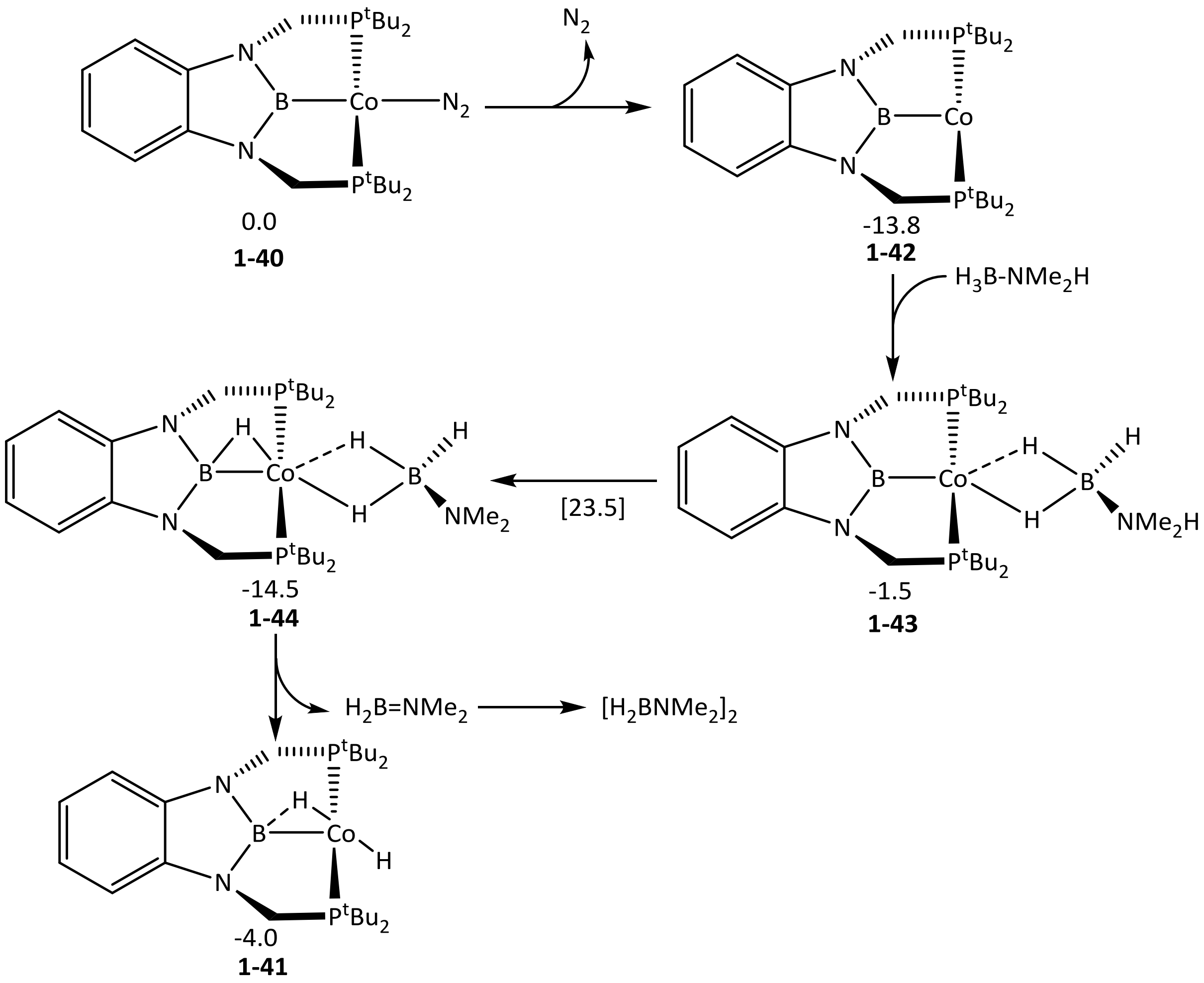

Scheme 1-9: *Proposed initiation pathway for reaction of H_3B-NMe_2H with **1-40**. Adapted from reference No. 81.*

1.1.2.3 – Concerted Activation Dehydrogenation Mechanisms

Once the catalytically active species **1-41** is formed, a concerted dehydrogenation mechanism was characterised (**Scheme 1-10**).[81] During the outer-sphere process, the B-H bond transfers a hydride to the metal centre as the N-H protonates a metal-hydride bond as seen in **1-45**. This forms di-hydride-dihydrogen complex **1-46**. This step has a calculated free energy barrier of 14.6 kcal mol^{-1} due to the lowest energy intermediate **1-44**. The complex then rearranges to intermediate **1-47** which is more stable than **1-46** by 8.3 kcal mol^{-1} before H_2 reductive elimination results in the loss of H_2 and the regeneration of catalyst **1-41**.

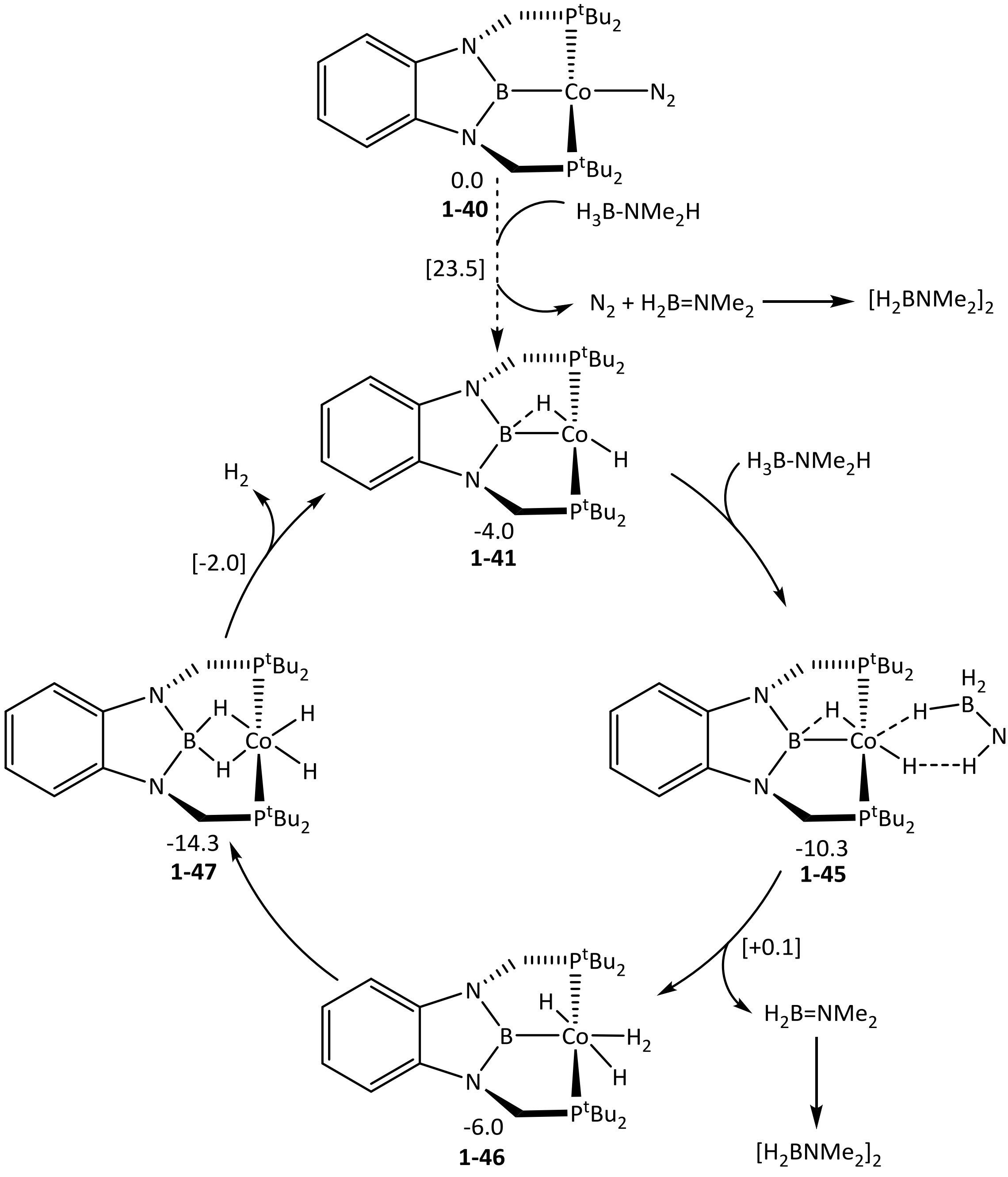

Scheme 1-10: *Proposed dehydrocoupling pathway for reaction of H_3B-NMe_2H with* ***1-41****. Free energies in kcal mol^{-1}. Adapted from reference No. 81.*

Concerted B-H/N-H activation mechanisms have also been proposed for H_3B-NH_3 dehydrocoupling by Esteruelas *et al.*[82, 83] who used [$OsH_2(CO)(\eta^2$-CH_2=CHEt)($P^iPr_3)_2$] **1-48** (**Figure 1-5**) as a catalyst. Calculations using the M06 functional and the lanl2dz/6-31g** basis sets suggests the H_3B-NH_3 would replace the CH_2=CHEt ligand before proceeding *via* a concerted activation with a free energy barrier of 14.4 kcal mol^{-1}. The rate limiting step of the reaction is the loss of the formed H_2 ligand which has a calculated barrier of 19.4 kcal mol^{-1}. Another example is found in Brookhart's catalyst [Ir(^{tBu}POCOP)H_2][84] **1-49** (^{tBu}POCOP = κ^3-P,C,P-1,3-

($OP^tBu_2)_2C_6H_3$) which is further discussed in **Section 1.1.2.5**. Reaction with this catalyst produces $[H_2BNH_2]_n$ oligomers (n ~ 20) from H_3B-NH_3 where the concerted B-H/N-H activation forms two new metal-hydride bonds.[85] This process was calculated to have a rate-limiting barrier of 24.3 kcal mol^{-1}. A rate-limiting barrier of 28.8 kcal mol^{-1} was calculated for the similar $[Ir(^{tBu}PCP)H_2]$ (PCP = κ^3-P,C,P-1,3-($(CH_2)P^tBu_2)_2C_6H_3C_6H_3$) catalyst **1-50**.[86] A different concerted process involving Ru catalyst, $[Ru(\kappa^4\text{-}N(CH_2CH_2PPh_2)_3)(H)_2]$ **1-51**, was proposed by Rossin, Peruzzini *et al.*[87] for the dehydrocoupling of H_3B-NH_3. The authors calculated using the M06(THF)/SDD(Ru,P),6-31g* level of theory that the N-H would protonate a metal-hydride to form H_2 which instantly dissociates. The B-H also transfers a hydride to the Ru centre to form a new Ru-H bond. This results in the formation of free H_2B=NH_2, H_2 and regeneration of the catalyst in the same step. The calculated free energy barrier for this process was calculated to be 21.6 kcal mol^{-1}. The same process was proposed for $[Co(\kappa^4\text{-}N(CH_2CH_2PPh_2)_3)(H)]$ **1-52**.[88]

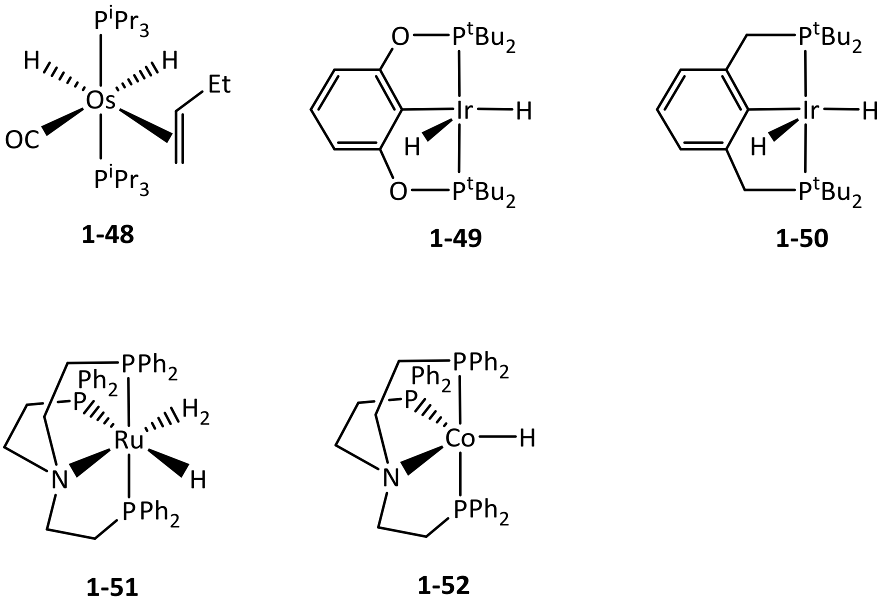

Figure 1-5: *Catalysts proposed to proceed via concerted activation mechanisms*

Schneider *et al.*[89] conducted a study using $[Ru(PNP)(H)PMe_3]$ **1-53** (PNP = $N(CH_2CH_2P^iPr_2)_2$) as a catalyst for amine-borane dehydrocoupling and found reaction with H_3B-NH_3 to produce polyamino-borane. In this study, $Ru(PNP^H)(H)PMe_3]$ **1-54** (PNP^H = $NH(CH_2CH_2P^iPr_2)_2$) (**Figure 1-6**) was observed as the resting state during catalysis. It was also found that complex **1-54** could be used as the starting catalyst. A later mechanistic study on catalysis with **1-54** (**Scheme 1-11**)[90] used DFT calculations at the B3LYP/6-31g+** level of theory on a PMe_2-truncated model. The proposed dehydrogenation occurs *via* a ligand-assisted concerted activation after an initiation process involving N-H activation. An outer-sphere H_3B-NH_3 unit protonates the metal-hydride to form an H_2 ligand and a {H_3B-NH_2} moiety which is stabilised by the proton on the pincer ligand **1-55**. The H_2 ligand then dissociates in the rate-limiting step to form **1-56** which proceeds through the concerted activation to yield free $H_2B{=}NH_2$ and regenerate **1-54**. Reaction with $Ru(PNP^{Me})(H)PMe_3]$ was found to be much slower which gives further evidence to the involvement of the ligand proton in the dehydrogenation process. The propagation of $H_2B{=}NH_2$ was also investigated and is discussed in **Section 1.1.2.5**.

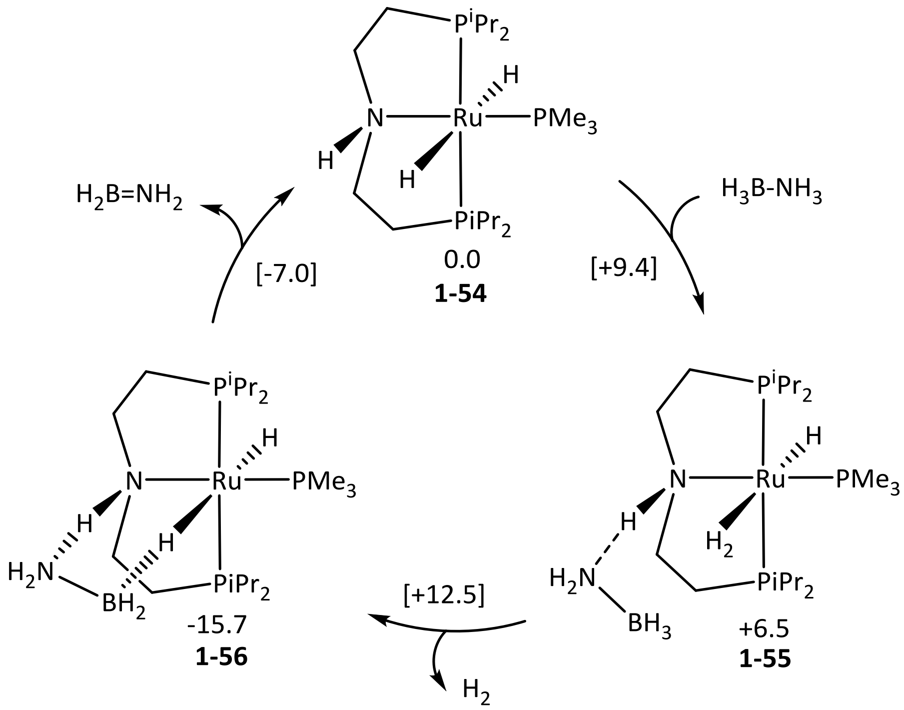

Scheme 1-11: *Proposed dehydrocoupling pathway for reaction of H_3B-NMe_2H with **1-53**. Free energies in kcal mol^{-1}. Adapted from reference No. 90.*

Schneider *et al.*[91] also studied $[Fe(PNP^H)(CO)(H)_2])$ catalyst **1-57** (**Figure 1-6**) and proposed the same ligand cooperativity mechanism for the dehydrocoupling of H_3B-NH_3. Other catalysts which are proposed to dehydrogenate amine-boranes through ligand-assisted concerted activation include a β-diketiminato complex **1-58** developed by Phillips *et al.*[92] and calculated by English *et al.*[93], Shvo's catalyst[94] **1-59** and $Fe(PNP)(BH_3)(CO)(H)]$ **1-60** studied by Beweries *et al.*[95] Paul *et al.*[96] also propose a concerted mechanism using [Ru(*fac*-κ^3-N,O,N-$(NC_5H_4)B(OH)(Me)(NC_5H_4)(NCMe)_3$] **1-61** developed by Williams *et al.*[97] where the N-H protonates the ligand as the $\{BH_3\}$ moiety transfers a hydride to the Ru centre.

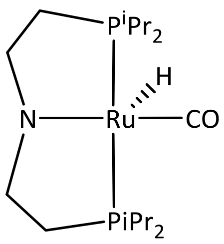

1-53

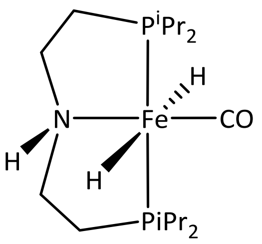

1-57

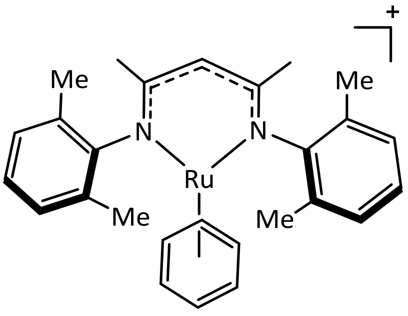

1-58

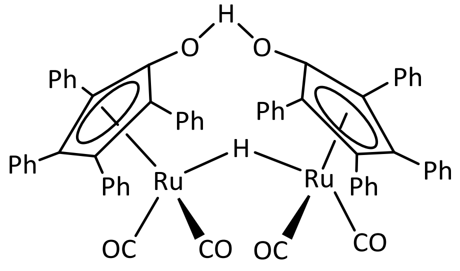

1-59

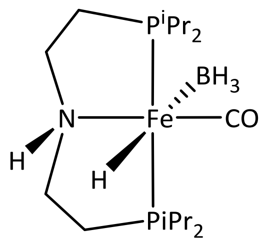

1-60

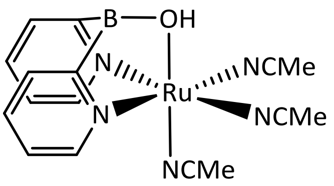

1-61

Figure 1-6: *Catalysts proposed to proceed via ligand assisted, concerted activation mechanisms*

1.1.2.4 – Dehydrogenation Mechanisms Involving Solvent and Boronium Cations

There are investigations into amine-borane dehydrocoupling that suggest that the reaction solvent and the *in situ* formation of boronium cations play an important role in the dehydrogenation of amine-boranes. For example, Conejero, Lopez-Serrano *et al.*[98] reported that platinum catalyst [Pt(I^{t}Bu')(I^{t}Bu)][BAr$^F_4$] (I^{t}Bu = 1,3-di-*tert*-butylimidazol-2-ylidene, I^{t}Bu' = cyclometalated I^{t}Bu) **1-62** could dehydrogenate H_3B-NMe_2H to form $[H_2BNMe_2]_2$ (**Scheme 1-12**). Experimental mechanistic studies identified the formation of an amine-borane σ-complex [Pt(I^{t}Bu')(I^{t}Bu)(η^1-H_3B-NMe_2H)][BAr$^F_4$] **1-63** (through the use of ^{1}H NMR spectroscopy) upon addition of H_3B-NMe_2H to catalyst **1-62**. Complex **1-63** was found to be unstable and would form hydride complex [Pt(I^{t}Bu')(I^{t}Bu)(H)] **1-64** within minutes at temperatures above 273 K. The formation of a second species was observed during this process which was later identified as boronium cation $[BH_2(NMe_2H)_2]^+$ through NMR spectroscopy. At the end of the reaction the boronium cation is again observed along with dimer $[H_2BNMe_2]_2$ and [Pt(I^{t}Bu)$_2$(H)][BAr$^F_4$] which is the hydrogenated product of **1-64**. DFT calculations where H_3B-NMe_2H was replaced with H_3B-NH_3 were performed with the M06(THF)/SDD(Pt),6-31g** level of theory. A concerted activation mechanism was calculated to proceed with a very large free energy barrier of 42.5 kcal mol^{-1}. The lowest energy reaction pathway calculated involved a Lewis base, such as NH_3, attacking the metal-bound H_3B-NH_3 to form boronium cation, $[(H_3N)_2BH_2]^+$ and complex **1-64** with a free energy barrier of 24.3 kcal mol^{-1}. A protonation of the Pt-H bond by the boronium cation then occurs with a barrier of 11.0 kcal mol^{-1} to afford complex **1-65** with free amino-borane (which is suggested to dimerise off-metal) and Lewis base produced. The newly formed dihydrogen ligand is then substituted with another molecule of H_3B-NH_3 to complete the cycle in what is the rate limiting step. Experimental studies found that directly reacting the boronium cation with **1-64** resulted in very slow dehydrogenation, however, directly reacting **1-64** with THF (the reaction solvent) adduct [THF-BH_2NMe_2H]$^+$ saw rapid dehydrogenation being observed at 273 K. This is because the N-H proton is more acidic in [THF-BH_2NMe_2H]$^+$ than in [$BH_2(NMe_2H)_2$]$^+$ and THF a better leaving group than NMe_2H which favours the hydride protonation step. It was suggested that the rapid reaction of [THF-BH_2NMe_2H]$^+$ with **1-64** explained the absence of NMR signals relating to the adduct.

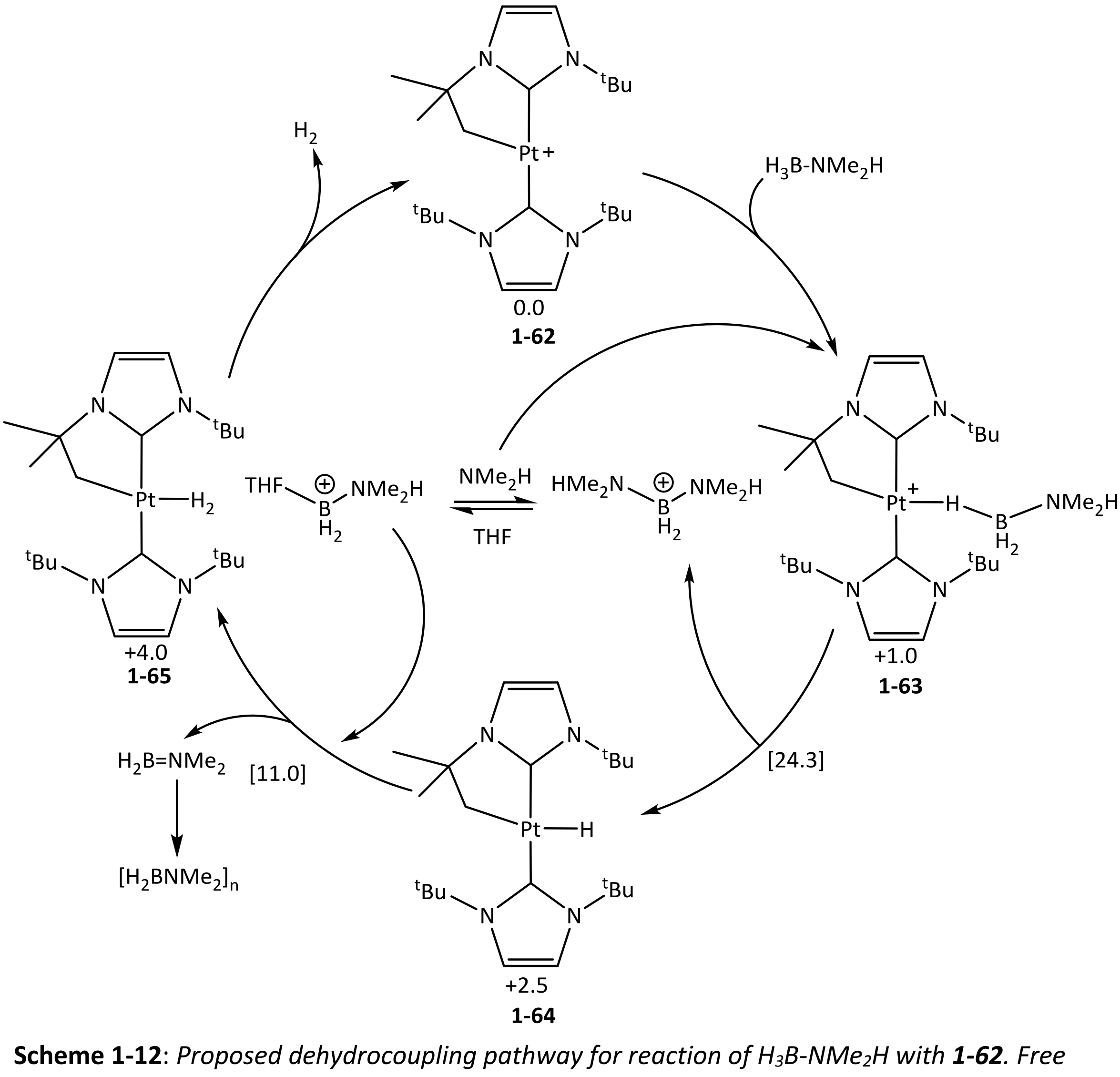

Scheme 1-12: *Proposed dehydrocoupling pathway for reaction of H_3B-NMe_2H with **1-62**. Free energies in kcal mol^{-1}. Adapted from reference No. 98.*

Freixa *et al.*[99] also propose dehydrocoupling of H_3B-NMe_2H through the formation of boronium cation [THF-BH_2NH_3]$^+$ which would then protonate the metal centre using [Ru(η^6-*p*-Cym)(bipy)Cl][Cl] (*p*-Cym = $CH_3C_6H_4CH(CH_3)_2$, bipy = $(NC_5H_4)_2$) **1-66** (**Figure 1-7**). Jagirdar *et al.*[100] also noted a hydride transfer mechanism when reacting H_3B-NH_3 with [RuCl(dppe)$_2$][OTf] (dppe

= $Ph_2PCH_2CH_2PPh_2$, OTf = $CF_3SO_3^-$) **1-67**. In this case, [$ClBH_2NH_3$] and [RuH(dppe)$_2$][OTf] are formed.

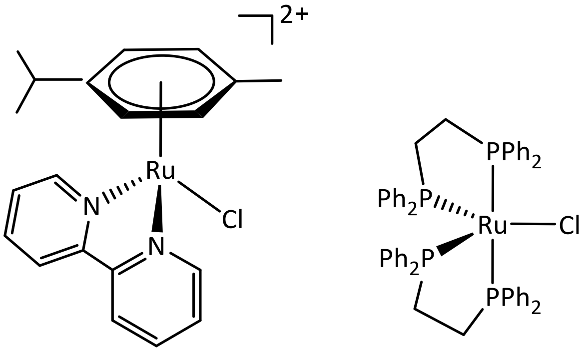

1-66 **1-67**

Figure 1-7: *Catalysts proposed to for boronium cations when reacting with amine-boranes.*

1.1.2.5 – Propagation Mechanisms

There are two basic types of propagation pathway to form polyamino-boranes: chain growth and step-wise polymerisation.[101] Chain growth polymerisation can proceed *via* two mechanisms: head-to-tail or co-ordination/insertion. Head-to-tail chain growth propagation is where a monomer binds to the metal centre which acts as a support as other monomer units attach to the growing polymer chain away from the metal centre. Co-ordination/insertion chain-growth involves each monomer binding to the metal centre before being inserted into the growing polymer chain at the metal centre. Step-wise propagation involves monomers reacting to form dimers, which then react to form tetramers which procced to form octamers towards forming long-chain polymers.

Mechanistic studies have also been conducted in order to gain information on the propagation mechanism for the formation of polyamino-boranes. For example, Gordon, Baker *et al.*[78] developed an iron catalyst [Fe($PCy_2CH_2CH_2PCy_2$)($NPhCH_2CH_2NPh$)], **1-38**, which was proposed to dehydrogenate H_3B-NH_3 *via* a N-H activation, ligand co-operativity mechanism as mentioned in **Section 1.1.2.2.** Selective formation of [H_2BNH_2]$_n$ from the dehydropolymerisation of H_3B-NH_3 was achieved using a 5 mol% loading of the catalyst with a TOF of ~80 h^{-1}. Iron nanoparticles in the form of a black precipitate were formed during the reaction which suggested the catalyst was decomposing through the full de-coordination of one of the chelating phosphines. Propagation was thought to be *via* a chain-growth process and two potential pathways were speculated (**Scheme 1-13(A)**). The initial dissociation of a phosphine arm enables coordination of H_3B-NH_3, in **1-68**. One arm of the amido ligand is then protonated by the H_3B-NH_3 to form **1-69** which contains an amido-borate complex normally only observed for early transition-metal amine-borane complexes[60] although the Ni(NHC)$_2$ systems developed by Baker *et al.*[70] are another exception. This results in dissociation of the ligand which allows a second molecule of H_3B-NH_3 to bind to the metal to form **1-70**. The propagation mechanism would then involve B-N coupling between the bound amine-borane and bound amido-borate which would create a vacant site for another H_3B-NH_3 unit to co-ordinate to the metal as in intermediate **1-71**. A series of insertion and co-ordination steps would then propagate the polymer chain. Alternatively, a H_2B=NH_2 moiety could bind to the Fe complex to form **1-72** as seen in **Scheme 1-13(B)**. Units of H_3B-NH_3 would then attach to the terminal {NH_2} moiety and release H_2 in order to grow the polymer chain in a head-to-tail propagation.

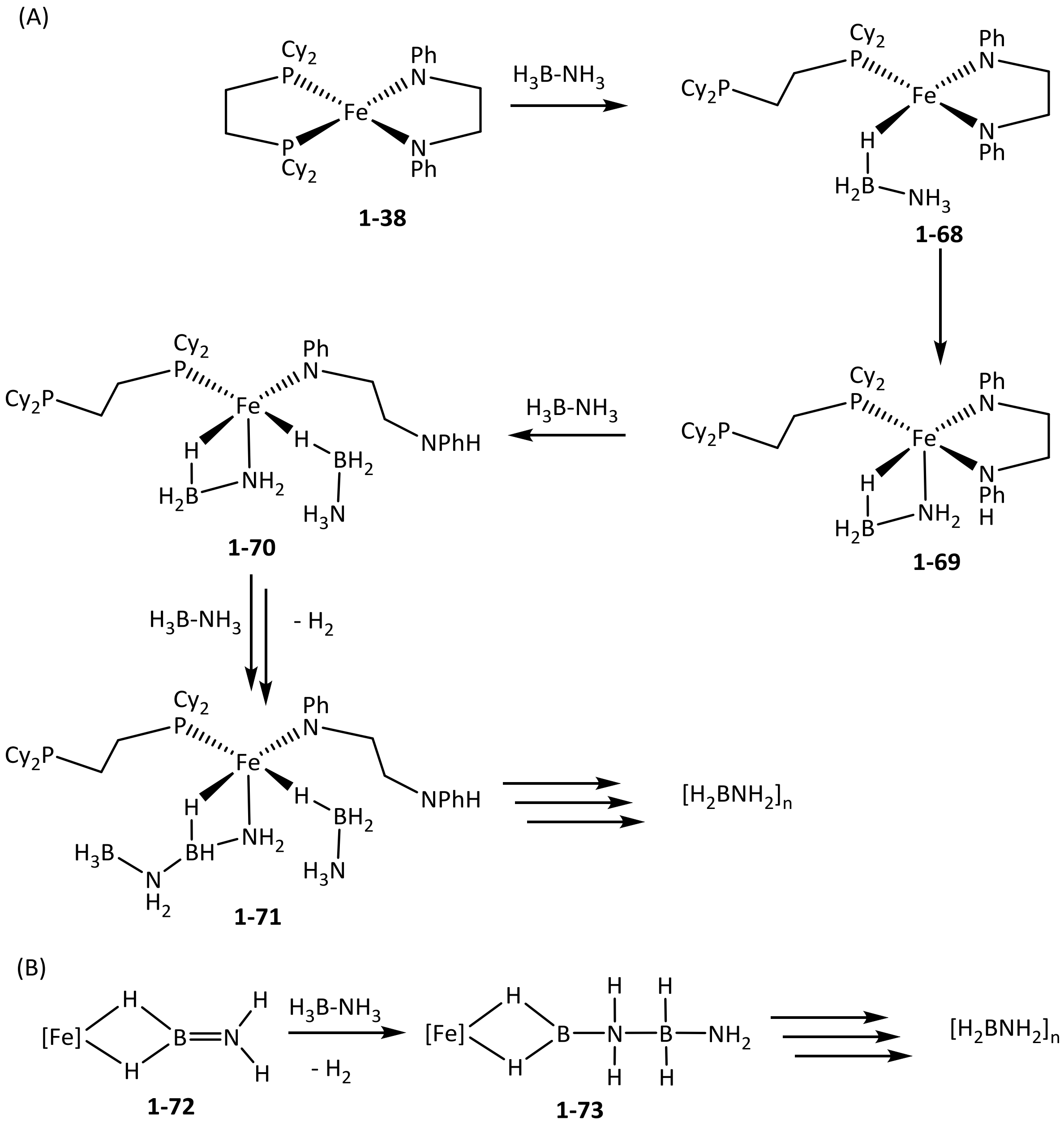

Scheme 1-13*: (A) Proposed initiation and co-ordination/insertion propagation mechanism for reaction with* ***1-38*** *(B) Proposed head-to-tail propagation mechanism. Adapted from reference No. 78.*

Paul *et al.*[102] proposed a propagation mechanism (shown in **Scheme 1-14**) when conducting a computational study on the reaction of H_3B-NH_3 with Brookhart's [Ir(^{tBu}POCOP)H_2] catalyst **1-49** (**Figure 1-5**).[84] Stationary points were optimised using the B3LYP//anl2dz(Ir),6-31g** followed by single point M06-L(THF)/lanl2dz(Ir),6-31g** calculations. Paul and Musgrave had previously conducted a study on the dehydrogenation of H_3B-NH_3 with **1-49** and concluded that dehydrogenation is achieved *via* a concerted activation mechanism.[85] The chain initiation is proposed to involve a free $H_2B{=}NH_2$ molecule binding to the catalyst to form a [IrH(POCOP)(η^1-

H_3B-NH_2)] complex **1-76**. The chain propagation then occurs *via* the lone pair on the terminal {NH_2} acting as a nucleophile at the electron-deficient {BH_2} of subsequent amino-borane units to grow the polymer chain, forming intermediates like **1-77**. This process was calculated to occur with a free energy barrier of 7.1 kcal mol^{-1} up to n = 5. The chain termination event is suggested to occur *via* a proton transfer from the NH_2 group adjacent to the metal-bound BH_2 moiety to the terminal NH_2 to form intermediate **1-78** which releases $H_2B{=}NH-(H_2B-NH_2)_n-BH_2-NH_3$ **1-79**. This molecule is then hydrogenated by a free amine-borane to afford the polyamino-borane with a free-energy barrier of 13.7 kcal mol^{-1} which is larger than the propagation barrier of 7.1 kcal mol^{-1} and is therefore the rate determining step of the proposed process. This computationally predicted pathway agrees with the experimental findings of Manners *et al.*[103] who observed chain-growth propagation behaviour with high molecular weight polymer even at low conversion.

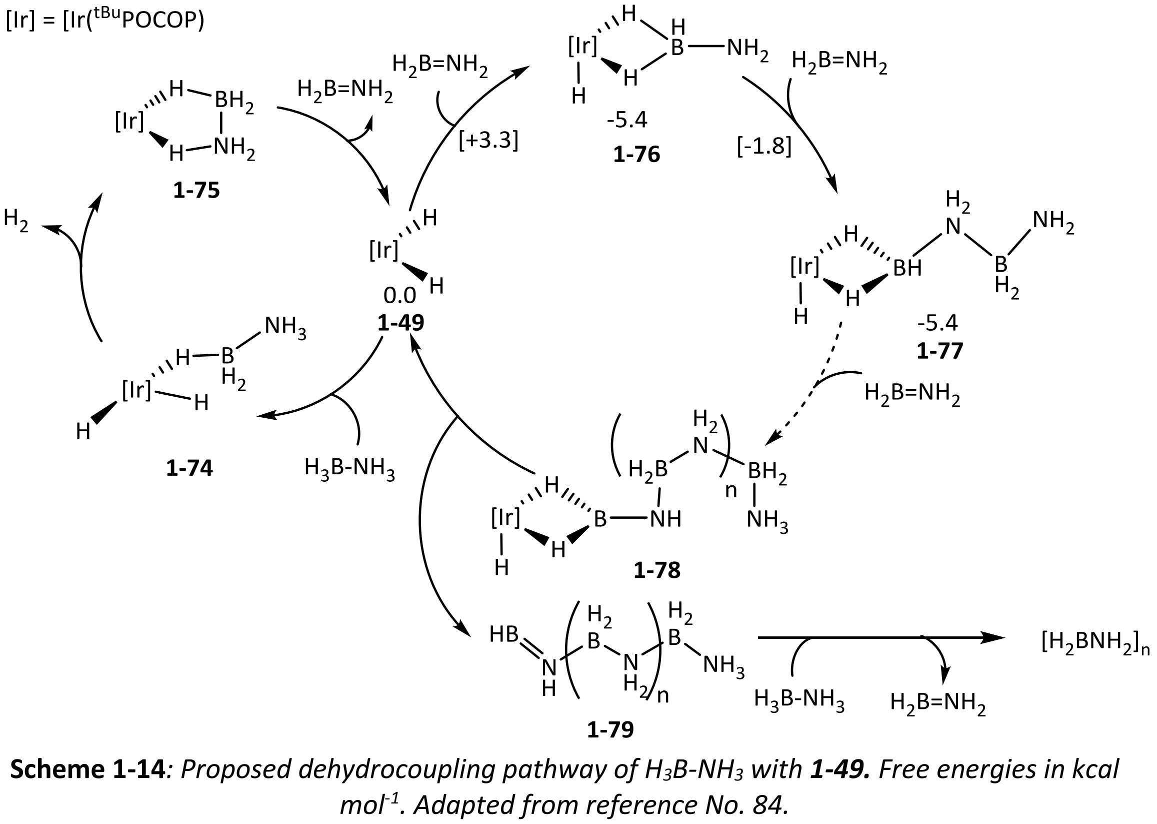

Scheme 1-14: *Proposed dehydrocoupling pathway of H_3B-NH_3 with* ***1-49.*** *Free energies in kcal mol^{-1}. Adapted from reference No. 84.*

During their study of amine-borane dehydrocoupling using catalyst **1-3**, Weller and Macgregor[55] proposed a propagation pathway (**Scheme 1-15**) as well as the dehydrogenation pathway discussed in **Scheme 1-5**. The same BP86-(D3)(C_6H_5F)/SDDALL(Rh,P),6-31g** level of theory was used on model system $[Ir(PMe_3)_2(H)_2]^+$. After the initial dehydrogenation to form **1-5**, which proceeds with a barrier of 26.7 kcal mol^{-1}, a second dehydrogenation of the other H_3B-NH_3 unit occurs with a lower energy barrier of 24.2 kcal mol^{-1}. This forms bis-amino-borane complex **1-80** where one $H_2B{=}NH_2$ is bound to the metal in an η^2-fashion and the other is outer-sphere. The {NH_2} moiety of the bound $H_2B{=}NH_2$ is able to act as a nucleophile towards the free $H_2B{=}NH_2$

and go through a B-N coupling event with a barrier of 17.9 kcal mol^{-1} which also involves a hydride transfer from the Ir centre to the terminal nitrogen of the growing oligomer chain. This forms intermediate **1-81**. Addition of H_2 produces intermediate **1-82** and facile B-H reductive coupling then results in the formation of intermediate **1-83** where the linear dimer is bound to the metal in an η^2-fashion. Addition of another H_3B-NH_3 molecule reforms active catalyst **1-4**. Subsequent oligomerisations were also shown to be possible with H_3B-NH_3. Propagation with H_3B-$NMeH_2$ and H_3B-NMe_2H saw B-N coupling barriers of 19.9 and 26.5 kcal mol^{-1} respectively, which fits with H_3B-NMe_2H not forming polymer.

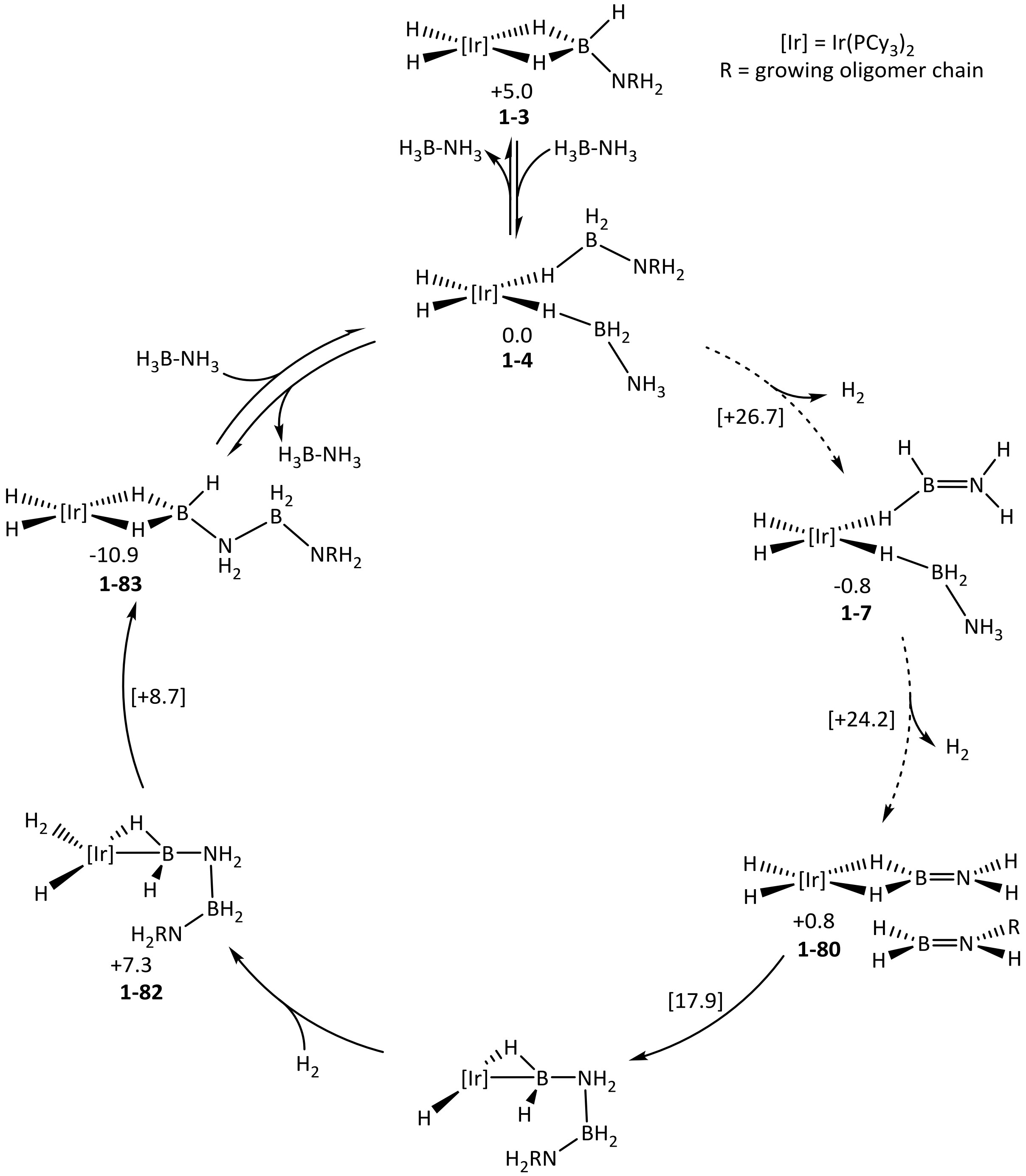

Scheme 1-15*: Proposed dehydrocoupling pathway of H_3B-NH_3 with* ***1-3****. Free energies in kcal mol^{-1}. Adapted from reference No.55.*

Schneider *et al.*[90] also conducted a mechanistic study into the propagation of H_2B=NH_2 with catalyst **1-54** (**Scheme 1-16**) after a ligand-assisted concerted dehydrogenation mechanism (**Scheme 1-11**). Here, a free H_2B=NH_2 unit approaches intermediate **1-55** and B-N couples with the {H_3B-NH_2} moiety through transition state **1-84**. This process occurs with a free energy barrier of 12.8 kcal mol^{-1} and produces linear dimer H_3B-NH_2BH_2-NH_3. Experimental amino-borane trapping experiments with cyclohexene saw no H_2N=BCy_2 adduct initially, however, adduct formation was observed after a few hours. The authors argue that due to the barriers of dehydrogenation (12.5 kcal mol^{-1}) and propagation (12.8 kcal mol^{-1}) being very similar, there is a small steady state concentration of $H_2B{=}NH_2$ present at any one time which is why no $H_2N{=}BCy_2$ adduct is initially observed. Formation of the adduct is seen after a few hours due to the degradation of the polyamino-borane with the B-N coupling being reversible which has been previously reported by Manners *et al.*[18]

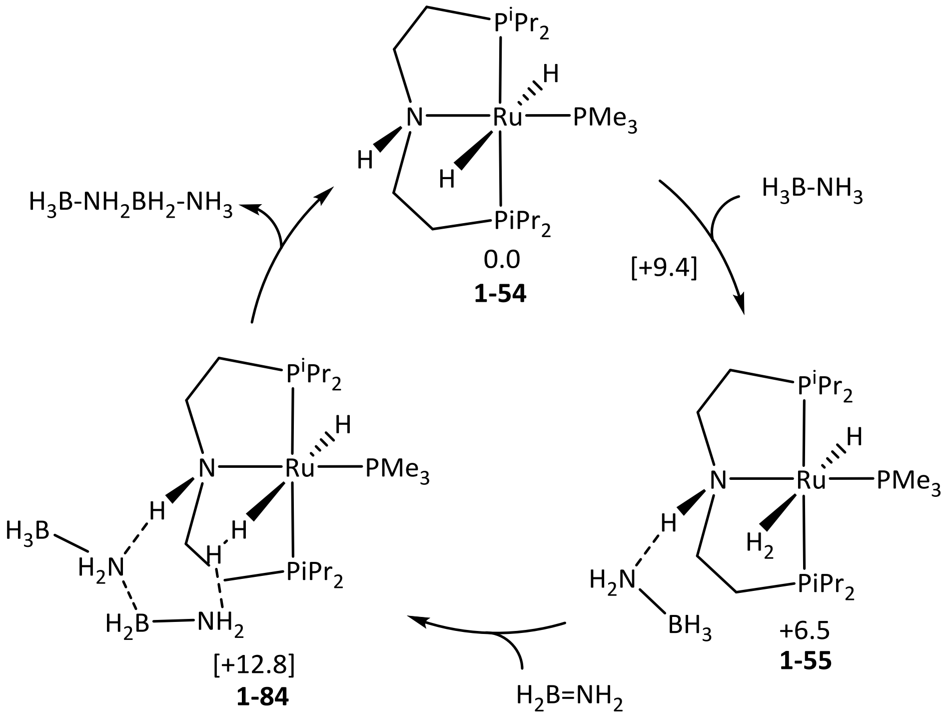

Scheme 1-16: *Proposed dehydrocoupling pathway of $H_3B\text{-}NH_3$ with **1-54**. Free energies in kcal mol^{-1}. Adapted from reference No. 90.*

There is also a possibility that free amino-borane units produced by the catalysed dehydrogenation of amine-borane could propagate *via* an off-metal polymerisation mechanism. It has already been stated that amino-boranes are unstable at room temperature as they react with themselves. This means that off-metal coupling processes should have low activation barriers. For example, Paul *et al.*[104] used the M05-2X(toluene)/6-311g++** level of theory, to calculate that $H_2B{=}NH_2$ would form borazine $[HBNH]_3$ with a free energy barrier of 9.9 kcal mol^{-1}. Therefore, any on-metal propagation process needs to have a just as low, if not lower, barrier to propagation if on-metal polymerisation is to become favoured over off-metal processes.

1.1.3 – Dehydrogenation and Dehydrocoupling of Amine-Boranes with Rhodium Complexes

The work in this thesis focusses on amine-borane dehydrocoupling using Rh catalysts of which there are many examples in the literature. Many studies use $H_3B\text{-}NMe_2H$ which only forms cyclic dimer $[H_2BNMe_2]_2$. This is due to the presence of one, easily-defined product being beneficial to experimental study. These studies are still included in this section, despite not involving any propagation process, due to the information they provide on dehydrogenation mechanisms.

Weller *et al.*[105] investigated the dehydrogenation of H_3B-NMe_2H with $[Rh(PCy_3)_2(H)_2Cl]$, **1-85**. Experiments found that 2 mol % of the catalyst will dehydrogenate H_3B-NMe_2H with a TOF of 28 h^{-1} to form $[H_2BNMe_2]_2$ (see **Scheme 1-17**). Mechanistic investigations led to the conclusion that after the initial coordination of H_3B-NMe_2H to the catalyst, B-H activation is followed by N-H activation or *vice versa* to form $H_2B{=}NMe_2$ which rapidly dimerises off-metal. The rate determining step for the reaction is thought to be the NH-activation step due to a large primary kinetic isotope effect.

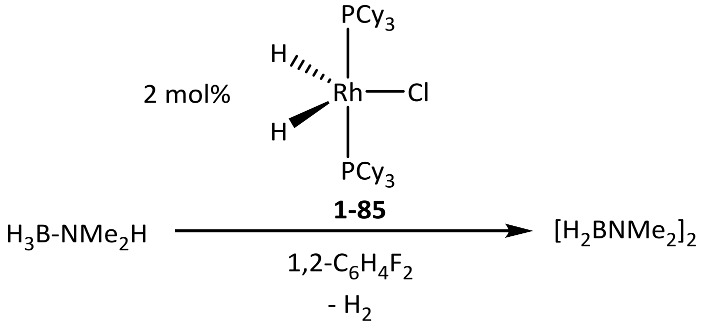

Scheme 1-17: *Dehydrocoupling of H_3B-NMe_2H with **1-85**. Adapted from reference No. 105.*

Weller, Hall *et al.*[106] studied the $\{Rh(P^iBu_3)_2\}^+$ fragment **1-86** for the dehydrogenation of H_3B-NMe_2H. It was observed that a 5 mol% loading of the catalyst produced $[H_2BNMe_2]_2$ from H_3B-NMe_2H with a TOF of 34 h^{-1} (see **Scheme 1-18**). A proposed pathway was calculated using the TPSS(C_6H_5Cl)/Def2-TZVP(Rh)/6-31g** level of theory. The pathway begins through coordination of H_3B-NMe_2H to form $[Rh(P^iBu_3)_2(\eta^2\text{-}H_3B\text{-}NMe_2H)][BAr^F_4]$ **1-87**. This was followed by either B-H activation and N-H transfer, or N-H activation and B-H transfer, to yield $[Rh(P^iBu_3)_2(H)_2(\eta^2\text{-}H_2B{=}NMe_2)][BAr^F_4]$ **1-88** with very similar barriers, suggesting the pathways are competitive. No matter the pathway, N-H activation was calculated to be the rate-limiting step with free energy barriers of 19.7 kcal mol^{-1} for the B-H activation first pathway and 19.9 kcal mol^{-1} for the N-H activation first pathway. This is followed by either H_2 loss or dissociation of $H_2B{=}NMe_2$ or dissociation of $H_2B{=}NMe_2$ followed by H_2 loss. The linear dimer H_3B-NMe_2BH_2-NMe_2H was observed experimentally and the complex $[Rh(P^iBu_3)_2(\eta^2\text{-}H_3B\text{-}NMe_2BH_2\text{-}NMe_2H)][BAr^F_4]$ was found to be stable in 1,2-$C_6H_4F_2$. However, when excess H_3B-NMe_2BH_2-NMe_2H was added, $[H_2BNMe_2]_2$ and $H_2B{=}NMe_2$ were formed. This suggests that B-N cleavage is occurring rather than on-metal dehydrocyclisation.

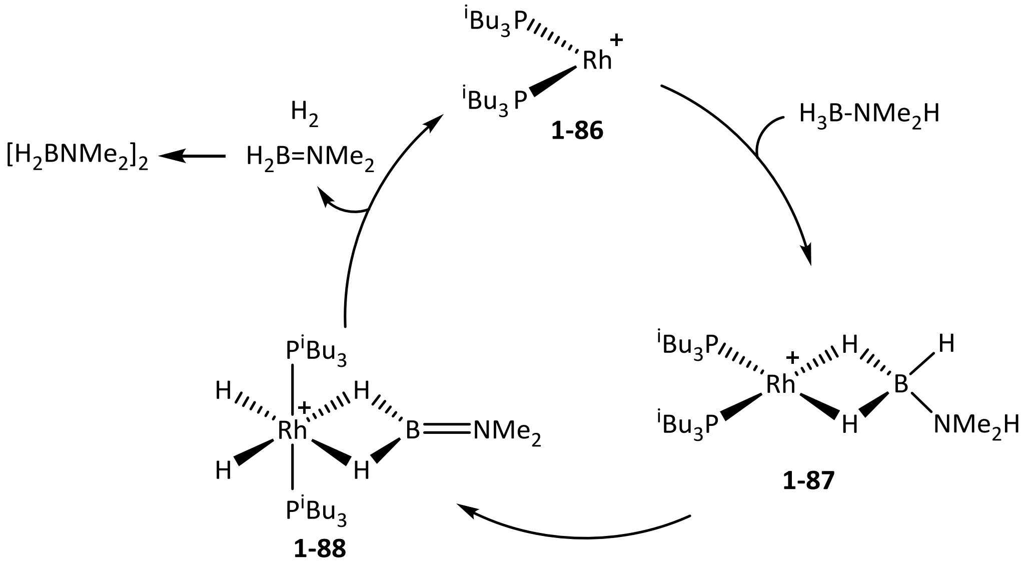

Scheme 1-18: *Proposed dehydrocoupling pathway for H_3B-NMe_2H with **1-86**. Adapted from reference No. 106.*

A further mechanistic study on the dehydrogenation of H_3B-NMe_2H to form $[H_2BNMe_2]_2$ using the $[Rh(PCy_3)_2L_n]^+$ **1-89** fragment was carried out by Weller, Lloyd-Jones *et al.*[107] Both free amino-borane H_2B=NMe_2 and the linear dimer H_3B-NMe_2BH_2-NMe_2H were seen as intermediates during reaction with 5 mol% of the catalyst. It was found that adding 2 equivalents of H_3B-NMe_2H to the reaction mixture would form $[Rh(PCy_3)_2(\eta^2$-H_3B-$NMe_2H)][BAr^F{}_4]$, **1-90** (**Scheme 19(A)**), where the metal is in the oxidation state Rh^I. This complex would proceed to form a Rh^{III} species $[Rh(PCy_3)_2(H)_2(\eta^2$-H_3B-$NMe_2H)][BAr^F{}_4]$ **1-91**, as well as free H_2B=NMe_2. Loss of H_2 does not occur easily which indicates that the active catalyst will remain at a Rh^{III} oxidation state after the initial dehydrocoupling. However, addition of the cyclic dimer product $[H_2BNMe_2]_2$ to Rh^{III} species $[Rh(PCy_3)_2(H)_2(\eta^2$-$H_2)_2][BAr^F{}_4]$, **1-92**, sees the immediate formation of Rh^I complex $[Rh(PCy_3)_2(\eta^2$-$(H_2BNMe_2)_2][BAr^F{}_4]$, **1-93**. This suggests that $[H_2BNMe_2]_2$ can accelerate the reductive elimination of H_2. Under catalytic conditions, it was found that $[H_2BNMe_2]_2$ has an autocatalytic role by acting as a modifier to produce a Rh^I catalytically active species alongside the Rh^{III} catalyst. Therefore, the dehydrocoupling reaction was shown to exist in both a constant, slower Rh^{III}/Rh^{III} cycle and a faster Rh^I/Rh^{III} cycle as seen in **Scheme 19(B)**.

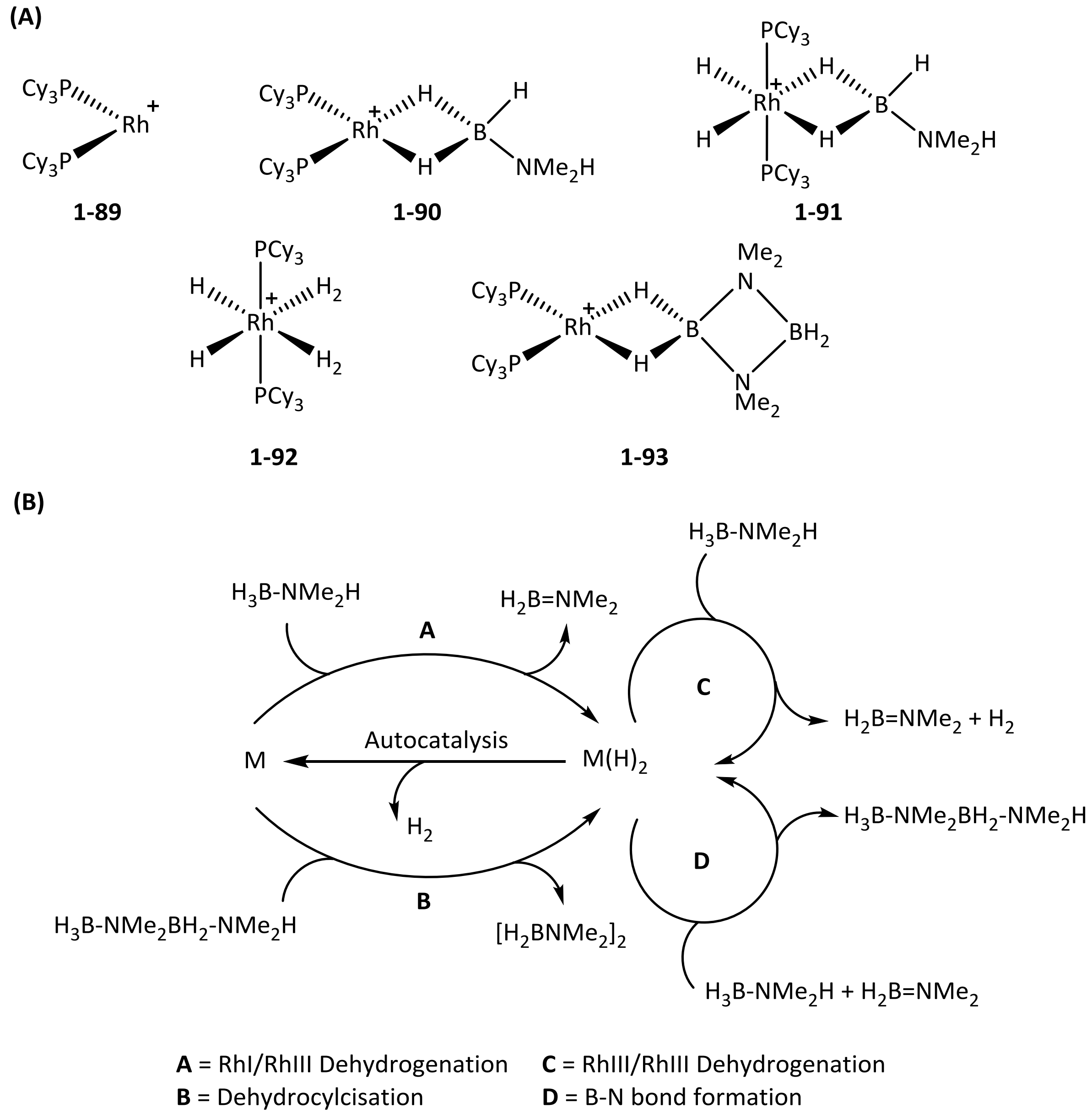

Scheme 1-19*: **(A)** Key interemdiates in the dehydrogenation of H_3B-NMe_2H with **1-89**. **(B)** General dehydrogenation scheme proposed by Weller, Lloyd-Jones et al. Adapted from reference No. 107.*

Investigations by Weller, Manners *et al.*[108] found that $[Rh(Ph_2P(CH_2)_xPPh_2)(\eta^6\text{-}C_6H_5F)][BAr^f_4]$ (x = 3 – 5), **1-94**, could dehydrocouple H_3B-$NMeH_2$ to form $[H_2BNMeH]_n$ (when x = 4, M_n = 144000 g mol^{-1}, PDI = 1.3) as seen in **Scheme 1-20(A)**. Replacing H_3B-$NMeH_2$ with H_3B-NMe_2H formed $[H_2BNMe_2]_2$ with a TOF of 1250 h^{-1} when x = 3. It was discovered that the bite angle correlated with the binding strength of the related σ-complexes $[Rh(Ph_2P(CH_2)_xPPh_2)(\eta^2\text{-}H_3B\text{-}NMe_3)][BAr^F_4]$ (x = 3 – 5) with the smallest bite angle (x = 3) having the weakest σ-bound H_3B-NMe_3 and the fastest dehydrocoupling of H_3B-NMe_2H. An initial induction period is thought to be due to the formation of an inactive amine-borane containing rhodium dimer, **1-95** (**Scheme 1-20(B)**) through dimerization. Sicilia *et al.*[109] conducted a computational study on catalyst **1-94** (n=3) and H_3B-NMe_2H at the B3PW91(C_9H_7N)//SDD/6-311g* level of theory. It was found that a concerted activation pathway was favoured for the dehydrogenation process, operating with a free energy barrier of 17.2 kcal mol^{-1}. The authors also attempted to account for the formation of dimer **1-95** but were unsuccessful.

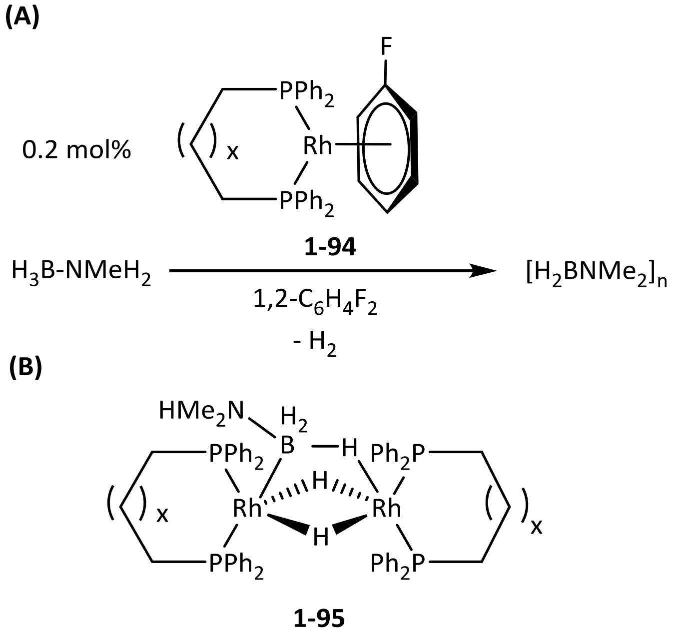

Scheme 1-20: ***(A)*** *Dehydrocoupling of H_3B-$NMeH_2$ with* ***1-94*** ***(B)*** *Isolated dimer during reaction with catalyst* ***1-94****. Adapted from reference No. 108.*

Furthermore, Weller, Manners and Lloyd-Jones *et al.*[110] have previously developed a dehydrogenation of H_3B-NMe_2H and H_3B-$NMeH_2$ using [Rh(κ^2-P,P-Xantphos-Ph)((^{t}BuCH_2CH_2)H_2B-NMe_3)][BAr^F], **1-96**, as a catalyst (see **Scheme 1-21**). Reaction with H_3B-NMe_2H in a system open to argon with **1-96** (0.2 mol %) in 1,2-$C_6H_4F_2$ rapidly produced [H_2B-NMe_2]$_2$ after an induction period of five minutes. Kinetic studies suggested that the reaction was operating under saturation kinetics in terms of both H_3B-NMe_2H and H_3B-$NMeH_2$ concentration. Furthermore, for reaction with H_3B-$NMeH_2$, molecular weight *versus* conversion experiments indicated propagation operated *via* a chain growth mechanism. In THF, the reaction proceeded at a lower rate but produced [H_2BNMeH]$_n$ with a higher molecular weight (M_n = 52200 gmol^{-1}, PDI = 1.4). Moreover, a closed system was found to produce [H_2BNMeH]$_n$ with lower molecular weight (M_n = 2800 gmol^{-1}, PDI = 1.8). The results of the kinetic studies led to the authors proposing a catalytic cycle for both the dehydrogenation of H_3B-NMe_2H and the dehydropolymerisation of H_3B-$NMeH_2$. The proposed mechanism begins with catalyst **1-96** undergoing a substitution with H_3B-$NMeH_2$ with release of (^{t}BuCH_2CH_2)H_2B-NMe_3. This is followed by addition of a second molecule of H_3B-$NMeH_2$ and the formation of H_2B=$NMeH$ in a dehydrogenation step to form intermediate **1-97**. The initiation step then occurs, which sees the slow release of H_2 and a rate-limiting N-H activation step which was supported by KIE experiments. This forms the active catalytic species **1-98**, which has yet to be isolated but is proposed to involve a Rh-N bond and could potentially involve an amido-borate species. The vacant site at **1-98** allows for the binding of another $H_3B\text{-}NMeH_2$ unit. Once bound, a co-ordination/insertion chain growth propagation mechanism would start to form the polymer chain. Chain termination is proposed to occur *via* the binding of H_2 to form **1-100** followed by heterolytic H_2 cleavage to reform **1-97** and release the $[H_2BNMeH]_n$ polymer. The formation of **1-100** is suggested to be competitive between H_2 and THF as using THF as solvent is known to slow the catalysis and lengthen the polymer chains.

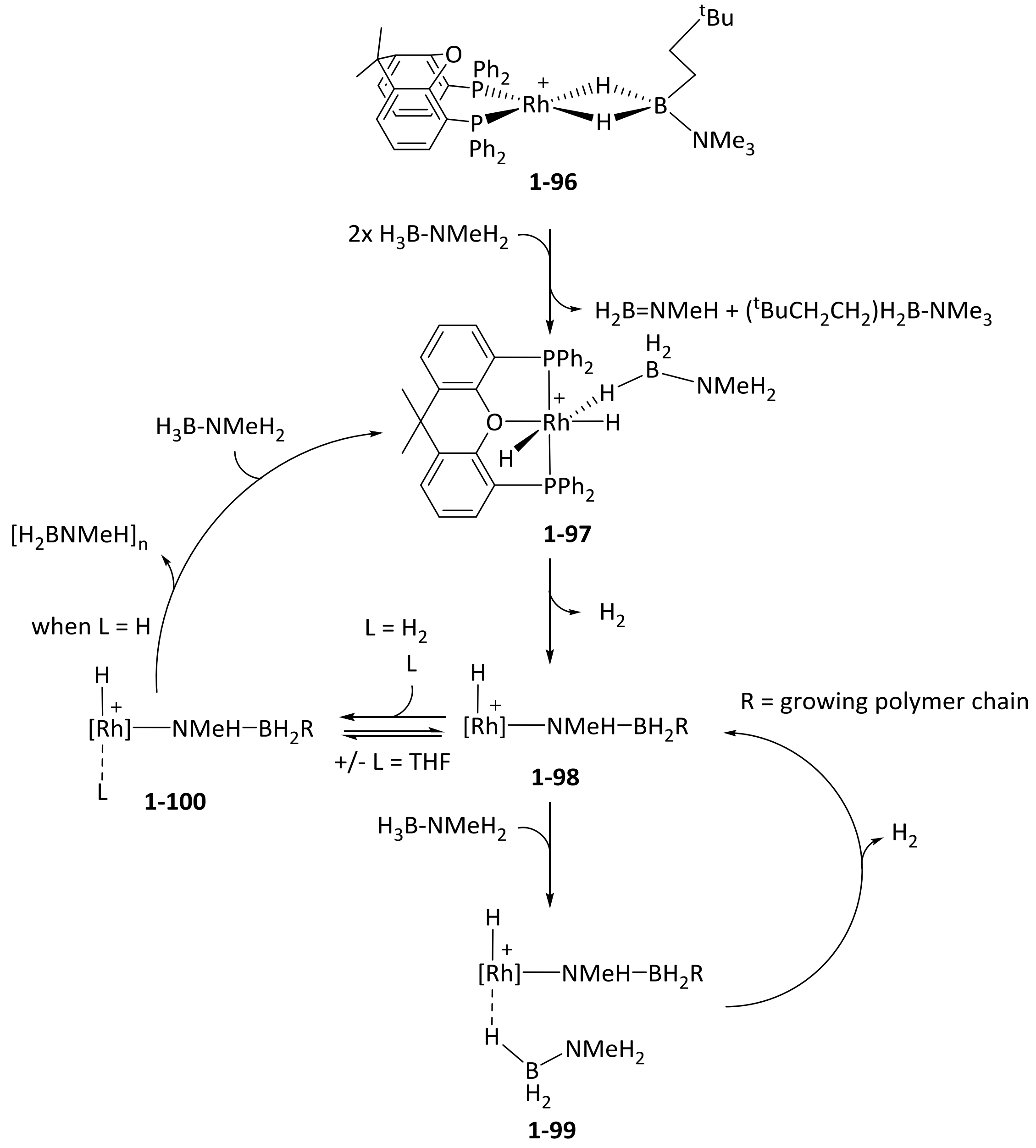

Scheme 1-21: *Proposed dehydrocoupling pathway for $H_3B\text{-}NMe_2H$ with **1-96**. Adapted from reference No. 110.*

The Weller group continued their study on the dehydrocoupling of amine-boranes with Rh-Xantphos catalysts by investigating the effects of alkyl-Xantphos ligands which has also been investigated by Esteruelas *et al.*[111] The computational work on this study, conducted in collaboration with the Weller group, is discussed in **Chapter 5** of this thesis.

1.2 – Background into the Dehydrocoupling of Phosphine-Boranes

Phosphine-boranes, R_3B-PR_3, are also isoelectronic with olefins and can react to form polyphosphino-boranes **1-101** (**Figure 1-8**). The formation of the polymer is less studied than the formation of polyamino-boranes but has similarities in that phosphino-borane species, $R_2B{=}PR_2$, are also too reactive to be used as a starting material and therefore have to be formed *in situ* through dehydrogenation processes from phosphine-boranes. The polyphosphino-borane materials produced from the dehydrocoupling process have shown potential as electron beam resists and precursors to boron-phosphide which has a semi-conducting properties.[10, 112, 113]

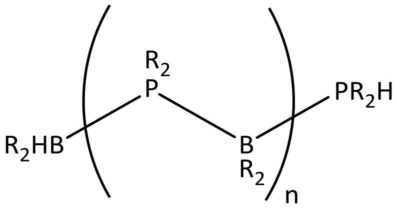

1-101

Figure 1-8: *General structure of polyphosphino-borane*

The first reported dehydrocoupling of phosphine-boranes was published in the 1950s by Burg and Wagner[114] where reaction with H_3B-PMe_2H was found to form cyclic trimers and tetramers in melt conditions. Formation of polyphosphino-boranes at higher temperatures was later reported by Burg.[115] The dehydrocoupling of phosphine-boranes can be catalysed using Lewis acids[116, 117] as well as transition-metal complexes.[64, 118-120] However, the melt conditions required for efficient formation of polyphosphino-boranes makes any experimental mechanistic study difficult as isolating key intermediates and retrieving kinetic data is challenging in high temperature conditions. Therefore, there are only a few examples of mechanistic studies to be found in the literature.

The first example of transition-metal catalysed phosphine-borane dehydrocoupling was conducted by Manners *et al.*[121] using $[Rh(1,5\text{-cod})(\mu\text{-Cl})]_2$ and $[Rh(1,5\text{-cod})_2][O_3SCF_3]$ as precatalysts (**Scheme 1-22**). Secondary phosphine-boranes such as H_3B-PPh_2H formed the linear dimer, H_3B-PPh_2BH_2-PPh_2H, in melt conditions at 363 K and cyclic oligomers at 393 K. Primary phosphine-boranes such as H_3B-$PPhH_2$ were found to form polyphosphino-boranes. Higher molecular weight polymer was formed if the reaction was performed in melt conditions compared to refluxing in toluene. A further investigation explored whether the catalysis was either heterogeneous or homogeneous in nature.[122] No evidence of the formation of a black material (which would indicate nanoparticle formation) was observed during a reaction in toluene which suggests homogeneous catalysis. Furthermore, no induction period and no decrease in catalytic activity upon poisoning the reaction with mercury was observed.

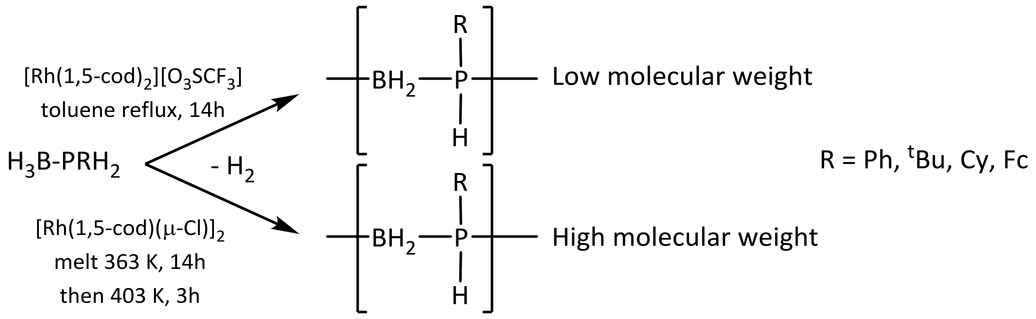

Scheme 1-22: *The dehydrocoupling of H_3B-PRH_2 published by Manners et al. Adapted from reference No. 120.*

The range of substituents tolerated by this catalytic system is broad, for example, polymer can be formed from the reaction of ferrocenylphosphine-boranes.[119] The Manners group also tested a range of organometallic catalysts for the dehydrocoupling of phosphine-boranes and found that $[Rh(1,5\text{-cod})(\mu\text{-Cl})]_2$ was one of the best performing catalysts investigated.[123]

Manners *et al.* also investigated the formation of polyphosphino-boranes using iron catalysts $[Fe(CO)_2(OTf)(\eta^5\text{-Cp})]$ and $[Fe(CO)_2(I)(\eta^5\text{-Cp})]$ (analogous to catalyst **1-9**)[39] to dehydrocouple H_3B-$PPhH_2$.[124] Mechanistic studies allowed the authors to isolate potential phosphido-borate intermediates $[Fe(CO)_2(\sigma\text{-PPhHBH}_3)]$ and $[Fe(CO)(\sigma,\eta^1\text{-PPhHBH}_3)]$. Furthermore, high molecular weight polymer was observed at low conversion rates suggesting that propagation was proceeding *via* a chain-growth mechanism.

Weller *et al.*[125] conducted a detailed mechanistic investigation into phosphine-borane dehydrocoupling using Manners' [Rh(1,5-cod)$_2$] system as a precatalyst. Secondary phosphine-borane, H_3B-P^tBu_2H was reacted at 413 K (melt conditions) for 20 h and formed the linear dimer H_3B-$P^tBu_2BH_2$-P^tBu_2H as the major product and phosphine-boronium salt $[H_2B(P^tBu_2H)_2][BH_4]$ as a side product. Adding 1,2-$C_6H_4F_2$ to act as a solvent allowed for investigation by ^{31}P NMR spectroscopy and ESI-MS. This led to the identification of two complexes present during the reaction: $[Rh(P^tBu_2H)_2(\eta^2\text{-}H_3B\text{-}P^tBu_2BH_2\text{-}P^tBu_2H)]^+$ **1-102** and $[Rh(P^tBu_2H)_2(\eta^6\text{-}C_6H_4F_2)]^+$ **1-103**. The results suggested that a $\{Rh(P^tBu_2H)_2\}^+$ fragment **1-104**, where the secondary phosphine ligands are the result of phosphine-boranes that have gone through P-B cleavage, was the active species in catalysis. This was confirmed by the independent synthesis of $[Rh(P^tBu_2H)_2(\eta^6\text{-}C_6H_5F)]^+$ **1-103** and its ability to catalyse the dehydrocoupling of H_3B-P^tBu_2H in the same conditions to form the same intermediates and products. A simple mechanism (**Scheme 1-23**) was postulated as a result of the study where H_3B-P^tBu_2H would bind to **1-104** to form intermediate **1-105**. A B-P coupling event would result in the formation of intermediate **1-102** which would be substituted with a unit of H_3B-P^tBu_2H to regenerate **1-105** and complete the cycle.

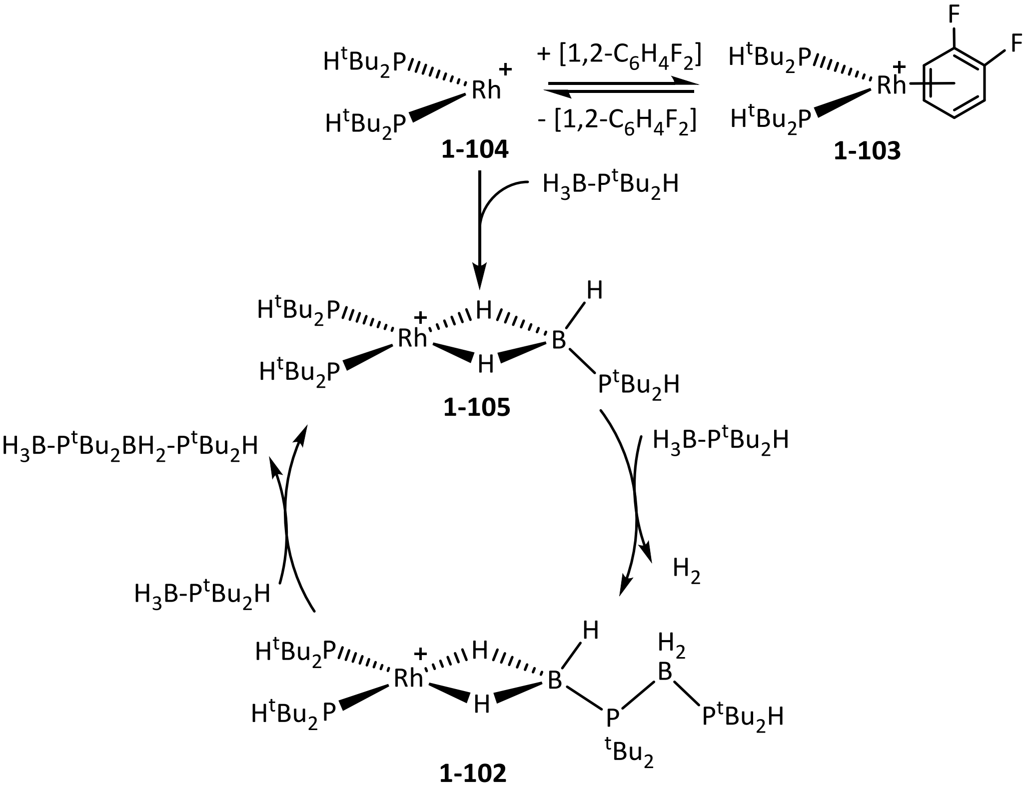

Scheme 1-23: *Proposed mechanism for dehydrocoupling of H_3B-P^tBu_2H by catalyst* ***1-102****. Adapted from reference No. 123.*

The Weller group have also conducted mechanistic studies on the dehydrocoupling of phosphine-boranes using $[Rh(Ph_2P(CH_2)_2PPh_2)(\eta^6\text{-}C_6H_5F)][BArF_4]$[126,127] and $[Rh(Me)(CH_2Cl_2)(PMe_3)(\eta\text{-}Cp^*)][BArF_4]$.[128] The computational mechanistic studies of these two systems are part of the work of this thesis and are discussed in **Chapters 3 & 4**. At the time of writing there were no other computational mechanistic investigations present in the literature.

1.3 – Conclusions

In conclusion, the formation of polyamino-boranes *via* the dehydrocoupling of amine-boranes is a burgeoning field. Their potential for H_2 storage sparked the recent increase in interest in the reaction and the formation and uses of polyamino-boranes has also become an active field as a result. Many catalytic examples are known in the literature and several experimental and computational mechanistic studies have been published. The dehydrogenation to form amino-boranes *in situ* generally proceeds through three pathways: i) B-H then N-H activation, ii) N-H then B-H activation, or iii) concerted B-H and N-H activation. Mechanistic work into the propagation of amino-borane to form polymer shows that it can proceed through a co-ordination / insertion mechanism, a head-to-tail chain growth pathway, or propagate off-metal. Compared to the formation of polyolefins, research into the formation of polyamino-boranes is still in its infancy and further mechanistic insight is needed to improve catalyst activity, reaction scale for industry and to expand the library of known polyamino-boranes.

The formation of polyphosphino-boranes is a much less explored field despite the polymers also having interesting uses. The high temperature, melt conditions required for efficient catalysis means mechanistic studies are scarce. Therefore, the field would also benefit from further mechanistic studies in the same way as the formation of polyamino-boranes.

This thesis aims to use computational techniques (namely density functional theory) in close collaboration with experimental results to gain more mechanistic information on the dehydrocoupling of amine- and phosphine-boranes.

Chapter 2: Theoretical Background

2.1 – Introduction

This chapter covers the theoretical background of the computational methodology used in this thesis. A brief overview of the quantum mechanical concepts behind the computation of chemical systems, Hartree-Fock Theory, and Density Functional Theory will be provided. Programs that provide an analysis of bonding used in this thesis such as the Quantum Theory of Atoms in Molecules and Natural Bond Orbital Theory will also be covered. This chapter draws on a number of well-known textbooks on the topic.[129-131]

2.2 – Background Quantum Mechanics

2.2.1 – Time Independent Schrödinger Equation

The aim of the majority of quantum chemistry approaches is to find the solution of the time-independent Schrödinger equation:[132]

$$\hat{H}\Psi = E\Psi$$

Eq. 2-1

Where $\hat{H}$ is the Hamiltonian operator representing the total energy for a molecular system with M nuclei and N electrons. The form of the Hamiltonian operator is:

$$\hat{H} = -\frac{1}{2}\sum_{i=1}^{N}\nabla_i^2 - \frac{1}{2}\sum_{A=1}^{M}\frac{1}{M_A}\nabla_A^2 - \sum_{i=1}^{N}\sum_{A=1}^{M}\frac{Z_A}{r_{iA}} + \sum_{i=1}^{N}\sum_{j>1}^{N}\frac{1}{r_{ij}} + \sum_{A=1}^{M}\sum_{B>A}^{M}\frac{Z_A Z_B}{R_{AB}}$$

Eq. 2-2

Where A and B are the M nuclei, i and j denote the N electrons in the molecular system, and M_A is the mass of nucleus A in multiples of the mass of an electron. The first two terms describe the kinetic energy of the electrons and nuclei respectively. The Laplacian operator, ∇_q^2, is the sum of differential operators in Cartesian co-ordinates:

$$\nabla_q^2 = \frac{\partial^2}{\partial x_q^2} + \frac{\partial^2}{\partial y_q^2} + \frac{\partial^2}{\partial z_q^2}$$

Eq. 2-3

The final three terms in **Equation 2-2** account for the attractive electrostatic interactions between the nuclei and the electrons as well as the repulsive potential due to electron-electron and nucleus-nucleus interactions.

2.2.2 – Atomic Units

The Schrödinger equation is simplified by not containing any physical constants. This is due to using the system of atomic units. Atomic units express physical expressions as multiples or combinations of fundamental constants. These constants, which are displayed in **Table 2-1**, are the mass of an electron (m_e), the modulus of its charge ($|e|$), Planck's constant h divided by 2π ($\hbar$), and the permittivity of the vacuum ($4\pi\varepsilon_0$).

Quantity	Atomic Unit	Value in SI Units	Symbol (name)
Mass	Rest mass of electron	9.1094 x 10^{-31} kg	m_e
Charge	Elementary charge	1.6022 x 10^{-19} C	e
Action	Planck's constant/2π	1.0546 x 10^{-34} J s	ħ
Length	$4\pi\varepsilon_0/m_e e^2$	5.2918 x 10^{-11} m	a_0 (bohr)
Energy	$\hbar^2/m_e a_0^2$	4.3597 x 10^{-18} J	E_h (hartree)

Table 2-1: *Atomic Units*

The atomic unit of 1 hartree corresponds to twice the ionisation energy of the hydrogen atom, which means the total energy of hydrogen is -0.5 E_h. Furthermore, 1 hartree is equivalent to 627.51 kcal mol^{-1} which is the unit of energy used throughout this thesis.

2.2.3 – Born-Oppenheimer Approximation

A further simplification of the Schrödinger equation can be made by using the Born-Oppenheimer approximation. The approximation is based on the fact that nuclei outweigh electrons to the point where the lightest nucleus (the proton, ^{1}H) is roughly 1800 times heavier than a single electron. Therefore, nuclei move more slowly than electrons and it can be assumed that electrons are moving so quickly in comparison to the nuclei that the nuclei positions can be fixed. This means that the kinetic energy of the nuclei can be considered to be zero, and the nuclei-nuclei repulsion term becomes a constant. Thus, **Equation 2-2** can be simplified to form the electronic Hamiltonian (**Equation 2-4**):

$$\hat{H}_{elec} = -\frac{1}{2}\sum_{i=1}^{N}\nabla_i^2 - \sum_{i=1}^{N}\sum_{A=1}^{M}\frac{Z_A}{r_{iA}} + \sum_{i=1}^{N}\sum_{j>1}^{N}\frac{1}{r_{ij}} = \hat{T} + \hat{V}_{Ne} + \hat{V}_{ee}$$

Eq. 2-4

The solution of the Schrödinger equation using $\hat{H}_{elec}$ and the electronic wavefunction, Ψ_{elec}, gives the electronic energy, E_{elec}. The total energy, E_{tot}, is the sum of the electronic energy and the constant nuclear repulsion term, E_{nuc}.

2.2.4 – The Variational Principle

Despite simplifying the Schrödinger equation through the use of atomic units and the Born-Oppenheimer approximation, it remains impossible to solve exactly for atomic and molecular systems beyond the simplest one electron examples. Inputting a guess wavefunction, Ψ_{guess}, into the Schrödinger equation will only obtain a guess energy, E_{guess}:

$$E_{guess} = \int \Psi_{guess} \hat{H} \Psi_{guess}$$

Eq. 2-5

The variational principle states that E_{guess} can only ever be greater or equal to the ground-state energy, E_0:

$$E_{guess} \geq E_0$$

Eq. 2-6

and E_{guess} can only be equal to E_0 when:

$$\Psi_{guess} = \Psi_0$$

Eq. 2-7

where Ψ_0 is the ground-state wave function. This means that the lower the value of E_{guess} the closer it must be to the exact value of E_0.

2.3 – The Hartree-Fock Approximation

The Hartree-Fock (HF) approximation is the basis for all wave function based quantum chemical methods as well as being an influence in the framework for density functional theory (discussed in **Section 2.4**). This section discusses the main concepts of the HF approximation.

2.3.1 – Spatial and Spin Orbitals

An orbital is defined as a wave function of an electron. A spatial orbital, $\varphi_i(r)$, is a function of the position vector, r, and describes the spatial distribution of an electron. This means that the square of the orbital, $|\varphi_i|^2 dr$, is the probability of finding the electron in the volume element, dr, surrounding r. Electrons cannot be fully described without defining their spin which can be achieved by using the functions $\alpha(\omega)$ and $\beta(\omega)$ to specify if the spin is spin up (↑) or spin down (↓). A wave function which describes both an electron's spatial distribution and spin is called a spin orbital, $\chi(x)$. A spatial orbital, $\varphi_i(r)$, can combine with the two spin functions, $\alpha(\omega)$ and $\beta(\omega)$, to form one spin orbital:

$$\chi(x) = \begin{cases} \varphi(r)\alpha(\omega) \\ \quad or \\ \varphi(r)\beta(\omega) \end{cases}$$

Eq. 2-8

2.3.2 – The Hartree Product

If each electron is assigned to a separate spin orbital then the total wave function could be described as the product of all the spin orbitals:

$$\Psi^{HP}(x_1, x_2, \cdots, x_N) = \chi_i(x_1)\chi_j(x_2)\cdots\chi_k(x_N)$$

Eq. 2-9

where $\Psi^{HP}(x_1, x_2, \cdots, x_N)$ is the Hartree product. A more correct electronic wave function should capture the indistinguishability of electrons. This is not the case for the Hartree product as placing specific electrons into specific spin orbitals make them distinguishable from each other. Another requirement for a more correct electronic wave function is that the antisymmetry principle must be satisfied. This requires that the electronic wave function should change sign upon the interchange of spatial and spin co-ordinates of any two electrons (or any half-spin particle). The Hartree product does not satisfy the antisymmetry principle.

2.3.3 – Slater Determinants

An electronic wave function that satisfies the antisymmetry principle and treats electrons as indistinguishable can be formed by using a Slater determinant. For example, when considering a two-electron case, each electron can be occupying either spin orbital, χ_i and χ_j which gives two possible Hartree Products:

$$\Psi_{12}^{HP}(x_1,x_2) = \chi_i(x_1)\chi_j(x_2)$$
$$\Psi_{21}^{HP}(x_1,x_2) = \chi_i(x_2)\chi_j(x_1)$$

Eq. 2-10

A wave function can be obtained by forming a linear combination of the two Hartree Products in **Equation 2-10**:

$$\Psi(x_1,x_2) = 2^{-\frac{1}{2}}[\chi_i(x_1)\chi_j(x_2) - \chi_j(x_1)\chi_i(x_2)]$$

Eq. 2-11

Where the value $2^{-\frac{1}{2}}$ is a normalisation factor. The wave function in **Equation 2-11** satisfies the antisymmetry principle as:

$$\Psi(x_1,x_2) = -\Psi(x_2,x_1)$$

Eq. 2-12

This antisymmetric wave function can be rewritten as a Slater determinant:

$$\Psi(x_1,x_2) = 2^{-\frac{1}{2}}\begin{bmatrix}\chi_i(x_1) & \chi_j(x_1)\\ \chi_i(x_2) & \chi_j(x_2)\end{bmatrix}$$

Eq. 2-13

The Slater determinant can be generalised for an N-electron system to:

$$\Psi(x_1,x_2,\cdots,\boldsymbol{x_N}) = (\boldsymbol{N}!)^{-\frac{1}{2}}\begin{vmatrix}\chi_i(x_1) & \chi_{\boldsymbol{j}}(x_1) & \cdots & \chi_{\boldsymbol{k}}(x_1)\\ \chi_i(x_2) & \chi_{\boldsymbol{j}}(x_2) & \cdots & \chi_{\boldsymbol{k}}(x_2)\\ \vdots & \vdots & & \vdots\\ \chi_i(x_{\boldsymbol{N}}) & \chi_{\boldsymbol{j}}(x_{\boldsymbol{N}}) & \cdots & \chi_{\boldsymbol{k}}(x_{\boldsymbol{N}})\end{vmatrix}$$

Eq. 2-14

The generalised Slater determinant (**Equation 2-14**) captures the indistinguishability of electrons as it describes every permutation of N electrons occupying N spin orbitals. The antisymmetry principle is also followed as interchanging two electrons is the equivalent of interchanging two rows within the determinant which changes the sign of the resulting wave function. Furthermore, assigning two electrons to the same spin orbital makes two columns of the determinant equivalent and gives the value of zero. This is consistent with the Pauli exclusion principle in that no more than one electron can occupy a single spin orbital. It is common practice for the Slater determinant to be written in a short-hand notation which contains a normalisation constant and only shows the diagonal values of the determinant:

$$\Psi(x_1, x_2, \cdots, x_N) = |\chi_i(x_1)\chi_j(x_2)\cdots\chi_k(x_N) >$$

Eq. 2-15

2.3.5 – The Hartree-Fock Equations

The wave function obtained from the Slater determinant is described by a series of spin orbitals. The electronic energy of the system is obtained through a series of minimisations based on the variational principle (**Section 2.2.4**). This is achieved through constructing a series of one-electron operators where each electron interacts with the static field of all other electrons. Applying this minimisation from a Slater determinant gives rise to the Fock operator (form for a one electron system shown in **Equation 2-16**):

$$\hat{F}(1) = \hat{h}(1) - \sum_{a}(\hat{J}\,\alpha(1) - \hat{K}\alpha(1))$$

Eq. 2-16

Where $\hat{h}$ is the one-electron Hamiltonian (under the Born-Oppenheimer approximation) which contains terms for the kinetic energy and potential energy due to electron-nuclei attractions, $\hat{J}$ is the Coulomb operator and $\hat{K}$ is the exchange operator. The Coulomb operator $\hat{J}$ takes the form:

$$\hat{J}_j(\vec{x}_1) = \int |\chi_j(\vec{x}_2)|^2 \frac{1}{r_{12}} d\vec{x}_2$$

Eq. 2-17

and accounts for the potential that an electron in position $\vec{x}_1$ experiences due to the average charge distribution of another electron in orbital χ_j. The exchange operator $\hat{K}$ takes the form:

$$\hat{K}_j(\vec{x}_1)\chi_i(\vec{x}_1) = \int \chi_j^*(\vec{x}_2)\frac{1}{r_{12}}\chi_i(\vec{x}_2)d\vec{x}_2\chi_j(\vec{x}_1)$$

Eq. 2-18

There is no classical interpretation for $\hat{K}$ (**Equation 2-18**) therefore, it can only be defined through the effect it has on a spin orbital. The exchange operator leads to an exchange of the variables between two spin orbitals and is a result of the antisymmetry of the Slater determinant. It only applies to electrons with the same spin as for opposite spins the spin orbitals are orthonormal and therefore would destroy the integral by containing a term which is zero. As part of the pauli exclusion Principle, electrons with the same spin cannot be in the same place at the same time. The exchange operator captures this effect as if electron 1 with spin α has a set of co-ordinates, electron 2 with spin α will see a reduced electron density around the co-ordinates of electron 1. This creates an 'electron hole' and means electrons of the same spin will be, on average, further away from each other than electrons with opposite spin which has a stabilising effect on the total energy.

The exchange operator, $\hat{K}$ also solves the self-interaction problem. This issue arises from the Coulomb operator describing the average repulsion of electrons against all spin and spatial co-ordinates of itself. The HF approximation eliminates this problem through the exchange operator, $\hat{K}$. Including the exchange operator perfectly cancels out the Coulomb interaction if electron 1 and 2 are the same and thus solves the self-interaction problem. This effect is not carried over into Density Functional Theory (discussed in **Section 2.4**) and therefore solving the self-interaction problem remains an issue for method development.

In order to solve the HF equations to obtain the energy of a chemical system, a set of orbitals is required. This is problematic as the solution to the HF equations is needed to solve them. The solution comes in the form of the self-consistent field (SCF) method. The SCF procedure takes a guess set of orbitals to form an initial Ψ_{guess}. Inputting Ψ_{guess} into the HF equations forms a new set of orbitals in order to obtain an E_{guess} value. The new set of orbitals can then be used to form a new Ψ_{guess} which provides another set of orbitals and value for E_{guess}. The process can then by repeated systematically until Ψ_{guess} reaches a convergence limit.

2.3.6 – Electron Correlation

Electron correlation mostly relates to the instantaneous repulsion of electrons. The main disadvantage of the HF approximation is that it does not capture most aspects of electron correlation. This is due to each electron being treated against an average electron repulsion independently rather than against the instantaneous repulsion of every other electron in the system. The correlation energy can be defined as the difference between the Hartree-Fock energy and the true ground state energy:

$$E_C^{HF} = E_0 - E_{HF}$$

Eq. 2-19

The result of HF not containing electron correlation is that electrons tend to be too close together when the HF Approximation is used. This has a destabilising effect as it increases the amount of potential energy due to electron-electron repulsion.

Electron correlation can be split into two categories: dynamic and non-dynamic. Dynamic correlation is related to the movement of electrons and how electrons which are further away from each other repulse each other less than those that are closer together (i.e. a Coulomb effect). Non-dynamic correlation is related to the fact that in some cases, the Slater determinant is not a good model of the true ground state as there are other Slater determinants with similar energies. An example where this becomes apparent is with the homolytic dissociation of the H_2 molecule. The equilibrium H···H distance is modelled reasonably well by the HF Approximation with a correlation error of 0.04 E_h, however, when the H···H distance is increased the correlation error also increases until it converges to a limit of 0.25 E_h. This is due to the relative weighting of the possible electron configurations which can be displayed pictorially as:

$$\left(H^{\uparrow} \cdots H^{\downarrow}\right) + \left(H^{\downarrow} \cdots H^{\uparrow}\right) + \left(H^{-\uparrow\downarrow} \cdots H^{+}\right) + \left(H^{+} \cdots H^{-\uparrow\downarrow}\right)$$

Eq. 2-20

In the first two terms of **Equation 2-20** the two electrons in the system are shared between the two protons and in the last two terms, both electrons are on one nucleus while the other is a proton. The Slater determinant is a good description of H_2 at the equilibrium H···H distance. However, it fails as the bond length increases as the relative weighting of the ionic terms in the wavefunction become greater. This is incorrect as the homolytic cleavage of H_2 should result with two H atoms with 1 electron and the weight of the ionic terms should tend to 0.

2.3.7 – Computational Methods to Account for Electron Correlation

A range of *ab initio* computational techniques have been developed in order to solve the electron correlation problem in the HF approximation. For example, the full configuration-interaction (CI) method[133] is currently considered to be the best *ab initio* approach. Full CI considers electron excitations from the ground state which enables other electronic configurations to be assessed. A Full CI calculation with a large enough basis set would result in a linear combination of every possible configuration of electrons and therefore the exact wave function. However, the computational cost for Full CI is so extreme that it is only viable for small systems. Other *ab initio* methods are couple cluster method such as: CCD[134] which only considers double excitation configurations, CCSD[135] which considers both single and double excitations, and CCSD(T)[136] which considered single, double and triple excitations. CASSCF[137] is another technique where the user selects a range of vacant and empty orbitals for the Full CI method to be applied to. Furthermore, it was found that electron correlation can be accounted for through using Møller-Plesset perturbation theory[138] to the second order in a method named MP2.[139] Perturbation to the fourth order in MP4[140] is also used but is more computationally expensive than MP2.

2.4 – Density Functional Theory (DFT)

2.4.1 – The Hohenberg-Kohn Theorems

Modern DFT began with a landmark paper by Hohenberg and Kohn published in 1964 where two theorems are proposed.[141] The first Hohenberg-Kohn Theorem proves that there cannot be two different values of V_{ext} that have the same ground state electron density (ρ_0) and therefore ρ_0 uniquely defines V_{ext} (**Equation 2-21**). They achieve this by using a *reduction ad absurdum* approach i.e. disproving a statement by showing it leads to an absurd or impractical conclusion. This is done by considering two external potentials, V_{ext} and V'_{ext}, which give the same electron density $\rho(\vec{r})$. The external potentials are part of two different Hamiltonians, $\hat{H}$ and $\hat{H}'$ (where they only differ in the external potential):

$$\hat{H} = \hat{T} + \hat{V}_{ee} + \hat{V}_{ext} \; and \; \hat{H}' = \hat{T} + \hat{V}_{ee} + \hat{V}'_{ext}$$

Eq. 2-21

Where $\hat{T}$ is the kinetic energy and $\hat{V}_{ee}$ is the potential energy caused by electron-electron repulsion. The Hamiltonians belong to two different ground state wavefunctions, Ψ and Ψ', and have different ground state energies, E_0 and E'_0. This means Ψ' can be used as a trial wavefunction for $\hat{H}$ and due to the variational principle (**Section 2.2.4**):

$$E_0 < \langle \Psi' | \hat{H} | \Psi' \rangle = \langle \Psi' | \hat{H}' | \Psi' \rangle + \langle \Psi' | \hat{H} - \hat{H}' | \Psi' \rangle$$

Eq. 2-22

Due to **Equation 2-21** this can be also written as:

$$E_0 < E'_0 + \langle \Psi' | (\hat{T} + \hat{V}_{ee} + \hat{V}_{ext}) - (\hat{T} + \hat{V}_{ee} + \hat{V}'_{ext}) | \Psi' \rangle$$

Eq. 2-23

Which yields:

$$E_0 < \; E'_0 + \int \rho(\vec{r}) \{V_{ext} - V'_{ext}\} d\vec{r}$$

Eq. 2-24

Repeating **Equations 2-22** and **2-23** for Ψ being used as a trial wavefunction for $\hat{H}'$ gives:

$$E'_0 < \; E_0 - \int \rho(\vec{r}) \{V_{ext} - V'_{ext}\} d\vec{r}$$

Eq. 2-25

Finally, adding **Equations 2-24** and **2-25** together produces:

$$E_0 + E'_0 < E'_0 + E_0$$

Eq. 2-26

Equation 2-26 contradicts itself and therefore acts as proof that there cannot be two different values of V_{ext} that have the same ground state electron density (ρ_0). This means that the ground state energy of a system is a functional of the ground state electron density and can be written as:

$$E_0[\rho_0] = \int \rho_0\,(\vec{r})V_{ext}d\vec{r} + T[\rho_0] + E_{ee}[\rho_0]$$

Eq. 2-27

Hohenberg and Kohn proved that the V_{ext} term determined from ρ_0 contained all the necessary information to obtain the electronic energy of the system. The distance between nuclei (R_A) could be measured by the distance between cusps in the electron density with the nuclei charges (Z) measured by the size and shape of those cusps. Furthermore, the number of electrons (N) can be found by integrating the electron density over the entire system. In theory, there should be a functional which allows for the ground state energy to be calculated from ρ_0. This hypothetical functional is named the Hohenberg-Kohn functional, $F_{HK}[\rho_0]$ and contains the terms for the kinetic energy, $T[\rho_0]$, and electron-interaction energy, $E_{ee}[\rho_0]$. The second Hohenberg-Kohn Theorem states that $F_{HK}[\rho_0]$ only provides the ground state energy of the system if its theoretical density is the true ground state electron density, otherwise, it gives a higher value. This problem is variational and therefore, the Variational Principle can be used:

$$E_0 \leq E[\tilde{\rho}] = T[\tilde{\rho}] + E_{ext}[\tilde{\rho}] + E_{ee}[\tilde{\rho}]$$

Eq. 2-28

If $F_{HK}[\rho_0]$ is known then the exact ground state electronic energy can be calculated. However, this is not the case and the rest of this section discusses approximations used in place of $F_{HK}[\rho_0]$.

2.4.2 – The Kohn-Sham Approach

In 1965, Kohn and Sham published an approach on how the Hohenberg-Kohn functional, F_{HK}, could be approximated. In order to solve the problem of not being able to determine the kinetic energy through an explicit functional, the Kohn-Sham approach proposed to include the majority of the total kinetic energy by calculating the kinetic energy of a non-interacting reference system with the same density as the real system being calculated:

$$T_S = -\frac{1}{2}\sum_{i}^{N} < \varphi_i|\nabla^2|\varphi_i >$$

Eq. 2-29

T_S does not equate to the total kinetic energy of the system as it does not take into account the correlated motion of electrons. The Kohn-Sham approach accounted for this by including the following separation of the functional F_{HK}:

$$F_{HK}[\rho(\vec{r})] = T_S[\rho(\vec{r})] + J[\rho(\vec{r})] + E_{XC}[\rho(\vec{r})]$$

Eq. 2-30

where $T_S[\rho(\vec{r})]$ is the solvable part of the kinetic energy (**Equation 2-29**) and $J[\rho(\vec{r})]$ is the classical Coulomb interaction which is also solvable. The term $E_{XC}[\rho(\vec{r})]$ is the exchange-correlation energy which takes the form:

$$E_{XC}[\rho] = T_C[\rho] + E_{ncl}[\rho]$$

Eq. 2-31

where $T_C[\rho]$ represents the correlated kinetic energy not included in the T_S term and $E_{ncl}[\rho]$ contains the effects of electron exchange, correlation and self-interaction. Solving $E_{XC}[\rho(\vec{r})]$ has been the focus of DFT method development ever since. The different ways this problem has been approached are detailed in the rest of this section.

2.4.3 – Local Density Approximation

The local density approximation (LDA) is one of the first and simplest approaches to an exchange-correlation functional. The model is based on the uniform electron gas (UEG) where electrons are present in a field of constant electronic potential and electron density. This means the functionals can be based on solely the electron density at a given point in space. For the UEG model, LDA models the exchange energy exactly. The exchange-correlation energy (E_{XC}) of a system can be written as:

$$E_{XC}^{LDA}[\rho] = \int \rho(\overrightarrow{r})\, \varepsilon_{XC}\big(\rho(\vec{r})\big)\, d\vec{r}$$

Eq. 2-32

In **Equation 2-32** $\varepsilon_{XC}\big(\rho(\vec{r})\big)$ is the exchange-correlation energy per particle of the UEG of density $\rho(\vec{r})$. The exchange-correlation energy can also be written as:

$$\varepsilon_{XC}\big(\rho(\vec{r})\big) = \varepsilon_X\big(\rho(\vec{r})\big) + \varepsilon_C\big(\rho(\vec{r})\big)$$

Eq. 2-33

Here, ε_X is the exchange term which in LDA has the explicit form of:

$$\varepsilon_X = -\frac{3}{4}\sqrt[3]{\frac{3\rho(\vec{r})}{\pi}}$$

Eq. 2-34

Equation 2-34 is also called Slater exchange and can be abbreviated to S. In 1980 Vosko, Wilk and Nusair published a very accurate approximation of the correlation energy for the UEG model. By combining the exchange (S) and correlation (VWN) approximations the SVWN LDA functional can be formed.[142]

LDA is useful when modelling chemical systems with a constant, uniform electron density such as metal lattices and simple materials and has therefore been used in solid-state physics since the 1970s.[131, 141] However, LDA is not a sufficient model for most chemical systems (such as molecules) whose electron density varies greatly over relatively small distances.

2.4.4 – General Gradient Approximation

The general gradient approximation (GGA) is an improvement on the LDA where the gradient of the electron density is taken into account. This is achieved by expanding the electron density using a Taylor expansion and truncating at the first term which takes into account the gradient of the electron density:

$$E_{XC}^{GGA}[\rho_\alpha, \rho_\beta] = \int f(\rho_\alpha, \rho_\beta, \nabla\rho_\alpha, \nabla\rho_\beta)\, d\vec{r}$$

Eq. 2-35

In **Equation 2-35** the electron densities of electrons with α and β spin are separated. This term can be further separated into exchange and correlation terms:

$$E_{XC}^{GGA} = E_X^{GGA} + E_C^{GGA}$$

Eq. 2-36

Becke used the general gradient approximation when deriving his exchange functional in 1988[143] as did Perdew when deriving his correlation functional in 1986.[144] These functionals are generally abbreviated to B (or B88) and P86 respectively. Combined they form the BP86 functional which is used in this thesis. Other popular GGA functionals are BLYP which combines Becke's exchange functional with the correlation functional published by Lee, Yang and Parr in 1988 (LYP) [145] and PBE[146], an exchange-correlation functional derived by Perdew, Burke and Ernzerhof in 1996.

2.4.5 – Hybrid Functionals

One disadvantage of GGA functionals is that they do not calculate exact exchange. As discussed in **Section 2.3**, Hartree-Fock theory does calculate exact exchange (within the HF Approximation) but neglects electron correlation completely. Therefore, a logical step would be to combine the Hartree-Fock exchange energy with the correlation energy from a GGA functional as shown in **Equation 2-37**:

$$E_{XC} = E_X^{HF} + E_C^{GGA}$$

Eq. 2-37

However, despite providing accurate atomisation energies, this method does not work well for molecular systems. This is due to treating electron exchange and correlation separately when the two terms cannot be decoupled from each other and mixing the delocalised exact exchange energy with a local correlation approximation leads to significant errors.

Further contributions to the field led to the development of tuning how much exact exchange energy to include in the functional by parametrising against experimental results. Through this method, Becke *et al.* published the hybrid functional known as B3LYP[147] which is one of the most commonly used functional in the literature.[148]

$$E_{XC}^{B3LYP} = (1-a)E_X^{LSD} + aE_{XC}^{\lambda=0} + bE_X^B + cE_C^{LYP} + (1-c)E_C^{LSD}$$

Eq. 2-38

Equation 2-38 has contributions from the exchange and correlation energies from the local spin density (LSD, a variation on LDA which takes into account spin orbitals) E_X^{LSD} and E_C^{LSD}, the exact exchange $E_X^{\lambda=0}$, Becke's exchange functional E_X^B and the LYP correlation functional E_C^{LYP}. There are also 3 parameters: *a*, *b*, and *c*. Parameter *a* controls the amount of exact exchange while *b* and *c* control exchange and correlation gradient corrections. For B3LYP these parameters are set at *a* = 0.20, *b* = 0.72 and *c* = 0.81. Another hybrid functional used in this thesis is PBE0, developed by Adaro and Barone in 1996.[149]

2.4.6 – Meta-GGA Functionals

Another logical progression from GGA functionals is to extend the Taylor expansion of the electron density to the second term to take into account the second derivative of the electron density. The B97 functional[150] used in this thesis uses this strategy. Another meta-GGA functional used in this thesis, TPSS[151], uses the exchange functional from the uniform electron gas model with an 'enhancement parameter' which takes into account the inhomogeneity of the electron density.

2.4.7 – Range-Separated Functionals

GGA and hybrid DFT functionals do not properly capture long-range interactions due to DFT being a 'local' method. This is sufficient when modelling small molecules. However, long-range interactions are not modelled as accurately. Range-separated functionals attempt to do so by including full Hartree-Fock exchange for long-range electron-electron interactions whilst continuing to use the GGA exchange energy for short-range electron-electron interactions:

$$E_{XC}^{LRCF} = E_X^{LR-HF} + E_X^{SR-GGA} + E_C^{GGA}$$

Eq. 2-39

Where E_{XC}^{LRCF} is the long-range corrected functional's exchange-correlation energy, E_X^{LR-HF} is the Hartree-Fock exchange at long range, and E_X^{SR-GGA} is the GGA exchange at short-range. An example of a long-range corrected functional is ωB97X, developed by Head-Gordon *et al*.[152] based on the B97 functional. The ω parameter defines the limit between short-range and long-range interactions. Furthermore, ωB97X contains around 16% short-range Hartree Fock exchange to match the improvement seen in short-range interactions with hybrid functionals compared to GGAs.

2.5 – Basis Sets

The spin orbitals used in the HF Approximation and DFT are constructed from a series of functions known as basis functions with a complete set of basis functions known as a basis set. Basis functions can have the form of Slater-type orbitals (STO) which take the following form for a 1s orbital of hydrogen:

$$\phi^{STO}(r) = \left(\frac{\varsigma^3}{\pi}\right)^{1/2} e^{-\varsigma r}$$

Eq. 2-40

Where r is the distance from the nucleus and ς is the orbital exponent which is what determines the rate of decay of the function. STOs have a cusp at r = 0 and therefore accurately replicate atomic orbitals. However, STOs are computationally expensive due to the need to integrate the $e^{-\varsigma r}$ term. Therefore, Gaussian-type orbitals (GTO) are more commonly used. For the 1s orbital of hydrogen they take the form:

$$\phi^{GTO}(r) = \left(\frac{2\alpha}{\pi}\right)^{3/4} e^{-\alpha r^2}$$

Eq. 2-41

where α is the orbital exponent for Gaussian functions. Integration involving GTOs is much easier to compute than STOs but they do not represent orbitals as accurately as at r = 0 no cusp is formed but the gradient does equal zero (**Figure 2-1**).

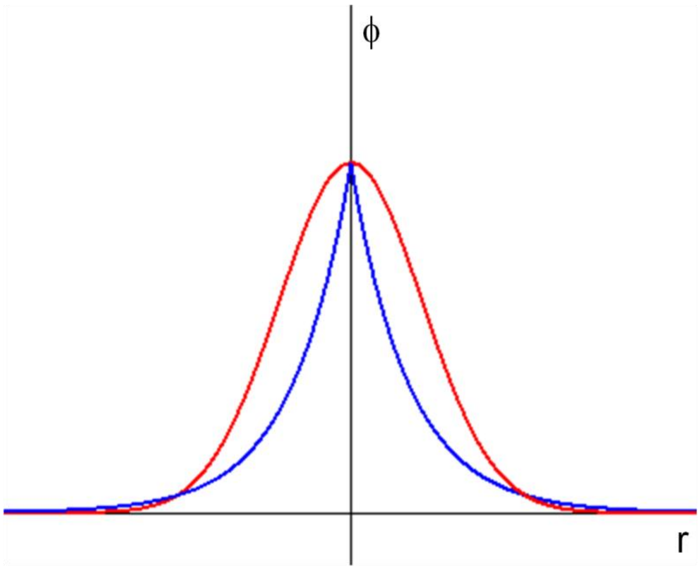

Figure 2-3: *The form of a STO (blue) vs. a GTO (red). ϕ = radial function, r = radius from nucleus*

Using one GTO in place of an STO is not a sufficient substitution. However, several primitive Gaussian functions can be combined into a linear combination in order to give a contracted Gaussian function (CGF):

$$\phi^{CGF}(r) = \sum^{M} c_a \, \phi^{GTO}(r)$$

Eq. 2-42

where M is the number of Gaussians used in the linear combination and c_a is the coefficient used to optimise the shape of the CGFs. These CGFs better resemble one STO and, despite containing several GTOs, are still more computationally efficient.

The minimum number of basis functions required to describe a system is one STO per atomic orbital (AO). One example of a minimal basis set (also known as single-ς basis sets) is STO-3G[153] which uses 3 GTOs combined into a CGF for each STO required. For example, the H_2 molecule has a linear combination of 2 1s AOs and therefore, requires a minimum of 2 STOs. STO-3G provides 2 CGFs in the form of 6 GTOs. Basis sets where two basis functions are formed for each AO (double-ς) and three basis functions for each AO (triple-ς) are also used.

In the STO-3G basis set, all orbitals have an equal number of basis functions whether they are core or valence orbitals. Core orbitals are generally not involved or influenced by chemical bonding while valence orbitals are greatly influenced. This effect led to the development of split-valence basis sets where the core orbitals are described using a single CGF while valence orbitals are split into more than one CGF. Pople *et al.* have developed the most popular split-valence basis sets which include 3-21G, 6-21G, 4-31G, 6-31G and 6-311G.[154, 155] The nomenclature indicates the number of CGFs used to describe the AOs. For example, 6-31G basis sets describe the core orbitals with 6 GTOs forming a single CGF and the valence electrons are described with a double-ς basis with 3 GTOs forming 1 CGF and 1 GTO forming another.

Further basis functions can be added through including polarisation functions which account for orbitals with higher angular momentum than the valence AOs of the neutral atom. For example, including d polarisation functions adds d-functions to p-block elements (indicated by a * after the basis set). A double ** indicates inclusion of d and p polarisation which adds p-functions to the H and He atoms. The 6-31G** basis set is used in this thesis.[156, 157]

All the basis sets discussed so far have been all electron basis sets as all the electrons of an atom are described. This is sufficient in terms of computational cost for lighter atoms. However, when moving to heavier atoms, especially transition-metal centres, describing every electron in the system becomes more computationally expensive. This problem is solved by using effective core potentials (ECPs) which capture the potential of the core electrons based on high-level calculations. This means that the core electrons of heavy atoms do not need to be explicitly calculated, saving computational time. ECPs also capture certain relativistic effects which are important in the description of the core electrons in heavier atoms and otherwise difficult to compute. These relativistic effects have been shown to be important in modelling transition-metal bonding as they also affect valence electrons of transition-metals.[131] This thesis describes heavy atoms (all elements beyond the 2nd row of the periodic table) with Stuttgart pseudopotentials.[158]

2.6 – Solvation and Dispersion

2.6.1 – Solvation Models

The majority of chemical reactions take place in solution and the nature of the solvent used can greatly affect the reactivity. Therefore, it is important to correctly model the effects of solvation in order to have a good description of the chemical system for calculation.

One approach is to only add the explicit solvent molecules that make up the first co-ordination sphere around the chemical species being calculated. However, difficulties arise when determining where the solvent molecules should be placed as there could be many potential conformations with similar kinetics, all of which would need to be taken into account. Furthermore, the number of solvent molecules to include is a factor that would need consideration with the cut-off not being clear and likely to change depending on the chemical species being studied. Another explicit approach to model solvation is to calculate a solvent box. This is where the chemical species being calculated is surrounded by explicitly included solvent molecules with periodic boundary conditions. The solvent box method is seldom used as it is expensive computationally due to each calculation including potentially thousands of atoms. However, Lledos, Ujaque *et al.*[159, 160] have managed to gain useful mechanistic information on the Wacker process by utilising this technique.

Implicit solvent models are much more commonly used when calculating the effects of solvent. These models simulate the effect of the bulk solvent on the chemical species (solute) being calculated. The implicit solvation model used in this thesis is the polarised continuum model (PCM).[161] This model calculates the solvent-solute boundary by probing the electron density isosurface of the solute. The solvent surface then polarises depending on the charges of the solute and the polarizability of the solvent. The PCM model achieves this using partial atomic charges. Another popular implicit solvation model used in the literature is solvation model density (SMD).[162]

Implicit solvation models give a value for the free energy of solvation, G_S, which is given by the equation:

$$G_S = G_{el} + G_{rep} + G_{dis} + G_{cav} + G_{tm}$$

Eq. 2-43

G_{el} (electrostatic), G_{rep} (repulsion) and G_{dis} (dispersion) all occur between the surface of the solute and the solvent surface. The cavitation energy (G_{cav}) arises from energetic cost of the formation of a cavity in a 3D continuum due to the presence of the solute as well as the change in structure of the solvent bulk. The term G_{tm} accounts for the thermal and molecular motions of the solute within the solvent cavity. Implicit solvent models are much less computationally expensive than explicit solvation whilst maintaining good modelling of solvation effects. The main disadvantage to the implicit solvent models is that they do not capture solvent-solute interactions such as hydrogen bonding or co-ordination to transition-metals. In cases where these effects are important to the chemical system being studied, a combination of implicit and explicit solvent models would have to be used.

2.6.2 – Dispersion Corrections

It has already been discussed in **Section 2.4** that DFT functionals fail when modelling long-range interactions. The most popular approach to solve this issue is to include an empirical dispersion correction to the DFT energy, so-called DFT-D. These DFT-D corrections are based on the attractive r^{-6} term of the Lennard-Jones 12-6 potential[163] and takes the form:

$$E_{disp}^{DFT-D} = -\frac{1}{2}\sum_{A\neq B}\sum_{n=6.8.10} s_n \frac{C_n^{AB}}{r_{AB}^n} f_{d,n}(r_{AB})$$

Eq. 2-44

where C_n^{AB} is the averaged *n*th order dispersion coefficient for atom pair AB and r_{AB}^n is their internuclear distance. For the commonly used empirical dispersion correction developed by Grimme *et al.*[164], D3, C_n^{AB} is used for n = 6 and 8. The value s_n is a scaling factor which is changed depending on the DFT functional being used in conjunction with the empirical dispersion correction. The damping function, $f_{d,n}$, is used to avoid short and medium ranged interactions being counted twice as they are already captured by DFT. For the D3 correction, a damping function was proposed by Becke and Johnson[165] denoted as BJ where the dispersion energy would be given by:

$$E_{disp}^{D3(BJ)} = -\frac{1}{2}\sum_{A\neq B} s_6 \frac{C_6^{AB}}{R_{AB}^6 + [f(R_{AB}^0)]^6} + s_6 \frac{C_8^{AB}}{R_{AB}^8 + [f(R_{AB}^0)]^8}$$

Eq. 2-45

where

$$f\left(R_{AB}^0\right) = a_1 R_{AB}^0 + a_2$$

Eq. 2-46

and a_1 and a_2 are fitted parameters. The D3(BJ) dispersion correction is what is used throughout this thesis.

Another approach to account for long-range interactions with DFT functionals is to parameterise against large molecules where long-range interactions are important. This is the basis for some

Minnesota functionals developed by Truhlar *et al*. The DFT functional M06[166] used in this thesis was parameterised against a data set of solid-state structural data. Furthermore, some DFT functionals contain an internal dispersion correction included within the functional itself. Dispersion-corrected functionals used in this thesis are B97D[167] and ωB97XD.[152]

2.7 – The Quantum Theory of Atoms in Molecules (QTAIM)

The discussion in this section involves the analyses of QTAIM calculations which utilises Bader's Quantum Theory of Atoms in Molecules.[168] The main sources for this section are Bader's textbook name "Atoms in Molecules"[169] and "The Quantum Theory of Atoms in Molecules" edited by C. F. Matta and R. J. Boyd.[170] These calculations are used to analyse chemical interactions on the basis of the topology of the electron density [ρ(**r**)]. This is achieved by studying the critical points of the electron density surface. Critical points arise where the gradient of the electron density, $\nabla\rho(\mathbf{r})$, is equal to zero in all directions **Equation 2-47.**

$$\nabla\rho = \mathbf{i}\frac{\partial\rho}{\partial x} + \mathbf{j}\frac{\partial\rho}{\partial y} + \mathbf{k}\frac{\partial\rho}{\partial z} = 0$$

Eq. 2-47

There are four different categories of critical points which can be distinguished by looking at the second derivative of the electron density, $\nabla\nabla\rho$. There are nine values of $\nabla\nabla\rho$ which can be arranged in a Hessian matrix and then diagonalised **Equation 2-48:**

$$\mathrm{A}(\mathrm{r_c}) = \begin{pmatrix} \frac{\partial^2\rho}{\partial x^2} & \frac{\partial^2\rho}{\partial x\partial y} & \frac{\partial^2\rho}{\partial x\partial z} \\ \frac{\partial^2\rho}{\partial y\partial x} & \frac{\partial^2\rho}{\partial y^2} & \frac{\partial^2\rho}{\partial y\partial z} \\ \frac{\partial^2\rho}{\partial z\partial x} & \frac{\partial^2\rho}{\partial z\partial y} & \frac{\partial^2\rho}{\partial z^2} \end{pmatrix}_{r'=r_c} \xrightarrow{Diagonalised} = \begin{pmatrix} \lambda_1 & 0 & 0 \\ 0 & \lambda_2 & 0 \\ 0 & 0 & \lambda_3 \end{pmatrix}$$

Eq. 2-48

The values of λ_1, λ_2, and λ_3 represent the curvature of the density in three directions. The sum of these three curvatures gives the Laplacian of the electron density $\nabla^2\rho(\mathbf{r})$ (**Equation 2-49**). The Laplacian value can provide some information when analysing a QTAIM calculation. This will be discussed later in **Section 2.7.1.2**.

$$\nabla^2\rho(r) = \lambda_1 + \lambda_2 + \lambda_3$$

Eq. 2-49

Critical points can be categorised by their rank (ω) and signature (σ) which are displayed as (ω,σ). The rank is defined by the number of non-zero curvatures at the critical point. In terms of the topology of the electron density it is very rare to find a value of ω that is not equal to three. The signature is the sum of the signs of the curvatures (λ_1, λ_2, λ_3).

One category of critical point has a rank, signature value of (3,-3), meaning that there are three negative curvatures as ρ is at a local maximum. This is called a nuclear critical point (ncp) as it signifies the position of an atomic nucleus in the surface of the electron density. Mathematically, this is not a true critical point as the electron density forms a cusp at the centre of a nucleus meaning the curvatures are not defined and the gradient of the electron density is not equal to zero. However, the maximum at the nucleus topologically acts as a critical point.

Other critical points are classified as (3,-1); meaning there are two negative curvatures and one positive curvature. This signifies that the critical point is at a saddle point in the electron density surface. Critical points of this category are called bond critical points (bcps) and generally indicate the presence of a bond between two atoms. BCPs are the minimum point of electron density along the bond path. The bond path is the line of maximum electron density between two nuclear critical points. Bond paths and bcps will be discussed in greater detail in **Section 2.7.1.5**.

Critical points classified as (3,+1) have two positive curvatures and one negative curvature. These are ring critical points (rcps) and are located in the centre of a ring of bonded atoms. The final classification of critical points are (3,+3). These cage critical points (ccps) are a local minimum in the electron density as all three curvatures are positive.

The number and type of critical points present in a single molecule or crystal follows the topological relationship seen in **Equation 2-50**:

$$\mathrm{n_{NCP}} - \mathrm{n_{BCP}} + \mathrm{n_{RCP}} - \mathrm{n_{CCP}} = \begin{cases} 1 & \text{(Isolated Molecules)} \\ 0 & \text{(Infinite Crystals)} \end{cases}$$

Eq. 2-50

In **Figure 2-2**, bond paths, ncps, bcps, rcps and ccps are displayed for cubane.

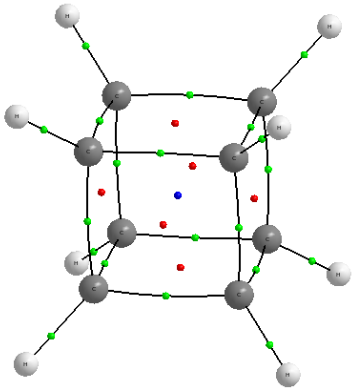

Figure 2-2: *Molecular graph for cubane. Nuclear critical points are shown by the atomic positions. Bond critical points (bcps) shown in green. Ring critical points (rcps) shown in red. Cage critical point (ccp) shown in blue.*

2.7.1 – Properties of the Bond Critical Point

2.7.1.1 – Electron Density

Every bcp will have a value of electron density (ρ). This can be displayed in atomic units (a.u.) or electrons per ångström cubed (e $Å^{-3}$). Generally, when ρ is greater than 0.10 a.u. it suggests a strong covalent bonding interaction. Values of less than 0.10 a.u. are indicative of a weak covalent interaction or a closed shell interaction. There is a strong correlation between the value of ρ and the strength of the interaction i.e. a larger ρ value correlates to a stronger bond.

2.7.1.2 – The Laplacian

Information on bonding can also be gained from the Laplacian, $\nabla^2\rho(r)$, at the bcp. It is typical for a covalent interaction to have a negative $\nabla^2\rho(r)$ value due to the two negative curvatures dominating. Closed shell interactions tend to have a positive $\nabla^2\rho(r)$ due to the depletion of electron density in a closed shell interaction. However, in cases where there is a strongly polar bond (e.g. C-O, C-N, C-F) or a large difference in electron density between two nuclei (e.g. a transition metal (TM) hydride) the $\nabla^2\rho(r)$ value can be either positive or negative. This means care is required when using the Laplacian to analyse certain bonds and other methods in determining the nature of the bonding interaction are used.

2.7.1.3 – Energy Densities

Energy densities are another way of analysing the bonding at a bcp. There are three types of energy density in QTAIM: potential (V(r)), kinetic (G(r)), and total (H(r)).[171] The potential energy density is the average effective potential field experienced by a single electron at point r in a many-particle system. V(r) is always negative and its integration over all space gives the total potential energy of the molecule. The value for V(r) is calculated using the virial theorem which expresses the relationship between, V(r), G(r) and $\nabla^2\rho(r)$ for a stationary state (**Equation 2-51**):

$$\left(\frac{\hbar^2}{4m}\right)\nabla^2\rho(r) = 2G(r) + V(r)$$

Eq. 2-51

where the kinetic energy density, G(r), is always positive and calculated from **Equation 2-52**:

$$G(r) = \frac{\hbar^2}{2m} N \int d\tau' \nabla\Psi^* \cdot \nabla\Psi$$

Eq. 2-52

where $d\tau'$ denotes summation over all spins and integration over all spatial co-ordinates. The total energy density, H(r), is simply the sum of G(r) and V(r) (**Equation 2-53**) and can be integrated over all space to give the total electronic energy of the molecule.

$$H(r) = G(r) + V(r)$$

Eq. 2-53

The total energy density is a negative value for interactions such as covalent bonds. This is caused by the potential energy, V(r), term dominating as there will be concentrated electron density in the region of the bond. The more negative the value of H(r), the stronger the covalent bond. Conversely, a positive H(r) value is indicative of interactions such as ionic bonding. In this case the kinetic energy, G(r), term dominates as there is no concentrated electron density and therefore less potential energy. Energy densities are not reliant on the second derivatives (curvatures: $\lambda_1, \lambda_2, \lambda_3$) of the electron density as the Laplacian seen in **Equations 2-50**. This makes them more reliable in analysing bonding with strong polarity or large disparity in nuclei electron densities.

2.7.1.4 – Bond Ellipticity

The bond ellipticity, ε, is defined in **Equation 2-54**:

$$\varepsilon = \frac{\lambda_1}{\lambda_2} - 1 \ (\text{where } |\lambda_1| \geq |\lambda_2|)$$

Eq. 2-54

The ellipticity can be used as a measure how much the electron density has accumulated in the plane containing the bond path i.e. how cylindrically symmetrical the interaction is. For example, **Figure 2-3** shows selected C-C natural bonding orbitals (NBO, **Section 2.8**) for ethane, ethene and acetylene. In ethane, $\lambda_1 = \lambda_2$ which means ε = 0 indicating a cylindrically symmetrical bond. This is no surprise as the C-C bond in ethane is a purely sigma interaction. Moving to ethene, the π C-C bond has an increased ellipticity of ε = 0.45 as $\lambda_1 \neq \lambda_2$ in this case. In acetylene, which has a bond order of 3, ε = 0 because the two equivalent π bonding interactions in acetylene are orthogonal which makes the overall interaction cylindrical.

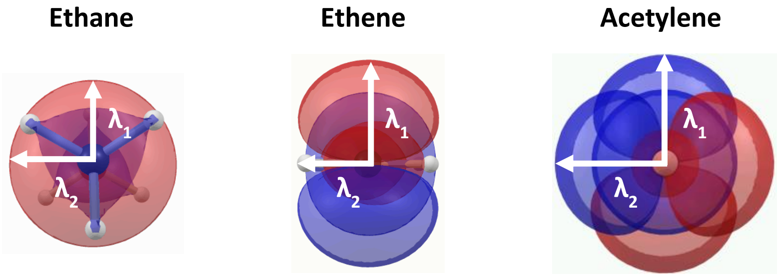

Ethane **Ethene** **Acetylene**

ε = 0 ε = 0.46 ε = 0

Figure 2-3: *Bonding NBOs (see **Section 2.8**) of Ethane, Ethene and Acetylene and λ values corresponding to the ellipticity.*

2.7.1.5 – Bond Paths

As previously stated, the bond path is the line of maximum electron density between two ncps with a bcp sitting at the minimum along this path. The length of the bond path does not necessarily equate to the length of the bond and can, in some cases, exceed it. One of these cases is when the bond is strained, which can be seen in the cubane in example in **Figure 2-2**. Furthermore, the bond path can also be curved if the bond is electron deficient. An example of this can be seen in B_2H_6 (**Figure 2-4**) which is a classic example of a molecule with 3c-2e bonds. The endocyclic curve of the bond path as seen in B_2H_6 is indicative of 3c-2e bonding.

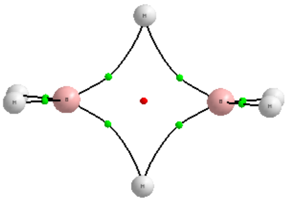

Figure 2-4: *Molecular graph of B_2H_6.*

Chapter 3: The Dehydrocoupling of Secondary Phosphine-Boranes using [Rh($Ph_2P(CH_2)_3PPh_2$)(**η**^{6}-C_6H_5F)][BAr$^F_4$] as a Precatalyst

3.1 – Introduction

3.1.1 – Experimental Background

The Weller group found that reacting [Rh(dppp)(η^6-C_6H_5F)][BAr$^F_4$], **3-1**, (dppp = $Ph_2P(CH_2)_3PPh_2$) with secondary phosphine-boranes H_3B-PPh_2H and H_3B-P^{t}Bu$_2$H in melt conditions would form linear dimers R_2HPBH_2-PR_2BH_3 (R = ^{t}Bu, Ph) (**Scheme 3-1**).[126] Reaction with H_3B-P^{t}Bu$_2$H required more forcing conditions and the reaction would also yield some side products such as boronium cation ([(P^{t}Bu$_2$H)$_2$BH$_2$]$^+$ while reaction with primary phosphine-borane, H_3B-$PPhH_2$ formed polyphosphino-borane.

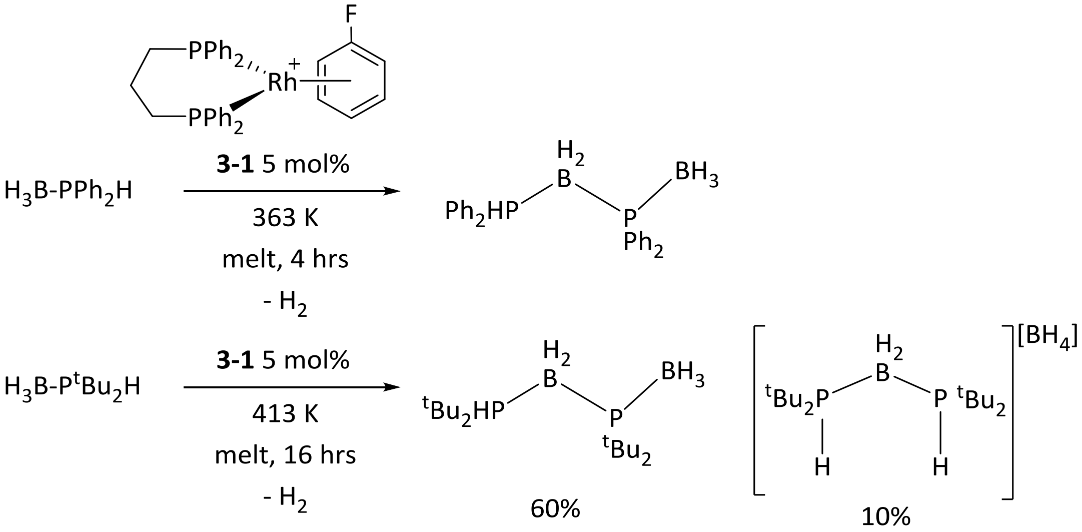

Scheme 3-1: *Reaction of H_3B-PR_2H (R = Ph, ^{t}Bu) with catalyst **3-1** in melt conditions. Adapted from reference No. 126.*

In an attempt to characterise likely intermediate complexes through NMR spectroscopy, the reaction was repeated at 298 K in toluene (**Scheme 3-2**). Reaction with H_3B-P^{t}Bu$_2$H formed phosphine-borane complex [Rh(dppp)(η^2-$H_3BP^tBu_2H$)][BAr$^F_4$], **3-2a$_{tBu}$** after displacing the fluorobenzene ligand. However, reaction with H_3B-PPh_2H formed two complexes. First, by adding 2 equivalents of H_3B-PPh_2H to **3-1**, a phosphido-borate, phosphine-borane complex [Rh(dppp)(σ,η^1-PPh_2BH_3)(η^1-H_3BPPh_2H)[BAr$^F_4$], **3-3**, where P-H activation has occurred was characterised. Complex **3-3** could also be formed in a 1:1 ratio with complex **3-1** upon reaction with one equivalent of H_3B-PPh_2H. Leaving intermediate **3-3** in toluene at 298 K for 4 hrs yields the second characterised complex which contained a phosphido-borate dimer [Rh(dppp)(σ,η^2-$PPh_2BH_2PPh_2BH_3$)][BAr$^F_4$], **3-7**, where the complex has undergone P-H activation, B-H activation and P-B coupling. Directly adding the linear dimer H_3B-PPh_2BH_2-PPh_2H to complex **3-1** also yields **3-7**.

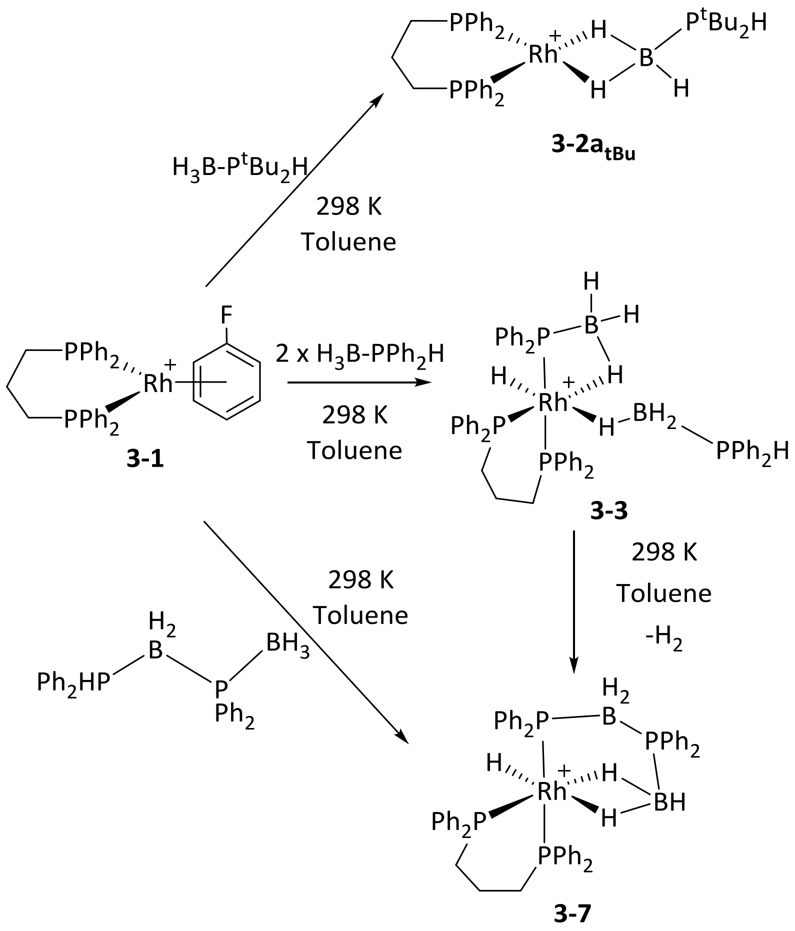

Scheme 3-2: *Reactions of H_3B-PR_2H (R = Ph, ^{t}Bu) and H_3B-PPh_2BH_2-PPh_2H with complex **3-1** in toluene*

Kinetic studies on the transformation of **3-3** to **3-7** suggested that the process occurs *via* intramolecular dehydrocoupling. An Eyring analysis, determined by measuring the rate of this process over a range of temperatures, gave experimental activation barriers of: $\Delta H^\ddagger = 27.4 \pm 0.4$ kcal mol^{-1}, $\Delta S^\ddagger = +13.1 \pm 1.3$ cal mol^{-1} K^{-1}, and $\Delta G(298)^\ddagger = 23.4 \pm 0.7$ kcal mol^{-1}. Reaction with D_3B-PPh_2H results in the incorporation of deuterium into all B-H, P-H and Rh-H positions in complexes **3-3** and **3-7**. The transformation of **3-3** (formed from reaction of D_3B-PPh_2H with **3-1**) to **3-7** occurs with a kinetic isotope effect (KIE) of 1.9 ± 0.1. When **3-3** was formed with D_3B-PPh_2D, the transformation to **3-7** proceeded with a KIE of 2.3 ± 0.2. A further study by the Weller group suggested that B-H activation/reorganisation prior to P-B bond formation could be rate-limiting.[127] Furthermore, **3-3**, does not undergo H/D exchange when under an atmosphere of D_2 indicating the rate determining process occurs before the loss of H_2 in the reaction. Putting intermediate **3-2a$_{tBu}$** in an atmosphere of D_2 sees H/D scrambling in the B-H positions but not the P-H position.

The experimental observations led to the Weller group proposing the mechanism shown in **Scheme 3-3**. One equivalent of H_3B-PPh_2H replaces the fluorobenzene in **3-1** to form **3-2a**. A second equivalent of phosphine-borane then binds and undergoes P-H activation to form **3-3** which has been characterised with NMR spectroscopy. A B-H isomerisation then occurs to form phosphido-borate, phosphine-borane complex **3-4**. Intermediate [Rh(dppp)(σ,η^1-PPh_2BH_3)(H_2BPPh_2H)(H_2)[BAr^F_4] **3-5** is then formed through B-H activation. The rate determining process occurs somewhere between complexes **3-3** and **3-5**. The reaction then proceeds through H_2 loss and P-B coupling to form **3-6** which exhibits a linear dimer bound to the metal through two σ-B-H interactions. It is then predicted that the stoichiometric reaction would form experimentally observed complex **3-7** through P-H activation while the catalytic cycle would see the linear dimer substituted by a phosphine-borane monomer to reform **3-2a**.

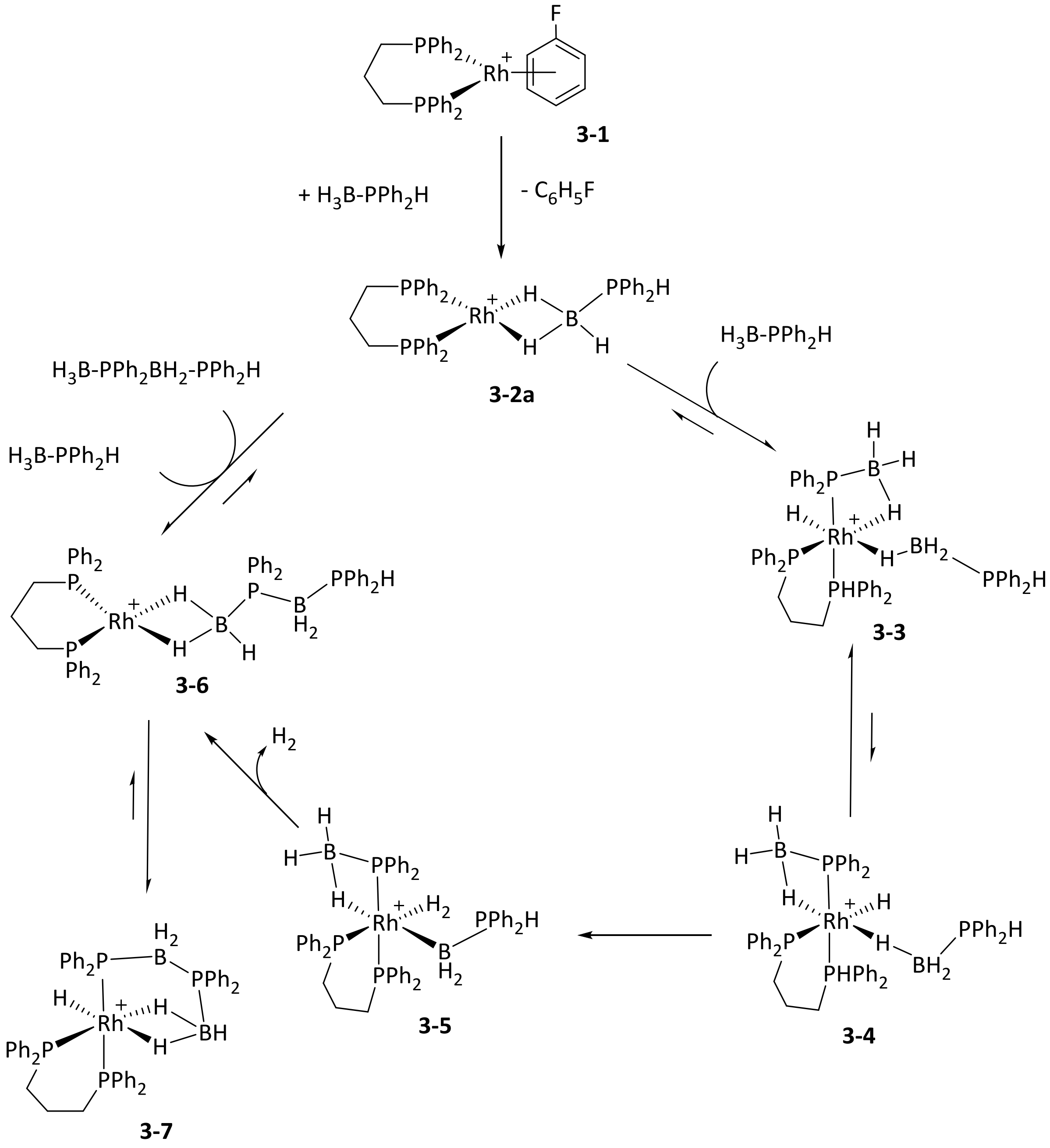

Scheme 3-3: *Proposed mechanism for the dehydrocoupling of H_3B-PPh_2H with catalyst **3-1**. Adapted from reference No 126.*

The DFT investigations conducted as part of this thesis aimed to characterise the dehydrocoupling mechanism with **3-1** and H_3B-PPh_2H. This system was chosen for study due to the availability of experimental activation parameters allowing any calculated barriers to be directly compared to experiment. A benchmarking study was also conducted in order to find the best computational approach to complement the experimental results.

3.1.2 – Computational Details

Calculations were run with Gaussian 03 Revision D.01.[173] Geometry optimisations were performed using the BP86 functional.[143, 144] The Rh and P centres were described with Stuttgart pseudopotentials and associated basis sets[158] (with added d-orbital polarisation on P (ς = 0.387))[174] and 6-31g** basis sets[156, 157] described all other atoms (referred to as BS1). All stationary points were fully characterised via analytical frequency calculations as either minima (all positive frequencies) or transition states (one imaginary frequency). IRC (intrinsic reaction co-ordinate) calculations and subsequent geometry optimisations were used to confirm the minima linked by each transition state. Frequency calculations also provided a free energy in the gas phase, computed at 298.15 K and 1 atm. Energies reported in the text are based on the gas-phase relative energies and incorporate a correction for dispersion effects using Grimme's D3 parameter set[164] with Becke-Johnson damping[165] as well as solvation (PCM approach)[161] in toluene. Both dispersion and solvation corrections were run as single points with Gaussian 09 Revision D.01.[175]

Throughout the chapter, the energy for $[Rh(dppp)(\eta^6\text{-}C_6H_5F)]^+$, **3-1**, and the phosphine-borane reactants are set to 0.0 kcal mol^{-1}.

3.2 – The Dehydrocoupling Mechanism of H_3B-PPh_2H with [Rh(dppp)(η^6-C_6H_5F)]$^+$

3.2.1 – Comparing the Molecular and Computed Structures of Complexes 3-3 and 3-7

To test whether the chosen computational model was a good fit for the system being studied, the computed structures for intermediate **3-3** and product **3-7** (**Figure 3-1**) were compared with available experimental structures. However, crystallographic data was not available for **3-3** and **3-7** so the optimised structures were compared with analogous complexes [Rh(dppp)(σ,η^1-PR_2BH_3)(η^1-H_3BPR_2H)][BAr$^F{}_4$] **3-3$_R$** and [Rh(dppp)(σ,η^1-$PR_2BH_2PR_2BH_3$)(H)][BAr$^F{}_4$] **3-7$_R$** (R = 3,5-$(CF_3)_2(C_6H_3)$).[127] The results displayed in **Table 3-1** show that the computed structures are in reasonable agreement with the available experimental molecular structures. For complex **3-3** the P^3-B^1 distance of 1.93 Å is similar to other published phosphido-borate species such as [Ti(Cp)$_2$(σ,η^1-PPh_2BH_3)] and [Fe(CO)(Cp)(PPh_2BH_3)] by Manners *et al.*[124, 176] who report a P-B distance of 1.951(4) and 1.892(3) Å respectively.

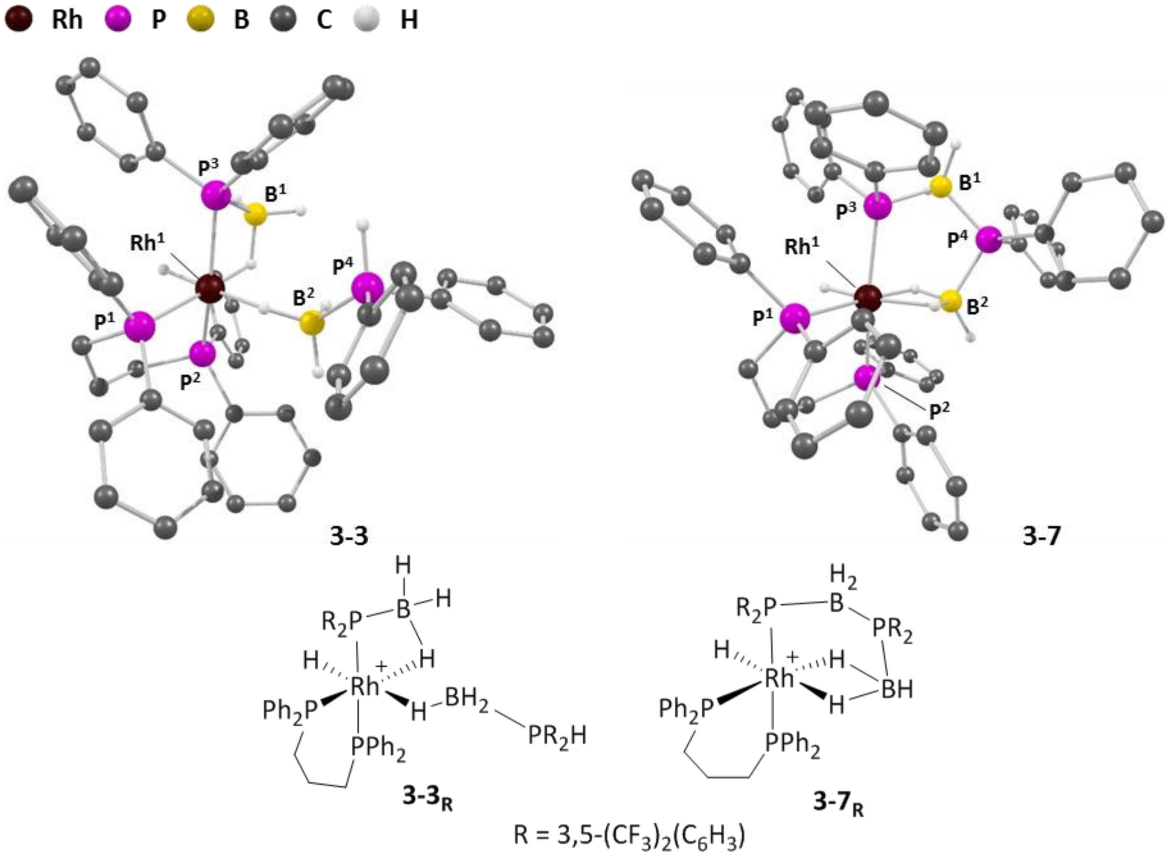

Figure 3-1: *Optimised structures of **3-3** and **3-7** and structures of **3-3$_R$** and **3-7$_R$**. Colour scheme shown in the legend above is adopted throughout the chapter.*

Key Bonds / Angles	3-3 Computed (Å / °)	 Experiment (Å / °)	3-7 Computed (Å / °)	 Experiment (Å / °)
Rh^1–P^1	2.33	2.278(10)	2.39	2.3241(11)
Rh^1–P^2	2.40	2.3163(9)	2.31	2.2650(11)
Rh^1–P^3	2.37	2.3045(10)	2.46	2.3925(10)
P^3–B^1	1.93	1.913(4)	1.99	--
P^4–B^2	1.96	1.918(4)	1.97	--
$Rh^1\cdots B^1$	2.52	2.515(4)	3.67	--
$Rh^1\cdots B^2$	2.79	2.740(4)	2.26	2.280(5)
Rh^1-P^3-B^1	70.93	72.54(14)	110.19	110.88(15)
Rh^1-B^2-P^4	128.15	121.3(2)	120.10	107.5(2)

Table 3-1: *Comparison between computed structures **3-3** and **3-7** with molecular structures **3-3$_R$** and **3-7$_R$**.*

3.2.2 – The Computed Dehydrocoupling Mechanism

The proposed pathway (**Scheme 3-4**) begins with the substitution of the η^6-bound fluorobenzene in **3-1** with one equivalent of H_3B-PPh_2H to form phosphine-borane complex, **3-2a** (G = -3.0 kcal mol^{-1}, **Figure 3-2**). The phosphine-borane binds in an η^2-fashion to the Rh centre with Rh-H bond lengths of 1.85 Å and elongated B-H bond lengths of 1.29 Å (compared to a calculated B-H bond length of 1.22 Å in free H_3B-PPh_2H). A second equivalent of H_3B-PPh_2H can then bind to form a bis-phosphine-borane complex, **3-2b** (G = -19.1 kcal mol^{-1}), where both phosphine-boranes are η^1-bound to the metal. Complex **3-2b** is more stable than **3-2a** by 16.1 kcal mol^{-1}. This suggests that the reaction will proceed from the bis-phosphine-borane complex, **3-2b** over the mono-phosphine-borane complex **3-2a**. Dehydrocoupling pathways from complex **3-2a** were investigated but no P-H activation transition state could be characterised.

From **3-2b**, the reaction proceeds through a facile step involving P-H activation and Rh-P bond formation *via* **3-TS(2b-3)** (G = -19.0 kcal mol^{-1}) to form the experimentally characterised complex, **3-3** (G = -36.9 kcal mol^{-1}). During this process the P···H distance increases from 1.43 Å in **3-2b**, to 1.72 Å in **3-TS(2b-3)** and finally 2.67 Å in **3-3** as the Rh···H distance decreases from 2.99 Å to 1.66 Å to 1.55 Å. The formed Rh-P bond in **3-3** has a length of 2.37 Å having previously had a distance of 2.99 Å in **3-2b**.

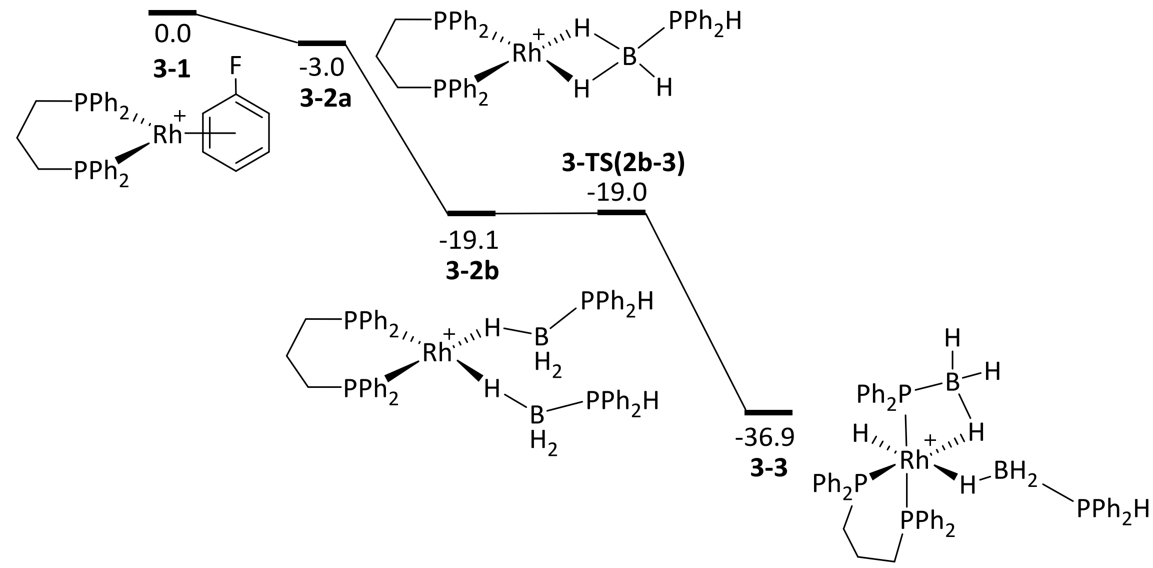

Scheme 3-4: *Reaction scheme for the formation of complex **3-3** from **3-1**. Free energies at BP86(D3BJ), CH_2Cl_2/BS1*

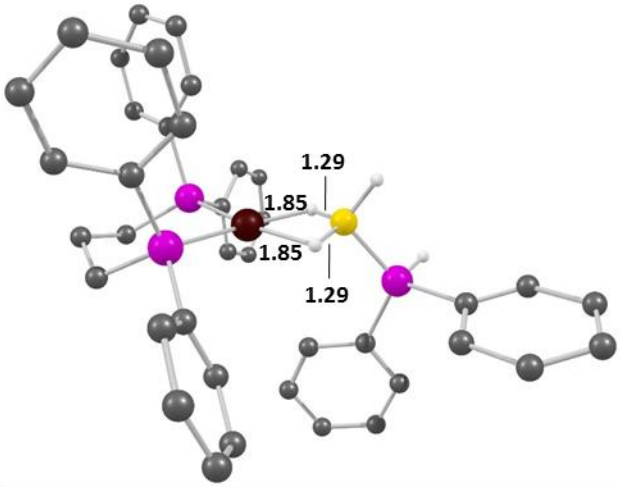

3-2a
G = -3.0 kcal mol^{-1}

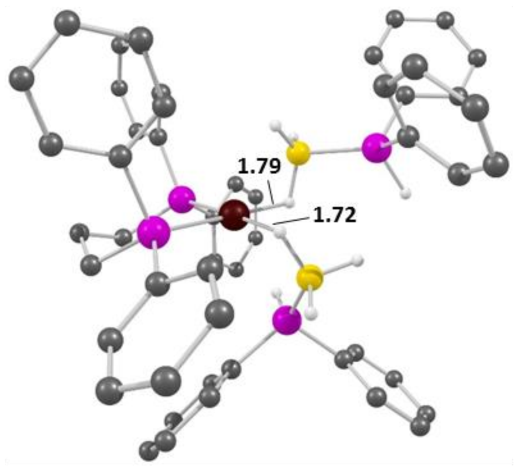

3-2b
G = -19.1 kcal mol^{-1}

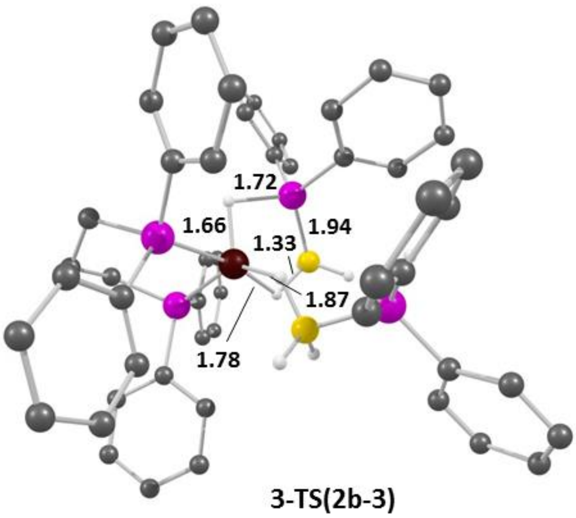

3-TS(2b-3)
G = -19.0 kcal mol^{-1}

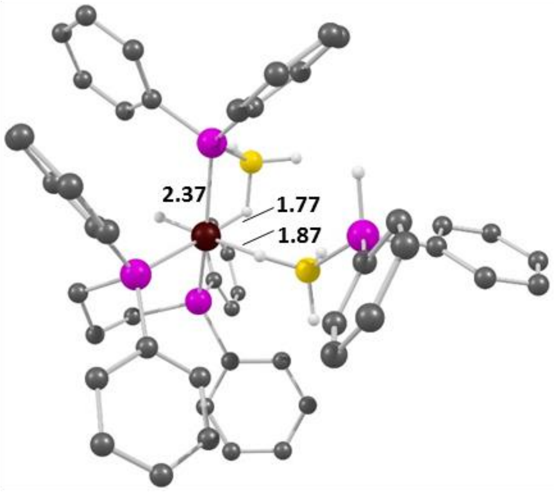

3-3
G = -36.9 kcal mol^{-1}

Figure 3-2: *Optimised structures of the H_3B-PPh_2H binding and P-H activation towards the formation of **3-3** including key distances in Å. Hydrogens bonded to carbon omitted for clarity.*

In intermediate **3-3** the phosphido-borate B-H σ-interaction is *trans* to one of the chelating phosphines. However, it can undergo an isomerisation *via* **3-TS(3-4)** (G = -18.1 kcal mol^{-1}, **Figure 3-3**, **Scheme 3-5**) where the boron migrates to the *cis*-hydride to form a σ-interaction *trans* to the phosphine-borane, **3-4** (G= -28.8 kcal mol^{-1}). At **3-TS(3-4)** the initial B-H bond has broken with a B···H distance of 2.15 Å with the new B···H interaction having a distance of 1.75 Å. From **3-4**, rotation around the phosphine-borane B-H bond occurs *via* **3-TS(4-4')** (G = -25.5 kcal mol^{-1}) to form lower energy intermediate **3-4'** (G =-31.6 kcal mol^{-1}). This rotation changes the torsion angle between Rh-H-B-P from 117.73 ° to -171.95 ° at **3-4'**.

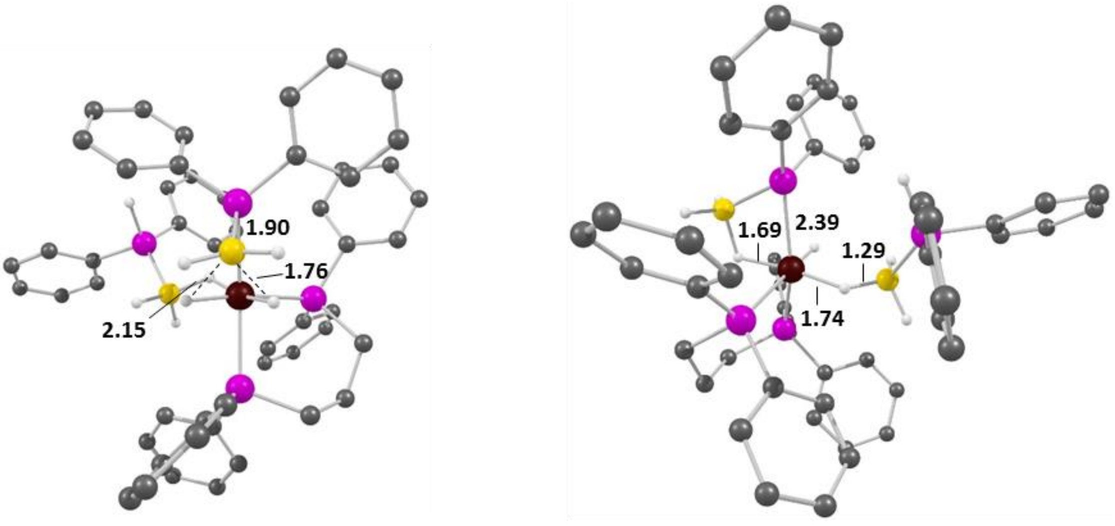

3-TS(3-4)
G = -18.1 kcal mol^{-1}

3-4
G = -28.8 kcal mol^{-1}

Figure 3-3: *Optimised structures of the B-H activation and rearrangement towards the formation of **3-4'** including key distances in Å. Hydrogens bonded to carbon omitted for clarity.*

Proceeding from intermediate, **3-4'**, B-P bond formation between the boron of the phosphine-borane and the metal-bound phosphorus of the phosphido-borate occurs through **3-TS(4'-7')1** (G = -16.2 kcal mol^{-1}, **Figure 3-4**) to form **3-INT(4'-7')1**. This process involves B-H activation with the breaking of the phosphine-borane B-H bond (B···H distance increasing from 1.31 Å to 4.90 Å), the breaking of the phosphido-borate Rh-P bond (Rh···P distance increasing from 2.37 Å to 3.85 Å), and the formation of the B-P bond (B···P distance decreasing from 3.34 Å to 1.96 Å) as well as the formation of a P-H σ-interaction (from the phosphine-borane) with the metal to afford complex **3-INT(4'-7')1** (G = -25.9 kcal mol^{-1}). Complex **3-INT(4'-7')1** contains a phosphine-borane dimer which is bound to the rhodium centre through a B-H σ-interaction and a P-H σ-interaction.

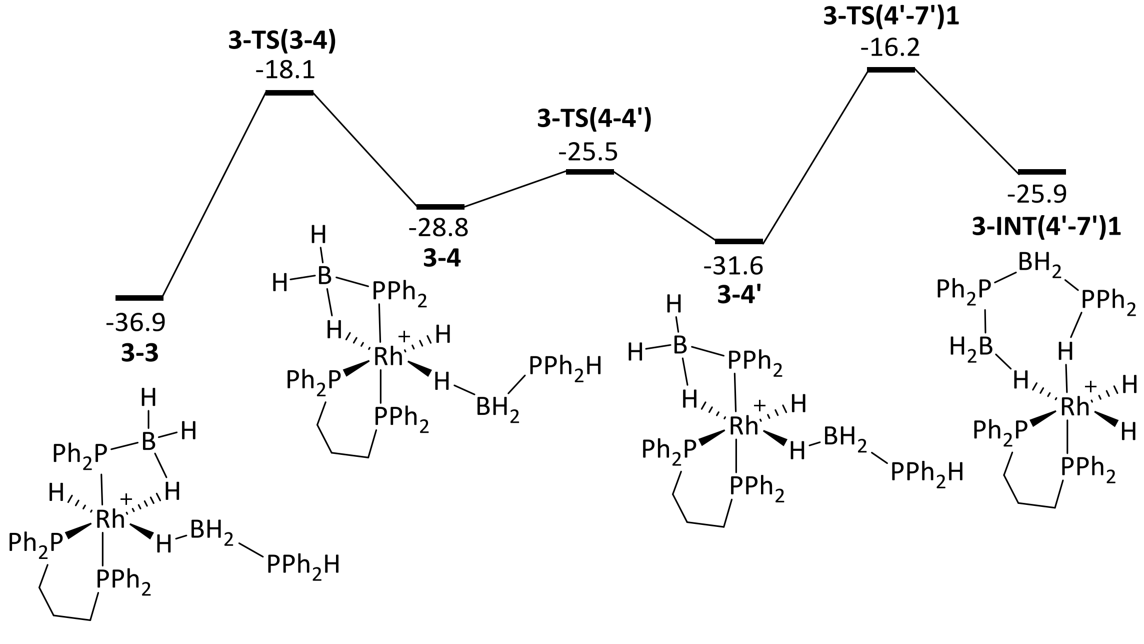

Scheme 3-5*: Reaction scheme for the B-H activation and P-B coupling towards the formation of complex **3-INT(4'-7')1** from **3-3**. Free energies at BP86(D3BJ), CH_2Cl_2/BS1*

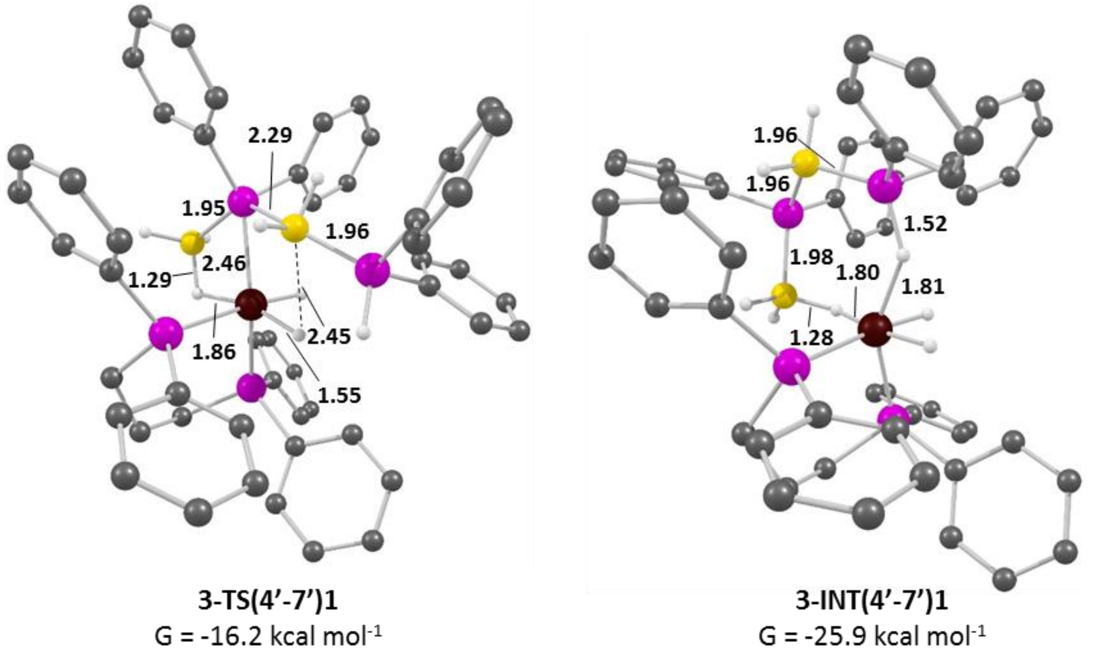

3-TS(4'-7')1
G = -16.2 kcal mol^{-1}

3-INT(4'-7')1
G = -25.9 kcal mol^{-1}

Figure 3-4: *Optimised structures of B-P coupling step towards the formation of **3-INT(4'-7')1** including key distances in Å. Hydrogens bonded to carbon omitted for clarity.*

In **Scheme 3-6**, intermediate **3-INT(4'-7')1** undergoes σ-complex assisted metathesis (σ-CAM)[177] of the P-H σ-interaction *via* **3-TS(4'-7')2** (G = -28.4 kcal mol^{-1}) to form dihydrogen intermediate **3-INT(4'-7')2** (G = -35.7 kcal mol^{-1}, **Figure 3-5**). The P···H distance increases from 1.52 Å in **3-INT(4'-7')1** to 2.87 Å in **3-INT(4'-7')2** (G = -35.7 kcal mol^{-1}) as the hydride goes on to form an H_2 ligand with the H···H distance decreasing from 1.99 Å to 0.91 Å in **3-INT(4'-7')2**. The energy of

3-TS(4'-7')2 is lower than that of preceding intermediate **3-INT(4'-7')1** making the process seem 'barrierless'. This is an effect caused by the zero point energy correction for **3-TS(4'-7')2**.

The H_2 ligand in **3-INT(4'-7')2** then dissociates through **3-TS(4'-7')3** (G = -22.9 kcal mol^{-1}) to afford **3-7'** (G = -17.6 kcal mol^{-1}). The complex can then rearrange to form **3-7'** (G = -41.2 kcal mol^{-1}) which is the product of the stoichiometric reaction.

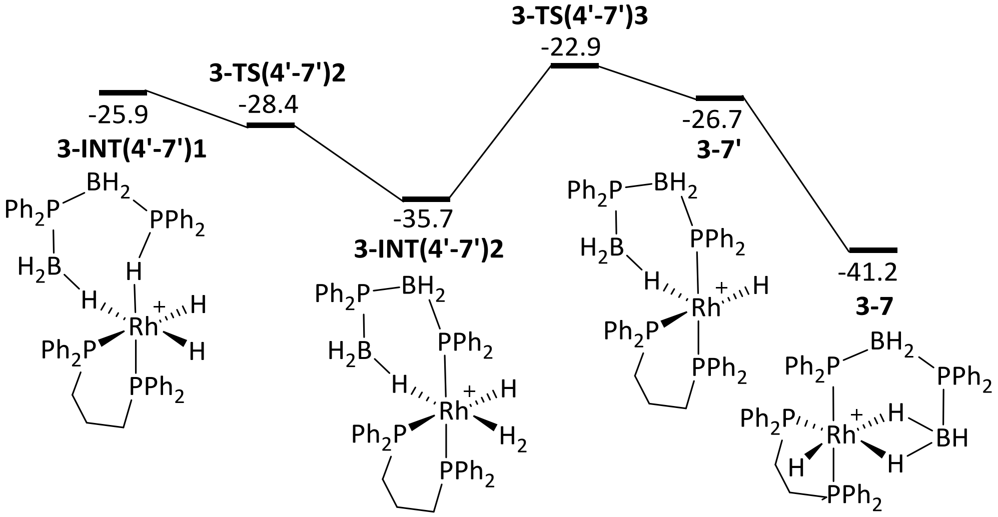

Scheme 3-6: *Reaction scheme for P-H activation and H_2 dissociation towards the formation of complex **3-7** from **3-INT(4'-7')1**. Free energies at BP86(D3BJ), CH_2Cl_2/BS1*

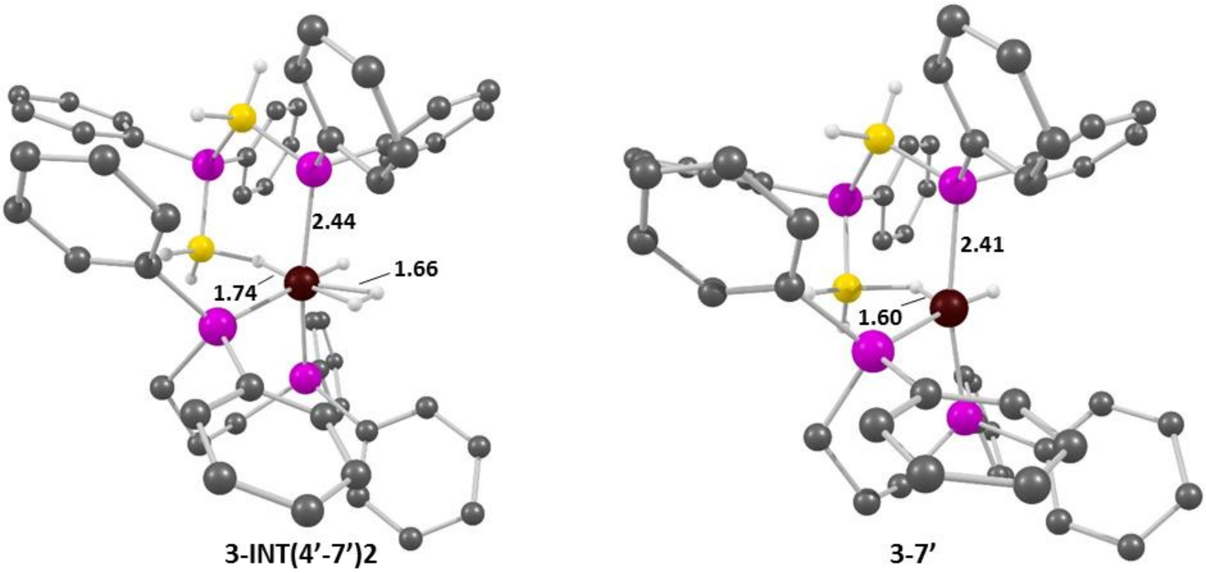

3-INT(4’-7’)2
G = -35.7 kcal mol^{-1}

3-7’
G = -26.7 kcal mol^{-1}

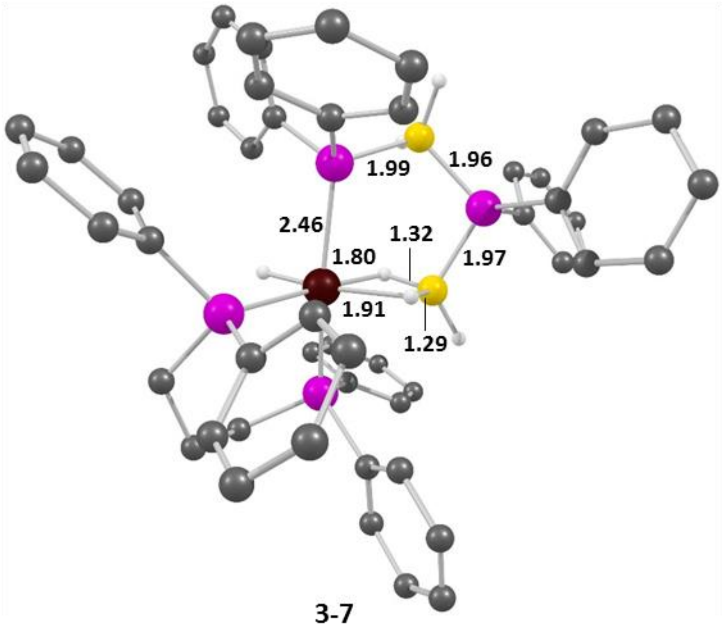

3-7
G = -41.2 kcal mol^{-1}

Figure 3-4: *Optimised structures of the P-H activation and H_2 dissociation towards the formation of* ***3-7*** *including key distances in Å. Hydrogens bonded to carbon omitted for clarity.*

The full proposed reaction pathway, shown in **Scheme 3-7**, coincides with the available experimental data. For example, the lowest energy intermediate, **3-3** and product **3-7**, are the two complexes stable enough to be characterised by NMR spectroscopy. Experimental studies predicted the rate-determining step to involve B-H activation/rearrangement before B-P coupling. In the computed pathway, the rate determining process arises from the highest energy transition state, **3-TS(4’-7’)1** (P-B coupling). However, this still coincides with experiment as B-H activation is involved in the P-B coupling process as well as in a preceding step *via* **3-TS(3-4)** which falls in between **3-3** and **3-TS(4’-7’)1**. The rate determining process occurs with an overall free energy barrier of 20.7 kcal mol^{-1} and an overall enthalpy barrier of 19.9 kcal mol^{-1}. KIE values of 2.98 and 3.07 were calculated from the computed free energy barrier for reaction with D_3B-PPh_2H and D_3B-PPh_2D respectively which also agrees with the experimental values.

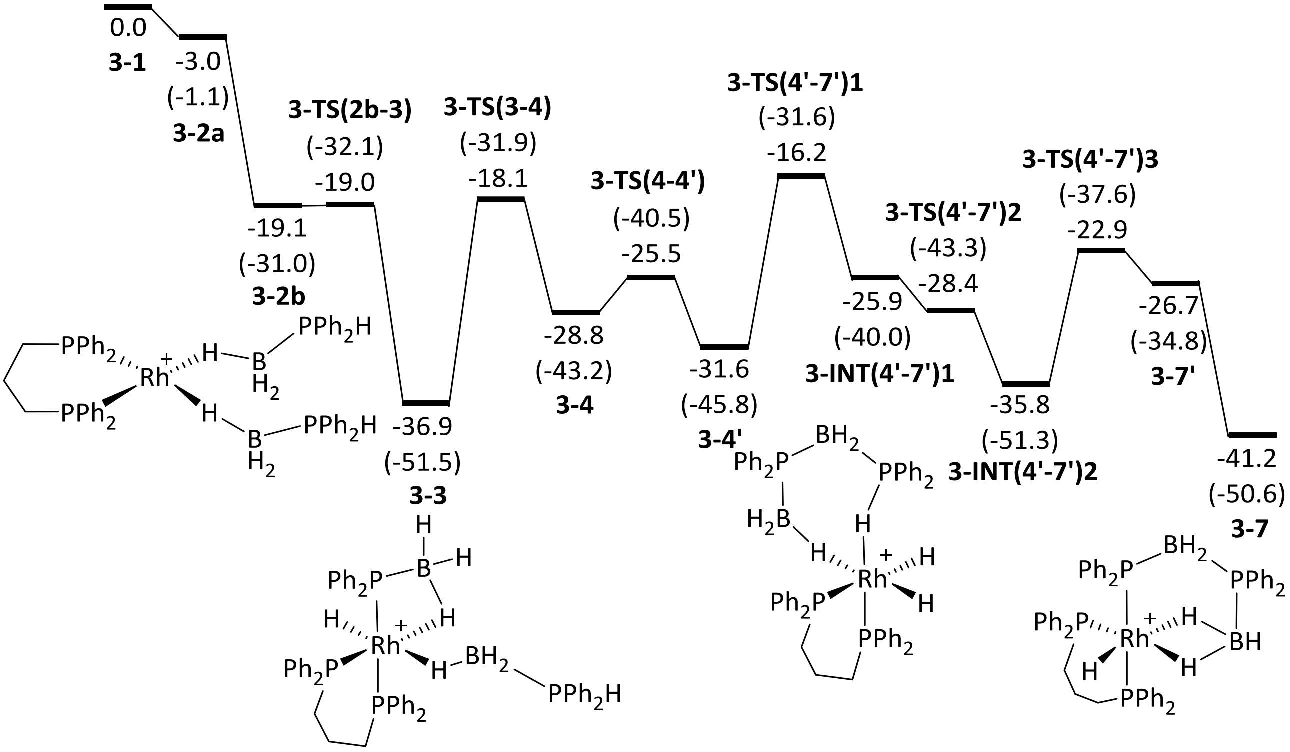

Scheme 3-7*: Reaction scheme for the formation of complex* ***3-7*** *from* ***3-1****. Free energies (enthalpies) at BP86(D3BJ), CH_2Cl_2/BS1*

Comparing the calculated free energy and enthalpy values with the experimental activation parameters (**Table 3-2**) shows that the free energy barrier is underestimated by 2.7 kcal mol^{-1} and the enthalpy barrier is underestimated by 7.5 kcal mol^{-1}. Furthermore, our calculations predict an entropy value with the incorrect sign compared to the experimental value. This is most likely due to the chemical model not capturing all the entropic contributions that occur in the experimental system. For example, due to the calculations being on the isolated molecule in the gas phase, contributions from solvent rearrangement will not be captured by the calculated entropy value. Having established this error in the entropy, all free energy values will also contain an error due to the free energies reliance on the entropy (**Equation 3-1**).

	Computed	**Eyring Analysis**
ΔH	19.9 kcal mol^{-1}	27.4 ± 0.4 kcal mol^{-1}
ΔG	20.7 kcal mol^{-1}	23.4 ± 0.7 kcal mol^{-1}
ΔS	-4.4 cal mol^{-1} K^{-1}	+13.1 ± 1.3 cal mol^{-1} K^{-1}

Table 3-2: *Comparison of computed barriers against the experimental Eyring analysis. Entropy value calculation using* ***Eq. 3-1*** *at 298 K*

$$\Delta G = \Delta H - (T\Delta S)$$

Eq. 3-1

Therefore, in the following benchmarking study, the enthalpy barrier was used as the benchmark due to the enthalpy not being affected by the known error in the entropy.

3.3 – Basis Set and Functional Testing on the Dehydrocoupling Mechanism

3.3.1 – Basis Set Testing on the Dehydrocoupling Mechanism

To test that the calculated free energies and enthalpies are not basis set dependent, a range of Pople basis sets for the smaller atoms (B, C, H) were tested.[156, 157, 178, 179] For these calculations Rh and P were described with Stuttgart pseudo-potentials with added d-orbital polarisation on P (ς = 0.387).[158, 174] These calculations were also run with added f-orbital polarisation on Rh (ς = 1.350)[174] for comparison. Furthermore, calculations with Ahlrich basis sets on all atoms were tested.[180, 181] The BP86 functional was used throughout, corrections for solvent and dispersion were not included.

The results in **Figure 3-6** show that the barriers of the proposed mechanism are not basis-set dependent and always underestimate the experimental value. The Pople basis sets tested (blue) only show a 0.6 kcal mol^{-1} deviation from the smallest (6-31g) to the largest (6-311g++**) basis set. The effect of adding f-orbital polarisation (ς = 1.350) to the Rh atom (red) is minimal. The agreement relative to the experimental enthalpy barrier of 27.4 kcal mol^{-1} are very similar, with the deviation between the smallest and largest basis sets tested being 0.5 kcal mol^{-1}. The same trend was exhibited with the Ahlrich basis sets (green) with the largest deviation in calculated enthalpy being 0.2 kcal mol^{-1} while displaying similar accuracy to the other basis sets. This study showed that using the basis set approach used in **Section 3.2** was sufficient as the free energies and enthalpies do not fluctuate greatly depending on the basis set used.

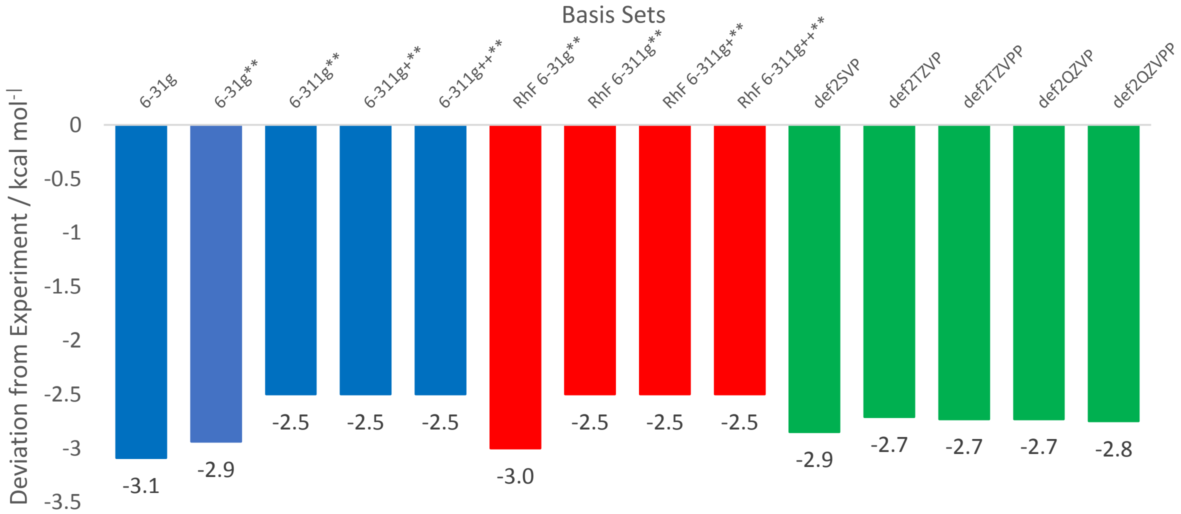

Figure 3-6: *Graph displaying the deviation from the experimental enthalpy of activation (27.4 kcal mol^{-1}) with a range of basis sets*

3.3.2 – Functional Testing on the Dehydrocoupling Mechanism

Single point and optimisation calculations were also run to test a range of DFT functionals. DFT functionals PBE[146], TPSS[151], B3LYP[147], PBE0[149], M06[166], B97D[167], and ωB97XD[152] were compared with the standard basis set approach used in **Section 3.2.** Corrections for solvent and dispersion (when required) were used throughout.

3.3.2.1 – Functional Testing with Single Point Calculations on the Dehydrocoupling Mechanism

The results of the single point calculations on the BP86 optimised geometries are shown in **Figure 3-7**. In terms of the enthalpy (blue), GGA functionals BP86 and PBE both underestimate the experimental value by 7.5 and 6.6 kcal mol^{-1} respectively. The agreement with experiment improves when moving to meta-GGA functionals such as TPSS which underestimates the enthalpy by 4.7 kcal mol^{-1}. An improvement is also seen with hybrid functionals PBE0 and B3LYP, with B3LYP only underestimating the experimental value by 0.7 kcal mol^{-1}. Functionals which incorporate a treatment of dispersion (M06, B97D, *ω*B97XD) were, in general, in better agreement than the previous functionals tested. The most accurate functional tested was range-separated functional *ω*B97XD which only underestimated the experimental enthalpy barrier of 27.4 kcal mol^{-1} by 0.5 kcal mol^{-1}

In terms of the free energy barrier (red), functionals such as TPSS and PBE0 appear to have a good agreement with the experimental free energy. However, due to the established error in calculating the entropy, this agreement is due to a cancellation of errors.

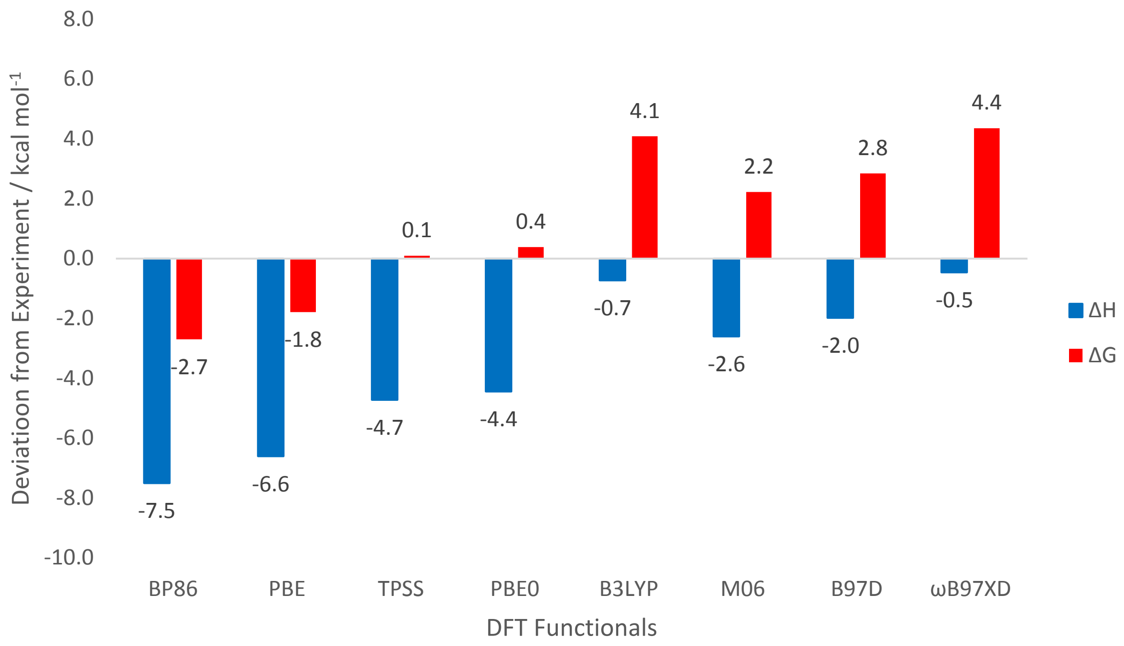

Figure 3-7: *Graph displaying the deviation from the experimental free enthalpy (27.4 kcal mol^{-1}, blue) and free energy (23.4 kcal mol^{-1}, red) of activation with a range of DFT functionals*

3.3.2.2 – Functional Testing with Optimisation Calculations on the Dehydrocoupling Mechanism

The optimisation calculations displayed in **Figure 3-8**, show the same trends as the single point calculations discussed previously. The hybrid functionals PBE0 and B3LYP still underestimate the enthalpy but improve in accuracy compared to the GGA BP86 value. The functionals that incorporate a treatment of dispersion still, in general, have better accuracy compared to the experimental value. However, B97D and *ω*B97XD now overestimate the enthalpy by 1.4 and 2.1 kcal mol^{-1} respectively. B3LYP is the best performing functional with a deviation of 0.2 kcal mol^{-1} from the experimental enthalpy of 27.4 kcal mol^{-1}. In terms of the free energy, TPSS and PBE0 appear to be in the best agreement with the experimental activation parameters. However this is due to a cancellation of errors due to the established entropy error.

Overall, the difference in values between the single point and optimised calculations are small for each functional especially when the extra computational time needed for full optimisation calculations is considered. Therefore, it was concluded that the most efficient computational approach for the dehydrocoupling mechanism would be to optimise with the BP86 functional and then run a single point calculation with the ωB97XD functional. The dehydrocoupling mechanism was not functional dependent and **3-TS4** remained the highest barrier compared to **3-TS2**.

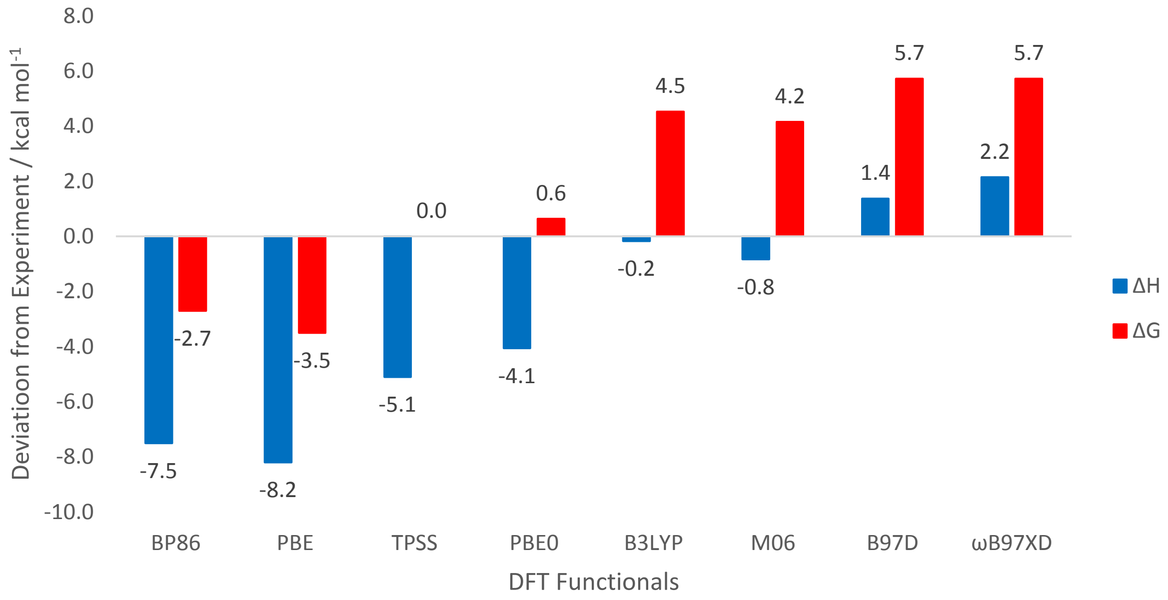

Figure 3-8: *Graph displaying the deviation from the experimental free enthalpy (27.4 kcal mol^{-1}, blue) and free energy (23.4 kcal mol^{-1}, red) of activation with a range of DFT functionals*

3.3.3 – Summary of Basis Set and Functional Testing

The basis set and functional testing concluded that the best computational approach would be to, at first, optimise with BP86, Stuttgart pseudopotentials on Rh and P (Ϛ = 0.387) and the 6-31g** basis set to describe B, C and H. This would be followed by a single calculation using ωB97XD and the same basis set approach including the correction for solvent. This would give the best compromise between agreement towards the experimental activation parameters and computational expense. The predicted pathway is unchanged but the energies are now different as can be seen in **Scheme 3-8**. Intermediate **3-3** (G = -37.3 kcal mol^{-1}) and product **3-7** (G = -47.8 kcal mol^{-1}) remain the lowest in free energy whilst the rate determining process remains between complex **3-3** and the P-B coupling step *via* **3-TS(4’-7’)1** (G = -10.3 kcal mol^{-1}) with an overall free energy barrier of 27.0 kcal mol^{-1} and an enthalpy barrier of 27.3 kcal mol^{-1}. The KIE values from the calculated free energy barriers also remain consistent with KIEs of 2.93 computed for reaction with $D_3B\text{-}PPh_2H$ and 3.01 for $D_3B\text{-}PPh_2D$.

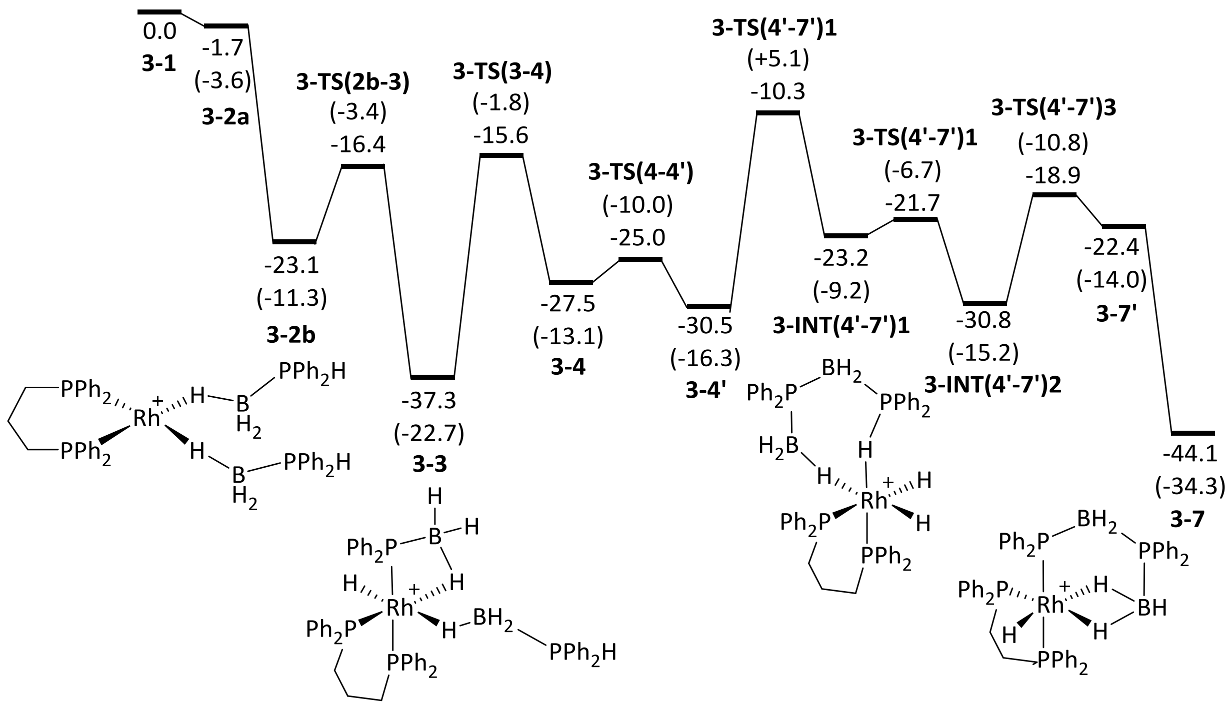

Scheme 3-8: *Reaction scheme for the formation of complex* ***3-7*** *from* ***3-1****. Free energies (enthalpies) at ωB97XD(toluene)/BS1 // BP86(D3BJ,toluene)/BS1*

3.6 – Conclusions

In conclusion, the stoichiometric dehydrocoupling of H_3B-PPh_2H with [Rh(dppp)(η^6-C_6H_5F)][BAr^F_4] to form [Rh(dppp)(σ,η^2-$PPh_2BH_2PPh_2BH_3$)][BAr^F_4], **3-7** was developed by the Weller group. An Eyring analysis predicted a free energy barrier of 23.4 ± 0.7 kcal mol^{-1} and an enthalpy barrier of 27.4 ± 0.4 kcal mol^{-1}.

The calculated pathway (**Section 3.2, Scheme 3-7**) predicts the reaction would proceed through the formation of [Rh(dppp)(σ,η^1-PPh_2BH_3)(η^1-H_3BPPh_2H)[BAr^F_4] **3-3** from **3-1**. B-H activation and B-P rotation precede the B-P coupling step *via* **3-TS(4’-7’)1** which also involves B-H activation to form **3-INT(4’-7’)1**. This is the rate limiting process with a free energy barrier of 20.7 kcal mol^{-1} and an enthalpy barrier of 19.9 kcal mol^{-1} at the BP86(D3-toluene)/SDDALL(Rh, P), 6-31g** level of theory. Product **3-7** is then formed through P-H activation and H_2 dissociation. The computed pathway is consistent with the experimental KIE data.

A functional and basis set testing study (**Section 3.3**) was undertaken in order to find the computational approach which would agree best with the experimental activation parameters. It was concluded that the most efficient computational approach for agreement with experiment was ωB97XD(toluene)/SDDALL(Rh, P), 6-31g**//BP86(D3BJ,toluene)/SDDALL(Rh, P), 6-31g**. The use of this approach predicts a free energy barrier of 27.0 kcal mol^{-1} and an enthalpy barrier of 27.3 kcal mol^{-1}.

Chapter 4: The Reactions of Secondary Phosphine-Boranes with $[Rh(Me)(CH_2Cl_2)(PMe_3)(\eta\text{-}Cp^*)][BAr^F_4]$

4.1 – Introduction

4.1.1 – Experimental Studies

This chapter details a study where experimental and computational techniques were used in parallel to investigate the reaction of phosphine-boranes with $[Rh(CH_2Cl_2)(Me)(PMe_3)(Cp^*)][BAr^F_4]$, **4-1** (see **Scheme 4-1**).[128] The experimental work was conducted by the Weller group from the University of Oxford. It was found that the catalytic reaction with primary phosphine borane, $H_3B\text{-}PPhH_2$, formed polyphosphinoborane $(H_2B\text{-}PPhH)_n$ whilst reaction with secondary phosphine borane $H_3B\text{-}PPh_2H$ would only yield the linear dimer, $H_3B\text{-}PPh_2BH_2\text{-}PPh_2H$. To further investigate the role of the metal fragment in the dehydrocoupling/dehydropolymerisation process, the stoichiometric reactivity was studied (**Scheme 4-2**). The stoichiometric reaction of **4-1** with $H_3B\text{-}PPh_2H$ resulted in the rapid formation of **4-2$_{Ph}$** which is a phosphido-borane complex with a βB-H-agostic interaction where the phosphine-borane has undergone a P-H activation step and methane loss is observed. The reaction was repeated with different phosphine-boranes: $H_3B\text{-}PCy_2H$ and $H_3B\text{-}P^tBu_2H$. Reaction with $H_3B\text{-}PCy_2H$ formed **4-2$_{Cy}$** within minutes. However, reaction with $H_3B\text{-}P^tBu_2H$ quickly formed a dark red intermediate before yielding complex **4-3$_{tBu}$** after two hours. In product **4-3$_{tBu}$** the phosphine-borane ligand appears to have undergone a further B-H activation step as well as B-P coupling with the PMe_3 group.

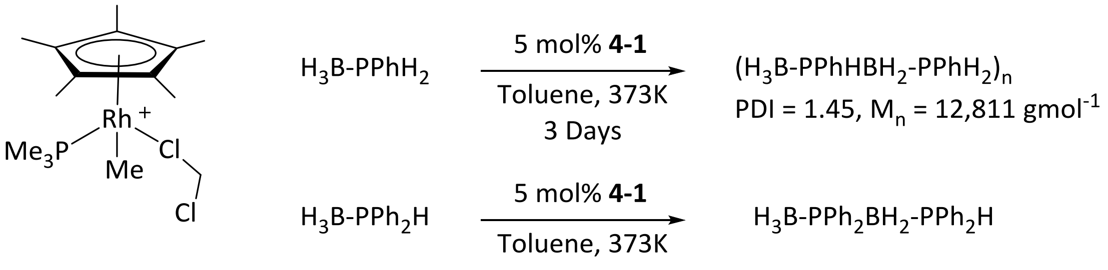

4-1

$$H_3B\text{-}PPhH_2 \xrightarrow[\text{Toluene, 373K}\ \text{3 Days}]{\text{5 mol\% }\mathbf{4\text{-}1}} (H_3B\text{-}PPhHBH_2\text{-}PPhH_2)_n \quad \text{PDI} = 1.45,\ M_n = 12{,}811\ \text{gmol}^{-1}$$

$$H_3B\text{-}PPh_2H \xrightarrow[\text{Toluene, 373K}\ \text{3 Days}]{\text{5 mol\% }\mathbf{4\text{-}1}} H_3B\text{-}PPh_2BH_2\text{-}PPh_2H$$

***Scheme 4-1**: Catalytic reactivity of $H_3B\text{-}PPhH_2$ and $H_3B\text{-}PPh_2H$ with **4-1**.*

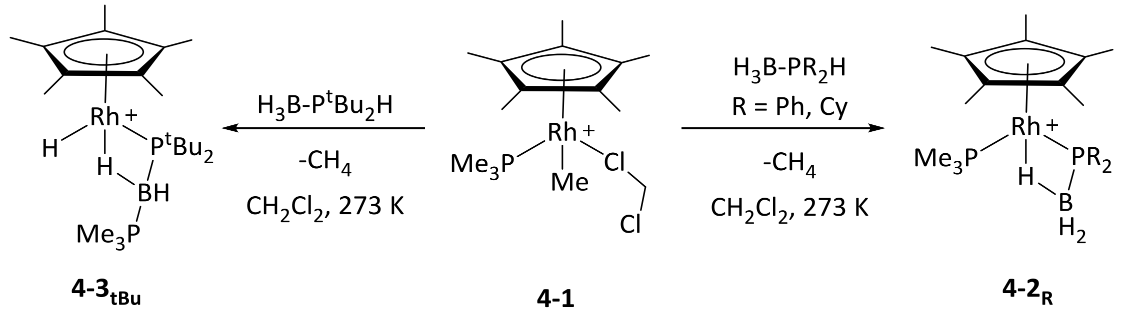

***Scheme 4-2**: Stoichiometric reaction of H_3B-P^tBu_2H and H_3P-PPh_2H with **4-1**.*

A low temperature NMR spectroscopy study was performed in order to identify the dark red intermediate towards the formation of B-P coupled product, **4-3$_{tBu}$** (**Scheme 4-3**). It was found that ligand exchange of CH_2Cl_2 and H_3B-P^tBu_2H occurred at 193 K to form a yellow solution containing **4-4$_{tBu}$.** At 233 K the loss of CH_4 is observed. Complex **4-5$_{tBu}$** formed dark red crystals, however, the crystal structure was highly disordered. The ^{11}B NMR shift of **4-5$_{tBu}$** suggested the molecular structure to be either an αB-H agostic boryl complex, **4-5$_{tBu}$**, or a hydrido base-stabilised borylene isomer, **4-5'$_{tBu}$**. Warming the reaction to 293 K over two hours resulted in the formation of the product, **4-3$_{tBu}$**. The low temperature NMR studies were not repeated for the formation of **4-2$_{Ph}$** and **4-2$_{Cy}$** as the reaction proceeded too quickly for study.

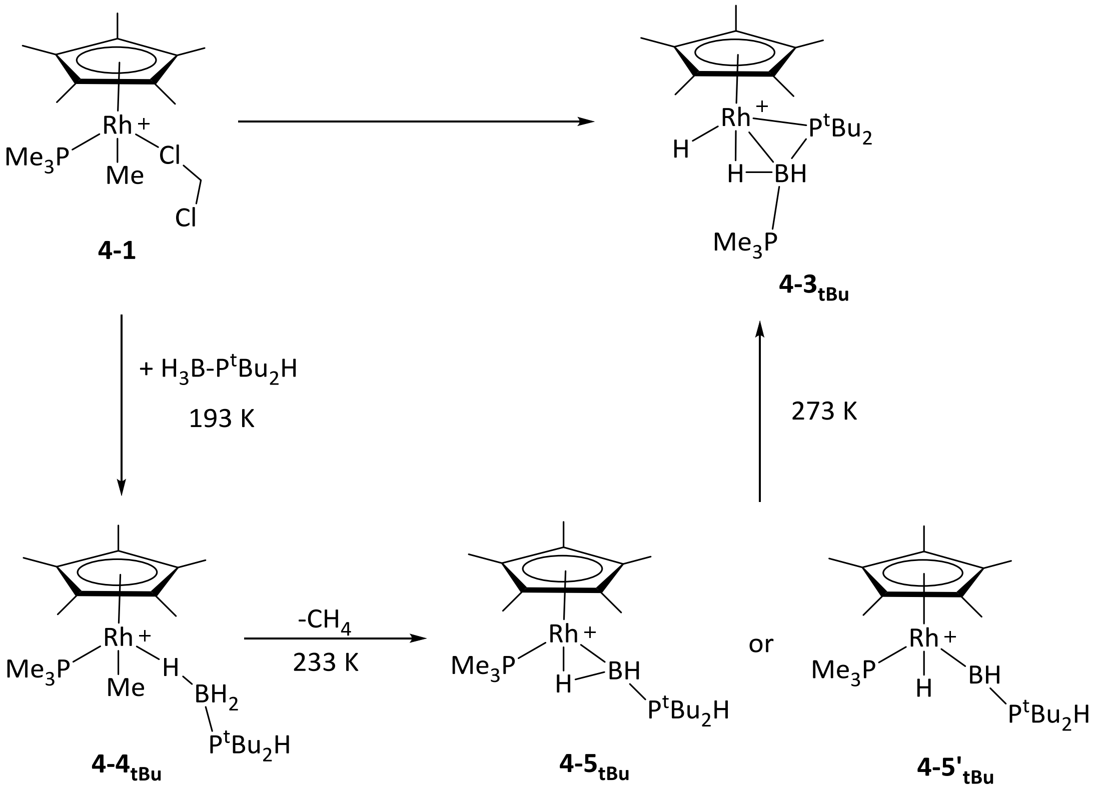

***Scheme 4-3:** Intermediates identified by the low temperature NMR study of the stoichiometric reaction between **4-1** and H_3B-P^tBu_2H. Adapted from reference No. 128.*

The parallel DFT investigations were conducted as part of this thesis. The aim of the study was to identify the favoured isomer of **4-5$_{\mathbf{tBu}}$** as well as characterise the stoichiometric reaction for H_3B-PR_2H (R = Ph, ^{t}Bu, Cy, Me). The formation of phosphido-borate, **4-2$_{\mathbf{R}}$** (crystal structure and NMR data obtained for R = Ph, Cy) and B-P coupled product, **4-3$_{\mathbf{R}}$** (crystal structure and NMR data obtained for R = ^{t}Bu) was also rationalised. Although not explored experimentally, reaction with H_3B-PMe_2H was calculated to study the effect of a less sterically hindered phosphine-borane on the stoichiometric reaction.

4.1.2 – Computational Details

Calculations were run with Gaussian 03 Revision D.01.[173] Geometry optimisations were performed using the BP86 functional.[143, 144] The Rh and P centres were described with Stuttgart pseudopotentials and associated basis sets[158] (with added d-orbital polarisation on P (ς = 0.387)[174]) and 6-31G** basis sets[156, 157] described all other atoms (**BS1**). All stationary points were fully characterised via analytical frequency calculations as either minima (all positive frequencies) or transition states (one imaginary frequency). IRC calculations and subsequent geometry optimisations were used to confirm the minima linked by each transition state. Frequency calculations also provided a free energy in the gas phase, computed at 298.15 K and 1 atm. Energies reported in the text are based on the gas-phase relative free energies and incorporate a correction for dispersion effects using Grimme's D3 parameter set[164] with Becke-Johnson damping[165] as well as solvation (PCM approach)[161] in CH_2Cl_2. Both dispersion and solvation corrections were run as single points with Gaussian 09 Revision D.01.[175]

^{11}B chemical shift calculations (**Section 4.2.2**) used the B3LYP[147] functional with a Rh and P centres described with Stuttgart pseudopotentials and associated basis sets (with added d-orbital polarisation on P (ς = 0.387)). All other atoms were described with the 6-311g++** basis set[178, 179] (**BS2**). Computed chemical shifts are relative to F_3BOEt_2.

DFT functionals B3LYP, PBE0[149], M06[166], B97D[167], and ωB97XD[152] were used during functional testing studies in **Section 4.4.**

Throughout the chapter, the energy for $[Rh(\eta^1\text{-}H_3B\text{-}PR_2H)(Me)(PMe_3)(Cp^*)]^+$, **4-4$_{\mathbf{R}}$**, is set to 0.0 kcal mol^{-1}. The $[BAr^F{}_4]$ anion is not included in the calculations.

4.2 – Identifying the Isomers of $[Rh(H_2B\text{-}PR_2H)(PMe_3)(\eta\text{-}Cp^*)]^+$ (R = ^{t}Bu, Ph, Cy, Me)

4.2.1 – Determining the Structure of $[Rh(H_2B\text{-}PR_2H)(PMe_3)(\eta\text{-}Cp^*)]^+$

The boryl isomer of the intermediate, **4-5$_{tBu}$** $[Rh(H_2B\text{-}P^tBu_2H)(PMe_3)(\eta\text{-}Cp^*)]^+$ (see **Figure 4-1**) was characterised. It was computed to have an Rh-B bond length of 2.03 Å and a Rh···H^1 distance of 1.79 Å indicating an α-agostic interaction with an elongated B-H^1 bond at 1.35 Å (the other B-H bond in **4-5$_{tBu}$** has a bond length of 1.21 Å). The borylene isomer, **4-5'$_{tBu}$** $[Rh(H)(HB\text{-}P^tBu_2H)(PMe_3)(\eta\text{-}Cp^*)]^+$, was also located. The optimised structure shows a rhodium-hydride bond is present due to a Rh-H distance of 1.58 Å (shorter than in the boryl isomer, **4-5$_{tBu}$**) and a B···H distance of 2.33 Å. Furthermore, calculation yielded a third possible isomer, **4-5''$_{tBu}$** $[Rh(H)(H_2B\text{-}P^tBu_2H)(PMe_3)(\eta\text{-}Cp^*)]^+$. This isomer exhibits a δC-H agostic interaction originating from the ^{t}Bu substituent with a Rh···H interaction distance of 2.07 Å and an elongated C-H distance of 1.13 Å. The C-H bond length is elongated which is typical of a C-H agostic interaction (a calculated C-H bond length being 1.09 Å). Comparing the relative free energies of the three structures suggests that the αB-H agostic boryl complex, **4-5$_{tBu}$** (G = -7.0 kcal mol^{-1}) is the most stable isomer compared to the borylene, **4-5'$_{tBu}$** (G = -4.9 kcal mol^{-1}), and δC-H agostic, **4-5''$_{tBu}$** (G = -1.6 kcal mol^{-1}), complexes. Due to the disorder in the crystal structure a comparison between crystal and optimised structures was not useful. The energies of these intermediates suggests that complex **4-5$_{tBu}$** $[Rh(\eta^1\text{-}H_2B\text{-}P^tBu_2H)(PMe_3)(\eta\text{-}Cp^*)]^+$, is the most stable isomer. Such αB-H agostic boryl complexes have been discussed in the literature as potential intermediates in the dehydrogenation of amine-boranes.[182, 183] No other monomeric base-stabilised αB-H agostic boryl complex has been reported, however, there is one example with a rhodium dimer motif $[Rh_2(H)_2(PCy_3)_2(\mu\text{-}H_2B\text{-}NMe_3)_2(\mu\text{-}H_3B\text{-}NMe_3)][BAr^F_4]_2$ reported by the Weller group.[184] The dimeric complex exhibits similar Rh-B distances (2.08 Å) to the Rh-B bond in **4-5$_{tBu}$** (2.03 Å).

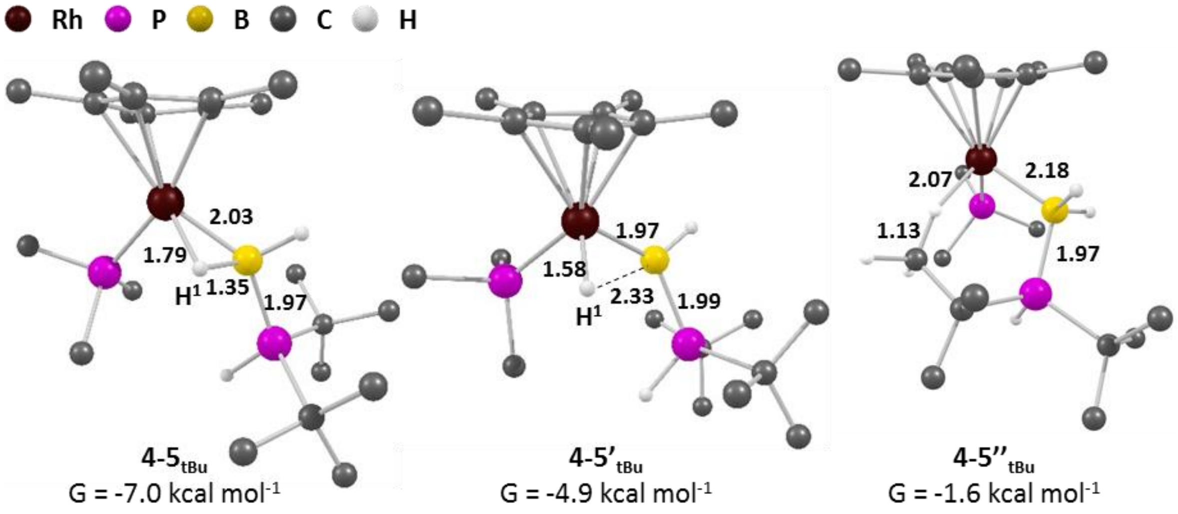

4-5$_{tBu}$ G = -7.0 kcal mol^{-1} **4-5'$_{tBu}$** G = -4.9 kcal mol^{-1} **4-5''$_{tBu}$** G = -1.6 kcal mol^{-1}

***Figure 4-1**: The three potential isomers of **4-5$_{tBu}$**. Hydrogens bonded to carbon omitted for clarity. Key distances in Å. Colour scheme shown in the legend above is adopted throughout the chapter.*

As seen in **Scheme 4-4**, the isomerisation pathways were also characterised. It was found that boryl, **4-5**$_{\mathbf{tBu}}$, can proceed to δC-H agostic complex **4-5''**$_{\mathbf{tBu}}$ *via* rotation of the B-P bond through **4-TS(5-5'')**$_{\mathbf{tBu}}$ (G = 5.5 kcal mol^{-1}, **Figure 4-2**). The isomerisation between **4-5**$_{\mathbf{tBu}}$ and borylene, **4-5'**$_{\mathbf{tBu}}$, occurs *via* B-H oxidative cleavage seen in **4-TS(5-5')**$_{\mathbf{tBu}}$ (G = -4.0 kcal mol^{-1}) with the B···H^{1} distance increasing from 1.35 Å (**4-5**$_{\mathbf{tBu}}$) to 2.33 Å (**4-5'**$_{\mathbf{tBu}}$). The two processes have free energy barriers of 12.5 kcal mol^{-1} and 3.0 kcal mol^{-1} respectively relative to complex **4-5**$_{\mathbf{tBu}}$**.** The low barriers indicate these isomerisations would be accessible at room temperature. No direct isomerisation pathway between **4-5'**$_{\mathbf{tBu}}$ and **4-5''**$_{\mathbf{tBu}}$ could be characterised.

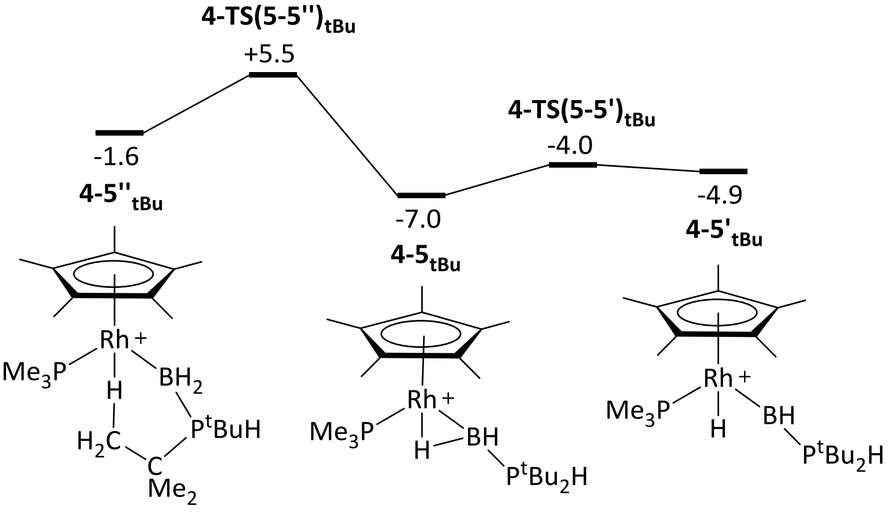

***Scheme 4-4**: Reaction scheme for the isomerisation of **4-5**$_{\mathbf{tBu}}$. Free energies at BP86(D3BJ, CH_2Cl_2)/BS1.*

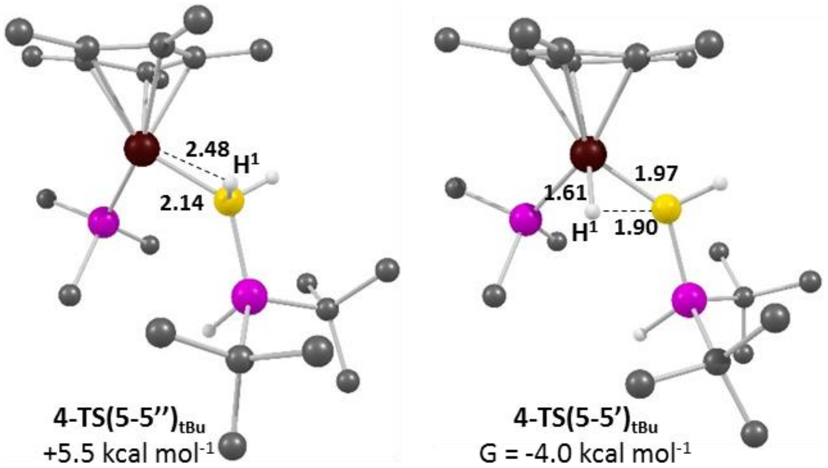

***Figure 4-2**: The two transition states of the isomerisation of **4-5**$_{\mathbf{tBu}}$. Hydrogens bonded to carbon omitted for clarity. Key distances in Å.*

Similar behaviour is also displayed for R = Ph, Cy and Me (see **Scheme 4-5**) with **4-5**$_{\mathbf{R}}$ being the most stable isomer and the isomerisation barriers remaining small and accessible at low temperatures. All isomers are structurally similar except for **4-5''**$_{\mathbf{Me}}$ (**Figure 4-3**) which displays no C-H agostic interaction (closest Rh···H distance at 3.78 Å) and is therefore unsaturated. No geometry of **4-5’’$_{Me}$** involving a γC-H agostic could be characterised as there are no δ hydrogens available.

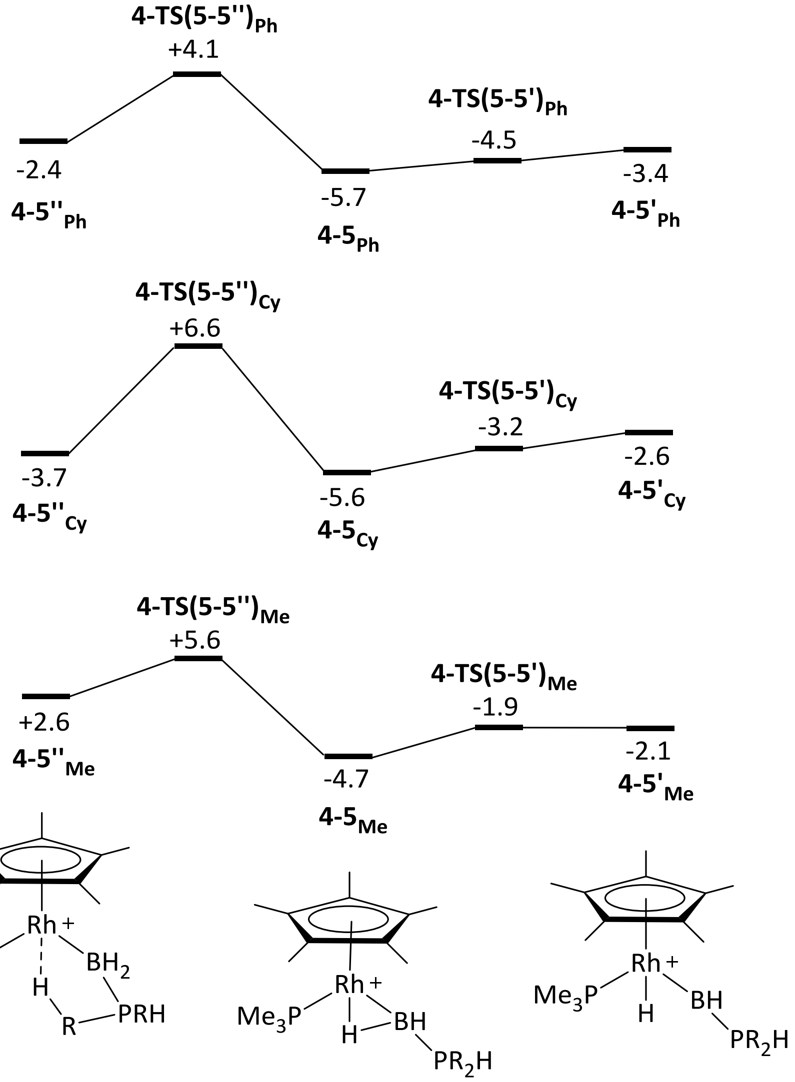

Scheme 4-5: *Reaction scheme for the isomerisation of **4-5$_R$** (R = Ph, Cy, Me). Free energies at BP86(D3BJ, CH_2Cl_2)/BS1.*

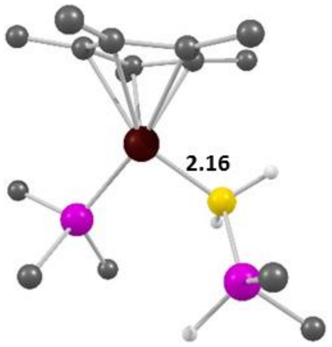

4-5’’$_{Me}$
G = +2.6 kcal mol^{-1}

Figure 4-3*: Complex **4-5’’$_{Me}$.** Hydrogens bonded to carbon omitted for clarity. Key distances in Å.*

4.2.2 – ^{11}B NMR Chemical Shift Calculations of 4-5$_{tBu}$

In order to confirm the computed prediction of boryl isomer, **4-5$_{tBu}$**, being the intermediate observed through experiment, the ^{11}B NMR chemical shift was calculated to compare with the experimental ^{11}B value of δ = +47.6 ppm. Chemical shift (CS) calculations were run with B3LYP/BS2 on the optimised BP86/BS1 geometries. The B3LYP/BS2 computational approach was used for the CS calculations as it is known that hybrid functionals perform better for NMR calculations due to work conducted by Bühl and co-workers.[185] The calculations gave ^{11}B δ values of +53.7 (boryl, **4-5$_{tBu}$**), +119.3 (borylene, **4-5'$_{tBu}$**) and -14.3 (δC-H agostic, **4-5''$_{tBu}$**) ppm. Comparing these values with that of experiment gives further indication that **4-5$_{tBu}$** is the experimentally observed isomer.

4.3 – The Stoichiometric Reaction of H_3B-PR_2H (R = ^{t}Bu, Ph, Cy, Me) with [Rh(CH_2Cl_2)(Me)(PMe_3)(η-Cp*)]$^+$: Rationalising the Selectivity between Products

4.3.1 – B-H Activation and the Formation of [Rh(η^1-$BH_2P^tBu_2H$)(PMe_3)(η-Cp*)]$^+$, 4-5$_{\text{tBu}}$

The mechanism for the formation of the boryl isomer, **4-5$_{\text{tBu}}$**, is detailed in **Scheme 4-6** using the computational procedure described in **Section 4.1.2**. Calculations found that the initial B-H activation can proceed through a σ-complex assisted metathesis (σ-CAM) process[177] *via* **4-TS(4-5'')1$_{\text{tBu}}$** (G = +14.1 kcal mol^{-1}, **Figure 4-4**). This involves the B···H^2 distance increasing from 1.30 Å (**4-4$_{\text{tBu}}$**) to 1.96 Å (**4-TS(4-5'')1$_{\text{tBu}}$**) showing the B-H bond has been broken. This forms a methane σ-complex, **4-INT(4-5'')$_{\text{tBu}}$**, with the C···H^2 distance decreasing from 1.48 Å (**4-TS(4-5'')1$_{\text{tBu}}$**) to 1.14 Å (**4-INT(4-5'')$_{\text{tBu}}$**). The elongated C-H^2 distance in the methane σ-complex, **4-INT(4-5'')$_{\text{tBu}}$** (other C-H distances are 1.10 Å) as well as the Rh···H distance of 1.97 Å are typical of a σ-interaction. The Rh···H distance in **4-INT(4-5'')$_{\text{tBu}}$** is elongated compared to a σ-methane complex synthesis by Brookhart *et al.* (Rh-H distance of 1.87 Å).[186] The methane then dissociates from **4-INT(4-5'')$_{\text{tBu}}$**, proceeding through **4-TS(4-5'')2$_{\text{tBu}}$** (G = +5.9 kcal mol^{-1}). This leaves a vacant site at the metal centre which allows a C-H agostic interaction to form resulting in δC-H agostic complex, **4-5''$_{\text{tBu}}$**. As previously discussed in **Section 4.2.1**, **4-5''$_{\text{tBu}}$** then isomerises to complex, **4-5$_{\text{tBu}}$**, through **4-TS(5-5'')$_{\text{tBu}}$**. The overall barrier to the formation of **4-5$_{\text{tBu}}$** is 14.1 kcal mol^{-1} as the σ-CAM step, *via* **4-TS(4-5'')1$_{\text{tBu}}$** is the highest energy process. This is indicative of the reaction proceeding at low temperature, agreeing with the experimental observation that this process would occur at 233 K and **4-5$_{\text{tBu}}$** to rapidly form at 298 K.

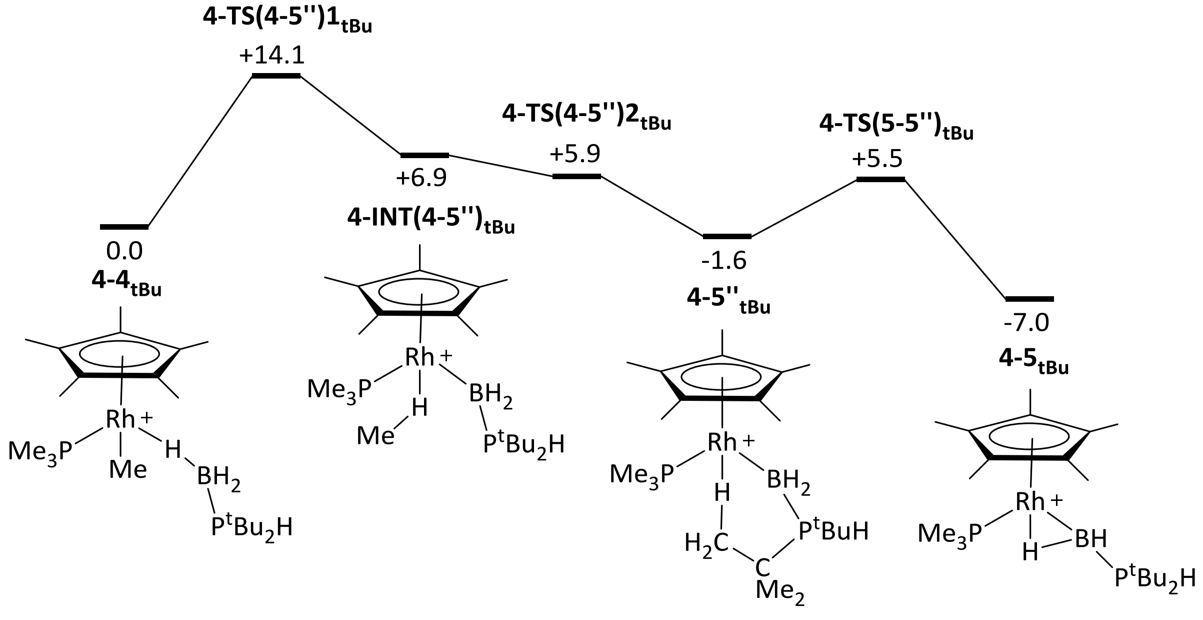

*Scheme 4-6: Reaction scheme for the formation of **4-5$_{\text{tBu}}$** from **4-4$_{\text{tBu}}$**. Relative free energies BP86(D3BJ, CH_2Cl_2)/BS1 in kcal mol^{-1}.*

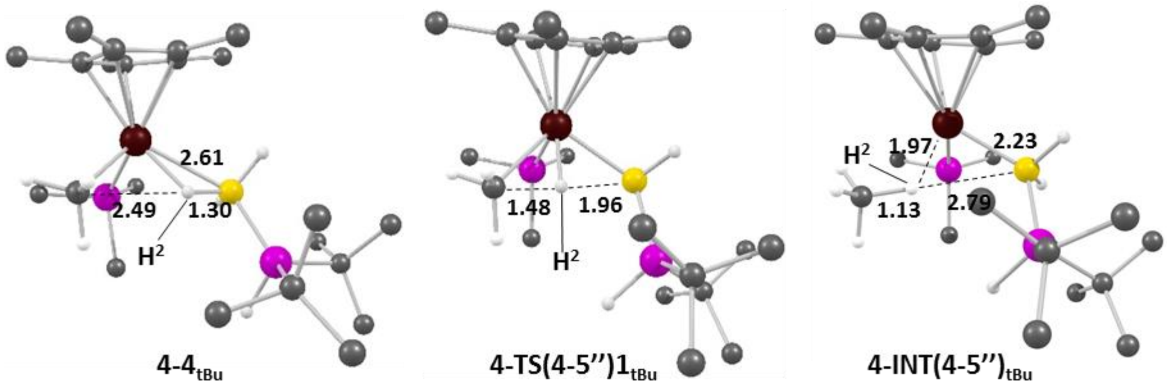

4-4$_{tBu}$
G = 0.0 kcal mol^{-1}

4-TS(4-5'')1$_{tBu}$
G = +14.1 kcal mol^{-1}

4-INT(4-5'')$_{tBu}$
G = +6.9 kcal mol^{-1}

***Figure 4-4**: Key stationary points in the formation of **4-5$_{tBu}$**. Hydrogens bonded to carbon omitted for clarity. Key distances in Å.*

4.3.2 – B-P Bond Coupling and the Formation of [Rh(H)(P^{t}Bu$_2$BH$_2$PMe$_3$)(Cp*)]$^+$, 4-3$_{tBu}$

Scheme 4-7 details the reaction pathway to form the B-P coupled product, **4-3$_{tBu}$**, starting from the δC-H agostic complex, **4-5''$_{tBu}$**. The reaction proceeds through a P-H activation step *via* **4-TS(5''-6)** (G = +17.2 kcal mol^{-1}) to form intermediate **4-6$_{tBu}$** (G = -4.0 kcal mol^{-1}, **Figure 4-5**) which contains an phosphino-borane motif bound to the metal through the boron and phosphorus atoms**.** In the characterised transition state, **4-TS(5''-6)$_{tBu}$**, the δC-H agostic interaction has been broken and replaced by a new Rh···H interaction at 2.09 Å (which becomes a Rh-H bond (1.56 Å) in **4-6$_{tBu}$**). Furthermore, as the hydrogen is transferred to the rhodium centre, the phosphorus moves closer to the rhodium which allows it to co-ordinate to the metal. This is observed through a decreasing Rh···P distance of 3.48 Å in **4-5''$_{tBu}$** to 2.75 Å in **4-TS(5''-6)**$_{tBu}$ and finally 2.47 Å in **4-6$_{tBu}$**. The phosphino-borane intermediate, **4-6$_{tBu}$**, has a B-P bond length of 1.87 Å which lies in between that of free H_3B-P^{t}Bu$_2$H (1.96 Å) and H_2B=P^{t}Bu$_2$ (1.83 Å) indicating a degree of back-bonding from the rhodium. The motif has been described as an ambiphillic ligand by Bourissou and co-workers.[187] Bourissou, Amgoune *et al.* have also reported platinum phosphino-borane complexes [Pt(R'$_2$PB(C$_6$F$_5$))(PPh$_3$)$_2$] (R' = ^{t}Bu, Cy) where the phosphino-borane motif exhibits similar bonding to **4-6$_{tBu}$**.[188] The platinum complexes also indicate a degree of back-bonding with the P-B distance in [Pt(Cy$_2$PB(C$_6$F$_5$)$_2$)(PPh$_3$)$_2$] of 1.92 Å increased from that of free (F$_5$C$_6$)$_2$B=PCy$_2$ (1.76 Å). Molecular orbital (MO) analysis conducted found the phosphino-borane interaction with the metal was similar to that of an η^2-ethene ligand however the donating π(BP) MO is centered towards the phosphorus and the accepting π* (BP) MO is centered towards the boron as would be expected in an ambiphillic ligand.

A B-P coupling step where the PMe$_3$ group couples to the {BH$_2$P^{t}Bu$_2$} moiety occurs through **4-TS(6-3')$_{tBu}$** (G = +7.7 kcal mol^{-1}) to form **4-3'$_{tBu}$** (G = -7.5 kcal mol^{-1}) from **4-6$_{tBu}$**. During this process the B···PMe$_3$ distance reduces from 2.76 Å (**4-6$_{tBu}$**) to 2.16 Å (**4-TS(6-3')$_{tBu}$**) and then 1.95 Å in **4-**

3’$_{tBu}$. The B-P coupling step also breaks the Rh-PMe$_3$ bond with the Rh···PMe$_3$ distance in **4-3’$_{tBu}$** of 3.85 Å increased from 2.37 Å in **4-6$_{tBu}$**. Intermediate **4-3’$_{tBu}$** is an unsaturated complex and rotation around the P^1-B bond *via* **4-TS(3’-3)$_{tBu}$** (G = -4.7 kcal mol^{-1}) allows the metal to become saturated by forming a βB-H agostic interaction. This gives the experimentally observed B-P coupled product **4-3$_{tBu}$** (G = -16.9 kcal mol^{-1}). The βB-H agostic interaction can form as the Rh···H^3 distance decreases (3.97 Å (**4-3’$_{tBu}$**) to 3.20 Å (**4-TS(3’-3)$_{tBu}$**) to 1.75 Å (**4-3$_{tBu}$**)) with the Rh-P^1-B-H^3 torsion angle (-88.7 ° (**4-3’$_{tBu}$**) to -54.9 ° (**4-TS(3’-3)$_{tBu}$**) to -3.0 (**4-3$_{tBu}$**).

The overall barrier for the formation of the B-P coupled product, **4-3$_{tBu}$**, is 24.2 kcal mol^{-1} relative to boryl complex **4-5$_{tBu}$**. This coincides with the experimental observation that product **4-3$_{tBu}$** is formed relatively slowly from **4-5$_{tBu}$**.

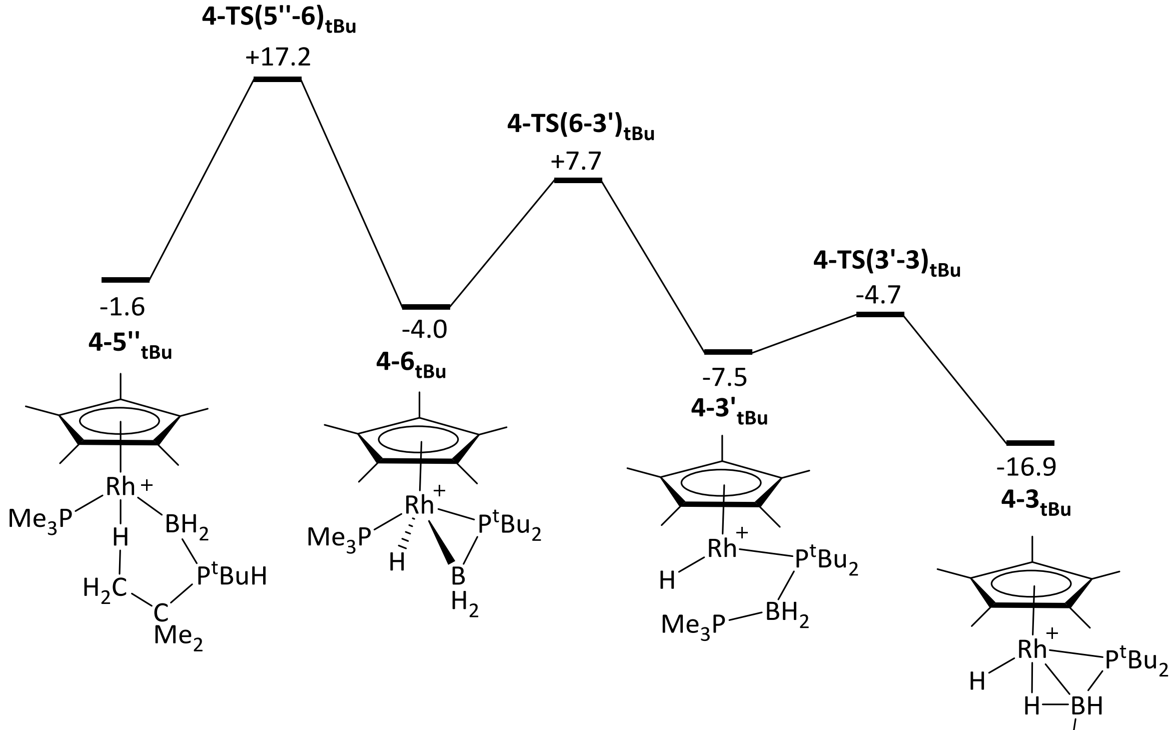

***Scheme 4-7**: Formation of **4-3$_{tBu}$** from **4-5’’$_{tBu}$**. Relative free energies BP86(D3BJ, CH$_2$Cl$_2$)/BS1 in kcal mol^{-1}.*

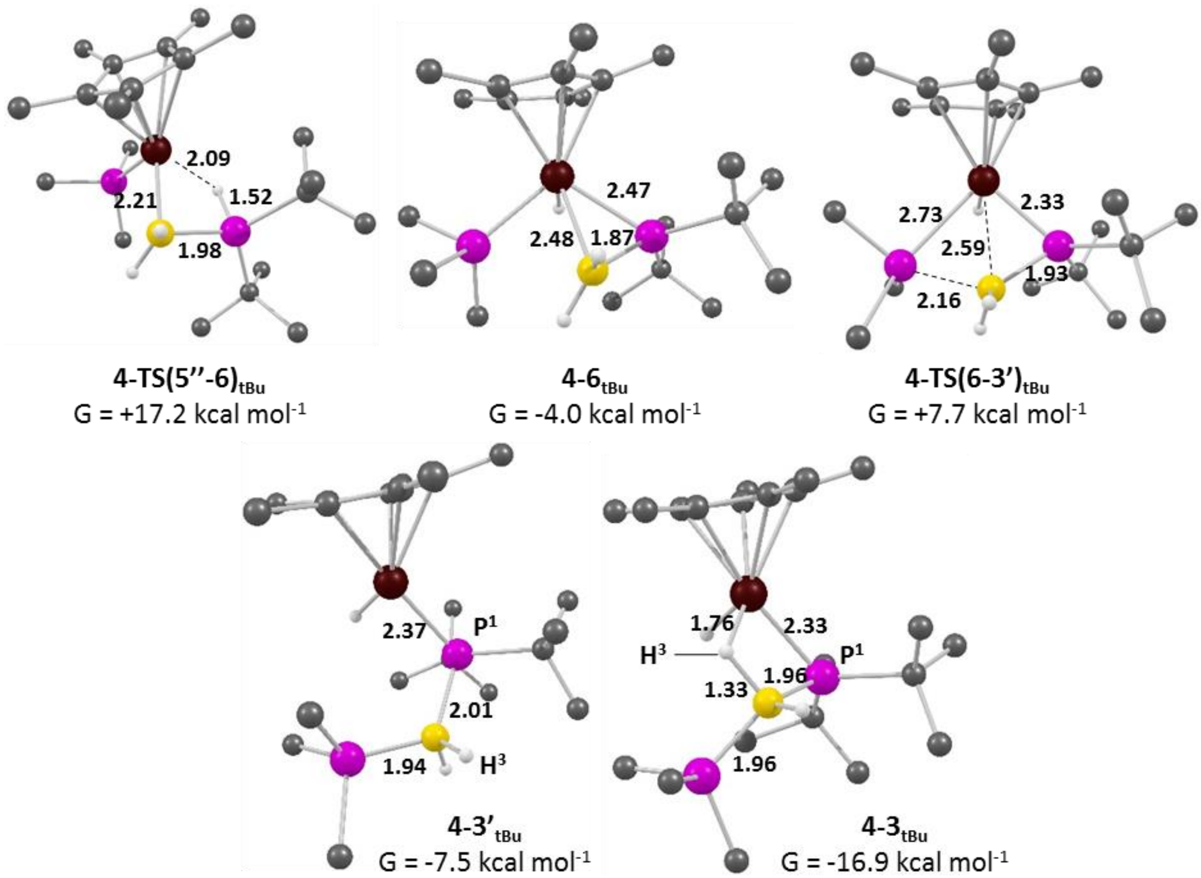

4-TS(5''-6)$_{tBu}$
G = +17.2 kcal mol^{-1}

4-6$_{tBu}$
G = -4.0 kcal mol^{-1}

4-TS(6-3')$_{tBu}$
G = +7.7 kcal mol^{-1}

4-3'$_{tBu}$
G = -7.5 kcal mol^{-1}

4-3$_{tBu}$
G = -16.9 kcal mol^{-1}

***Figure 4-5**: Key stationary points in the formation of **4-3$_{tBu}$**. Hydrogens bonded to carbon omitted for clarity. Key distances in Å.*

The calculated structure for the B-P coupled product **4-3$_{tBu}$** is compared with the experimental molecular structure in **Table 4-2.** The results show that the computed structure is a good fit for the experimentally determined structure. Similar structures, known as Lewis-base stabilised phosphino-boranes, are reported in the literature as either free molecules synthesised by Burg *et al.*[189] or co-ordinated to tungsten, [W(CO)$_5$(PH$_2$BH$_2$NMe$_3$)], and iron [Fe(CO$_4$)(PH$_2$BH$_2$NMe$_3$)] synthesised by Scheer *et al*.[190, 191] Both complexes exhibit a P-B bond length of 1.96 Å which is similar to the P^1-B bond length of 1.99 Å in the molecular structure of **4-3$_{tBu}$.**

Key Bonds / Angles	Computed (Å / °)	Experiment (Å / °)
P^1-B	1.96	1.99(2)
P^2-B	1.96	1.918(5)
Rh-P^1	2.33	2.30(3)
Rh-B	2.43	2.43(5)
P^1-B-P^2	129.65	126.7

***Table 4-2**: Comparison between computed and experimental structures for **4-3$_{tBu}$**.*

4.3.3 – Formation of [Rh(η^1-H_3BPtBu_2)(PMe_3)(Cp*)]$^+$, 4-2$_{tBu}$, from 4-6$_{tBu}$ (i) Rotation

A pathway to form the phosphido-borane product, **4-2$_{tBu}$**, was also calculated. The mechanism follows the same pathway as that of the B-P coupled product, **4-3$_{tBu}$** (**Section 4.3.2**) up to the formation of the phosphino-borane intermediate, **4-6$_{tBu}$** (**Scheme 4-7**). To form **4-2$_{tBu}$** from **4-6$_{tBu}$**, the η^2-($BH_2P^tBu_2$) moiety proceeds through a two-step rotation (**Scheme 4-8**). The rotation proceeds *via* **4-TS(6-2)1** (G = +0.7 kcal mol^{-1}) where the {P^tBu_2} passes next to the Cp* ring with the P-Rh-P-B torsion angle decreasing from -35.5 ° in **4-6$_{tBu}$** to -4.5 ° in **4-TS(6-2)1$_{tBu}$** (**Figure 4-6**). An intermediate, **4-INT(6-2)$_{tBu}$** (G = -1.3 kcal mol^{-1}), was computed when the P-Rh-P-B torsion angle was +15.7 °. The rotation continues through **4-TS(6-2)2$_{tBu}$** (G = +1.8 kcal mol^{-1}); (P-Rh-P-B = +38.2 °) and results in the formation of product, **4-2$_{tBu}$** (G = -4.5 kcal mol^{-1}) (P-Rh-P-B = +61.3 °). This process also involves the formation of a B-H bond as the B···H distance decreases from 2.56 Å (**4-INT(6-2)$_{tBu}$**) and 2.06 Å (**4-TS(6-2)2$_{tBu}$**) to 1.41 Å (**4-2$_{tBu}$**), forming a phosphido-borate in **4-2$_{tBu}$**.

The barrier for the formation of the phosphido-borane product, **4-2$_{tBu}$**, from **4-6$_{tBu}$** is 5.8 kcal mol^{-1}. The barrier for the reverse process (**4-2$_{tBu}$** to **4-6$_{tBu}$**) is 6.3 kcal mol^{-1} due to the thermodynamic instability of **4-2$_{tBu}$** which indicates the two-step rotation is reversible. The overall barrier of the formation of **4-2$_{tBu}$** from **4-4$_{tBu}$** is 24.2 kcal mol^{-1} relative to **4-5$_{tBu}$**. Phosphido-borates such as **4-2$_{tBu}$** are known in the literature and have been observed as intermediates in the dehydrocoupling of phosphido-boranes (**Chapter 3**).

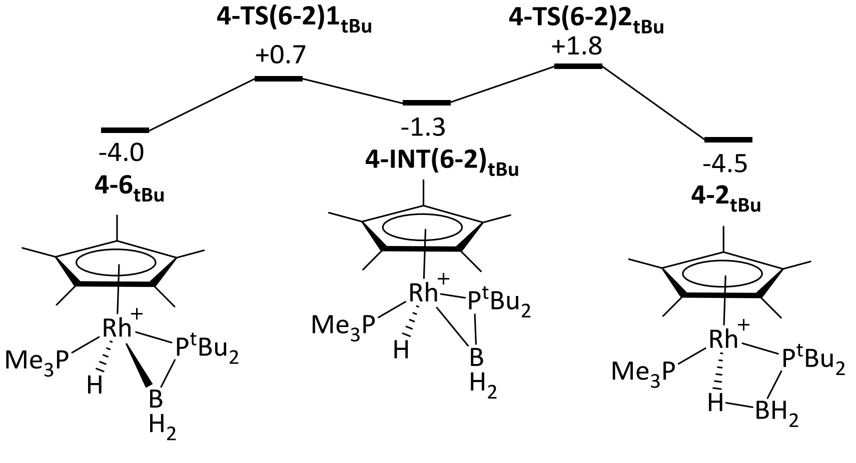

Scheme 4-8: *Formation of**4-2$_{tBu}$**from **4-6$_{tBu}$**. Relative free energies BP86(D3BJ, CH_2Cl_2)/BS1 in kcal mol^{-1}.*

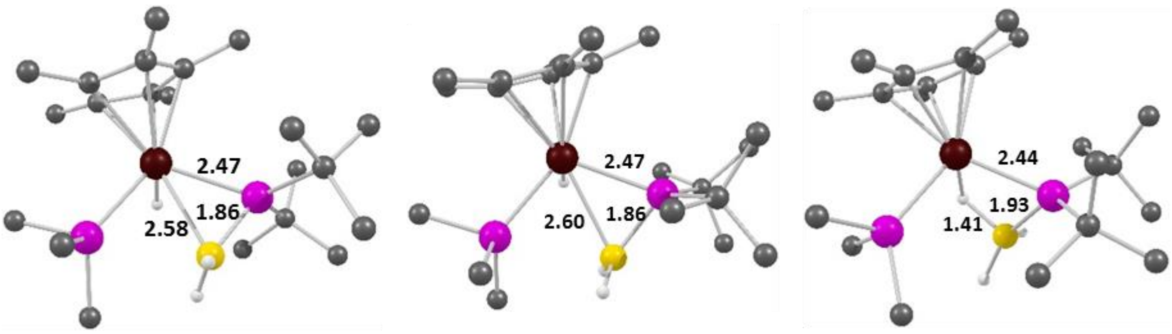

4-TS(6-2)1$_{tBu}$
G = +0.7 kcal mol^{-1}

4-INT(6-2)$_{tBu}$
G = -1.3 kcal mol^{-1}

4-2$_{tBu}$
G = -4.5 kcal mol^{-1}

Figure 4-6: *Key stationary points in the formation of **4-2$_{tBu}$**. Hydrogens bonded to carbon omitted for clarity. Key distances in Å.*

4.3.4 – Formation of [Rh(η^1-H_3BPtBu_2)(PMe_3)(Cp*)]$^+$, 4-2$_{tBu}$, from 4-6$_{tBu}$ (ii) P-H Transfer

An alternative pathway to the formation of **4-2$_{tBu}$** directly from **4-5$_{tBu}$** was also characterised (**Scheme 4-9**). From the boryl isomer, **4-5$_{tBu}$,** a hydrogen transfer between the phosphorus and boron of the phosphine-boryl proceeds through **4-TS(5-2)1$_{tBu}$** (G = 24.6 kcal mol^{-1}, **Figure 4-7**) to form **4-INT(5-2)$_{tBu}$** (G = -1.1 kcal mol^{-1}). Complex **4-INT(5-2)$_{tBu}$** contains a phosphido-borate ligand which is η^2-bound through two B-H σ-interactions with the rhodium centre. It is also a higher energy isomer of product, **4-2$_{tBu}$** (where the phosphido-borate is bound to the metal through one σ-BH interaction and a Rh-P bond). In **4-TS(5-2)1$_{tBu}$** the hydrogen is almost equidistant between the rhodium and boron atoms (2.03 Å and 2.04 Å respectively). The phosphorus of the phosphido-borate in **4-INT(5-2)$_{tBu}$** then co-ordinates to the rhodium in a separate step *via* **4-TS(5-2)2$_{tBu}$** (G = 11.9 kcal mol^{-1}) which results in the formation of the phosphide-borate product **4-2$_{tBu}$**.The Rh···P distance decreased from 3.91 Å to 2.44 Å during this process.

The overall barrier for the alternate formation of product, **4-2$_{tBu}$**, is 31.6 kcal mol^{-1} relative to boryl complex, **4-5$_{tBu}$**. The barrier is 7.4 kcal mol^{-1} higher in free energy than the two-step rotation mechanism characterised in **Section 4.3.3** (overall free energy barrier of 24.2 kcal mol^{-1}) and is therefore the reaction is not proposed to proceed through this mechanism.

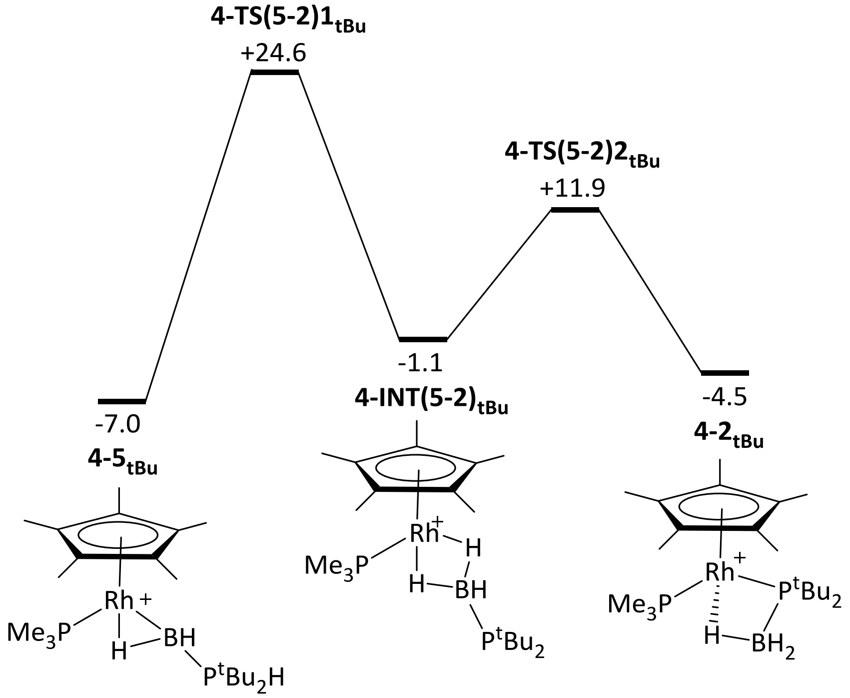

***Scheme 4-9**: Alternative formation of **4-2$_{tBu}$** from **4-5$_{tBu}$**. Relative free energies BP86(D3BJ, CH_2Cl_2)/BS1 in kcal mol^{-1}.*

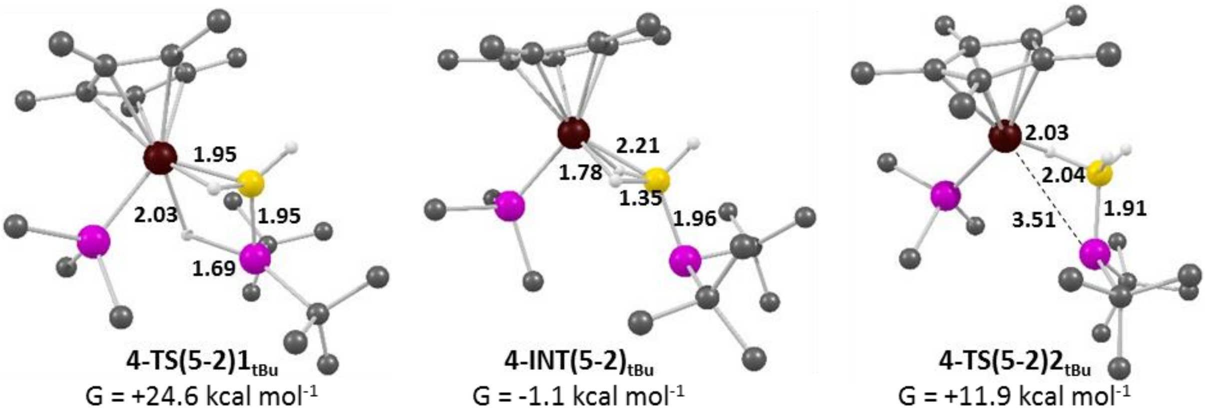

***Figure 4-7**: Key stationary points in the alternative formation of **4-2$_{tBu}$**. Hydrogens bonded to carbon omitted for clarity. Key distances in Å.*

4.3.5 – Summary of the Stoichiometric Reaction with H_3B-P^{t}Bu$_2$H

The formation of αB-H agostic boryl complex, **4-5$_{tBu}$** and phosphino-borane complex, **4-6$_{tBu}$**, are detailed in **Scheme 4-10**. The stoichiometric reaction is predicted to begin *via* an initial substitution of the CH_2Cl_2 ligand in **4-1** with H_3B-P^{t}Bu$_2$H to from **4-4$_{tBu}$**. This is followed by B-H activation through a σ-CAM process *via* **4-TS(4-5'')1$_{tBu}$** (G = +14.1 kcal mol^{-1}), and loss of methane, **4-TS(4-5'')2$_{tBu}$** (+5.9 kcal mol^{-1}), to form a δC-H agostic intermediate, **4-5''$_{tBu}$** (-1.6 kcal mol^{-1}). Complex **4-5''$_{tBu}$** can then isomerise to form **4-5$_{tBu}$** (G = -7.0 kcal mol^{-1}) through **4-TS(5-5'')** (G = +5.5 kcal mol^{-1}). This process has a free energy barrier of 14.1 kcal mol^{-1} which agrees with the experimental observation that **4-5$_{tBu}$** forms rapidly in the reaction solution. Complex **4-5''$_{tBu}$** can also yield the phosphino-borane intermediate, **4-6$_{tBu}$**. Complex **4-6$_{tBu}$** is formed *via* a P-H activation process through **4-TS(5''-6)** (G = +17.2 kcal mol^{-1}) with a free energy barrier of 24.2 kcal mol^{-1} relative to **4-5$_{tBu}$**.

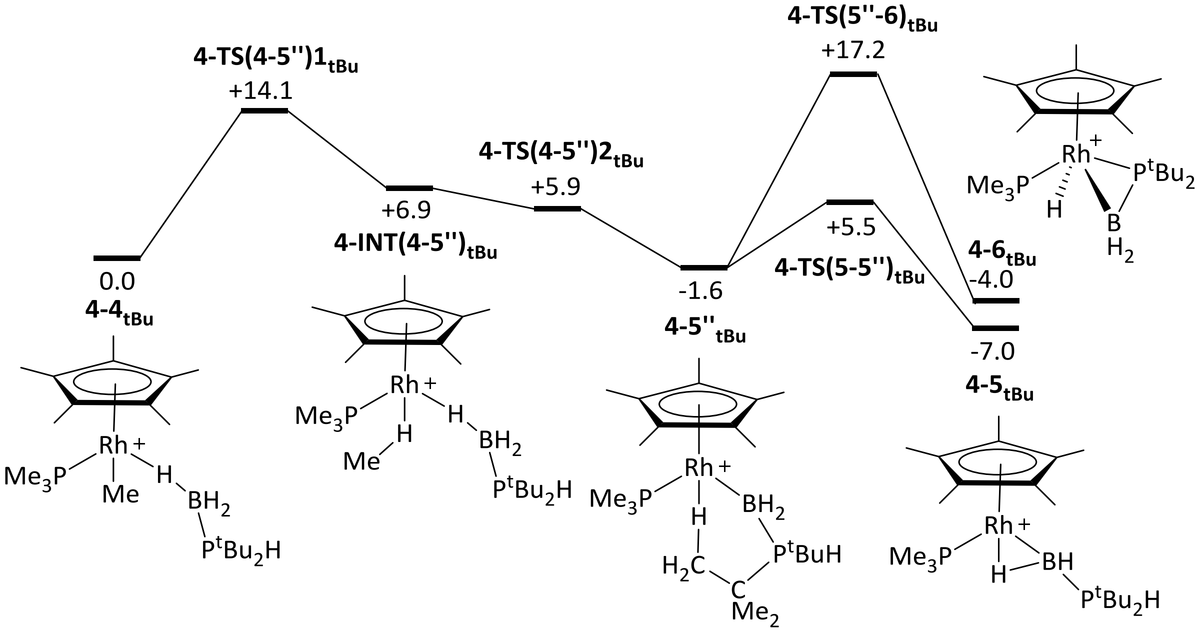

***Scheme 4-10**: Formation of **4-5$_{tBu}$** and **4-6$_{tBu}$** from **4-4$_{tBu}$**. Relative free energies BP86(D3BJ, CH2Cl2)/BS1 in kcal mol^{-1}.*

Intermediate **4-6$_{tBu}$** is the key intermediate in the stoichiometric reaction as the pathways to form phosphide-borate complex **4-2$_{tBu}$** (G = -4.5 kcal mol^{-1}) and B-P coupled product **4-3$_{tBu}$**(G = -16.9 kcal mol^{-1}) deviate from the phosphino-borane complex (**Scheme 4-11**). To form **4-2$_{tBu}$**, the {$H_2BP^tBu_2$} moiety undergoes a two-step rotation through **4-TS(6-2)1$_{tBu}$** (G = +0.7 kcal mol^{-1}) and **4-TS(6-2)2$_{tBu}$** (G = +1.8 kcal mol^{-1}) with an overall barrier of 5.8 kcal mol^{-1} with respect to intermediate **4-6$_{tBu}$**. The B-P coupled product, **4-3$_{tBu}$**, is formed through B-P coupling *via* **4-TS(6-3')$_{tBu}$** (G = +7.7 kcal mol^{-1}) and P-B bond rotation through **4-TS(3'-3)** (G = -4.7 kcal mol^{-1}) with a barrier of 11.7 kcal mol^{-1} relative to **4-6$_{tBu}$**. In both cases, the formation of phosphino-borane complex, **4-6$_{tBu}$** (with a free energy barrier of 24.2 kcal mol^{-1}) remains the rate determining process for both pathways. Therefore, **4-2$_{tBu}$** is the kinetic pathway from intermediate **4-6$_{tBu}$**. However, the formation of **4-2$_{tBu}$** is reversible due to the low barriers of rotation and the similar free energies of **4-2$_{tBu}$** and **4-6$_{tBu}$** (G = -4.5 kcal mol^{-1} *vs.* G = -4.0 kcal mol^{-1}). Complex, **4-3$_{tBu}$** is the thermodynamically more stable product compared to **4-2$_{tBu}$** with a free energy of -16.9 kcal mol^{-1}. This could be due to there being more steric clashing between the ^{t}Bu group and the Cp* ring in **4-2$_{tBu}$** compared to **4-3$_{tBu}$**. This is further discussed in **Section 4.3.7**. An indication of the increased steric clashing is the longer Rh···P distance in **4-2$_{tBu}$** (2.44 Å, **Figure 4-6**) compared to **4-3$_{tBu}$** (2.33 Å, **Figure 4-5**).

In conclusion, the rationale behind the B-P coupled product, **4-3$_{tBu}$** being the experimentally observed product is its thermodynamic stability in comparison to phosphido-borate **4-2$_{tBu}$** as well as the formation of **4-2$_{tBu}$** being reversible. The overall barrier for the reaction is 24.2 kcal mol^{-1} with the P-H activation step preceeding **4-6$_{tBu}$** formation proving to be the rate determining process. This is in agreement with the experimental observation of rapid formation of **4-5$_{tBu}$** followed by slow formation of **4-3$_{tBu}$.**

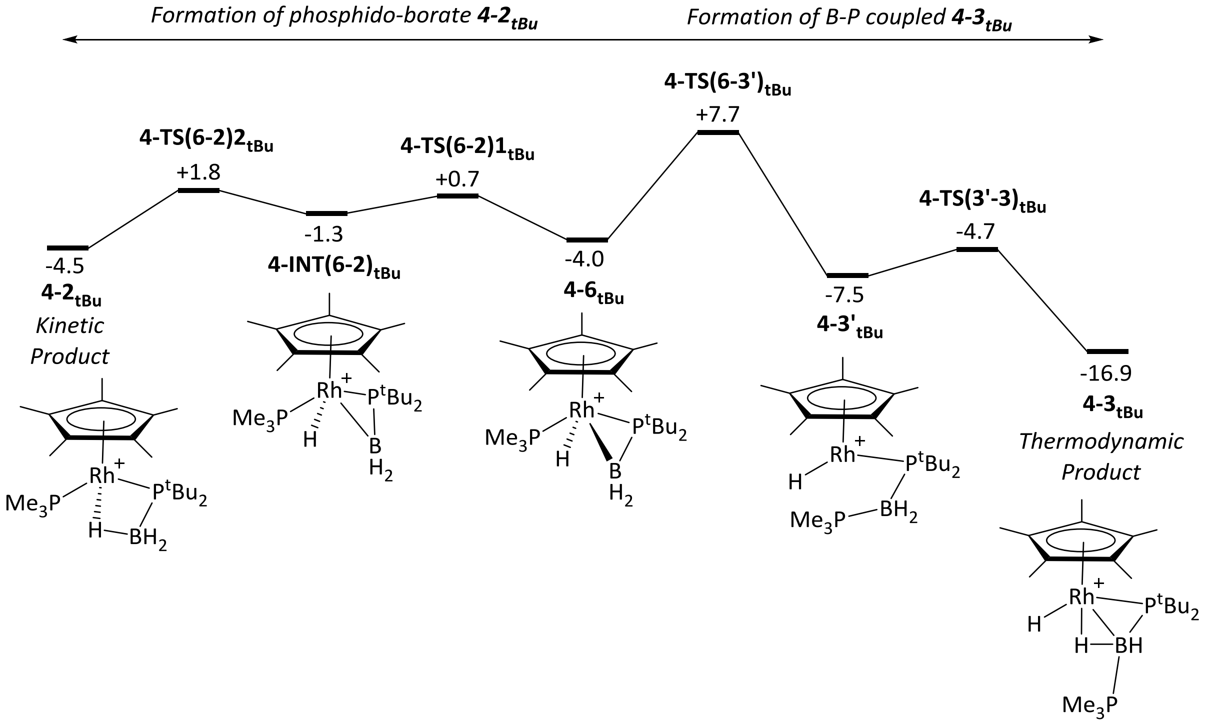

***Scheme 4-11**: Formation of **4-2$_{tBu}$** and **4-3$_{tBu}$** from **4-6$_{tBu}$**. Relative free energies BP86(D3BJ, CH2Cl2)/BS1 in kcal mol^{-1}.*

4.3.6 – The Stoichiometric Reaction with H_3B-PR_2H (R = Ph, Cy, Me)

The mechanistic pathways were also characterised for H_3B-PR_2H with R = Ph, Cy and Me. Experimental results showed H_3B-PPh_2H and H_3B-PCy_2H rapidly formed phosphido-borate product **4-2$_R$** at room temperature. The formation of αB-H agostic boryl complexes, **4-5$_R$**, and phosphino-borane complexes, **4-6$_R$**, from phosphine-borane complexes, **4-4$_R$**, are detailed in **Scheme 4-12**. For all phosphine-boranes the formation of complex **4-5$_R$** follows the same pathway as for H_3B-P^tBu_2H (**Section 4.3.5**). A σ-CAM process still proceeds through **4-TS(4-5'')1$_R$** to form methane σ-complex **4-INT(4-5'')$_R$**. The methane then dissociates *via* **4-TS(4-5'')2$_R$** to yield a δC-H agostic complex **4-5''$_R$** (or a unsaturated complex in the case of R = Me) which can then isomerise to the favoured boryl isomer **4-5$_R$** *via* B-P bond rotation **4-TS(5-5'')$_R$**. The highest energy process is the σ-CAM step (as with R = ^{t}Bu) *via* **4-TS(4-5'')1$_R$** with an overall free energy barrier of 12.0 kcal mol^{-1} for R = Ph, 12.3 kcal mol^{-1} for R = Cy and 12.8 kcal mol^{-1} for R = Me. This is similar to the barrier of 14.1 kcal mol^{-1} calculated for R =^{t}Bu and still agrees with the loss of methane occurring rapidly at room temperature.

There are differences in the energetics of the formation of the phosphino-borane complex, **4-6$_R$**. The complex is still formed through a P-H activation step from complex, **4-5''$_R$**, *via* **4-TS(5''-6)$_R$**. However, this step proceeds with much lower barriers for R = Ph (0.8 kcal mol^{-1}), Cy (3.4 kcal mol^{-1}), and Me (0.2 kcal mol^{-1}) than for R = ^{t}Bu (24.2 kcal mol^{-1}). This is suggested to be a steric effect which is further studied in **Section 4.3.7**. Therefore, when R = Ph, Cy and Me the rate determining process for the formation of intermediate **4-6$_R$**, is not the P-H activation step through **4-TS(5''-6)$_R$**) as with R = ^{t}Bu but is the σ-CAM process *via* **4-TS(4-5'')1$_R$**. Furthermore, for R = Ph, Cy, and Me the barrier for the P-H activation step through **4-TS(5''-6)$_R$** towards the formation of intermediate **4-6$_R$** is lower than the P-B rotation step *via* **4-TS(5-5'')$_R$** for the formation of complex **4-5$_R$**. This indicates that isolating and characterising complex **4-5$_R$** experimentally for R = Ph, Cy and Me would not be possible. This fits with the experimental data that no intermediates were observed during the rapid formation of **4-2$_R$** with R = Ph and Cy.

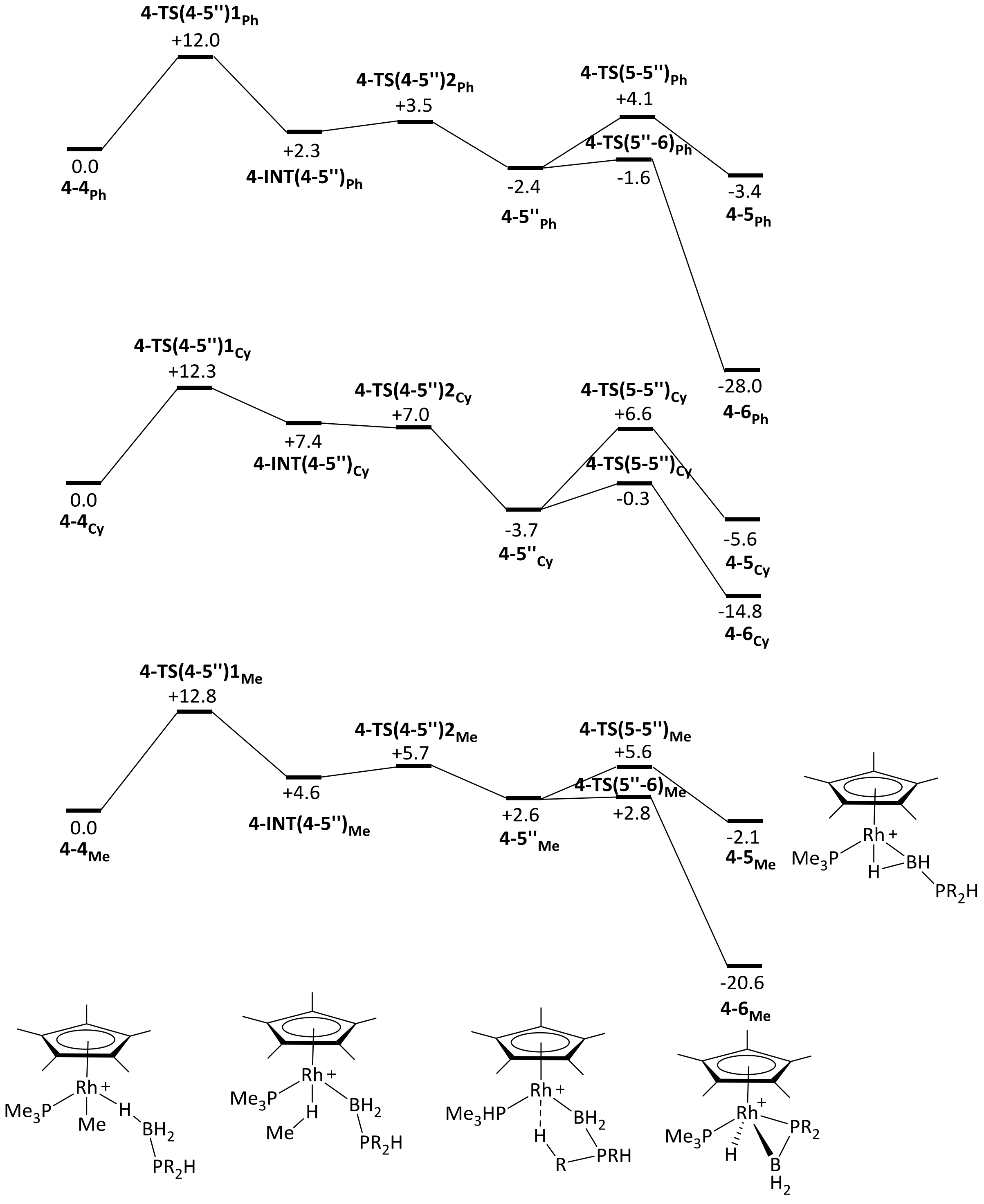

***Scheme 4-12**: Formation **of 4-5$_R$** and **4-6$_R$** from **4-4$_R$** (R = Ph, Cy, Me). Relative free energies BP86(D3BJ, CH2Cl2)/BS1 in kcal mol^{-1}.*

The relative free energies for intermediate, **4-6$_R$** also vary between the four phosphine-boranes calculated, with R = ^{t}Bu being significantly higher in energy (G = -4.5 kcal mol^{-1} compared to R = Ph (G = -28.0 kcal mol^{-1}), Cy = (G = -14.8 kcal mol^{-1}) and Me (-20.6 kcal mol^{-1}). This is suggested to be due to steric interactions between the phosphino-borane and the Cp* and PMe$_3$ ligands which will be discussed further in **Section 4.3.7**. This is reflected in the Rh-P bond distances displayed in **Figure 4-8** with **4-6$_{\mathbf{tBu}}$** displaying the longest distance of 2.44 Å (**Figure, 4-5**) compared to 2.43 Å in **4-6$_{\mathbf{Cy}}$,** 2.37 Å in **4-6$_{\mathbf{Ph}}$** and 2.36 Å in **4-6$_{\mathbf{Me}}$**. Despite **4-6$_{\mathbf{tBu}}$** and **4-6$_{\mathbf{Cy}}$** displaying similar bond lengths, the respective Tolman cone angles of 182 ° (P^tBu_3) and 170 ° (PCy_3) could explain the difference in relative free energies.[192]

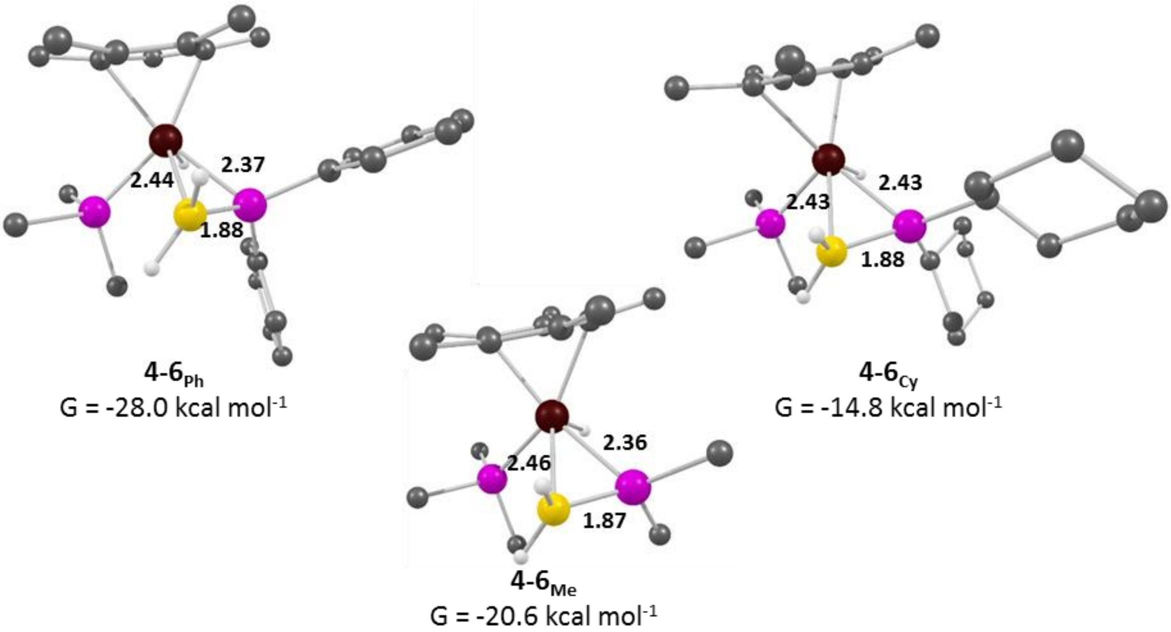

4-6$_{\mathbf{Ph}}$
G = -28.0 kcal mol^{-1}

4-6$_{\mathbf{Cy}}$
G = -14.8 kcal mol^{-1}

4-6$_{\mathbf{Me}}$
G = -20.6 kcal mol^{-1}

***Figure 4-8**: Optimised geometries of **4-6$_{\mathbf{R}}$** (R = Ph, Cy, Me). Hydrogens bonded to carbon omitted for clarity. Key distances in Å.*

The reaction selectivity is determined proceeding from **4-6$_{\mathbf{R}}$.** The formation of phosphido-borate complex **4-2$_{\mathbf{R}}$** (the experimentally observed product for R = Ph and Cy) and the B-P coupled complex, **4-3$_{\mathbf{R}}$** from **4-6$_{\mathbf{R}}$** is shown in **Scheme 4-13**. The formation of **4-2$_{\mathbf{R}}$** still occurs *via* a two-step rotation of the {BH_2PR_2} moiety through **4-TS(6-2)1$_{\mathbf{R}}$** and **4-TS(6-2)1$_{\mathbf{R}}$.** During the rotation of the {BH_2PR_2} moiety for R = Ph, Cy and Me the BH_2 group passes closer to the Cp* ring and not the PR_2 group as with R = ^{t}Bu. This is thought to be a steric effect. The free energy barriers of the formation of **4-2$_{\mathbf{R}}$** from **4-6$_{\mathbf{R}}$** are 15.3 kcal mol^{-1}, 10.2 kcal mol^{-1}, and 12.8 kcal mol^{-1} respectively (relative to **4-6$_{\mathbf{R}}$**). Furthermore, unlike with R = ^{t}Bu the formation of **4-2$_{\mathbf{R}}$** is irreversible. The alternative formation of complex **4-2$_{\mathbf{R}}$** through P-H transfer, as characterised for R = ^{t}Bu in **Section 4.3.4**, were also calculated for R = Ph, Cy and Me and found to be similarly disfavoured. The formation of the B-P coupled complex, **4-3$_{\mathbf{R}}$** occurs as before with B-P bond coupling through **4-TS(6-3')** and B-P bond rotation *via* **4-TS(3'-3)**. This process has a free energy barrier of 22.5 kcal mol^{-1} for R = Ph, 14.7 kcal mol^{-1} for R = Cy and 21.7 kcal mol^{-1} for R = Me relative to **4-6$_{\mathbf{R}}$**. This means that the formation of **4-2$_{\mathbf{R}}$** is the kinetically favoured pathway proceeding from **4-6$_{\mathbf{R}}$**. This was also the case for R = ^{t}Bu. However, **4-2$_{\mathbf{R}}$** is also more thermodynamically favoured than **4-3$_{\mathbf{R}}$** with G = -35.3 *vs.* -28.8 kcal mol^{-1} for R = Ph, G = -25.4 *vs.* -20.9 kcal mol^{-1} for R = Cy, and G = -

27.6 kcal mol^{-1} *vs.* -20.3 kcal mol^{-1} for R = Me. Therefore, **4-2$_R$** is the kinetic and thermodynamic product of the reaction for R = Ph, Cy, and Me.

In conclusion, phosphido-borate complex **4-2$_R$** is the experimentally observed product for reaction with H_3B-PR_2H (R = Ph, Cy) because it is kinetically and thermodynamically more stable than the B-P coupling product, **4-3$_R$** (experimentally observed for R = ^{t}Bu). This is thought to be caused by increased steric interactions between the ^{t}Bu and Cp* ring which destabilises **4-2$_{tBu}$** and **4-6$_{tBu}$** compared to the other phosphine-boranes. The rate determining process for R = Ph, Cy and Me is the first step of the two step rotation *via* **4-TS(6-1)2$_R$** with free energy barriers of 15.3 kcal mol^{-1}, 10.2 kcal mol^{-1} and 12.8 kcal mol^{-1} respectively. This differs from the rate determining process when R = ^{t}Bu. Furthermore, this is in agreement with the experimental observation that **4-2$_{Ph}$** and **4-2$_{Cy}$** are formed rapidly in the reaction conditions.

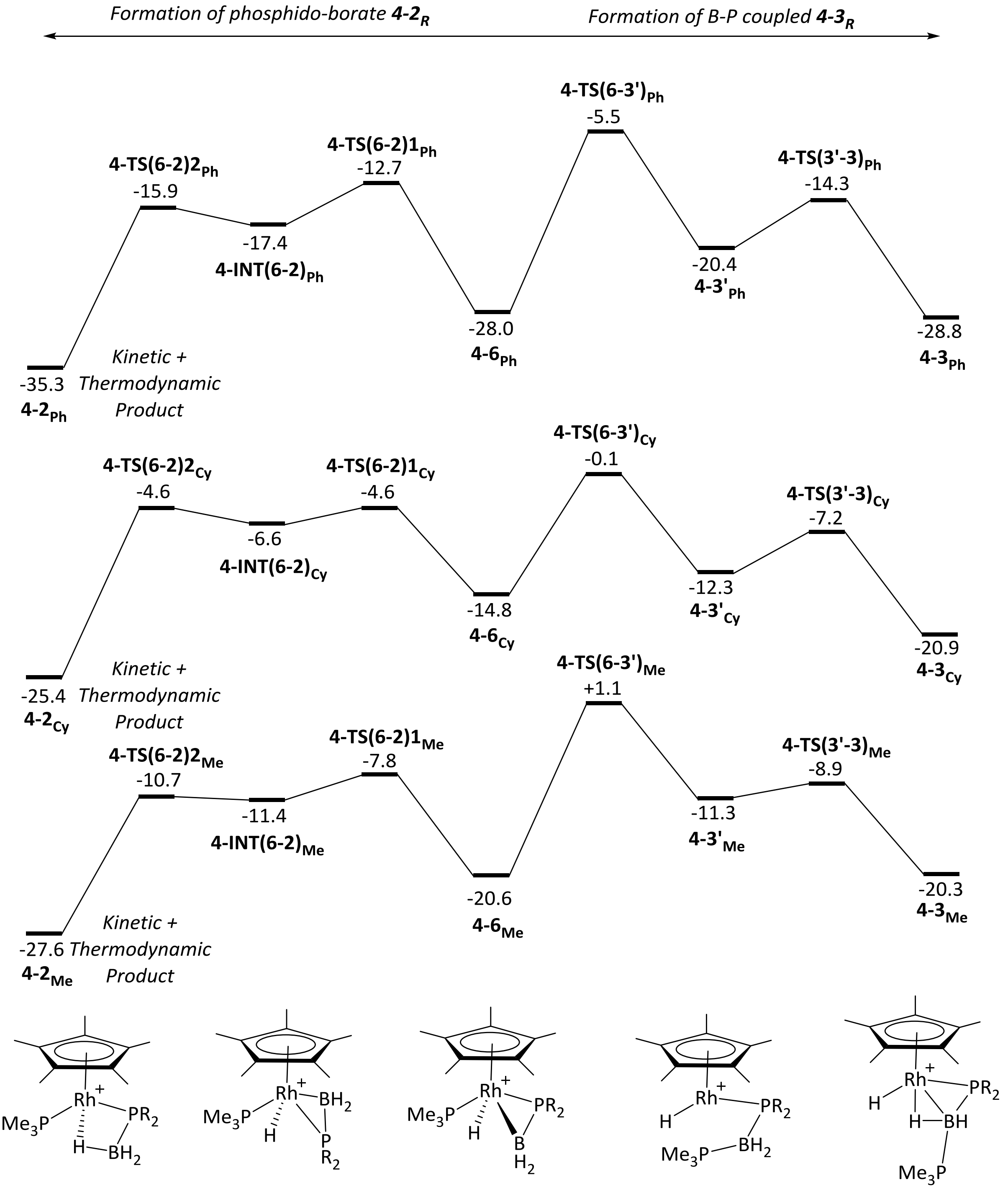

Scheme 4-13*: Formation of* ***4-2***$_R$ *and* ***4-3***$_R$ *from* ***4-6***$_R$ *(R = Ph, Cy, Me). Relative free energies BP86(D3BJ, CH2Cl2)/BS1 in kcal mol*$^{-1}$*.*

4.3.7 – Investigating the Effect of Sterics on Reaction Selectivity

In order to understand the influence of sterics in determining the reaction, phosphido-borate product **4-2**$_R$, η^2-phosphino-borane complex **4-6**$_R$, and P-H activation transition state **TS(5''-6)**$_R$ were optimised for R = ^{t}Bu and R = Me with Cp replacing the Cp* ring (**Table 4-1**). It has already been noted in **Section 4.3.6** that **4-2**$_{Me}$ has a free energy of -27.6 kcal mol^{-1} (**Table 4-1**)**.** Therefore **4-2**$_{Me}$ is more thermodynamically stable than **4-2**$_{tBu}$ (G = -4.5 kcal mol^{-1}) by 23.1 kcal mol^{-1}.

Furthermore, **4-Cp2$_{\mathbf{tBu}}$** (G = -17.5 kcal mol^{-1}) and **4-Cp2$_{\mathbf{Me}}$** (G = -29.7 kcal mol^{-1}) are relatively more thermodynamically stable than **4-2$_{\mathbf{tBu}}$** by 13.0 and 25.2 kcal mol^{-1} respectively. This shows that reducing the steric bulk of the ^{t}Bu group and Cp* ring stabilises the complex. The energy difference between **4-2$_{\mathbf{Me}}$** and **4-Cp2$_{\mathbf{Me}}$** is small which suggests the electronic change from Cp* to Cp does not have a large effect on the stability of **4-2$_{\mathbf{R}}$**. The same trends were observed for **4-6$_{\mathbf{tBu}}$** (G = -4.0 kcal mol^{-1}), **4-6$_{\mathbf{Me}}$** (G = -20.6 kcal mol^{-1}), **4-Cp6$_{\mathbf{tBu}}$** (G = -12.7 kcal mol^{-1}), and **4-Cp6$_{\mathbf{Me}}$** (G = -24.1 kcal mol^{-1}). Reducing the sterics in **4-6$_{\mathbf{R}}$** does not stabilise the complex as much as for **4-2$_{\mathbf{R}}$** which indicates that steric interactions are not as important in this case.

The results for transition state **4-TS(5''-6)$_{\mathbf{tBu}}$** (G = +17.2 kcal mol^{-1}) and **4-CpTS(5''-6)$_{\mathbf{tBu}}$** (G = +16.3 kcal mol^{-1}) suggest that steric interactions between the ^{t}Bu group and Cp* are not significant enough to destabilise the P-H activation transition state. However, **4-TS(5''-6)**$_{\mathrm{Me}}$ (G = +2.8 kcal mol^{-1}) is 14.4 kcal mol^{-1} more stable than **4-TS(5''-6)$_{\mathbf{tBu}}$** suggesting that the increased steric bulk of the ^{t}Bu is still a factor. It is likely that in this case, the steric interactions between the ^{t}Bu groups and the PMe_3 ligand destabilise the transition state. Furthermore, **4-CpTS(5''-6)$_{\mathbf{Me}}$** has a relative free energy of +1.7 kcal mol^{-1} which is similar to that of **4-TS(5''-6)$_{\mathbf{Me}}$** suggesting that the inductive effect of Cp* does no affect the stability of **4-TS(5''-6)$_{\mathbf{R}}$**.

	L = Cp*, R = ^{t}Bu	**L = Cp, R = ^{t}Bu**	**L = Cp*, R = Me**	**L = Cp, R = Me**
4-L2$_{\mathbf{R}}$	-4.5	-17.5	-27.6	-29.7
4-L6$_{\mathbf{R}}$	-4.0	-12.7	-20.6	-24.1
4-LTS(5''-6)$_{\mathbf{R}}$	+17.2	+16.3	+2.8	+1.7

***Table 4-1**: Relative free energies in kcal mol^{-1} of selected intermediates and transition states.*

In conclusion, the instability of phosphido-borate, **4-2$_{\mathbf{tBu}}$**, and η^2-(H_2B-P^tBu_2) complex, **4-6$_{\mathbf{tBu}}$**, compared to **4-2$_{\mathbf{R}}$ and 4-6$_{\mathbf{R}}$** (R = Ph, Cy, Me) is primarily due to the increased steric interactions between the ^{t}Bu group and the Cp* ring compared to the other R groups.

4.4 – Functional Testing of Key Intermediates and Transition States

Functional testing was carried out to check if the trends observed from the computed pathways were dependent on the computational set-up (**Section 4.1.2**). The difference in energy between phosphido-borate **4-2$_{tBu}$**, and B-P coupled product, **4-3$_{tBu}$**, was selected for testing because it is a key difference in the interpretation of the stoichiometric mechanism detailed above. Furthermore, the P-H activation transition state **4-TS(5''-6)$_{R}$** (R = ^{t}Bu, Ph) was tested. This was due to the large energy difference between ^{t}Bu and Ph proving to be the reason behind reaction with R = ^{t}Bu being considerably slower than reaction with R = Ph. Therefore, single point calculations were run on **4-2$_{tBu}$**, **4-3$_{tBu}$**, **4-TS(5''-6)$_{tBu}$**, and **4-TS(5''-6)$_{Ph}$** with a variety of functionals both with and without dispersion corrections (when applicable). Results are displayed in **Table 4-2**.

The calculations show that adding dispersion stabilises **4-2$_{tBu}$** and de-stabilises **4-3$_{tBu}$**. This could be a result of the PMe$_3$ group being bonded to the metal in **4-2$_{tBu}$** (**Figure 4-6**) compared to **4-3$_{tBu}$** (**Figure 4-5**) where it is not. Treating for dispersion would capture stabilising long range H⋯H interactions between the PMe$_3$ and Cp* ligands in **4-2$_{tBu}$** that would not be present in **4-3$_{tBu}$**. Despite this, **4-3$_{tBu}$** is always more thermodynamically stable than **4-2$_{R}$** regardless of functional choice or treatment of dispersion with the energy difference between **4-2$_{tBu}$** and **4-3$_{tBu}$** ranging from 9.7 kcal mol^{-1} (B97D) to 20.1 kcal mol^{-1} (PBE0). Therefore, **4-3$_{tBu}$** would always be predicted to be the observed product which fits the experimental observations. Furthermore, **4-TS(5''-6)$_{tBu}$** is always significantly higher in free energy compared to **4-TS(5''-6)$_{Ph}$**. Adding dispersion destabilises both transition states but affects **4-TS(5''-6)$_{Ph}$** more than **4-TS(5''-6)$_{tBu}$** meaning that, as with **4-2$_{tBu}$** and **4-3$_{tBu}$**, adding a treatment of dispersion reduces the relative free energy difference. This means that reaction with R = ^{t}Bu would always be predicted to take significantly longer than reaction with R = Ph which agrees with the experimental data. Overall, the trends in the thermodynamics and kinetics of the stoichiometric reaction are not dependent on functional or dispersion.

Functional	**4-2$_{tBu}$**	**4-3$_{tBu}$**	**ΔG^1**	**4-TS(5''-6)$_{tBu}$**	**4-TS(5''-6)$_{Ph}$**	**ΔG^2**
BP86	-3.1	-21.7	18.6	+15.0	-6.4	21.4
BP86-D3	-4.5	-16.7	12.2	+17.2	-1.6	18.8
PBE0	-0.7	-20.8	20.1	+22.5	-4.6	27.1
PBE0-D3	-2.9	-18.7	15.8	+23.4	-1.8	25.2
B3LYP	-0.2	-19.4	19.2	+20.3	-8.1	28.4
B3LYP-D3	-2.9	-15.0	12.1	+21.5	-3.2	24.7
M06	-3.8	-13.6	9.8	+19.7	-5.3	25.0
B97D	-4.0	-13.7	9.7	+18.1	-3.8	21.9
***ω*B97XD**	-1.1	-16.3	15.2	+25.0	-2.5	27.5

Table 4-2: *Functional testing on the relative free energies (kcal mol^{-1}) of* ***4-2$_{tBu}$, 4-3$_{tBu}$, 4-TS(5''-6)$_{tBu}$,*** *and* ***4-TS(5''-6)$_{Ph}$.*** *ΔG^1 = (**4-2$_{tBu}$** – **4-3$_{tBu}$**). ΔG^2 = (**4-TS(5''-6)$_{tBu}$** – **4-TS(5''-6)$_{Ph}$**).*

Following the results from the benchmarking study conducted in **Chapter 3**, the isomerisation mechanisms between the boryl, **4-5$_R$**, borylene, **4-5'$_R$**, and δC-H agostic **4-5''$_R$**, complexes (**Scheme 4-14**) as well as the formation of phosphido-borate **4-2$_R$** and B-P coupled **4-3$_R$** products from phosphino-borane intermediate **4-6$_R$**, (**Scheme 4-15**) were calculated with *ω*B97XD single point using the same basis set approach and correcting for solvation for R = ^{t}Bu and Ph. The calculations show that the calculated free energies using the *ω*B97XD functional continues to predict isomer **4-5$_R$** as more favourable than isomers **4-5'$_R$** and **4-5''$_R$**. Furthermore, the isomerisation pathways, **4-TS(5-5')$_R$** and **4-TS(5-5'')$_R$**, remain accessible at low temperatures.

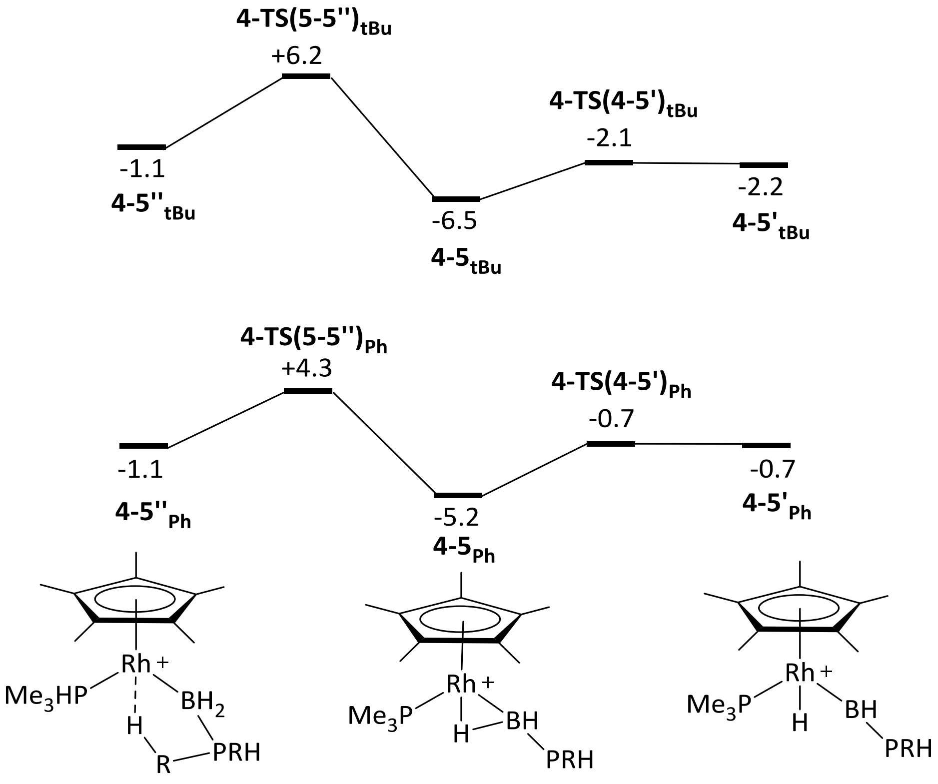

***Scheme 4-14**: Isomerisation of **4-5$_R$** (R = ^{t}Bu, Ph). Relative free energies ωB97XD(CH_2Cl_2)/BS1 (on previously BP86 optimised geometries) in kcal mol^{-1}.*

Scheme 4-15 shows that complex **4-2$_R$** is still the kinetically favoured pathway from **4-6$_R$** for R = ^{t}Bu and Ph with barriers of 4.2 and 13.4 kcal mol^{-1} respectively compared to barriers of 9.3 and 21.1 kcal mol^{-1} towards the formation of **4-3$_R$**. For R = ^{t}Bu, **4-2$_{tBu}$** (G = -0.6 kcal mol^{-1}) remains thermodynamically disfavoured compared to **4-3**$_{tBu}$ (G = -17.1 kcal mol^{-1}) and close in energy to **4-6$_{tBu}$** (G = +1.7 kcal mol^{-1}). For R = Ph, **4-2$_{Ph}$** (G = -32.7 kcal mol^{-1}) is more thermodynamically stable than **4-3$_{Ph}$** (G = -28.7 kcal mol^{-1}) and **4-6$_{Ph}$** (G = -22.7 kcal mol^{-1}). Furthermore, the rate determining process for R = ^{t}Bu is still the P-H activation step *via* **4-TS(5''-6)** with a free energy barrier of 28.1 kcal mol^{-1} while for R = Ph it is the first step of the two-step rotation (ΔG = 13.4 kcal mol^{-1}). Therefore, the agreement with the experimental observations discussed in **Section 4.3** is not functional dependant.

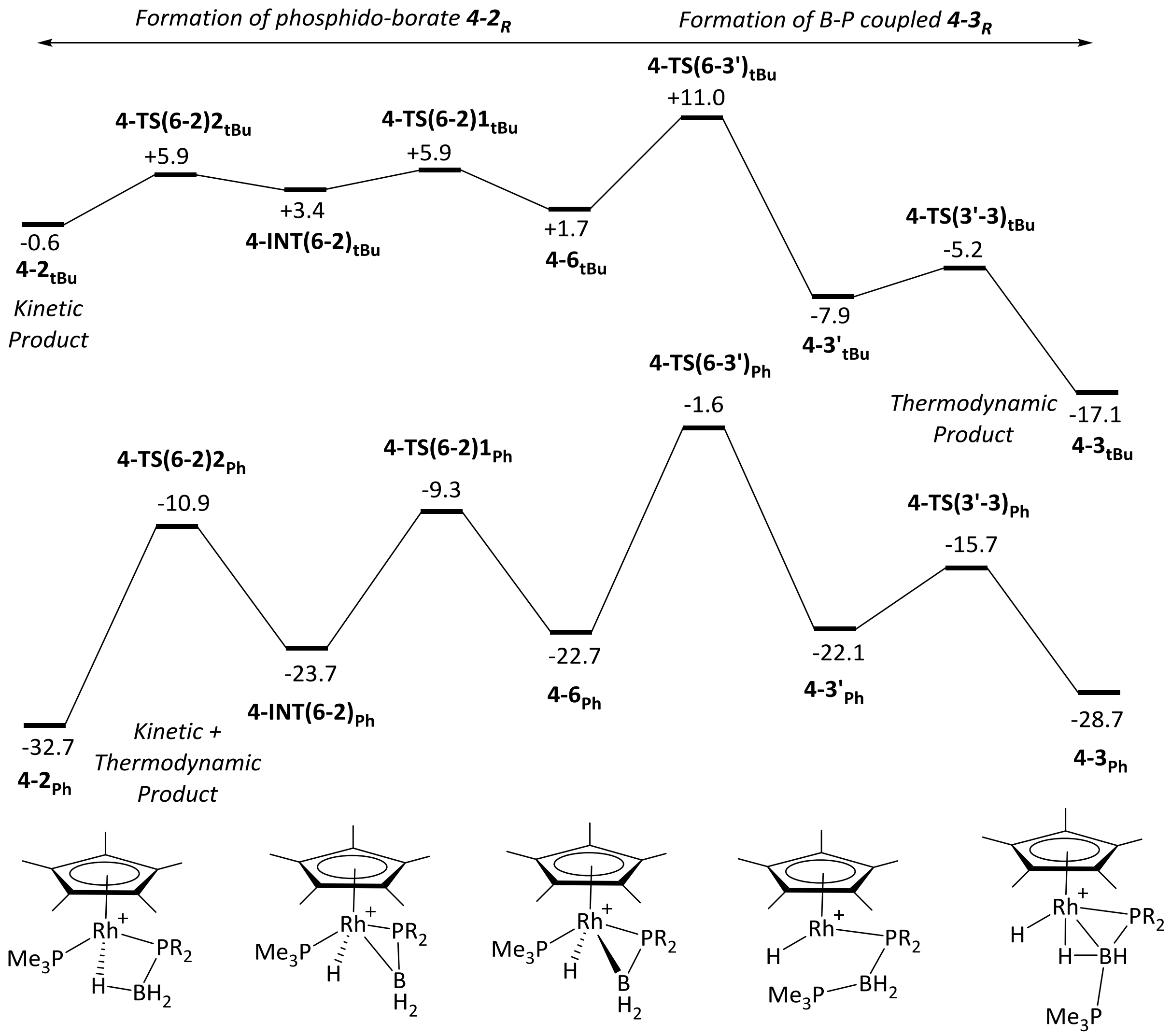

Scheme 4-15: *Formation of **4-2$_R$** and **4-3$_R$** from **4-6$_R$** (R = ^{t}Bu, Ph). Relative free energies ωB97XD(CH_2Cl_2)/BS1 (on previously BP86 optimised geometries) in kcal mol^{-1}.*

4.5 – Conclusions

Geometry optimisation and chemical shift calculations were utilised in order to determine the structure of **$4\text{-}5_R$,** $[Rh(H_2B\text{-}PR_2H)(PMe_3)(Cp^*)]^+$. Calculations concluded the most stable isomer is that of a boryl complex containing an αB-H agostic interaction ($[Rh(\eta^1\text{-}H_2B\text{-}PR_2H)(PMe_3)(Cp^*)]^+$, **$4\text{-}5_R$**) rather than either a borylene complex ($[Rh(H)(HB\text{-}PR_2H)(PMe_3)(Cp^*)]^+$, **$4\text{-}5'_R$**) or a δC-H agostic complex ($[Rh(H_2B\text{-}PR_2H)(PMe_3)(Cp^*)]^+$, **$4\text{-}5''_R$**) (**Figure 4-1**) as it had: i) the lowest relative free energy and ii) the closest calculated ^{11}B chemical shift to the experimental value. Pathways between the three isomers were also calculated (**Scheme 4-4**). Oxidative cleavage of the αB-H agostic in **$4\text{-}5_R$** would result in the formation of **$4\text{-}5'_R$** while a B-P bond rotation pathway forms **$4\text{-}5''_R$** from **$4\text{-}5_R$**. These results were found to be consistent when R = ^{t}Bu, Ph, Cy, and Me.

The mechanism of the formation of the boryl complex, **$4\text{-}5_R$**, from phosphine-borane complex, **$4\text{-}4_R$** was characterised (**Section 4.3.1**). A σ-CAM process and loss of methane yields δC-H agostic complex, **$4\text{-}5''_R$**, which can then isomerise to **$4\text{-}5_R$**. This mechanism is similar energetically for R = ^{t}Bu, Ph, Cy and Me. Complex **$4\text{-}5''_R$** can also go through a P-H activation step to from phosphino-borane complex **$4\text{-}6_R$** (**Section 4.3.2**). Due to their reduced steric bulk, R = Ph, Cy and Me exhibit easier P-H activation steps. Regardless, the differing selectivity in the stoichiometric reaction is not determined prior to the formation of **$4\text{-}6_R$.**

From complex **$4\text{-}6_R$** the reaction selectivity is determined. Phosphido-borate **$4\text{-}2_R$** (**Section 4.3.3**) can be formed through a two-step rotation of the $\{BH_2PR_2\}$ moiety. This proceeds with a barrier of 5.8 (R = ^{t}Bu), 15.3 (R = Ph), 10.2 (R = Cy), and 12.8 (R = Me) kcal mol^{-1} from **$4\text{-}6_{tBu}$**. For R = ^{t}Bu the rotation is a reversible process, this is not the case for R = Ph, Cy and Me. The B-P coupled complex, **$4\text{-}3_R$** (**Section 4.3.2**) is formed *via* P-B bond formation between the phosphino-borane and PMe_3 group followed by P-B bond rotation. This proceeds with a barriers of 11.7 (R = ^{t}Bu), 22.5 (R = Ph), 14.7(R = Cy), and 21.7 (R = Me) kcal mol^{-1} from **$4\text{-}6_{tBu}$.** The formation of **$4\text{-}2_R$** from **$4\text{-}6_R$** is always kinetically favoured than the formation of **$4\text{-}3_R$**. However, for R = ^{t}Bu, **$4\text{-}3_{tBu}$** (G = -16.9 kcal mol^{-1}) is more thermodynamically favoured than **$4\text{-}2_{tBu}$** (G = -4.5 kcal mol^{-1}). Therefore **$4\text{-}3_{tBu}$** is the experimentally observed product. This is not the case for R = Ph, Cy, and Me where **$4\text{-}2_R$** is always thermodynamically more favoured than **$4\text{-}3_R$** and therefore, the experimentally observed product.

The rate determining step for the formation of **$4\text{-}3_{tBu}$** from **$4\text{-}4_{tBu}$** is the P-H activation *via* **4-TS(5''-6)$_{tBu}$** with an overall free energy barrier of 24.2 kcal mol^{-1}. This coincides with the rapid formation of **$4\text{-}5_{tBu}$** followed by the relatively slow formation of **$4\text{-}3_{tBu}$**. The rate determining step for the formation of **$4\text{-}2_R$** from **$4\text{-}4_R$** (R = Ph, Cy, Me) is the first step of the two-step rotation, **4-TS(6-2)1$_R$**

with overall free energy barriers of 15.3, 10.2, and 12.8 kcal mol^{-1} respectively. This fits with the experimental observation that **4-2$_R$** (R = Ph, Cy) forms rapidly at room temperature.

In conclusion, the increased steric bulk of ^{t}Bu compared to Ph, Cy and Me is the main factor in the deviation in the selectivity of the stoichiometric reaction. The calculations show that increased steric clashing between the ^{t}Bu group and the Cp* ring destabilises **4-2$_{tBu}$** so it is no longer the thermodynamically favoured product. The computed mechanisms fit the experimental observations of rapid formation of **4-2$_{Ph}$** and **4-2$_{Cy}$** and the slower formation of **4-3$_{tBu}$**. Functional testing calculations allows the conclusion that the proposed mechanism and trends in thermodynamics and kinetics are not functional dependant (**Section 4.4**).

Chapter 5: The Dehydropolymerisation of Amine-Boranes with Cationic and Neutral Alkyl-Xantphos-Rhodium Catalysts

5.1 – Introduction

5.1.1 – Experimental Studies

5.1.1.1 – Catalysis with Neutral [Rh(*mer*-κ^3-P,O,P-Xantphos-^{i}Pr)H], 5-1$_{iPr}$

The Weller group found that reacting H_3B-$NMeH_2$ with 0.2 mol% of **5-1$_{iPr}$** in 1,2-$F_2C_6H_4$ at room temperature produced polyamino-borane with an M_n of 28,000 g mol^{-1} and a PDI of 1.9 in 30 minutes.[16] Catalysis was also carried out using THF as a solvent, however, this resulted in slower reaction times due to the greater co-ordinating ability of THF. Therefore, 1,2-$F_2C_6H_4$ was used as the reaction solvent for the mechanistic studies. Only a small amount of borazine side-products was observed. Mechanistic studies into the polymerisation mechanism found long polymer chains of M_n *10,000* g mol^{-1} at low H_3B-$NMeH_2$ conversion with no evidence of short chain oligomers. This suggested a chain-growth propagation mechanism was taking place. Furthermore, addition of two successive batches of H_3B-$NMeH_2$ did not result in increased polymer length which indicates the polymerisation is not living, but is rechargeable. This contrasts with aryl-Xantphos catalyst [Rh(κ^2-P,P-Xantphos-Ph)((^{t}BuCH$_2$CH$_2$)H$_2$B-NMe$_3$)] (**Chapter 1, Section 1.1.3**) which is proposed to proceed via a coordination-insertion propagation mechanism.[193] Catalyst **5-1$_{iPr}$** was found to be so sensitive that repeat runs using the same batch of solvent differed significantly making obtaining consistent KIE values impossible. The authors suggest this is due to irreversible catalyst decomposition due to unavoidable impurities entrained in the reaction vessels (O_2). Speciation studies saw the rapid formation of several hydride-containing species including what is thought to be a complex containing five metal-hydrogen interactions, [Rh(Xantphos-^{i}Pr)H$_5$] (also observed by Esteruelas *et al.*).[111] An induction period of between 20 and 90 seconds was observed during H_2 evolution studies.

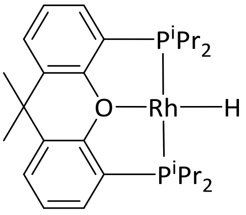

5-1$_{iPr}$

Figure 5-4: *[Rh(mer-κ^3-P,O,P-Xantphos-^{i}Pr)H],* ***5-1$_{iPr}$***

Esteruelas *et al.*[111] conducted a DFT mechanistic study on the reaction of **5-1$_{iPr}$** with H_3B-NH_3 and proposed the mechanism shown in **Scheme 5-1**. In their study they quote energies from the M06/6-311g**,SDD(Rh, P) level with a solvent correction for THF from geometries optimised using the M06//6-31g**,lanl2dz(Rh,P) level of theory. They propose that the Xantphos ligand isomerises from *mer*-κ^3-P,O,P-Xantphos to *cis*-κ^2-P,P-Xantphos **5-I**. This allows a molecule of H_3B-NH_3 to bind to the vacant site and form **5-II**. An initial B-H activation with a calculated barrier of 22.0 kcal mol^{-1} then occurs to form **5-III** before a harder N-H activation forms dihydrogen, hydride complex **5-IV** and free $H_2B=NH_2$.The H_2 ligand then dissociates to reform the active catalyst **5-I**. This process was calculated to have an overall barrier of 31.7 kcal mol^{-1}.

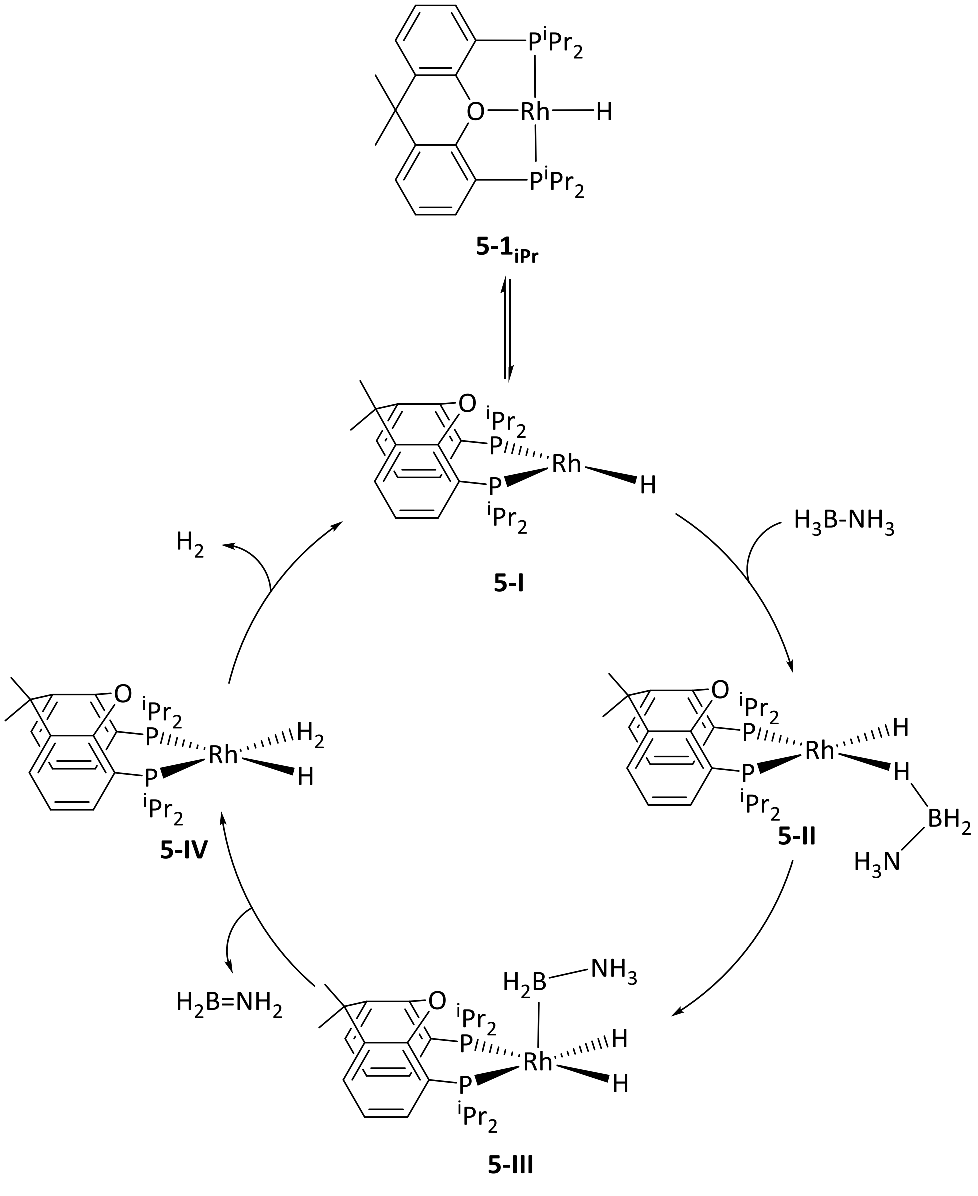

Scheme 5-1: *Proposed mechanism for the dehydrogenation of H_3B-NH_3 with **5-1$_{iPr}$** by Esteruelas et al. Adapated from reference No. 111*

5.1.1.2 – Catalysis with Neutral [Rh(*mer*-κ^3-P,O,P-Xantphos-^{t}Bu)H], 5-1$_{tBu}$

The Weller group found that reacting H_3B-$NMeH_2$ with catalyst **5-1$_{tBu}$** would form polyaminoborane under the same catalytic conditions used for **5-1$_{iPr}$**. The bulkier substituents on the Xantphos ligand meant that reaction times increased to 270 minutes and more dehydrocoupling side-products such as borazine, $[HBNMe]_3$, were produced. Speciation studies indicated that **5-**

1_{tBu} is the resting state during catalysis as it was the sole organometallic species observed. This differs from the speciation studies with **5-1_{iPr}** which observes several hydride-containing species.

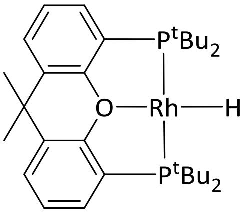

5-1_{tBu}

Figure 5-2: *[Rh(mer-κ^3-P,O,P-Xantphos-^{t}Bu)H],* ***5-1_{tBu}***

5.1.1.3 – Catalysis with Cationic [Rh(*mer*-κ^3-P,O,P-Xantphos-^{i}Pr)(H)$_2$(η^1-H_3B-NMe_3)][BAr$^F{}_4$], 5-2_{iPr}

The Weller group also investigated cationic alkyl-Xantphos complexes in the catalytic dehydrocoupling of amine-boranes. Reaction of **5-2_{iPr}** with H_3B-$NMeH_2$ in the same conditions as previously discussed formed polyamino-boranes with a M_n of 9,000 g mol^{-1}and a PDI of 2.9 in 20 minutes. This is a lower M_n and higher PDI than reported for catalyst **5-1_{iPr}**. Mechanistic studies indicate that despite the difference in polymer lengths, the two catalysts operate *via* a chain-growth propagation mechanism. Catalyst **5-2_{iPr}** was less sensitive to the unavoidable impurities entrained in the reaction vessel than **5-1_{iPr}** allowing for KIE values to be reported. A low KIE of 0.8 ± 0.4 for BH/BD substitution and a large KIE of 4.6 ± 0.2 for NH/ND substitution was recorded. This suggests that N-H activation is involved in the rate limiting step of the reaction. As with neutral catalyst **5-1_{iPr}** an induction period of between 20 and 90 seconds was observed. Speciation studies found an organometallic species formed at the end of catalysis which was identified to be dimer [(Rh(κ^3-P,O,P-Xantphos-^{i}Pr))$_2$μ-B][BAr$^F{}_4$] which is further discussed in **Chapter 6**. The fact that the isolated dimer is mono-cationic indicates that there are neutral organometallic species present in the catalytic solution. Therefore, potential hydride transfer mechanisms (as discussed in **Chapter 1, Section 1.1.2.4**) could be taking place in order to form these neutral species.

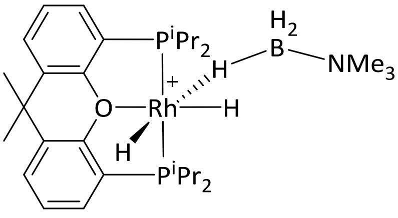

5-2_{iPr}

Figure 5-3: *[Rh(mer-κ^3-P,O,P-Xantphos-^{i}Pr)(H)$_2$(η^1-H_3B-$NMeH_2$)]$^+$,* ***5-2_{iPr}***

5.1.1.4 – Catalysis with Cationic [Rh(*mer*-κ^3-P,O,P-Xantphos-^{t}Bu)H_2][BAr$^F_4$], 5-3$_{tBu}$

Complex [Rh(κ^3-P,O,P-Xantphos-^{t}Bu)(H)$_2$][BAr$^F_4$], **5-3$_{tBu}$** (**Figure 5-4**) was used as the active catalyst to compare with catalyst **5-2$_{iPr}$**. This is because the equivalent complex [Rh(κ^3-P,O,P-Xantphos-^{t}Bu)(H)$_2$(η^1-H_3B-NMe_3)], **5-2$_{tBu}$**, could not be isolated. This is thought to be due to the increased steric hindrance provided by the ^{t}Bu groups making the H_3B-NMe_3 binding disfavoured. However, H/D exchange reactions suggested that complex **5-2$_{tBu}$** is kinetically accessible in the reaction conditions. Catalyst **5-3$_{tBu}$** was found to form polyamino-borane upon reaction with H_3B-$NMeH_2$ but, as with neutral catalyst **5-1$_{tBu}$**, it required longer reaction times and produced more dehydrocoupling side-products than its ^{i}Pr analogue. Speciation studies found that catalyst **5-3**$_{tBu}$ was the only organometallic species in solution at the end of catalysis as well as a small amount of boronium cation [$BH_2(NMeH_2)_2$]$^+$. This gives further indication to a hydride abstraction process occurring in the cationic catalysis.

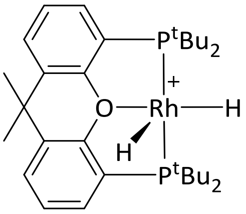

5-3$_{tBu}$

Figure 5-4: *[Rh(mer-κ^3-P,O,P-Xantphos-^{t}Bu)(H)$_2$]$^+$,* ***5-3$_{tBu}$***

5.1.2 – Proposed Dehydrocoupling Mechanism

From the mechanistic evidence obtained through experiment, the Weller group proposed the dehydrocoupling mechanism shown in **Scheme 5-2**. For cationic catalysts, initial B-H activation occurs from **5-V** to form **5-VI**. This intermediate can then proceed through an N-H activation to form H_2, amino-borane and regenerate the catalyst (Pathway A). Another possibility is for a free $NMeH_2$ molecule to attack the {H_2B-$NMeH_2$} moiety resulting in the formation of neutral complex [Rh(κ^3-P,O,P-Xantphos-^{t}Bu)H_3] **5-VII** and boronium cation [$BH_2(NMeH_2)_2$]$^+$ (Pathway B). The formed boronium cation could either protonate [Rh(*mer*-κ^3-P,O,P-Xantphos-^{t}Bu)H_3] to form a cationic dihydride **5-VIII** or be dormant in the reaction and become off-cycle. Neutral catalysts **5-IX** proceed through a B-H, then N-H activation mechanism to form amino-borane and H_2 before regenerating the catalyst. The propagation mechanism is proposed to involve a chain-growth mechanism for both neutral and cationic catalysts.

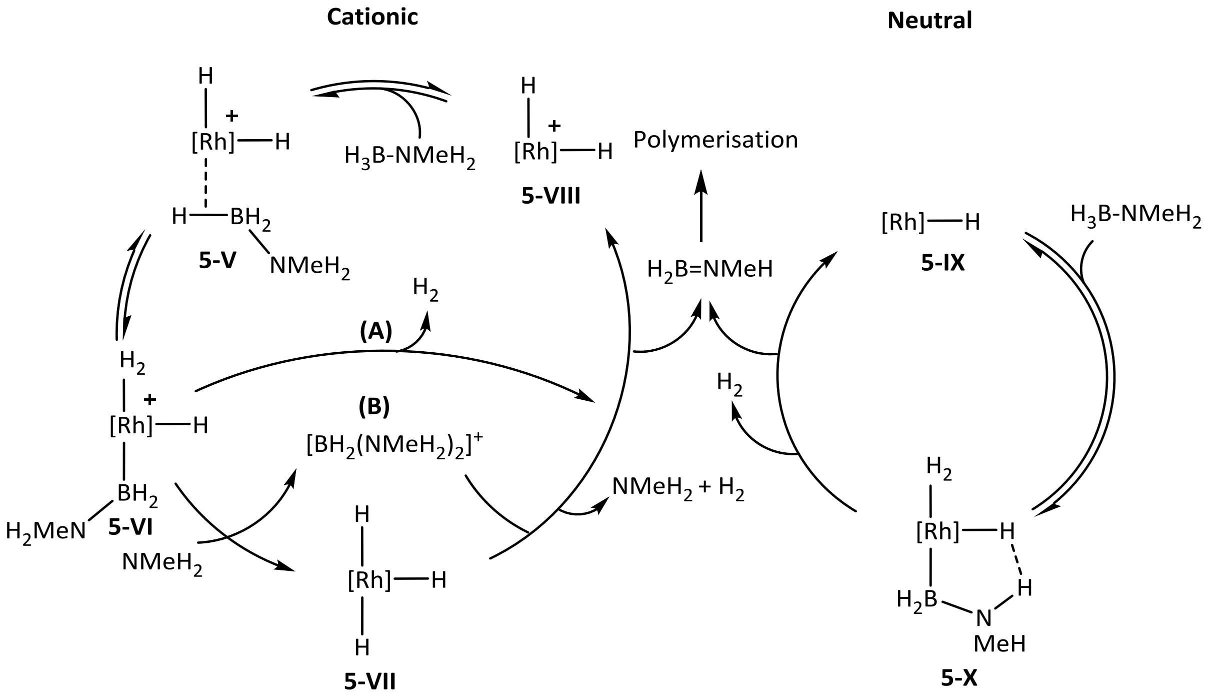

Scheme 5-5: Proposed mechanism for the dehydrocoupling of H_3B-$NMeH_2$ using *alkyl-Xantphos catalysts. Adapted from reference No. 16.*

5.1.3 – Computational Details

Calculations were run with Gaussian 09 Revision D.01.[175] Geometry optimisations were performed using the BP86 functional. The Rh and P centres were described with the Stuttgart pseudopotentials and associated basis sets[158] (with added d-orbital polarisation on P (ς = 0.387))[174] and 6-31G** basis sets[156, 157] described all other atoms. All stationary points were fully characterised *via* analytical frequency calculations as either minima (all positive frequencies) or transition states (one imaginary frequency). IRC calculations and subsequent geometry optimisations were used to confirm the minima linked by each transition state. Frequency calculations also provided a free energy in the gas phase, computed at 298.15 K and 1 atm. Energies reported in this chapter are based on the gas-phase relative free energies and incorporate a correction for dispersion effects using Grimme's D3 parameter set[164] with Becke-Johnson damping[165] as well as solvation (PCM approach)[161] in THF. This was due to 1,2-$C_6H_4F_2$ not being available on Gaussian. Both dispersion and solvation corrections were run as single points with Gaussian 09 Revision D.01.[175]

5.2 – Dehydropolymerisation of H_3B-$NMeH_2$ Using [Rh(*mer*-κ^3-P,O,P-Xantphos-iPr)(H)]

5.2.1 – Dehydrogenation of H_3B-$NMeH_2$ with 5-1$_{iPr}$

To begin the computational studies conducted as part of this thesis, the mechanism proposed by Esteruelas *et al.* **(Pathway IS1$_{iPr}$, Scheme 5-1**) was explored and is shown in **Scheme 5-3**. The isomerisation of the Xantphos ligand from the *mer*-κ^3-P,O,P binding mode in catalyst **5-1$_{iPr}$** (G set to 0.0 kcal mol^{-1}, **Figure 5-5**) to *cis*-κ^2-P,P in **5-INT(1-4)$_{iPr}$** (G = +9.8 kcal mol^{-1}) occurs *via* **5-TS(1-4)1$_{iPr}$** (G = +16.2 kcal mol^{-1}) with the P-Rh-P angle decreasing from 162.6 ° to 113.6 °. This creates a vacant site at the metal centre which allows for the formation of a C-H agostic interaction between the Rh centre and one of the ^{i}Pr groups. This agostic interaction is substituted with a molecule of H_3B-$NMeH_2$ which binds through **5-TS(1-4)2$_{iPr}$** to form amine-borane σ-complex **5-4$_{iPr}$** (G = -0.5 kcal mol^{-1}). The σ-bound B-H bond then proceeds through a facile oxidative addition process *via* **5-TS(4-5)1$_{iPr}$** (G = +4.4 kcal mol^{-1}) to form five-co-ordinate complex **5-INT(4-5)$_{iPr}$** (G = -9.0 kcal mol^{-1}). The dehydrogenation is completed by a N-H activation step through **5-TS(4-5)2$_{iPr}$** (G = +4.4 kcal mol^{-1}) to form intermediate **5-5$_{iPr}$** (G = -11.3 kcal mol^{-1}) and free amino-borane H_2B=NMeH. During this process, the Rh···H(N) distance decreases from 3.03 Å to 1.59 Å as a new Rh-H bond is formed. The structure of **5-TS(4-5)2$_{iPr}$** looks similar to intermediate **5-IV** proposed by Esteruelas *et al.* (**Scheme 5-1**) but no minimum was found, with the H_2 ligand formed instantly proceeding through oxidative addition to form **5-5$_{iPr}$**.

Overall, **Pathway IS1$_{iPr}$** was calculated to proceed with a free energy barrier of 16.2 kcal mol^{-1} with the rate limiting step being the isomerisation of the Xantphos ligand in **5-TS(1-4)1$_{iPr}$.** This is different from the work by Esteruelas *et al.* who predict the N-H activation step to be rate-limiting with a barrier of 31.7 kcal mol^{-1}. It is thought this difference is down to the different computational methodologies used between the two studies.

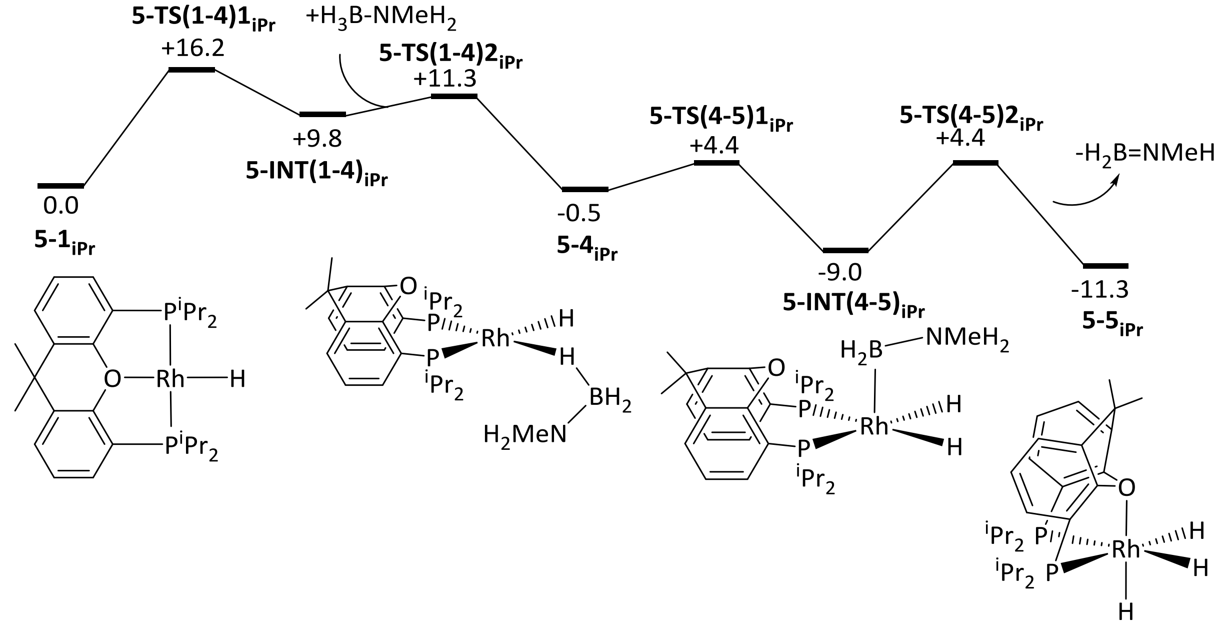

Scheme 5-3: *Inner-sphere, stepwise pathway 1 (**IS1$_{iPr}$**) from **5-1$_{iPr}$** to form **5-5$_{iPr}$**. Relative free energies BP86(D3BJ, THF)/BS1 in kcal mol^{-1}.*

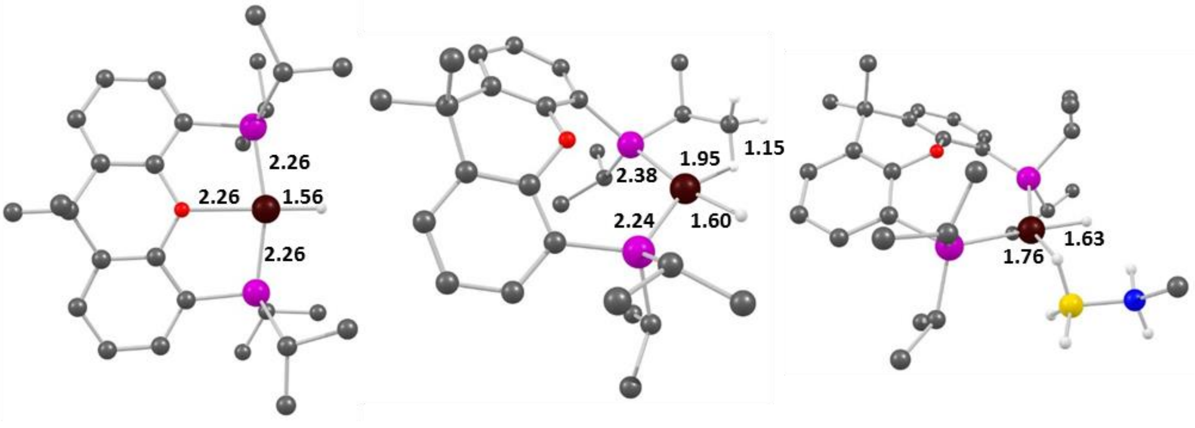

5-1$_{iPr}$
G = 0.0 kcal mol^{-1}

5-INT(1-4)$_{iPr}$
G = +9.8 kcal mol^{-1}

5-INT4$_{iPr}$
G = -0.5 kcal mol^{-1}

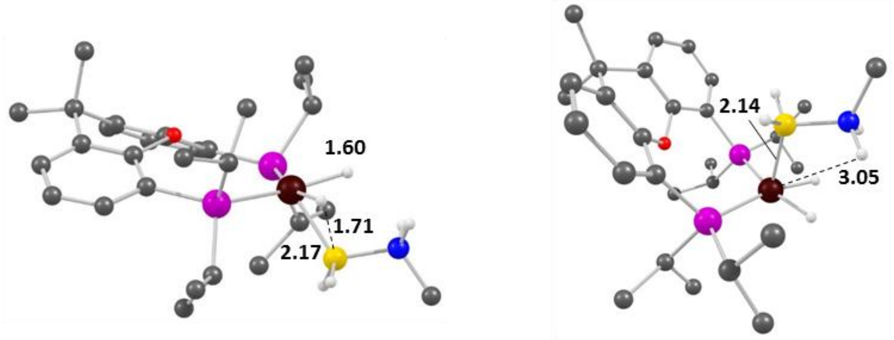

5-TS(4-5)1$_{iPr}$
G = +4.4 kcal mol^{-1}

5-INT(4-5)$_{iPr}$
G = -9.0 kcal mol^{-1}

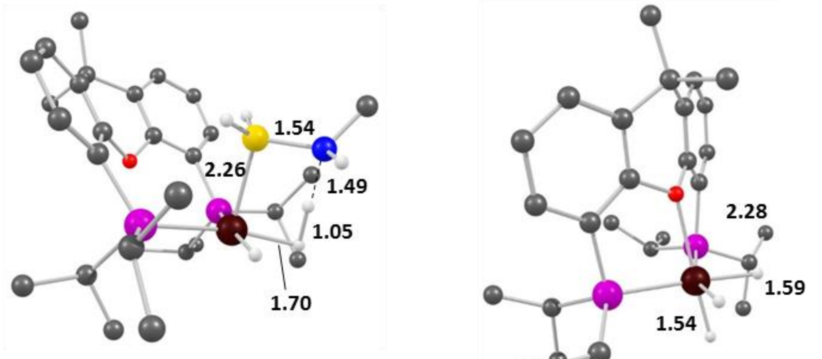

5-TS(4-5)2$_{iPr}$
G = +4.4 kcal mol^{-1}

5-5$_{iPr}$
G = -11.3 kcal mol^{-1}

Figure 5-5: *Key stationary points in **Pathway IS1$_{iPr}$** of **5-1$_{iPr}$**. Hydrogens bonded to carbon omitted for clarity. Key distances in Å. Colour scheme shown in the legend above is adopted throughout the chapter.*

Alternative dehydrogenation pathways from **5-1$_{iPr}$** were also explored. It was found that instead of proceeding through **Pathway IS1$_{iPr}$** as in **Scheme 5-3**, the H_3B-$NMeH_2$ molecule in **5-4$_{iPr}$** could dehydrogenate through a concerted activation mechanism (**Pathway IC1$_{iPr}$**, **Scheme 5-4**). Here, intermediate **5-4$_{iPr}$** is formed as previously discussed before proceeding through **5-TS(4-5)3$_{iPr}$** (G = +6.8 kcal mol^{-1}, **Figure 5-6**) to directly form *fac*-tri-hydride **5-5$_{iPr}$** and free H_2B=NMeH. During this process two new Rh-H bonds are formed from the Rh⋯H(N) and Rh⋯H(B) distances decreasing from 3.03 Å to 1.54 Å and 1.76 Å to 1.59 Å respectively. The rate-limiting step is the Xantphos ligand isomerisation process through **5-TS(1-4)1$_{iPr}$** which proceeds with a free energy barrier of 16.2 kcal mol^{-1} as in **Pathway IS1$_{iPr}$**. However, the concerted activation *via* **5-TS(4-5)3$_{iPr}$** in **Pathway IC1$_{iPr}$** is calculated to be more favoured than **5-TS(4-5)1$_{iPr}$** and **5-TS(4-5)2$_{iPr}$** in **Pathway IS1$_{iPr}$** with a barrier of 7.3 kcal mol^{-1} compared to 13.1 kcal mol^{-1}.

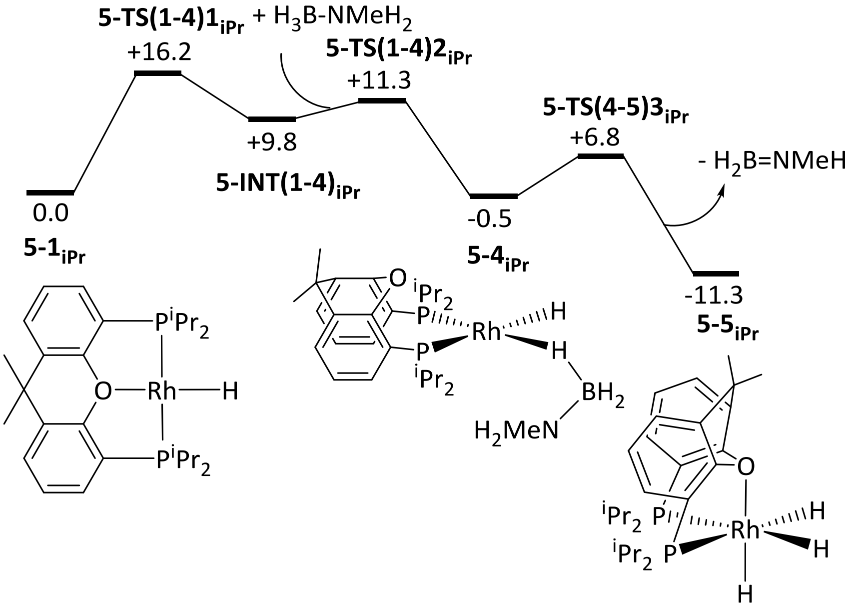

Scheme 5-4: *Inner-sphere, concerted pathway 1 (**IC1$_{iPr}$**) from **5-1$_{iPr}$** to form **5-5$_{iPr}$**. Relative free energies BP86(D3BJ, THF)/BS1 in kcal mol^{-1}.*

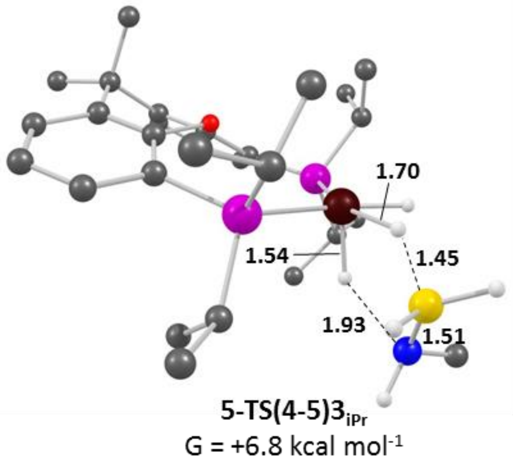

Figure 5-6: *Optimised structure of **5-TS(4-5)3$_{iPr}$**. Hydrogens bonded to carbon omitted for clarity. Key distances in Å.*

Two concerted outer-sphere dehydrogenation mechanisms (**Pathways OC1$_{iPr}$** and **OC2$_{iPr}$**) were also characterised and are shown in **Scheme 5-5**). **Pathway OC1$_{iPr}$** found that *fac*-tri-hydride intermediate **5-5$_{iPr}$** could be formed directly *via* **5-TS(1-5)$_{iPr}$** (G = +12.5 kcal mol^{-1}, **Figure 5-7**) before H_2 loss regenerates **5-1$_{iPr}$**. This type of concerted mechanism is common in the literature.[83, 85] Pathway **OC2** proceeds through **5-TS(1-1)$_{iPr}$** (G = +14.0 kcal mol^{-1}) and regenerates catalyst **5-1$_{iPr}$** (G = -5.3 kcal mol^{-1}), free H_2B=NMeH and H_2 in just one step. Here, the N-H protonates the Rh centre as the B-H transfers a hydride onto the Rh-H bond to directly form H_2.

The regenerated **5-1**$_{\mathbf{iPr}}$ has a lower free energy due to the thermodynamics of dehydrogenating a molecule of $H_3B\text{-}NMeH_2$ to form $H_2B{=}NMeH$ and H_2**.** This transition state has not been reported in the literature before, however, a similar transition state has been published by Rossin, Peruzzini *et al.* for $[Ru(\kappa^4\text{-}N(CH_2CH_2PPh_2)_3)(H)_2]$[87] and $[Co(\kappa^4\text{-}N(CH_2CH_2PPh_2)_3)(H)]$.[88] In these examples, the N-H protonates a metal-hydride to form H_2 while the B-H transfers a hydride to the metal centre. Transition states of this type were searched for during this study but none could be located. The transition state **5-TS(1-5)**$_{\mathbf{iPr}}$ is an earlier TS which is evident from the shorter B···H and N···H interactions of 1.32 and 1.46 Å respectively in **5-TS(1-5)**$_{\mathbf{iPr}}$ compared to 1.35 and 1.81 Å in **5-TS(1-1)**$_{\mathbf{iPr}}$. **Pathway OC1** has a lower activation energy of 12.5 kcal mol^{-1} than **Pathways IS1** (16.2 kcal mol^{-1}, **Scheme 5-3**), **IC1** (16.2 kcal mol^{-1} **Scheme 5-4**), and **OC2** (14.0 kcal mol^{-1}) and is therefore the most favoured mechanism for the formation of *fac*-tri-hydride **5-5**$_{\mathbf{iPr}}$.

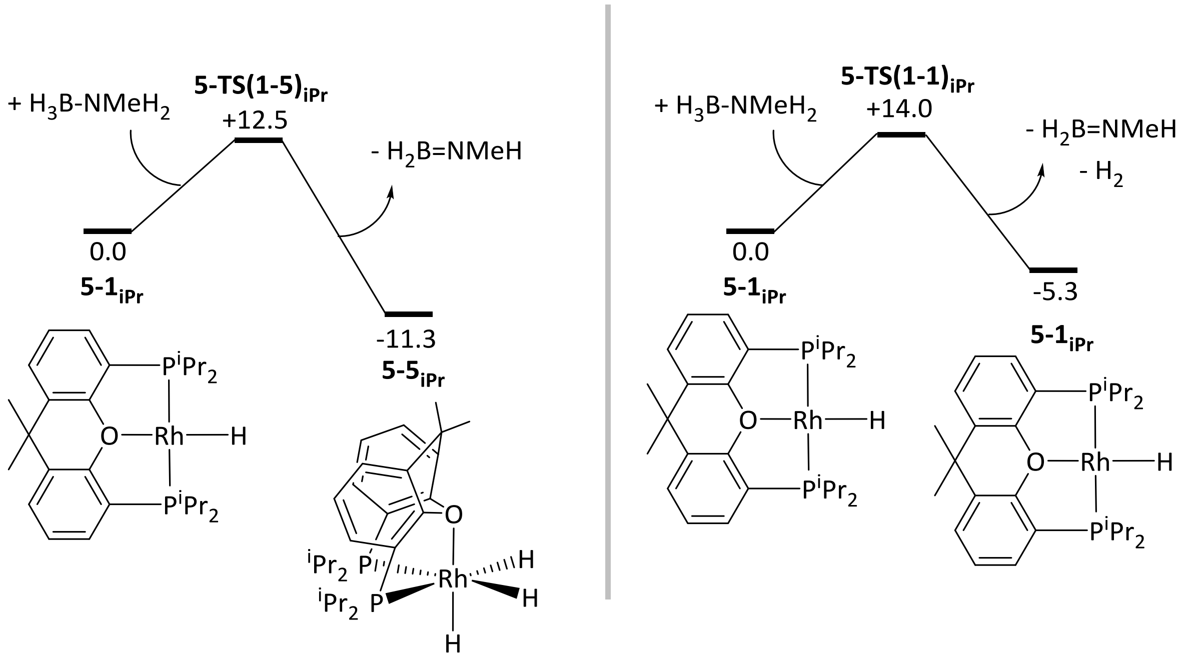

Scheme 5-5: *Outer-sphere, concerted pathway 1 (**OC1**$_{iPr}$, left) and 2 (**OC2**$_{iPr}$, right) from **5-1**$_{iPr}$. Relative free energies BP86(D3BJ, THF)/BS1 in kcal mol^{-1}.*

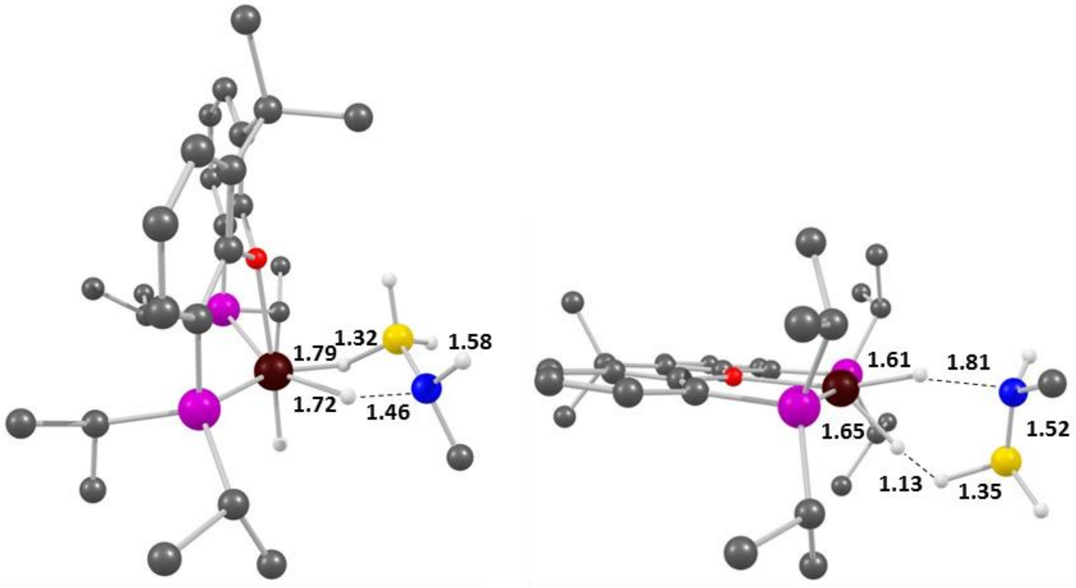

5-TS(1-5)$_{iPr}$
G = +12.5 kcal mol^{-1}

5-TS(1-1)$_{iPr}$
G = +14.0 kcal mol^{-1}

Figure 5-7: *Optimised structures of **5-TS(1-5)$_{iPr}$** and **5-TS(1-1)$_{iPr}$**. Hydrogens bonded to carbon omitted for clarity. Key distances in Å.*

The regeneration of catalyst **5-1$_{iPr}$** (**Pathway R1$_{iPr}$**) shown in **Scheme 5-6** shows that complex **5-5$_{iPr}$** can go through an H_2 reductive coupling *via* **5-TS(5-1)1$_{iPr}$** (G = -4.1 kcal mol^{-1}) to form **5-INT(5-1)$_{iPr}$** (G = -11.7 kcal mol^{-1}) which contains a dihydrogen ligand. This is similar to the dihydrogen complex **5-IV** (**Scheme 5-1**) computed by Esteruelas *et al.* with the Xantphos ligand adopting the *fac*-κ^3-P,O,P over the *cis*-κ^2-P,P binding mode. The dihydrogen ligand then dissociates through **5-TS(5-1)2$_{iPr}$** (G = +2.1 kcal mol^{-1}) to regenerate **5-1$_{iPr}$** (G = -5.3 kcal mol^{-1}). This process occurs with a barrier of 13.8 kcal mol^{-1}.

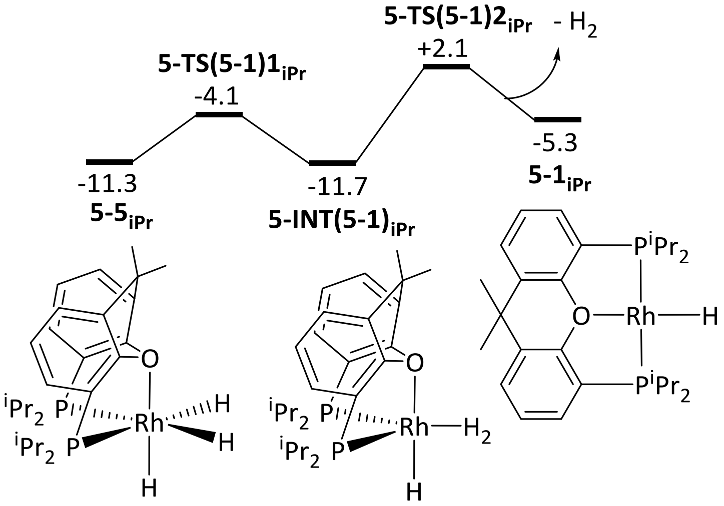

Scheme 5-6: *Regeneration of **5-1$_{iPr}$** from **5-5$_{iPr}$** (**R1$_{iPr}$**). Relative free energies BP86(D3BJ, THF)/BS1 in kcal mol^{-1}.*

Due to its kinetic and thermodynamic accessibility, if the concentration of H_2 builds up in the system, *fac*-tri-hydride **5-5**$_{\mathbf{iPr}}$ could be the active catalyst. Therefore, dehydrogenation pathways proceeding from **5-5**$_{\mathbf{iPr}}$ were also explored. It is shown in **Scheme 5-7** (**Pathway IC2**) that the Rh···O interaction in **5-5**$_{\mathbf{iPr}}$ can be displaced by a molecule of H_3B-$NMeH_2$ *via* **5-TS(5-6)**$_{\mathbf{iPr}}$ (G = -3.9 kcal mol^{-1}) to form amine-borane σ-complex **5-6**$_{\mathbf{iPr}}$ (G = -11.4 kcal mol^{-1}, **Figure 5-8**). The Rh···O bond distance can be seen to increase from 2.28 Å to 3.32 Å as the Xantphos changes binding mode to *cis*-κ^2-P,P. This process occurs with a free energy barrier of 7.4 kcal mol^{-1} which is lower than the loss of H_2 calculated in **Pathway R1**$_{\mathbf{iPr}}$. Two of the hydride ligands on **5-6**$_{\mathbf{iPr}}$ can then proceed through a reductive coupling process *via* **5-TS(6-4)1**$_{\mathbf{iPr}}$ (G = +6.3 kcal mol^{-1}) to form intermediate **5-INT(6-4)**$_{\mathbf{iPr}}$ (G = +2.8 kcal mol^{-1}). The H_2 ligand then dissociates *via* **5-TS(6-4)2**$_{\mathbf{iPr}}$ (G = +4.2 kcal mol^{-1}) which results in the formation of **5-4**$_{\mathbf{iPr}}$ (G = -5.8 kcal mol^{-1}). Concerted activation then proceeds as in **Pathway IS1**, **Scheme 5-3** to reform *fac*-tri-hydride **5-5**$_{\mathbf{iPr}}$ (G = -16.6 kcal mol^{-1}). The H_2 reductive coupling step *via* **5-TS(6-4)1**$_{\mathbf{iPr}}$ proves to be the rate-limiting process with a barrier of 17.7 kcal mol^{-1}.

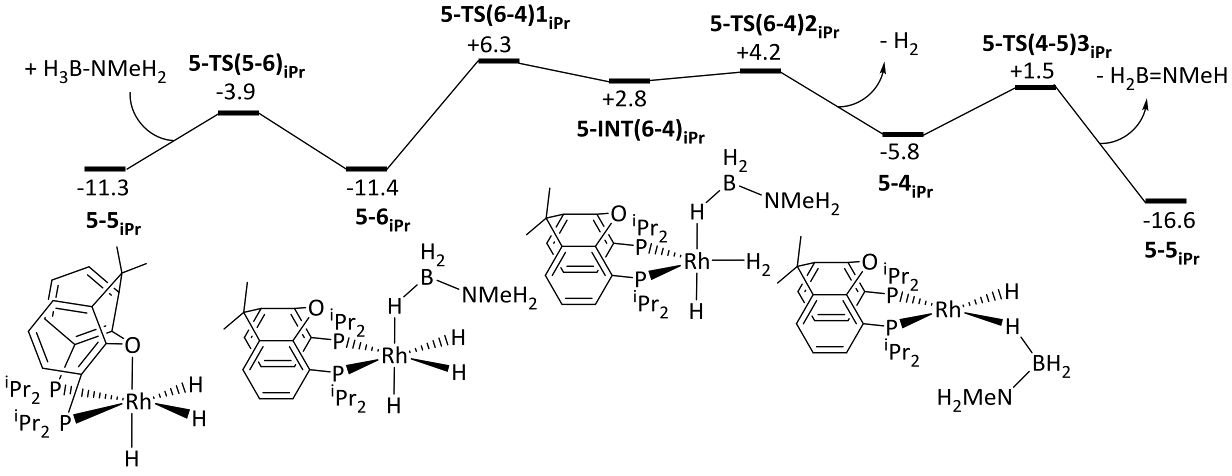

Scheme 5-7: *Inner-sphere concerted pathway 2 (**IC2**$_{\mathbf{iPr}}$) from **5-5**$_{\mathbf{iPr}}$. Relative free energies BP86(D3BJ, THF)/BS1 in kcal mol^{-1}.*

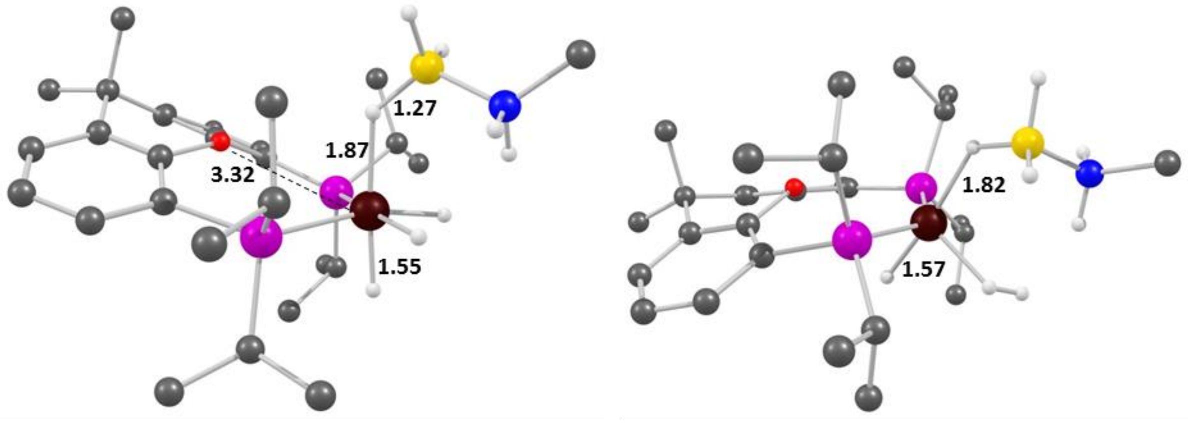

5-6$_{iPr}$
G = -11.4 kcal mol^{-1}

5-TS(6-4)1$_{iPr}$
G = +6.3 kcal mol^{-1}

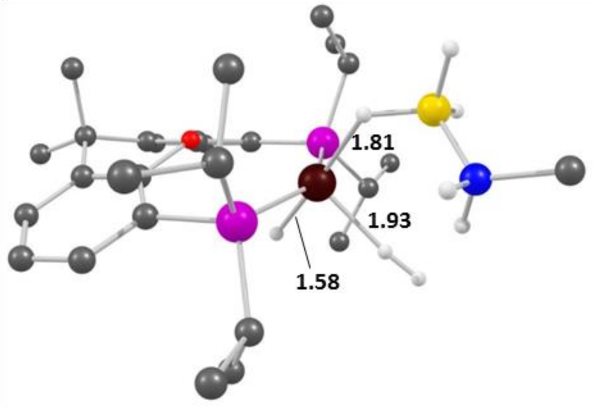

5-INT(6-4)$_{iPr}$
G = +2.8 kcal mol^{-1}

Figure 5-8: *Key stationary points for **Pathway IC2$_{iPr}$** from **5-5$_{iPr}$**. Hydrogens bonded to carbon omitted for clarity. Key distances in Å.*

Instead of going through loss of H_2 followed by concerted activation, the dehydrogenation process from **5-5$_{iPr}$** could also proceed *via* **Pathway IC3$_{iPr}$** which involves concerted activation then H_2 loss (**Scheme 5-8**). From intermediate **5-6$_{iPr}$**, concerted B-H and N-H activation can occur through **5-TS(6-5)1$_{iPr}$** (G = +7.7 kcal mol^{-1}, **Figure 5-9**) . This forms *fac*-tri-hydride dihydrogen complex **5-INT(6-5)$_{iPr}$** (G = -12.5 kcal mol^{-1}) which is the lowest energy intermediate calculated throughout this study. The H_2 ligand on **5-INT(6-5)$_{iPr}$** then dissociates *via* **5-TS(6-5)2$_{iPr}$** to regenerate intermediate **5-5$_{iPr}$. Pathway IC3$_{iPr}$** is calculated to have a free energy barrier of 19.1 kcal mol^{-1} with the concerted activation proving to be the rate-limiting process. This is a higher activation energy than **Pathway IC2$_{iPr}$** (**Scheme 5-6**) which is the favoured dehydrogenation cycle from intermediate **5-5$_{iPr}$**.

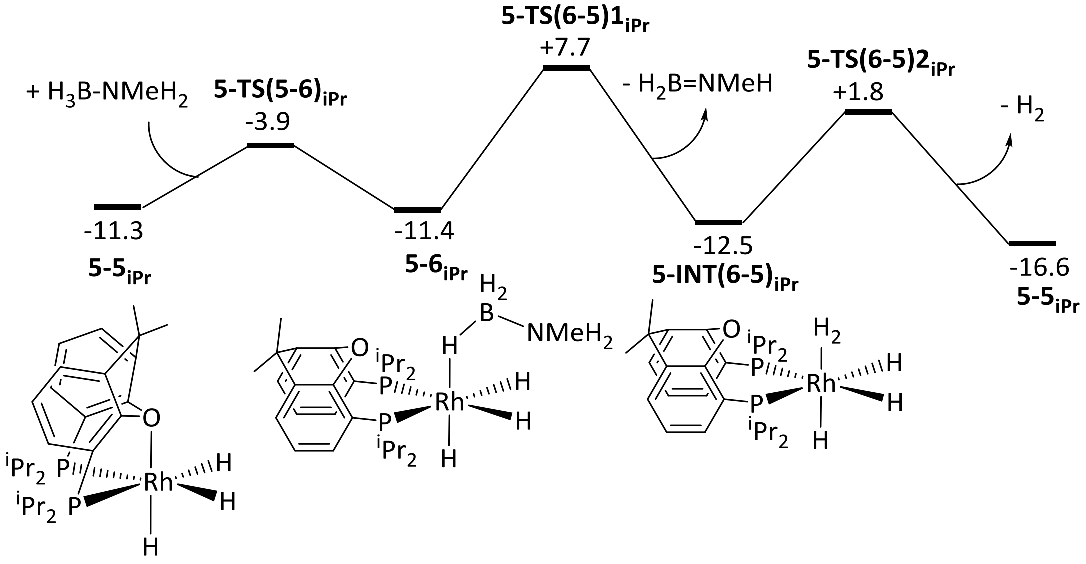

Scheme 5-8: *Pathway **IC3$_{iPr}$** from **5-5$_{iPr}$**. Relative free energies BP86(D3BJ, THF)/BS1 in kcal mol^{-1}.*

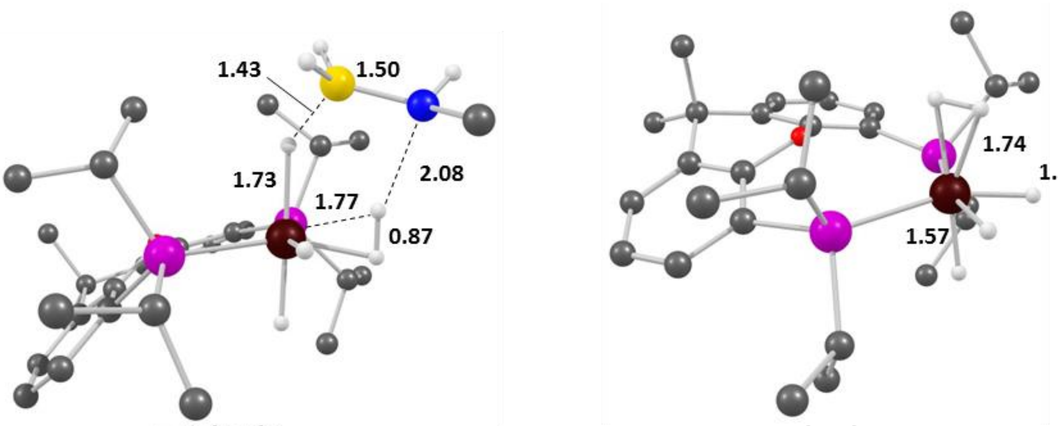

5-TS(6-5)1$_{iPr}$
G = +7.7 kcal mol^{-1}

5-INT(6-5)$_{iPr}$
G = -12.5 kcal mol^{-1}

Figure 5-9: *Key stationary points **Pathway IC3$_{iPr}$** from **5-5$_{iPr}$**. Hydrogens bonded to carbon omitted for clarity. Key distances in Å.*

In summary, the dehydrogenation of H_3B-$NMeH_2$ with catalyst **5-1$_{iPr}$** initially proceeds through **Pathway OC1$_{iPr}$** (**Scheme 5-5**) with a free energy barrier of 12.5 kcal mol^{-1} to form complex **5-5$_{iPr}$**. If H_2 is released, then the dehydrogenation can then proceed *via* **Pathway R1** (**Scheme 5-6**) to regenerate catalyst **5-1$_{iPr}$** and **Pathway OC1$_{iPr}$** with a barrier of 18.9 kcal mol^{-1}. If the H_2 concentration in the system builds up the dehydrogenation could go through **Pathway IC2$_{iPr}$** (**Scheme 5-7**) with a barrier of 17.7 kcal mol^{-1}. The lowest energy intermediate is *fac*-tri-hydride, dihydrogen complex **5-INT(5-6)$_{iPr}$** (**Figure 5-9**) which lies off-cycle, but can be formed from **5-5$_{iPr}$** when H_2 is present in the catalytic system.

5.2.2 – Propagation of H_2B=NMeH with 5-1$_{iPr}$

The polymerisation mechanism was initially explored by investigating potential amino-borane adducts between H_2B=NMeH and catalyst **5-1$_{iPr}$**. Attempts to optimise complex [Rh(κ^3-P,O,P-Xantphos-^{i}Pr)(η^1-H_3B-NMeH)], **5-7$_{iPr}$** (**Figure 5-10**) were unsuccessful with no minima located. However, repeating the calculation with the linear dimer H_2B-NMeH-BH_2-NMeH co-ordinating to **5-1$_{iPr}$** to form **5-8$_{iPr}$** (G = 0.0 kcal mol^{-1}, **Figure 5-11**) was successful in locating an optimised minimum. It is believed that a minimum is found for **5-8$_{iPr}$** and not **5-7$_{iPr}$** because the formation of **5-7$_{iPr}$** would involve breaking the double bond between the boron and nitrogen which is unfavourable. In the linear dimer, this double bond has already been reduced and therefore the formation of **5-8$_{iPr}$** is more favourable.

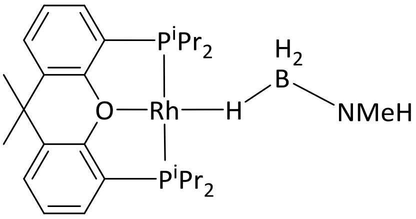

5-7$_{iPr}$

Figure 5-10: *[Rh(κ^3-P,O,P-Xantphos-^{i}Pr)(η^1-H_3B-NMeH)], **5-7$_{iPr}$***

Calculations from intermediate **5-8$_{iPr}$** then allowed for propagation mechanism **Pathway P1** (**Scheme 5-9**) to be characterised. **Pathway P1** was found to proceed through **5-TS(1-8)$_{iPr}$** (G = +6.0 kcal mol^{-1}). During this process, the hydride of **5-1$_{iPr}$** acts as a nucleophile and attacks the boron of a H_2B=NMeH unit which breaks the B-N double bond which can be seen through the bond distance of 1.48 Å (the computed B-N bond length in free H_2B=NMeH is 1.40 Å). This allows the NMeH group to act as a nucleophile and attack a second H_2B=NMeH to form **5-8$_{iPr}$** directly. A third H_2B=NMeH molecule was found to add to the growing polymer chain through **5-TS(8-9)$_{iPr}$** (G = +5.0 kcal mol^{-1}) to form **5-9$_{iPr}$** (G = -2.4 kcal mol^{-1}). It is proposed that the terminal NMeH group will continue the propagation process through nucleophilic attack at free amino-borane units to form the polymer. Polymerisation would only become thermodynamically favourable once the growing polymer chain becomes lower in energy than the lowest energy intermediate **5-INT(6-5)** (**Figure 5-8**). This occurs with [Rh(*mer*-κ^3-P,O,P-Xantphos-^{i}Pr)(η^1-$BH_3(NMeHBH_2)_3$NMeH)] (G = -15.1 kcal mol^{-1}). This head-to-tail chain growth polymerisation towards the formation of polyamino-boranes has previously been postulated by Paul *et al.*[102] with an [Ir(POCOP)] catalyst.

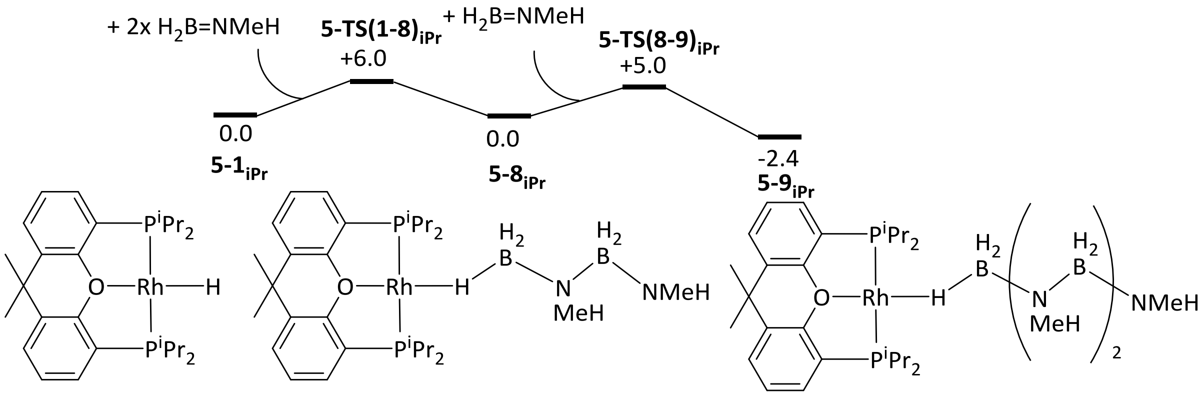

Scheme 5-9: *Head-to-tail propagation mechanism (**Pathway P1$_{iPr}$**) from **5-1$_{iPr}$**. Relative free energies BP86(D3BJ, THF)/BS1 in kcal mol^{-1}.*

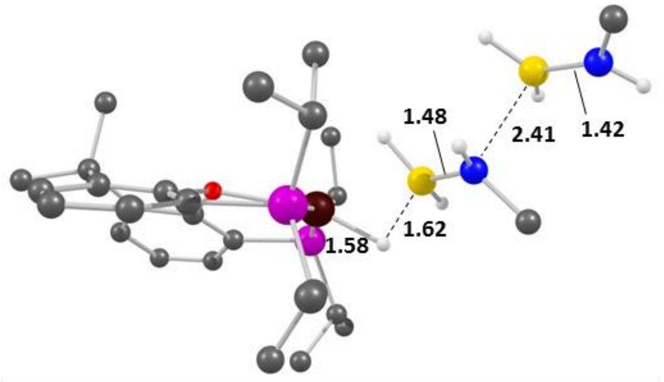

5-TS(1-8)$_{iPr}$
G = +6.0 kcal mol^{-1}

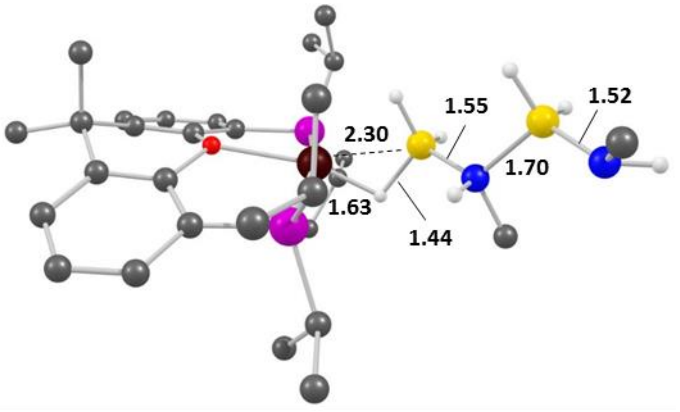

5-8$_{iPr}$
G = 0.0 kcal mol^{-1}

Figure 5-11: *Key stationary points from **Pathway P1$_{iPr}$** from **5-1$_{iPr}$**. Hydrogens bonded to carbon omitted for clarity. Key distances in Å.*

5.2.3 – Summary of the Dehydropolymerisation Pathway of $H_3B\text{-}NMeH_2$ with 5-1$_{iPr}$

Overall, the dehydropolymerisation of $H_3B\text{-}NMeH_2$ is predicted to proceed *via* the pathway shown in **Scheme 5-10.** The $H_3B\text{-}NMeH_2$ is initially dehydrogenated *via* **Pathway OC1$_{iPr}$** (**Scheme 5-5**) to form *fac*-tri-hydride complex **5-5$_{iPr}$** and free $H_2B=NMeH$ with a free energy barrier of 12.5 kcal mol^{-1}**.** The catalytic dehydrogenation of $H_3B\text{-}NMeH_2$ can then proceed through regeneration of catalyst **5-1$_{iPr}$** through **Pathway R1** and **Pathway OC1$_{iPr}$**. This occurs with a free energy barrier of 19.8 kcal mol^{-1} due to the lowest energy intermediate **5-INT(5-6)$_{iPr}$** which lies off-cycle. If the concentration of H_2 builds up in the system, complex **5-5$_{iPr}$** could become the active catalyst with dehydrogenation proceeding by **Pathway IC2$_{iPr}$** (**Scheme 5-7**) with a free energy barrier of 18.8 kcal mol^{-1}. As both dehydrogenation pathways are close in energy they cannot be distinguished from each other and both are possibly occurring in catalysis. The propagation pathway proceeds from **5-1$_{iPr}$** *via* **Pathway P1$_{iPr}$** (**Scheme 5-9**) which is a head-to-tail chain growth mechanism with a free energy barrier of 18.5 kcal mol^{-1}.

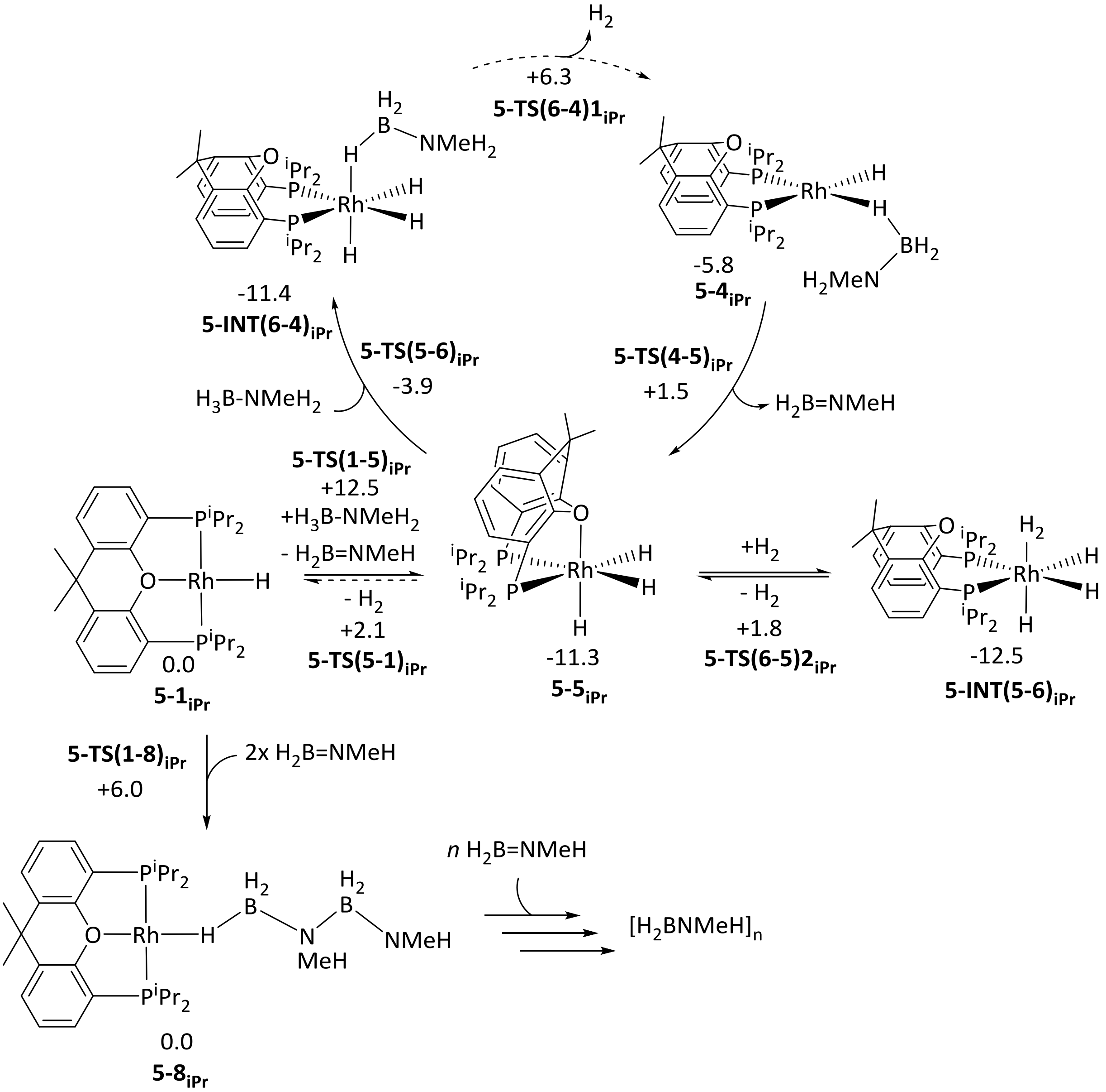

Scheme 5-10: *Proposed mechanism for the dehydropolymerisation of H_3B-$NMeH_2$ with catalyst **5-1$_{iPr}$**. Relative free energies BP86(D3BJ, THF)/BS1 in kcal mol^{-1}. Dashed arrows indicate steps that include multiple processes. In these cases the highest energy transition state is quoted.*

The calculated pathway is consistent with the available experimental data. The rate limiting process is the free energy difference between the lowest energy intermediate (**5-INT(5-6)$_{iPr}$**) and the highest energy transition state (**5-TS(1-5)1**) which is 19.8 kcal mol^{-1}. This is consistent with efficient reaction at room temperature. Speciation studies also observed a range of [Rh-H] complexes which are consistent with **5-5$_{\mathbf{iPr}}$** and **5-INT(5-1)$_{\mathbf{iPr}}$** being low energy intermediates. Furthermore, the lowest energy intermediate across all pathways was intermediate **5-INT(6-5)$_{\mathbf{iPr}}$** which, although off-pathway, would be predicted to be observable in speciation studies.

5.3 – Dehydropolymerisation of H_3B-$NMeH_2$ with [Rh(*mer*-κ^3-P,O,P-Xantphos-^{t}Bu)(H)], 5-1$_{tBu}$

5.3.1 – Dehydrogenation of H_3B-$NMeH_2$ with 5-1$_{tBu}$

The computational investigation into dehydrogenation pathways for **5-1$_{tBu}$** began by exploring **Pathway IS1** (**Scheme 5-11**). The Xantphos ligand isomerises from the *mer*-κ^3-P,O,P to *cis*-κ^2-P,P binding mode through **5-TS(1-4)1$_{tBu}$** (G = +24.3 kcal mol^{-1}) to yield **5-INT(1-4)$_{tBu}$** (G = +20.3 kcal mol^{-1}, **Figure 5-12**) which forms a C-H agostic complex between the Rh and one of the ^{t}Bu groups. This is a higher energy process than for **5-1$_{iPr}$**. A molecule of H_3B-$NMeH_2$ then replaces the agostic interaction *via* **5-TS(1-4)2$_{tBu}$** (G = +24.0 kcal mol^{-1}) to form **5-4$_{tBu}$** (G = +17.2 kcal mol^{-1}). B-H activation then occurs through **5-TS(4-5)1$_{tBu}$** (G = +20.4 kcal mol^{-1}) to form base-stabilised boryl species **5-INT(4-5)**$_{tBu}$ (G = +14.2 kcal mol^{-1}). This intermediate is different to **5-INT(4-5)$_{iPr}$** (**Figure 5-5**) as a Rh-O interaction is present as the Xantphos ligand is in the *fac*-κ^3-P,O,P binding mode over the *cis*-κ^2-P,P binding mode. The equivalent intermediate to **5-INT(4-5)$_{iPr}$, 5-INT(4-5)'$_{tBu}$** (G = +22.0 kcal mol^{-1}) was found to be 7.8 kcal mol^{-1} higher in energy. This could be because the increased steric bulk of ^{t}Bu-Xantphos compared to ^{i}Pr-Xantphos makes the *fac*-κ^3-P,O,P binding mode more favourable as it has a wider P-Rh-P angle (122.35 °) in **5-INT(4-5)$_{tBu}$** compared to 114.01 ° in **5-INT(4-5)'$_{tBu}$**. N-H activation *via* **5-TS(4-5)2$_{tBu}$** then yields *fac*-tri-hydride complex **5-5$_{tBu}$** (G = 0.0 kcal mol^{-1}) with the Xantphos ligand in a *fac-κ^3-P,O,P* binding mode. **Pathway IS1$_{tBu}$** occurs with a free energy barrier of 31.8 kcal mol^{-1} with the rate limiting process being the N-H activation step *via* **5-TS(4-5)2$_{tBu}$.**

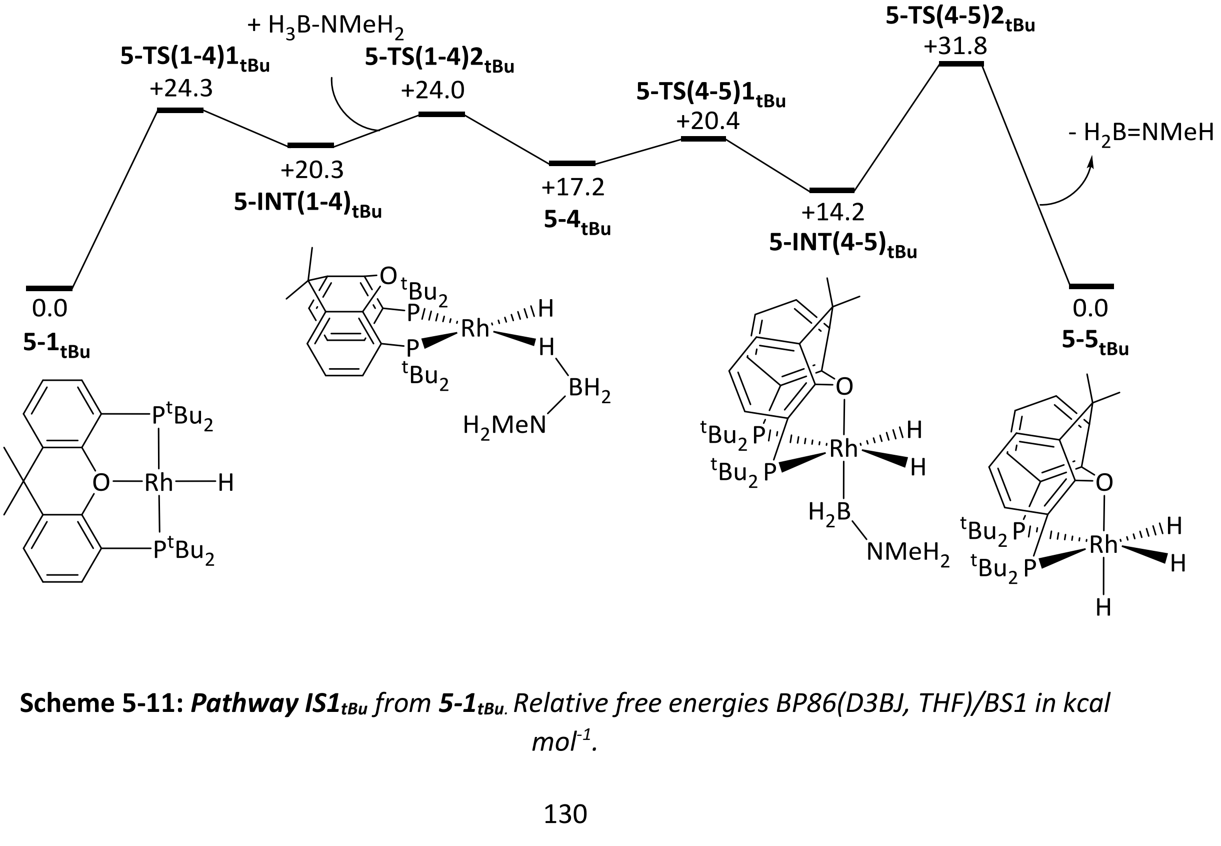

Scheme 5-11: ***Pathway IS1$_{tBu}$*** *from* ***5-1$_{tBu}$****. Relative free energies BP86(D3BJ, THF)/BS1 in kcal mol^{-1}.*

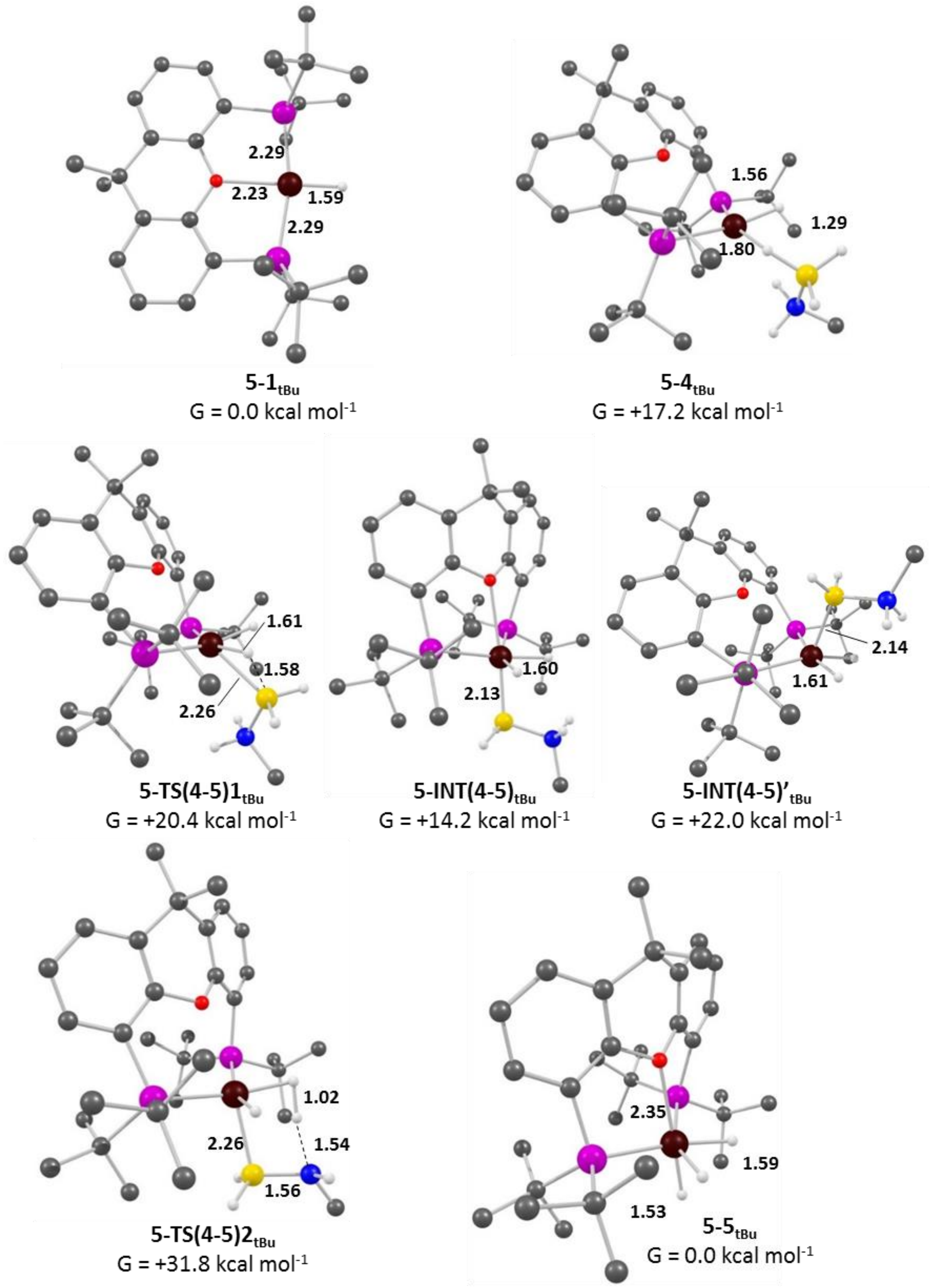

5-1$_{tBu}$
G = 0.0 kcal mol^{-1}

5-4$_{tBu}$
G = +17.2 kcal mol^{-1}

5-TS(4-5)1$_{tBu}$
G = +20.4 kcal mol^{-1}

5-INT(4-5)$_{tBu}$
G = +14.2 kcal mol^{-1}

5-INT(4-5)'$_{tBu}$
G = +22.0 kcal mol^{-1}

5-TS(4-5)2$_{tBu}$
G = +31.8 kcal mol^{-1}

5-5$_{tBu}$
G = 0.0 kcal mol^{-1}

Figure 5-12: *Key stationary points from **Pathway IS1$_{tBu}$** from **5-1$_{tBu}$**. Hydrogens bonded to carbon omitted for clarity. Key distances in Å.*

Pathway IC1$_{tBu}$ was also calculated and is shown in **Scheme 5-12**. Intermediate **5-4$_{tBu}$** is formed as detailed in **Pathway IS1$_{tBu}$, Scheme 5-11**. Concerted activation would then take place instead of step-wise B-H then N-H activation *via* **5-TS(4-5)3$_{tBu}$** (G = +23.7 kcal mol^{-1}, **Figure 5-13**) to form *fac*-tri-hydride **5-5$_{\mathbf{tBu}}$.** This is the analogous process to **5-TS(4-5)3$_{\mathbf{iPr}}$** (**Figure 5-7**) and the transition states are similar. One difference is the H_3B-$NMeH_2$ molecule is further away from the Rh metal in **5-TS(4-5)3$_{\mathbf{tBu}}$** which is likely to be due to the increased steric hindrance brought by the ^{t}Bu groups. Pathway **IC1$_{\mathbf{tBu}}$** has a free energy barrier of 24.3 kcal mol^{-1} with the rate limiting process being the initial isomerisation of the Xantphos ligand *via* **5-TS(1-4)1$_{\mathbf{tBu}}$**. This makes it more favoured than **Pathway IS1$_{\mathbf{tBu}}$** which has a higher free energy barrier of 31.8 kcal mol^{-1}.

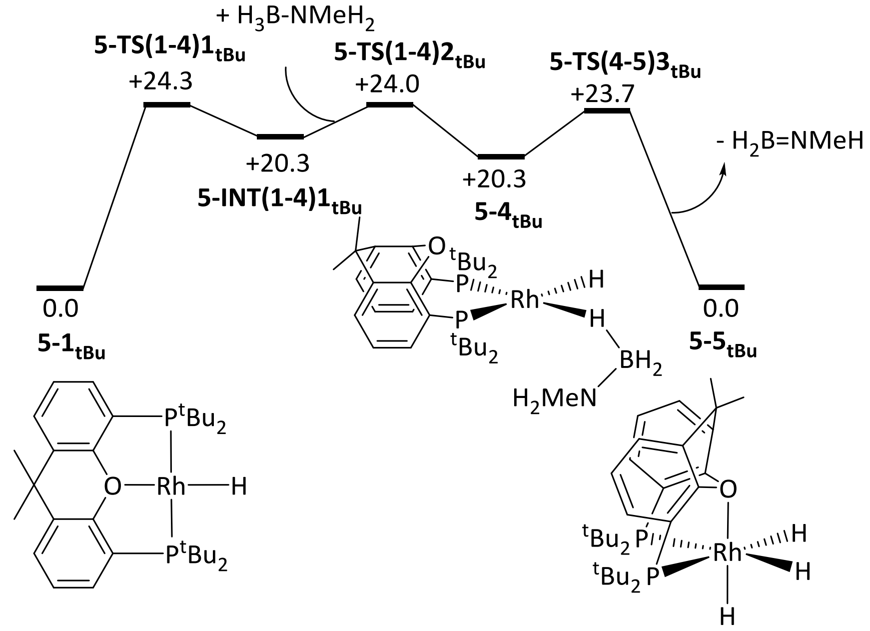

Scheme 5-12: ***Pathway IC1*** *from* ***5-1$_{\mathbf{tBu}}$****. Relative free energies BP86(D3BJ, THF)/BS1 in kcal mol^{-1}.*

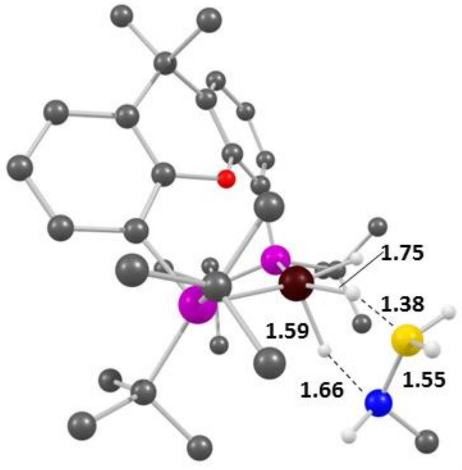

Figure 5-13: *Optimised structure for* ***5-TS(4-3)$_{\mathbf{tBu}}$****. Hydrogens bonded to carbon omitted for clarity. Key distances in Å.*

Two outer-sphere concerted dehydrogenation pathways, **OC1$_{\mathbf{tBu}}$** and **OC2$_{\mathbf{tBu}}$**, were also characterised for reaction with **5-1$_{\mathbf{tBu}}$** (**Scheme 5-13**). **Pathway OC1$_{\mathbf{tBu}}$** occurs *via* **5-TS(1-5)$_{\mathbf{tBu}}$** (G

= +23.8 kcal mol^{-1}, **Figure 5-14**) to directly form **5-5$_{tBu}$** and proceeds with a barrier lower than that of the **Pathway IC1$_{tBu}$** (**Scheme 5-12**) by 0.5 kcal mol^{-1}. **Pathway OC2$_{tBu}$** directly forms **5-1$_{tBu}$** $H_2B{=}NMeH$ and H_2 in the same step and proceeds through **5-TS(1-1)$_{tBu}$** (G = +19.9 kcal mol^{-1}). This is therefore the most favoured dehydrogenation pathway from mono-hydride **5-1$_{tBu}$** over **Pathways IS1**$_{tBu}$ (31.8 kcal mol^{-1}, **Scheme 5-11**), **IC1$_{tBu}$** (24.3 kcal mol^{-1}, **Scheme 5-12)**, and **OC1$_{tBu}$** (23.8 kcal mol^{-1}). This is in contrast to the reaction with catalyst **5-1$_{iPr}$** where **Pathway OC1$_{iPr}$** is favoured. The reason for this is likely that the increased steric bulk provided by the ^{t}Bu groups results in the transition state where the $H_3B\text{-}NMeH_2$ unit is further away from the metal complex is more favoured. The Rh···N and Rh···B distances in **5-TS(1-1)$_{tBu}$** are 3.36 and 3.69 Å compared to 2.93 and 2.69 Å in **5-TS(1-5)$_{iPr}$**.

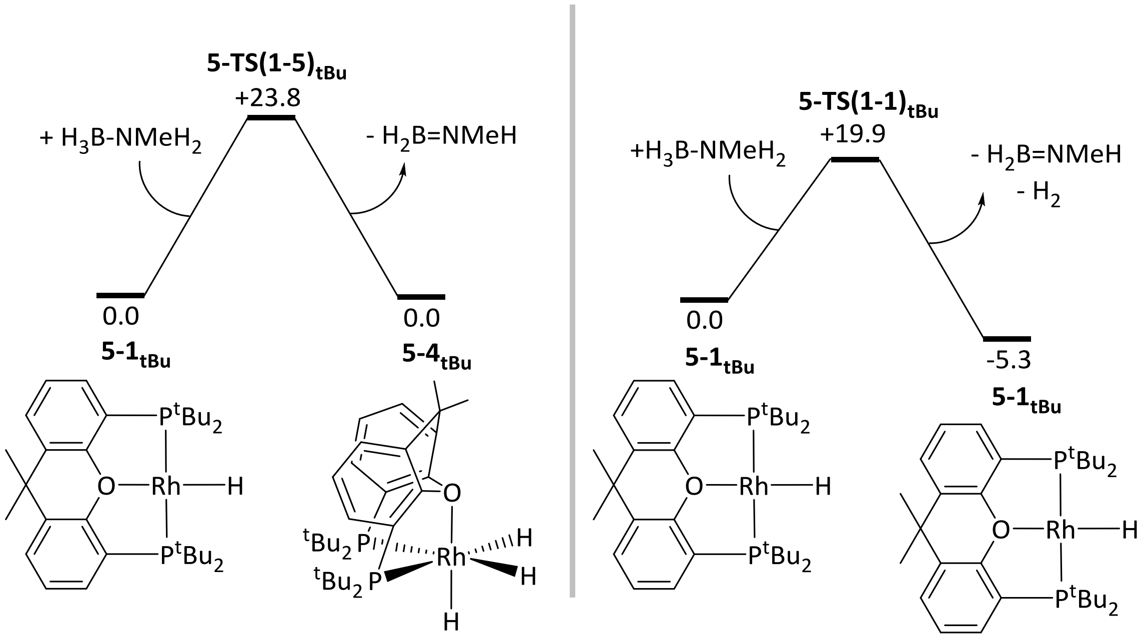

Scheme 5-13: *Outer-sphere, concerted pathway 1 (**OC1$_{iPr}$**, left) and 2 (**OC2$_{iPr}$**, right) from **5-1$_{iPr}$**. Relative free energies BP86(D3BJ, THF)/BS1 in kcal mol^{-1}.*

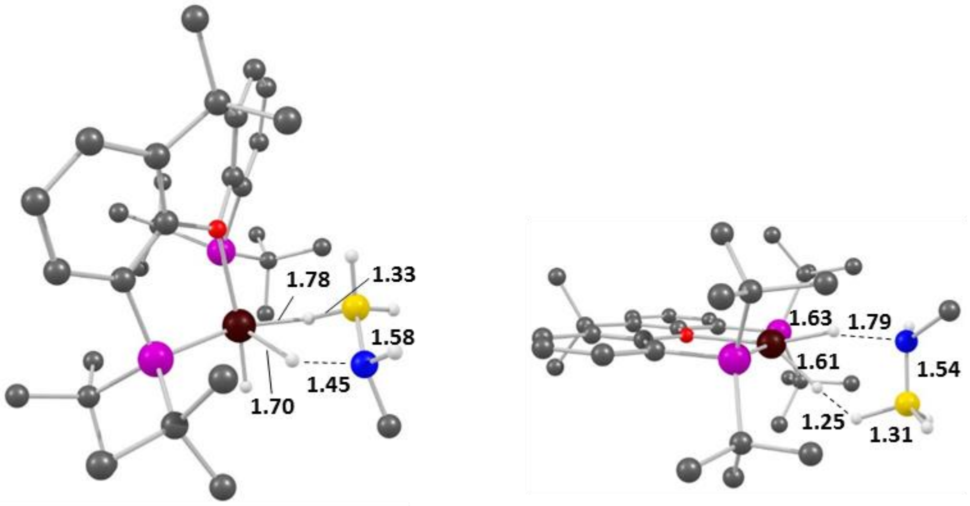

5-TS(1-5)$_{tBu}$
G = +23.8 kcal mol^{-1}

5-TS(1-1)$_{tBu}$
G = +19.9 kcal mol^{-1}

Figure 5-14: *Optimised structures of **5-TS(1-5)$_{tBu}$** and **5-TS(1-1)$_{tBu}$**. Hydrogens bonded to carbon omitted for clarity. Key distances in Å.*

In the case of catalyst **5-1$_{iPr}$**, the initial dehydrogenation proceeds through **Pathway OC1$_{iPr}$** to form *fac*-tri-hydride intermediate **5-5$_{iPr}$** which could then be the active catalyst in the catalytic dehydrogenation. However, in the case of catalysis with **5-1$_{tBu}$** it is now predicted that the initial dehydrogenation would proceed *via* **Pathway OC2$_{tBu}$** and therefore, **5-5$_{tBu}$** would not be formed in the reaction mixture. Furthermore, **5-5$_{tBu}$** is higher in energy than **5-1$_{tBu}$** unlike **5-5$_{iPr}$** which is lower in energy than **5-1$_{iPr}$** so it is no longer thermodynamically accessible. This means that the dehydrogenation mechanism would operate through **Pathway OC2$_{tBu}$** regardless of the concentration of H_2 in this system. In order to confirm that there was no other mechanism that needed to be considered, the pathways proceeding from intermediate **5-5$_{tBu}$**: **R1$_{tBu}$**, **IC1$_{tBu}$**, and **IC2$_{tBu}$** were characterised.

Pathway R1$_{tBu}$, where catalyst **5-1$_{tBu}$** is reformed from **5-5$_{tBu}$**, is shown in **Scheme 5-14.** A H_2 reductive coupling step occurs *via* **5-TS(5-1)1$_{tBu}$** (G = +4.4 kcal mol^{-1}) to form dihydrogen complex **5-INT(5-1)$_{tBu}$** (G = +4.9 kcal mol^{-1}) before H_2 is lost through **5-TS(5-1)2$_{tBu}$** (G = +5.7 kcal mol^{-1}) to yield **5-1$_{tBu}$** (-5.3 kcal mol^{-1}). This process occurs with a free energy barrier of 5.7 kcal mol^{-1}. The reverse reaction shows that complex **5-5$_{tBu}$** is still kinetically accessible from **5-1$_{tBu}$**.

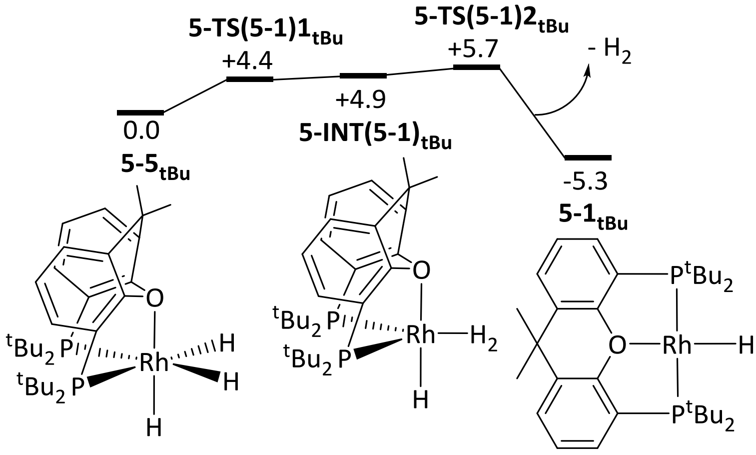

Scheme 5-14: ***Pathway R1$_{tBu}$*** *from* ***5-5$_{tBu}$****. Relative free energies BP86(D3BJ, THF)/BS1 in kcal mol^{-1}.*

In **Pathway IC2$_{tBu}$** (**Scheme 5-15**) the Rh-O interaction in **5-5$_{tBu}$** can be substituted with a unit of H_3B-$NMeH_2$ *via* **5-TS(5-6)$_{tBu}$** (G = +5.2 kcal mol^{-1}) to form **5-6$_{tBu}$** (G = +1.4 kcal mol^{-1}, **Figure 5-15**). This changes the Xantphos binding mode from *fac-κ^3-P,O,P* to *cis-κ^2-P,P*. A H_2 reductive coupling process can then form **5-INT(6-4)$_{tBu}$** (G = +13.8 kcal mol^{-1}) *via* **5-TS(6-4)1$_{tBu}$** before dissociation of the newly formed H_2 ligand through **5-TS(6-4)2$_{tBu}$** (G = +15.3 kcal mol^{-1}) yields square planar amine-borane complex **5-4$_{tBu}$** (G = +11.9 kcal mol^{-1}). Concerted activation *via* **5-TS(4-5)3$_{tBu}$** (G = +18.2 kcal mol^{-1}) regenerates **5-5$_{tBu}$** (G = -5.3 kcal mol^{-1}) as seen in **Scheme 5-13** to complete the cycle. The overall free energy barrier for this dehydrogenation is +18.2 kcal mol^{-1} associated with the concerted activation step *via* **5-TS(4-5)3$_{tBu}$**.

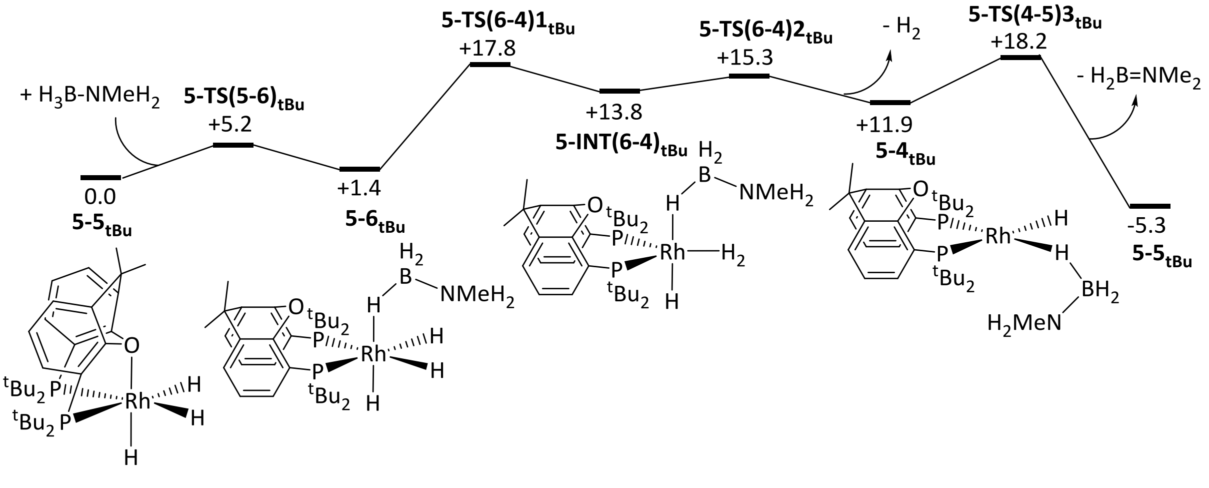

Scheme 5-15: ***Pathway IC2$_{tBu}$*** *from* ***5-5$_{tBu}$****. Relative free energies BP86(D3BJ, THF)/BS1 in kcal mol^{-1}.*

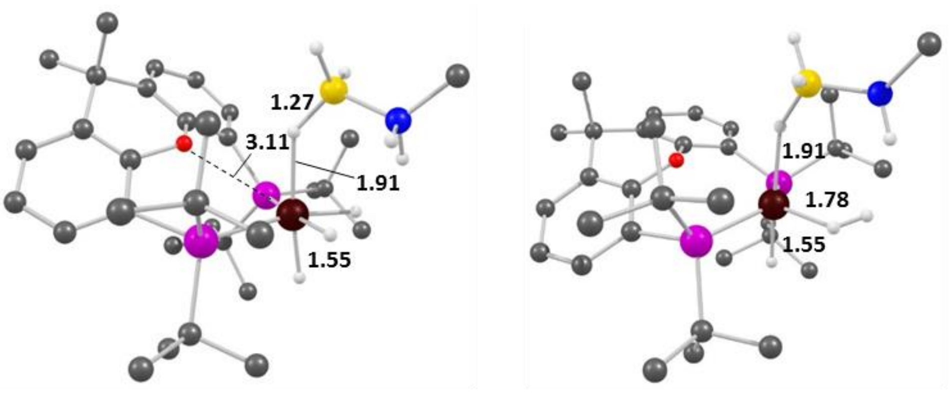

5-6$_{\text{tBu}}$
G = +1.4 kcal mol^{-1}

5-TS(6-4)1$_{\text{tBu}}$
G = +17.8 kcal mol^{-1}

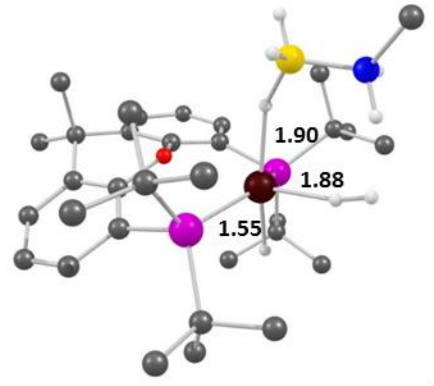

5-INT(6-4)$_{\text{tBu}}$
G = +13.8 kcal mol^{-1}

Figure 5-15: *Key stationary points for* ***Pathway IC2***$_{\textit{\textbf{tBu}}}$ *from* ***5-5***$_{\textit{\textbf{tBu}}}$*. Hydrogens bonded to carbon omitted for clarity. Key distances in Å.*

The dehydrogenation from **5-5**$_{\text{tBu}}$ can also proceed through concerted activation before H_2 loss after forming **5-6**$_{\text{tBu}}$ (**Pathway IC3**$_{\text{tBu}}$**, Scheme 5-16**). Here, the concerted activation occurs *via* **5-TS(6-1)1**$_{\text{tBu}}$ (G = +21.6 kcal mol^{-1}, **Figure 5-16**) to give *fac*-tri-hydride dihydrogen complex **5-INT(6-5)**$_{\text{tBu}}$ (G = +1.5 kcal mol^{-1}). The H_2 ligand then dissociates through **5-TS(6-5)2**$_{\text{tBu}}$ (G = +11.7 kcal mol^{-1}) with the Rh-O bond reforming to fill the formed vacant site and yielding **5-5**$_{\text{tBu}}$ (G = -5.3 kcal mol^{-1}). The highest free energy barrier for this dehydrogenation process involves the concerted activation *via* **5-TS(6-5)1**$_{\text{tBu}}$ with a free energy barrier of 21.6 kcal mol^{-1}.

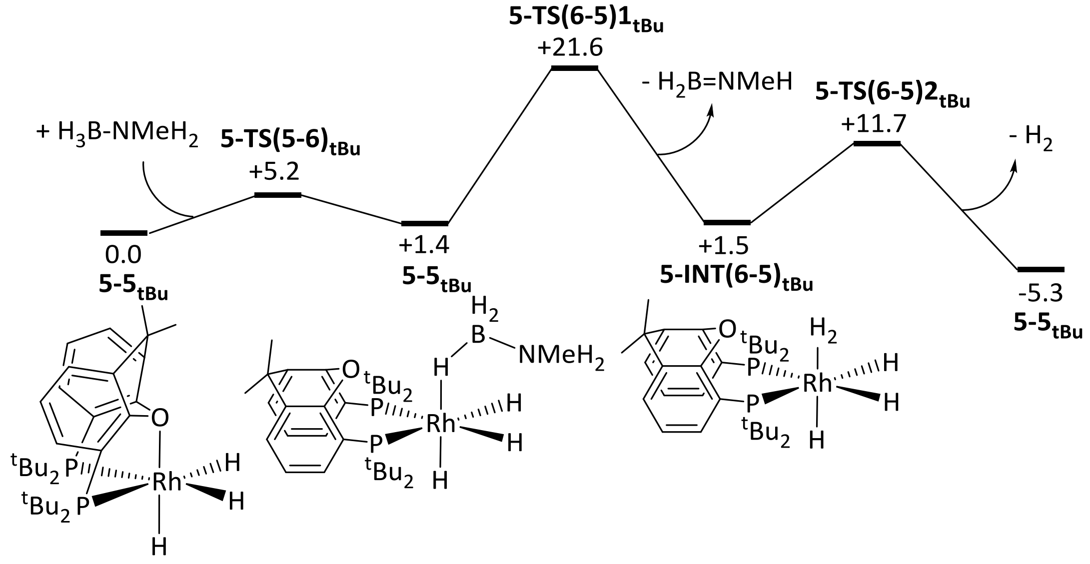

Scheme 5-16: ***Pathway IC3$_{tBu}$*** *from* ***5-5$_{tBu}$****. Relative free energies BP86(D3BJ, THF)/BS1 in kcal mol^{-1}.*

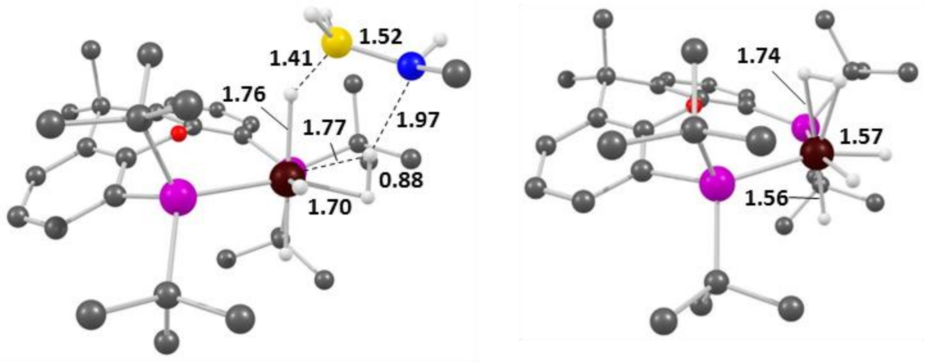

5-TS(6-5)1$_{tBu}$
G = +21.6 kcal mol^{-1}

5-INT(6-5)$_{tBu}$
G = +1.5 kcal mol^{-1}

Figure 5-16: *Key stationary points for* ***Pathway IC3$_{tBu}$*** *from* ***5-5$_{tBu}$****. Hydrogens bonded to carbon omitted for clarity. Key distances in Å.*

In summary, dehydrogenation of H_3B-$NMeH_2$ with catalyst **5-1$_{tBu}$** occurs *via* **Pathway OC2$_{tBu}$** (**Scheme 5-13**) which forms **5-1$_{tBu}$** and free H_2B=NMeH and H_2 in one step. This proceeds with a free energy barrier of 19.9 kcal mol^{-1}. **Pathway IS2$_{tBu}$** (a predicted catalytic cycle for reaction with catalyst **5-1$_{iPr}$**) is the favoured dehydrogenation mechanism proceeding from complex **5-5$_{tBu}$**. Intermediate **5-5$_{tBu}$** is kinetically accessible through the addition of H_2 to catalyst **5-1$_{tBu}$** but isn't thermodynamically accessible being 5.3 kcal mol^{-1} higher in energy. Therefore, **Pathway IS2$_{tBu}$** has a free energy barrier of 23.5 kcal mol^{-1} and is predicted not to occur during catalysis.

5.3.2 – Propagation of H_2B=NMeH with 5-1$_{tBu}$

The propagation pathway for **5-1$_{tBu}$** was found to proceed by a head-to-tail chain growth pathway (**Pathway P1$_{tBu}$, Scheme 5-17**). A minimum for [Rh(*mer*-κ^3-P,O,P-Xantphos-^{t}Bu)(η^1-H_3B-NMeH)] **5-7$_{tBu}$** could not be located, and instead **5-TS(1-8)$_{tBu}$** (G = +12.5 kcal mol^{-1}, **Figure 5-17**) is predicted to proceed to directly give **5-8**$_{tBu}$ (G = +9.8 kcal mol^{-1}). A third molecule of $H_2B{=}NMeH$ can then be attacked by the terminal NMeH moiety *via* **5-TS(8-9)$_{tBu}$** (G = +13.8 kcal mol^{-1}) to give the metal bound trimer **5-9$_{tBu}$** (G = +7.0 kcal mol^{-1}). The polymerisation would only become thermodynamically favoured when the growing polymer chain becomes lower in energy than the lowest energy intermediate, **5-1$_{tBu}$**. This occurs with [Rh(*mer*-κ^3-P,O,P-Xantphos-^{t}Bu)(η^1-$BH_3(NMeHBH_2)_3NMeH$)] (G = -6.0 kcal mol^{-1}).

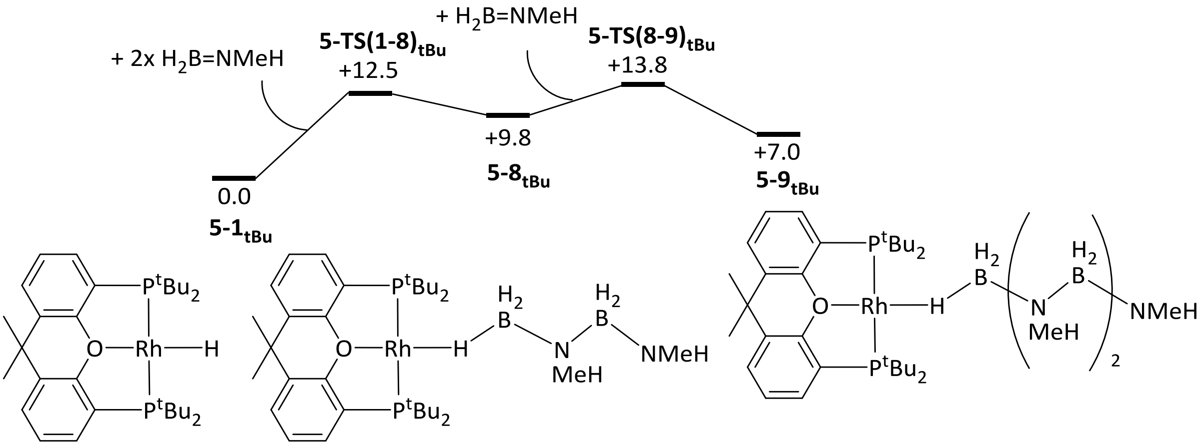

Scheme 5-17: ***Pathway P1$_{tBu}$*** *from* ***5-1$_{tBu}$****. Relative free energies BP86(D3BJ, THF)/BS1 in kcal mol^{-1}.*

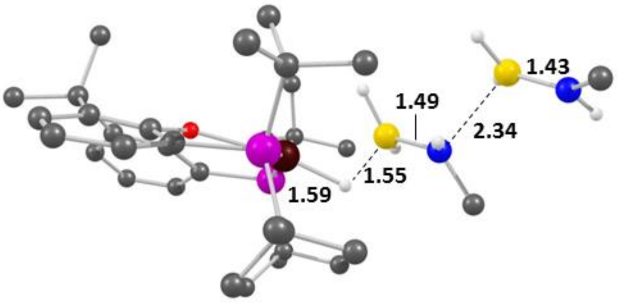

5-TS(1-8)$_{tBu}$
G = +12.5 kcal mol^{-1}

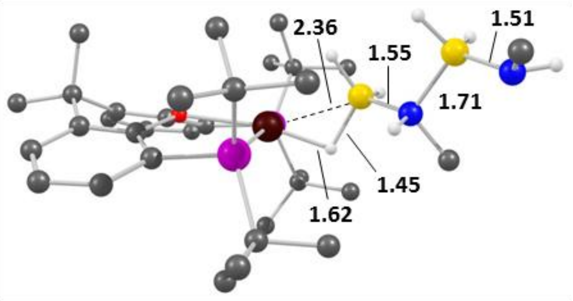

5-TS8$_{tBu}$
G = +9.8 kcal mol^{-1}

Figure 5-17: *Key stationary points from* ***Pathway P1$_{tBu}$*** *from* ***5-1$_{tBu}$****. Hydrogens bonded to carbon omitted for clarity. Key distances in Å.*

5.3.3 – Summary of Dehydropolymerisation Pathways of H_3B-$NMeH_2$ with 5-1$_{tBu}$

The predicted overall dehydropolymerisation pathway for reaction of H_3B-$NMeH_2$ with **5-1$_{tBu}$** is shown in **Scheme 5-18**. The dehydrogenation mechanism involves an outer-sphere concerted activation of the H_3B-$NMeH_2$ molecule which forms free H_2B=NMeH and H_2 as well as catalyst **5-1$_{tBu}$** in one step which passes through **5-TS(1-1)$_{tBu}$** (**Pathway OC2$_{tBu}$, Scheme 5-13**). This occurs with a barrier of 19.9 kcal mol^{-1}. The dehydrogenation mechanism is not predicted to change with higher concentrations of H_2 which is in contrast to the predicted reaction with **5-1$_{iPr}$** (**Scheme 5-10**). The propagation mechanism is predicted to proceed *via* a head-to-tail chain growth polymerisation (**Pathway P1$_{tBu}$, Scheme 5-16**). The rate-limiting step for the dehydropolymerisation mechanism is predicted to be the dehydrogenation with a free energy barrier of 19.9 kcal mol^{-1}.

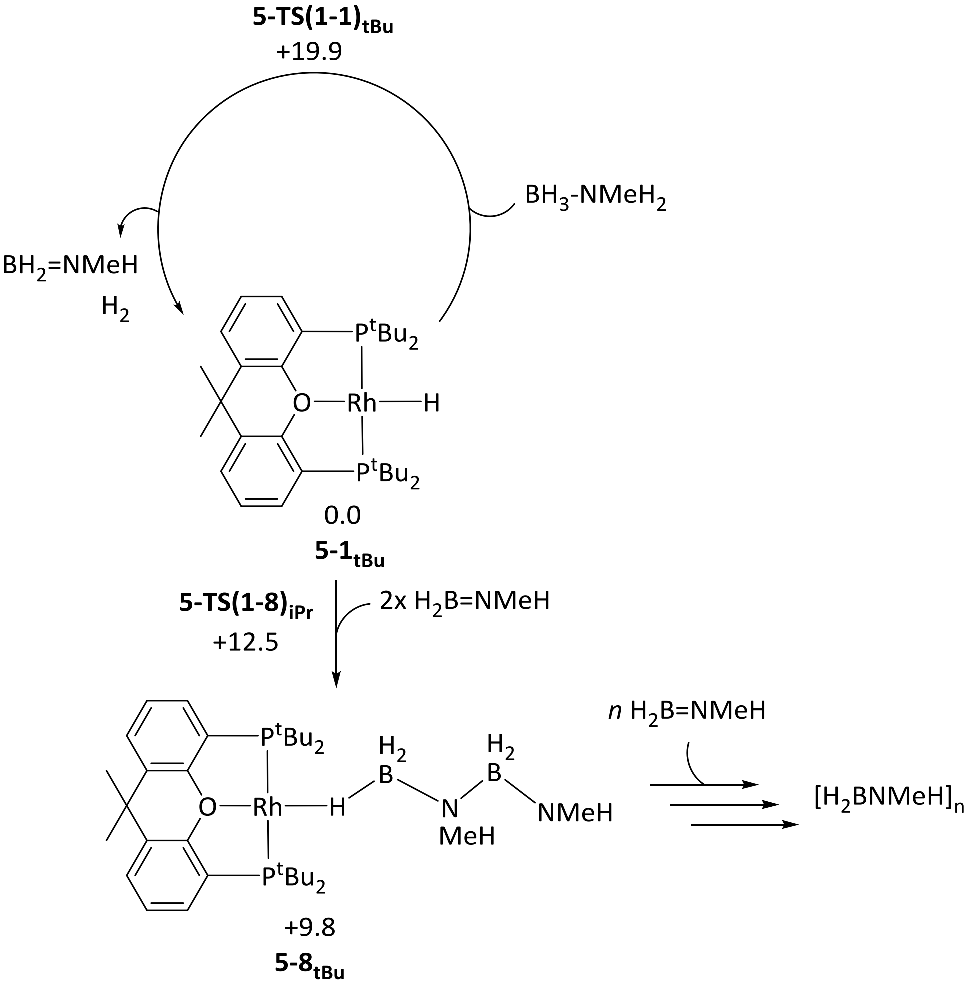

Scheme 5-18: *Proposed mechanism for the dehydropolymerisation of H_3B-$NMeH_2$ with catalyst **5-1$_{tBu}$**. Relative free energies BP86(D3BJ, THF)/BS1 in kcal mol^{-1}.*

The calculated pathway is consistent with the available experimental data. The overall barrier of 19.9 kcal mol^{-1} coincides with the reaction proceeding at room temperature. Furthermore, speciation studies showed that **5-1$_{tBu}$** was the only observed reaction intermediate which is consistent with the predicted pathway and all calculated intermediates being higher in energy than **5-1$_{tBu}$**. *Fac*-tri-hydride **5-5$_{tBu}$** is of similar relative energy to **5-1$_{tBu}$** (G = 0.0 kcal mol^{-1}) but due to the low energy barriers proceeding from **5-5$_{tBu}$** in **Pathways R1$_{tBu}$**, **IC2$_{tBu}$**, **and IC3$_{tBu}$** it is not predicted to be long-lived in the reaction.

5.4 – Dehydropolymerisation of H_3B-$NMeH_2$ with [Rh(*mer*-κ^3-P,O,P-Xantphos-^{t}Bu)(H)$_2$(η^1-H_3B-NMe_3)]$^+$, 5-2$_{\text{iPr}}$

5.4.1 – Dehydrogenation of H_3B-$NMeH_2$ with 5-2$_{\text{iPr}}$

During the computational investigations into the dehydropolymerisation of H_3B-$NMeH_2$ with catalyst **5-2$_{\text{iPr}}$** it was assumed that the H_3B-NMe_3 would rapidly exchange with H_3B-$NMeH_2$ to form [Rh(*mer*-κ^3-P,O,P-Xantphos-^{t}Bu)(H)$_2$(η^1-H_3B-$NMeH_2$)]$^+$ **5-2'$_{\text{iPr}}$**. Therefore, amine-borane complex **5-2'$_{\text{iPr}}$** and the reactants are set at 0.0 kcal mol^{-1} for this study.

Considering the results of the study on neutral alkyl-Xantphos catalysts discussed in **Sections 5.2** and **5.3**, investigations into the dehydrogenation of H_3B-$NMeH_2$ with **5-2'$_{\text{iPr}}$** (G = 0.0 kcal mol^{-1}, **Figure 5-18**) began by exploring possible outer-sphere mechanisms. No such pathways could be characterised from **5-2'$_{\text{iPr}}$.** However, an outer-sphere pathway was characterised when starting from complex **5-3$_{\text{iPr}}$** (G = +16.2 kcal mol^{-1}), which is formed through H_3B-$NMeH_2$ dissociation from **5-2'$_{\text{iPr}}$** (**Pathway OC3$_{\text{iPr}}$, Scheme 5-19**). This outer-sphere, concerted activation proceeds *via* **5-TS(3-3)$_{\text{iPr}}$** (G = +35.6 kcal mol^{-1}) and involves protonation of the metal centre to form a new Rh-H bond and a hydride transfer to directly yield free H_2. **Pathway OC3$_{\text{iPr}}$** is analogous to **Pathway OC2$_{\text{iPr}}$** (**Scheme 5-5**) which occurs with a lower free energy barrier of 14.0 kcal mol^{-1}. It is thought that this process is more difficult in the cationic system partly due to the binding of H_3B-$NMeH_2$ being 16.2 kcal mol^{-1} more stable and partly due to the more electron poor Rh would disfavour the hydride transfer to form H_2 and the proton transfer to the metal. Catalyst **5-2'$_{\text{iPr}}$** (G = -5.3 kcal mol^{-1}) would be regenerated by a molecule of H_3B-$NMeH_2$ co-ordinating to the vacant site in **5-3$_{\text{iPr}}$**.

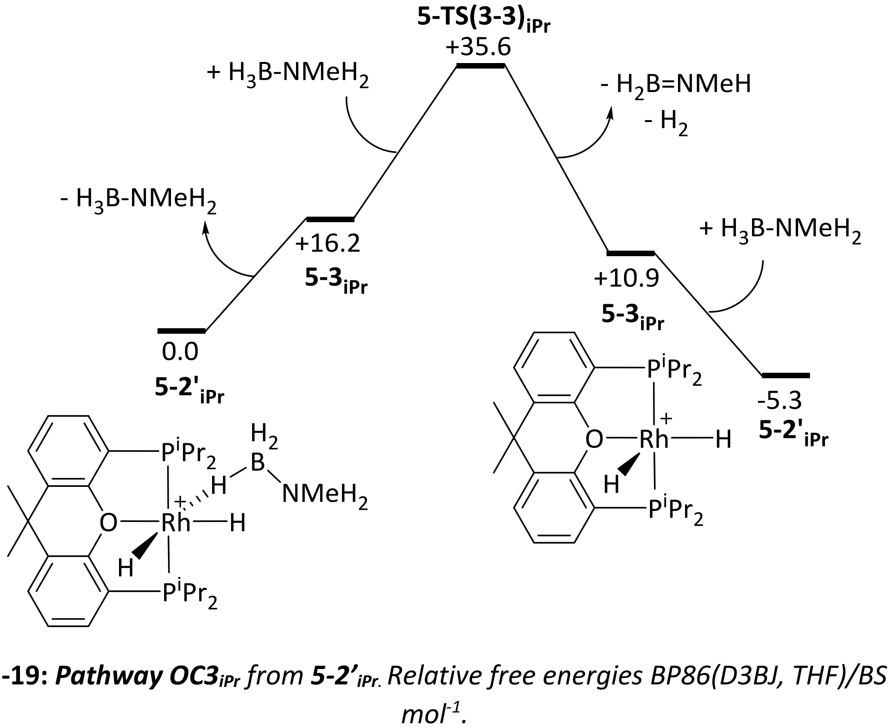

Scheme 5-19: ***Pathway OC3$_{\text{iPr}}$*** *from* ***5-2'$_{\text{iPr}}$****. Relative free energies BP86(D3BJ, THF)/BS1 in kcal mol^{-1}.*

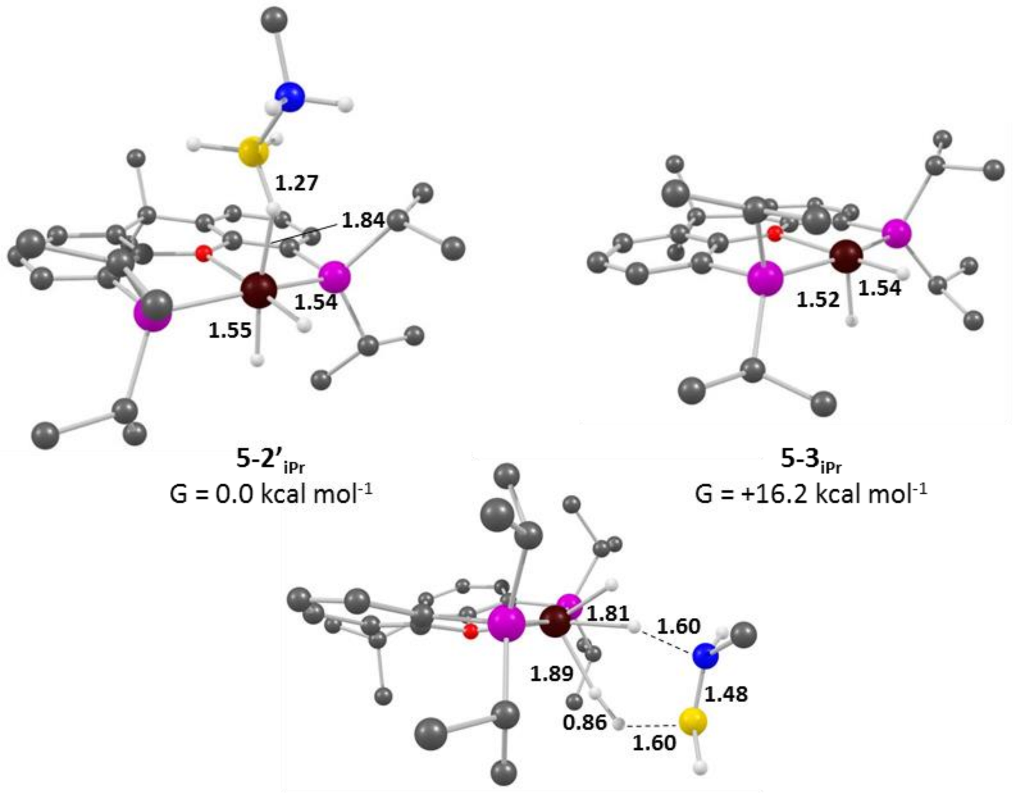

5-2'$_{\mathbf{iPr}}$
G = 0.0 kcal mol^{-1}

5-3$_{\mathbf{iPr}}$
G = +16.2 kcal mol^{-1}

5-TS(3-3)$_{\mathbf{iPr}}$
G = +35.6 kcal mol^{-1}

Figure 5-18: *Key stationary points from* ***Pathway OC3***$_{\mathbf{iPr}}$ *from* ***5-2'***$_{\mathbf{iPr}}$*. Hydrogens bonded to carbon omitted for clarity. Key distances in Å.*

Inner-sphere dehydrogenation mechanisms were also explored. A step-wise B-H/N-H activation pathway (**Pathway IS2**$_{\mathbf{iPr}}$) was characterised and shown in **Scheme 5-20**. From catalyst, **5-2'**$_{\mathbf{iPr}}$, B-H activation was found to proceed through **5-TS(2'-3)1**$_{\mathbf{iPr}}$ (G = +23.5 kcal mol^{-1}, **Figure 5-19**) to form **5-INT(2'-3)1**$_{\mathbf{iPr}}$ (G = +13.4 kcal mol^{-1}). Interestingly, this causes the two metal-hydrides to reductively couple with the H···H distance decreased from 1.99 Å to 0.81 Å as the B···H distances increases from 1.27 Å to 2.63 Å. This forms a dihydrogen ligand *trans* to the {BH_2-$NMeH_2$} moiety rather than *trans* to the Rh-O bond. The newly formed H_2 ligand then dissociates through **5-TS(2'-3)3**$_{\mathbf{iPr}}$ (G = +14.7 kcal mol^{-1}) to form five-coordinate species **5-INT(2'-3)2**$_{\mathbf{iPr}}$ (G = +6.1 kcal mol^{-1}). N-H activation *via* **5-TS(2'-3)3**$_{\mathbf{iPr}}$ (G = +21.4 kcal mol^{-1}) would then yield **5-3**$_{\mathbf{iPr}}$ (G = +10.9 kcal mol^{-1}) which would regenerate **5-2'**$_{\mathbf{iPr}}$ (G = -5.3 kcal mol^{-1}) by binding H_3B-$NMeH_2$. The rate-limiting step for this process was found to be the B-H activation step through **5-TS(2'-3)1**$_{\mathbf{iPr}}$ with a free energy barrier of 23.5 kcal mol^{-1}.

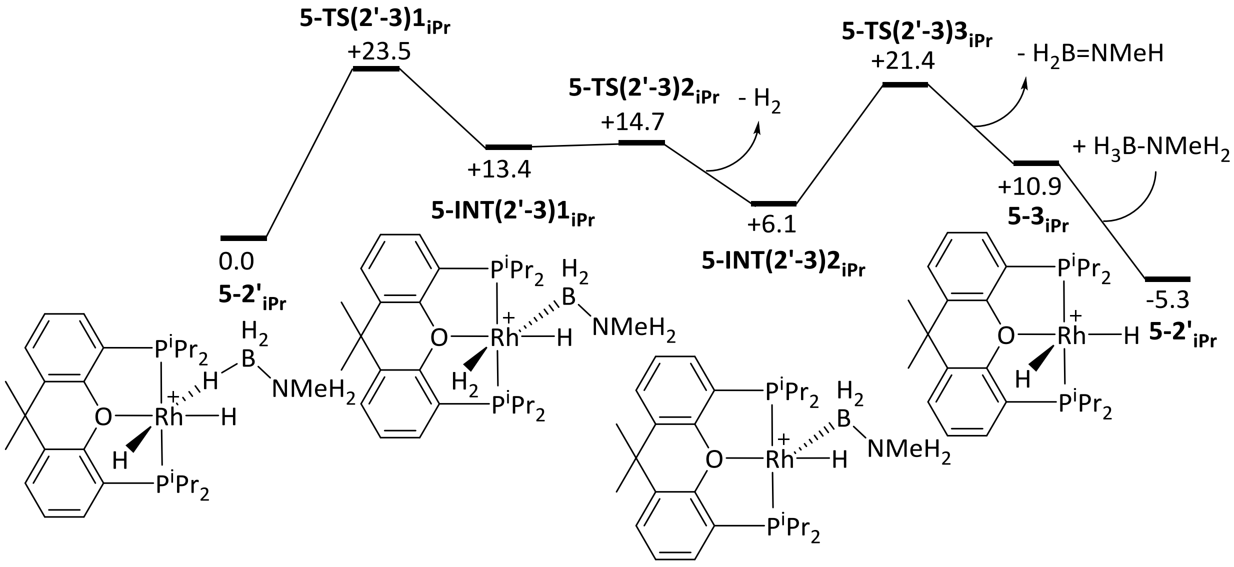

Scheme 5-20: ***Pathway IS2$_{iPr}$*** *from* ***5-2'$_{iPr}$***. *Relative free energies BP86(D3BJ, THF)/BS1 in kcal mol^{-1}.*

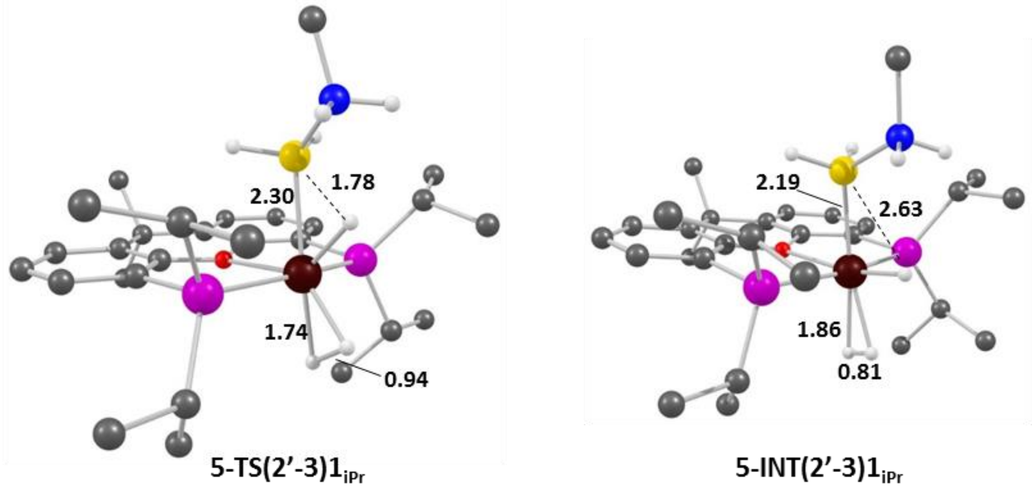

5-TS(2'-3)1$_{iPr}$
G = +23.5 kcal mol^{-1}

5-INT(2'-3)1$_{iPr}$
G = +13.4 kcal mol^{-1}

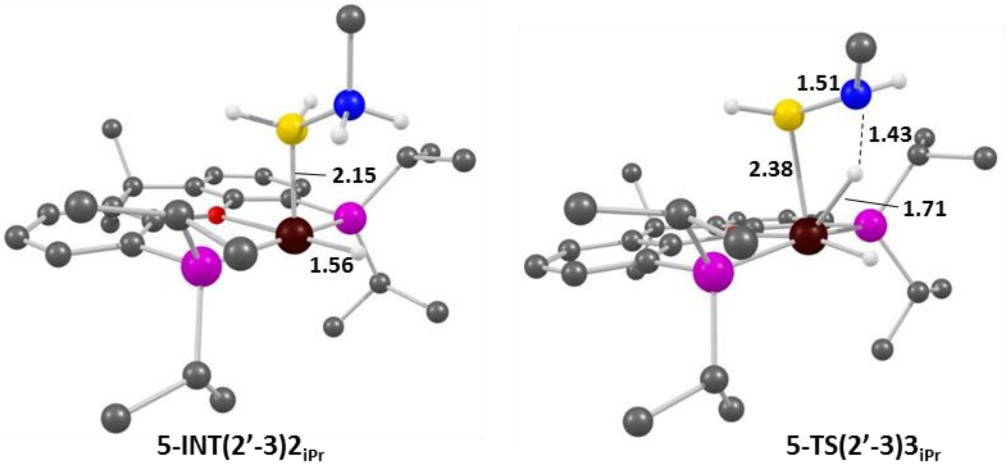

5-INT(2'-3)2$_{iPr}$
G = +6.1 kcal mol^{-1}

5-TS(2'-3)3$_{iPr}$
G = +21.4 kcal mol^{-1}

Figure 5-19: *Key stationary points from* ***Pathway IS2$_{iPr}$*** *from* ***5-2'$_{iPr}$***. *Hydrogens bonded to carbon omitted for clarity. Key distances in Å.*

An inner-sphere concerted mechanism was also calculated (**Pathway IC4$_{iPr}$, Scheme 5-21**). The concerted activation proceeds through **5-TS(2'-10)$_{iPr}$** (G = +36.7 kcal mol^{-1}, **Figure 5-20**) forming free $H_2B{=}NMeH$ and dihydrogen di-hydride complex **5-10$_{iPr}$** (G +9.1 kcal mol^{-1}). Dissociation of the H_2 ligand *via* **5-TS(10-3)$_{iPr}$** (G = +15.6 kcal mol^{-1}) generates **5-3$_{iPr}$** which completes the cycle by binding H_3B-$NMeH_2$ to form **5-2'$_{iPr}$.** The rate limiting step for **Pathway IC4$_{iPr}$** is the concerted activation with a free energy barrier of 36.7 kcal mol^{-1}.

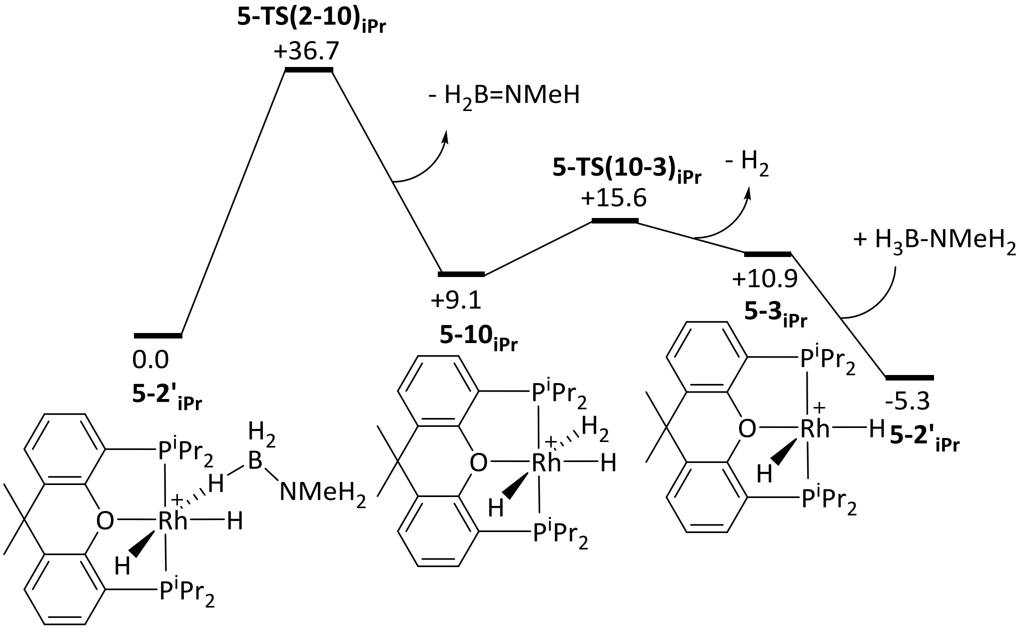

Scheme 5-21: ***Pathway IC4$_{iPr}$*** *from* ***5-2$_{iPr}$****. Relative free energies BP86(D3BJ, THF)/BS1 in kcal mol^{-1}.*

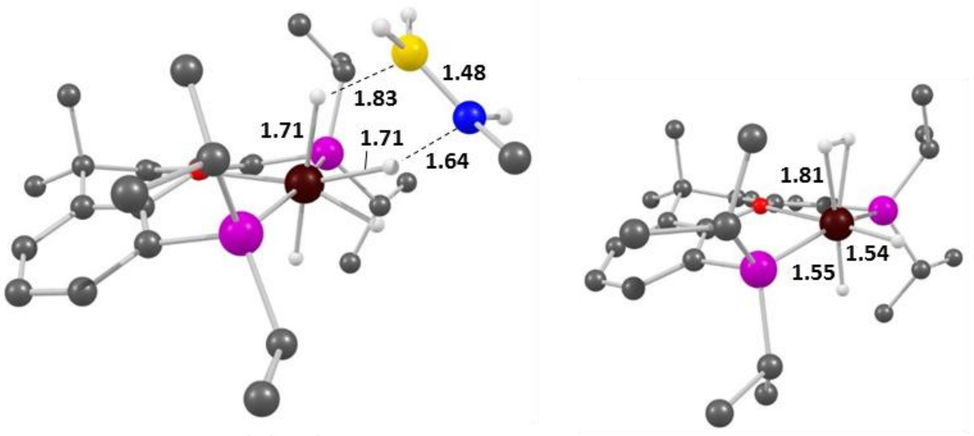

5-TS(2'-10)$_{iPr}$
G = +36.7 kcal mol^{-1}

5-10$_{iPr}$
G = +9.1 kcal mol^{-1}

Figure 5-20: *Key stationary points for* ***Pathway IC4$_{iPr}$*** *from* ***5-2'$_{iPr}$****. Hydrogens bonded to carbon omitted for clarity. Key distances in Å.*

Inspired by the formation of mono-cationic dimer [(Rh(*mer*-κ^3-P,O,P-Xantphos-^{i}Pr))$_2$μ-B][BAr$^F{}_4$], dehydrogenation mechanisms involving the formation of a boronium cation $[(NMeH_2)_2BH_2]^+$ were explored. This requires a free $NMeH_2$ molecule to be present in solution of which there is precedent in the literature.[194, 195] The groups of Conejero and Freixa have also suggested mechanisms of this kind taking place in the dehydrocoupling of amine-boranes.[98, 99] One such mechanism, **Pathway BF1$_{iPr}$**, is displayed in **Scheme 5-22**. The free amine can attack the boron of the H_3B-$NMeH_2$ moiety in **5-2'$_{iPr}$** through an S_N2 type transition state **5-TS(2'-11)$_{iPr}$** (G = +27.0 kcal mol^{-1}, **Figure 5-21**) where the N···B distance is 2.20 Å and the B···H distance 1.81 Å. This forms the boronium cation $[(NMeH_2)_2BH_2]^+$ and neutral *mer*-tri-hydride species **5-11$_{iPr}$** (G = +4.5 kcal mol^{-1}). One of the N-H bonds of the boronium cation is then predicted to protonate the metal centre *via* **5-TS(11-10)$_{iPr}$** (G = +9.1 kcal mol^{-1}) to form cationic complex **5-10$_{iPr}$** (G = +9.1 kcal mol^{-1}) and $[(HMeN)BH_2(NMeH_2)]$ in a process that appears barrier-less. The $[(HMeN)BH_2(NMeH_2)]$ molecule is then calculated to dissociate to free H_2B=NMeH and $NMeH_2$ in a process that is thermodynamically favourable by 1.2 kcal mol^{-1}. This makes the free $NMeH_2$ catalytic in this process. Intermediate **5-10$_{iPr}$** would regenerate **5-2'$_{iPr}$** through H_2 loss and H_3B-$NMeH_2$ co-ordination as discussed in **Scheme 5-20**. The boronium formation *via* **5-TS(2'-11)$_{iPr}$** is the rate limiting step for this process with a free energy barrier of 27.0 kcal mol^{-1}.

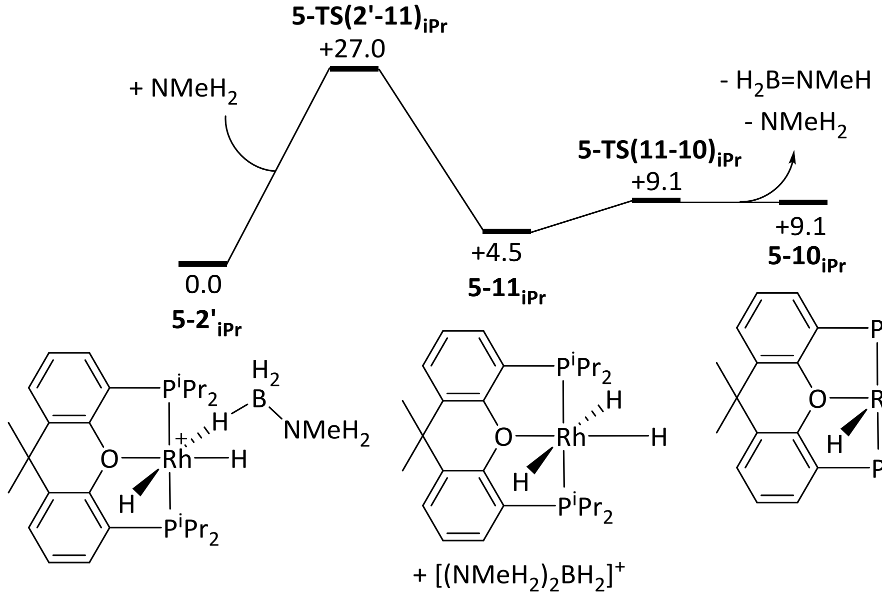

Scheme 5-22: ***Pathway BF1$_{iPr}$*** *from* ***5-2'$_{iPr}$****. Relative free energies BP86(D3BJ, THF)/BS1 in kcal mol^{-1}.*

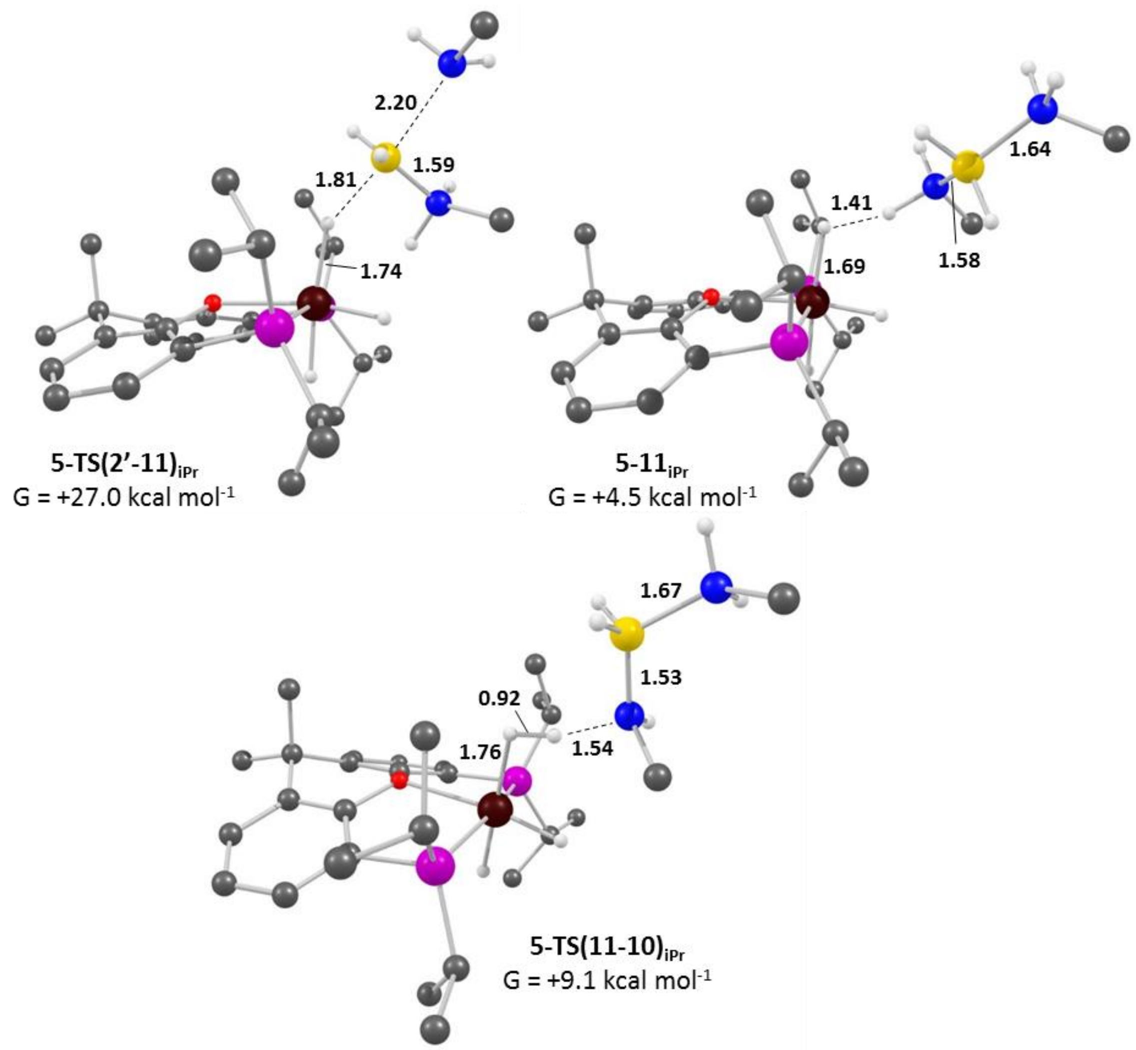

Figure 5-21: *Key stationary points from **Pathway BF1$_{iPr}$** pathway from **5-2'$_{iPr}$**. Hydrogens bonded to carbon omitted for clarity. Key distances in Å.*

Another pathway involving boronium formation, **Pathway BF2$_{iPr}$**, is outlined in **Scheme 5-23**. Here, catalyst **5-2'$_{iPr}$** proceeds through B-H activation and H_2 loss to form **5-INT(2'-3)2$_{iPr}$** as in **Pathway IS2$_{iPr}$** (**Scheme 5-20**) before boronium formation takes place. The free $NMeH_2$ attacks the {H_2B-$NMeH_2$} moiety *via* **5-TS(2'-1)$_{iPr}$** (G = 20.2 kcal mol^{-1}, **Figure 5-22**) in an S_N2 type transition state. This forms the boronium cation and neutral mono-hydride species **5-1$_{iPr}$** (G = +1.6 kcal mol^{-1}). In contrast to neutral tri-hydride **5-11$_{iPr}$**, a process involving proton transfer of the boronium cation of **5-1$_{iPr}$** could not be located. This suggests that neutral mono-hydride **5-1$_{iPr}$** would then become the catalytically active species and catalysis would proceed as described in **Scheme 5-10**. The boronium formation through **5-TS(2'-1)$_{iPr}$** occurs with a barrier of 20.2 kcal mol^{-1} which is 6.8 kcal mol^{-1} lower in energy than the boronium formation in **Pathway BF1$_{iPr}$** *via* **5-TS(2'-11)$_{iPr}$**. This makes the initial B-H activation *via* **5-TS(2'-3)1$_{iPr}$** the rate-limiting step for this process with a free energy barrier of 23.5 kcal mol^{-1}.

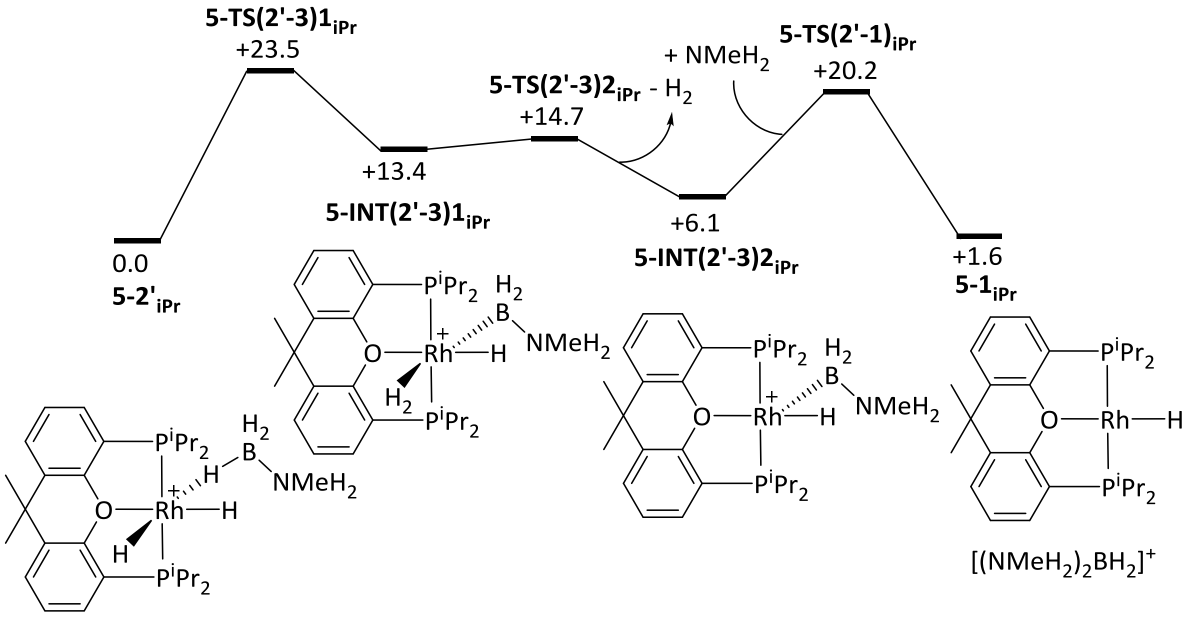

Scheme 5-23: ***Pathway BF2$_{iPr}$*** *from* ***5-2$_{iPr}$****. Relative free energies BP86(D3BJ, THF)/BS1 in kcal mol^{-1}.*

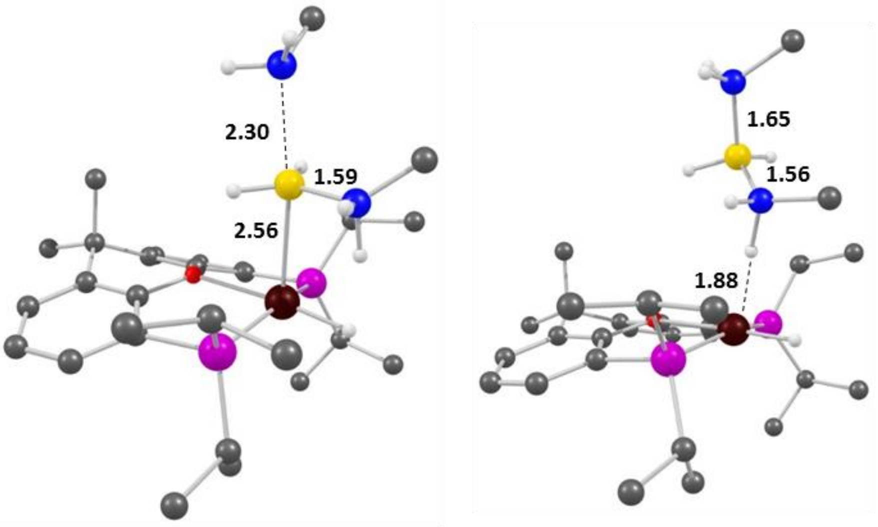

5-TS(2'-1)$_{iPr}$
G = +20.2 kcal mol^{-1}

5-1$_{iPr}$ + [BH$_2$(NMeH$_2$)$_2$]$^+$
G = +6.1 kcal mol^{-1}

Figure 5-22: *Key stationary points for* ***Pathway BF2$_{iPr}$*** *from* ***5-2$_{iPr}$****. Hydrogens bonded to carbon omitted for clarity. Key distances in Å.*

5.4.2 – Summary of the Dehydropolymerisation of H_3B-NMeH$_2$ with 5-2$_{iPr}$

Overall, there are two dehydrogenation pathways with the same overall free energy barrier: **Pathway IS2$_{iPr}$** (**Scheme 5-20**) and **Pathway BF2$_{iPr}$** (**Scheme 5-23**). In both cases, the initial B-H activation *via* **5-TS(2'-3)1$_{iPr}$** was the rate limiting process with a barrier of 23.5 kcal mol^{-1}. Neither of these computationally predicted pathways agree well with the experimental data. Namely, the calculated rate-limiting step being a B-H activation process contradicts the experimental KIE values which show only a small B-H KIE and predict N-H activation to be rate-limiting. This means that other dehydrogenation mechanisms need to be explored. It has been noted previously that introducing a second amine-borane molecule to the metal centre can facilitate lower free energy barriers for B-H and N-H activation.[55] Furthermore, the dehydrogenation pathways for the neutral catalyst **5-1$_{iPr}$** discussed in **Section 5.2** involve the Xantphos ligand adopting different binding modes during the reaction. This does not occur in any of the dehydrogenation pathways characterised so far for catalyst **5-2'$_{iPr}$** with the Xantphos remaining in the *mer*-κ^3-P,O,P binding mode throughout. Therefore, it is suggested that dehydrogenation pathways involving the addition of a second amine-borane and isomerisation of the Xantphos ligand would provide the best chance of characterising a pathway which complements the available experimental data.

Propagation pathways from **5-2'$_{iPr}$** or other cationic intermediates have also yet to be explored. However, some work has been conducted into the propagation mechanism involving catalyst **5-3$_{tBu}$** which is discussed in **Section 5.5.2**.

5.5 – Dehydropolymerisation of H_3B-$NMeH_2$ with [Rh(*mer*-κ^3-P,O,P-Xantphos-^{t}Bu)(H)$_2$]$^+$, 5-3$_{tBu}$

5.5.1 – Dehydrogenation of H_3B-$NMeH_2$ with 5-3$_{tBu}$

Computational studies were also conducted on catalyst **5-3$_{tBu}$** for comparison with **5-2$_{iPr}$** and **5-1$_{tBu}$.** Experimentally, [Rh(*mer*-κ^3-P,O,P-Xantphos-^{t}Bu)(H)$_2$(η^1-H_3B-NMe_3)]$^+$ **5-2$_{tBu}$** and [Rh(*mer*-κ^3-P,O,P-Xantphos-^{t}Bu)(H)$_2$(η^1-H_3B-$NMeH_2$)]$^+$ **5-2'$_{tBu}$** could not be isolated, presumably due to the increased steric effect of the ^{t}Bu groups disfavouring the binding of amine-boranes. The optimised geometries of **5-2'$_{tBu}$** (G = +1.1 kcal mol^{-1}, **Figure 5-23**) and **5-3$_{tBu}$** (G = 0.0 kcal mol^{-1}) fit this experimental observation as **5-2'$_{tBu}$** is higher in energy. Furthermore, the energy difference is small enough to remain consistent with the experimental observation that it is accessible in solution due to H/D exchange experiments.

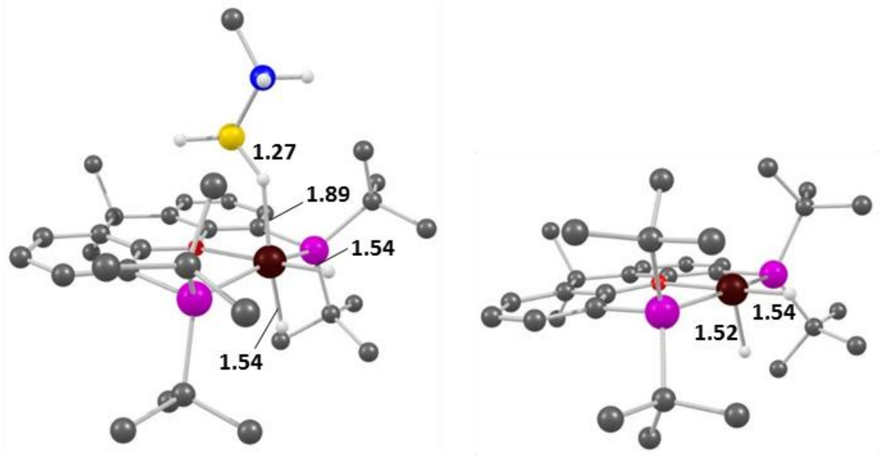

5-2'$_{tBu}$
G = +1.1 kcal mol^{-1}

5-3$_{tBu}$
G = 0.0 kcal mol^{-1}

Figure 5-23: *Optimised structures of **5-2'$_{tBu}$** and **5-3$_{tBu}$**. Hydrogens bonded to carbon omitted for clarity. Key distances in Å.*

As with **5-2'$_{iPr}$,** outer-sphere, concerted dehydrogenation mechanisms were explored. A transition state analogous to **Pathway OC1$_{tBu}$** (**Scheme 5-13**) could not be located. However, a concerted process *via* **5-TS(3-3)$_{tBu}$** (G = +29.0 kcal mol^{-1}, **Figure 5-24**) was calculated (**Pathway OC3$_{tBu}$, Scheme 5-24**). This process forms H_2B=NMeH, H_2 and regenerates **5-3$_{tBu}$** (G = -5.3 kcal mol^{-1}) in one step as in **Pathway OC2$_{tBu}$** which was the most favoured dehydrogenation pathway for catalyst **5-1$_{tBu}$**. The same trend between **Pathway OC2$_{iPr}$** (**Scheme 5-5**) and **Pathway OC3$_{iPr}$** (**Scheme 5-19**) is observed where this outer-sphere, concerted process is more difficult for cationic **5-3$_{tBu}$** compared to **5-1$_{tBu}$** with a free energy barrier of 29.0 kcal mol^{-1} compared to 19.9 kcal mol^{-1}.

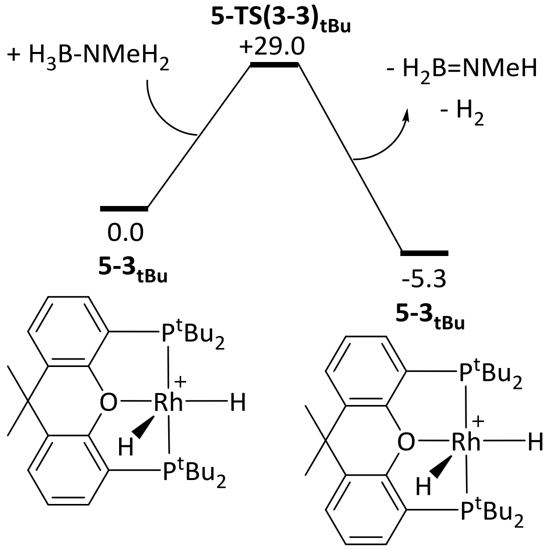

Scheme 5-24: ***Pathway OC3$_{tBu}$*** *from* ***5-3$_{tBu}$****. Relative free energies BP86(D3BJ, THF)/BS1 in kcal mol^{-1}.*

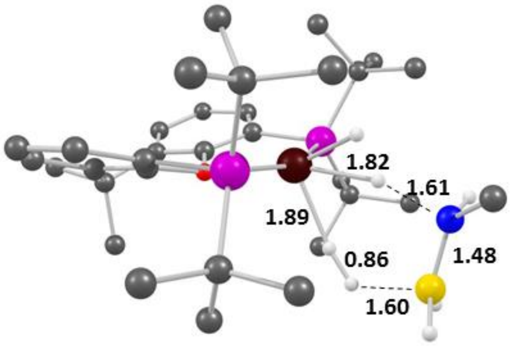

5-TS(3-3)$_{tBu}$
G = +29.0 kcal mol^{-1}

Figure 5-24: *Optimised structure of* ***5-TS(3-3)$_{tBu}$****. Hydrogens bonded to carbon omitted for clarity. Key distances in Å.*

Pathway IS2$_{tBu}$ was also calculated as seen in **Scheme 5-25**. A molecule of H_3B-$NMeH_2$ must first co-ordinate to the metal centre to form **5-2'$_{tBu}$** before any inner-sphere mechanism can proceed. B-H activation is then predicted to proceed through **5-TS(2'-3)1$_{tBu}$** (G = +29.8 kcal mol^{-1}, **Figure 5-25**) with concerted H_2 reductive coupling occurring to form **5-INT(2'-3)1$_{tBu}$** (G = +27.5 kcal mol^{-1}) where the H_2 is *trans* to the {BH_2-NH_3} moiety. A transition state involving the dissociation of H_2 could not be characterised for this system, however, it is calculated to be thermodynamically favourable to form **5-INT(2'-3)2$_{tBu}$** (G = +6.9 kcal mol^{-1}). The N-H activation step then occurs *via* **5-TS(2'-3)3$_{tBu}$** (G = +23.0 kcal mol^{-1}) to form free H_2B=NMeH and regenerate **5-3$_{tBu}$** (G = -5.3 kcal mol^{-1}). The B-H activation is the rate-limiting step in this process with a free energy barrier of 29.8 kcal mol^{-1}.

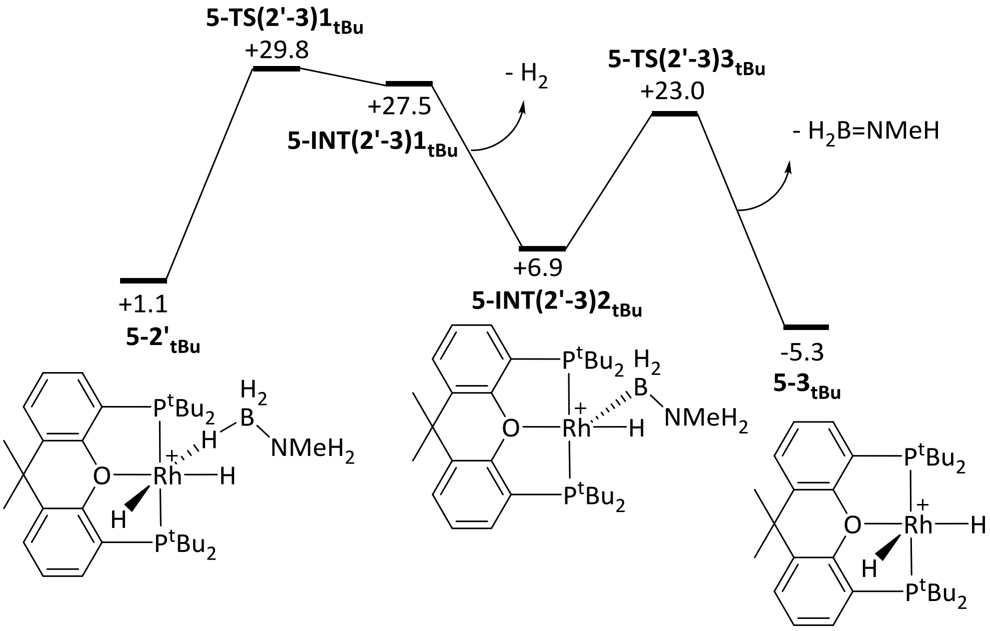

Scheme 5-25: ***Pathway IS2$_{tBu}$*** *from* ***5-2'$_{tBu}$****. Relative free energies BP86(D3BJ, THF)/BS1 in kcal mol^{-1}.*

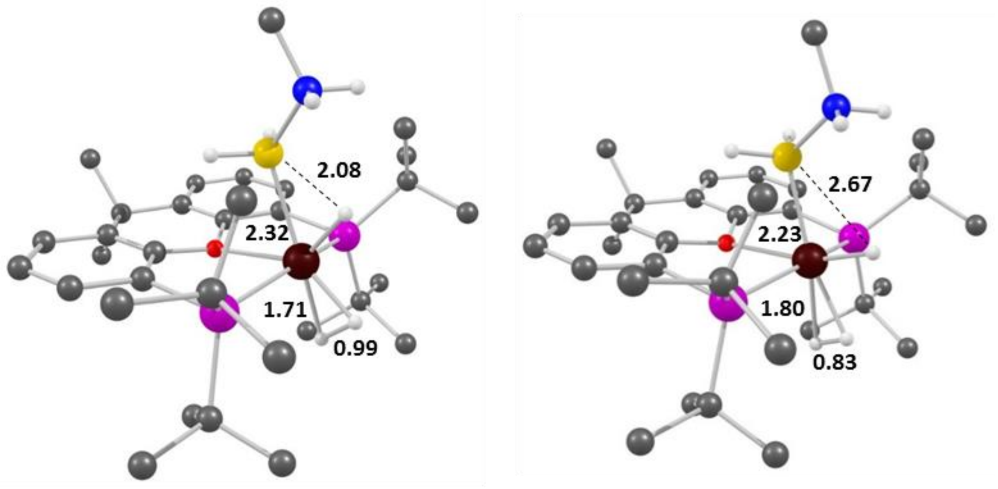

5-TS(2’-3)1$_{\text{tBu}}$
G = +29.8 kcal mol^{-1}

5-INT(2’-3)1$_{\text{tBu}}$
G = +27.5 kcal mol^{-1}

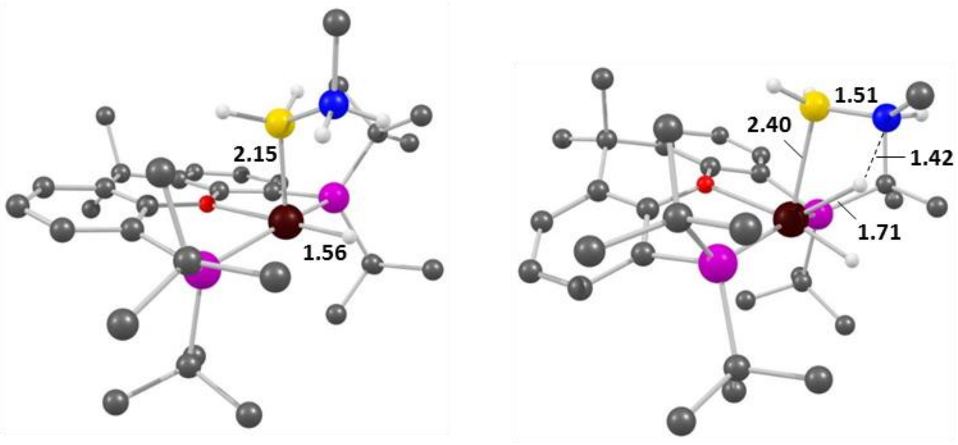

5-INT(2’-3)2$_{\text{tBu}}$
G = +6.9 kcal mol^{-1}

5-TS(2’-3)3$_{\text{tBu}}$
G = +23.0 kcal mol^{-1}

Figure 5-25: *Key stationary points for* ***Pathway IS2$_{\text{tBu}}$*** *from* ***5-2$_{\text{tBu}}$****. Hydrogens bonded to carbon omitted for clarity. Key distances in Å.*

An inner-sphere, concerted activation mechanism, **Pathway IC4$_{\text{tBu}}$**, was also characterised (**Scheme 5-26**). This process occurs *via* **5-TS(2’-10)$_{\text{tBu}}$** (G = +29.3 kcal mol^{-1}, **Figure 5-26**) to form dihydrogen di-hydride complex **5-10$_{\text{tBu}}$** (G = -1.2 kcal mol^{-1}) and free $H_2B{=}NMeH$. The dissociation of H_2 through **5-TS(10-3)$_{\text{tBu}}$** (G = +5.0 kcal mol^{-1}) regenerates catalyst **5-3$_{\text{tBu}}$** (G = -5.3 kcal mol^{-1}). The free energy barrier for this process in 29.3 kcal mol^{-1} due to the concerted dehydrogenation through **5-TS(2’-10)$_{\text{tBu}}$** being rate limiting.

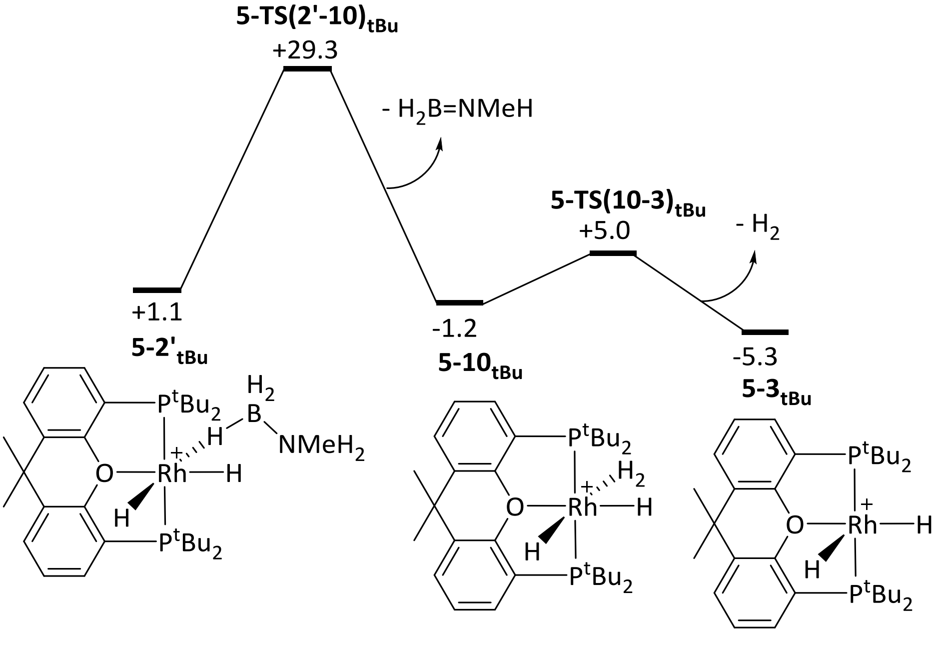

Scheme 5-26: ***Pathway IC4*$_{tBu}$** *from* **5-2'$_{tBu}$**. *Relative free energies BP86(D3BJ, THF)/BS1 in kcal mol^{-1}.*

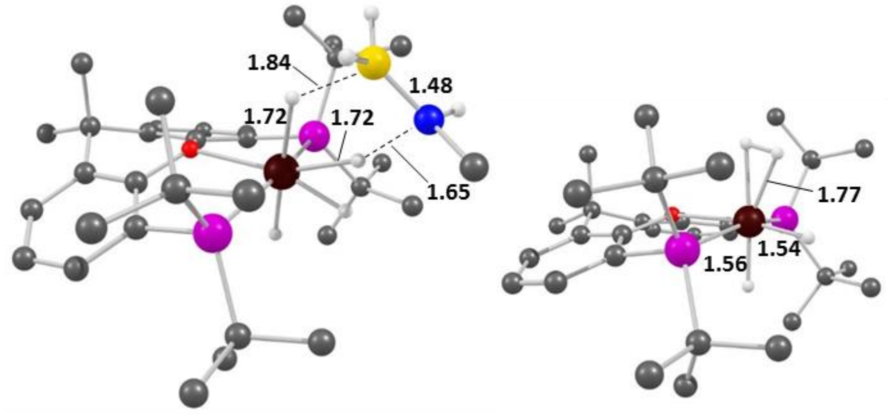

5-TS(2'-10)$_{tBu}$
G = +29.3 kcal mol^{-1}

5-10$_{tBu}$
G = -1.2 kcal mol^{-1}

Figure 5-26: *Key stationary points for* ***Pathway IC4*$_{tBu}$** *from* **5-2'$_{tBu}$**. *Hydrogens bonded to carbon omitted for clarity. Key distances in Å.*

Mechanisms involving the formation of boronium cation $[(NMeH_2)_2BH_2]^+$ were also explored. In **Pathway BF1$_{tBu}$** (**Scheme 5-27**) it was found that free $NMeH_2$ would attack the H_3B-$NMeH_2$ in **5-2'$_{tBu}$** *via* **5-TS(2'-11)$_{tBu}$** (G = +18.5 kcal mol^{-1}, **Figure 5-27**) which is an S_N2 like transition state. This forms neutral *mer*-tri-hydride **5-11$_{tBu}$** (G = -6.0 kcal mol^{-1}) and $[(NMeH_2)_2BH_2]^+$. The boronium cation then protonates the metal centre in a facile process through **5-TS(11-10)$_{tBu}$** (G = -1.5 kcal mol^{-1}) to yield **5-10$_{tBu}$.** Catalyst **5-3$_{tBu}$** would then be formed by the H_2 dissociation process covered in **Pathway IC4$_{tBu}$** (**Scheme 5-26**). The rate limiting step for this process is the formation of **5-11$_{tBu}$** *via* **5-TS(2'-11)$_{tBu}$** with a free energy barrier of 18.5 kcal mol^{-1}. An equivalent process to **Pathway BF2$_{iPr}$** (**Scheme 5-23**) proceeding from **5-INT(2-3)2$_{tBu}$** could not be characterised for this system.

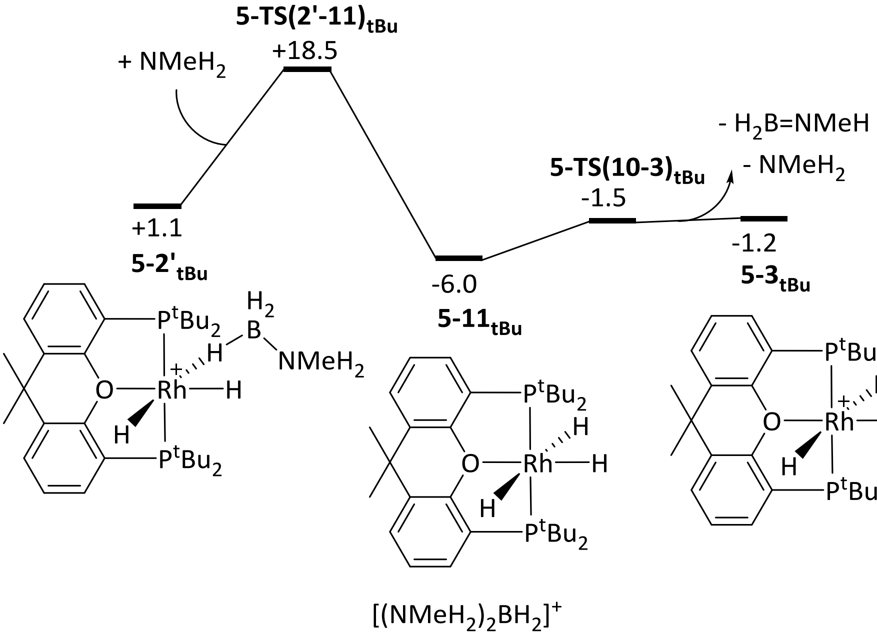

Scheme 5-27: ***Pathway BF1$_{tBu}$*** *from* ***5-2'$_{tBu}$****. Relative free energies BP86(D3BJ, THF)/BS1 in kcal mol^{-1}.*

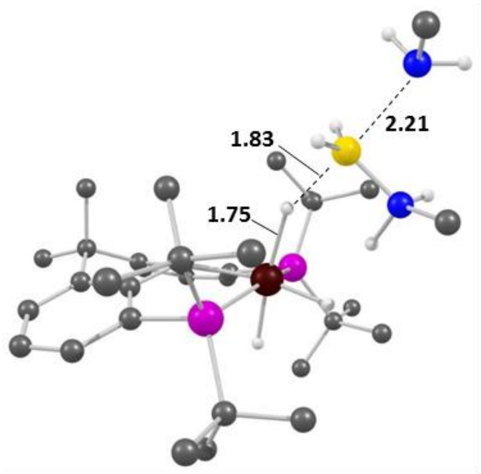

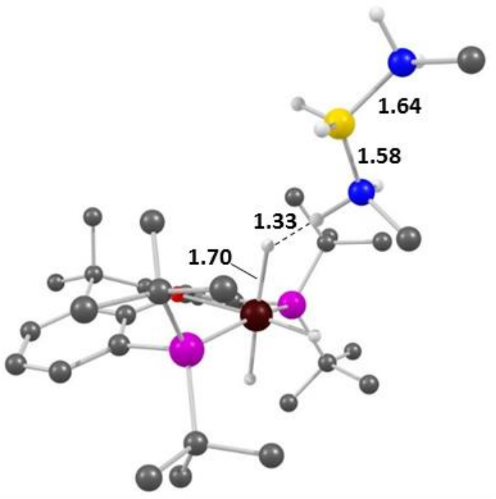

5-TS(2'-11)$_{tBu}$
G = +18.5 kcal mol^{-1}

5-11$_{tBu}$
G = -6.0 kcal mol^{-1}

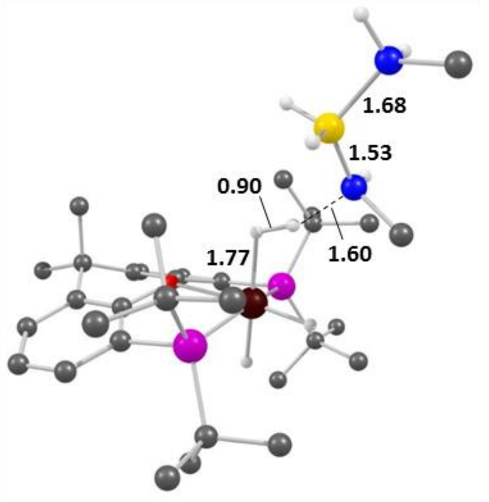

5-TS(11-10)$_{tBu}$
G = -1.5 kcal mol^{-1}

Figure 5-27: *Key stationary points for **Pathway BF1$_{tBu}$** from **5-2'$_{tBu}$**. Hydrogens bonded to carbon omitted for clarity. Key distances in Å.*

In summary, the most favoured mechanism for the dehydrogenation of H_3B-$NMeH_2$ with **5-3$_{tBu}$** is **Pathway BF1$_{tBu}$** (**Scheme 5-27**) where free $NMeH_2$ facilitates the formation of boronium cation $[(NMeH_2)_2BH_2]^+$ and neutral *mer*-tri-hydride **5-11$_{tBu}$**. The boronium would then protonate the metal centre to form free H_2B=NMeH, $NMeH_2$ and cationic dihydrogen dihydride **5-10$_{tBu}$** which would regenerate catalyst **5-3$_{tBu}$** by losing H_2. This process is favoured as it proceeds with a free energy barrier of 18.5 kcal mol^{-1} compared to **Pathways OC3$_{tBu}$** (29.0 kcal mol^{-1}), **IS2$_{tBu}$** (29.8 kcal mol^{-1}), and **IC4$_{tBu}$** (29.3 kcal mol^{-1}).

5.5.2 – Propagation of H_2B=NMeH with 5-3$_{tBu}$

Pathways were also investigated for the propagation of H_2B=NMeH with **5-3$_{tBu}$**. An equivalent pathway to **Pathway P1$_{tBu}$** (**Scheme 5-17**) from either **5-2'$_{tBu}$** or **5-3$_{tBu}$** could not be characterised. It was found that a free H_2B=NMeH moiety could bind to the vacant site of **5-3$_{tBu}$** to give **5-13$_{tBu}$**

(G = -4.5 kcal mol^{-1}, **Figure 5-28**). The mechanism (**Pathway P2$_{tBu}$**) shown in **Scheme 5-28** then predicts that a second H_2B=NMeH would approach and proceed through a B-N coupling process *via* **5-TS(13-14)$_{tBu}$** (G = +15.0 kcal mol^{-1}) to form intermediate **5-14** (G = +6.3 kcal mol^{-1}) which features the newly formed H_3B-NMeHBH_2-NMeH moiety being η^2-bound to the Rh through B-H σ-interactions from both boron atoms. This occurs with a free energy barrier of 19.5 kcal mol^{-1}.

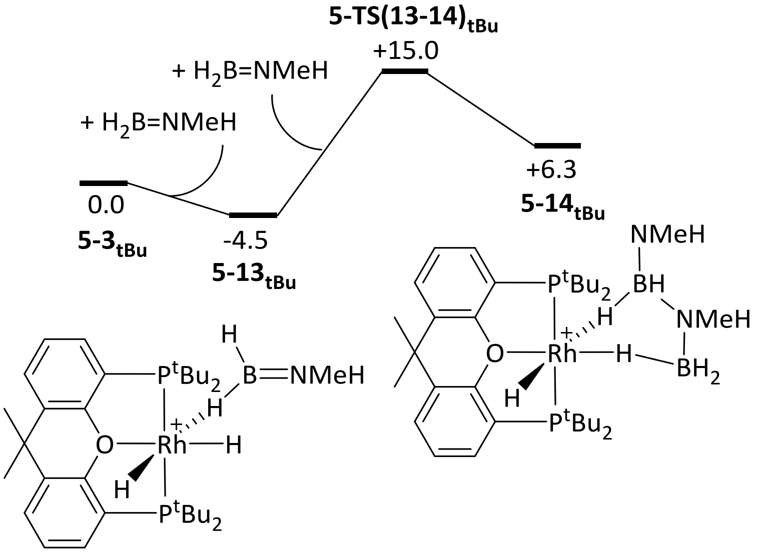

Scheme 5-28: ***Pathway P2$_{tBu}$****from* ***5-3$_{tBu}$****. Relative free energies BP86(D3BJ, THF)/BS1 in kcal mol^{-1}.*

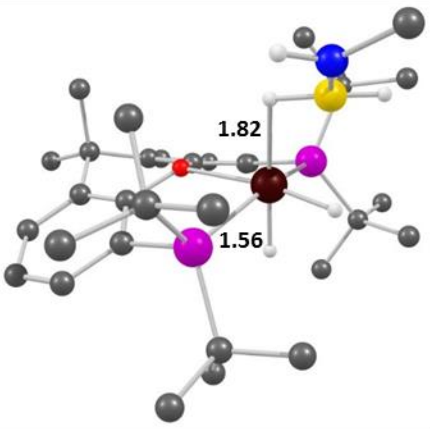

5-13$_{tBu}$
G = -4.5 kcal mol^{-1}

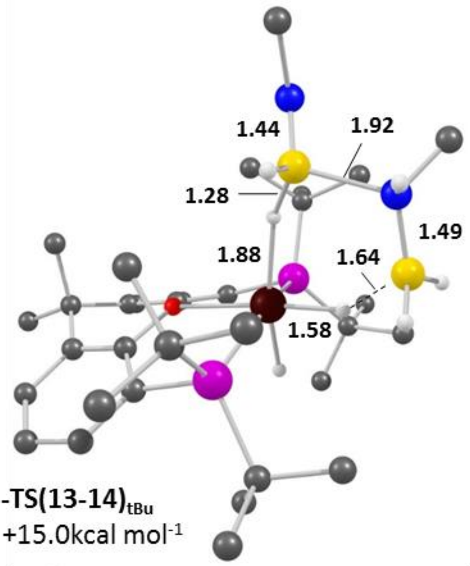

5-TS(13-14)$_{tBu}$
G = +15.0kcal mol^{-1}

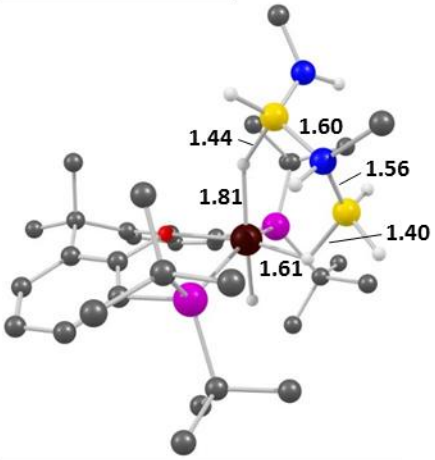

5-14$_{tBu}$
G = +6.3 kcal mol^{-1}

Figure 5-28: *Key stationary points for* ***Pathway P2$_{tBu}$*** *from* ***5-3$_{tBu}$****. Hydrogens bonded to carbon omitted for clarity. Key distances in Å.*

From **5-14$_{tBu}$** two propagation pathways could take place. First, a head-to-tail chain growth propagation mechanism would see the terminal NMeH unit act as a nucleophile against other free H_2B=NMeH molecules in a similar process to **Pathway P1$_{tBu}$** (**Scheme 5**-**17**) for **5-1$_{tBu}$**. This kind of propagation could also occur from amino-borane complex **5-13$_{tBu}$**. An alternative mechanism would involve **5-14$_{tBu}$** B-H activating to form a complex analogous to **5-13$_{tBu}$** where the linear dimer H_2B-NMeHBH$_2$-NMeH is in place of the H_2B=NMeH molecule. Equivalent transition states to **5-TS(13-14)$_{tBu}$** could then take place to grow the polymer chain in a co-ordination/insertion propagation pathway.

5.5.3 – Summary of the Dehydropolymerisation of H_3B-NMeH$_2$ with 5-3$_{tBu}$

The computationally predicted pathway for the dehydropolymerisation of H_3B-NMeH$_2$ with catalyst **5-3$_{tBu}$** is shown in **Scheme 5-29**. The dehydrogenation proceeds *via* **Pathway BF1$_{tBu}$** (**Scheme 5-27**) with an initial free energy barrier of 18.5 kcal mol^{-1}. It then proceeds through a slightly larger barrier of 19.2 kcal mol^{-1} due to the energy difference between the lowest energy intermediate **5-11$_{\mathbf{tBu}}$** and the second cycle of boronium formation through **5-TS(2’-11)$_{\mathbf{tBu}}$** (G = 13.2 kcal mol^{-1}). One of the $H_2B{=}NMeH$ molecules formed from the dehydrogenation is then predicted to bind to the vacant site of the metal to give intermediate **5-13$_{\mathbf{tBu}}$**. **Pathway P2$_{\mathbf{tBu}}$** (**Scheme 5-28**) has been calculated to proceed with a barrier of 21.0 kcal mol^{-1}, higher than that of dehydrogenation. This means that propagation is unlikely to proceed *via* this mechanism. However, amino-borane complex **5-13$_{\mathbf{tBu}}$** is currently the most likely propagating species characterised and it is suggested that any propagation mechanism will stem from this intermediate.

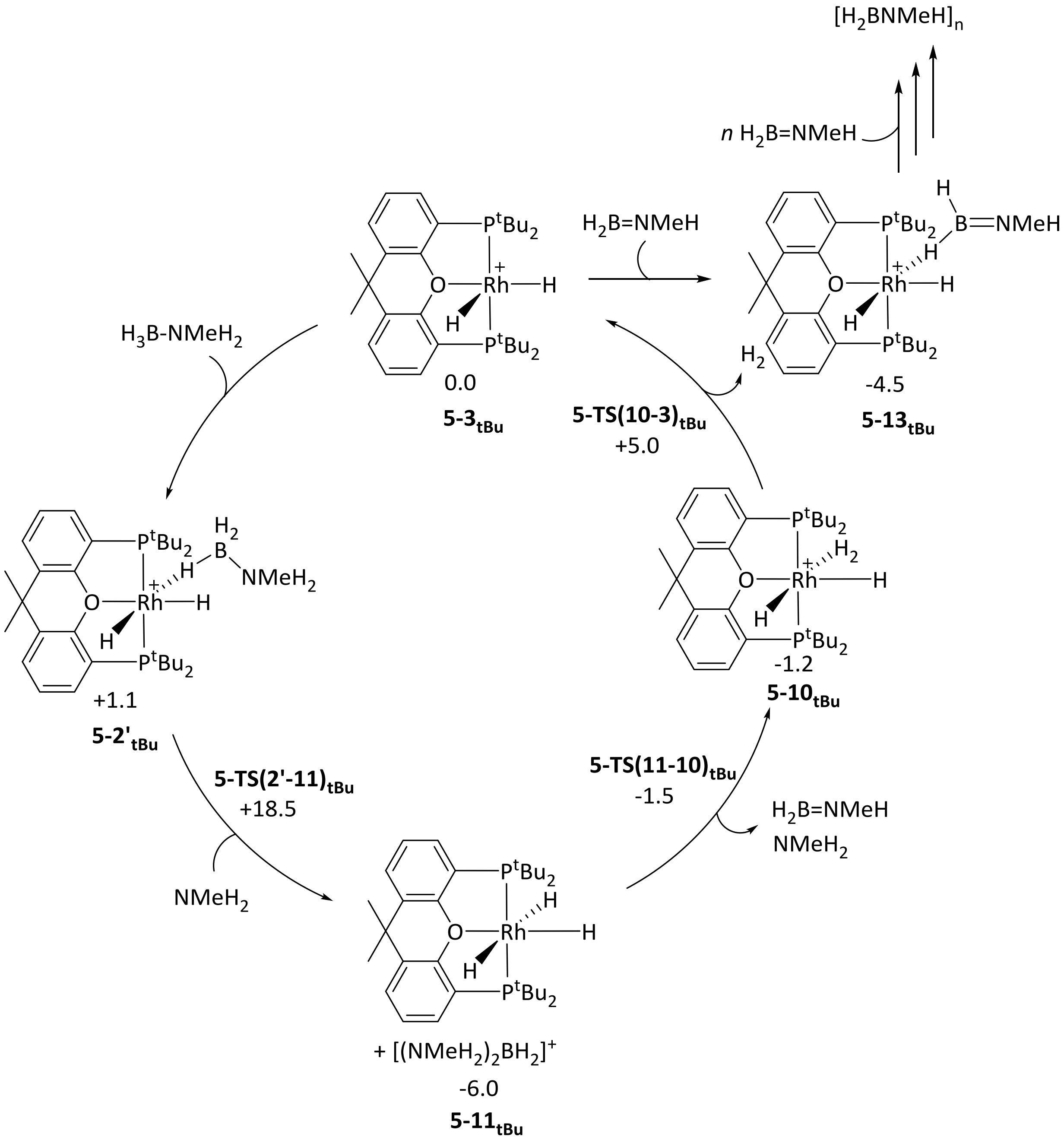

Scheme 5-29: *Proposed mechanism for the dehydropolymerisation of $H_3B\text{-}NMeH_2$ with catalyst* **5-3$_{\text{tBu}}$**. *Relative free energies BP86(D3BJ, THF)/BS1 in kcal mol^{-1}.*

The proposed pathway is consistent with most of the available experimental data. For example, the pathway involves the formation of boronium cation $[(NMeH_2)_2BH_2]^+$ which is observed at the end of catalysis. Catalyst **5-3$_{\text{tBu}}$** was the only organometallic complex observed during speciation studies, however, neutral *mer*-tri-hydride, **5-11$_{\text{tBu}}$** is predicted to be more stable than 0.7 kcal mol^{-1} and therefore, observable through experiment. However, with the energy difference between **5-11$_{\text{tBu}}$** and **5-3$_{\text{tBu}}$** being so small and the protonation by the boronium cation (**5-TS(11-**

10)$_{\text{tBu}}$) being low in energy, complex **5-11$_{\text{tBu}}$** is predicted to be short-lived which could explain only **5-1$_{\text{tBu}}$** being observed. The current rate-limiting step being part of the dehydrogenation process also fits the experimental observation with the free energy barrier of 19.2 kcal mol^{-1} coincides with the dehydropolymerisation being accessible at room temperature. This fits with both catalysts displaying similar reaction times. There are no KIE values for this reaction to compare with the calculated pathway, however, it is predicted that a large B-H/B-D KIE should be observed. This would be in contrast to the neutral catalysts **5-1$_{\text{iPr}}$** and **5-1$_{\text{tBu}}$** which would predict larger N-H/N-D KIE values as well as **5-2$_{\text{iPr}}$** which has an experimentally observed large N-H/N-D KIE value.

5.6 – Conclusions

In conclusion, DFT techniques have been used to explore and characterise pathways for the dehydropolymerisation of H_3B-$NMeH_2$ with four alkyl-Xantphos catalysts: [Rh(*mer*-κ$_3$-P,O,P-Xantphos-^{i}Pr)H], **5-1$_{\mathbf{iPr}}$** (**Section 5.2**). [Rh(*mer*-κ$_3$-P,O,P-Xantphos-^{t}Bu)H], **5-1$_{\mathbf{tBu}}$** (**Section 5.3**), [Rh(*mer*-κ$_3$-P,O,P-Xantphos-^{i}Pr)(H)$_2$(η^1-H_3B-$NMeH_2$)]$^+$, **5-2$_{\mathbf{iPr}}$** (**Section 5.4**), and [Rh(*mer*-κ$_3$-P,O,P-Xantphos-^{t}Bu)(H)$_2$]$^+$, **5-3$_{\mathbf{tBu}}$** (**Section 5.5**).

For neutral catalyst **5-1$_{\mathbf{iPr}}$** catalysis is predicted to proceed initially *via* an outer-sphere, concerted process to form catalytically active species [Rh(*fac*-κ$_3$-P,O,P-Xantphos-^{t}Bu)H$_3$], **5-5$_{\mathbf{iPr}}$** with a free energy barrier of 12.5 kcal mol^{-1}. In low H_2 concentrations catalyst **5-1$_{\mathbf{iPr}}$** is regenerated and the cycle continues with a barrier of 19.8 kcal mol^{-1}. In high H_2 concentrations, **5-5$_{\mathbf{iPr}}$,** is the active catalyst and a inner-sphere concerted dehydrogenation proceeds with a barrier of 18.8 kcal mol^{-1}. The propagation, from mono-hydride **5-1$_{\mathbf{iPr}}$** follows a head-to-tail chain growth pathway involving nucleophilic attack of free H_2B=NMeH units by the terminal NMeH moiety of the growing polymer chain.

Catalyst **5-1$_{\mathbf{tBu}}$** follows a different and novel outer-sphere, concerted dehydrogenation where the metal is protonated by the N-H bond as the B-H transfers a hydride to the existing Rh-H bond. This mechanism forms free H_2B=NMeH and H_2 directly as well as **5-1$_{\mathbf{tBu}}$**. This process occurs with a free energy barrier of 19.9 kcal mol^{-1} and predicted to proceed regardless of H_2 concentration. The propagation is predicted to follow the same head-to-tail chain growth mechanism as **5-1$_{\mathbf{iPr}}$**.

A dehydropolymerisation pathway for cationic catalyst **5-2$_{\mathbf{iPr}}$** with realistic free energy barriers has not yet been fully characterised. All dehydrogenation pathways calculated predict free energy barriers that are too high and involve rate-limiting B-H activation while KIE experiments show small B-H and large N-H KIE values. It is suggested that pathways involving multiple units of H_3B-$NMeH_2$ and the isomerisation of the Xantphos ligand should be explored. No propagation pathway has been characterised.

Finally, catalyst **5-3$_{\mathbf{tBu}}$** is predicted to follow a dehydrogenation mechanism involving the formation of boronium cation [$(NMeH_2)_2BH_2$]$^+$ through the attack of free $NMeH_2$ on complex [Rh(*mer*-κ$_3$-P,O,P-Xantphos-^{t}Bu)(H)$_2$(η^1-H_3B-$NMeH_2$)]$^+$ **5-2'$_{\mathbf{tBu}}$**. The boronium then protonates the metal to form H_2B=NMeH and $NMeH_2$ before H_2 dissociation completes the cycle. This proceeds with a free energy barrier of 19.2 kcal mol^{-1}. The propagation mechanism is proposed begin from amino-borane complex [Rh(*mer*-κ^3-P,O,P-Xantphos-^{t}Bu)(H)$_2$(η^1-H_2B=NMeH)]$^+$ **5-13$_{\mathbf{tBu}}$**. This predicted mechanism is consistent with the limited amount of experimental data available on the system but further study into the propagation mechanism is also required.

Chapter 6: Studies into the Structure and Bonding of Boron Bridging, Cationic, Rhodium Dimers

6.1 – Introduction

During studies into the dehydropolymerisation of amine-boranes using a range of cationic rhodium catalysts the Weller group were able to isolate three cationic rhodium dimers: $[\{Rh(dipp)\}_2(H)(BH_2NH_2)]^+$ (dipp = $^iPr_2P(CH_2)_3P^iPr_2$)[196], $[\{RhH\}_2(\mu\text{-}BNMe_2)(\mu\text{-}dpcm)_2(\mu\text{-}H)]^+$ (dpcm = $Cy_2PCH_2PCy_2$)[197], and $[\{Rh(\kappa^3\text{-}P,O,P\text{-}Xantphos\text{-}^iPr)\}_2B]^+$.[196] In all cases, the experimental NMR and crystallographic data were complimented with computational studies (included as part of this thesis) in order to determine the structure and bonding of the three rhodium dimers.

This chapter details the QTAIM analysis and NBO calculations used in order to determine the structure and bonding in the dimers isolated by the Weller group. Furthermore, a study in calculating the ^{11}B NMR shift was also conducted.

6.2 – Computational Details

Geometry optimisations were run with Gaussian 03 D.01[173] with the BP86 functional.[143] Rh, P, Cl, and Si centres were described with Stuttgart pseudopotentials and associated basis sets[158] (with added d-orbital polarisation on P (ς = 0.387), Cl (ς = 0.640), and Si (ς = 0.284))[174] and 6-31g** basis sets described all other atoms[156, 157]. All fully optimised stationary points were fully characterised via analytical frequency calculations as either minima (all positive frequencies) or transition states (one imaginary frequency). IRC calculations and subsequent geometry optimisations were used to confirm the minima linked by the transition state in **Section 6.3.4**. A frequency calculation also provided a free energy in the gas phase, computed at 298.15 K and 1 atm. The energies reported in the text are based on the gas-phase relative free energies and incorporate a correction for dispersion effects using Grimme's D3 parameter set[164] with Becke-Johnson damping[165] as well as solvation (PCM approach)[161] in THF. Both dispersion and solvation corrections were run as single points with Gaussian 09 Revision D.01.[175]

Quantum Theory of Atoms in Molecules (QTAIM) analyses were performed with the AIMALL program[168] and employed partially optimised structures based on the experimental heavy atom positions derived from the molecular structure with fully optimised H atom positions. The partially optimised structures were chosen for study over full optimised structures as they give a more accurate representation of the molecular structure as the heavy atom positions remain the same. Comparison between the QTAIM results of the fully optimised and partially optimised structures showed little difference between the two. NBO localised orbitals were computed using the NBO program version 6.0.[172]

6.3 – $[\{Rh(dipp)\}_2(H)(BH_2NH_2)]^+$, 6-1

6.3.1 – Experimental Background

The Weller group synthesised $[(Rh(dipp))_2(H)(BH_2NH_2)][BAr^F_4]$ (**6-1**) whilst investigating the dehydrogenation of $H_3B\text{-}NH_3$ with $[Rh(P^iPr_2(CH_2)_3P^iPr_2)(\eta\text{-}C_6H_5F)][BAr^F_4]$.[198] X-ray crystallography of the molecular crystals confirmed the heavy atoms positions but the hydrogen atoms were poorly defined. This meant the molecular structure was proposed to be either a bridging amino-borane, **6-1a** (**Figure 6-1**) or a bridging borylene complex, **6-1b**.

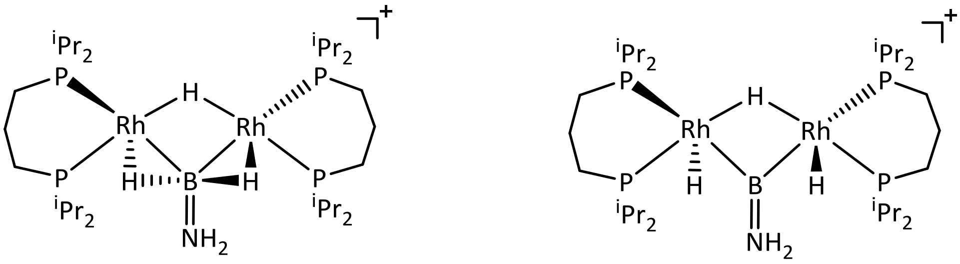

6-1a **6-1b**

Figure 6-1: *Potential structures for Dimer **6-1**.*

The ^{11}B NMR shift of **6-1** was 51.1 ppm. Amino-borane complexes involving one transition metal typically exhibit a ^{11}B shift of around 40 ppm[199, 200] whilst bridging borylene complexes usually have ^{11}B shifts of between 90-110 ppm.[201-203] Although the ^{11}B NMR is similar to amino-borane complexes, there were no known bridging amino-borane complexes in the literature for direct comparison. Therefore, further investigation was required in order to determine the structure of the dimer.

Further NMR studies suggested that dimer **6-1** exhibits a fluxional process at room temperature. The ^1H NMR spectrum at 298 K shows one peak at δ -8.64 ppm which corresponds to the 3 hydrogens located around the rhodium atoms. However, at 180 K, two broad signals at δ -8.16 (2H) and δ -9.02 (1H) ppm are observed. Splitting was also seen in the $^{31}P\{^1H\}$ NMR spectrum where one doublet at δ 40.82 ppm which corresponded to all four P atoms was present at 298 K, whilst two broad doublets at δ 36.38 and δ 41.48 ppm were present at 180 K. This indicates that the fluxional mechanism involves both the phosphine groups and the hydrides around the rhodium atoms becoming equivalent. An Eyring plot yielded an activation free energy of 9.37 ± 0.38 kcal mol^{-1}.

The DFT investigations conducted as part of this thesis aimed to use QTAIM analysis to determine the structure of **6-1** and characterise the fluxional process observed in the NMR studies.

6.3.2 – QTAIM Results

A full molecular graph with a 2D contour plot of the Rh-B-Rh plane for **6-1** is shown in **Figure 6-2A.** There is effective C_2 symmetry in the computed structure of the complex and therefore the hydrogen interactions with the rhodium and boron centres can be treated as equivalent on each side of the molecule and average values for ρ(r), $\nabla^2 \rho$(r), ε, H(r), V(r), and G(r) have been reported. The hydrogens bonded to the boron are labelled as H^1 and $H^{1'}$ and the bridging hydride has been labelled H^2. **Figure 6-2B** displays a 2D contour plot of the electron density in the Rh-H^1-B plane. Bond critical points (bcps) are observed between Rh-H^1, Rh-B and B-H^1 indicating there is a bonding interaction between the three atoms. The presence of a ring critical point (rcp) in the Rh-H^1-B plane is consistent with the presence of 3 bcps in a triangle. Furthermore, the bond paths between Rh-B and B-H^1 contain an endocyclic curve which indicates that the bonding interactions are electron deficient and potentially an agostic interaction or 3-centre-2-electron interaction. The same observations are made for the Rh-$H^{1'}$-B interaction. **Figure 6-2C** displays a 2D contour plot of the electron density in the Rh-H^2-Rh plane. As well as the Rh-B bonding interactions, bcps are observed between Rh and H^2 indicating a bonding interaction. The presence of a rcp in the Rh-H^2-Rh-B plane suggests there in no Rh-Rh bonding in the structure. These results are consistent with what would be expected for a bridging amino-borane structure, **6-1a**.

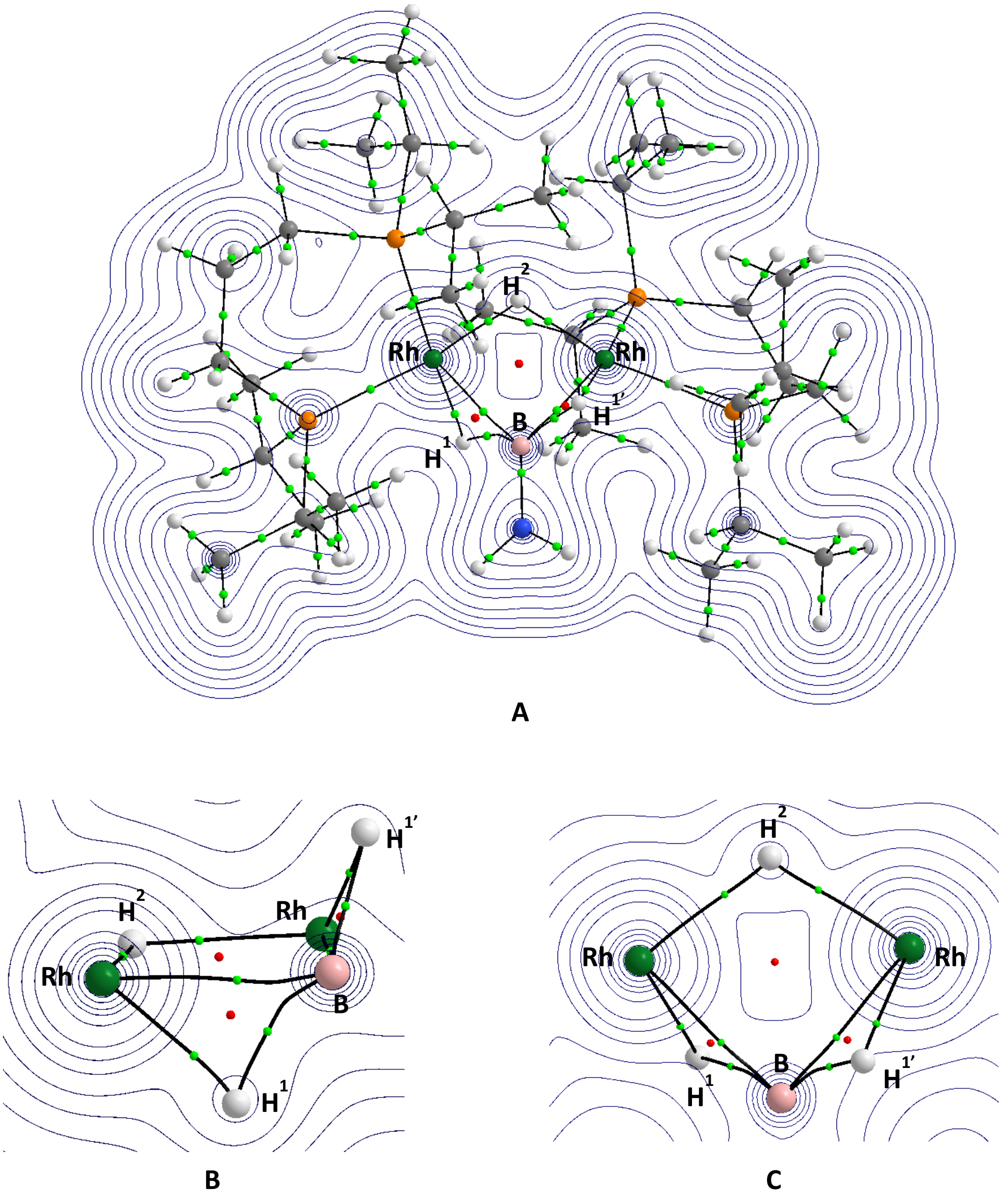

Figure 6-2: ***A****)Full molecular graph and electron density contour plot in Rh-B-Rh for* ***6-1****. Weak bond paths and chemically less–relevant rcps are omitted for clarity.* ***B****)2D electron density contour plot of Rh-H^1-B plane.* ***C****)2D electron density contour plot of Rh-H^2-Rh plane.*

Analysis of the bcps (**Table 6-1**) suggests that all of the bonding interactions are covalent in nature. This is due to their values of electron density, ρ(r), being around 0.10 e Å^{-3} and the negative value of the total electron density, H(r). The ellipticity, ε, value for the B-Rh interaction is 0.61 which means the bonding is not spherical in the plane of the bond. This suggests the bonding orbitals involved in the B-Rh interaction will also be involved in the B-H$^{1/1'}$ and Rh-H$^{1/1'}$ bonding interactions which would be expected for an agostic interaction or 3-centre-2-electron bond. Further evidence of this are the ε values of 0.38 and 0.45 for the B-H$^{1/1'}$ and Rh-H$^{1/1'}$ interactions. This data is all consistent with a bridging amino-borane complex, **6-1a**.

	Distance	**$\rho(r)$**	**$\nabla^2\rho(r)$**	**ε**	**H(r)**	**V(r)**	**G(r)**
B – Rh	2.08	0.10	0.04	0.61	-0.04	-0.10	0.07
B – H$^{1/1'}$	1.48	0.11	-0.13	0.38	-0.06	-0.10	0.03
H$^{1/1'}$ – Rh	1.66	0.11	0.25	0.45	-0.04	-0.15	0.10
H^{2} – Rh	1.76	0.09	0.16	0.10	-0.03	-0.10	0.07

Table 6-1: *Bond distances and values of electron density, Laplacian, ellipticity and energy densities at selected bcps in **6-1**. Obtained from the QTAIM analysis. Units in Å (Distance), e Å^{-3} ($\rho(r)$, $\nabla^2\rho(r)$) , or a.u (H(r), V(r), and G(r)).*

Overall, the results suggest that **6-1** is a bridging amino-borane complex (**6-1a, Figure 6-1**) rather than a bridging borylene complex (**6-1b**). Dimer **6-1** is the only published example of an amino-borane being trapped by a transition-metal dimer. However, there are monomeric examples: [Ru(H)$_2$(PCy$_3$)$_2$(η^2-H$_2$BNH$_2$)] by Sabo-Etienne, Clot *et. al.*[199], [Ru(H)$_2$(P^{i}Pr$_3$)$_2$(η^2-H$_2$BNH$_2$)], [Ru(H)(Cl)(PCy$_3$)$_2$(η^2-H$_2$BNH$_2$)] by Sabo-Etienne, Clot, Alcaraz *et al.*,[182] and [Ru(H)(η^2-H$_2$BNH$_2$)(Cy-PSiP)] (Cy-PSiP = κ^3-(Cy$_2$PC$_6$H$_4$)$_2$SiMe)) by Turculet, Tobisch *et al.*[200] A published QTAIM analysis[182] on [Ru(H)$_2$(P^{i}Pr$_3$)$_2$(η^2-H$_2$BNH$_2$)] and [Ru(H)(Cl)(PCy$_3$)$_2$(η^2-H$_2$BNH$_2$)] showed bcps for Rh-B and B-H interactions. No bcp was present between the Rh and H of the amino-borane but there was still evidence of an interaction due to the endocyclic curve of the B-H bond path indicating donation of electron density to the metal centre.

6.3.3 – Comparison with Related Bridging Boron Rhodium Dimers

After analysing the QTAIM results for **6-1**, a benchmarking study was conducted against the partially optimised structures of three well-defined Rh dimers in order to further clarify the structure and confirm that QTAIM can distinguish between different binding modes. The complexes (**Figure 6-3**) selected were: [{Rh(H)(PPh$_3$)$_2$}$_2$(μ-Cl)$_2$(μ-H)]$^+$, **6-2** (**Section 6.3.3.1**), for comparison with a rhodium dimer with both bridging and terminal hydrides, [{Rh(dipp)}$_2$(μ-H)(μ-H$_3$BCMe$_2$(^{i}Pr))], **6-3** (**Section 6.3.3.2**), for comparison with a rhodium dimer containing a bridging borate, and [{Rh(CO)(Cp)}$_2$(μ-BN(SiMe$_3$)$_2$)], **6-4** (**Section 6.3.3.3**), for comparison with a rhodium dimer with a bridging borylene.

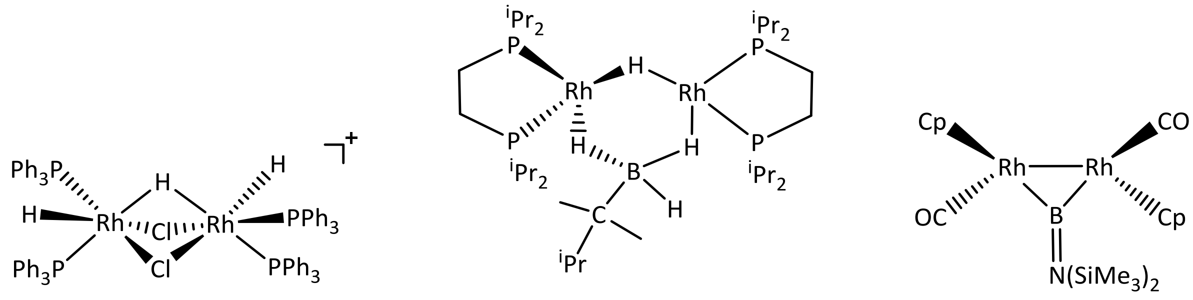

6-2 **6-3** **6-4**

Figure 6-3: *The rhodium dimers selected for the benchmarking study in this section.*

6.3.3.1 – $[\{Rh(H)(PPh_3)_2\}_2(\mu\text{-}Cl)_2(\mu\text{-}H)]^+$, 6-2

Dimer **6-2** was reported by Weller and co-workers.[204] The full molecular graph and 2D contour plot of the electron density in the Rh-H^2-Rh plane for **6-2** is displayed in **Figure 6-4** and the properties of selected bcps are in **Table 6-2**. The complex exhibits approximate, non-crystallographic C_2 symmetry, therefore, the terminal hydrides are considered equivalent and labelled H^1 and $H^{1'}$. The bridging hydride was labelled as H^2. The terminal $H^{1/1'}$-Rh interaction is covalent in nature due to the values of $\rho(r) = 0.16$ e Å^{-3} and $H(r) = -0.09$ a.u. Furthermore, the ellipticity of the terminal $H^{1/1'}$-Rh interaction in **6-2** is 0.01 which is very close to the expected value for a terminal σ-bonding (0.00). The H^2-Rh bonding interaction is seen to be covalent with H(r) being negative and mostly spherical with an ellipticity of 0.11.

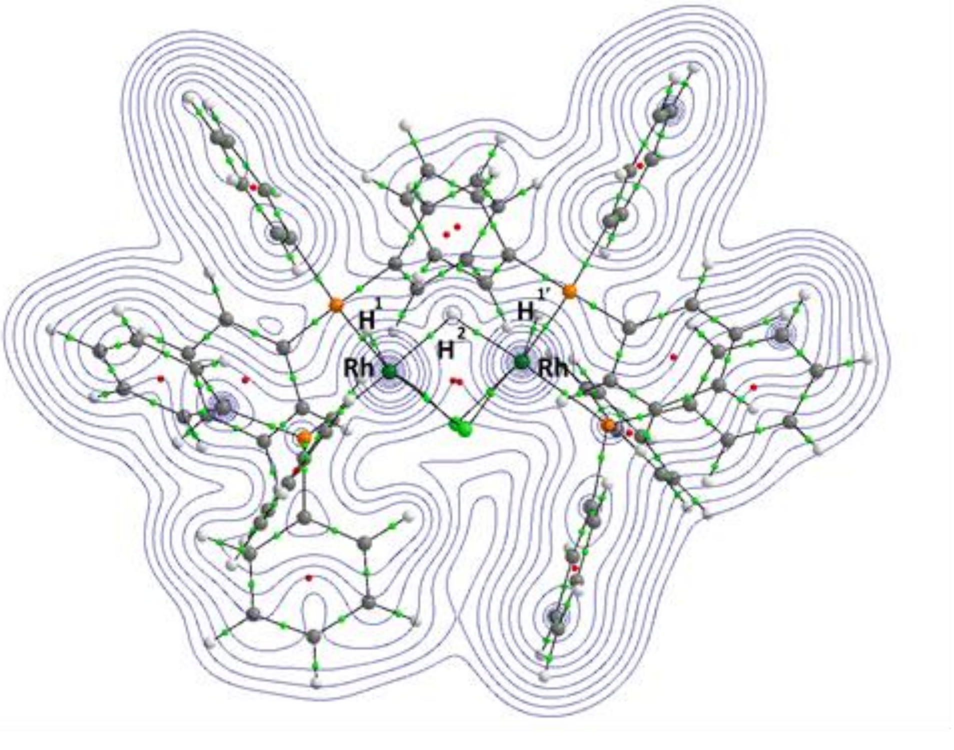

Figure 6-4: *Full molecular graph and electron density contour plot in the Rh-H^2-Rh plane for **6-2**. Weak bond paths and chemically less–relevant rcps are omitted for clarity.*

	Distance	**ρ(r)**	**∇^2ρ(r)**	**ε**	**H(r)**	**V(r)**	**G(r)**
$H^{1/1'}$ – Rh	1.60	0.16	0.05	0.01	-0.09	-0.19	0.10
H^2 – Rh	1.75	0.09	0.16	0.11	-0.02	-0.09	0.07

Table 6-2: *Bond distances and values of electron density, Laplacian, ellipticity and energy densities at selected bcps in **6-2**. Obtained from the QTAIM analysis. Units in Å (Distance), e $Å^{-3}$ (ρ(r), ∇^2ρ(r)) , or a.u (H(r), V(r), and G(r)).*

In comparison, when compared to the $H^{1/1'}$-Rh bcp values in **6-1** (ρ(r) = 0.11 e $Å^{-3}$, H(r) = -0.04 a.u.) the $H^{1/1'}$-Rh bonding in **6-2** is stronger than in **6-1** due to the larger and more negative values respectively. This is reflected in the computed $H^{1/1'}$-Rh bond lengths in **6-1** (1.66 Å) and **6-2** (1.60 Å). Furthermore, the ellipticity of 0.01 is in direct contrast with the ellipticity of $H^{1/1'}$-Rh in **6-1** (ε = 0.45). This is consistent with complex **6-1** being a bridging amino-borane structure and not a bridging borylene with terminal hydrides. The H^2-Rh bonding interaction is seen to be very similar to that in complexes **6-1** and **6-2** which is also observed in the computed H^2-Rh bond lengths of 1.76 Å and 1.75 Å respectively.

6.3.3.2 – [{Rh(dipp)}$_2$(μ-H)(μ-H_3BCMe_2(^{i}Pr))], 6-3

Complex **6-3** was reported by Baker *et al.*[205] The molecular graph containing the 2D contour of the electron density in the Rh-B-Rh plane for **6-3** is displayed in **Figure 6-5** and the properties of selected bcps are in **Table 6-3**. In the computed structure, the two hydrogens bonded to the boron atom and a rhodium centre are symmetrical and therefore treated equivalently and labelled H^1 and $H^{1'}$. The bridging hydride was labelled H^2 and the terminal B-H hydride denoted as H^3.The B-$H^{1/1'}$ interaction has a negative value of H(r) (-0.12 a.u.) suggesting it is covalent and has an ε of 0.18 indicating the bonding is not spherical. As in complex **6-1**, this is likely due to the bonding orbitals of the B-$H^{1/1'}$ bond being involved in another bonding interaction not in the plane of the B-$H^{1/1'}$ bond. This interaction is the Rh-$H^{1/1'}$ bonding interaction which is also elliptical with an ε of 0.41. This indicates that B-$H^{1/1'}$ forms an agostic interaction with the Rh atoms. The terminal B-H^3 bond is stronger than the B-$H^{1/1'}$ bond (ρ(r) = 0.15 e $Å^{-3}$ *vs.* 0.13 e $Å^{-3}$ and H(r) = -0.16 a.u. *vs.* -0.12 a.u.) and more spherical (ε = 0.13 *vs.* 0.18) which is typical of a terminal bonding interaction compared to an agostic bond. The bridging Rh-H^2-Rh interaction is also covalent with H(r) being -0.03 a.u. with fairly spherical bonding (ε = 0.12) while no bcp was present between Rh and B indicating there is no bonding interaction.

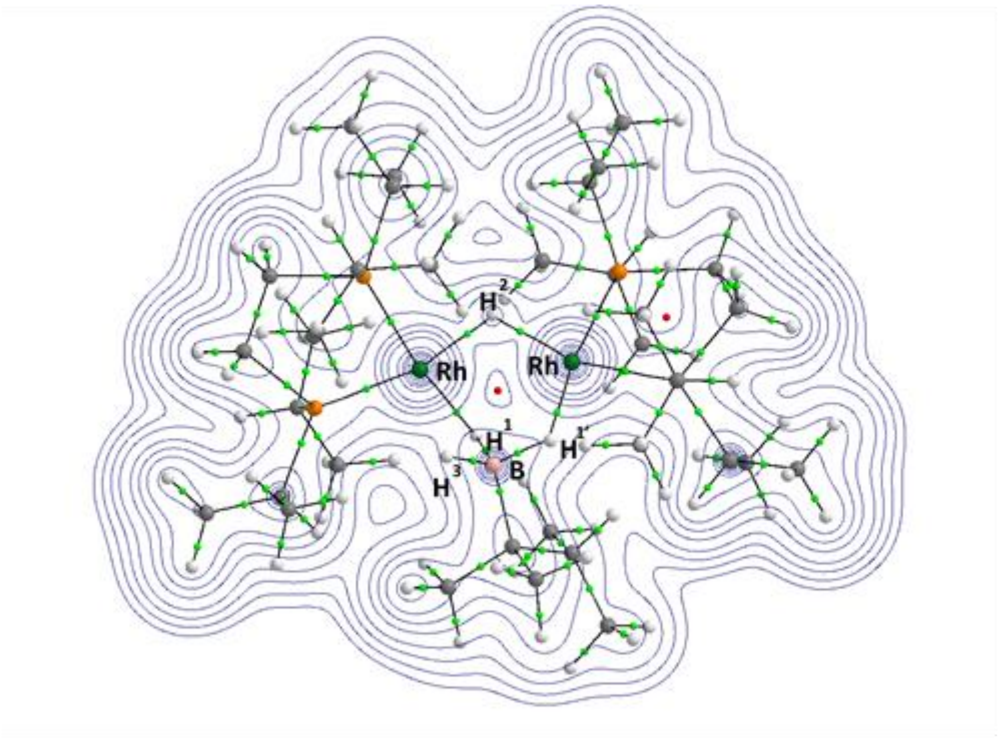

Figure 6-5: *Full molecular graph and electron density contour plot in the Rh-B-Rh plane for **6-3**. Weak bond paths and chemically less–relevant rcps are omitted for clarity.*

	Distance	ρ(r)	$\nabla^2\rho(r)$	ε	H(r)	V(r)	G(r)
B – Rh		-	-	-	-	-	-
B – H$^{1/1'}$	1.33	0.13	-0.10	0.18	-0.12	-0.21	0.09
B – H^{3}		0.15	-0.21	0.13	-0.16	-0.26	0.10
H$^{1/1'}$ – Rh	1.76	0.09	0.23	0.41	-0.03	-0.12	0.09
H^{2} – Rh		0.09	0.15	0.12	-0.03	-0.10	0.07

Table 6-3: *Bond distances and values of electron density, Laplacian, ellipticity and energy densities at selected bcps in **6-3**. Obtained from the QTAIM analysis. Units in Å (Distance), e Å^{-3} (ρ(r), $\nabla^2\rho(r)$) , or a.u (H(r), V(r), and G(r)).*

In comparison, the bcps between B-H$^{1/1'}$ show some similarities between complexes **6-1** and **6-3**. The B-H$^{1/1'}$ interaction in **6-3** is not as elliptical as **6-1** (ε = 0.18 *vs.* 0.38) and this is likely due to the lack of bonding interaction between Rh and B in complex **6-3**. This can also be attributed to the B-H$^{1/1'}$ interaction in **6-3** being stronger than in **6-1** (H(r) = -0.12 *vs.* -0.04 a.u.) which is reflected in the B-H$^{1/1'}$ bond lengths of 1.33 Å compared to 1.48 Å in **6-1**. There are also similarities when comparing the Rh-H$^{1/1'}$ interactions of the two complexes even through the trends in ρ(r), H(r) and bond distance indicate that the Rh-H$^{1/1'}$ in **6-3** is weaker than that in **6-1** (0.09 e Å^{-3}, -0.03 a.u., and 1.76 Å *vs.* 0.11 e Å^{-3}, -0.04 a.u., 1.66 Å). This acts as further evidence that complex **6-1** is a bridging amino-borane. The Rh-H^2 bonding interaction is similar to that in complexes **6-1** and **6-2.**

6.3.3.3 – [{Rh(CO)(Cp)}$_2$(µ-BN(SiMe$_3$)$_2$)], 6-4

Complex **6-4** was reported by Braunschweig and co-workers.[206] **Figure 6-6** shows the full molecular graph with a 2D contour plot of the electron density in the Rh-B-Rh plane and the properties of selected bcps are displayed in **Table 6-4**. The B-Rh bonding interactions are equivalent due to the *C2/c* space group of the crystal structure. The ρ(r) of 0.11 e Å^{-3} and H(r) of -0.05 a.u. indicate the B-Rh is covalent in nature. Furthermore, the bonding can be described as spherical in the plane of the bond as the ε is near zero (0.08). These results are typical for what would be expected from a bridging borylene complex.

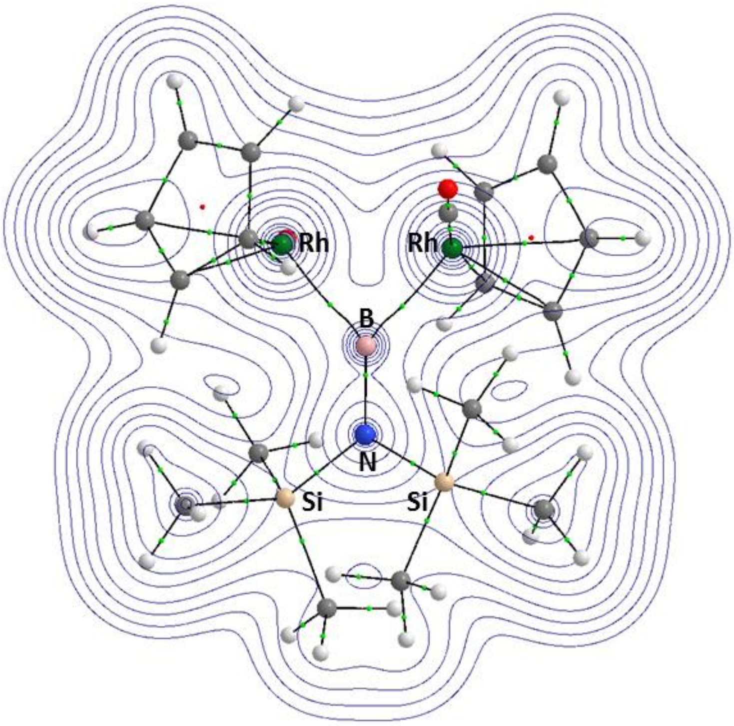

Figure 6-6: *Full molecular graph and electron density contour plot of the electron density in the Rh-B-Rh plane for **6-4**. Weak bond paths and chemically less–relevant rcps are omitted for clarity.*

	Distance	ρ(r)	∇^{2} ρ(r)	ε	H(r)	V(r)	G(r)
B – Rh		0.11	-0.02	0.08	-0.05	-0.10	0.05

Table 6-4: *Bond distances and values of electron density, Laplacian, ellipticity and energy densities at selected bcps in **6-4**. Obtained from the QTAIM analysis. Units in Å (Distance), e Å^{-3} (ρ(r), **∇**^{2} ρ(r)), or a.u (H(r), V(r), and G(r)).*

The B-Rh interaction in **6-4** is similar to that in **6-1** in terms of ρ(r) (0.11 and 0.10 e Å^{-3}) and H(r) (-0.05 and -0.04 a.u.) but differs in terms of ε (0.08 *vs.* 0.61). This is due to the Rh-H$^{1/1'}$-B bonding in **6-1** making the Rh-B interaction more elliptical due to the interaction being in a different plane to the Rh-B bond. Complex **6-4** is a bridging borylene so there is no B-H or Rh-H interaction to cause the increase in ε. Therefore, this is evidence that complex **6-1** is not a bridging borylene structure.

The QTAIM analysis of **6-4** does not contain a bcp between the two Rh atoms (**Figure 6-6**). However, in this case Braunschweig *et al.* report that there should be a metal-metal bond as the Rh···Rh distance of 2.67 Å is "remarkably short" and the presence of a metal-metal bond would satisfy the 18 electron rule for both Rh centres. If both Rh centres had an electron count of 17 electrons the complex would be paramagnetic of which there is no evidence in the NMR. The failure of QTAIM to locate bcps in organometallic complexes where the metal-metal bond is supported by bridging ligands (which is the case in **6-4**) is known and has been reported.[207] For example, Macchi and co-workers have found that in $[Co_4(CO)_{11}(PPh_3)]$ only unsupported Co-Co interactions displayed bcps and bond paths.[208] Therefore, the lack of bcp between the Rh^7 and Rh^8 in **6-4** is not indicative of there being no metal-metal bond present. A natural bond orbital (NBO) calculation confirmed the presence of a metal-metal bond between two Rh d-orbitals (**Figure 6-7**). The NBO has an occupancy of 1.69 electrons of which 86% is localised to the Rh atoms.

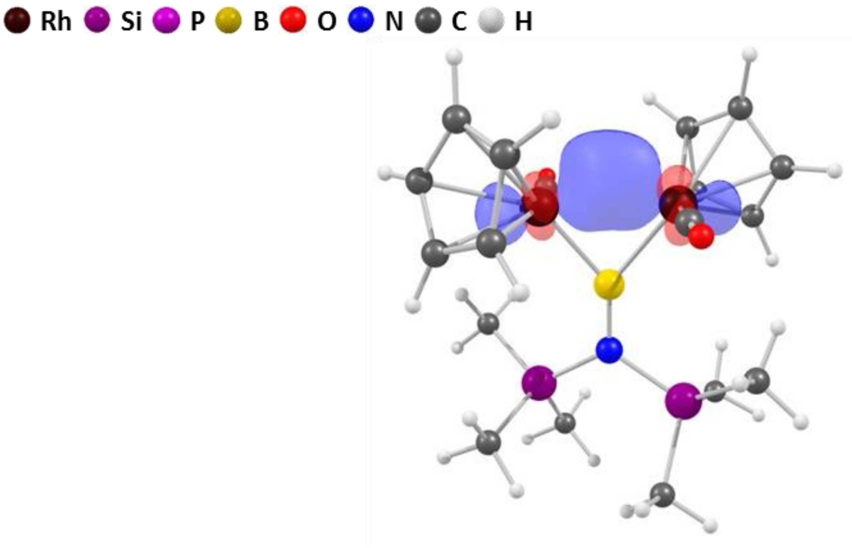

Figure 6-7: *NBO for the Rh-Rh interaction in complex* ***6-4****. Colour scheme shown in the legend above is adopted throughout the chapter.*

6.3.4 – Characterising the Room Temperature Fluxional Process

A mechanism for the fluxional process occurring at room temperature in bridging amino-borane complex, **6-1**, was characterised (**Scheme 6-1**). Starting from the fully optimised structure of **6-1** (**Figure 6-8**), the amino-borane group begins to rotate which breaks the $B-H^1$ bond, increasing the distance from 1.48 Å to 2.38 Å in **6-TS1** (G = 13.2 kcal mol^{-1}). In **6-TS1** the $B\cdots H^2$ distance has decreased to 2.27 Å as has the $Rh-H^1$ distance (Rh-H = 1.88 Å). The process yields **6-1'** which is the same structure as complex **6-1** with two hydrogen positions, H^1 and H^2, switched. The process can be described as a rotation of a $\{HBNH_2\}$ moiety around the Rh-Rh vector with the Rh-H^2-Rh-B torsion decreasing from 0.57 ° in **6-1** to -49.57 ° in **6-TS1** and -98.36 ° in **6-1'**. The overall barrier for this process is 13.2 kcal mol^{-1} which agrees with the mechanism being accessible during room temperature NMR studies and agrees reasonably well with the experimental free energy activation of 9.37 ± 0.38 kcal mol^{-1}. The mechanism also coincides with the experimental observations of the varying temperature NMR studies. At room temperature, all hydrides would be equivalent as the $HBNH_2$ moiety continues to rotate around the Rh-Rh vector the hydrogens switch between being bonded to the boron or both Rh centres. The phosphorus atoms become equivalent as at **6-1**, P^1 and P^4 are *trans* to a B-H bond, whilst P^2 and P^3 are *trans* to the bridging hydride, but after the rotation, **P1** and **P4** become *trans* to the bridging hydride whilst P^2 and P^3 are *trans* to the B-H bonds, as in **6-1'**.

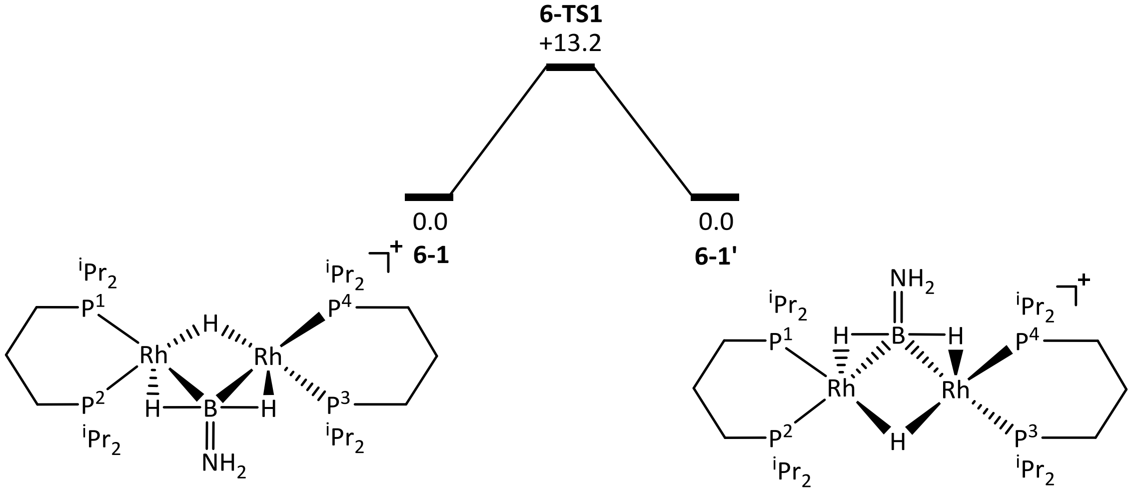

Scheme 6-1: *Reaction scheme for the fluxional process at room temperature on the NMR timescale. Values quoted are free energies in kcal mol^{-1}.*

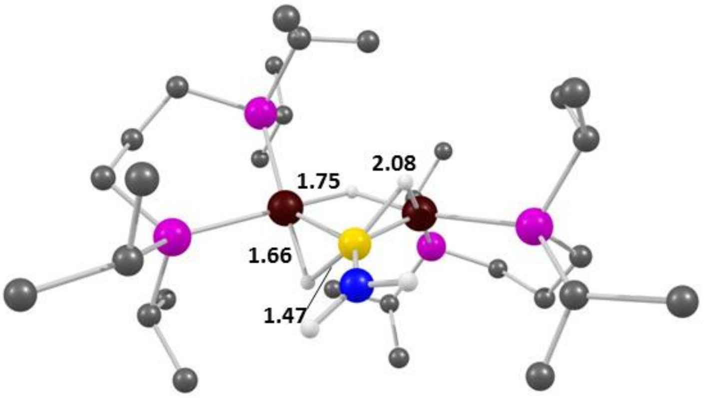

6-1
G = 0.0 kcal mol^{-1}

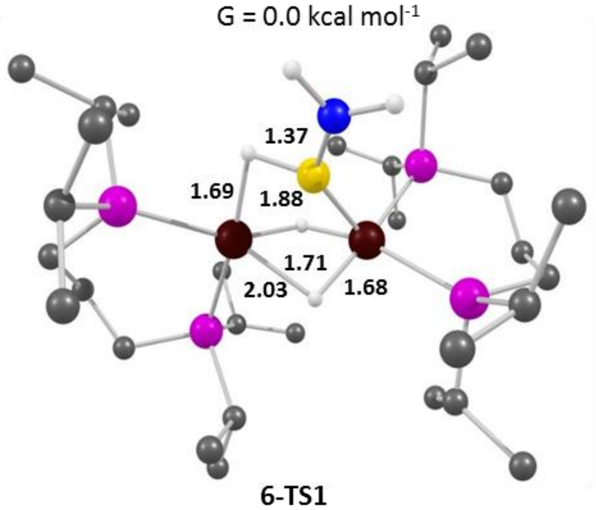

6-TS1
G = +13.2 kcal mol^{-1}

Figure 6-8: *Computed structures of **6-1** and **6-TS1** including key distances in Å. Hydrogens bonded to carbon omitted for clarity.*

6.4 – [{RhH}2(μ-BNMe2)(μ- dpcm)2(μ-H)]+, 6-5

6.4.1 – Experimental Background

Investigation of the dehydrocoupling of H_3B-NMe_2H with small bite angle bisphosphine complexes such as [Rh(dpcm)(η^6-C_6H_5F)][Al(OC(CF_3)$_3$)] (dpcm = $Cy_2PCH_2PCy_2$) was conducted by the Weller group.[196] During the reaction, one major species was observed through ^{31}P{1H} NMR with a shift of 55.9 ppm. The same complex was found to give a ^{11}B NMR shift of 59.0 ppm and ^{1}H NMR shifts of -4.87 and -7.93 ppm (integration 2:1). This species was crystallised and found to be dimeric species **6-5**. However, the hydrogen locations could not be determined crystallograpically. Therefore, the structure could possibly be either a bridging amino-borane, **6-5a** (**Figure 6-9**) or a bridging borylene di-hydride, **6-5b**. A Rh-Rh bond was not postulated due to each Rh centre having 16 electrons without the presence of any Rh-Rh interaction. These questions about the structure of **6-5** would also be investigated using QTAIM calculations. Due to disorder in the molecular crystal structure from the cyclohexyl substituents, the fully optimised calculated structure was used for the QTAIM calculations.

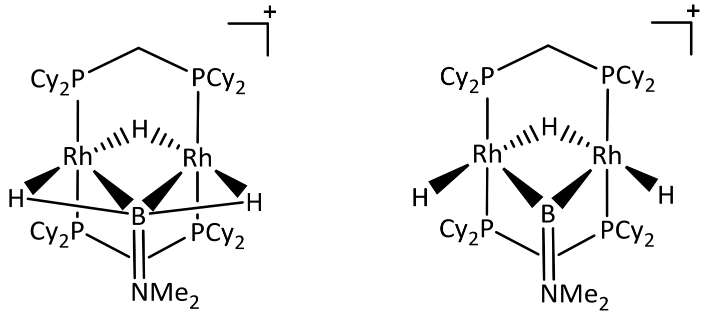

6-5a **6-5b**

Figure 6-9*: Proposed structures of* ***6-5****.*

6.4.2 – QTAIM Results

The 2D contour plot of the electron density in the Rh-B-Rh plane (**A**) and the full molecular graph (**B**) are shown in **Figure 6-10** with properties of selected bcps in **Table 6-5.** The complex has non-crystallographic C_{2V} symmetry making the bonding interactions at each Rh centre equivalent. The hydrogens potentially bound to boron were labelled H^1 and $H^{1'}$ while the bridging hydride was labelled H^2. The properties of the Rh-B bcps (H(r) = -0.08 a.u., ε = 0.05) suggest the bonding is covalent in nature and spherical in the plane of the bond. The Rh-$H^{1/1'}$ interaction is also covalent and has an ε near 0 which is typical of a terminal Rh-H bond. No bcp or bond path were observed between B and $H^{1/1'}$ which indicates no B-$H^{1/1'}$ bond in the complex. This is all evidence that complex **6-5** is a bridging borylene (**6-5b**) and not a bridging amino-borane (**6-5a**).

Comparison with the other Rh dimers already discussed in this chapter confirm this conclusion. For example, when compared to complex **6-1**, the Rh-B interaction is similar in terms of ρ(r) and H(r), however, the ε is much more similar to bridging borylene complex **6-4** (0.05 *vs.* 0.08) than bridging amino-borane complex **6-1** (0.61). Furthermore, the Rh-$H^{1/1'}$ interaction in **6-5** is very similar to the terminal Rh-$H^{1/1'}$ interaction in complex **6-2** (H(r) of -0.08 *vs.* -0.09 a.u. and ε of 0.01 *vs.* 0.01). The Rh-H^2 interaction in **6-5** is comparable with other bridging hydrides studied in this chapter (**6-1**, **6-2,** and **6-3**).

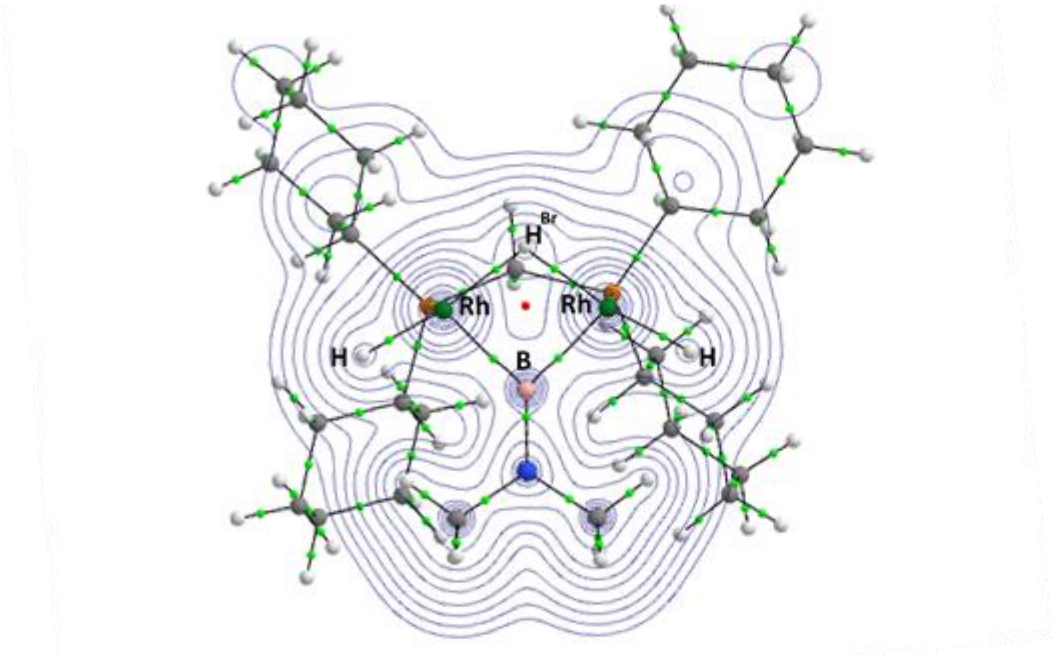

Figure 6-10: *Molecular graph and electron density contour plot in the Rh-B-Rh plane for **6-5**. Weak bond paths, chemically less–relevant rcps, and one μ-dpcm unit are omitted for clarity.*

	ρ(r)	**∇^2ρ(r)**	**ε**	**H(r)**	**V(r)**	**G(r)**
Rh-B	0.12	-0.09	0.05	-0.08	-0.13	0.05
Rh-H	0.13	0.13	0.01	-0.06	-0.15	0.09
Rh-H^{Br}	0.08	0.16	0.02	-0.02	-0.09	0.07
B-H	-	-	-	-	-	-

Table 6-5: *Bond distances and values of electron density, Laplacian, ellipticity and energy densities at selected bcps in **6-5**. Obtained from the QTAIM analysis. Units in Å (Distance), e Å^{-3} (ρ(r), ∇^2 ρ(r)) , or a.u (H(r), V(r), and G(r)).*

The rcp found in the middle of the Rh-H^2-Rh-B plane in the 2D contour plot of the electron density suggests there is no Rh···Rh interaction in **6-5**. However, as seen in the study of bridging borylene complex, **6-4** (**Section 6.3.3.3**), QTAIM can be unreliable in characterising metal-metal bonding where there are bridging ligands. An NBO calculation showed no NBO or natural localised molecular orbital (NLMO) containing an Rh-Rh bond in complex **6-5**.

Overall, the QTAIM sudy predicts that **6-5** is a bridging borylene complex with two terminal metal-hydride bonds. The only other structurally characterised dimer with a μ-$BNMe_2$ unit is [{Mn(η^5-C_5H_5)$(CO)_2$}$_2$(μ-$BNMe_2$) published by Braunschweig *et al.*[209]

6.5 – [{Rh(*mer*-κ^3-P,O,P-Xantphos-^{i}Pr)}$_2$B]$^+$, 6-6

6.5.1 – Experimental Background

The Weller group used catalyst [Rh(*mer*-κ^3-P,O,P-Xantphos-^{i}Pr)(H)$_2$(η^1-H$_3$B-NMe$_3$)][BAr$^F{}_4$] to dehydropolymerise H$_3$B-NMeH$_2$ at 0.4 mol% catalyst loading for 20 minutes at 298 K.[196] At the end of catalysis a weak ^{31}P{^{1}H} NMR shift of 47.5 ppm was observed from the major remaining metal-containing species. This complex was then separately prepared by addition of [NBu$_4$][BH$_4$] to [Rh(*mer*-κ^3-P,O,P-Xantphos-^{i}Pr)(H)$_2$(η^1-H$_3$B-NMe$_3$)][BAr$^{Cl}{}_4$] which allowed for NMR (^{11}B δ = 139.0 ppm) and crystallographic data to be obtained. The molecular structure was found to be [{Rh(*mer*-0κ^3-P,O,P-Xantphos-^{i}Pr)}$_2$B]$^+$, **6-6**. The DFT studies in this thesis aims to clarify if complex **6-6** can be described as a dimetalloborylene where the boron participates in multiple bonding between two Rh(I) centres, **6-6a** (**Figure 6-11**) or a cationic borinium which would display no multiple bonding with the boron atom, **6-6b**. A third possibility, a dimetalloboride **6-6c**, was not considered due to the high symmetry of the molecular structure.

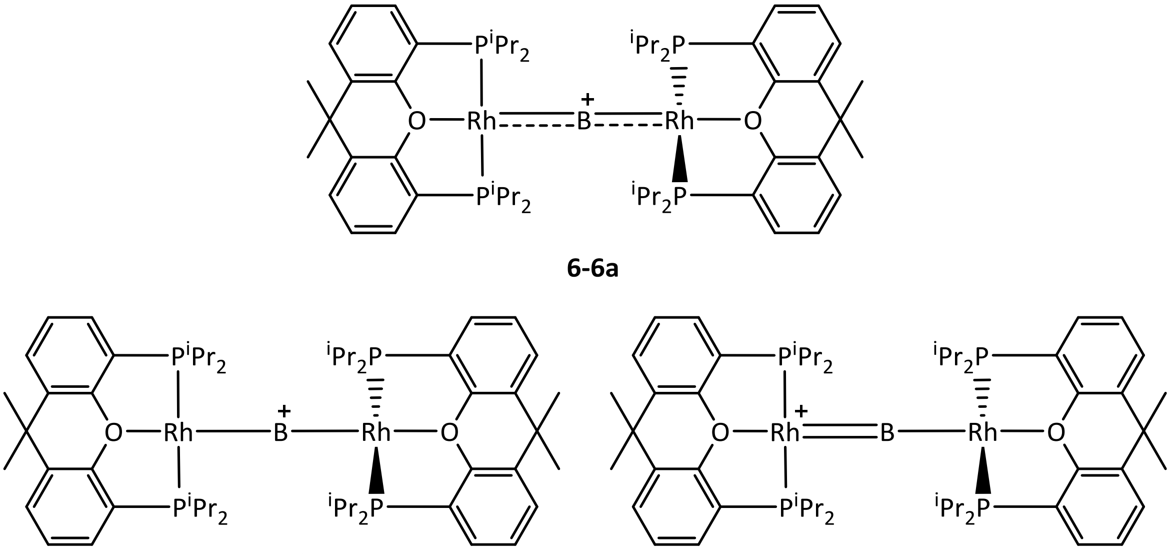

6-6a

6-6b

6-6c

Figure 6-11: *Possible bonding schemes for complex **6-6**.*

6.5.2 – QTAIM Results

The full molecular graph with a 2D contour plot of the electron density in the Rh-B-P plane is displayed in **Figure 6-12** with properties of selected bcps in **Table 6-6**. There is effective C$_2$ symmetry in the fully optimised computed structure so the B-Rh bonds are considered equivalent. The results show that the B-Rh interaction in **6-6** is covalent in nature due to the value of H(r) being -0.15 a.u. The ellipticity of 0.03 suggests a spherical interaction at the bcp. This could be interpreted as either a σ-bonding interaction or multiple bonding where the π-bonding has a similar contribution in perpendicular planes. Therefore, distinguishing complex **6-**

6 as either a metalloborylene **6-6a** or a boride **6-6b** is not possible when only considering the QTAIM analysis.

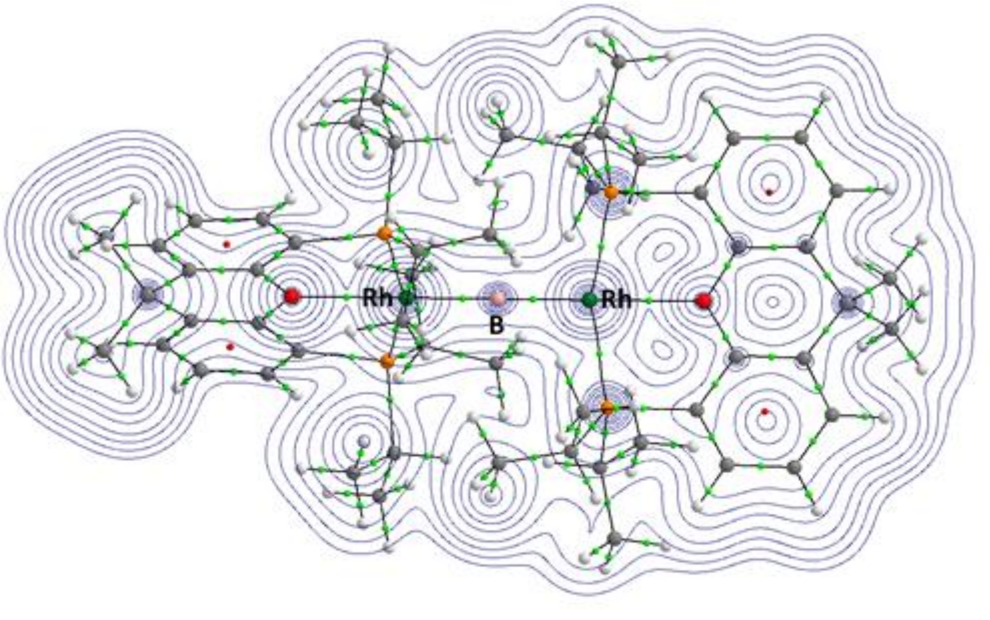

Figure 6-12: Full *molecular graph and electron density contour plot in the Rh-B-P plane for* ***6-6****. Weak bond paths, chemically less–relevant rcps, and one μ-dpcm unit are omitted for clarity*

	ρ(r)	**∇^2ρ(r)**	**ε**	**H(r)**	**V(r)**	**G(r)**
Rh-B	0.15	-0.15	0.03	-0.11	-0.19	-0.08

Table 6-6: *Values of electron density, Laplacian, ellipticity and energy densities at selected bcps in* ***6-6****. Obtained from the QTAIM analysis. Units in e Å^{-3} (ρ(r), ∇^2 ρ(r)) , or a.u (H(r), V(r), and G(r)).*

An NBO calculation found that the NBO charge on the boron atom was +0.45 which is consistent with the proposed metallaborylene (**6-6a**) and boride (**6-6b**) structures. Furthermore, a Wiberg Bond Index (WBI)[210] of 1.11 was calculated for both Rh-B interactions which suggests there is multiple bonding present. The NBO Lewis structure exhibits no direct Rh-B bond, however, there are 4 donor-acceptor interactions between rhodium lone pairs and the 4 boron orbitals which are labelled as 'low valency' (**Figure 6-13**). One Rh d-orbital donates electrons to the boron 2s with a donor-acceptor interaction energy (E) of 75.6 kcal mol^{-1} as well as the p-orbital in the plane of the bond (E = 25.7 kcal mol^{-1}). A second Rh d-orbital donates electrons to the two perpendicular p-orbitals of the boron atoms (E = 15.1 and 12.9 kcal mol^{-1}). This is further evidence of the presence of multiple bonding in the Rh-B interaction.

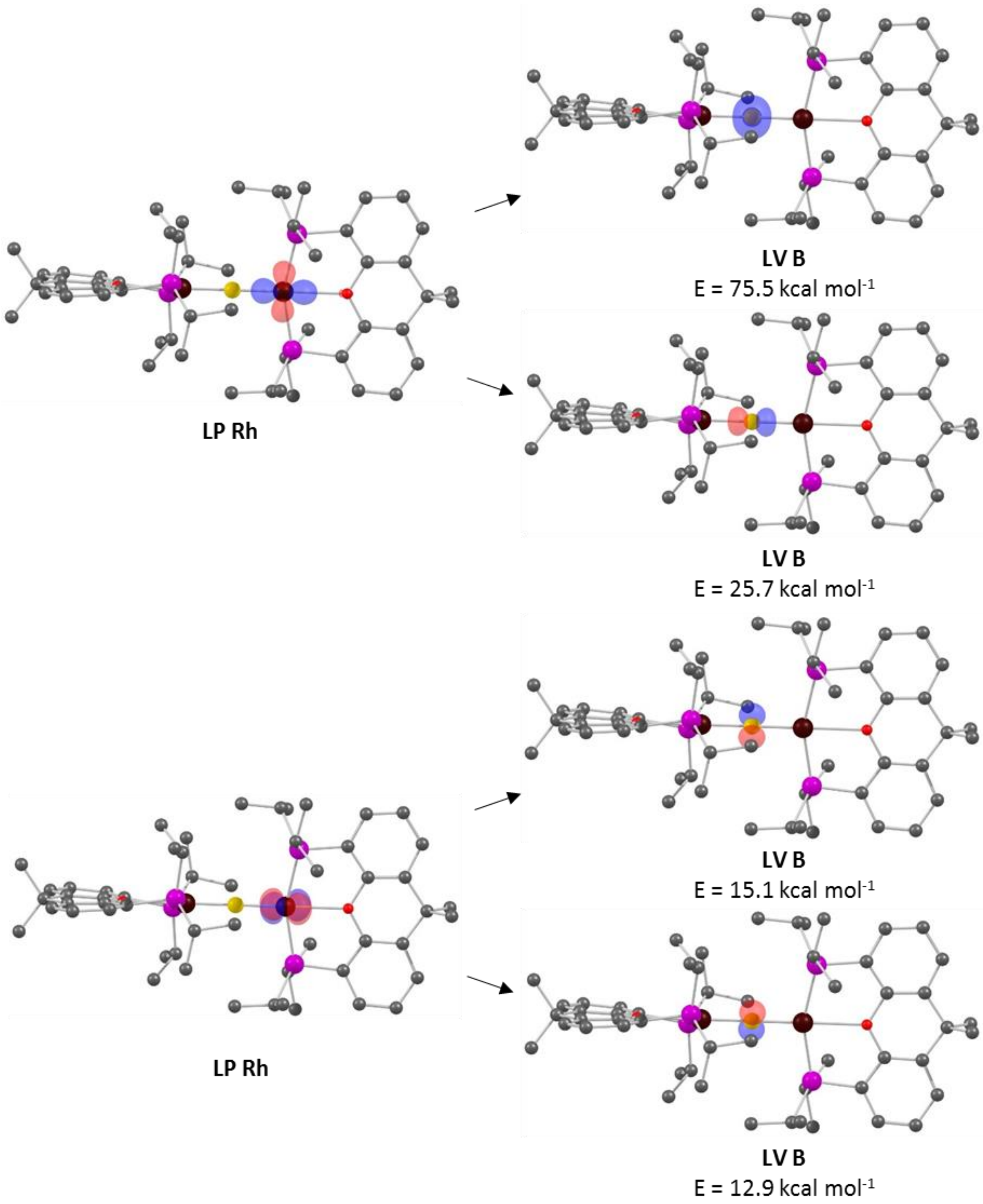

Figure 6-13: *The donator-acceptor interactions of a Rh-B interaction in complex* ***6-6*** *with interaction energies. NBOs shown of relevant Rh LPs and B LVs.*

Overall, complex **6-6** can be described as a metalloborylene **6-6a** as there is evidence of multiple bonding in the Rh-B-Rh interaction in both the QTAIM and NBO analysis. The NBO charge; of the boron and WBI of the Rh-B interaction also supports this conclusion. There are several examples of metalloborylenes in the literature which exhibit similar boron natural charges and WBI values than complex **6-6**. For example, $[\{Fe(CO)_2Cp^*\}B\{Ir(CO)Cp^*\}]^+$ synthesised by Braunschweig *et al.*[211] has a boron natural charge of +0.22 and a WBI value of 1.22 for the Ir-B interaction and 0.63 for the Fe-B interaction, both of which suggest multiple bonding. Braunschweig *et al.* also reported [$\{Mn(CO)_2(C_6H_7)\}_2B$]^{212} which has a natural charge of +0.46 on the boron with the Mn-B interactions having a WBI of 0.84. Furthermore, [$\{Ru(CO)_2Cp\}_2B$]$^+$ published by Aldridge *et al.*[213] has a natural charge of +0.43 on the boron and a WBI of 0.85 for the Ru-B interaction.

6.6 – Calculating the ^{11}B NMR Chemical Shift

6.6.1 – Computational Details

In this section, NMR calculations were run using the ADF modelling suite[214-216] due to the ability of ADF to include relativistic effects such as spin-orbit coupling. Calculations were run on truncated model systems with the PBE0 functional[149] and a Slater type triple-ς (TZP) basis set on small model systems.[217] Scalar relativistic and spin-orbit coupling effects were treated by the 2-component zeroth-order regular approximation (ZORA).[218] The truncated models were initially fully optimised using Gaussian 09 revision D.01[175] with the PBE0 functional[149] with transition metals and P centres described with Stuttgart pseudopotentials[158] and associated basis sets (with added d-orbital polarisation on P (ς = 0.387))[174] and all other atoms described with Jensen's polarized valence triple zeta basis set, pcseg2.[219] Dispersion effects were included in the optimisation using Grimme's D3 parameter set[164] with Becke-Johnson damping.[165] The optimised full models were then truncated and re-optimised using the same computational set-up with all heavy atom positions fixed. Complexes that have been optimised in this way have been assigned a prime. Calculations using Gaussian in this chapter were run with Gaussian 09 revision D.01[175] using the B3LYP functional.[147] Transition-metal and P centres were described with Stuttgart pseudopotentials[158] and associated basis sets (with added d-orbital polarisation on P (ς = 0.387))[174] and all other atoms with the 6-311g++**.[178, 179]

6.6.2 – Calculating the ^{11}B Chemical Shift

During the computational studies into the structure of bridging amino-borane **6-1**, bridging borylene **6-5**, and metalloborylene **6-6**, calculations to predict the ^{11}B chemical shift were attempted (**Table 6-7**). ^{11}B NMR calculations run with G09, that did not include spin-orbit coupling effects, of **6-1**, **6-5**, and **6-6** were calculated to be +51.3, +86.2, and +180.1 ppm respectively. The experimental shift for complex **6-1** was accurately reproduced by the calculation, however, there were large errors of +27.2 ppm for complex **6-5** and +41.1 ppm for **6-6**. The calculations were repeated using ADF where spin-orbit coupling relativistic effects were accounted for. This allowed for calculated ^{11}B NMR shifts of +45.4 (**6-1'**), +50.7 (**6-5'**), and +135.5 (**6-6'**) ppm to be obtained. This improves the accuracy to the experimental values with smaller errors of -8.3 and -3.5 for complexes **6-5** and **6-6** respectively. The observation of improving the accuracy of calculated NMR shifts when including spin-orbit relativistic effects has been noted before in a study on ^{1}H NMR shifts of ruthenium hydrides by Raynaud, Macgregor, Whittlesey *et al.*[220]

	Calculated ^{11}B shift (no spin-orbit coupling)	Calculated ^{11}B shift (w/ spin-orbit coupling)	Experimental ^{11}B shift
6-1	+51.3	+45.4	+51.1
6-5	+86.2	+50.7	+59.0
6-6	+180.1	+135.5	+139.0

Table 6-7: *Comparison between calculated and experimental ^{11}B chemical shifts. Values in ppm.*

Following the results shown in **Table 6-7**, a larger study was conducted to investigate the importance of including spin-orbit relativistic effects on the calculation of ^{11}B chemical shifts.

6.6.3 – The Importance of Spin-Orbit Coupling

A range of cationic, group 9, amine- and amino-borane complexes synthesised by the Weller group at The University of Oxford were chosen for the study including complexes **6-1**, **6-5**, and **6-6** (**Figure 6-14**). This included amine-borane complexes $[Rh(H_2)(PCy_3)_2(\eta^2\text{-}H_3BNMe_3)]^+$ **6-7**,[184] $[Ir(H_2)(PCy_3)_2(\eta^2\text{-}H_3BNMe_3)]^+$ **6-8**,[55, 221] and, $[Rh(P^iPr_3)_2(\eta^2\text{-}H_3BNMe_3)]^+$ **6-9**[**222**], amino-borane complex $[Ir(H)_2(PCy_3)_2(\eta^2\text{-}H_2BNMe_2)]^+$ **6-10**,[55, 221] and boryl complex $[Rh(\kappa^3\text{-P,O,P-Xantphos-Ph})(H)(HBNMe_2)(\eta^1\text{-}H_3B\text{-}NMe_3)]^+$ **6-11**.[193] In the truncated models, $\{PR_2\}$ moieties are replaced with $\{PMe_2\}$ units and $\{NMe_3\}$ or $\{NMe_2\}$ fragments are replaced with $\{NH_3\}$ and $\{NH_2\}$ groups.

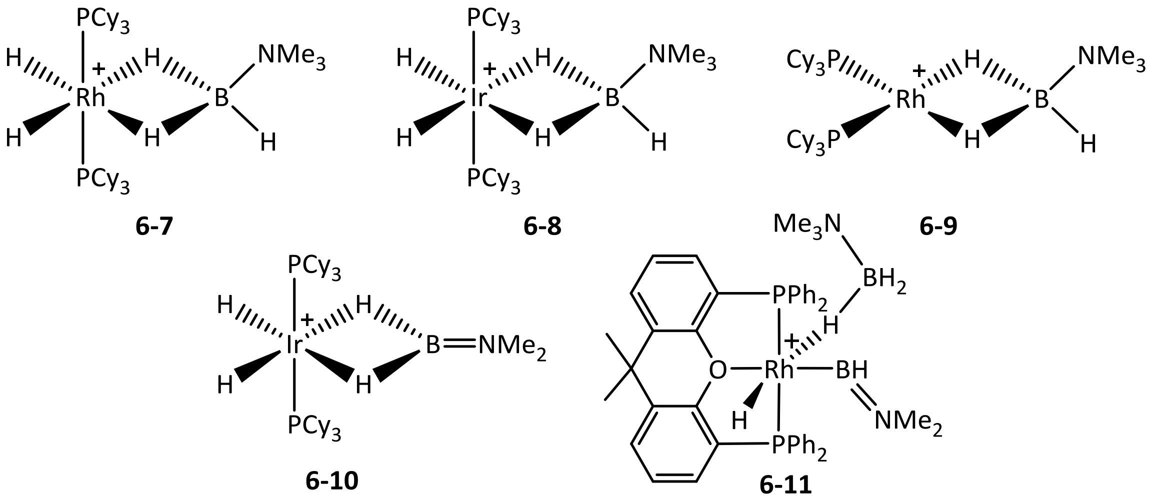

Figure 6-14: *Transition-metal amine- and amino-borane complexes used in the NMR study.*

The ^{11}B NMR shifts were calculated with and without spin-orbit relativistic effects being included. The results are shown in **Figure 6-15**. It was observed that the calculations which included spin-orbit relativistic effects were more accurate with the gradient of the best fit line (0.9492) being closer to 1 (which would indicate perfect correlation) than that of the calculations with no spin-orbit relativistic effects (1.3698). Including spin-orbit relativistic effects also gives an R^2 value of 0.9913 compared to 0.9614 when they were not included. For transition-metal amine-borane complexes **6-7’** and **6-8’**, which have saturated boron centres, the addition of spin-orbit coupling to the NMR calculation has little effect to the accuracy of the ^{11}B chemical shift with errors of -3.1 and -3.7 ppm respectively improving to +0.34 and +5.2 when including spin-orbit relativistic effects. For amino-borane complex **6-10’**, which has an unsaturated boron centre, there is a larger discrepancy in error when accounting for spin-orbit coupling (-16.0 *vs.* +1.1 ppm). This is in contrast with the error differences seen in amino-borane dimer **6-1’**. The largest discrepancies were observed for dimers **6-5’** and **6-6’** which have already been discussed.

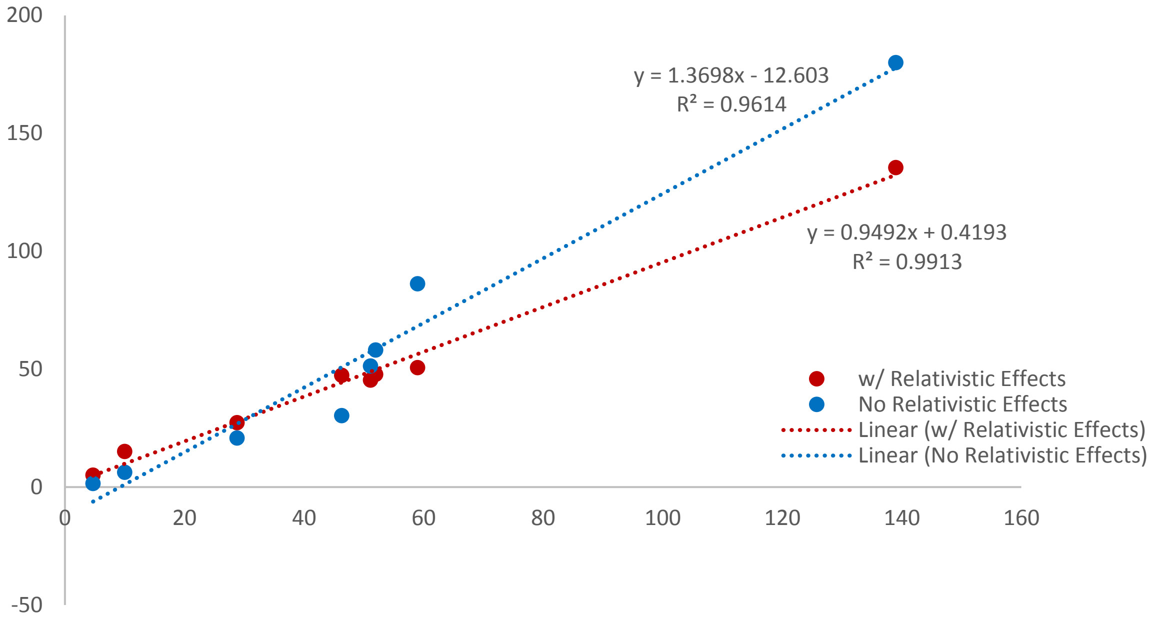

Figure 6-15: *Graph of Calculated vs Experimental ^{11}B shifts in ppm.*

Overall, there is a trend that the effects of spin-orbit coupling are more important for transition metal complexes containing unsaturated boron atoms within amino-boranes, boryls and borylenes than for saturated boron centres such as amine-borane complexes. In order to test that the trends observed above were due to including spin-orbit relativistic effects and not a factor of changing program, ^{11}B NMR calculations using the ADF procedure detailed in **Section 6.6.1** but with no spin-orbit relativistic effects account for on complexes **6-1’**, **6-5’**, and **6-11’** (**Table 6-8**). The results show the largest difference between the Gaussian and ADF calculations is 3.9 ppm for boryl complex **6-11’**. This gives confidence that it is the inclusion of spin-orbit coupling effects that is improving the accuracy of the ^{11}B NMR calculations and not the change in software program.

	Gaussian ^{11}B shift (no spin-orbit coupling)	ADF ^{11}B shift (no spin-orbit coupling)	ADF ^{11}B shift (w/ spin-orbit coupling)
6-1’	+51.3	+55.0	+45.4
6-5’	+86.2	+86.8	+50.7
6-11’	+58.1	+62.2	+47.8

Table 6-8: *Comparison between ^{11}B NMR calculations using Gaussian with no relativistic effects, ADF with no spin-orbit relativistic effects, and ADF with spin-orbit relativistic effects.*

6.7 – Conclusions

In conclusion, DFT has been used to analyse and confirm the structure of three boron containing rhodium dimers which were isolated from and active in amine-borane dehydropolymerisation catalysis.

Dimer $[\{Rh(dipp)\}_2(H)(\mu\text{-}BH_2NH_2)]^+$ **6-1** (**Section 6.3**) was confirmed as the first isolated bridging amino-borane complex through the use of QTAIM analysis. Benchmarking against other rhodium dimers ($[\{Rh(H)(PPh_3)_2\}_2(\mu\text{-}Cl)_2(\mu\text{-}H)]^+$ **6-2**, $[\{Rh(dipp)\}_2(\mu\text{-}H)(\mu\text{-}H_3BCMe_2(^iPr))]$ **6-3** and, $[\{Rh(CO)(Cp)\}_2(\mu\text{-}BN(SiMe_3)_2)]$ **6-4** helped confirm the findings of the study. The ellipticity of the Rh-H and Rh-B bcps in complex **6-1** (ε = 0.45 and 0.61) were important in defining the bonding as they did not compare with the terminal rhodium-hydride bonds in **6-2** (ε = 0.01) and the bridging borylene in **6-4** (ε = 0.08). A room temperature fluxional process was also characterised to involve rotation of a $[HBNMe_2]$ moiety around the Rh-Rh vector. The calculated free energy activation barrier of 13.2 kcal mol^{-1} was similar to the experimentally obtained value of 9.37 ± 0.38 kcal mol^{-1}.

QTAIM analysis also helped confirm that complex **6-5** (**Section 6.4**), $[\{RhH\}_2(\mu\text{-}BNMe_2)(\mu\text{-}dpcm)_2(\mu\text{-}H)]^+$, was a bridging borylene dimer with two terminal rhodium-hydride bonds. A NBO calculation confirmed there was no Rh-Rh bonding in the dimer. Similar techniques were used to define the Rh-B-Rh interaction in metalloborylene complex **6-6** (**Section 6.5**), $[\{Rh(\textit{mer}\text{-}\kappa^3\text{-}P,O,P\text{-}Xantphos\text{-}^iPr)\}_2B]^+$.

In **Section 6.6** a study into the accuracy of ^{11}B chemical shift calculations found that using the including spin-orbit coupling relativistic effects provided better accuracy to the experimental values. This was found to be particularly important in accurately calculating the ^{11}B chemical shift of transition-metal complexes with unsaturated boron centres.

Overall Conclusions

DFT calculations have been successfully used to characterise the dehydrogenation and dehydrocoupling of phosphine-boranes towards the formation of polyphosphino-boranes with two different catalyst systems. This has helped increase the understanding of the dehydrogenation process and could aid in the development of more efficient catalysts for the dehydrocoupling process.

Mechanisms for the formation of polyamino-borane from amine-boranes with a range of alkyl-Xantphos Rh catalysts have also been characterised. For neutral catalysts the dehydrogenation was found to proceed *via* an outer-sphere concerted activation with the mechanism changing depending on the sterics of the Xantphos ligand. The propagation process was characterised to proceed through a head-to-tail chain growth mechanism. Amine-borane dehydrocoupling with cationic catalysts were also investigated but remain less clear. It is suggested that the sterics of the Xantphos ligand continues to influence the dehydrogenation mechanism, which is likely to involve the formation of a neutral species through the formation of a boronium cation. For these systems further investigation is required.

The electronic structure and bonding of boron-containing Rh dimers was investigated using QTAIM and NBO analyses. This helped clarify the structure of intermediates during the amine-borane dehydrocoupling process. Furthermore, an investigation into the origins of the ^{11}B NMR chemical shift in amine-borane transition-metal complexes highlighted the importance in taking spin-orbit coupling relativistic effects into account for an accurate calculation, especially when investigating unsaturated boron centres.

Chemical Science

ROYAL SOCIETY OF CHEMISTRY

EDGE ARTICLE

View Article Online
View Journal | View Issue

Cite this: Chem. Sci., 2016, 7, 2414

Dehydrocoupling of phosphine–boranes using the $[RhCp^*Me(PMe_3)(CH_2Cl_2)][BAr^F_4]$ precatalyst: stoichiometric and catalytic studies†

Thomas N. Hooper,[a] Andrew S. Weller,*[a] Nicholas A. Beattie[b]
and Stuart A. Macgregor*[b]

Received 2nd November 2015
Accepted 19th December 2015

DOI: 10.1039/c5sc04150c

www.rsc.org/chemicalscience

We report a detailed, combined experimental and computational study on the fundamental B–H and P–H bond activation steps involved in the dehydrocoupling/dehydropolymerization of primary and secondary phosphine–boranes, $H_3B\cdot PPhR'H$ (R = Ph, H), using $[RhCp^*(PMe_3)Me(ClCH_2Cl)][BAr^F_4]$, to either form polyphosphino-boranes $[H_2B\cdot PPhH]_n$ (M_n ~ 15 000 g mol^{-1}, PDI = 2.2) or the linear diboraphosphine $H_3B\cdot PPh_2BH_2\text{-}PPh_2H$. A likely polymer-growth pathway of reversible chain transfer step-growth is suggested for $H_3B\text{-}PPhH_2$. Using secondary phosphine–boranes as model substrates a combined synthesis, structural (X-ray crystallography), labelling and computational approach reveals: initial bond activation pathways (B–H activation precedes P–H activation); key intermediates (phosphido-boranes, α-B-agostic base-stabilized boryls); and a catalytic route to the primary diboraphosphine ($H_3B\cdot PPhHBH_2\cdot PPhH_2$). It is also shown that by changing the substituent at phosphorus (Ph or Cy *versus* ^{t}Bu) different final products result (phosphido-borane or base stabilized phosphino-borane respectively). These studies provide detailed insight into the pathways that are operating during dehydropolymerization.

Introduction

The polymerization of alkenes using transition metal-based catalysts to afford societally and technologically ubiquitous polyolefins is well-established, yet equivalent catalytic routes to polymeric materials containing main-group elements is considerably less developed.[1,2] In particular, the group 13/15 mixed polymers provide one example that promises to lead to significant scientific and technological opportunities, given that polyphosphino-boranes, along with polyamino-boranes,[3] are (valence) isoelectronic with polyolefins and are finding uses in a variety of applications from lithography to pre-ceramics.[4,5] Ill-defined polyphosphino-boranes were first synthesised in 1959 through thermal dehydrocoupling of primary phosphine–boranes,[6] but a faster and more selective dehydrocoupling/dehydropolymerization process was reported by Manners and co-workers in the early 2000's using transition metal pre-catalysts primarily based upon $[Rh(COD)Cl]_2$ and $[Rh(COD)_2][OTf]$, operating under melt conditions.[7–10] Others have since used similar catalyst systems to prepare related polyphosphino-boranes, or elegant demonstrations of highly selective cross-dehydrocouplings.[11,12] For primary phosphine–boranes, $H_3B\cdot PRH_2$, polyphosphino-boranes are formed, whereas for secondary phosphine–boranes, $H_3B\cdot PR_2H$, linear diboraphosphines or cyclic oligomers form (Scheme 1). Although catalysis has been shown to be homogenous rather than heterogeneous,[13,14] the melt conditions required for effective dehydrocoupling meant that resolving intermediates/resting states or kinetics was challenging. In contrast, the mechanism of amine–borane dehydrocoupling using transition metal catalysts is much better understood as catalysis can be performed in solution at room temperature.[15] Very recently the non-metal-catalyzed addition polymerization of *in situ* generated phosphino-boranes, such as $[H_2BP^tBu_2]$, has been described,[16] that avoids the use of melt conditions.

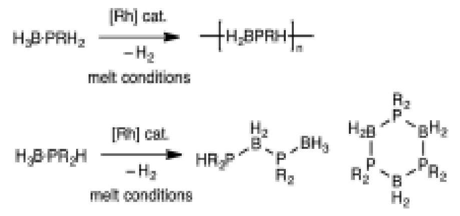

Scheme 1 Rh-catalyzed dehydrocoupling of primary and secondary phosphine–boranes.

---

[a] Department of Chemistry, Chemistry Research Laboratories, University of Oxford, Mansfield Road, Oxford, OX1 3TA, UK. E-mail: andrew.weller@chem.ox.ac.uk

[b] Institute of Chemical Sciences, Heriot Watt University, Edinburgh, EH14 4AS, UK. E-mail: S.A.Macgregor@hw.ac.uk

† Electronic supplementary information (ESI) available: Synthesis and characterisation data, computational details. CCDC 1423368–1423370. For ESI and crystallographic data in CIF or other electronic format see DOI: 10.1039/c5sc04150c

Recently, *in situ* sampling using ESI-MS (electrospray ionisation mass spectrometry) led to the identification of a $[Rh(PHR_2)_2]^+$ fragment as an active species in the dehydrocoupling of secondary phosphine–boranes under melt conditions to form $H_3B\cdot PR_2H_2B\cdot PHR_2$ when using $[Rh(COD)_2][BAr^F{}_4]$ as the precatalyst [R = Ph, ^{t}Bu; $Ar^F = 3,5\text{-}(CF_3)_2C_6H_3$].[17] This arises from cleavage of the relatively weak P–B bond in the substrate.[18] Simple replacement of the monodentate phosphine ligands with a bidentate phosphine produced a metal fragment, *i.e.* $[Rh(Ph_2P(CH_2)_3PPh_2)]^+$, which did not suffer from ligand redistribution, allowing for a detailed study of the mechanism, including isolation of intermediates, isotopic labelling studies and determination of activation parameters.[19,20] Thus intermediate complexes that relate to overall P–H activation of $H_3B\cdot PPh_2H$ at a Rh(I) center (**A** Scheme 2), and subsequent P–B bond formation (**B**), were isolated, while B–H activation of the second phosphine–borane to form a boryl intermediate was proposed to be involved in the rate-determining step that follows from **A**. However, because of relatively rapid H/D exchange between P and B the elementary P–H/B–H activation steps could not be delineated using labelling studies. In addition, although this dehydrocoupling occurred at room temperature, melt conditions were required for turnover. This same fragment was also found to dehydrocouple primary phosphine–boranes under melt conditions to produce ill-defined low molecular weight polymer. The mechanism was proposed to be the same as with secondary phosphine–boranes, but with the added complexity of diastereomer formation caused by P–H activation of the prochiral phosphorus centre.[20]

A catalytic system which does not require melt conditions, produces well-defined, high molecular weight polyphosphinoborane (M_n = 59 000 g mol^{-1}, PDI = 1.6) and operates *via* a chain growth process was reported in 2015 by Manners *et al.* using the $FeCp(CO)_2(OTf)$ catalyst.[5] Heating (toluene, 100 °C) in the presence of phosphine–borane was required to promote CO and $[OTf]^-$ loss and the formation of an initial phosphidoborane complex (**C**, Scheme 3, isolated for the $H_3B\cdot PPh_2$ analogue). In the mechanism it was suggested that the Fe centre adopts a constant oxidation state with B–H/P–H activation and P–B coupling proposed (**D** and **E**), using DFT calculations, to proceed *via* multiple sigma-complex assisted metathesis steps.[21,22]

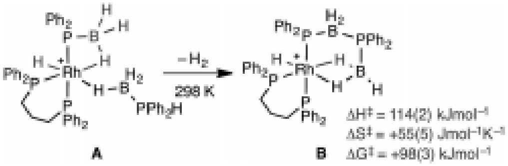

Scheme 2 Intermediates observed in the dehydrocoupling of $H_3B\cdot PPh_2H$ using the $[Rh(Ph_2P(CH_2)_3PPh_2)]^+$ fragment. $[BAr^F{}_4]^-$ anions not shown.

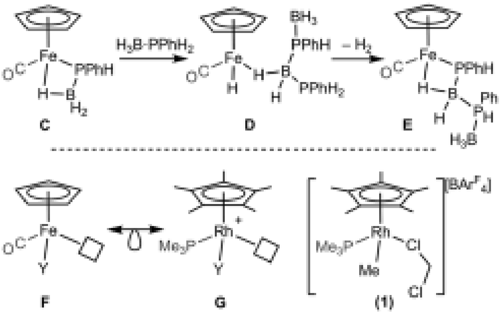

Scheme 3 (Top) Intermediates (isolated and suggested) in the dehydropolymerization of $H_3B\cdot PPhH_2$ as catalysed by $FeCp(CO)_2OTf$. (Bottom) Relationship between FeCp(CO)Y and $[RhCp^*(PMe_3)Y]^+$ (Y = anionic ligand).

Central to control of the dehydropolymerization process is a detailed understanding of the fundamental, elementary, steps that are occurring. Inspired by this recent report by Manners on the $FeCp(CO)_2(OTf)$ system, and also aware that this system still required heating to promote CO loss, we turned to $[RhCp^*Me(PMe_3)(CH_2Cl_2)][BAr^F{}_4]$ (**1**, Scheme 3, Cp* = η^5-C_5Me_5)[23,24] as an alternative entry point (*cf.* structures **F** and **G**), proposing that B–H/P–H activation may be studied at ambient temperature under solution conditions. This complex provides a latent vacant site through CH_2Cl_2 dissociation and also a methyl group that is well set up for loss as methane after B–H or P–H transfer. It is also well-established to mediate bond activation processes *via* sigma-bond metathesis, and related, processes,[23,24] while the {RhCp*} fragment more generally catalyzes C–H, B–H, and P–H activation and bond coupling.[25–28]

We report here that complex **1** is an effective precatalyst for the dehydropolymerization of $H_3B\cdot PPhH_2$, and also allows for a study of the elementary B–H/P–H activation processes occurring *via* a combined experimental and computational approach. In particular the order of B–H/P–H activation is determined in these systems, as well as a subsequent isomerization and P–B bond forming events. This provides insight into both the order of events and the likely intermediates involved in dehydropolymerization of phosphine–boranes.

Results and discussion

Catalysis: dehydrocoupling of $H_3B\cdot PPhH_2$

Initial catalytic screening showed that complex **1** was an active precatalyst (1 mol%, 0.01 M, toluene, 100 °C, 72 h, system open to Ar) for the dehydropolymerization of $H_3B\cdot PPhH_2$. After work-up, by precipitation into hexanes, the $^{31}P\{^1H\}$ NMR spectrum of the resulting solid shows a well-defined peak at δ −49.5, while in the ^{11}B NMR spectrum a broad peak at δ −34.0 is observed ($CDCl_3$), in good agreement with that reported by Manners *et al.* for polymer formed using the $FeCp(CO)_2(OTf)$[5] and $[Rh(COD)_2][OTf]$[8] catalysts. A simple doublet observed in the ^{31}P NMR spectrum [J(HP) = 346 Hz] suggests a linear $[H_2BPPhH]_n$ structure to the polymer, rather than a branched structure that would invoke a quaternary phosphorus;[8,29] although a low intensity ill-defined broad shoulder is observed between δ −50 to −60 that is suggestive of a small proportion of shorter chain oligomers or some branching. Consistent with this NMR data, the isolated polymer was shown by GPC to consist of a moderate molecular weight fraction (M_n = 15 000 g mol^{-1}, PDI = 2.2) alongside lower molecular weight material (less than 1000 g mol^{-1}). Although similar to that reported for the [Rh(COD)$_2$][OTf] catalyst (M_w = 30 000 g mol^{-1})[7,8] it falls short of the FeCp(CO)$_2$(OTf) system at 1 mol% (M_n = 59 000 g mol^{-1}, PDI = 1.6).[5] The organometallic species in the catalytic mixture could not be identified. However, a signal corresponding to $H_3B\cdot PMe_3$ was observed,[30] suggesting dissociation (or substitution) of PMe_3 in complex **1** during catalysis. If dehydropolymerization is carried out at a higher catalyst loading (5 mol%, 0.05 M, 72 hours) moderate molecular weight polymer is also formed as measured by GPC of hexane-precipitated material (M_n = 13 000 g mol^{-1}, PDI = 1.5), and low molecular weight polyphosphinoborane is again present (less that 1000 g mol^{-1}). The isolated polymer was also analysed by ESI-MS with a broad range of molecular weight chains $[H\{PPhHBH_2\}_nPPhH_2]^+$ and clear repeat units of $\{PHPhBH_2\}$ (m/z = 122) observed. The highest molecular weight polymer measured by this technique was n = 20, m/z = 2551.9.

Monitoring this reaction by ^{11}B NMR spectroscopy shows that the $H_3B\cdot PPhH_2$ monomer is consumed after only four hours, suggesting its relatively rapid oligomerization, but the slower formation of higher molecular weight polymer. If dehydropolymerization is stopped after only 1 hour the $^{11}B\{^1H\}$ NMR spectrum now shows signals due to $H_3B\cdot PPhH_2$, a broad signal at δ −33.6 assigned to oligomer/polymer, $H_3B\cdot PMe_3$ and significant amounts of a new compound assigned to the primary diboraphosphine $H_3B\cdot PPhHBH_2\cdot PPhH_2$ **2** (Scheme 4). Compound **2** is present in significantly greater amounts at 5 mol% loading [$H_3B\cdot PPhH_2$: **2**; 1 : 1, 5 mol%; 6 : 1, 1 mol%], and could be isolated in 25% yield by removing the toluene *in vacuo* and extracting with hexane to give a very pale yellow oil that could be fully characterized by NMR spectroscopy [*e.g.* $^{11}B\{^1H\}$ δ −36.5 vt, J (PB) ~ 70 Hz; −38.9 (d, J (PB) ~ 50 Hz)], with data similar to both the secondary diboraphosphine $H_3B\cdot PPh_2BH_2\cdot PPh_2H$,[8] and the primary analogue, $H_3B\cdot PCyHBH_2\cdot PCyH_2$.[20] The thermal dehydrogenation of $H_3B\cdot PPhH_2$ in the absence of **1** (toluene, 0.625 M) produces **2** only slowly (~50% conversion after 16 h) alongside a small amount of oligomeric product and unreacted $H_3B\cdot PPhH_2$.

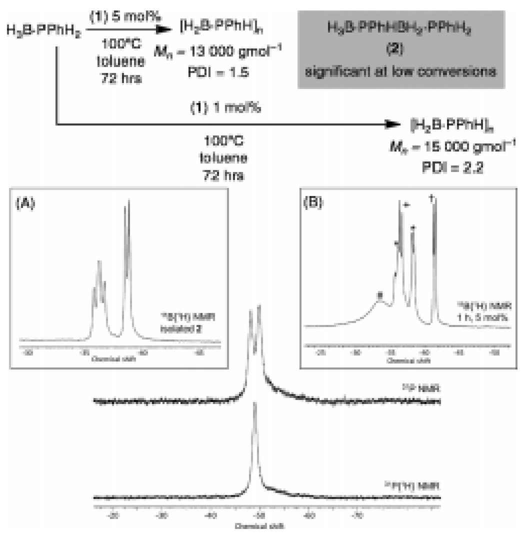

Scheme 4 Purified $[H_2BPPhH]_n$ from the dehydrocoupling of $H_3B\cdot PPhH_2$ catalysed by **1**, 1 mol%. Inset (A) purified **2**; (B) $^{11}B\{^1H\}$ NMR after 1 h: * $H_3B\cdot PPhHBH_2\cdot PPhH_2$ **2**, † $H_3B\cdot PPhH_2$, + $H_3B\cdot PMe_3$, # short chain oligomers.

The lack of significant change in M_n on increasing the catalyst loading from 1 to 5 mol% suggests that a coordination chain-growth type mechanism is not operating, in which the polymer chain grows on the metal centre by successive monomer insertion events, as suggested for FeCp(CO)$_2$(OTf) system for phosphine–borane and [Rh(xanthphos)]$^+$ for amine–borane dehydropolymerization.[5,31] Under this mechanistic model lower catalyst loadings would be expected to lead to higher molecular weight polymer, although such an analysis can be complicated by the fact that the metal has to both dehydrogenate and couple the reactive monomers.[32] Instead, that at short reaction times **2** is observed in significant quantities, especially at higher catalyst loadings, and $H_3B\cdot PPhH_2$ is completely consumed after only 4 hours hints at a step-growth-type mechanism, as suggested for [Rh(COD)Cl]$_2$-catalyzed systems.[29] Under this regime, a greater catalyst loading might be expected to increase the molecular weight of the resulting polymer.[29,32] However the analysis of the mechanism of polymer growth is further complicated by the fact that both isolated **2** and higher M_n polymer undergo P–B bond cleavage in the presence of **1**. For example, heating **2** in the presence of 5 mol% **1** for 1 hour (100 °C, toluene) resulted in a mixture of **2**, $H_3B\cdot PPhH_2$ (approx. 3 : 1 ratio by $^{11}B\{^1H\}$ NMR spectroscopy) and signals assigned to oligomers. Further heating overnight resulted in complete consumption of **2** and $H_3B\cdot PPhH_2$ to reveal signals in the ^{11}B NMR spectrum consistent with low molecular weight polymer, Scheme 5. Heating a sample of high molecular weight polymer (100 °C, toluene) with 5 mol% **1** also resulted in P–B cleavage events, with lower molecular weight species observed by ^{31}P NMR spectroscopy. Linear diborazanes have also been observed to undergo B–N bond cleavage and product redistribution processes through both thermal and metal catalysed pathways, with a mixture of monomeric amine–borane and oligomeric products generated.[33]

On balance we thus suggest that a process in which reversible chain transfer between an oligomer (polymer) bound to a metal centre and free $H_3B\cdot PPhH_2$, either initially present or

Scheme 5 P–B bond cleavage and polymerisation of **2** as catalysed by **1**.

generated by P–B bond cleavage, accounts best for these observations. We have previously demonstrated similar behaviour (as monitored by ESI-MS) using $H_3B{\cdot}NH_3$ and a $[Ir(PCy_3)_2(H)_2]^+$ fragment.[34]

Catalysis: dehydrocoupling of $H_3B{\cdot}PPh_2H$

To further probe the mechanism of dehydrocoupling using **1** the secondary phosphine–borane $H_3B{\cdot}PPh_2H$ was used, which has been shown to afford the diboraphosphine $H_3B{\cdot}PPh_2BH_2{\cdot}PPh_2H$ **3** or cyclic species depending on dehydrocoupling conditions.[8] Treatment of precatalyst **1** (5 mol%, 0.0313 M, 100 °C, toluene, 16 h) with $H_3B{\cdot}PPh_2H$ resulted in almost full conversion to **3** (95% by ^{31}P and ^{11}B NMR spectroscopy), Scheme 6. Analysis of the $^{31}P\{^1H\}$ NMR spectrum post-catalysis showed one dominant phosphine-containing organometallic species, as a doublet at δ 26.7 [J (RhP) = 139 Hz] which splits into a doublet of doublets in the ^{31}P NMR spectrum [J (PH) = 391 Hz], demonstrating a direct P–H bond. $H_3B{\cdot}PMe_3$ was also observed to be formed. The ^1H NMR spectrum of the reaction mixture showed a doublet of triplets at δ −11.36 which simplified to a doublet upon ^{31}P decoupling, suggesting a rhodium-bound hydride coupling to two phosphorus centres. ESI-MS showed one dominant peak at m/z = 611.15, with an isotope pattern that corresponds to the cation $[RhCp^*(H)(PPh_2H)_2]^+$, $\mathbf{4}^+$, fully consistent with the NMR data. Species closely related to cationic $\mathbf{4}^+$ have been previously structurally characterised.[35,36] Addition of Hg to the catalytic mixture after 4 hours resulted in no significant change to the overall conversion or rate, suggesting that the catalyst is not colloidal.[14]

The diphenylphosphine ligands required for the formation of cation $\mathbf{4}^+$ likely result from P–B cleavage of the starting material $H_3B{\cdot}PPh_2H$ and resulting exchange at the metal centre to release PMe_3, which is trapped as $H_3B{\cdot}PMe_3$. Following the temporal evolution of catalysis using $^{31}P\{^1H\}$ NMR spectroscopy and ESI-MS[37] showed that after 1 hour $\mathbf{4}^+$ was present, but also a pair of doublet of doublet resonances at δ 19.2 and 2.3 were observed, that correlate with signals in the ESI-MS spectrum assigned to the cation $[RhCp^*(H)(PMe_3)(PPh_2H)]^+$ ($\mathbf{5}^+$). After 4 hours at 100 °C complex $\mathbf{4}^+$ was dominant, suggesting that the cation $\mathbf{5}^+$ evolves to give $\mathbf{4}^+$ during catalysis. The ESI-MS also revealed signals with isotopic patterns which correspond to $[RhCp^*(PPh_2{\cdot}BH_3)(PPh_2H)_2]^+$ (at m/z = 809.23) and $[RhCp^*(PPh_2{\cdot}BH_2PPh_2{\cdot}BH_3)(PPh_2H)_2]^+$ (m/z = 1007.31) which we assume are Rh–P bound (*vide infra*). Phosphido-borane species have been detected and proposed as catalytic intermediates in phosphine–borane dehydrocoupling in systems based on the $\{Rh(Ph_2P(CH_2)_3PPh_2)\}^+$ and $\{FeCp(CO)\}^+$ fragments.[5,19,20] Addition of a further 20 equivalents of $H_3B{\cdot}PPh_2H$ to this reaction mixture post catalysis and heating to 100 °C resulted in complete conversion to diboraphosphine **3** after 22 h, suggesting that cation $\mathbf{4}^+$ is active in catalysis. Further evidence for complexes of general formula $[RhCp^*(H)(PR_3)_2]^+$ being the active species comes from the isolation of **5** as pure material as the $[BAr^F{}_4]^-$ salt (*vide infra*). Complex **5** is also a competent precatalyst for the dehydrocoupling of $H_3B{\cdot}PPh_2H$ (5 mol%, 100 °C) reaching completion within 22 hours. Again, cation $\mathbf{4}^+$ is observed to be formed in the reaction mixture by ^{31}P NMR spectroscopy, and the associated release of PMe_3 was confirmed by the detection of $H_3B{\cdot}PMe_3$. Addition of PPh_3 (10 equivalents) to complex **5** and monitoring by ESI-MS shows, after 2 hours at 298 K, the formation of $[RhCp^*(H)(PMe_3)(PPh_3)]^+$ (m/z = 577.17) showing that phosphine exchange also occurs at 298 K. At room temperature, neither *in situ* generated **4**, or pure **5**, displayed any reactivity towards one equivalent of $H_3B{\cdot}PPh_2H$. This suggests that under these conditions phosphine–borane is not a competitive ligand with phosphine, requiring higher temperatures and a large excess to promote reactivity at the metal center when there are two phosphines bound. The generation of vacant sites has been suggested to be important in the mode of action of $FeCp(CO)_2(OTf)$ in dehydrocoupling.[5] Consistent this we show next that **1**, which is a masked source of $\{RhCp^*Me(PMe_3)\}^+$ and thus does not require phosphine dissociation, reacts very rapidly with $H_3B{\cdot}PHPh_2$.

Overall these data show that the $\{RhCp^*Me(PMe_3)\}^+$ precatalyst, and related species formed during catalysis such as cation $\mathbf{4}^+$, are implicated in the dehydrocoupling/dehydropolymerization of both primary and secondary phosphine–boranes. In order to determine the role the metal fragment plays in this, the stoichiometric reactivity was studied, as is described next.

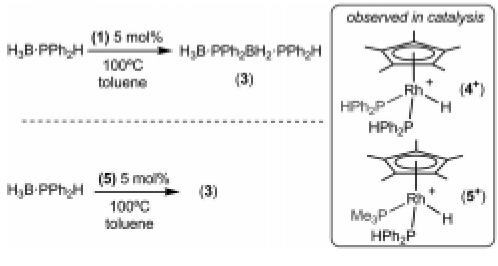

Scheme 6 The dehydrocoupling of $H_3B{\cdot}PPh_2H$ as catalysed by **1** and **5** to form **3**.

Stoichiometric reactivity with $H_3B{\cdot}PPh_2H$

Reaction of 1 equivalent of $H_3B{\cdot}PPh_2H$ with **1** at room temperature in CD_2Cl_2 solution resulted in rapid effervescence and a colour change from orange to yellow. $^{31}P\{^1H\}$ NMR spectroscopy of the resulting solution showed one sharp doublet of doublets at δ −6.6 [J (RhP) = 139 Hz, J (PP) = 22 Hz] assigned to the PMe_3 ligand and one broad peak at δ 6.9 [fwhm = 222 Hz] assigned to a phosphine–borane moiety, which was essentially unchanged in line shape in the ^{31}P NMR spectrum. The ^1H NMR spectrum demonstrated a lack of P–H and Rh–Me signals, and dissolved CH_4 was detected (δ 0.21[38]). A very broad peak was observed at δ 0.3 (relative integral 2H) which sharpens on ^{11}B decoupling and splits into two distinct resonances at δ 0.49 and δ −0.03 in a 1 : 1 ratio. A broad peak is observed at δ −10.81 that also sharpens on decoupling ^{11}B, under which conditions it also resolves into a broad doublet of doublet of doublets. These 3 upfield resonances are assigned to a BH_3 unit binding to the metal centre through one Rh–H–B 3 centre-2 electron bond that is not undergoing exchange on the NMR timescale between terminal and bridging environments. In the ^{11}B NMR spectrum a signal at δ −45.5 was observed, shifted slightly upfield from $H_3B{\cdot}PPh_2H$ [δ −40.1]. Overall, these data are consistent with the formation of a phosphido-borane complex which also has a rather tight β-B-agostic interaction: $[RhCp^*(PPh_2{\cdot}BH_3)(PMe_3)][BAr^F{}_4]$ (**6**), Scheme 7.

Yellow crystals were grown from the reaction mixture and isolated in good yield (76%). A resulting single-crystal X-ray diffraction study (Fig. 1) confirmed the structure as a phosphido-borane species with a β-B-agostic interaction. Although the B–H hydrogen atoms were located in the difference map, in the final refinement they were placed at fixed positions. The P–B distance in **6** [1.896(4) Å] is slightly shorter than the reported P–B bonds in $H_3B{\cdot}P(Mes)_2H$ [1.938 Å][39] and in $H_3B{\cdot}P(p\text{-}CF_3C_6H_4)_2H$ [1.917(2) Å][10] (the structure of $H_3B{\cdot}PHPh_2$ has not been reported) but longer than most of the crystallographically characterised monomeric phosphino-boranes, which usually bear bulky substituents to prevent oligomerisation (1.76–1.88 Å).[40,41] The NMR data are also characteristic of a four-coordinate boron, indicating a β-B-agostic structure rather a phosphino-borane complex with concomitant hydride transfer to Rh. Further evidence for a β-B-agostic structure was obtained from DFT calculations[42] which revealed a significant lengthening of the agostic B(1)–H(1A) bond (1.39 Å) compared to the non-agostic B(1)–H(1B)/H(1C) bonds (both 1.21 Å), as well as a short Rh(1)L–H(1A) contact of 1.72 Å. Other heavy atom bond metrics were in good agreement with experiment, including a computed P(1)–B(1) distance of 1.92 Å (see ESI† for full details). β-B-agostic interactions of this type have been previously observed in phosphido-borane complexes with Mo,[43,44] Fe,[45] Ti,[46] Rh[20] and alkaline earth metals,[47–49] but the structure of **6**, and the salient NMR data, most closely resemble the neutral compound $[FeCp(PPh_2{\cdot}BH_3)(CO)]$.[5] Finally, the β-B-agostic interaction observed in **6** is in contrast with valence isoelectronic $[RhCp^*(H)(H_2C{=}CH_2)P(OMe)_3][BF_4]$ that although in equilibrium with the corresponding β-agostic complex, favours the former.[50] Complex **6** is stable in CD_2Cl_2 solution for at least 2 weeks.

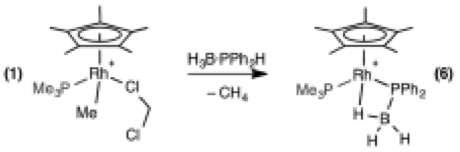

Scheme 7 Complex **6**. $[BAr^F{}_4]^-$ anions are not shown.

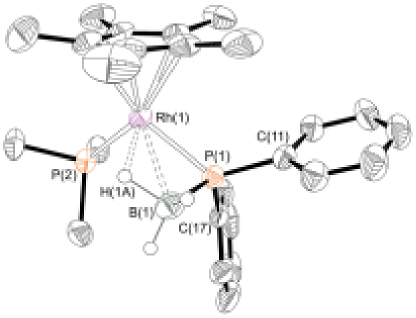

Fig. 1 X-ray molecular structure of $[RhCp^*(PPh_2{\cdot}BH_3)(PMe_3)][BAr^F{}_4]$ **6**. $[BAr^F{}_4]^-$ anion and selected hydrogen atoms omitted for clarity. Ellipsoids shown at 50% probability. Selected bond lengths (Å) and angles (°): P(1)–B(1) 1.896(4), Rh(1)–P(1) 2.302(1), Rh(1)–B(1) 2.464(4), Rh(1)–P(2) 2.3241(10), Rh(1)–Cp* (centroid) 1.859; P(1)–Rh(1)–P(2) 95.35(3), Rh(1)–P(1)–B(1) 71.13(13), B(1)–P(1)–C(11) 116.09(19), B(1)–P(1)–C(17) 119.55(19), C(11)–P(1)–C(17) 103.34(15).

The β-B-agostic interaction in **6** could be viewed as a source of masked highly reactive, phosphino-borane *i.e.* $\{H_2BPPh_2\}/\{Cp^*RhH(PMe_3)\}^+$ in which Rh–H acts as a Lewis base to boron and phosphorus a Lewis base to the Rh-center. The parent H_2BPH_2 has been shown to oligomerise at [Ti] centres,[51–53] or form polymeric materials when generated *in situ*.[16] To explore whether phosphino-borane H_2BPPh_2 could be liberated, as signalled by the formation of $[Ph_2PBH_2]_n$ ($n = 3$ or 4),[8,16] complex **6** was heated to 100 °C in toluene for 4 hours. However, the only product that could be observed by NMR spectroscopy was the P–B cleavage product **5**, while the fate of the remaining {BH} is unclear (Scheme 8). This process is therefore the likely route to formation of **5** from **1** under catalytic conditions. Complex **5** could also be formed cleanly by pressurising a 1,2-difluorobenzene solution of **6** with H_2 (~4 atm) at room temperature for 16 hours. In this case the boron-containing by-product of P–B cleavage was determined to be B_2H_6 by ^{11}B NMR spectroscopy.[54] Complex **6** does not react with $H_3B{\cdot}PPh_2H$ at 298 K, reflecting the strong Rh⋯H–B interaction.

Stoichiometric reactivity with $H_3B{\cdot}PCy_2H$

Reaction of one equivalent of $H_3B{\cdot}PCy_2H$ with **1** in CD_2Cl_2 resulted in rapid effervescence (methane). Analysis by NMR spectroscopy after 5 minutes indicated the formation of a complex very similar to **6**: $[RhCp^*(PCy_2{\cdot}BH_3)(PMe_3)][BAr^F{}_4]$, **7**, in particular an upfield signal in the ^1H NMR spectrum is observed at δ −11.42, assigned to the β-B-agostic interaction. Single crystals of **7** suitable for X-ray diffraction were grown from a cooled CH_2Cl_2/pentane solution, and the solid state structure confirms a β-B-agostic phosphido-borane ligand chelating with the rhodium centre (Fig. 2). The bond lengths and angles in the structure were broadly similar to those found

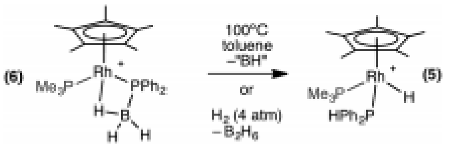

Scheme 8 Reactivity of complex **6**. $[BAr^F{}_4]^-$ anions are not shown.

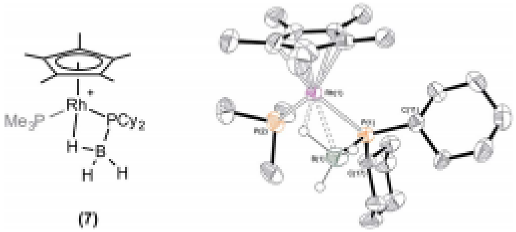

Fig. 2 X-ray molecular structure of [RhCp*(PCy$_2$·BH$_3$)(PMe$_3$)][BAr$^F{}_4$] (7). [BAr$^F{}_4$]$^-$ anion and selected hydrogen atoms omitted for clarity. Ellipsoids shown at 50% probability. Selected bond lengths (Å) and angles (°): P(1)–B(1) 1.910(7), Rh(1)–P(1) 2.3425(14), Rh(1)–B(1) 2.468(7), Rh(1)–P(2) 2.2878(16), Rh(1)–Cp*(centroid) 1.875; P(1)–Rh(1)–P(2) 93.94(6), Rh(1)–P(1)–B(1) 70.1(2), B(1)–P(1)–C(11) 109.3(3), B(1)–P(1)–C(17) 118.3(3), C(11)–P(1)–C(17) 110.0(2).

in **6**, and this was also borne out when comparing the DFT-optimised structures (ESI†). In contrast to complex **6**, **7** is not stable in CD$_2$Cl$_2$ solution, decomposing fully after approximately 24 hours to form a mixture, from which the major component could be characterised spectroscopically as [RhCp*(H)(PCy$_2$H)(PMe$_3$)][BAr$^F{}_4$] **8**, *i.e.* the analogue of **5**. This low temperature instability to P–B cleavage can be contrasted with **6**, that only decomposes upon heating. P–B bond cleavage in phosphine–borane complexes has previously been noted to be a function of both the electron withdrawing nature and the steric bulk of the P-substituents, the latter suggested to be dominating here.[3,20]

Stoichiometric reactivity of H$_3$B·P^{t}Bu$_2$H

One equivalent of H$_3$B·P^{t}Bu$_2$H was added to complex **1** to explore further the effect of increasing the steric bulk at the phosphorus center. After mixing, the yellow solution rapidly turned dark red and effervescence was observed. Over the course of two hours at 298 K this intense colour was lost to give a yellow/orange solution. Analysis by ^{31}P{^{1}H} NMR spectroscopy of this final solution showed two broad peaks at δ 54.8 and −7.8, alongside minor unidentified species. The ^{1}H NMR spectrum showed two resonances in the hydride region at δ −10.79 and −13.76 (the former being considerably broader but sharpened on decoupling ^{11}B) which, in contrast to **6** and **7**, suggest the presence of both Rh–H–B and Rh–H groups respectively. A broad peak at δ 0.50 (BH, integral 1H) was also observed, in addition to phosphine and Cp* resonances. Moreover the ^{11}B{^{1}H} NMR spectrum revealed a broad virtual triplet at δ −45.4 [*J*(BP) ≈ 95 Hz] suggestive of coupling to two phosphorus centres. The structure of this new species was resolved by a single-crystal X-ray diffraction study (Fig. 3) to be [RhCp*(H)(P^{t}Bu$_2$BH$_2$·PMe$_3$)][BAr$^F{}_4$] **9**, in which the PMe$_3$ ligand has migrated to the boron centre to afford a Lewis-base stabilised phosphino-borane, chelating to the rhodium centre through P^{t}Bu$_2$ and a β-B-agostic interaction. The P^{t}Bu$_2$ unit is disordered over two sites meaning that the P–B bond metrics cannot be discussed in detail, but it is similar to those observed in the phosphido-borane species **6** and **7**, suggesting a single P–B bond. DFT calculations on **9** provide optimised P(1A)–B(1) and P(2)–B(1) distances of 1.95 Å and 1.96 Å, respectively, consistent with single bond character. Lewis-base stabilised phosphino-boranes were first synthesised by Burg in 1978,[33] and have recently been used by Scheer and coworkers to form metal complexes[16,31,33] that can also undergo P–B coupling reactions.[32] Similar phosphine ligand migration to a boron centre in a transient phosphino-borane has been previously proposed in the formation of [Rh(PPh$_3$)$_2$(PPh$_2$BH$_2$·PPh$_3$)][BAr$^F{}_4$][36] which also has a Lewis base-stabilised phosphino-borane with a β-B-agostic interaction to the Rh(I) centre [Rh–B: 2.407(5); B–P: 1.915(5), 1.945(5) Å].

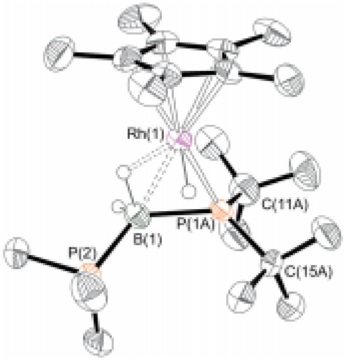

Fig. 3 X-ray molecular structure of (9). The P^{t}Bu$_2$ unit is disordered over 2 sites, only the major component labelled, *i.e.* P(1A), C(11A), is shown. [BAr$^F{}_4$]$^-$ anion and selected hydrogen atoms omitted for clarity. Selected bond lengths (Å) and angles (°): P(1A)–B(1) 1.99(2), P(1B)–B(1) 1.901(14), B(1)–P(2) 1.918(5), Rh(1)–P(1A) 2.30(3), Rh(1)–P(1B) 2.258(14), Rh(1)–B(1) 2.431(5), Rh(1)–Cp* (centroid) 1.870; P(1A)–B(1)–P(2) 126.2(7).

A low temperature NMR spectroscopy study was performed to help elucidate the mechanism by which **9** is formed, and in particular the identity of the observed dark red intermediate. CD$_2$Cl$_2$ solutions of H$_3$B·P^{t}Bu$_2$H and **1** were combined at −78 °C to form a yellow solution after mixing. After loading into a precooled NMR spectrometer the ^{31}P{^{1}H} NMR spectrum at −80 °C showed a new species by a sharp doublet δ 8.3 and a broad signal δ 35.4, consistent with Rh–PMe$_3$ and H$_3$B·PR$_2$H environments respectively. The ^{1}H NMR spectrum was more revealing with a very broad upfield peak observed at δ −4.01 (3H relative integral) consistent with a Rh···H$_3$B unit. A broad signal was also observed at δ 0.79 (3H relative integral), assigned to Rh–Me. The P–H bond is still intact, as shown by a doublet at δ 4.08 [*J*(HP) = 363 Hz] which collapsed to a singlet on ^{31}P decoupling. These data suggest that this species is an η^1-sigma complex with the bound dichloromethane molecule of **1** replaced by the phosphine–borane to form [RhCp*Me(PMe$_3$)(η^1-H$_3$B·P^{t}Bu$_2$H)][BAr$^F{}_4$], **10**, Scheme 9 That only one B–H environment is observed, even at −80 °C, suggests rapid terminal/bridging B–H exchange on the NMR timescale. η^1-Sigma binding with a variety of metal-ligand fragments has been observed for both phosphine- and amine–boranes, with

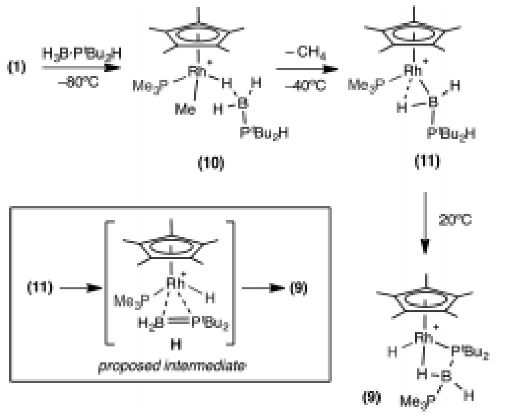

Scheme 9 Formation of complex (9). Observed and proposed intermediates. $[BAr^F_4]^-$ anions are not shown.

low–energy exchange between bridging and terminal B–H sites observed on the NMR timescale.[57–60] The $^{11}B\{^1H\}$ NMR spectrum shows a chemical shift at δ −44.8, characteristic[61] of an η^1-M···$H_3B\cdot PR_3$ interaction, being barely shifted from free phosphine–borane (δ −42.9).

When this solution was warmed to −40 °C inside the spectrometer after approximately one hour a new species, **11**, was formed at the expense of complex **10**. The $^{31}P\{^1H\}$ NMR spectrum showed two new resonances at δ 25.1 and −1.9, as a broad peak and a sharp doublet respectively. The ^1H NMR spectrum revealed the disappearance of the Rh–Me signal with concomitant appearance of dissolved CH_4 (δ 0.15).[58] Two broad peaks (both 1H relative integral) at δ 7.1 and δ −12.76 [d, *J* (RhH) = 38 Hz] were observed, both of which sharpen on decoupling ^{11}B, and a doublet of multiplets at δ 4.68 [*J* (RhP) 380 Hz], consistent with a P–H group. In the $^{11}B\{^1H\}$ NMR spectrum there is a peak at δ 47.6, downfield shifted by 92.4 ppm compared to **10**. These data suggest that **11** corresponds to a base-stabilized boryl complex, $[RhCp^*(PMe_3)(H_2B\cdot P^tBu_2H)][BAr^F_4]$, featuring a strong α-B-agostic interaction, as the two, now diastereotopic, B–H groups do not undergo exchange.

As far as we are aware there is only one other reported base-stabilised α-B-agostic boryl complex, albeit featuring a dimeric motif,[62] although examples that may be described as having α-B-agostic amino-boryl limiting structures have been discussed.[63,64] DFT calculations on the dehydrogenation of $H_3B\cdot NMe_2H$ using the $\{Ir(PCy_3)_2(H)_2\}^+$ fragment suggest intermediates with structures closely related to **11**.[65] Similar B–H activation and elimination of methane (under photolytic conditions) has been reported by Shimoi and co-workers to form $M(\eta^5\text{-}C_5R_5)(CO)_n(BH_2\cdot PMe_3)$ [n = 2, M = Mn; n = 3 W, Mo, R = H, Me] from the corresponding metal methyl precursors.[66,67] Interestingly these, and other closely related complexes,[68,69] only show small (*ca.* 13 ppm) downfield shifts, when compared to free $H_3B\cdot PMe_3$, on formation of the boryl moiety, in contrast to the *ca.* 92 ppm shift observed between **10** and **11**. In fact the ^{11}B chemical shift is more similar to complexes featuring 3-coordinate boron (*e.g.* δ 30–50).[61,70–72] The ^1H NMR spectrum of **11** shows a large *J* (RhH) coupling in the low field hydride-like signal [*J* (RhH) 38 Hz], whereas in complexes **6** and **7** no such coupling is observed. Moreover the other BH group resonates at rather low field (δ 7.11), compared with **6** (δ 0.49 and −0.03). In comparison, Shimoi's $M(\eta^5\text{-}C_5R_5)(CO)_n(BH_2\cdot PMe_3)$ species (which do not feature an α-B-agostic interaction) exhibit BH chemical shifts around 1.5,[66] whereas hydrido-amino-boryls $Ir(PMe_3)_2(H)Cl\{B(H)(NCy_2)\}$[70] and $[Rh(\kappa^3\text{-}_{P,O,P}\text{-xantphos})(H)\{B(H)(N^iPr_2)\}(NCMe)][BAr^F_4]$[71] (featuring 3-coordinate boron) show B–H and ^{11}B chemical shifts more like **11** [$\delta(^{11}B)$ 43, 49 respectively]. These data suggest that complex **11** could also be described as a hydrido base–stabilised borylene complex, at least in a limiting form. However, it is also possible that a tight α-B-agostic interaction could induce a downfield shift in the ^{11}B NMR spectrum, similar to α-C-agostic interactions probed by ^{13}C NMR spectroscopy.[73]

In an attempt to resolve this structural ambiguity, dark red single crystals of **11** were grown at −20 °C, however the resulting structure was of poor quality and only showed the connectivity of the heavy atoms that demonstrate a Rh–B interaction (see ESI†). Instead both limiting forms were characterized *via* DFT calculations which revealed the α-B-agostic boryl (**11**) to lie 2.1 kcal mol^{-1} below the hydrido base-stabilised borylene complex (**11′**, see Fig. 4).[74,75] This preference was reproduced with a range of other functionals. A third form, **11″**, featuring an agostic interaction with one ^{t}Bu C–H bond was also located and was 5.4 kcal mol^{-1} above **11** (see ESI†). Computed barriers suggest rapid interconversion between all three species, with **11** being the dominant species in solution. The computed structure of **11** exhibits a strong α-B-agostic interaction, with a short RhL–H^1 contact of 1.79 Å and significant elongation of the B^1–H^1 bond (1.35 Å) compared to the terminal B^1–H^2 bond (1.22 Å). Further

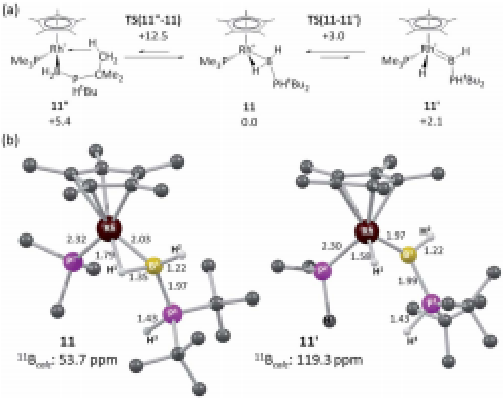

Fig. 4 (a) Computed isomers and interconversions of $[RhCp^*(PMe_3)(H_2B\text{-}PH^tBu_2)]^+$; (b) computed structures of α-B-agostic boryl complex **11** and hydrido base-stabilised borylene complex, **11′**. Selected distances are in Å and C-bound H atoms are omitted for clarity. Free energies are quoted relative to **11** set to 0.0 kcal mol^{-1} and are at the BP86-D3 (CH_2Cl_2) level; computed ^{11}B chemical shifts are at the B3LYP(BS2)//BP86(BS1) level (see ESI for full details).†

support for the α-B-agostic assignment was seen in the computed ^{11}B chemical shifts, the value for **11** (δ 53.7 ppm) being both in good absolute agreement with experiment (δ 47.6) and significantly better than that computed for **11′** (δ 119.3 ppm).

Removal of the NMR tube from the spectrometer while at low temperature showed complex **11** to be responsible for the intermediate deep red colour observed. Warming to room temperature over two hours produced the yellow/orange solution in which **9** was the major product (Scheme 9). The formation of complex **9** was signalled in the ^{11}B NMR spectrum by a dramatic upfield shift to δ −45.4 (computed value = −49.1). Complex **9** forms from **11** by P–H activation and migration of the PMe_3 ligand to the boron centre. We suggest that this may occur *via* a phosphino-borane intermediate (**H**, Scheme 9) that then undergoes intramolecular attack by PMe_3. A structural analogue of **H** has been reported by Bourissou and co-workers in $[Cy_2PB(C_6F_5)_2Pt(PMe_3)_2]$.[76]

DFT calculations were employed to assess this proposed mechanism and the results are summarised in Fig. 5 (which also presents data for the analogous reaction of $H_3B\cdot PHPh_2$ that will be discussed below). Starting from species **10** (set to 0.0 kcal mol^{-1}) B–H activation involves a sigma-CAM process[21] *via* **TS(10-11″)** (G = +14.1 kcal mol^{-1}) to generate intermediate **Int(10-11″)** (G = +6.9 kcal mol^{-1}) featuring both phosphine-stabilised boryl and methane ligands. **TS(10-11″)** exhibits a short Rh–H^3 distance of 1.61 Å, indicative of significant Rh(V) character at this point (see Fig. 6(a) which also gives the labelling scheme employed). Facile loss of CH_4 initially yields the C–H agostic species **11″** (G = −1.6 kcal mol^{-1}) which readily isomerizes to **11** at −7.0 kcal mol^{-1}.

The onward reaction of **11** requires an initial rearrangement back to **11″**. This proves to be necessary as it swaps the strong α-B-agostic interaction in **11** for a weak C–H agostic in **11″** which then allows the transfer of H^4 from P^1 to Rh *via* **TS(11″-9′)1** (G = +17.2 kcal mol^{-1}). The intermediate generated, **Int(11″-9′)** (G = −4.0 kcal mol^{-1}, Fig. 6(b)), features a $\{^tBu_2PBH_2\}$ phosphinoborane moiety and is equivalent to the postulated intermediate **H** of Scheme 8. **Int(11″-9′)** exhibits a P^1–B^1 distance of 1.89 Å, lying between the computed B–P distances of H_3B–P^tBu_2H (1.96 Å) and $H_2B{=}P^tBu_2$ (1.83 Å), see ESI.† This suggests a degree of back-bonding from the metal to the phosphinoborane, but perhaps less than is implied in $[Cy_2PB(C_6F_5)_2Pt(PMe_3)_2]$,[76] for which a P–B distance of 1.917(3) Å has been determined crystallographically. It is also notable that the hydride and $\{BH_2\}$ unit in **Int(11″-9′)** are orientated *trans*, while the PMe_3 and BH_2 are *cis*. Thus B^1–P^2 coupling can occur *via* **TS(11″-9′)2** with a modest barrier of only +11.7 kcal mol^{-1} to give **9′**, which is related to the observed species **9** (G = −16.9 kcal mol^{-1}) *via* rotation about the new B–PMe_3 bond. The overall barrier for the formation of **9** from **11** is 24.2 kcal mol^{-1}, and so is somewhat higher than that for the formation of **11** from **10** (14.1 kcal mol^{-1}). These relative barriers are qualitatively consistent with the rapid formation of **11** at low temperature, compared to the onwards slower generation of **9** (room temperature, 2 hours). The higher barrier for P–H activation (from **11**), compared to the initial B–H activation (from **10**) is also consistent with previous experimental and computational studies on related amine–borane chemistry,[65,77] and for $H_3B\cdot P^tBu_2H$ dehydrocoupling using the $[Rh(Ph_2P(CH_2)_3PPh_2)]^+$ fragment.[79]

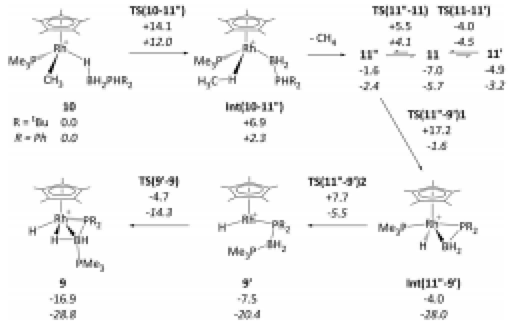

Fig. 5 Computed free energy reaction profile (kcal mol^{-1}, BP86-D3 (CH_2Cl_2) level) for formation of **9** from **10** (R = ^{t}Bu) with equivalent data for R = Ph provided in italics. All free energies are quoted relative to **10** + free H_3B-PHR_2 at 0.0 kcal mol^{-1}; see Fig. 4 for details of species **11**, **11′** and **11″** when R = ^{t}Bu.

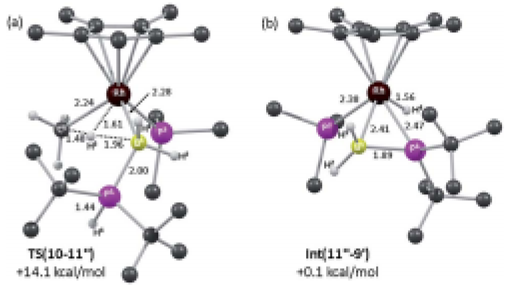

Fig. 6 Computed structures and free energies (BP86-D3 (CH_2Cl_2)) for (a) TS(10-11″) and (b) Int(11″-9′); selected distances are in Å and C-bound H atoms are omitted for clarity.

Reactions with H_3BPCy_3

In an attempt to produce a stable boryl complex, $H_3B\cdot PCy_3$ was reacted with **1** in the anticipation that the lack of a P–H group would stop onward reactivity. Reaction formed a deep red phosphine–boryl complex which was characterised spectroscopically as $[RhCp^*(PMe_3)(H_2B\cdot PCy_3)][BAr^F_4]$, **12**, which was stable at room temperature for 4 hours before any decomposition (to unidentified products) was observed (Scheme 10). The NMR spectra of complex **12** are very similar to **11**. In particular in the ^1H NMR spectrum a broad upfield peak at δ −13.57 is observed,[78] along with the characteristic downfield shift of the ^{11}B NMR resonance (δ 53.0). Attempts to crystallise **12** resulted in intractable oils. Addition of H_2 (4 atm) to **12** resulted in loss of the deep red colour to form an orange/brown solution, which was characterised spectroscopically as $[RhCp^*H(PMe_3)(H_3B\cdot PCy_3)][BAr^F_4]$, **13**. ^{11}B NMR spectroscopy at room

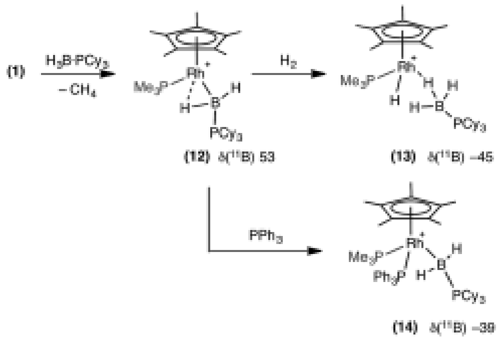

Scheme 10 Spectroscopically observed boryl complex (12) and reactivity with H_2 and PPh_3. $[BAr^F{}_4]^-$ anions are not shown.

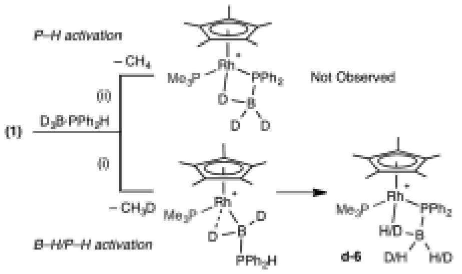

Scheme 11 D-labelling experiments.

temperature revealed a considerable upfield shift in the ^{11}B NMR shift in which the boryl signal had been replaced by one at δ −45.6, characteristic of a σ-phosphine–borane. In the ^1H NMR spectrum (under a H_2 atmosphere) one very broad upfield signal was observed at δ −4.14. Cooling to −60 °C resolved this into a quadrupolar broadened peak at δ −4.07 (relative integral 3H), assigned to a $Rh\cdots H_3B$ unit, and a sharp doublet of doublets at δ −11.53 (integral 1H), assigned to Rh–H. These are exchanging at room temperature, and we suggest that the mechanism for this is likely be through a boryl-dihydrogen complex $[RhCp^*(PMe_3)(H_2B\cdot PCy_3)(H_2)][BAr^F{}_4]$, operating *via* a sigma-CAM mechanism.[21] Addition of PPh_3 to **12** results in a loss of the high-field signal, and the appearance of two signals at δ 2.42 and 0.23 in the $^1H\{^{11}B\}$ NMR spectrum assigned to $RhB\mathit{H}_2PCy_3$. Furthermore the ^{11}B NMR spectrum shows a significant upfield shift to δ −39.5, consistent with previously reported, non-α-B-agostic, base-stabilised boryls.[66–69] These, and associated $^{31}P\{^1H\}$ NMR data, signal the formation of complex **14**: $[RhCp^*(PMe_3)(PPh_3)(H_2B\cdot PCy_3)][BAr^F{}_4]$.

D-labelling experiments

The observation of the α-B-agostic boryl intermediate **11** en route to complex **9** led us to speculate upon the mechanism of formation of the phosphido-borane species **6** (and **7**), and whether Ph- and Cy-analogues of **11** are intermediates in the formation of these species from **1** and the corresponding phosphine–borane. To probe this $D_3B\cdot PHPh_2$ was added to **1**. Two scenarios follow: (i) B–D activation followed by P–H activation would lead to a $\{HD_2BPR_2\}$ unit in the final product and the release of CH_3D, or (ii) initial P–H activation would result in liberation of CH_4 and no incorporation of ^1H into the borane (Scheme 11). ^{31}P and ^{11}B NMR spectroscopy confirmed clean formation of the phosphido-borane product; while ^1H and ^2H NMR spectroscopy (ESI†) showed H and D in all positions of the β-B-agostic borane, with an overall relative integral of 1H measured from the ^1H NMR spectrum indicating a H : D ratio of 1 : 2. This suggests route (i) is operating, as observed spectroscopically for complex **11**. That ^1H signals are observed in all 3 B–H positions of the final product **d-6** suggests slow exchange between terminal and bridging positions which was confirmed by a spin saturation ^1H NMR exchange experiment.[70] CH_3D is observed [δ 0.19, t, *J* (HD) 2.0 Hz, CD_2Cl_2], that disappears on degassing the solution.

The observation of a phosphido-borane complex $[RhCp^*(PR_2\cdot BH_3)(PMe_3)]^+$ when R = Ph (**6**) and Cy (**7**) is in sharp contrast to the formation of $[RhCp^*(H)(PR_2\cdot BH_2\cdot PMe_3)]^+$ when R = ^tBu (**9**). The above labelling studies (R = Ph) and calculations (R = ^tBu and Ph, Fig. 5) are all consistent with initial B–H activation to form $[RhCp^*(H_2B\cdot PHR_2)(PMe_3)]^+$, $\mathbf{11_R}$, as a common intermediate. Fig. 5 also indicates that the reaction profile for the formation of $\mathbf{9_{Ph}}$ from $\mathbf{11_{Ph}}$ would follow a similar course to the ^tBu system, although significantly different energetics are seen around the β-H transfer step from $\mathbf{11''_R}$, which has a much lower barrier and is far more exergonic when R = Ph. The onward reactivities of the resultant phosphino-borane intermediates $\mathbf{Int(11''\text{-}9')_R}$ are compared in Fig. 7. The stability of $\mathbf{Int(11''\text{-}9')_{Ph}}$ (G = −28.0 kcal mol^{-1}) means the subsequent P–B coupling step towards $\mathbf{9_{Ph}}$ encounters a significant barrier of 22.5 kcal mol^{-1} *via* $\mathbf{TS(11''\text{-}9')2_{Ph}}$ at −5.5 kcal mol^{-1}. Alternatively, we found that the phosphino-borane ligand in $\mathbf{Int(11''\text{-}9')_{Ph}}$ can undergo a two-step rotation that leads directly to $\mathbf{6_{Ph}}$. This process involves first a transition state $\mathbf{TS(11''\text{-}6)2_{Ph}}$ at −12.7 kcal mol^{-1} which leads to an intermediate in which the phosphino-borane ligand lies parallel to the Rh–Cp* (centroid) direction with the $\{BH_2\}$ moiety adjacent to the Cp* ring ($\mathbf{Int(11''\text{-}6)2_{Ph}}$, G = −17.4 kcal mol^{-1}). The rotation is completed *via* a transition state at −15.9 kcal mol^{-1} and this second step was also found to be coupled to B–H bond formation involving the Rh–H ligand, resulting in the formation of $\mathbf{6_{Ph}}$. Note that for clarity only the energy of $\mathbf{TS(11''\text{-}6)2_{Ph}}$ (the highest point in the rotation process) is indicated in Fig. 7; full details are provided in the ESI.† Overall this rotation process is kinetically favoured over P–B bond coupling towards $\mathbf{9_{Ph}}$ by 7.2 kcal mol^{-1}; moreover the formation of $\mathbf{6_{Ph}}$ is also thermodynamically favoured over $\mathbf{9_{Ph}}$ by 6.5 kcal mol^{-1}.

In the light of these results phosphino-borane rotation in $\mathbf{Int(11''\text{-}9)2\mathit{t}_{Bu}}$ was also assessed and was found to proceed with a low overall barrier of 5.8 kcal mol^{-1}. This also involves two steps, although in this case the rotated phosphino-borane intermediate has the $\{P^tBu_2\}$ moiety adjacent to the Cp* ring. The resultant phosphido-borane, $\mathbf{6\mathit{t}_{Bu}}$, is located at −4.5 kcal mol^{-1} and so can readily revert to $\mathbf{Int(11''\text{-}9)2\mathit{t}_{Bu}}$ with a barrier

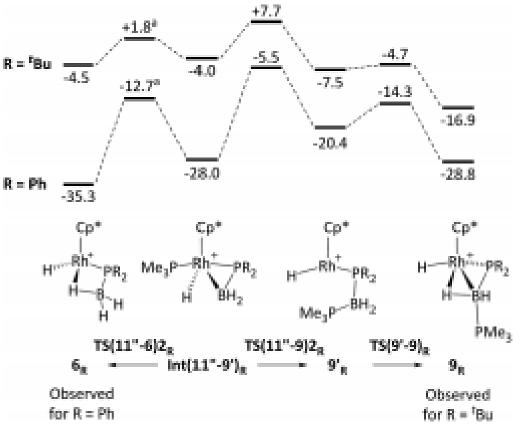

Fig. 7 Computed free energy reaction profiles (kcal mol^{-1}, BP86-D3 (DCM) level) for formation of $\mathbf{6_R}$ and $\mathbf{9_R}$ from phosphino-borane adducts $\mathbf{Int(11''\text{-}9')_R}$: (R = ᵗBu and Ph). All free energies are quoted relative to **10** set to 0.0 kcal mol^{-1}. ᵃAn intermediate corresponding to a *ca.* 90° rotation of the phosphino-borane ligand was located between $\mathbf{Int(11''\text{-}9')_R}$ and $\mathbf{6_R}$ and only the energy of the higher-lying transition state is indicated. See text and ESI† for full details.

of only 6.3 kcal mol^{-1}, from which it can access the competing P–B bond coupling *via* $\mathbf{TS(11''\text{-}9)2}t_{\mathbf{Bu}}$. The overall barrier for this (from $\mathbf{6}t_{\mathbf{Bu}}$) is therefore only 12.2 kcal mol^{-1} and leads to first $\mathbf{9'}t_{\mathbf{Bu}}$ and then $\mathbf{9}t_{\mathbf{Bu}}$ in processes that are both significantly exergonic. The calculations therefore suggest rapid, but reversible formation of $\mathbf{6}t_{\mathbf{Bu}}$ before the thermodynamically favoured pathway to $\mathbf{9}t_{\mathbf{Bu}}$ takes over.[80]

The differences in the reaction profiles when R = ᵗBu and Ph in Fig. 7 can be attributed to the greater steric encumbrance of the ᵗBu system. This is particularly apparent for $\mathbf{6}t_{\mathbf{Bu}}$, the formation of which is 31 kcal mol^{-1} less accessible than $\mathbf{6_{Ph}}$. The combination of the steric bulk derived from both the ᵗBu substituents and the Cp* ligands is important in this: thus with $H_3B\cdot PMe_2H$ (*i.e.* exchanging Me for ᵗBu) the formation of $\mathbf{6_{Me}}$ becomes exergonic by 17.5 kcal mol^{-1}, while the equivalent reaction of $[RhCp(Me)(H_3B\cdot P^tBu_2H)(PMe_3)]^+$ (*i.e.* retaining the ᵗBu substituents but exchanging Cp for Cp*) is downhill by 27.6 kcal mol^{-1}. Similar arguments explain the greater relative stability of $\mathbf{9_{Ph}}$ over $\mathbf{9}t_{\mathbf{Bu}}$. In these systems, however, a PMe_3 ligand has migrated from Rh onto B to be replaced by a much smaller hydride. The accumulative steric effect around the metal is therefore much less significant meaning that $\mathbf{9}t_{\mathbf{Bu}}$ is only 11.9 kcal mol^{-1} less accessible than $\mathbf{9_{Ph}}$; moreover, the formation of $\mathbf{9}t_{\mathbf{Bu}}$ becomes thermodynamically viable. Calculations also show that $H_3B\cdot PHCy_2$ follows the pattern of behaviour computed for $H_3B\cdot PHPh_2$, consistent with the observed formation of **7** in this case (see ESI† for full details).

Comments on mechanism of dehydropolymerization of $H_3B\cdot PRH_2$

These studies suggest that the two likely limiting mechanisms for dehydropolymerization of $H_3B\cdot PPhH_2$, step-growth-like *via* reversible chain transfer or coordination chain-growth, both likely flow from a common phosphido-borane intermediate (**I**, Scheme 12) that is an analogue of complex **6**. Stoichiometric, labelling and computational studies on secondary phosphine–borane systems suggest that such a species is likely formed from initial B–H activation of a phosphine-borane, followed by P–H transfer and rearrangement of a resultant hydrido phosphino-borane intermediate, modelled in this study as $\mathbf{Int(11''\text{-}9')}$.

The observation of significant amounts of oligomer **2** at short reaction times, alongside the rapid consumption of $H_3B\cdot PPhH_2$, point to reversible chain transfer (Scheme 12B) as a likely mechanism. That M_n is essentially unchanged with catalyst loading suggests this mechanism could be further modified by (observed) increasingly more P–B cleavage of the polymer at higher catalyst loadings. Based on our observations a coordination chain growth mechanism (Scheme 12C) appears less likely; as $H_3B\cdot PPhH_2$ would be expected to be consumed gradually throughout the whole polymerization, **2** should not form in significant quantities, and M_n should increase with decreased catalyst loadings. If chain growth was occuring, slow propagation and faster termination/chain transfer steps would be required to account for our observations. We cannot discount a scenario where both mechanisms operate in ensemble, or there is a change from reversible chain transfer (step growth) to chain growth at lower $[H_3B\cdot PPhH_2]$/higher [oligomer]. Related dual mechanisms have been discussed before with regard to polymer growth kinetics.[81,82]

The contrast with Manners' $FeCp(CO)_2(OTf)$ system is interesting,[8] as this shows coordination chain-growth-type polymerisation kinetics. We currently do not have a clear reason why this would be, although cationic Rh *versus* neutral Fe, and PR_3 *versus* CO ligands, are obvious electronic differences. Common to both Rh and Fe systems is the implication of β-B-agostic phosphido-borane complexes of the type $[MCp(L)(PRHBH_3)]^{n+}$, and we thus suggest that such species, as well as precursor metal-bound phosphino-boranes such as $[MCp(L)(H)(PRHBH_2)]^{n+}$, play a role in dehydropolymerization.

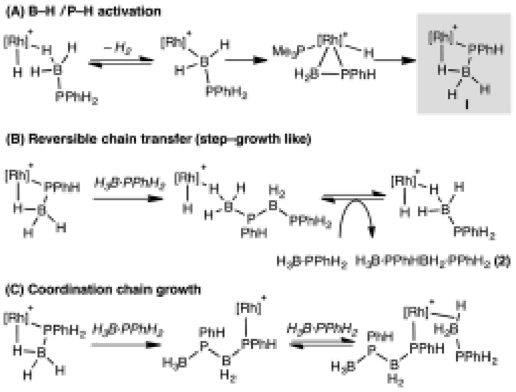

Scheme 12 Suggested mechanisms for dehydropolymerization. [Rh] = Rh(PR_3)Cp* (PR_3 = PMe_3 or $PPhH_2$).

Scheme 13 Manners and co-workers observations on polymer molecular weight and P–R substituent.

As shown here the reactivity of such phosphino-borane intermediates is dependent on the steric bulk at phosphorus: for R = Ph phosphido-boranes are favoured thermodynamically, whereas for bulkier R = ^{t}Bu this is the kinetic product, and the thermodynamic product arises from transfer of a metal bound ancillary ligand (PMe_3) to the phosphino-borane. In this regard it is interesting to compare the differences in reported dehydropolymerization efficacy for $FeCp(CO)_2(OTf)$.[5,16] For $H_3B \cdot PPhH_2$ high molecular weight polymer is formed (M_n 59 000 g mol^{-1} in 24 h), whereas for $H_3B \cdot P^tBuH_2$ only short chain oligomers $[H_2BP^tBuH]_x$ ($x < 10$) are formed after 172 h. Given our observations presented here we speculate that this may be due to deactivation routes that are modelled by complexes such as **9** when R = ^{t}Bu (Scheme 13), that in turn arise from differing reactivity pathways of the corresponding phosphino-boranes.

Conclusions

By choosing a system that can produce well-defined, moderate molecular weight, poly-$[H_2BPPhH]_n$, and is also designed to be latent low-coordinate, the intimate details of initial phosphine–borane activation in dehydropolymerization can be studied. Studies on model systems with secondary phosphine–boranes show that B–H activation precedes P–H activation, to give the kinetic product of a base-stabilised α-B-agostic boryl complex, subsequent P–H transfer, that operates *via* a hydrido-phosphino-borane species, leads to the observed phosphido-borane as the thermodynamic product. Together these three species offer many possibilities for pathways operating during dehydropolymerization.

Given the ambiguity related to the mechanism of dehydropolymerisation (step or chain growth-like) in this system we are reluctant to say definitively which mechanism is operating, but our general observations are consistent with those recently proposed mechanisms operating for $FeCp(CO)_2(OTf)$ and $[Rh(Ph_2P(CH_2)_3PPh_2)]^+$,[5,19] in as much that the proposed species that undergo the P–B bond forming event have M–P bonds (*i.e.* phosphido-boranes). Moreover, given that boryl, phosphino-borane and phosphido-boranes are all accessible they should all be considered as viable intermediates in catalytic dehydrocoupling and dehydropolymerization processes. This work also lends insight into related amine–borane dehydropolymerization in which amido–boranes, structurally related to **6** have been proposed as actual catalysts, and proposed to form *via* a N–H activation from a sigma-amine borane precursor,[11,63] similar to that described in detail here for phosphido-boranes. The ubiquity of B-agostic interactions in the systems discussed here, whether α- or β-, also shows that such interactions also need to be explicitly considered when discussing the mechanism of dehydropolymerization. This mirrors olefin polymerisation, in which α- and β-agostic interactions play key roles in migratory insertion and polymerization processes.[64,65] Such detail makes a further step towards fully understanding the mechanisms of group 13/15 dehydropolymerizations, and thus the further development of catalysts that can deliver tailored new polymeric materials.[2]

Acknowledgements

The EPSRC for funding through EP/J02127X (ASW, TNH) and, with Heriot-Watt University, for a DTP studentship (NAB). Professor Ian Manners and Dr Titel Jurca (University of Bristol) for GPC analysis and useful discussions.

Notes and references

1 T. Chivers and I. Manners, *Inorganic Rings and Polymers of the p-Block Elements: From Fundamentals to Applications*, Royal Soc. Chem., Cambridge, 2009.
2 E. M. Leitao, T. Jurca and I. Manners, *Nat. Chem.*, 2013, **5**, 817.
3 A. Staubitz, A. P. M. Robertson, M. E. Sloan and I. Manners, *Chem. Rev.*, 2010, **110**, 4023.
4 T. J. Clark, K. Lee and I. Manners, *Chem. - Eur. J.*, 2006, **12**, 8634.
5 A. Schäfer, T. Jurca, J. Turner, J. R. Vance, K. Lee, V. A. Du, M. F. Haddow, G. R. Whittell and I. Manners, *Angew. Chem., Int. Ed.*, 2015, **54**, 4836.
6 A. B. Burg and R. I. Wagner, *J. Am. Chem. Soc.*, 1953, **75**, 3872.
7 H. Dorn, R. A. Singh, J. A. Massey, A. J. Lough and I. Manners, *Angew. Chem., Int. Ed.*, 1999, **38**, 3321.
8 H. Dorn, R. A. Singh, J. A. Massey, J. M. Nelson, C. A. Jaska, A. J. Lough and I. Manners, *J. Am. Chem. Soc.*, 2000, **122**, 6669.
9 H. Dorn, E. Vejzovic, A. J. Lough and I. Manners, *Inorg. Chem.*, 2001, **40**, 4327.
10 T. L. Clark, J. M. Rodezno, S. B. Clendenning, S. Aouba, P. M. Brodersen, A. J. Lough, H. E. Ruda and I. Manners, *Chem. - Eur. J.*, 2005, **11**, 4526.
11 S. Pandey, P. Lönnecke and E. Hey-Hawkins, *Inorg. Chem.*, 2014, **53**, 8242.
12 S. Pandey, P. Lönnecke and E. Hey-Hawkins, *Eur. J. Inorg. Chem.*, 2014, 2456.
13 C. A. Jaska and I. Manners, *J. Am. Chem. Soc.*, 2004, **126**, 1334.
14 C. A. Jaska and I. Manners, *J. Am. Chem. Soc.*, 2004, **126**, 9776.
15 H. C. Johnson, T. N. Hooper and A. S. Weller, *Top. Organomet. Chem.*, 2015, **49**, 153.
16 C. Marquardt, T. Jurca, K.-C. Schwan, A. Stauber, A. V. Virovets, G. R. Whittell, I. Manners and M. Scheer, *Angew. Chem., Int. Ed.*, 2015, **54**, 13782.
17 M. A. Huertos and A. S. Weller, *Chem. Commun.*, 2012, **48**, 7185.
18 D. J. Grant and D. A. Dixon, *J. Phys. Chem. A*, 2006, **110**, 12955.
19 M. A. Huertos and A. S. Weller, *Chem. Sci.*, 2013, **4**, 1881.

20 T. N. Hooper, M. A. Huertos, T. Jurca, S. D. Pike, A. S. Weller and I. Manners, *Inorg. Chem.*, 2014, **53**, 3716.
21 R. N. Perutz and S. Sabo-Etienne, *Angew. Chem., Int. Ed.*, 2007, **46**, 2578.
22 R. Waterman, *Organometallics*, 2013, **32**, 7249.
23 F. L. Taw, H. Mellows, P. S. White, F. J. Hollander, R. G. Bergman, M. Brookhart and D. M. Heinekey, *J. Am. Chem. Soc.*, 2002, **124**, 5100.
24 B. K. Corkey, F. L. Taw, R. G. Bergman and M. Brookhart, *Polyhedron*, 2004, **23**, 2943.
25 A. H. Roy, C. P. Lenges and M. Brookhart, *J. Am. Chem. Soc.*, 2007, **129**, 2082.
26 J. F. Hartwig, K. S. Cook, M. Hapke, C. D. Incarvito, Y. Fan, C. E. Webster and M. B. Hall, *J. Am. Chem. Soc.*, 2005, **127**, 2538.
27 V. P. W. Böhm and M. Brookhart, *Angew. Chem., Int. Ed.*, 2001, **40**, 4694.
28 F. Wang and X. Li, *J. Am. Chem. Soc.*, 2012, **134**, 3651.
29 H. Dorn, J. M. Rodezno, B. Brunnhöfer, E. Rivard, J. A. Massey and I. Manners, *Macromolecules*, 2003, **36**, 291.
30 A. H. Cowley and M. C. Damasco, *J. Am. Chem. Soc.*, 1971, **93**, 6815.
31 H. C. Johnson, E. M. Leitao, G. R. Whittell, I. Manners, G. C. Lloyd-Jones and A. S. Weller, *J. Am. Chem. Soc.*, 2014, **136**, 9078.
32 A. Staubitz, M. E. Sloan, A. P. M. Robertson, A. Friedrich, S. Schneider, P. J. Gates, J Schmedt auf der Günne and I. Manners, *J. Am. Chem. Soc.*, 2010, **132**, 13332.
33 A. P. M. Robertson, E. M. Leitao, T. Jurca, M. F. Haddow, H. Helten, G. C. Lloyd-Jones and I. Manners, *J. Am. Chem. Soc.*, 2013, **135**, 12670.
34 A. Kumar, H. C. Johnson, T. N. Hooper, A. S. Weller, A. G. Algarra and S. A. Macgregor, *Chem. Sci.*, 2014, **5**, 2546.
35 D. Michael, P. Mingos, P. C. Minshall, M. B. Hursthouse, K. M. A. Malik and S. D. Willoughby, *J. Organomet. Chem.*, 1979, **181**, 169.
36 Z.-J. Yao, X.-K. Huo and G.-X. Jin, *Chem. Commun.*, 2012, **48**, 6714.
37 A. T. Lubben, J. S. McIndoe and A. S. Weller, *Organometallics*, 2008, **27**, 3303.
38 G. R. Fulmer, A. J. M. Miller, N. H. Sherden, H. E. Gottlieb, A. Nudelman, B. M. Stoltz, J. E. Bercaw and K. I. Goldberg, *Organometallics*, 2010, **29**, 2176.
39 E. M. Pelczar, E. A. Nytko, M. A. Zhuravel, J. M. Smith, D. S. Glueck, R. Sommer, C. D. Incarvito and A. L. Rheingold, *Polyhedron*, 2002, **21**, 2409.
40 R. T. Paine and H. Noeth, *Chem. Rev.*, 1995, **95**, 343.
41 J. A. Bailey and P. G. Pringle, *Coord. Chem. Rev.*, 2015, **297–298**, 77.
42 DFT calculations were performed with the Gaussian 03 and 09 suites and optimisations employed the BP86 functional. See ESI† for full details.
43 W. F. McNamara, E. N. Duesler, R. T. Paine, J. V. Ortiz, P. Koelle and H. Noeth, *Organometallics*, 1986, **5**, 380.
44 I. Amor, D. García-Vivó, M. E. García, M. A. Ruiz, D. Sáez, H. Hamidov and J. C. Jeffery, *Organometallics*, 2007, **26**, 466.
45 M. A. Alvarez, M. E. Garcia, R. Gonzalez and M. A. Ruiz, *Dalton Trans.*, 2012, **41**, 14498.
46 H. Helten, B. Dutta, J. R. Vance, M. E. Sloan, M. F. Haddow, S. Sproules, D. Collison, G. R. Whittell, G. C. Lloyd-Jones and I. Manners, *Angew. Chem., Int. Ed.*, 2013, **52**, 437.
47 M. S. Hill, M. Hodgson, D. J. Liptrot and M. F. Mahon, *Dalton Trans.*, 2011, **40**, 7783.
48 D. J. Liptrot, M. S. Hill, M. F. Mahon and D. J. MacDougall, *Chem. - Eur. J.*, 2010, **16**, 8508.
49 J. Spielmann, D. F. J. Piesik and S. Harder, *Chem. - Eur. J.*, 2010, **16**, 8307.
50 M. Brookhart and D. M. Lincoln, *J. Am. Chem. Soc.*, 1988, **110**, 8719.
51 U. Vogel, P. Hoemensch, K.-C. Schwan, A. Y. Timoshkin and M. Scheer, *Chem. - Eur. J.*, 2003, **9**, 515.
52 C. Thoms, C. Marquardt, A. Y. Timoshkin, M. Bodensteiner and M. Scheer, *Angew. Chem., Int. Ed.*, 2013, **52**, 5150.
53 K.-C. Schwan, A. Y. Timoskin, M. Zabel and M. Scheer, *Chem. - Eur. J.*, 2006, **12**, 4900.
54 B. Wrackmeyer, *Z. Naturforsch. (B)*, 2004, **59**, 1192.
55 A. B. Burg, *Inorg. Chem.*, 1978, **17**, 593.
56 T. A. Shuttleworth, M. A. Huertos, I. Pernik, R. D. Young and A. S. Weller, *Dalton Trans.*, 2013, **42**, 12917.
57 Y. Kawano, T. Yasue and M. Shimoi, *J. Am. Chem. Soc.*, 1999, **121**, 11744.
58 Y. Kawano, M. Hashiva and M. Shimoi, *Organometallics*, 2006, **25**, 4420.
59 H. C. Johnson, R. Torry–Harris, L. Ortega, R. Theron, J. S. McIndoe and A. S. Weller, *Catal. Sci. Technol.*, 2014, **4**, 3486.
60 H. C. Johnson, C. L. Mcmullin, S. D. Pike, S. A. Macgregor and A. S. Weller, *Angew. Chem., Int. Ed.*, 2013, **52**, 9776.
61 N. Merle, G. Koicok-Köhn, M. F. Mahon, C. G. Frost, G. D. Ruggerio, A. S. Weller and M. C. Willis, *Dalton Trans.*, 2004, 3883.
62 A. B. Chaplin and A. S. Weller, *Angew. Chem., Int. Ed.*, 2010, **49**, 581.
63 C. Y. Tang, A. L. Thompson and S. Aldridge, *J. Am. Chem. Soc.*, 2010, **132**, 10578.
64 G. Bénac-Lestrille, U. Helmstedt, L. Vendier, G. Alcaraz, E. Clot and S. Sabo-Etienne, *Inorg. Chem.*, 2011, **50**, 11039.
65 C. J. Stevens, R. Dallanegra, A. B. Chaplin, A. S. Weller, S. A. Macgregor, B. Ward, D. Mckay, G. Alcaraz and S. Sabo-Etienne, *Chem. - Eur. J.*, 2011, **17**, 3011.
66 T. Yasue, Y. Kawano and M. Shimoi, *Angew. Chem., Int. Ed.*, 2003, **42**, 1727.
67 Y. Kawano, T. Yasue and M. Shimoi, *J. Am. Chem. Soc.*, 1999, **121**, 1.
68 T. Yasue, Y. Kawano and M. Shimoi, *Chem. Lett.*, 2000, 58.
69 H. Nakazawa, M. Ohba and M. Itazaki, *Organometallics*, 2006, **25**, 2903.
70 M. O'Neill, D. A Addy, I. Riddlestone, M. Kelly, N. Phillips and S. Aldridge, *J. Am. Chem. Soc.*, 2011, **133**, 11500.
71 H. Braunschweig, K. Radacki, F. Seeler and G. R. Whittell, *Organometallics*, 2004, **23**, 4178.
72 G. Alcaraz and S. Sabo-Etienne, *Coord. Chem. Rev.*, 2008, **252**, 2395.

73 M. Etienne, *Organometallics*, 1994, **13**, 410.

74 H. Braunschweig, R. D. Dewhurst and V. H. Gessner, *Chem. Soc. Rev.*, 2013, **42**, 3197.

75 H. Braunschweig, K. Radacki, D. Rais and D. Scheschkewitz, *Angew. Chem., Int. Ed.*, 2005, **44**, 5651.

76 A. Amgoune, S. Ladeira, K. Miqueu and D. Bourissou, *J. Am. Chem. Soc.*, 2012, **134**, 6560.

77 T. M. Douglas, A. B. Chaplin, A. S. Weller, X. Yang and M. B. Hall, *J. Am. Chem. Soc.*, 2009, **131**, 15440.

78 We could not observe the corresponding B–H (terminal) signal for (**12**), and it may be obscured by the anion resonances, as the equivalent signal in (**11**) comes at δ 7.11.

79 The $^{1}H\{^{11}B\}$ spectra of complex **6**/**d-6** are suggestive of an isotopic perturbation of equilibrium. Relative integrals of the BH signals at 0.50 (BH), −0.02 (BH) and −10.80 (BH···Rh) ppm: **6**, 0.30 : 0.31 : 0.39; **d-6**, 0.26 : 0.25 : 0.49. This suggests a preference for Rh···H–B rather than Rh···D–B in **d-6**.

80 A process involving P–H activation with direct H-transfer onto B was also characterised but exhibited significantly higher barriers (see ESI†).

81 M. Mizutani, K. Satoh and M. Kamigaito, *J. Am. Chem. Soc.*, 2010, **132**, 7498.

82 L. You and J. Ling, *Macromolecules*, 2014, **47**, 2219.

83 R. T. Baker, J. C. Gordon, C. W. Hamilton, N. J. Henson, P.-H. Lin, S. Maguire, M. Murugesu, B. L. Scott and N. C. Smythe, *J. Am. Chem. Soc.*, 2012, **134**, 5598.

84 M. Brookhart, M. L. H. Green and G. Parkin, *Proc. Nat. Acad. Sci USA*, 2007, **104**, 6908.

85 M. Brookhart, A. F. Volpe, D. M. Lincoln, I. T. Horvath and J. M. Millar, *J. Am. Chem. Soc.*, 1990, **112**, 5634.

JACS JOURNAL OF THE AMERICAN CHEMICAL SOCIETY

Article

pubs.acs.org/JACS

Synthesis of Functionalized 1,4-Azaborinines by the Cyclization of Di-*tert*-butyliminoborane and Alkynes

Marius Schäfer,† Nicholas A. Beattie,‡ K. Geetharani,†,⊥ Julian Schäfer,§ William C. Ewing,† Mirjam Krahfuß,† Christian Hörl,† Rian D. Dewhurst,† Stuart A. Macgregor,*,‡ Christoph Lambert,*,§ and Holger Braunschweig*,†

†Institut für Anorganische Chemie, Julius-Maximilians-Universität Würzburg, Am Hubland, 97074 Würzburg, Germany
‡Institute of Chemical Sciences, Heriot-Watt University, Edinburgh EH14 4AS, U.K.
§Insitute für Organische Chemie, Julius-Maximilians-Universität Würzburg, Am Hubland, 97074 Würzburg, Germany

Supporting Information

ABSTRACT: Di-*tert*-butyliminoborane is found to be a very useful synthon for the synthesis of a variety of functionalized 1,4-azaborinines by the Rh-mediated cyclization of iminoboranes with alkynes. The reactions proceed via [2 + 2] cycloaddition of iminoboranes and alkynes in the presence of $[RhCl(PiPr_3)_2]_2$, which gives a rhodium η^4-1,2-azaborete complex that yields 1,4-azaborinines upon reaction with acetylene. This reaction is compatible with substrates containing more than one alkynyl unit, cleanly affording compounds containing multiple 1,4-azaborinines. The substitution of terminal alkynes for acetylene also led to 1,4-azaborinines, enabling ring substitution at a predetermined location. We report the first general synthesis of this new methodology, which provides highly regioselective access to valuable 1,4-azaborinines in moderate yields. A mechanistic rationale for this reaction is supported by DFT calculations, which show the observed regioselectivity to arise from steric effects in the B–C bond coupling en route to the rhodium η^4-1,2-azaborete complex and the selective oxidative cleavage of the B–N bond of the 1,2-azaborete ligand in its subsequent reaction with acetylene.

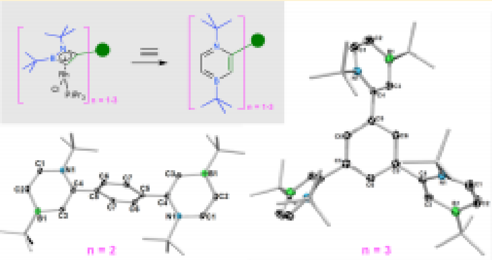

INTRODUCTION

BN/CC isosterism has attracted a great deal of attention in recent years because of the isoelectronic nature of BN and CC units in conventional organic compounds.[1] Benzene-like cyclics wherein two of the carbon atoms have been replaced by one boron and one nitrogen atom are known as azaborinines and have three isomeric forms: 1,2-, 1,3-, and 1,4-azaborinines. Of the three, 1,2-azaborinines have been known the longest, having been reported in the early 1960s by Dewar[2] and White.[3] Recent years have witnessed spectacular development in the chemistry of these compounds by the groups of Ashe,[4] Piers,[5] Yamaguchi,[6] Perepichka[7] and Liu,[8] extending the initial synthetic breakthroughs (the unsubstituted parent 1,2-dihydro-1,2-azaborinine was isolated only recently[9]) into more applied areas such as biomedical research and materials science. Comparatively little research has focused on the chemistry of 1,3- and 1,4-azaborinines[10,11] because of a lack of suitable methodologies for their syntheses.

The development of 1,4-azaborinines has been predominantly limited to polycyclic frameworks (Figure 1, top), such as the anthracene analogue first reported by Maitlis.[12] A few years later, the same anthracene core was synthesized by Clark via the reaction of *o*,*o*′-dilithiodiphenylmethylamine with $BF_3{\cdot}Et_2O$ followed by treatment with mesityllithium.[13] Kawashima and co-workers extended these systems, reporting the syntheses, optical properties, and reactivities of polycylic 1,4-azaborinines and related polycycles.[14] Though several approaches exist for

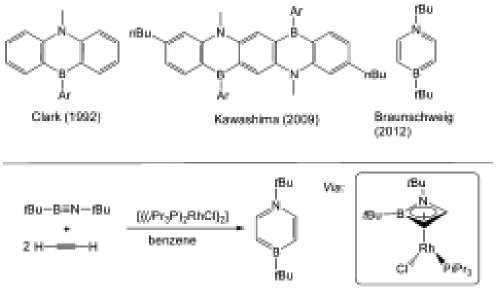

Figure 1. (top) Isolated 1,4-azaborinines. (bottom) Rh-mediated synthesis of a 1,4-azaborinine via a 1,2-azaborete complex.

Received: April 22, 2016
Published: June 10, 2016

ACS Publications

DOI: 10.1021/jacs.6b04128
J. Am. Chem. Soc. 2016, 138, 8212–8220

the syntheses of such polycyclic systems,[15] strategies for the syntheses of monocyclic derivatives have only recently been revealed. In 2012, we reported a new synthetic route to monocyclic 1,4-azaborinines through Rh-catalyzed cyclization reactions of alkynes and iminoboranes.[11] These reactions involve tandem [2 + 2]/[2 + 4] cycloaddition of the iminoborane *t*BuB≡N*t*Bu (**1**) with acetylene in a sequence involving rupture of the B≡N bond. We recently extended this approach, showing the system to be capable of selectively producing 1,2-azaborinines through simple variation of the alkyne.[16]

The isolation of a rhodium 1,2-azaborete complex from reactions leading to the formation of 1,4-azaborinines led us to envisage the use of this intermediate in the syntheses of a much wider range of functionalized materials with fine regiochemical control. In this paper we describe these efforts and likewise demonstrate the formation of unusual bis- and tris-1,4-azaborinines through judicious choice of the alkyne. In total, this work vastly extends the range of known compounds within this class of fascinating BN/CC isosteric aromatic structures.

■ RESULTS AND DISCUSSION

Synthesis of Phenyl and Ferrocenyl 1,4-Azaborinine Derivatives. The recent work on the catalytic pathways leading to functionalized 1,2-azaborinines led us to investigate the regioselectivity of this reaction in more detail, particularly using terminal alkynes. The phenyl-substituted 1,4-azaborinine **4** can be synthesized in moderate yield in two steps. The first is a stoichiometric reaction of iminoborane **1** and phenylacetylene in the presence of $[RhCl(PiPr_3)_2]_2$ (**2**), yielding the rhodium η^4-1,2-azaborete intermediate **3**. When this complex is then reacted with acetylene, 2-phenyl-1,4-azaborinine **4** is formed in moderate yield (Scheme 1). Compounds **3** and **4** were characterized by standard spectroscopic methods, and their solid-state structures were confirmed by single-crystal X-ray diffraction.

Scheme 1. Synthesis of Rhodium η^4-1,2-Azaborete Complexes 3 and 5 and Substituted 1,4-Azaborinines 4 and 6; the Numbering Scheme for Ring Substituents Is Also Provided

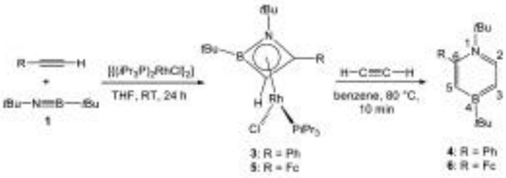

During the course of the reaction, the ^{11}B NMR shift changed from 5 ppm in **1** to 25 ppm in **3** and finally to 46 ppm in **4**, in agreement with previously reported data for 1,4-azaboretes and 1,4-azaborinines.[11] The ^1H NMR spectra of **3** and **4** display resonances characteristic of their phenyl groups (**3**: $\delta = 7.86$ and 7.01 ppm; **4**: $\delta = 7.17$ and 7.01 ppm) as well as BN heterocycle ring protons (**3**: 3.24 ppm; **4**: 7.84, 6.74, and 6.62 ppm).

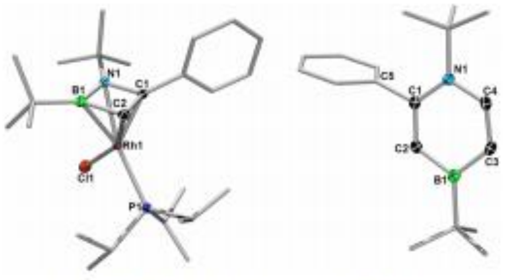

Figure 2. Molecular structures of $[\eta^4$-1,2-{B(*t*Bu)N(*t*Bu)C(Ph)C(H)}RhCl(P*i*Pr$_3$)] (**3**) and 1,4-di-*tert*-butyl-2-phenyl-1,4-azaborinine (**4**). The two crystallographically independent molecules in the asymmetric unit of **4** have nearly identical geometries, only one of which is displayed. Ellipsoids are set at 50% probability; hydrogen atoms and some ellipsoids have been omitted for clarity. Selected bond lengths (Å) and angles (deg) in **3**: B1−N1 1.5254(18), B1−C2 1.5542(19), N1−C1 1.4744(16), C1−C2 1.4280(18), Rh1−B1 2.2837(15), Rh1−N1 2.1290(11), Rh1−C1 2.0369(12), Rh1−C2 2.1358(13); N1−B1−C2 87.42(10), C1−N1−B1 88.78(10). In **4**: B1−C3 1.504(2), B1−C2 1.5170(18), N1−C1 1.3892(16), N1−C4 1.3808(15), C1−C2 1.3710(17), C3−C4 1.3611(17); C2−B1−C3 110.71(11), C4−N1−C1 117.69(10).

Orange crystals of **3** and colorless crystals of **4** suitable for single-crystal X-ray crystallography (Figure 2) were obtained by recrystallization from saturated benzene solutions. The N−C, B−C, and C−C bond lengths in **4** are comparable to those of previously reported 1,4-azaborinines.[11] The phenyl ring is positioned roughly perpendicular to the azaborinine ring (the dihedral angle between the two rings is 82.20°), and the 1,4-azaborinine ring itself is planar. The four-membered ring of **3** is distorted, showing two longer bonds (B1−C2, 1.5542(19) Å; N1−C1, 1.4744(16) Å) and two shorter bonds (B1−N1, 1.526(2) Å; C2−C1, 1.425(2) Å), although the latter two distances indicate significant lengthening compared with the B≡N and C≡C triple bonds of the substrates. This distortion is typical of rhodium η^4-1,2-azaborete complexes[11] and other rhodium complexes of boron heterocycles.[17,18]

To further probe the scope of the sequential reaction, we employed ethynylferrocene, a monosubstituted polar alkyne, as a substrate. As previously reported, the stoichiometric reaction of **1** and **2** in the presence of ethynylferrocene resulted in the formation of azaborete **5**.[16] Gratifyingly, the reaction of **5** with acetylene proceeded smoothly to furnish 2-ferrocenyl-1,4-azaborinine **6** in 55% yield (Scheme 1). Notably, the reaction of **1** with ethynylferrocene alone in the presence of **2** as a catalyst led exclusively to 1,2-di-*tert*-butyl-4,6-diferrocenyl-1,2-azaborinine.

6 was isolated as an air-stable orange solid displaying a singlet at $\delta = 46$ ppm in its ^{11}B NMR spectrum, which is shifted significantly downfield with respect to that in **5** ($\delta = 23.5$ ppm). The ^1H NMR spectrum of **6** showed characteristic resonances for the ferrocenyl and azaborinine rings as multiplets at $\delta = 4.38–3.94$ and 7.75–6.63 ppm, respectively. The C═C stretching frequencies of the azaborinine ring were observed in the IR spectrum, and the presence of both *tert*-butyl and ferrocenyl groups was confirmed by ^{13}C NMR spectroscopy.

The proposed structure of **6** was confirmed by crystallographic studies (Figure 3). The average B−C and N−C bond distances (1.510 and 1.388 Å, respectively) are slightly shorter than those reported for 1,2-di-*tert*-butyl-4,6-diferrocenyl-1,2-azaborinine (1.523(4) and 1.410(3) Å, respectively).[16] The azaborinine ring is slightly twisted from planarity, with an average displacement of the ring atoms of 0.02 Å, as a result of

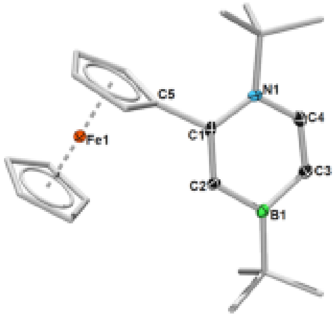

Figure 3. Molecular structure of 1,4-di-*tert*-butyl-2-ferrocenyl-1,4-azaborinine (**6**). The thermal ellipsoids of the *t*Bu, ferrocenyl ring, and hydrogen atoms have been omitted for clarity. Thermal ellipsoids are displayed at the 50% probability level. Selected bond lengths (Å) and angles (deg): B1−C2 1.516(2), B1−C3 1.505(2), N1−C1 1.397(1), N1−C4 1.379(2), C1−C2 1.372(2), C3−C4 1.356(2); C2−B1−C3 111.1(1), C4−N1−C1 118.0(1).

the steric congestion imposed by the bulky *N*-*t*Bu and ferrocenyl substituents.

To further improve our understanding of the synthesis of 1,4-azaborinines, a rhodium η^4-1,2-azaborete compound formed through the reaction of **1** and acetylene ([η^4-1,2-{B(*t*Bu)N(*t*Bu)C(H)C(H)}RhCl(P*i*Pr$_3$)])[11] was reacted with 4,4,5,5-tetramethyl-2-ethynyl-1,3,2-dioxaborolane (Bpin) and also 4-ethynyl-*N*,*N*-bis(4-methoxyphenyl)aniline, resulting in the formation of **7** and **8**, respectively (Scheme 2). Surprisingly,

Scheme 2. Synthesis of Substituted 1,4-Azaborinines 7 and 8

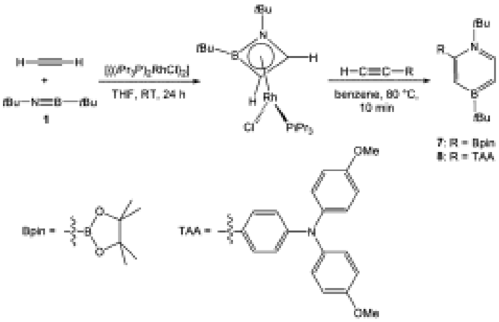

the reactions with the same rhodium azaborete complex and phenylacetylene or ethynylferrocene yielded 1,4-azaborinines also with substituents at the 2-position (as in Scheme 1). This indicates that the regiochemistry of the products is invariant to changes in the order of addition of reagents. Both **7** and **8** adopt a relatively planar structure in the solid state (see Figure S1 and Figure 4, respectively) with bond angles and distances falling within the typical ranges for 1,4-azaborinine compounds.

Synthesis of Bis- and Tris-1,4-azaborinines. In order to further extend the scope of the products available through sequential addition, reactions involving diynes were carried out, culminating in the synthesis of a bis-1,4-azaborinine (Scheme 3). The reaction of **1** and 1,4-diethynylbenzene in the presence of **2** furnished the dirhodium bis(η^4-1,2-azaborete) complex **9** in moderate yield (24%). Subsequent reaction with acetylene gave the 1,4-phenylene-bridged bis-1,4-azaborinine **10** in 43% yield. To our knowledge, very few examples of bis(BN)-azaborinine compounds have been reported beyond a fused bis(BN-phenanthrene)azaborinine[19] and, more recently, a tolan analogue of bis(azaborinine) systems.[20] Compound **10** is stable in air at temperatures up to 110 °C in toluene.

The ^{11}B NMR spectra of **9** and **10** display signals at δ = 26 and 46 ppm, respectively, indicative of the formation of the Rh−azaborete and azaborinine compounds. The ^{1}H NMR spectrum of **10** reveals the presence of aromatic protons at δ = 6.61−7.84 ppm along with the presence of four inequivalent *tert*-butyl groups, clearly confirming the presence of *cis* and *trans* atropisomers in solution. Unfortunately, variable-temperature ^{1}H NMR spectroscopy did not provide any further information about the interconversion between the *cis* and *trans* atropisomers.[21] The structure of **10** shows a *trans*-anti orientation with dihedral angles of approximately 68° between the spacer (phenyl) and azaborinine units, which is significantly more acute than found in the all-organic analogue (93°).[21] The geometries of the azaborinine rings in **10** resemble those of **6**, displaying B−C separations of 1.511(3) and 1.517(2) Å, and NC distances of 1.378(2) and 1.394(2) Å. Interestingly, the length of 1.499(2) Å for the carbon−carbon bond connecting the NCC and phenyl rings is comparable to that observed for the corresponding C−C single bond linking the two sp^2-hybridized C atoms in butadiene (1.483(1) Å).[22] Reactions of 1,7-octadiyne with **1** and **2** led to bis-1,4-azaborinine **11** in moderate yield after final acetylene insertion. The presence of a

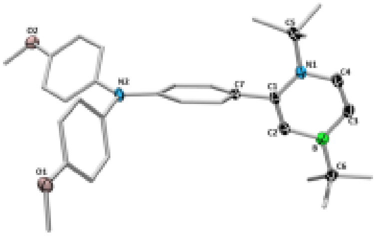

Figure 4. Molecular structure of 4-(1,4-di-*tert*-butyl-1,4-azaborinin-2-yl)-*N*,*N*-bis(4-methoxyphenyl)aniline (**8**). The thermal ellipsoids of the methyl, phenyl, and hydrogen atoms have been omitted for clarity. Thermal ellipsoids are displayed at the 50% probability level. Selected bond lengths (Å) and angles (deg): B−C3 1.503(3), B−C2 1.514 (3), N1−C1 1.385(2), N1−C4 1.387(3), C1−C2 1.372 (3), C3−C4 1.355(3) C1−C7 1.495 (3); C2−B1−C3 110.2 (2), C4−N1−C1 117.6(2).

Scheme 3. Synthesis of Bis-1,4-azaborinines 10 and 11

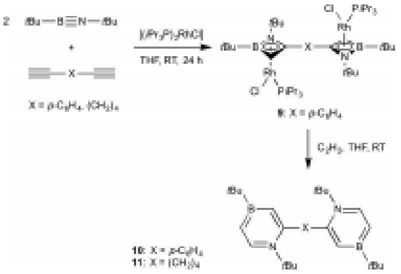

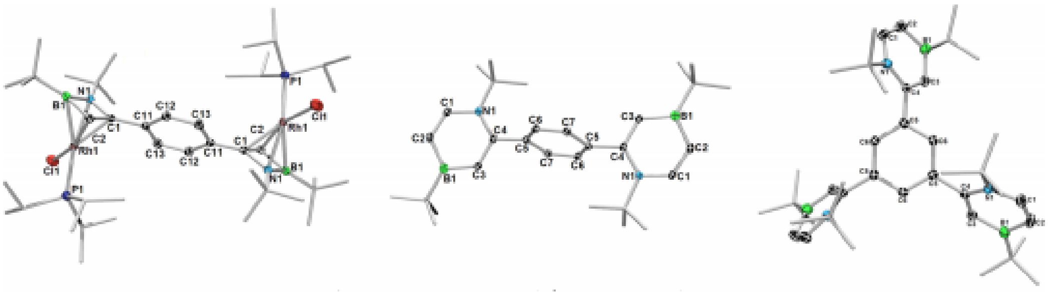

Figure 5. Molecular structures of 1,4-phenylene-bridged bis(η^4-1,4-azaborete) complex **9**, bis-1,4-azaborinine **10**, and tris-1,4-azaborinine **12**. The thermal ellipsoids of the *t*Bu, *i*Pr, and hydrogen atoms have been omitted for clarity. Thermal ellipsoids are displayed at the 50% probability level. Selected bond lengths (Å) and angles (deg) in **9**: B1−N1 1.541(2), B1−C2 1.533(2), N1−C1 1.4685(19), C1−C2 1.422(2), Rh1−B1 2.2784(18), Rh1−N1 2.1212(13), Rh1−C1 2.0369(12), Rh1−C2 2.1495(15); N1−B1−C2 87.67(12), C1−N1−B1 87.67(11). In **10**: B1−C3 1.517(2), B1−C2 1.511(3), N1−C1 1.378(2), N1−C4 1.394(2), C1−C2 1.356(2), C3−C4 1.365(2), C4−C5 1.499(2); C2−B1−C3 110.52(15), C4−N1−C1 118.05(14). In **12**: B1−C3 1.517(4), B1−C2 1.506(4), N1−C1 1.370(3), N1−C4 1.390(3), C1−C2 1.376(3), C3−C4 1.351(4), C4−C5 1.493(3); C2−B1−C3 111.0(2), C4−N1−C1 118.18(19).

^{11}B NMR resonance at δ = 46.0 ppm is consistent with the formation of a 1,4-azaborinine, while the ^{1}H NMR resonances for the *t*Bu groups at δ = 1.49 and 0.99 ppm indicate a highly symmetrical compound.

Single crystals of **9** and **10** suitable for X-ray diffraction were obtained from a pentane solution at −30 °C. The solved structures are presented in Figure 5. Single crystals of **11** suitable for X-ray diffraction analysis were grown, but the centrosymmetric nature of **11** resulted in substantial disorder. For the sake of confirming the structural assignment of **11**, the disordered structure is given in Figure S2 (see the Supporting Information for details).

With the optimized conditions determined, we next turned our attention to the synthesis of a tris-1,4-azaborinine through reactions involving 1,3,5-triethynylbenzene. These reactions yielded compound **12**, which was characterized by comparison of its spectroscopic data with those of related compounds reported here. The ^{11}B NMR spectrum of **12** shows the presence of a single resonance at δ = 47.5 ppm, which is in good agreement with the data for other 1,4-azaborinines. The ^{1}H NMR spectrum of **12** shows four resonances for the *B*- and *N*-*t*Bu protons at δ = 1.54 (18H), 1.45 (9H), 1.00 (9H), and 0.99 (18H) ppm, the latter two signals being those from the *N*-*t*Bu protons. This suggests that in solution one BN-containing ring is flipped relative to the other two.

Crystals of **12** were obtained by cooling a concentrated pentane solution to −30 °C. The solid-state structure of **12** (Figure 5) confirms the structural inferences made on the basis of the spectroscopic data. The molecule crystallizes in the triclinic space group *P*1 and thus lies on a crystallographic inversion center. The bond distances in the six-membered azaborinine ring are consistent with previously reported bond lengths for mono- and bis-1,4-azaborinines. The dihedral angles of 58.93° between the phenyl and azaborinine units are slightly smaller than in **10**.

Computational Mechanistic Studies. Density functional theory calculations were performed to model the formation of Rh−azaborete complex **3** from the reaction of phenylacetylene and *t*BuB≡N*t*Bu (**1**) with [RhCl(P*i*Pr$_3$)$_2$]$_2$ as well as the onward reaction of **3** with acetylene to form 2-phenyl-1,4-azaborinine **4**.[23] Alternative regioselectivities were also considered in order to account for the selective formation of this product isomer. All of the geometries were optimized with the BP86 functional, and the reported free energies incorporate corrections for benzene solvent (PCM approach) and dispersion (Grimme's D3 parameter set) (see the Supporting Information for full details).

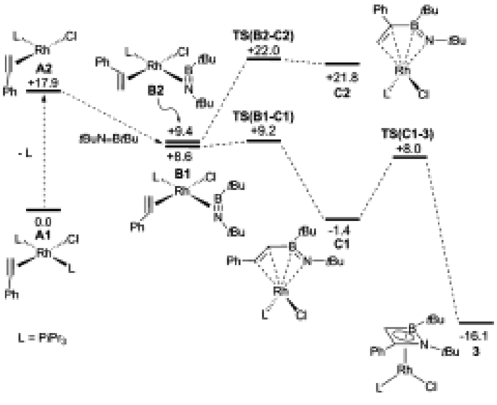

Figure 6. Computed free energy profile (BP86-D3(C$_6$H$_6$)//BP86, in kcal/mol) for the formation of Rh−azaborete complex **3** from *trans*-[RhCl(P*i*Pr$_3$)$_2$(η^2-PhC≡CH)] (**A1**) and iminoborane **1**. The alternative B−C(Ph) coupling to give **C2** is also shown.

The reaction profile for the formation of **3** is shown in Figure 6 and starts from the intermediate *trans*-[RhCl(P*i*Pr$_3$)$_2$(η^2-PhC≡CH)] (**A1**), which may be formed upon opening of the [RhCl(P*i*Pr$_3$)$_2$]$_2$ dimer in the presence of PhC≡CH. All subsequent free energies are quoted relative to the combined energies of **A1** and the other reagents set to 0.0 kcal/mol. As expected, the *cis* isomer of **A1** (*G* = +15.4 kcal/mol) is less stable as a result of the presence of two adjacent bulky P*i*Pr$_3$ ligands. In addition, iminoborane binding is not competitive at this stage, with [RhCl(P*i*Pr$_3$)$_2$(η^2-*t*BuB≡N*t*Bu)] being high in energy as either its *trans* isomer (*G* = +19.5 kcal/mol) or *cis* isomer (*G* = +16.8 kcal/mol), reflecting the additional steric encumbrance arising from the *t*Bu substituents. P*i*Pr$_3$/

DOI: 10.1021/jacs.6b04128
J. Am. Chem. Soc. 2016, 138, 8212−8220

iminoborane substitution in **A1** can proceed via [RhCl(P*i*Pr$_3$)(η^2-PhC≡CH)] (**A2**) at +17.9 kcal/mol and leads to the relatively accessible species [RhCl(P*i*Pr$_3$)(η^2-*t*BuB≡N*t*Bu)(η^2-PhC≡CH)] (**B**), in which both the alkyne and the iminoborane lie approximately perpendicular to the Rh coordination plane. Two rotamers of **B** were located, with that in which the C(H) group lies adjacent to the *t*BuB group (**B1**) being slightly more stable (*G* = +8.6 kcal/mol). The iminoborane ligand in these structures binds in an unsymmetrical fashion (**B1**: Rh−N = 2.20 Å, Rh−B = 2.25 Å; see Figure 7) with the N center lying in the square-planar coordination plane. This appears to be an electronic preference arising from the greater Lewis basicity of the N center, as a similar distortion is retained in the computed structure of the small model complex [RhCl(PMe$_3$)(η^2-MeB≡NMe)(η^2-HC≡CH)]. From **B1** a very facile B−C(H) bond coupling can be accessed via **TS(B1−C1)** (*G* = +9.2 kcal/mol) that forms **C1** at −1.4 kcal/mol. The alternative rotamer, **B2** (*G* = +9.4 kcal/mol), has the C(Ph) group adjacent to *t*BuB and thus is set up for B−C(Ph) bond coupling; however, this process has a much higher barrier (via **TS(B2−C2)** at +22.0 kcal/mol) and is strongly endergonic, giving **C2** at +21.8 kcal/mol. Transition states for the potential N−C bond coupling processes were also located from **B1** and **B2** but were found to be even higher in energy (*G* > 33 kcal/mol; see the Supporting Information).

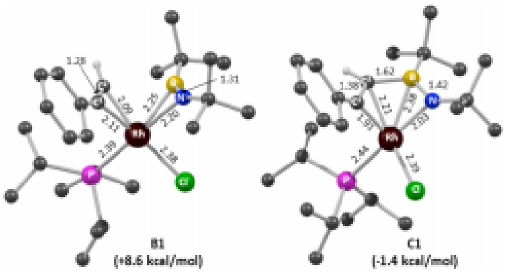

Figure 7. Computed structures of intermediates **B1** and **C1**. Selected distances are in Å, and H atoms (with the exception of that derived from the terminal alkyne position) have been omitted for clarity.

The formation of **C1** can be considered as an oxidative coupling proceeding with B−C(H) bond formation to give a Rh^{3+} species. The {(Ph)C═C(H)−(*t*Bu)B═N(*t*Bu)} moiety is therefore considered as a dianionic ligand with formal negative charges on the C(Ph) and B centers. The major interaction with the Rh center occurs through short Rh−N and Rh−C(Ph) σ bonds (2.03 and 1.91 Å, respectively; see Figure 7), and these are supported by additional Rh−C(H) and Rh−B contacts of 2.21 and 2.38 Å, respectively. The C(Ph)−C(H) and B−N distances of 1.38 and 1.42 Å, respectively, indicate significant double-bond character with little delocalization across the central B−C(H) bond (1.62 Å). N−C(Ph) bond formation can then proceed from **C1** and occurs via **TS(C1−3)** with a modest barrier of 9.4 kcal/mol. This reductive coupling process forms complex **3** at −16.1 kcal/mol in which a neutral 1,2-azaborete ligand is bound to a Rh$^+$ center. The computed structure of **3** agrees well with that determined experimentally, the main discrepancy being a slight overestimation of the distances between Rh and the azaborete ligand by ca. 0.04 Å (see the Supporting Information).

Overall, the formation of complex **3** from intermediate **A1** is computed to proceed via P*i*Pr$_3$/iminoborane substitution and sequential B−C(H) and N−C(Ph) bond-coupling events. The highest point on the profile is at +17.9 kcal/mol and corresponds to the species [RhCl(P*i*Pr$_3$)(η^2-PhC≡CH)] (**A2**) formed upon loss of P*i*Pr$_3$ from **A1**. The subsequent B−C(H) coupling is highly selective, with the alternative B−C(Ph) coupling (and the potential C(R)−N couplings) being clearly higher in energy. B−C(H) coupling in **B1** is computed to have a much lower barrier than N−C(Ph) coupling in **C1**, although the latter is more thermodynamically favorable, presumably because it is driven by the formation of the delocalized 1,2-azaborete ligand.

Several possibilities were considered for the onward reaction of the 1,2-azaborete complex **3** with acetylene to form the 1,4-azaborinine product. Pathways were characterized for B−N bond cleavage of the azaborate moiety either directly in **3** or after the facile addition of acetylene to give intermediate **D**; details of these processes (and those for the related B−C bond cleavage processes in **3** and **D**) are provided in Scheme S2. However, the most accessible pathway (see Figures 8 and 9, which also provide the labeling scheme employed) involves the

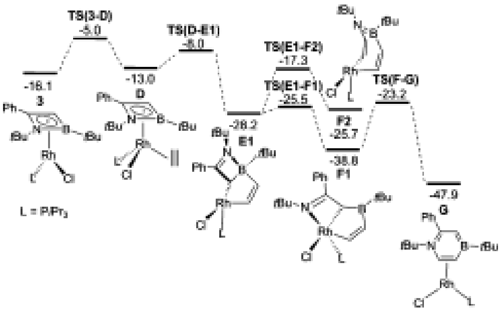

Figure 8. Computed free energy profile (BP86-D3(C$_6$H$_6$)//BP86, in kcal/mol) for the formation of rhodium η^2-(*C*,*C*)-1,4-azaborinine complex **G** from 1,2-azaborete complex **3** and acetylene. The alternative B−C(H) bond cleavage in **E1** to form **F2** is also indicated.

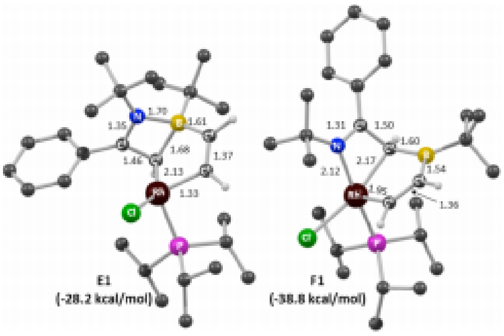

Figure 9. Computed structures of intermediates **E1** and **F1**. Selected distances are in Å, and H atoms (with the exception of those derived from the alkyne positions) have been omitted for clarity.

DOI: 10.1021/jacs.6b04128
J. Am. Chem. Soc. 2016, 138, 8212−8220

formation of **D** followed by insertion of the alkyne into the Rh−B bond with a barrier of only 5 kcal/mol to produce intermediate **E1** at −28.2 kcal/mol. Transition states for the alternative insertions into the Rh−C^1(Ph) and Rh−C^2(H) bonds proved to be significantly higher in energy (see Scheme S2). **E1** features a five-membered metallaboracycle fused with the still-intact imine-stabilized borane moiety, which is bound in an η^1 fashion to Rh via C^2 (Rh−C^2 = 2.13 Å; Figure 9). The B−N bond in **E1** is now significantly elongated to 1.70 Å, and its cleavage readily occurs via **TS(E1-F1)** with a barrier of only 2.7 kcal/mol to form **F1** at −38.8 kcal/mol. This bond cleavage is accompanied by a rotation about the C^1(Ph)−C^2(H) bond of the azaborete moiety such that the N(*t*Bu) group migrates back onto the Rh center. The Rh−C^2 bond noted in **E1** is therefore retained such that **F1** features a new bicyclic structure with {RhN(*t*Bu)C^1(Ph)C^2(H)} and {RhC^2(H)B(*t*Bu)C^4(H)-C^3(H)} rings. These fold along the shared Rh−C^2 bond to give a tridentate ligand that is bound in a facial manner, with overall square-pyramidal coordination at Rh. C^3−N bond-forming reductive coupling in **F1** proceeds with a barrier of 15.6 kcal/mol to give **G**, in which the 2-phenyl-1,4-azaborinine product is bound in an η^2 fashion to the {RhCl(P*i*Pr$_3$)} fragment. Displacement of the azaborinine by P*i*Pr$_3$ forms the free product and *trans*-RhCl(P*i*Pr$_3$)$_2$ at −46.7 kcal/mol, to which PhCCH can bind to reform **A1** at −71.8 kcal/mol.

Intermediate **E1** may also potentially undergo a B−C^2 bond cleavage that could ultimately lead to the alternative 1,2-azaborinine product. Characterization of this process, however, revealed it to be disfavored both kinetically ($\Delta G^{\ddagger}$ = 10.9 kcal/mol) and thermodynamically, with the putative seven-membered metallacycle **F2** lying 13.1 kcal/mol above **F1** (and 2.5 kcal/mol above **E1**). This preference for B−N bond cleavage in **E1** is consistent with the regioselective formation of the 1,4-azaborinine product.

The computed reaction profile for the formation of 1,4-azaborinine adduct **G** from **3** and acetylene is strongly exergonic (ΔG = −31.8 kcal/mol) and involves a series of low-energy processes of which the largest barrier is 15.6 kcal/mol, corresponding to the final N−C bond-coupling event. In comparison, the formation of the 1,2-azaborete is less exergonic (ΔG = −16.1 kcal/mol) and, aside from the initial P*i*Pr$_3$ dissociation, has lower barriers to its formation. The regioselectivity for 2-phenyl-1,4-azaborinine formation derives from the selective B−C(H) reductive coupling seen in intermediate **B1** in conjunction with the selective oxidative cleavage of the B−N bond in **E1**.

It is of interest to contrast the mechanism proposed here for 1,4-azaborinine formation with those put forward in the literature for Rh- and Ir-catalyzed alkyne trimerization.[24] The latter are initiated via oxidative coupling of two alkynes to give planar metallacyclopentadiene intermediates, equivalent to the (nonplanar) intermediate **C1** proposed here. Onward reaction with a third alkyne can involve a direct [4 + 2] cycloaddition or insertion to give a metallacycloheptatriene, from which C−C reductive coupling forms the arene product. This latter mechanism can feature a metallabicyclo[3.2.0]heptatriene intermediate that is isoelectronic with **F1**;[25] indeed, such a species has been characterized experimentally.[26] An all-carbon analogue of bicyclic **E1** has not been proposed, however, and this may reflect the fact that **E1** is formed via reaction of acetylene with the 1,2-azaborete ligand in **3**. In contrast, the isoelectronic cyclobutadiene complex, if it forms, is thought to lie off the catalytic cycle for alkyne trimerization. The regioselective formation of the 1,4-azaborinines formed here contrasts with the observation of 1,2-azaborinines seen in the direct reaction of ethynylferrocene with *t*BuB≡N*t*Bu, indicating a significant role of substituent effects in dictating the selectivity.[11] Work to understand these different outcomes is currently underway.

Electrochemical and Photophysical Characterization of 8. In view of the results of the recently published 1,2-azaborinine **13** and **Ref**[27] (Figure 10), we investigated the 1,4-azaborinine **8** by cyclic voltammetry and UV/vis/NIR absorption and emission spectroscopy in order to elucidate the influence of the azaborinine isomers on the electronic properties in such donor−acceptor chromophores.

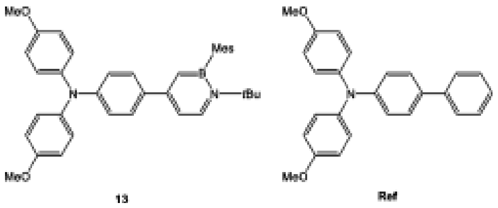

Figure 10. Structures of **13** and **Ref**.

Electrochemical Properties. The cyclic voltammograms of **8** (Figure 11A) show a first oxidation wave at 256 mV vs ferrocene/ferrocenium (Fc/Fc$^+$) as an internal standard in CH$_2$Cl$_2$/0.15 M tetrabutylammonium hexafluorophosphate (TBAH). The first oxidation can be assigned to a one-electron oxidation of the nitrogen atom in the triarylamine (TAA)[26] unit and is reversible even under thin-film conditions. In the square-

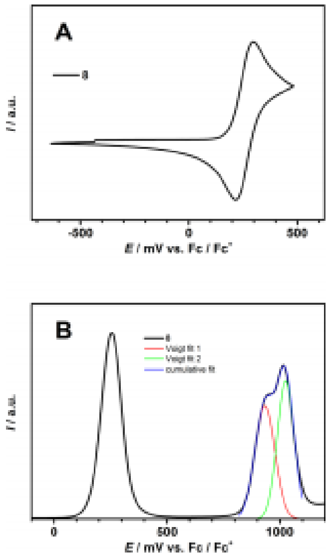

Figure 11. (A) Cyclic voltammogram of **8** in CH$_2$Cl$_2$ (TBAH) at a scan rate of 100 mV s^{-1}. (B) Square-wave voltammogram (black line) of **8** in CH$_2$Cl$_2$ at a scan rate of 50 mV s^{-1}. Voigt fits (red and green lines) and the cumulative fit (blue line) are also shown.

Table 1. Optical Steady-State and Emission Decay Data for 8 in MeCN, CH_2Cl_2, and Toluene

solvent	$\tilde{\nu}_{abs}$/cm^{-1} (nm)	ε/M^{-1} cm^{-1}	$\tilde{\nu}_{fl}$/cm^{-1} (nm)	ϕ_f	τ_{fl}/ns
MeCN	32900 (304); 38300 (261)[a]	23900	20600 (485)	0.33 ± 0.014	5.62
CH_2Cl_2	32600 (307); 38600 (259)[a]	23000	21700 (461)	–[c]	–[c]
toluene	32500 (308); –[b]	23700	23600 (424)	0.10 ± 0.001	0.68

[a]Less intense maximum. [b]Could not be measured because of insufficient solvent transparency. [c]Could not be measured because of decomposition.

wave voltammogram (Figure 11B), an additional double peak associated with irreversible oxidation processes at higher potential (800–1100 mV vs Fc/Fc$^+$) is visible (Figure S4). A fit with two Voigt functions revealed two processes at 934 and 1026 mV vs Fc/Fc$^+$. We assume that one of these potentials refers to the second oxidation of the TAA unit and the other one to oxidation of the 1,4-azaborinine unit. However, a discrete assignment is impossible.

The electrochemical behavior of 1,4-azaborinine **8** is similar to that of 1,2-azaborinine **13** and the all-carbon compound **Ref**, but the first oxidation wave is at a ca. 30 mV higher potential in **8** (**13**: 224 mV; **Ref**: 228 mV), indicating a greater electron-withdrawing strength of the 1,4-azaborinine unit compared with the 1,2-azaborinine unit. In addition, the two peaks around 800–1100 mV vs Fc/Fc$^+$ in **8** are slightly more separated than those in **13** and **Ref**.

UV/Vis/NIR Spectroscopy. The steady-state absorption spectra of **8** in MeCN, CH_2Cl_2, and toluene are shown in Figure 13. These absorption spectra display two π–π^* absorption bands typical of TAA.[28,29] The first absorption band at ca. 32800 cm^{-1} is caused by a HOMO → LUMO ($S_1 \leftarrow S_0$) transition and the second at ca. 38600 cm^{-1} by a HOMO → LUMO+1 ($S_2 \leftarrow S_0$) transition (Table 1).[29] Both peaks depend on the solvent polarity. They are broader in nonpolar solvents and show a weak negative solvatochromism. The $S_1 \leftarrow S_0$ transition rises from 32500 cm^{-1} in toluene to 32900 cm^{-1} in MeCN and the $S_2 \leftarrow S_0$ transition from 38300 cm^{-1} in MeCN to 38600 cm^{-1} in CH_2Cl_2, which indicates some charge transfer (CT) character of both electronic transitions. This absorption behavior is also in good agreement with calculations of the frontier molecular orbitals (Figure 12), which were carried out using the Gaussian 09 software suite (see the Supporting Information for details). The ground-state molecular geometries were optimized at the B3LYP/6-311G(d) level of theory, and were found to be true minima through frequency analyses. The HOMO is TAA-localized, while the LUMO and the LUMO+1 show more contribution from the azaborinine unit. Excitation from a HOMO to the LUMO or LUMO+1 should be associated with a change in dipole moment, and consequently, both transitions depend on the solvent polarity.

The absorption spectra of **13** and **Ref** show quite similar characteristics, but in the case of **8** the difference in energy between the two π–π^* absorptions (and thus the difference in the energies of the LUMO and LUMO+1) are smaller than in **13**. While in MeCN the two absorption maxima of **8** are separated by 5400 cm^{-1}, in **13** they are only 3400 cm^{-1} apart. In **Ref** the maxima are so close together that only a broad band with a shoulder in the lower-wavelength regime is visible. The $S_2 \leftarrow S_0$ transition of **8** illustrates another difference. Whereas the $S_2 \leftarrow S_0$ transition of **8** is dependent on the polarity of the solvent, in **13** and **Ref** nearly no CT is visible and the transition is independent of the solvent.

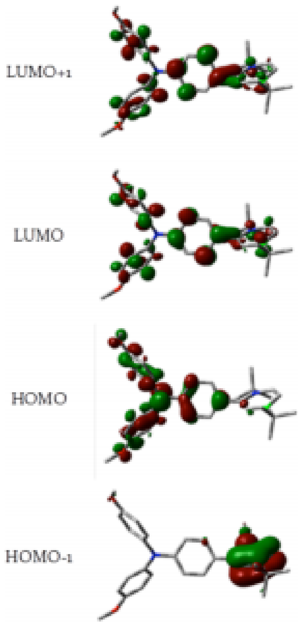

Figure 12. Isosurface plots of the HOMO–1, HOMO, LUMO, and LUMO+1 for **8**.

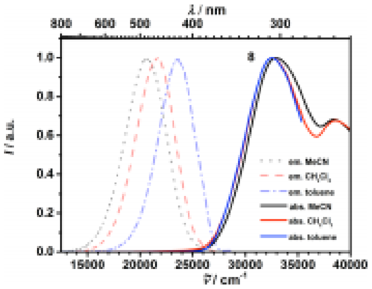

Figure 13. Normalized absorption spectra (solid lines) and emission spectra (dashed lines) of **8** in MeCN (black), CH_2Cl_2 (red), and toluene (blue).

Emission spectra of **8** were measured in MeCN, CH_2Cl_2, and toluene (Figure 13).[28,30] The fluorescence spectra were recorded by excitation at the absorption maxima, but excitation at lower excitation wavenumbers resulted in the same emission. The emission maxima of **8** shift from 20600 cm^{-1} in toluene and 21700 cm^{-1} in CH_2Cl_2 to 23600 cm^{-1} in MeCN. This strong positive solvatochromism fluorescence of **8** is accompanied by a large apparent Stokes shift (8900 cm^{-1} in toluene and 12300 cm^{-1} in MeCN), indicating a major reorganization of the excited state in the more polar solvents. The fact that there is only weak solvatochromism in the absorption spectra but strong solvatochromism in the fluorescence spectra speaks for a vanishing ground-state dipole moment but a large excited-state dipole moment.

Fluorescence lifetimes were measured by time-correlated single photon counting with excitation at 31600 cm^{-1}. Compound **8** shows a fluorescence lifetime of a few nanoseconds with a monoexponential decay (Table 1). The fluorescence lifetime was also found to be dependent on the solvent polarity: in the polar solvent MeCN the excited state is stabilized and the lifetime rises to 5.62 ns, whereas in toluene the lifetime drops to 0.68 ns (Figure S3). The fluorescence quantum yield (QY) of **8** is surprisingly low (see Table 1). In MeCN, **8** shows a QY of 33%, which in toluene drops to 10%. Because of slow decomposition of **8** in CH_2Cl_2, we were unable to perform accurate fluorescence lifetime or fluorescence quantum yield measurements in this solvent.

The emission maximum of **8** is between those of 1,2-azaborinine **13** and the all-carbon analogue **Ref** (e.g., in MeCN: **13**, 19500 cm^{-1}; **8**, 20600 cm^{-1}; **Ref**, 21400 cm^{-1}). The Stokes shift of **8** is significantly higher and the fluorescence lifetime of **8** is shorter than those of **13** and **Ref** (both in toluene and MeCN). Here the all-carbon chromophore has the longest lifetime in the respective solvent (e.g., in MeCN: **Ref**, 8.20 ns; **13**, 7.34 ns; **8**, 5.62 ns). However, the largest difference in the emission behavior of these compounds is the fluorescence quantum yield. The 1,4-azaborinine compound **8** was found to be significantly less fluorescent than the 1,2-azaborinine compound and the all-carbon analogue (e.g., in toluene: **13**, 0.47%; **Ref**, 0.30%; **8**, 0.10%).

■ CONCLUSION

We have demonstrated the utility of iminoboranes for the construction of 1,4-azaborinines with a range of architectures. The scope of the reaction with respect to the inclusion of terminal alkynes is broad and allows the use of substrates with functional groups not tolerated by previous synthetic routes to 1,4-azaborinines. This methodology has also enabled the synthesis and characterization of bis- and (the first) tris-1,4-azaborinines, which are BN analogues of *p*-terphenyl and 1,3,5-triphenylbenzene, respectively. The structural, spectroscopic, and chemical data presented in this work were fully supported by high-level calculations. Our current efforts are directed toward expanding the scope of this reaction in the context of 1,4-azaborinines. The results described herein further open the door to the wide and uncharted field of BN heterocycle chemistry, and it is anticipated that this study will provide new avenues in BN-doped molecular architectures of importance to medicinal and materials chemistry.

■ ASSOCIATED CONTENT

Ⓢ Supporting Information

The Supporting Information is available free of charge on the ACS Publications website at DOI: 10.1021/jacs.6b04128.

Procedures and additional data (PDF)
Computed Cartesian coordinates (XYZ)
Crystallographic data for **3**, **4**, **6**, **8**–**10**, and **12** (CIF)

■ AUTHOR INFORMATION

Corresponding Authors

*s.a.macgregor@hw.ac.uk
*christoph.lambert@uni-wuerzburg.de
*h.braunschweig@uni-wuerzburg.de

Present Address

$^{\perp}$Department of Inorganic & Physical Chemistry, Indian Institute of Science, Bangalore 560012, India.

Notes

The authors declare no competing financial interest.

■ ACKNOWLEDGMENTS

This work was financially supported by the Deutsche Forschungsgemeinschaft (DFG grant to H.B.). K.G. thanks the Alexander von Humboldt Foundation for a postdoctoral fellowship. N.A.B. thanks the EPSRC and Heriot-Watt University for a DTP studentship.

■ REFERENCES

(1) (a) Lepeltier, M.; Lukoyanova, O.; Jacobson, A.; Jeeva, S.; Perepichka, D. F. *Chem. Commun.* **2010**, *46*, 7007–7009. (b) Bosdet, M. J. D.; Piers, W. E. *Can. J. Chem.* **2009**, *87*, 8–29. (c) Campbell, P. G.; Marwitz, A. J. V.; Liu, S.-Y. *Angew. Chem., Int. Ed.* **2012**, *51*, 6074–6092. (d) Fritsch, A. J. *Chem. Heterocycl. Compd.* **1977**, *30*, 381–440.

(2) (a) Dewar, M. J. S.; Kubba, V. P.; Pettit, R. *J. Chem. Soc.* **1958**, 3073–3076. (b) Dewar, M. J. S.; Dietz, R. *J. Chem. Soc.* **1959**, 2728–2730. (c) Dewar, M. J. S.; Marr, P. A. *J. Am. Chem. Soc.* **1962**, *84*, 3782. (d) Davies, K. M.; Dewar, M. J. S.; Rona, P. *J. Am. Chem. Soc.* **1967**, *89*, 6294–6297.

(3) White, D. G. *J. Am. Chem. Soc.* **1963**, *85*, 3634–3636.

(4) (a) Ashe, A. J., III; Fang, X. *Org. Lett.* **2000**, *2*, 2089–2091. (b) Ashe, A. J., III; Fang, X.; Fang, X.; Kampf, J. W. *Organometallics* **2001**, *20*, 5413–5418.

(5) (a) Jaska, C. A.; Emslie, D. J. H.; Bosdet, M. J. D.; Piers, W. E.; Sorensen, T. S.; Parvez, M. *J. Am. Chem. Soc.* **2006**, *128*, 10885–10896. (b) Bosdet, M. J. D.; Piers, W. E.; Sorensen, T. S.; Parvez, M. *Angew. Chem., Int. Ed.* **2007**, *46*, 4940–4943.

(6) Taniguchi, T.; Yamaguchi, S. *Organometallics* **2010**, *29*, 5732–5735.

(7) Lepeltier, M.; Lukoyanova, O.; Jacobson, A.; Jeeva, S.; Perepichka, D. F. *Chem. Commun.* **2010**, *46*, 7007–7009.

(8) (a) Liu, L.; Marwitz, A. J. V.; Matthews, B. W.; Liu, S.-Y. *Angew. Chem., Int. Ed.* **2009**, *48*, 6817–6819. (b) Abbey, E. R.; Zakharov, L. N.; Liu, S.-Y. *J. Am. Chem. Soc.* **2010**, *132*, 16340–16342. (c) Abbey, E. R.; Zakharov, L. N.; Liu, S.-Y. *J. Am. Chem. Soc.* **2011**, *133*, 11508–11511.

(9) Marwitz, A. J. V.; Matus, M. H.; Zakharov, L. N.; Dixon, D. A.; Liu, S.-Y. *Angew. Chem., Int. Ed.* **2009**, *48*, 973–977.

(10) Xu, S.; Zakharov, L. N.; Liu, S.-Y. *J. Am. Chem. Soc.* **2011**, *133*, 20152–20155.

(11) Braunschweig, H.; Damme, A.; Jimenez-Halla, J. O. C.; Pfaffinger, B.; Radacki, K.; Wolf, J. *Angew. Chem., Int. Ed.* **2012**, *51*, 10034–10037.

(12) Maitlis, P. M. *J. Chem. Soc.* **1961**, 425–429.

(13) Kranz, M.; Hampel, F.; Clark, T. *J. Chem. Soc., Chem. Commun.* **1992**, 1247–1248.

(14) (a) Agou, T.; Arai, H.; Kawashima, T. *Chem. Lett.* **2010**, *39*, 612–613. (b) Agou, T.; Kojima, T.; Kobayashi, J.; Kawashima, T. *Org. Lett.* **2009**, *11*, 3534–3537. (c) Agou, T.; Sekine, M.; Kobayashi, J.; Kawashima, T. *Chem. - Eur. J.* **2009**, *15*, 5056–5062. (d) Agou, T.; Sekine, M.; Kobayashi, J.; Kawashima, T. *Chem. Commun.* **2009**, 1894–1896.

(15) Xu, S.; Haeffner, F.; Li, B.; Zakharov, L. N.; Liu, S.-Y. *Angew. Chem., Int. Ed.* **2014**, *53*, 6795–6799.

(16) Braunschweig, H.; Geetharani, K.; Jimenez-Halla, J. O. C.; Schaefer, M. *Angew. Chem., Int. Ed.* **2014**, *53*, 3500–3504.

(17) (a) Hitchcock, P. B.; Maah, M. J.; Nixon, J. F. *J. Chem. Soc., Chem. Commun.* **1986**, 737–738. (b) Meidine, M. F.; Pombeiro, A. J. L.; Nixon, J. F. *J. Chem. Soc., Dalton Trans.* **1999**, 3041–3045.

(18) (a) Xu, S.; Zakharov, L. N.; Liu, S.-Y. *J. Am. Chem. Soc.* **2011**, *133*, 20152−20155. (b) Huttner, G.; Krieg, B. *Chem. Ber.* **1972**, *105*, 3437−3444. (c) Delpy, K.; Schmitz, D.; Paetzold, P. *Chem. Ber.* **1983**, *116*, 2994−2999.

(19) (a) Jaska, C. A.; Piers, W. E.; McDonald, R.; Parvez, M. J. *J. Org. Chem.* **2007**, 72, 5234−5243. (b) Lukoyanova, O.; Lepeltier, M.; Laferrière, M.; Perepichka, D. F. *Macromolecules* **2011**, *44*, 4729−4734.

(20) Marwitz, A. J. V.; Lamm, A. N.; Zakharov, L. N.; Vasiliu, M.; Dixon, D. A.; Liu, S.-Y. *Chem. Sci.* **2012**, *3*, 825−829.

(21) Lunazzi, L.; Mazzanti, A.; Minzoni, M.; Anderson, J. E. *Org. Lett.* **2005**, *7*, 1291−1294.

(22) Marais, D. J.; Sheppard, N.; Stoicheff, B. P. *Tetrahedron* **1962**, *17*, 163−169.

(23) A computational study on the metal-free [2+2] cycloadditions of iminoboranes and alkynes indicates that such processes encounter a significant barrier. See: Bissett, K. M.; Gilbert, T. M. *Organometallics* **2004**, *23*, 5048−5053.

(24) (a) Dahy, A. A.; Koga, N. *Organometallics* **2015**, *34*, 4965−4974. (b) Guo, C.-H.; Wu, H.-S.; Hapke, M.; Jiao, H. *J. Organomet. Chem.* **2013**, *748*, 29−35. (c) Dachs, A.; Osuna, S.; Roglans, A.; Sola, M. *Organometallics* **2010**, *29*, 562−569. (d) Dachs, A.; Torrent, A.; Roglans, A.; Parella, T.; Osuna, S.; Sola, M. *Chem. - Eur. J.* **2009**, *15*, 5289−5300.

(25) For computational characterization of an equivalent process involving the reaction of a rhodapentadiene and acetonitrile, see: Orian, L.; van Stralen, J. N. P.; Bickelhaupt, F. M. *Organometallics* **2007**, *26*, 3816−3830.

(26) Paneque, M.; Poveda, M. L.; Rendon, N.; Mereiter, K. *J. Am. Chem. Soc.* **2004**, *126*, 1610−1611.

(27) Schäfer, M.; Schäfer, J.; Dewhurst, R. D.; Ewing, W. C.; Krahfuß, M.; Kuntze-Fechner, M. W.; Wehner, M.; Lambert, C.; Braunschweig, H. *Chem. - Eur. J.* **2016**, *22*, 8603−8609.

(28) Amthor, S.; Noller, B.; Lambert, C. *Chem. Phys.* **2005**, *316*, 141−152.

(29) Amthor, S.; Lambert, C. *J. Phys. Chem. A* **2006**, *110*, 1177−1189. (b) Dapperheld, S.; Steckhan, E.; Brinkhaus, K.-H. G.; Esch, T. *Chem. Ber.* **1991**, *124*, 2557−2567. (c) Seo, E. T.; Nelson, R. F.; Fritsch, J. M.; Marcoux, L. S.; Leedy, D. W.; Adams, R. N. *J. Am. Chem. Soc.* **1966**, *88*, 3498−3503. (d) Schmidt, W.; Steckhan, E. *Chem. Ber.* **1980**, *113*, 577−585.

(30) Amthor, S.; Lambert, C.; Dümmler, S.; Fischer, L; Schelter, J. *J. Phys. Chem. A* **2006**, *110*, 5204−5214.

Amine–Borane Dehydropolymerization

International Edition: DOI: 10.1002/anie.201600898
German Edition: DOI: 10.1002/ange.201600898

The Simplest Amino-borane $H_2B{=}NH_2$ Trapped on a Rhodium Dimer: Pre-Catalysts for Amine–Borane Dehydropolymerization

Amit Kumar, Nicholas A. Beattie, Sebastian D. Pike, Stuart A. Macgregor, and Andrew S. Weller**

Abstract: *The μ-amino–borane complexes $[Rh_2(L^R)_2(\mu\text{-}H)(\mu\text{-}H_2B{=}NHR')][BAr^F_4]$ ($L^R{=}R_2P(CH_2)_3PR_2$; $R = Ph$, ${}^iPr$; $R' = H$, Me) form by addition of $H_3B{\cdot}NMeR'H_2$ to $[Rh(L^R)(\eta^6\text{-}C_6H_5F)][BAr^F_4]$. DFT calculations demonstrate that the amino–borane interacts with the Rh centers through strong Rh-H and Rh-B interactions. Mechanistic investigations show that these dimers can form by a boronium-mediated route, and are pre-catalysts for amine-borane dehydropolymerization, suggesting a possible role for bimetallic motifs in catalysis.*

Polyamino-boranes ($[H_2BNRH]_n$) are potentially exciting new materials that are isoelectronic with technologically pervasive polyolefins, but are chemically distinct because of (δ−)HB−NH(δ+) polarization. They are formed by the dehydropolymerization of amine-boranes ($H_3B{\cdot}NRH_2$; R = H or Me, for example; Scheme 1 A),[1] and metal-catalyzed routes to polyamino-boranes offer the potential for fine control over molecular weight and polymer stereochemistry. There is recent evidence that these processes occur at a metal center in which the catalyst needs to perform two roles: 1) formal dehydrogenation of amine-borane to form a latent source of amino-borane ($H_2B{=}NRH$), and 2) subsequent B−N bond formation.[2–6] For some systems a coordination/insertion mechanism is proposed, although the precise structure of the propagating species is currently unresolved (Scheme 1 B).[3,5,6] This is in contrast to olefin polymerization, in which the feedstock (for example, ethene or propene) is already unsaturated, and the active species and propagating mechanisms are well-defined.[7] A clearer understanding of how the catalyst dehydrogenates amine-borane, traps intermediate amino-boranes, and promotes B−N bond-formation, is central to harnessing the full potential of systems that ultimately deliver new well–defined B−N polymeric materials on a useful scale.

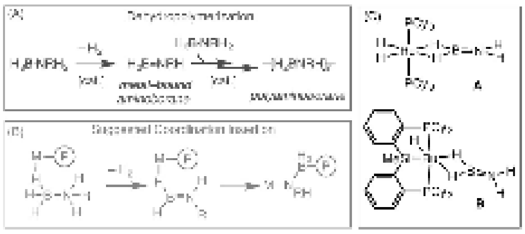

Scheme 1. A) Amine-borane dehydropolymerization; B) a suggested coordination/insertion mechanism, P = polymer chain; C) examples of $H_2B{=}NH_2$ coordinated to a metal center.

Unlike ethene ($H_2C{=}CH_2$), which is stable under ambient conditions, the isoelectronic amino-borane ($H_2B{=}NH_2$) has only been prepared in low temperature matrices and oligomerizes above −150 °C.[2,8] Adding steric bulk to the nitrogen atom increases stability, so that, for example, $H_2B{=}NMeH$[9] or $H_2B{=}N^tBuH$[10] can be observed as transient species using in situ NMR spectroscopy before they also oligomerize. There are two examples where unstable $H_2B{=}NH_2$ can be trapped by coordination to a single metal center. These originate after dehydrogenation of a putative σ-ammonia borane[11] complex, forming $Ru(PCy_3)_2(H)_2(\eta^2\text{-}H_2B{=}NH_2)$ **A**[12] and (Cy-PSiP)-$Ru(H)(\eta^2\text{-}H_2B{=}NH_2)$ **B**, Cy-PSiP = $\kappa^3\text{-}(Cy_2PC_6H_4)_2SiMe$).[13]

We now report that $H_2B{=}NH_2$ can be trapped by a bimetallic $[Rh_2(R_2PCH_2CH_2CH_2PR_2)_2]^{2+}$ fragment to give a novel bridging amino-borane bonding motif. We provide mechanistic evidence for formation of the complex from a monometallic precursor, and show that such dimeric amino-borane species may be important in dehydropolymerization pathways. This report builds upon previous observations that indirectly implicate bimetallic motifs during catalysis.[14–16]

Addition of a slight excess of $H_3B{\cdot}NH_3$ to a $[D_8]$THF solution of $[Rh(L^{Ph})(\eta^6\text{-}C_6H_5F)][BAr^F_4]$ **1** ($L^{Ph} = Ph_2P(CH_2)_3PPh_2$, $Ar^F = 3{,}5\text{-}(CF_3)_2C_6H_3$) resulted in the rapid formation of a bimetallic monocation, which was identified by NMR spectroscopy, electrospray ionization mass spectrometry (ESI-MS), and single-crystal X-ray diffraction, as $[Rh_2(L^{Ph})_2(\mu\text{-}H)(\mu\text{-}H_2B{=}NH_2)][BAr^F_4]$ **3**. One equivalent of the boronium[8,17–20] cation $[THF{\cdot}BH_2{\cdot}NH_3][BAr^F_4]$ was also formed ($\delta(^{11}B)$ 0.5 (t), $J_{BH} = 108$ Hz; lit.[19] $[Et_2O{\cdot}BH_2{\cdot}NH_3][BAr^F_4]$ $\delta(^{11}B)$ 0.2, $J_{BH} = 125$ Hz).

In situ solution NMR data for **3** show a signal at $\delta(^{11}B)$ 51.5, a single ^{31}P environment ($\delta(^{31}P)$ 18.2, $J_{RhP} = 142$ Hz), and a broad peak at $\delta(^1H)$ −7.45 (integral ca. 3H relative to the

---

[*] A. Kumar, Dr. S. D. Pike, Prof. A. S. Weller
Department of Chemistry, Chemistry Research Laboratories, University of Oxford, Mansfield Road, Oxford, OX1 3TA (UK)
E-mail: andrew.weller@chem.ox.ac.uk

N. A. Beattie, Prof. S. A. Macgregor
Institute of Chemical Sciences, Heriot Watt University, Edinburgh, EH14 4AS (UK)
E-mail: S.A.Macgregor@hw.ac.uk

Supporting information for this article can be found under: http://dx.doi.org/10.1002/anie.201600898.

phenyl groups). ESI-MS shows a mono-cation at $m/z = 1060.16$ (calcd 1060.16) with the correct isotope pattern. Crystallization (THF/pentane/-18 °C) gave a small number of crystals, for which a single-crystal X-ray diffraction study showed a $H_2B{=}NH_2$ unit bridging a $\{(Rh_2(L^{Ph})_2(\mu\text{-}H)\}$ unit (Supporting Information, Figure S21). However, insufficient material was obtained upon which to collect reliable NMR data. Complex **3** is unstable in solution at room temperature, decomposing after four hours to give a mixture in which $[Rh(L^{Ph})(THF)_2][BAr^F_4]$ **6** was present in approximately 30 % yield.[21] To put the structure and spectroscopic data on a firm footing, the equivalent reaction using the ^{i}Pr-substituted chelating phosphine gave complex **4**, $[Rh_2(L^{iPr})_2(\mu\text{-}H)(\mu\text{-}H_2B{=}NH_2)][BAr^F_4]$, and **5** (Scheme 2).

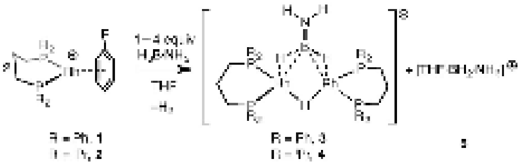

Scheme 2. Formation of amino-borane coordinated dimers **3** and **4**. $[BAr^F_4]^-$ anions are not shown.

This reaction was slower than that observed for L^{Ph}. Complex **4** can also be isolated in 78 % yield as orange crystalline material using an alternative route (see below, Scheme 5). In the absence of $H_3B{\cdot}NH_3$, complex **4** is stable for at least two days in [D$_8$]THF solution. However, when formed in situ **4** decomposes over 24 hrs into a mixture of products, one of which can be characterized as $[Rh_2(L^{iPr})_2(H)_2(\mu\text{-}H)_3][BAr^F_4]$.[22] The room temperature solution NMR data obtained for **4** are very similar to those for **3**: $\delta(^{11}B)$ 51.1; $\delta(^{31}P)$ 40.8, $J_{RhP} = 142$ Hz; $\delta(^1H)$ −8.64 (3H, broad). Progressive cooling to 180 K splits the high field hydride resonance into two signals, in a 2:1 ratio; while two ^{31}P environments were also observed, suggesting a fluxional process at room temperature. An Eyring plot yields the activation data: $\Delta H^{\ddagger} = 31.1 \pm 1.3\ kJ\,mol^{-1}$, $\Delta S^{\ddagger} = -27 \pm 1\ J\,K^{-1}mol^{-1}$, $\Delta G(298\ K)^{\ddagger} = 39.2 \pm 1.6\ kJ\,mol^{-1}$; where the negative entropy of activation suggests an intramolecular process (Supporting Information, Figures S2–3).

The solid-state structure of complex **4** is shown in Figure 1 A. A dimeric Rh$_2$ unit is accompanied by one $[BAr^F_4]^-$ anion, confirming that it is a mono-cation. Two $\{Rh(L^{iPr})\}^+$ fragments are bridged by a hydride and a $H_2B{=}NH_2$ unit. The B−N distance (1.377(6) Å) is consistent with a significant B−N π-interaction, and is similar to that measured in **A** (1.396(3) Å) and **B** (1.359(8) Å), as well as the bridging borylene complex **C** (1.399(3) Å; Scheme 3).[23] The Rh−B distances (2.070(5) and 2.055(5) Å) are similar to those found in the amino-borane complexes **A**, **B**, and $[Ir(PCy_3)_2(H)_2(H_2B{=}NMe_2)][BAr^F_4]$[24] (spanning 1.956(2) to 2.140(13) Å), but significantly shorter than those measured in the bridging thexylborohydride complex **D** (2.330(3) Å).[25] The hydrogen atoms were located but refined using a riding model. Within the limits of X-ray diffraction the B−H distances suggest lengthened, but unbroken bonds (for example, 1.360 Å). The NH$_2$ group is slightly twisted with respect to the BH$_2$ group (24.3°; Figure 1 B). The whole $H_2B{=}NH_2$ fragment lies 54.1° from the Rh-Rh vector so as to accommodate appropriate overlap between the B−H bonds and the two rhodium centers. These are best described as being two distorted square planes (for example, P1/P2/H3/H1) twisted with respect to one another by 102° (Figure 1 C). This motif, which is similar to that observed for **D**, is fully consistent with the low temperature NMR data, and are recreated well in the DFT calculated structure (Supporting Information, Figures S24–26). Each metal center in **4** is best described as Rh^{I}, with no M−M bond.[26] The end-on $\{Rh_2(\mu\text{-}H_2B{=}NH_2)\}$ binding mode contrasts with $H_2C{=}CH_2$ that bridges two metal centers symmetrically using both

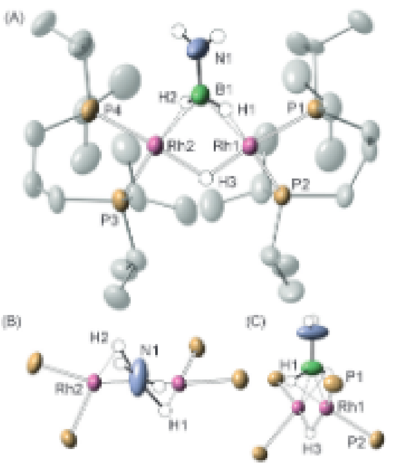

Figure 1. Solid-state structure of the cationic portion of complex **4**. Displacement ellipsoids are shown at the 50 % probability level. Selected bond distances (Å) and angles (°): Rh1−Rh2, 2.7874(4); Rh1−B1, 2.070(5); Rh2−B1, 2.055(5); B1−N1 1.377(6); P1−Rh1, 2.2550(10); P2−Rh1, 2.3063(10); Rh1−H1, 1.718; Rh2−H2, 1.723; ∠ plane (N1B1H1H2)/plane (N1B1Rh1Rh2), 54.1; ∠ plane (Rh1P1P2)/plane (Rh2P3P4), 100.2; ∠ (NH$_2$)/(BH$_2$) 24.3°.

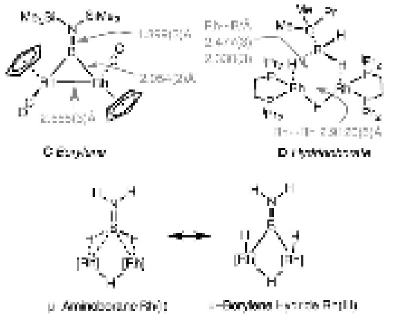

Scheme 3. Limiting valence bond descriptions for complex **4**, and examples of bridging hydridoborate and borylene complexes. [Rh] = $\{Rh(L^{iPr})\}$, charge not shown.

carbon atoms, in either μ-η^2:η^2 or μ-η^1:η^1 bonding modes,[27,28] highlighting the differences between these isosteres.[29]

Surprisingly, the amino-borane in **4** is quite strongly bound. It is only slowly displaced by excess acetonitrile (7% in 50 min) to give a mixture of species, one of which is $[Rh(L^{iPr})(NCMe)_2][BAr^F_4]$.[22] No reaction occurs with toluene, which might be expected to form a $[Rh(L^{iPr})(\eta^6\text{-}C_6H_5Me)]^+$ complex if a monomeric $\{Rh(L^{iPr})\}^+$ fragment were accessible.[30] Addition of cyclohexene, shown to be a probe for free $H_2B{=}NH_2$,[9] gave no reaction. In contrast, H_2 rapidly reacts with **4** to form $[Rh_2(L^{iPr})_2(H)_2(\mu\text{-}H)_3][BAr^F_4]$.[22]

There are two limiting forms for the structure of **4** (and quasi-isostructural 3): 1) a bridging amino-borane at two Rh^I centers, or 2) a bridging borylene dihydride (Rh^{III}), Scheme 3. The observed $\delta(^{11}B)$ chemical shift of 51 ppm is more consistent with the former as amino-boranes bound to one metal center show chemical shifts around 40–50 ppm,[12,13,24,31] while bridging borylenes[32] are generally observed between 90 and 100 ppm.[23,33]

To probe the bonding of the amino-borane ligand in **4**, DFT calculations were used as the basis for a Quantum Theory of Atoms in Molecules (QTAIM) analysis of the total electron density. The results are presented in Figure 2A, along with selected bond critical point (BCP) metrics. Figure 2B provides comparative BCP data for the bridging borylene complex **C**, the hydridoborate complex **D**, and $[(PPh_3)_2Rh(H)(\mu\text{-}H)(\mu\text{-}Cl)_2Rh(H)(PPh_3)_2]^+$, **E**, a well-defined Rh^{III} dimer with both terminal and bridging hydrides.[34] Average data are presented for all complexes where appropriate, although the discussion will focus on the bonding around a single rhodium center (Rh1).

In **4**, the {Rh1/B1/H1} moiety displays bond paths between all three centers, and these enclose a ring critical point (RCP). Thus, **4** has direct Rh1−B1 and Rh1−H1 bonding interactions, while the B1−H1 bond is also intact. Comparison with the Rh1−B1 interaction in **C** provides similar $\rho(r)$ and $H(r)$ values, but highlights a much reduced bond ellipticity (ε) of 0.08; this low value indicates dominant σ-bond character, whereas the value of 0.47 in **4** reflects the asymmetry introduced by the B1-H1 unit. In **D**, the absence of Rh-B BCPs confirms a lack of any direct Rh-B interaction, and this also reduces the average ellipticity of the Rh1−H1 and B1−H1 bonds. Also noticeable are the higher values of $\rho(r)$ and $H(r)$ for the terminal B1-H4 bond in **D** compared to the bridging B-H bonds in both that structure and, in particular, **4**, all of which is consistent with a weakening of the latter. For **E**, the Rh1-H1 BCP has larger values for $\rho(r)$ and $H(r)$ than the Rh1-H1 BCP in **4**, as well as a minimal ε value. These data indicate a terminal Rh−H σ-bond and stress the differences in bridging character of H1 and H2 in **4**. BCP data for the Rh1−H3−Rh2 bonds in **4**, **D**, and **E** are very similar, suggesting that this moiety varies little across these three systems.

Taken together, the QTAIM analyses suggest that **4** is best described as a μ-amino-borane Rh^I species; a μ-borylene hydride Rh^{III} formulism can certainly be ruled out in light of the intact B1−H1/B1−H2 bonds and the lack of Rh1−H1/Rh2−H2 terminal hydride character. The μ-amino-borane ligand in **4** interacts with the rhodium centers through stretched B−H bonds that engage in strong Rh-H and Rh-B interactions. Further support for this assertion comes from the computed $\delta(^{11}B)$ chemical shifts (Figure 2) and the Pipek–Mezey localized orbitals, where a strong bonding interaction spanning all three Rh1, B1, and H1 centers was identified (see Figure 3).

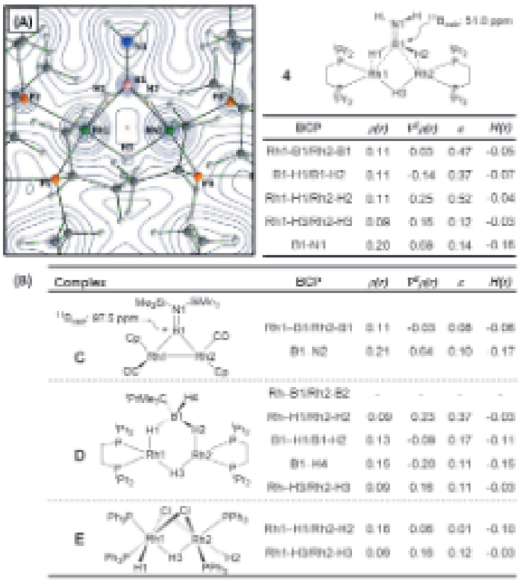

BCP	$\rho(r)$	$\nabla^2\rho(r)$	ε	$H(r)$
Rh1-B1/Rh2-B1	0.11	0.03	0.47	-0.05
B1-H1/B1-H2	0.11	-0.14	0.37	-0.07
Rh1-H1/Rh2-H2	0.11	0.25	0.52	-0.04
Rh1-H3/Rh2-H3	0.09	0.15	0.17	-0.03
B1-N1	0.20	0.08	0.14	-0.15

Complex	BCP	$\rho(r)$	$\nabla^2\rho(r)$	ε	$H(r)$
C	Rh1−B1/Rh2-B1	0.11	-0.03	0.08	-0.06
	B1-N2	0.21	0.04	0.10	-0.17
D	Rh-B1/Rh2-B2	-	-	-	-
	Rh-H1/Rh2-H2	0.09	0.23	0.37	-0.03
	B1-H1/B1-H2	0.13	-0.09	0.17	-0.11
	B1-H4	0.15	-0.20	0.11	-0.15
	Rh-H3/Rh2-H3	0.09	0.16	0.11	-0.03
E	Rh1−H1/Rh2-H2	0.16	0.06	0.01	-0.10
	Rh1-H3/Rh2-H3	0.09	0.16	0.12	-0.03

Figure 2. A) Contour plot of the electron density of the central part of **4** presented in the {Rh1B1Rh2} plane with projected stationary points, bond paths, bond critical points (BCP; green), and ring critical points (RCP; red); the associated table shows selected BCP metrics (a.u.; average data for indicated bonds) and computed $\delta(^{11}B)$ chemical shifts. B) Calculated BCP metrics (a.u.; average data for indicated bonds) for comparator complexes **C** (including the computed ^{11}B chemical shift), **D** and **E** ($\rho(r)$ = electron density, $\nabla\rho(r)$ = Laplacian of electron density, ε = bond ellipticity, $H(r)$ = local energy density). All geometries are based on the crystallographically determined heavy atom positions with hydrogen atoms optimized with the BP86 functional. For a full summary of parameters see Figures S24–27 and associated Tables in the Supporting Information.

The mechanism of the room temperature fluxional process observed for **4** was also probed with DFT calculations and a single transition state was found to account for this process (Scheme 4). This is accessed by cleavage of one (blue) B-H bond to give a transition state structure featuring two Rh-H-Rh bridging hydrides; movement of the original (red) Rh-H-Rh hydride into a Rh-H-B bridging position then completes the exchange (**4′**). Repeating this process from **4′** exchanges a second B-H hydrogen (black) into the Rh-H-Rh bridging position (**4″**). The computed free energy of activation is 55.2 kJ mol^{-1}, somewhat higher than the experimental value (39.2 ± 1.6 kJ mol^{-1}) but still consistent with facile room temperature exchange.

Understanding how bimetallic species such as **3** and **4** are formed, and subsequently react, is important for delineating

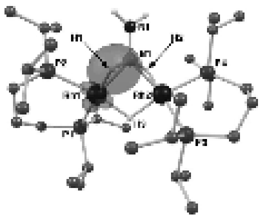

Figure 3. Pipek–Mezey localized orbital, highlighting the bonding interaction of the B1–H1 bond with center Rh1 (see Supporting Information, Figure S28, for details and related orbitals spanning the {Rh2B1H2} and {Rh1H3Rh2} moieties).

Scheme 4. Proposed fluxional process occurring in 4 (and 3). Hydrogen atoms shown by filled circles. See Supporting Information for DFT calculated geometries and energies.

their role in amine-borane dehydrocoupling. The single equivalent of boronium [THF·BH$_2$·NH$_3$][BAr$^F_4$] (5) formed indicates that a hydride abstraction route may be operating, as recently outlined by Conejero and co-workers for the dehydrocoupling of H$_3$B·NMe$_2$H by cationic {Pt-NHC}$^+$ catalysts,[17] as well as that occurring in cationic Ru/Ir-systems[38] or with B(C$_6$F$_5$)$_3$.[19] We reasoned that a similar process would yield 5 by B-H activation[36] and subsequent attack by THF (Scheme 5), alongside {Rh(L^R)H}

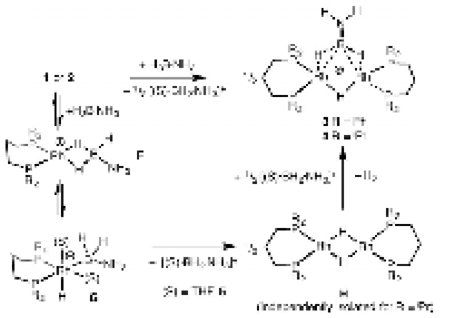

Scheme 5. Mechanism of formation of 3 and 4 by boronium protonation of neutral dimer H. (S) = THF or Et$_2$O. [BAr$^F_4$]$^-$ anions are not shown.

that would dimerize to give neutral [Rh(L^R)H]$_2$ (for example, complex H). Subsequent protonation[17] by boronium 5 and elimination of H$_2$ would give H$_2$B=NH$_2$ trapped on a rhodium dimer. To test this hypothesis, addition of 5 to the neutral dimer is required. [Rh(L^{Ph})H]$_2$ is unknown, and our attempts to prepare it have not been successful. [Rh(L^{iPr})H]$_2$ is a known complex, first prepared by Fryzuk in 1989,[36] and addition of one equivalent of the known boronium salt [Et$_2$O·BH$_2$·NH$_3$][BAr$^F_4$][19] to [Rh(L^{iPr})H]$_2$ in Et$_2$O solvent, resulted in the immediate formation of 4 and gas evolution (H$_2$), which is consistent with the mechanism shown.

A dimeric species similar to 3 was also formed when one equivalent of H$_3$B-NMeH$_2$ was added to 1 in THF solution. This was characterized by in situ NMR spectroscopy and ESI-MS as [Rh$_2$(L^{Ph})$_2$(μ-H)(μ-H$_2$B=NMeH)][BAr$^F_4$] 8: δ(^{1}H) −6.84; δ(^{31}P{^{1}H}) 22.2, 21.5; δ(^{11}B) 50.6.[21] [THF·BH$_2$·NMeH$_2$][BAr$^F_4$] was also formed (δ(^{11}B) 2.8 (t), J_{HB} = 123 Hz; lit. Et$_2$O adduct δ(^{11}B, CD$_2$Cl$_2$) 1.7 (t), J_{HB} = 121 Hz[9]). A more complex mixture of species was formed with H$_3$B-NMe$_2$H, suggesting steric factors may be important in the formation of these aminoborane dimers, although a signal observed at δ(^{11}B) 52.7 suggests dimer formation. Complexes 3, 4, and 8 presumably form via a σ-complex [Rh(L^R)(H$_3$B-NRH$_2$)][BAr$^F_4$], R = H (F Scheme 5) or Me. In THF solution, using the L^{Ph} ligand, these σ-complexes were not observed as boronium formation and subsequent formation of 3 is fast. For L^{iPr}, an intermediate σ-complex could be observed on the way to 4, [Rh(L^{iPr})(H$_3$B·NH$_3$)][BAr$^F_4$], presenting NMR data consistent with structure F.[21] Using H$_3$B·NMe$_3$ (in which the N–H bonds are absent) [Rh(L^{iPr})(H$_3$B·NMe$_3$)][BAr$^F_4$] (7) was isolated and structurally characterized, confirming the in situ NMR studies (Supporting Information, Figure S23). The rapid reaction of [Et$_2$O·BH$_2$·NH$_3$][BAr$^F_4$] with [Rh(L^{iPr})H]$_2$ to form 4 suggests protonation is not slow for this system; currently we cannot determine whether B–H activation or boronium formation is the rate limiting process, although it is likely that either could be promoted by excess amine-borane via N-H···H-B interactions.[37] Calculations on the {Pt-NHC}$^+$/H$_3$B·NMe$_2$H system suggest boronium formation is rate limiting.[17]

Complex 1 (0.5 mol %, THF, 3 hrs, open system) promoted the dehydrocoupling of H$_3$B·NH$_3$ (1.2 equiv of H$_2$ evolved by gas burette; Supporting Information, Figures S4–S7) to form oligomeric species such as *B*-(cyclotriborazanyl)amine-borane (BCTB),[5,38] and insoluble polyaminoborane.[5] With more soluble H$_3$B-NMeH$_2$, polymethylamino-borane was formed [H$_2$BNMeH]$_n$, which was isolated by precipitation from hexanes (M_w = 30600 g mol^{-1}, $Đ$ = 2.6), alongside H$_2$ (1.1 equiv, gas burette). Consistent with the rapid formation of dimers such as 8 in THF, no induction period was observed (as measured by H$_2$ evolution) and similar TOF values were recorded (ca. 200 hr^{-1} for 1 equiv H$_2$), starting from monomeric 1 or in situ formed dimeric 8 (Scheme 6).[39] Changing the solvent to non-nucleophilic 1,2-F$_2$C$_6$H$_4$, and using 1 or in situ generated 8 as a catalyst, did not present an induction period and also revealed a faster TOF (for 8, ca. 1000 hr^{-1} with 1 equiv of H$_2$ released).[40] Sub-catalytic in situ experiments in this solvent[21] show that dimer 8, [(BH$_2$)$_2$NMeH(μ-H)] and boronium [(NH$_2$Me)$_2$BH$_2$][BAr$^F_4$] are present;[41] the latter is suggested to arise from NMeH$_2$ formed from B–N bond cleavage in H$_3$B·NMeH$_2$.[17] Thus, it is likely that similar active species are present in THF or 1,2-F$_2$C$_6$H$_4$. The lack of induction period is in direct contrast to xantphos-based rhodium catalysts, which show induction periods for H$_3$B·NMeH$_2$ dehydrocoupling in C$_6$H$_5$F,[5,15] suggesting that a different kinetics regime or mechanism is in operation.

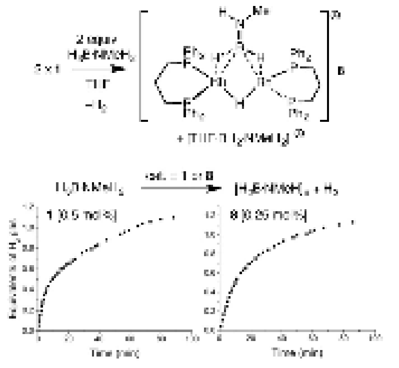

Scheme 6. H_2 evolution experiments using **1** or **8**, and $H_3B{\cdot}NMeH_2$ (0.5 mol% [Rh], 0.41 M amine-borane, THF, 298 K). $[BAr^F_4]^-$ anions are not shown.

Determination of the resting state in catalysis was hampered by the addition of excess amine-borane ($H_3B{\cdot}NH_3$ or $H_3B{\cdot}NMeH_2$) to the preformed dimeric species **3** or **4** in THF, resulting in a mixture of products that have been resistant to characterization. Turning to the pure and well-characterized dimer **4**, initial rate measurements in a closed system (4 mol% rhodium, THF) were more informative, and a first-order dependence for either $H_3B{\cdot}NH_3$ or $H_3B{\cdot}NMeH_2$, as well as catalyst **4**, were measured for the early pseudo zero-order phase of catalysis (Supporting Information, Figures S19 and 20). Such behavior is not consistent with a rapid dimer–monomer equilibrium for which an order of [**4**]$^{1/2}$ would be expected,[22,38,43] a view supported by the stoichiometric reactions with acetonitrile or toluene (see above). Under these conditions complexes **2** or **4** do not promote full conversion of amine-borane (for **4**, 70% conversion of $H_3B{\cdot}NH_3$ after 10 hrs). Informed by the sub-catalytic experiments and H_2 addition studies, we propose that $[Rh_2(L^{iPr})_2(H)_2(\mu\text{-}H)_3][BAr^F_4]$[23] is formed during catalysis. Consistent with this hypothesis, isolated $[Rh_2(L^{iPr})_2(H)_2(\mu\text{-}H)_3][BAr^F_4]$ is a poorer catalyst for $H_3B{\cdot}NH_3$ dehydrocoupling in a sealed system (4 mol% [Rh], 30% conversion after 10 hrs) than both **2** and **4**. Interestingly, degassing the closed system restarted catalysis, indicating that inhibition by the H_2 formed during dehydrocoupling is partially reversible (Supporting Information, Figure S10). Co-promotion of dehydrocoupling by boronium is discounted, as these studies show that isolated **4** is an active pre-catalyst in its absence. Consistent with this statement, dehydrocoupling of $H_3B{\cdot}NH_3$ is not catalyzed by $[Et_2O{\cdot}BH_2{\cdot}NH_3][BAr^F_4]$ under the conditions used here (0.5 mol%, THF, 298 K, 3 hrs).[19] Overall, these observations do not let us discriminate between active catalysts derived from dimeric **4** (or **3**) or monomeric species that result from irreversible, but fast, consumption of **4** (or **3**), under the conditions of excess amine-borane.[43]

The ambiguity surrounding mono/bimetallic catalysis has parallels with xantphos-based amine-borane dehydropolymerization catalysts, where P-C activated phosphido-bridged species are formed that are also active catalysts, in contrast to the amino-borane-bridged dimers observed here.[15] Deconvoluting these systems under conditions of high amine-borane concentration is thus a significant challenge to address if precise control over the resulting polyamino-borane is to be achieved by metal/ligand design. Nevertheless, the observation of novel and unexpected bridging amino-borane complexes as the first-formed species, offers tantalizing clues as to the nature of the actual catalysts; and also suggests that boronium cations may play a more general role in amine-borane dehydrocoupling than generally appreciated.[17,19]

Acknowledgements

The EPSRC (A.S.W. and S.A.M., EP/M024210/1; N.A.B., DTP Studentship), the Rhodes Trust (A.K.), G. M. Adams (G. P. C. analysis).

Keywords: amino-borane · dehydrocoupling · DFT · catalytic mechanisms · rhodium dimers

How to cite: *Angew. Chem. Int. Ed.* **2016**, *55*, 6651–6656
Angew. Chem. **2016**, *128*, 6763–6768

---

[1] E. M. Leitao, T. Jurca, I. Manners, *Nat. Chem.* **2013**, *5*, 817; H. C. Johnson, T. N. Hooper, A. S. Weller, *Top. Organomet. Chem.* **2015**, *49*, 153; A. Staubitz, A. P. M. Robertson, M. E. Sloan, I. Manners, *Chem. Rev.* **2010**, *110*, 4023.

[2] V. Pons, R. T. Baker, N. K. Szymczak, D. J. Heldebrant, J. C. Linehan, M. H. Matus, D. J. Grant, D. A. Dixon, *Chem. Commun.* **2008**, 6597.

[3] A. Staubitz, M. E. Sloan, A. P. M. Robertson, A. Friedrich, S. Schneider, P. J. Gates, J. Schmedt auf der Günne, I. Manners, *J. Am. Chem. Soc.* **2010**, *132*, 13332.

[4] R. T. Baker, J. C. Gordon, C. W. Hamilton, N. J. Henson, P.-H. Lin, S. Maguire, M. Murugesu, B. L. Scott, N. C. Smythe, *J. Am. Chem. Soc.* **2012**, *134*, 5598; A. N. Marziale, A. Friedrich, I. Klopsch, M. Drees, V. R. Celinski, J. Schmedt auf der Günne, S. Schneider, *J. Am. Chem. Soc.* **2013**, *135*, 13342.

[5] H. C. Johnson, E. M. Leitao, G. R. Whittell, I. Manners, G. C. Lloyd-Jones, A. S. Weller, *J. Am. Chem. Soc.* **2014**, *136*, 9078.

[6] A. Glüer, M. Förster, V. R. Celinski, J. Schmedt auf der Günne, M. C. Holthausen, S. Schneider, *ACS Catal.* **2015**, *5*, 7214.

[7] J. F. Hartwig, *OrganoTransition Metal Chemistry*, University Science Books, Sausalito, **2010**.

[8] H. A. McGee, C. T. Kwon, *Inorg. Chem.* **1970**, *9*, 2458; J. S. Wang, R. A. Geanangel, *Inorg. Chim. Acta* **1988**, *148*, 185.

[9] O. J. Metters, A. M. Chapman, A. P. M. Robertson, C. H. Woodall, P. J. Gates, D. F. Wass, I. Manners, *Chem. Commun.* **2014**, *50*, 12146.

[10] H. C. Johnson, A. S. Weller, *J. Organomet. Chem.* **2012**, *721–722*, 17.

[11] G. J. Kubas, *Metal Dihydrogen and σ-bond complexes*, Kluwer, New York, **2001**; M. Shimoi, S. Nagai, M. Ichikawa, Y. Kawano, K. Katoh, M. Uruichi, H. Ogino, *J. Am. Chem. Soc.* **1999**, *121*, 11704.

[12] G. Alcaraz, L. Vendier, E. Clot, S. Sabo-Etienne, *Angew. Chem. Int. Ed.* **2010**, *49*, 918; *Angew. Chem.* **2010**, *122*, 930.

[13] M. C. MacInnis, R. McDonald, M. J. Ferguson, S. Tobisch, L. Turculet, *J. Am. Chem. Soc.* **2011**, *133*, 13622.

[14] R. Dallanegra, A. P. M. Robertson, A. B. Chaplin, I. Manners, A. S. Weller, *Chem. Commun.* **2011**, *47*, 3763.

[15] H. C. Johnson, A. S. Weller, *Angew. Chem. Int. Ed.* **2015**, *54*, 10173; *Angew. Chem.* **2015**, *127*, 10311.

[16] A. B. Chaplin, A. S. Weller, *Angew. Chem. Int. Ed.* **2010**, *49*, 581; *Angew. Chem.* **2010**, *122*, 591.

[17] M. Roselló-Merino, J. López-Serrano, S. Conejero, *J. Am. Chem. Soc.* **2013**, *135*, 10910.

[18] W. E. Piers, S. C. Bourke, K. D. Conroy, *Angew. Chem. Int. Ed.* **2005**, *44*, 5016; *Angew. Chem.* **2005**, *117*, 5142.

[19] F. H. Stephens, R. T. Baker, M. H. Matus, D. J. Grant, D. A. Dixon, *Angew. Chem. Int. Ed.* **2007**, *46*, 746; *Angew. Chem.* **2007**, *119*, 760.

[20] T. A. Shuttleworth, M. A. Huertos, I. Pernik, R. D. Young, A. S. Weller, *Dalton Trans.* **2013**, *42*, 12917.

[21] See the Supporting Information.

[22] A. Kumar, J. S. A. Ishibashi, T. N. Hooper, T. C. Mikulas, D. A. Dixon, S. Y. Liu, A. S. Weller, *Chem. Eur. J.* **2016**, *22*, 310.

[23] H. Braunschweig, M. Forster, T. Kupfer, F. Seeler, *Angew. Chem. Int. Ed.* **2008**, *47*, 5981; *Angew. Chem.* **2008**, *120*, 6070.

[24] G. Alcaraz, A. B. Chaplin, C. J. Stevens, E. Clot, L. Vendier, A. S. Weller, S. Sabo-Etienne, *Organometallics* **2010**, *29*, 5591.

[25] R. T. Baker, D. W. Ovenall, R. L. Harlow, S. A. Westcott, N. J. Taylor, T. B. Marder, *Organometallics* **1990**, *9*, 3028.

[26] J. C. Green, M. L. H. Green, G. Parkin, *Chem. Commun.* **2012**, *48*, 11481.

[27] W. H. Monillas, G. P. A. Yap, L. A. MacAdams, K. H. Theopold, *J. Am. Chem. Soc.* **2007**, *129*, 8090.

[28] O. P. Anderson, B. R. Bender, J. R. Norton, A. C. Larson, P. J. Vergamini, *Organometallics* **1991**, *10*, 3145.

[29] C. Y. Tang, A. L. Thompson, S. Aldridge, *Angew. Chem. Int. Ed.* **2010**, *49*, 921; *Angew. Chem.* **2010**, *122*, 933.

[30] S. D. Pike, I. Pernik, R. Theron, J. S. McIndoe, A. S. Weller, *J. Organomet. Chem.* **2015**, *784*, 75.

[31] G. Bénac-Lestrille, U. Helmstedt, L. Vendier, G. Alcaraz, E. Clot, S. Sabo-Etienne, *Inorg. Chem.* **2011**, *50*, 11039; C. Y. Tang, A. L. Thompson, S. Aldridge, *J. Am. Chem. Soc.* **2010**, *132*, 10578.

[32] H. Braunschweig, R. D. Dewhurst, V. H. Gessner, *Chem. Soc. Rev.* **2013**, *42*, 3197.

[33] H. Braunschweig, Q. Ye, A. Damme, K. Radacki, *Chem. Commun.* **2013**, *49*, 7593; H. Braunschweig, M. Colling, *Coord. Chem. Rev.* **2001**, *223*, 1.

[34] A. Rifat, N. J. Patmore, M. F. Mahon, A. S. Weller, *Organometallics* **2002**, *21*, 2856.

[35] R. Kumar, B. R. Jagirdar, *Inorg. Chem.* **2013**, *52*, 28; A. Rossin, M. Caporali, L. Gonsalvi, A. Guerri, A. Lledos, M. Peruzzini, F. Zanobini, *Eur. J. Inorg. Chem.* **2009**, *2009*, 3055.

[36] M. D. Fryzuk, W. E. Piers, F. W. Einstein, T. Jones, *Can. J. Chem.* **1989**, *67*, 883.

[37] A. Kumar, H. C. Johnson, T. N. Hooper, A. S. Weller, A. G. Algarra, S. A. Macgregor, *Chem. Sci.* **2014**, *5*, 2546; X. Chen, J.-C. Zhao, S. G. Shore, *Acc. Chem. Res.* **2013**, *46*, 2666; V. S. Nguyen, M. H. Matus, D. J. Grant, M. T. Nguyen, D. A. Dixon, *J. Phys. Chem. A* **2007**, *111*, 8844.

[38] H. A. Kalviri, F. Gärtner, E. Ye, I. Korobkov, R. T. Baker, *Chem. Sci.* **2015**, *6*, 618.

[39] An induction period for H_3B-NMe_2H dehydrocoupling using catalyst **1** in 1,2-$F_2C_6H_4$ solvent has been reported. See Ref. 14 and supporting materials. The lack of induction period observed using H_3B-$NMeH_2$ may be a result of reduced steric effects that promote boronium formation. Related calculations using **1**/H_3B-NMe_2H have suggested that dimeric rhodium species are unlikely to be formed, in contrast to observations reported here: V. Butera, N. Russo, E. Sicilia, *ACS Catal.* **2014**, *4*, 1104.

[40] We were unable to fit the temporal evolution of H_2 to a simple kinetic profile in THF solvent. Interestingly, in 1,2-$F_2C_6H_4$ H_2 evolution appears to follow a zero-order profile, perhaps suggestive of saturation kinetics operating in this non-nucleophilic solvent.

[41] K. R. Graham, M. E. Bowden, T. Kemmitt, *Inorg. Chem.* **2011**, *50*, 932.

[42] Z. Lu, B. L. Conley, T. J. Williams, *Organometallics* **2012**, *31*, 6705.

[43] Heterobimetallic systems have been reported for the dehydrogenation of H_3B-NMe_2H, see: T. Miyazaki, Y. Tanabe, M. Yuki, Y. Miyake, Y. Nishibayashi, *Organometallics* **2011**, *30*, 2394.

Received: January 26, 2016
Revised: March 22, 2016

Metallacarboranes

International Edition: DOI: 10.1002/anie.201602440
German Edition: DOI: 10.1002/ange.201602440

14-Vertex Heteroboranes with 14 Skeletal Electron Pairs: An Experimental and Computational Study

Alasdair P. M. Robertson, Nicholas A. Beattie, Greig Scott, Wing Y. Man, John J. Jones, Stuart A. Macgregor, Georgina M. Rosair, and Alan J. Welch**

Abstract: *Three isomers of [(Cp*Ru)$_2$C$_2$B$_{10}$H$_{12}$], the first examples of 14-vertex heteroboranes containing 14-skeletal electron pairs, have been synthesized by the direct electrophilic insertion of a {Cp*Ru$^+$} fragment into the anion [4-Cp*-4,1,6-RuC$_2$B$_{10}$H$_{12}$]$^-$. All three compounds have the same unique polyhedral structure having an approximate C$_s$ symmetry and featuring a four-atom trapezoidal face. X-ray diffraction studies could confidently identify only one of the two cage C atoms in each structure. The other C atom position has been established by a combination of i) best fitting of computed and experimental ^{11}B and ^{1}H NMR chemical shifts, and ii) consideration of the lowest computed energy for series of isomers studied by DFT calculations. In all three isomers, one cage C atom occupies a degree-4 vertex on the short parallel edge of the trapezium.*

The structures of boranes and heteroboranes are usually interpreted in terms of the electron-counting principles, established by Wade and Mingos more than 40 years ago.[1] These rules rationalize families of clusters, such as *closo* structures with $n+1$ skeletal electron pairs (SEPs), *nido* structures with $n+2$ SEPs, and *arachno* structures with $n+3$ SEPs (where n is the number of cluster vertices).

A small but interesting further family of heteroboranes is that in which the members possess only n SEPs, and these species, generally referred to as *hypercloso*, have been the subject of significant interest in the literature.[2] In general these clusters do not have the structures normally encountered for $n+1$ SEP species but rather they are related to them by a single diamond-square-diamond (d-s-d) isomerization.[3] An excellent early example is [(CpFe)$_2$C$_2$B$_6$H$_8$],[4] a 10-vertex (10-v) 10-SEP species structurally related to the bicapped square antiprismatic 10-v 11-SEP cobalt analogue [(CpCo)$_2$C$_2$B$_6$H$_8$][5] by a d-s-d rearrangement of the 2-6-10-9 diamond of the latter polyhedron (Figure 1).

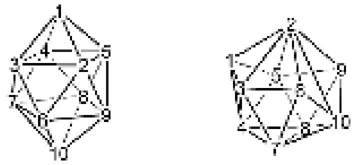

Figure 1. Left: The 10-v 11-SEP bicapped square antiprismatic structure of 2,6-Cp$_2$-2,6,1,10-Co$_2$C$_2$B$_6$H$_8$. Right: The 10-v 10-SEP structure of 2,10-Cp$_2$-2,10,1,9-Fe$_2$C$_2$B$_6$H$_8$, featuring a degree-6 metal atom at vertex 2. The two polyhedra are related by applying a d-s-d sequence to the 2-6-10-9 diamond of the left structure.

A number of these *hypercloso* clusters have been reported by Kennedy et al.[6] who argued that they are actually $n+1$ SEP compounds in which the metal utilizes four, as opposed to the usual three, orbitals in cluster bonding. In this approach the compounds are simply regarded as differently structured *closo* species and, accordingly, the authors used the descriptor *isocloso*. Although MO calculations by Mingos and coworkers support the *hypercloso* view[7] and the fact that Spencer et al. have shown that the simple addition of two electrons to [*hypercloso*-(η-C$_6$Me$_6$)RuB$_9$H$_9$] converts it into [*closo*-(η-C$_6$Me$_6$)RuB$_9$H$_9$]$^{2-}$,[8] the *isocloso* descriptor is still in use in the present day.[6,8]

To date, the small library of *hypercloso* heteroboranes has almost exclusively been composed of clusters with between 9 and 12 vertices, limiting the possibility of an extensive study of such species. The *hypercloso* electron count distorts the cluster from a geometry associated with an $n+1$ SEP species to one in which at least one vertex, usually a transition metal, becomes highly connected. Accordingly we believe that the supraicosahedral area holds promise with respect to a systematic study of *hypercloso* compounds since supraicosahedra necessarily contain highly connected vertices. Currently this field is relatively under-developed, the only confirmed[9] examples of supraicosahedral *hypercloso* metallacarboranes[10] being the 13-v 13-SEP species [4,5-Cp*$_2$-4,5,2,3-Ru$_2$C$_2$B$_9$H$_{11}$] (I) and [4,5-Cp*$_2$-6-SMe$_2$-4,5,2,3-Ru$_2$C$_2$B$_9$H$_{10}$]$^+$ (II) isolated by Kudinov and co-workers.[11] In this Communication we describe the synthesis of the first 14-v 14-SEP *hypercloso* metallacarboranes and their characterization by a combination of spectroscopic, crystallographic, and computational studies.

The two-electron reduction of [1,2-C$_2$B$_{10}$H$_{12}$] with Na in THF followed by treatment with [Cp*Ru(MeCN)$_3$]Cl and cation metathesis afforded the 13-v 14-SEP ruthenacarborane [BTMA][4-Cp*-4,1,6-RuC$_2$B$_{10}$H$_{12}$] (1) in 76% yield (BTMA = PhCH$_2$NMe$_3$). Salt **1** was fully characterized spectroscopically and crystallographically (see the Supporting Information).[12] As is common for 4,1,6-MC$_2$B$_{10}$ species, the anion in **1** is fluxional in solution at room temperature

---

[*] Dr. A. P. M. Robertson, N. A. Beattie, Dr. G. Scott, Dr. W. Y. Man, J. J. Jones, Prof. S. A. Macgregor, Dr. G. M. Rosair, Prof. A. J. Welch
Institute of Chemical Sciences, Heriot-Watt University
Edinburgh EH14 4AS (UK)
E-mail: s.a.macgregor@hw.ac.uk
a.j.welch@hw.ac.uk

Supporting information (containing the experimental, spectroscopic, crystallographic, and computational details of all new compounds reported herein) and the ORCID identification number(s) for the author(s) of this article can be found under http://dx.doi.org/10.1002/anie.201602440.

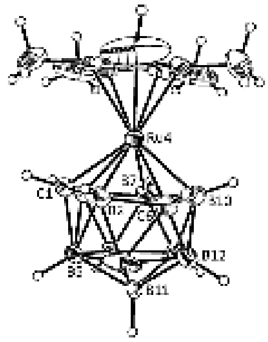

Figure 2. Solid-state structure of the anion of 1.[21] The structure is partially disordered and only the major component is shown. Selected bond lengths [Å]: Ru4–C1 2.213(4), Ru4–B2 2.301(4), Ru4–C6 2.259(4), Ru4–B10 2.242(3), Ru4–B7 2.267(3), Ru4–B3 2.256(2), Ru4–C(Cp*) 2.192(5)–2.242(5).

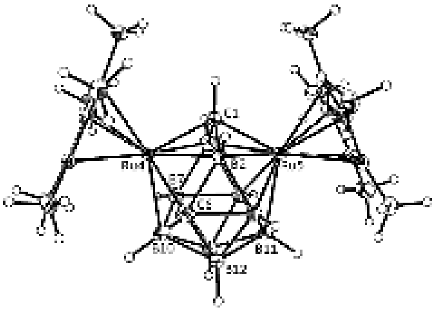

Figure 3. Solid-state structure of compound 2.[21] Selected bond lengths [Å]: Ru4–C1 2.0254(16), Ru4–B2 2.2788(19), Ru4–C6 2.204(2), Ru4–B10 2.2167(19), Ru4–B7 2.2117(19), Ru4–B3 2.2801(19), Ru5–C1 2.0342(16), Ru5–B2 2.2786(19), Ru5–B9 2.2029(19), Ru5–B11 2.2119(19), Ru5–B8 2.2229(19), Ru5–B3 2.299(2), Ru4–C(Cp*) 2.2308(16)–2.2510(15), Ru5–C(Cp*) 2.2294(16)–2.2469(17).

through a double d-s-d process,[22] with NMR spectra revealing time-averaged C_s symmetry. A perspective view of the anion is shown in Figure 2.

Treatment of **1** in THF with 0.25 equiv $[Cp^*RuCl]_4$ followed by heating to reflux over 16 h produced a complex mixture of products with eight well-defined species clearly visible by thin-layer chromatography (see Plate S1 in the Supporting Information). Four of these species have been successfully characterized by a combination of mass spectrometry, multinuclear NMR spectroscopy, X-ray diffraction, and DFT calculations.

The seventh fastest moving band is an orange compound (**2**) which was assigned as $[(Cp^*Ru)_2C_2B_9H_{11}]$ by mass spectrometry and NMR spectroscopy. Notably, however, NMR spectroscopy indicated this was clearly not the 4,5,2,3-$Ru_2C_2B_9$ species **I** isolated by Kudinov et al. since both the ^1H and ^{11}B NMR spectra reveal no molecular symmetry. Moreover there is no very high-frequency ^{11}B NMR resonance signal in the spectrum of **2** ($\delta_{max} = 31$ ppm in **2**; $\delta_{max} = 97$ ppm in the 4,5,2,3 compound). Instead, there is a high frequency resonance signal in the ^1H NMR spectrum ($\delta = 16.6$ ppm) attributable to the $C_{cage}H$ proton. A crystallographic study (Figure 3) established that **2** is $[4,5\text{-}Cp^*_2\text{-}4,5,1,6\text{-}Ru_2C_2B_9H_{11}]$, a 13-v 13-SEP *hypercloso* species and a positional isomer of **I**.[21] We assume that **2** is formed by loss of the {B5H} fragment from the anion of **1** or (possibly more likely) its 4,1,8-RuC_2B_{10} isomer,[13] and capping of the open face thus produced by a $\{Cp^*Ru^+\}$ fragment.

The diruthenacarborane cage in **2** has a docosahedral structure, essentially the same structure as found in 13-v 14-SEP species, and the origin of this superficially unusual result has been traced to the fact that the C_{2v}-symmetric docosahedron necessarily has nondegenerate molecular orbitals.[14] We have shown that the HOMO of the parent borate $[B_{13}H_{13}]^{2-}$ is strongly bonding with respect to the 1-2 and 1-3 edges, and moderately strongly bonding with respect to the 6-9 and 7-8 edges.[15] This allows us to rationalize the facts that the 1-2 and 1-3 distances in **2** are about 0.09–0.10 Å longer, and the 6-9 and 7-8 distances in **2** are about 0.02–0.04 Å longer, than the equivalent distances in crystallographically characterized 13-v 14-SEP 4,5,1,6-$M_2C_2B_9$ species (see the Supporting Information).[15,16]

The fastest moving band (identified as purple compound **3**), the third fastest band (dark green compound **4**), and the sixth fastest moving band (purple compound **5**) were also studied, with elemental analysis and/or mass spectrometry suggesting the formula $[(Cp^*Ru)_2C_2B_{10}H_{12}]$ for all three. The ^1H NMR spectra of **3**–**5** contain one relatively high frequency $C_{cage}H$ resonance signal ($\delta = 8.6$ to 10.5 ppm) and two resonance signals corresponding to the Cp* H atoms. The asymmetry of all three compounds is confirmed by their ^{11}B NMR spectra which exhibit ten equal-integral resonance signals for **4** and **5** and nine resonance signals for **3** (one less signal as a result of the overlapping of two signals). In all three compounds, the range of ^{11}B chemical shifts is relatively large, $\delta = 76.0$ to -13.6 ppm for **3**, 54.8 to -22.9 ppm for **4**, and 72.1 to -12.1 ppm for **5**.

Thus compounds **3**–**5** appear to be the first examples of 14-v 14-SEP *hypercloso* species, presumably formed by direct electrophilic insertion (DEI)[11,10b,17] of a $\{Cp^*Ru^+\}$ fragment into the anion of **1**, and it was clearly of importance to characterize each of them crystallographically. To our initial surprise, compounds **3**, **4**, and **5** are all isomorphous with **2** but the origin of this became clear when the structures were solved. Compounds **3**–**5**, isomers of each other differing only in the positions of the cage C atoms, share the same basic skeleton, which is shown together with an arbitrary numbering scheme in Figure 4. As in **2**, the carborane central cores in **3**–**5** are flanked by two large {Cp*Ru} fragments whose Cp* rings are inclined at about 47°. The isomorphism presumably results from the packing of molecules in the crystal being determined by the same overall shape of the molecules and not the relatively minor differences in dipole moment that arise from different C atom positions or the presence (in **3**–**5**) of one additional BH unit. The 14-vertex cluster has two degree-6 vertices (i.e., 6-connected with respect to the polyhedron, vertices 2 and 7) occupied by the Ru atoms, ten degree-5 vertices, and two degree-4 vertices (1 and 4)

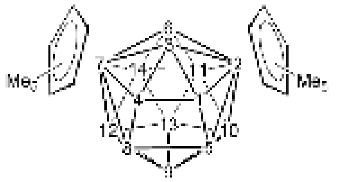

Figure 4. Generalized representation of compounds 3–5 and atomic numbering scheme.

occupying the short parallel edge of an approximate trapezium (1-4-8-5). The 1-4 distances are 1.642(4), 1.618(6), and 1.612(4) Å and the 5-8 distances 2.196(6), 2.024(9), and 2.049(5) Å for compounds 3, 4 and 5, respectively. The whole molecule has approximate C_s symmetry about the plane containing vertices 3, 6, 9, and 13. To the best of our knowledge this is the first time such a cluster structure has been reported. It is clearly distinct from the bicapped hexagonal antiprism (bha) typical of 14-v 15-SEP species,[17,18] again reflecting the unique structures of *hypercloso* clusters. Formally, a bha structure could be formed from this unique polyhedron by making the 4–5 connection and applying a d-s-d process to the 1-2-10-5 diamond.

It is clearly important to identify which $[(Cp^*Ru)_2C_2B_{10}H_{12}]$ isomer is which for each of compounds 3–5 by establishing the positions of the cage C atoms. Analysis of the various NMR spectra confirms that in none of the compounds do both cage C atoms occupy vertices on the approximate mirror plane of symmetry (that is, vertices 3, 6, 9, and 13), nor are they related by that plane of symmetry. Distinguishing between BH and CH vertices in (hetero)carborane structures studied crystallographically is well-known to be challenging, and it is particularly so in the case of compounds 3–5. This arises because 76% of the X-ray scattering power of the molecules is localized in the two peripheral {Cp*Ru} fragments which are effectively symmetry-related, resulting in a degree of pseudo-symmetry overall and comparatively poor definition of the asymmetric $\{C_2B_{10}\}$ fragments.

We have recently described two new approaches, the vertex–centroid distance (VCD)[19] and boron–hydrogen distance (BHD)[17] methods, that are useful in distinguishing cage B and cage C atoms in carboranes and heterocarboranes. Both methods analyze the "Prostructure", the result of refinement in which all B or C vertices are treated as B. The VCD method works by comparing distances from topologically equivalent vertices to the polyhedral centroid, whereas in the BHD method each B−H distance is compared against all others. Although both methods were successfully used to identify the cage C atoms in 1 and 2, the relatively low symmetry of the polyhedra in compounds 3–5 (C_1 at best) means that for these compounds the more useful approach is the BHD method. B−H distances in the Prostructures of 3–5 are given in the Supporting Information.

The compound in which the clearest indication is given of the position of one of the cage C atoms is compound 4, which has B12−H12 0.33(6) Å in the Prostructure. The next shortest B−H distance is at vertex 1 (0.73(4) Å). However, although we are fully confident that in 4 one cage C atom is at vertex 12, we have sought further evidence for the position of the second C atom through DFT calculations. Using DFT, the crystallographically determined skeleton was used to build ten isomers $[2,7\text{-}Cp^*\text{-}2,7,12,a\text{-}Ru_2C_2B_{10}H_{12}]$ (with $a=1$, 3, 4, 5, 6, 8, 9, 11, 13, and 14; $a=10$ can be disregarded since that would be mirror-symmetric) and each isomer was optimized using the BP86 functional. Following optimization, the ^1H and ^{11}B NMR chemical shifts of each isomer were calculated at the B3LYP level and compared with those measured experimentally.[20] In summary, the isomer $[2,7\text{-}Cp^*\text{-}2,7,1,12\text{-}Ru_2C_2B_{10}H_{12}]$ very clearly gave the best agreement between theory and experiment. Thus linear regression of the computed and experimental ^{11}B NMR shifts yields an R^2 value for the 2,7,1,12 isomer of 0.9954, compared with $R^2=0.8676$ for the next-best isomer (2,7,3,12). In terms of ^1H NMR shifts, the difference in the sum ($\Delta\Sigma\delta$) of the calculated and actual chemical shifts for the two $C_{cage}H$ resonance signals is only 1.21 ppm for the 2,7,1,12 isomer, compared with 5.01 ppm for the next-best isomer (2,7,4,12). Finally, of all of the ten isomers the lowest free energy computed (BP86-D3 with a correction for the THF solvent) was for the 2,7,1,12 isomer, which had a value 3.5 kcal mol−1 below that of the next most stable isomer (2,7,4,12). Thus compound 4 is identified as $[2,7\text{-}Cp^*\text{-}2,7,1,12\text{-}Ru_2C_2B_{10}H_{12}]$. The position of the second cage C atom at vertex 1 is, moreover, chemically sensible in that vertex 1 is the degree-4 vertex in the trapezoidal face which subtends an acute angle, B4-C1-B5 = 86.7(4)°, consistent with B4⋯B5 being an incipient connectivity, 2.220(11) Å. A perspective view of 4 is given in Figure 5.

In the Prostructure of compound 5 there is also one strong indication of a cage carbon atom since the B6−H6 distance is only 0.50(3) Å (the next shortest B−H distance is at vertex 1 and measures 0.96(3) Å). Since vertex 6 lies on the effective mirror plane of the molecule, there are only four possible isomers for compound 5, $[2,7\text{-}Cp^*\text{-}2,7,6,b\text{-}Ru_2C_2B_{10}H_{12}]$ (with $b=1$, 5, 11, and 12). DFT calculations strongly suggest that $b=1$. R^2 is 0.9899 for the 2,7,1,6 isomer compared to 0.8611 for the next-best fit (2,7,6,11). Only one resonance signal

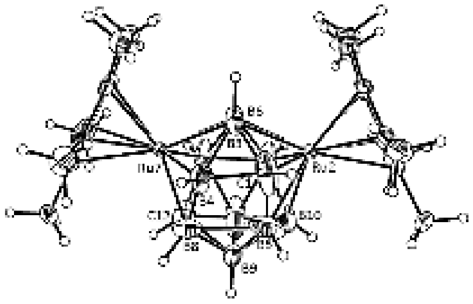

Figure 5. Solid-state structure of compound 4.[21] Selected bond lengths [Å]: Ru2−C1 2.049(4), Ru2−B5 2.315(7), Ru2−B10 2.127(5), Ru2−B11 2.187(4), Ru2−B6 2.264(4), Ru2−B3 2.258(4), Ru7−B3 2.253(4), Ru7−B4 2.132(4), Ru7−B8 2.197(5), Ru7−C12 2.147(4), Ru7−B14 2.158(4), Ru7−B6 2.265(4), Ru2−C(Cp*) 2.236(3)–2.271(3), Ru7−C(Cp*) 2.243(3)–2.261(3), B4⋯B5 2.220(11).

attributed to $C_{cage}H$ protons was evident in the ^{1}H NMR spectrum of 5 (see the Supporting Information) but it fits best ($\Delta\delta = 0.61$ ppm) with one of the computed shifts for the 2,7,1,6 isomer (next smallest $\Delta\delta = 4.90$ ppm). Finally, the 2,7,1,6 isomer has the lowest computed free energy of all four isomers considered, being 4.9 kcal mol^{-1} more stable than the next most stable isomer (2,7,5,6). We therefore conclude that compound 5 is [2,7-Cp*-2,7,1,6-$Ru_2C_2B_{10}H_{12}$]. There is partial disorder between the C1 and B4 centers in the crystallographically determined structure of 5 but this does not change the isomer since 2,7,1,6 and 2,7,4,6 are enantiomeric.

For compound 3 the BHD analysis is complicated by three apparently short B–H distances, measuring 0.58(4), 0.74(3), and 0.87(4) Å at vertices 5, 1, and 13 respectively, although the significance of the short B5–H5 distance may be questioned since B5 is disordered over two positions (see the Supporting Information). Nevertheless, for this compound DFT calculations were performed on two sets of isomers, [2,7-Cp*-2,7,5,*c*-$Ru_2C_2B_{10}H_{12}$] (with $c = 1, 3, 4, 6, 9, 10, 11, 12, 13$, and 14), and [2,7-Cp*-2,7,1,*d*-$Ru_2C_2B_{10}H_{12}$] (with $d = 3, 5, 6, 8, 9, 10, 11, 12, 13$, and 14). In the latter case, these calculations gave strong support for the second cage C atom being located at vertex 13. Location of this atom at vertex 13 afforded the best fit between calculated and actual ^{11}B NMR chemical shifts ($R^2 = 0.9939$), the lowest free energy, and the third best fit between calculated and actual ^{1}H NMR chemical shifts ($\Delta\Sigma\delta = 0.93$ ppm). In the former case (that is, with one cage C atom at vertex 5), the situation was anomalous, with the 2,7,3,5 isomer being best in terms of ^{11}B NMR shifts, the 2,7,4,5 isomer best in terms of ^{1}H NMR shifts, and the 2,7,5,13 isomer having the lowest free energy. None of these, however, was either better or lower in value than the corresponding measure for the 2,7,1,13 isomer and therefore we tentatively suggest that compound 3 is [2,7-Cp*-2,7,1,13-$Ru_2C_2B_{10}H_{12}$] based on the available data.

In conclusion, we have prepared the first examples of 14-v 14-SEP (*hypercloso*) heteroboranes and established that they have unique cluster structures. By a combination of spectroscopic, crystallographic, and computational studies, we have determined the isomeric nature of three examples, establishing that in all cases one cage C atom occupies a degree-4 vertex (vertex 1 in our arbitrary numbering scheme shown in Figure 4) on the short parallel edge of a trapezoidal polyhedral face. The formation of multiple isomers by a DEI reaction has precedent[17] and is to be expected since there are likely to be multiple sites on the surface of the *closo* anionic cage where the electrophile can attack, unlike the conventional reduction–metalation synthesis of metallacarboranes in which an open face is presented to the incoming electrophile. Future contributions will develop this theme and expand further the unique chemistry of supraicosahedral *hypercloso* metallacarboranes.

Acknowledgements

We thank the Leverhulme Trust for support of A.P.M.R. and J.J.J. (project RPG-2014-286) and the Engineering and Physical Sciences Research Council both for support of W.Y.M. (project EP/I031545/1) and for DTP studentships supporting N.A.B. and G.S.

Keywords: cage compounds · carboranes · density functional calculations · ruthenium · structure elucidation

How to cite: *Angew. Chem. Int. Ed.* **2016**, *55*, 8706–8710
Angew. Chem. **2016**, *128*, 8848–8852

---

[1] a) K. Wade, *J. Chem. Soc. D* **1971**, 792–793; b) D. M. P. Mingos, *Nat. (London) Phys. Sci.* **1972**, *236*, 99–102.
[2] See, for example: a) R. T. Baker, *Inorg. Chem.* **1986**, *25*, 109–111; b) J. D. Kennedy, *Inorg. Chem.* **1986**, *25*, 111–112.
[3] a) A. Kaczmarczyk, R. D. Dobrott, W. N. Lipscomb, *Proc. Natl. Acad. Sci. USA* **1962**, *48*, 729–733; b) W. N. Lipscomb, *Science* **1966**, *153*, 373–378.
[4] K. P. Callahan, W. J. Evans, F. Y. Lo, C. E. Strouse, M. F. Hawthorne, *J. Am. Chem. Soc.* **1975**, *97*, 296–302.
[5] E. L. Hoel, C. E. Strouse, M. F. Hawthorne, *Inorg. Chem.* **1974**, *13*, 1388–1392.
[6] See, for example: a) J. Bould, N. N. Greenwood, J. D. Kennedy, W. S. McDonald, *J. Chem. Soc. Chem. Commun.* **1982**, 465–467; b) J. E. Crook, M. Elrington, N. N. Greenwood, J. D. Kennedy, M. Thornton-Pett, J. D. Woollins, *J. Chem. Soc. Dalton Trans.* **1985**, 2407–2415; c) E. J. Ditzel, X. L. R. Fontaine, N. N. Greenwood, J. D. Kennedy, M. Thornton-Pett, *J. Chem. Soc. Chem. Commun.* **1988**, 1262–1264; d) J. Bould, N. N. Greenwood, J. D. Kennedy, *J. Chem. Soc. Dalton Trans.* **1990**, 1451–1458; e) J. Bould, J. D. Kennedy, M. Thornton-Pett, *J. Chem. Soc. Dalton Trans.* **1992**, 563–576; f) J. Bould, R. W. Harrington, W. Clegg, J. D. Kennedy, *J. Organomet. Chem.* **2012**, *721–722*, 155–163; and references therein.
[7] a) R. L. Johnston, D. M. P. Mingos, *Inorg. Chem.* **1986**, *25*, 3321–3323; b) R. L. Johnston, D. M. P. Mingos, P. Sherwood, *New J. Chem.* **1991**, *15*, 831–841.
[8] R. Littger, U. Englich, K. Ruhlandt-Senge, J. T. Spencer, *Angew. Chem. Int. Ed.* **2000**, *39*, 1472–1474; *Angew. Chem.* **2000**, *112*, 1532–1534.
[9] The compound [$(CpFe)_2C_2B_7H_{11}$] (13-v 13-SEP) is proposed to have a 4,5,2,3-$Fe_2C_2B_7$ structure based on spectroscopic data, but no crystallographic study has been reported. C. G. Salentine, M. F. Hawthorne, *Inorg. Chem.* **1978**, *17*, 1498–1501.
[10] 15-v 15-SEP and 16-v 16-SEP metallaboranes have been reported. See: a) D. K. Roy, B. Mondal, P. Shankhari, R. S. Anju, K. Geetharani, S. M. Mobin, S. Ghosh, *Inorg. Chem.* **2013**, *52*, 6705–6712; b) D. K. Roy, S. K. Bose, R. S. Anju, B. Mondal, V. Ramkumar, S. Ghosh, *Angew. Chem. Int. Ed.* **2013**, *52*, 3222–3226; *Angew. Chem.* **2013**, *125*, 3304–3308.
[11] a) A. R. Kudinov, D. S. Perekalin, S. S. Rynin, K. A. Lyssenko, G. V. Grintselev-Knyazev, P. V. Petrovskii, *Angew. Chem. Int. Ed.* **2002**, *41*, 4112–4114; *Angew. Chem.* **2002**, *114*, 4286–4288; b) A. R. Kudinov, M. I. Rybinskaya, D. S. Perekalin, V. I. Meshcheryakov, Yu. A. Zhuravlev, P. V. Petrovskii, A. A. Korlyukov, D. G. Golovanov, K. A. Lyssenko, *Russ. Chem. Bull.* **2004**, *53*, 1958–1962.
[12] a) D. F. Dustin, G. B. Dunks, M. F. Hawthorne, *J. Am. Chem. Soc.* **1973**, *95*, 1109–1115; b) A. Burke, D. Ellis, D. Ferrer, D. L. Ormsby, G. M. Rosair, A. J. Welch, *Dalton Trans.* **2005**, 1716–1721.
[13] D. F. Dustin, M. F. Hawthorne, *J. Am. Chem. Soc.* **1974**, *96*, 3462–3467; See also Ref. [16].
[14] M. E. O'Neill, K. Wade, *Polyhedron* **1984**, *3*, 199–212.
[15] M. E. Lopez, M. J. Edie, D. Ellis, A. Horneber, S. A. Macgregor, G. M. Rosair, A. J. Welch, *Chem. Commun.* **2007**, 2243–2245.

[16] a) W. Y. Man, S. Zlatogorsky, H. Tricas, D. Ellis, G. M. Rosair, A. J. Welch, *Angew. Chem. Int. Ed.* **2014**, *53*, 12222–12225; *Angew. Chem.* **2014**, *126*, 12418–12421; b) W. Y. Man, D. Ellis, G. M. Rosair, A. J. Welch, *Angew. Chem. Int. Ed.* **2016**, *55*, 4596–4599; *Angew. Chem.* **2016**, *128*, 4672–4675.

[17] A. McAnaw, M. E. Lopez, D. Ellis, G. M. Rosair, A. J. Welch, *Dalton Trans.* **2014**, *43*, 5095–5105.

[18] a) W. J. Evans, M. F. Hawthorne, *J. Chem. Soc. Chem. Commun.* **1974**, 38–39; b) W. M. Maxwell, R. Weiss, E. Sinn, R. N. Grimes, *J. Am. Chem. Soc.* **1977**, *99*, 4016–4029; c) J. R. Pipal, R. N. Grimes, *Inorg. Chem.* **1978**, *17*, 6–10; d) D. Ellis, M. E. Lopez, R. McIntosh, G. M. Rosair, A. J. Welch, *Chem. Commun.* **2005**, 1917–1919; e) L. Deng, H.-S. Chan, Z. Xie, *Angew. Chem. Int. Ed.* **2005**, *44*, 2128–2131; *Angew. Chem.* **2005**, *117*, 2166–2169; f) R. D. McIntosh, D. Ellis, G. M. Rosair, A. J. Welch, *Angew. Chem. Int. Ed.* **2006**, *45*, 4313–4316; *Angew. Chem.* **2006**, *118*, 4419–4422; g) J. Zhang, L. Deng, H. S. Chan, Z. Xie, *J. Am. Chem. Soc.* **2007**, *129*, 18–19; h) A. McAnaw, M. E. Lopez, D. Ellis, G. M. Rosair, A. J. Welch, *Dalton Trans.* **2013**, *42*, 671–679.

[19] A. McAnaw, G. Scott, L. Elrick, G. M. Rosair, A. J. Welch, *Dalton Trans.* **2013**, *42*, 645–664.

[20] Full computational details including the calculated chemical shifts and test calculations based on the B3LYP-optimized structures are given in the Supporting Information.

[21] CCDC 1458452–1458456 contain the supplementary crystallographic data for this paper. These data are provided free of charge by The Cambridge Crystallographic Data Centre.

Received: March 9, 2016
Revised: April 19, 2016

ChemPubSoc Europe
DOI: 10.1002/ejic.201700600
EurJIC European Journal of Inorganic Chemistry
Full Paper

Aminoborylene Complexes

CLUSTER ISSUE

Fluoroarene Complexes with Small Bite Angle Bisphosphines: Routes to Amine–Borane and Aminoborylene Complexes

Annie L. Colebatch,[a] Alasdair I. McKay,[a] Nicholas A. Beattie,[b] Stuart A. Macgregor,*[b] and Andrew S. Weller*[a]

Abstract: Fluoroarene complexes of the small bite angle bisphosphine $Cy_2PCH_2PCy_2$ (dcpm) have been prepared: $[Rh(dcpm)(\eta^6\text{-}1,2\text{-}F_2C_6H_4)][Al\{OC(CF_3)_3\}_4]$ and $[Rh(dcpm)(\eta^6\text{-}1,2,3\text{-}F_3C_6H_3)][Al\{OC(CF_3)_3\}_4]$. These complexes act as precursors to a previously inaccessible σ-amine–borane complex $[Rh(dcpm)(\eta^2\text{-}H_3B{\cdot}NMe_3)][Al\{OC(CF_3)_3\}_4]$ of a small bite-angle phosphine. This complex is a poor catalyst for the dehydrocoupling of $H_3B{\cdot}NMe_2H$. Instead, formation of the bridging borylene complex $[\{RhH(\mu\text{-}dcpm)\}_2(\mu\text{-}H)(\mu\text{-}BNMe_2)][Al\{OC(CF_3)_3\}_4]$ occurs, which has been studied by NMR, mass spectrometry, crystallographic and DFT techniques. This represents a new route to bridging borylene complexes.

Introduction

The transition metal catalysed dehydrocoupling and dehydropolymerisation of amine–boranes has been the subject of considerable recent attention due to both fundamental interest in BH/NH activation processes and as routes to new BN-based materials.[1–3] Amine–borane σ-complexes[4] are often implicated as intermediates in such processes. Although a wide variety of amine–borane σ-complexes are now known,[4–6] previous attempts to prepare such species with small bite angle bisphosphine coligands have been unsuccessful.[7] Studying the reactivity of $[Rh\{Ph_2P(CH_2)_xPPh_2\}(\eta^6\text{-}FC_6H_5)][BAr^F_4]$ with $H_3B{\cdot}NMe_3$ to form $[Rh\{Ph_2P(CH_2)_xPPh_2\}(\eta^2\text{-}H_3B{\cdot}NMe_3)][BAr^F_4]$ [x = 2–5, Ar = $3,5\text{-}(CF_3)_2C_6H_3$] revealed a dependence of the relative strengths of the metal-borane/metal–arene interactions on the P–Rh–P bite angle (Scheme 1a).[8,9] Larger bite angles were noted to give rise to stronger Rh–B and Rh–H interactions, as evidenced by downfield ^{11}B NMR chemical shifts and upfield ^1H NMR chemical shifts. Notably, a σ-borane complex did not form for $x = 2$ (i.e. $Ph_2PCH_2CH_2PPh_2$), which demonstrates the tipping point where η^6-binding of the FC_6H_5 solvent outcompetes $\eta^2\text{-}H_3B{\cdot}NMe_3$ coordination. These weak rhodium-borane interactions were found to be advantageous in catalysis, with small bite angles promoting faster dehydrocoupling of $H_3B{\cdot}NMe_2H$ to form $[H_2BNMe_2]_2$, e.g. TOFs from 180 h^{-1} ($x = 5$) to 1250 h^{-1} ($x = 3$).[7] For $x = 2$ no dehydrocoupling was observed, likely due to preferential binding of FC_6H_5 over σ-complexation of the amine–borane. Demonstration of this comes from comparison of the binding mode of the *B*-phenyl-substituted amine–borane $H_2PhB{\cdot}NMe_3$ with $\{Rh(PR_3)_2\}^+$ fragments: wide bite angles favour amine–borane σ-coordination, tighter ones arene coordination, e.g. $[Rh(PiPr_3)_2(\eta^2\text{-}(BH)\text{-}H_2PhB{\cdot}NMe_3)][BAr^F_4]$, [P–Rh–P =

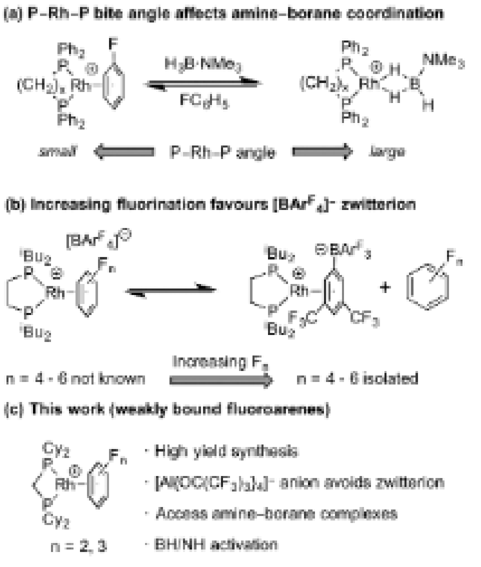

Scheme 1. (a) Displacement of FC_6H_5 by $H_3B{\cdot}NMe_3$ (x = 3–5). $[BAr^F_4]^-$ anion not shown.[7] (b) Zwitterion formation from fluoroarene complexes.[11] (c) Preparation of fluoroarene complexes in this work. $[Al\{OC(CF_3)_3\}_4]^-$ anion not shown.

---

[a] Department of Chemistry, Chemistry Research Laboratory,
University of Oxford,
Mansfield Road, Oxford OX1 3TA, UK
E-mail: andrew.weller@chem.ox.ac.uk
http://research.chem.ox.ac.uk/andrew-weller.aspx
[b] Institute of Chemical Sciences, Heriot Watt University,
Edinburgh EH14 4AS, UK
E-mail: S.A.Macgregor@hw.ac.uk
http://cic.eps.hw.ac.uk/

Supporting information and ORCID(s) from the author(s) for this article are available on the WWW under https://doi.org/10.1002/ejic.201700600.

101.86(3)°], and [Rh(*i*Pr$_2$P(CH$_2$)$_3$P*i*Pr$_2$)(η^6-H$_2$PhB-NMe$_3$)][BAr$^F_4$] [P–Rh–P = 94.04(4)°].[10]

Empirically the P–Rh–P bite angle has an inverse effect on arene binding in [Rh(bisphosphine)(arene)]$^+$ cations, with η^6-arene binding more favourable for smaller bite angle ligands,[7,12,13] for which we also suggest amine–borane σ-complexation is weaker. One way to mitigate these competing effects is to use more weakly binding arene ligands. η^6-Fluoroarenes are increasingly popular as weakly binding ligands that offer an operationally unsaturated metal centre.[14] However, the vast majority of cases are limited to FC$_6$H$_5$ examples, with a few examples of F$_2$C$_6$H$_4$ ligation,[7,14–17] due to the generally weaker binding of arenes with increasing degrees of fluorination.[18,19] Recently, the binding strength of fluoroarenes has been assessed using the [Rh(*t*Bu$_2$PCH$_2$CH$_2$P*t*Bu$_2$)(η^6-F$_n$C$_6$H$_{6-n}$)]-[BAr$^F_4$] scaffold. These studies showed that complexes could be accessed in situ for *n* = 0–3 (Scheme 1b),[11] whereas for more highly fluorinated analogues (*n* = 4–6) the reduced coordinating ability of the arene means that π complexation of the [BAr$^F_4$]$^-$ counterion becomes more favourable, and the zwitterionic complex [Rh(*t*Bu$_2$PCH$_2$CH$_2$P*t*Bu$_2$)(η^6-(3,5-(CF$_3$)$_2$C$_6$H$_3$)BAr$^F_3$)] was observed as the sole product. Similar π-coordination of [BAr$^F_4$]$^-$ is now well established.[16,20–23]

With these observations in hand, we speculated that in order to synthesise an amine–borane complex with small bite angle bisphosphine supporting co-ligand a very weakly ligating fluoroarene would be needed to be coupled with manipulation of the anion to avoid zwitterion formation. In this contribution we demonstrate that Rh-complexes with the exceptionally small bite angle Cy$_2$PCH$_2$PCy$_2$ (dcpm) ligand[13,24] combined with moderately fluorinated arenes can be accessed using the [Al(OC(CF$_3$)$_3$)$_4$]$^-$ anion, thus providing a route to synthetically useful quantities of a trifluorobenzene complex (Scheme 1c). From such complexes flows the coordination chemistry of amine–boranes, and subsequent BH/NH activation, that results in a new dehydrocoupling route to bridging borylene complexes.

Results and Discussion

To avoid competition from zwitterion formation through coordination of [BAr$^F_4$]$^-$, the very weakly coordinating anion [Al(OC(CF$_3$)$_3$)$_4$]$^-$ was employed, the use of which has been pioneered and widely applied by Krossing.[25,26] Hydrogenation of [Rh(dcpm)(COD)][Al(OC(CF$_3$)$_3$)$_4$] (COD = cyclooctadiene) in 1,2-F$_2$C$_6$H$_4$ or 1,2,3-F$_3$C$_6$H$_3$ solution gave the corresponding fluoroarene complexes [Rh(dcpm)(F$_n$C$_6$H$_{6-n}$)][Al(OC(CF$_3$)$_3$)$_4$] [*n* = 2 (**1**), 3 (**2**)], Scheme 2. Trace quantities of other, more strongly coordinating, arenes in the commercially available solvents lead to impurities of the form [Rh(dcpm)(arene)][Al(OC(CF$_3$)$_3$)$_4$].[27] In the case of **1** these are minimal (<10 %), but for **2** considerable quantities are observed. This can be simply overcome by performing the synthesis of **2** in concentrated solution (0.17 M, 100 mg in 0.4 cm^3), thereby decreasing the ratio of [impurities]:[Rh] such that **2** is formed in >95 % spectroscopic yield. Both complexes **1** and **2** can be isolated as analytically pure yellow crystals in 78 % and 82 % yields respectively after crystallisation by addition of pentane. For comparison, the analogous [BAr$^F_4$]$^-$ complexes [Rh(dcpm)(F$_n$C$_6$H$_{6-n}$)][BAr$^F_4$] (*n* = 2, 3) were similarly prepared. Both species were observed in situ, and [Rh(dcpm)(1,2-F$_2$C$_6$H$_4$)][BAr$^F_4$] (**3**) could be isolated in 82 % yield as the only product. However, [Rh(dcpm)(1,2,3-F$_3$C$_6$H$_3$)][BAr$^F_4$] (**4**) forms the zwitterion complex [Rh(dcpm)(η^6-(3,5-(CF$_3$)$_2$C$_6$H$_3$)-BAr$^F_3$)], (**5**), upon standing (Scheme 2). For [Rh(dcpm)(1,2-F$_2$C$_6$H$_4$)][BAr$^F_4$] slower partial conversion to **5** occurs over days,[28] and a single crystal X-ray structural determination confirmed its formulation (Scheme 2). To avoid such complications all future work was conducted exclusively with the [Al(OC(CF$_3$)$_3$)$_4$]$^-$ anion.

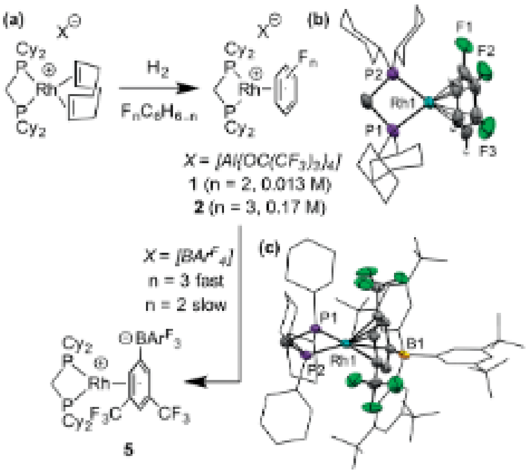

Scheme 2. (a) Preparation of η^6-fluoroarene complexes [Rh(dcpm)(η^6-F$_n$C$_6$H$_{6-n}$)]-[X] (X = [Al(OC(CF$_3$)$_3$)$_4$]: *n* = 2 (**1**), 3 (**2**); X = [BAr$^F_4$]: *n* = 2 (**3**), 3 (**4**)) and η^6-zwitterion [Rh(dcpm)(η^6-(3,5-(CF$_3$)$_2$C$_6$H$_3$)BAr$^F_3$)] (**5**). (b) Solid-state structure of the cationic portion of complex **2**, alkyl hydrogen atoms omitted. Major disorder component shown only. Displacement ellipsoids are shown at the 50 % probability level. Selected bond lengths [Å] and angles [°]: Rh–C$_{aryl}$ range: 2.346(5)–2.263(5); Rh1–P1, 2.2452(10); Rh1–P2, 2.2397(10); P1–Rh1–P2, 73.06(4). (c) Solid-state structure of **5**, hydrogen atoms omitted, [BAr$^F_4$] simplified. Displacement ellipsoids are shown at the 50 % probability level. Selected bond lengths [Å] and angles [°]: Rh–C$_{aryl}$ range 2.425(6)–2.274(6); Rh1–P1, 2.2512(17); Rh1–P2, 2.2478(16); P1–Rh1–P2, 72.44(6).

In the ^{31}P{^{1}H} NMR spectra of **1** and **2** downfield shifts and increased Rh–P couplings relative to the precursor complexes are observed (**1**: δ –10.4, *J*(RhP) 168 Hz; **2**: δ –10.9, *J*(RhP) 167 Hz; cf. [Rh(dcpm)(COD)][Al(OC(CF$_3$)$_3$)$_4$]: δ –27.4, *J*(RhP) 126 Hz). In the ^{19}F{^{1}H} NMR spectrum the fluoroarene resonances shift downfield upon complexation, with those of **2** observed at δ –146.7 (2 F) and –167.1 (1 F), relative to free 1,2,3-F$_3$C$_6$H$_3$ (δ –136.8, –163.5), as described previously for related systems.[29–31]

Characterisation of **1** and **2** included a single-crystal X-ray crystallographic study (Scheme 2b for **2**, supporting materials for **1**), and complex **2** is the first structurally characterised example of an F$_3$C$_6$H$_3$-transition metal complex. Significant disorder of the fluoroarene ring between different rotomers means that discussion of the geometric parameters is not appropriate, but the structure does demonstrate arene binding and the acute nature of the P–Rh–P angle [73.06(4)°]. The only previously reported example of 1,2,3-$F_3C_6H_3$ binding to a transition metal is $[Rh(tBu_2PCH_2CH_2PtBu_2)(\eta^6\text{-}1,2,3\text{-}F_3C_6H_3)][BAr^F_4]$, the characterisation of which was limited to in situ NMR spectroscopy and mass spectrometry as it is formed in equilibrium with its $[BAr^F_4]^-$ coordinated zwitterion.[11] Here, for **2**, the combination of synthesis using concentrated solutions to overcome trace impurities and employing the very weakly coordinating anion $[Al\{OC(CF_3)_3\}_4]^-$ to obviate zwitterion formation allows for reliable access to such highly fluorinated arene complexes.

After establishing an effective route to weakly bound fluoroarene species **1** and **2** their reactivity with amine–boranes was investigated. Starting with $H_3B\text{-}NMe_3$, which has no N–H groups and thus does not undergo dehydrocoupling, treatment of **1** with one equivalent of $H_3B\text{-}NMe_3$ in 1,2-$F_2C_6H_4$ solution gave a mixture of **1** and the target complex $[Rh(dcpm)(\eta^2\text{-}H_3B\text{-}NMe_3)][Al\{OC(CF_3)_3\}_4]$ (**6**) in a ratio of 9:1 (as measured by $^{31}P\{^1H\}$ NMR spectroscopy). Addition of a second equivalent of $H_3B\text{-}NMe_3$ decreased this ratio to 4:1, demonstrating that 1,2-$F_2C_6H_4$ binding is competitive with that of $H_3B\text{-}NMe_3$. In contrast, for the more weakly bound 1,2,3-$F_3C_6H_3$ complex (**2**) reaction with $H_3B\text{-}NMe_3$ in 1,2,3-$F_3C_6H_3$ solvent afforded **6** as the major product (81 % by $^{31}P\{^1H\}$ NMR spectroscopy), Scheme 3, alongside a collection of uncharacterised $[Rh(dcpm)(arene)][Al\{OC(CF_3)_3\}_4]$ species (13 %) and other minor impurities. Moving to more concentrated solutions [0.17 M] did not significantly increase the yield of **6**, and clearly these minor impurities bind slightly more strongly than the amine–borane.

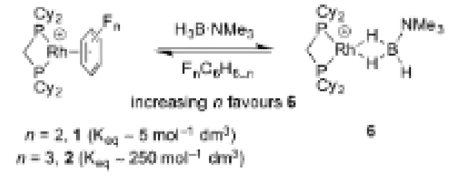

Scheme 3. Formation of $[Rh(dcpm)(\eta^2\text{-}H_3B\text{-}NMe_3)][Al\{OC(CF_3)_3\}_4]$ (**6**) (*n* = 2, 3). $[Al\{OC(CF_3)_3\}_4]^-$ anion not shown.

The NMR spectra of **6** resemble those of the analogous $[Rh(Ph_2P(CH_2)_nPPh_2)(\eta^2\text{-}H_3B\text{-}NMe_3)][BAr^F_4]$ complexes (*n* = 3–5).[7] In the $^{31}P\{^1H\}$ NMR spectrum of **6** a doublet is observed at δ –3.7 [*J*(RhP) 145 Hz]. The ^{11}B NMR spectrum contains a broad resonance at δ = 16.3; and the corresponding σ-bound Rh···H–B resonances appear at δ –1.75 as a very broad singlet (integral 3 H) in the ^1H NMR spectrum indicating rapid exchange between bridging and terminal B–H. Unfortunately, **6** did not survive ESI-MS conditions, and attempts to crystallise **6** resulted in decomposition, an indication of its relative instability.

Having access to small bite angle bisphosphine complexes that were capable of binding amine–boranes, albeit made in situ, their ability to dehydrocouple $H_3B\text{-}NMe_2H$ was evaluated, as we have previously shown that the P–Rh–P bite angle has an influence on the rate of this process.[7] The dehydrocoupling of $H_3B\text{-}NMe_2H$ in 1,2,3-$F_3C_6H_3$ solvent was investigated using 5 mol-% **2** (Scheme 4). The dehydrocoupling proved to be slow with only 14 % $H_3B\text{-}NMe_2H$ consumption over 21 h to provide the dimeric aminoborane $[H_2BNMe_2]_2$ (8 %), alongside small quantities of other common dehydrocoupling products including transient $H_2B{=}NMe_2$, $H_3BNMe_2BH_2NMe_2H$, $[BH_2(NMe_2H)_2]^+$ and $H_2B(\mu\text{-}H)NMe_2BH_2$ as measured by ^{11}B NMR spectroscopy.[15,32–34] In the $^{31}P\{^1H\}$ NMR spectrum only one major phosphorus-containing species was observed (**7**), as a complex second-order multiplet at δ = 55.9, hinting at the formation of a dimeric species.[35] A very broad resonance is observed in the ^{11}B NMR spectrum at δ = 59.0, with nothing observed to lower field. In the ^1H NMR spectrum two very well resolved multiplets were observed in the high field region at δ = –4.87 and –7.91, with relative integrals of 2:1 respectively, which do not sharpen upon ^{11}B decoupling, but do simplify on decoupling ^{31}P. This suggests there are no significant $^{11}B\cdots{}^1H$ interactions. In the ESI–MS spectrum, a peak at *m/z* = 1080.51 is observed, with an isotope pattern consistent with the gross formulation of a bimetallic monocation $[\{Rh(dcpm)\}_2H_3(BNMe_2)]^+$. A similar dimerisation has been seen upon reaction of $[Rh(R_2P(CH_2)_3PR_2)(\eta^6\text{-}FC_6H_5)][BAr^F_4]$ (R = *i*Pr, Ph) with $H_3B\text{-}NH_3$, where the bridging aminoborane $[\{Rh(R_2P(CH_2)_3PR_2)\}_2(\mu\text{-}H)(\mu\text{-}H_2BNH_2)][BAr^F_4]$ [R = *i*Pr (**I**), Ph (**II**)] is formed, and the data for **7** are similar.[36]

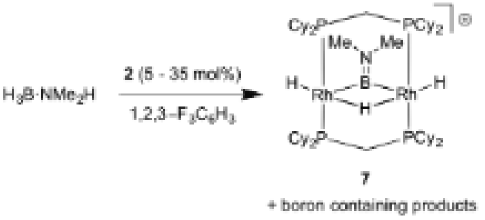

Scheme 4. Attempted dehydrocoupling of $H_3B\text{-}NMe_2H$ and formation of $[\{RhH(\mu\text{-}dcpm)\}_2(\mu\text{-}H)(\mu\text{-}BNMe_2)][Al\{OC(CF_3)_3\}_4]$ (**7**). $[Al\{OC(CF_3)_3\}_4]^-$ anion not shown.

Crystalline material of complex **7** was obtained by recrystallisation from 1,2,3-$F_3C_6H_3$/pentane. In the bulk this was always contaminated with a boron-containing species identified as the boronium salt $[H_2B(NMe_2H)_2]^+$ [$\delta(^{11}B)$ = –2.0 ppm, *J*(BH) = 115 Hz; lit. $\delta(^{11}B)$ = –2.8 ppm, *J*(BH) = 113 Hz],[32] but this did allow a single-crystal X-ray diffraction study to be performed, the results of which are shown in Figure 1. The solid-state structure shows a rearrangement of the bisphosphine ligands upon dimerisation, and complex **7** contains bridging dcpm ligand in an A-frame motif[37] and an aminoborylene $BNMe_2$ group. The $\{Rh(\mu\text{-}dcpm)\}_2$ construct resembles that of other binuclear rhodium systems with similar ligands.[38,39] Although the hydride ligands were not located in the final Fourier difference map, the combination of NMR spectroscopic evidence and DFT studies (vide infra) confirm the presence of one bridging hydride *trans*-disposed to one terminal Rh–H at each Rh centre, with the overall formulation $[\{RhH(\mu\text{-}dcpm)\}_2(\mu\text{-}H)(\mu\text{-}BNMe_2)][Al\{OC(CF_3)_3\}_4]$ (**7**). The geometry about each Rh is *pseudo*-square pyramidal, interestingly with a vacant coordination site *trans* to the borylene ligand. The cation has overall non-crystallographic C_{2v} symmetry. The Rh–B distances [2.015(6) and 1.983(7) Å] are shorter than those in the related bridging aminoborylene complex $[\{Rh(\eta^5\text{-}C_5H_5)(CO)\}_2\{\mu\text{-}BN(SiMe_3)_2\}]$ [2.054(2) Å][40] and aminoborane complex $[\{Rh(PiPr_2(CH_2)_3\text{-}$

$P(iPr_2)\}_2(\mu\text{-}H)(\mu\text{-}BH_2NH_2)][BAr^F{}_4]$ [I, 2.055(5), 2.070(5) Å][36] but fall within the range seen for monomeric rhodium aminoboryl complexes of 2.034–1.929 Å.[10,41,42] The B–N distance in **7** [1.379(8) Å] is comparable to that measured in bridging aminoborylenes, for example $[\{Rh(\eta^5\text{-}C_5H_5)(CO)\}_2\{\mu\text{-}BN(SiMe_3)_2\}]$ [1.399(6) Å],[40] and the only structurally characterised μ-$BNMe_2$ example $[\{Mn(\eta^5\text{-}C_5H_5)(CO)_2\}_2(\mu\text{-}BNMe_2)]$ [1.39(1) Å].[43]

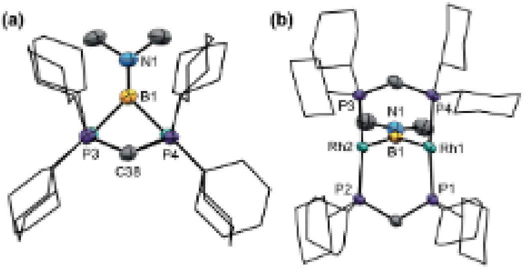

Figure 1. Solid-state structure of the cationic portion of complex **7**, hydrogen atoms omitted. (a) Viewed down the P–Rh–P axis. (b) Viewed down the B–N axis. Displacement ellipsoids are shown at the 50 % probability level. Selected distances [Å] and angles [°]: Rh1–Rh2, 2.8266(5); Rh1–B1, 2.015(6); Rh2–B1, 1.983(7); B1–N1 1.379(8); Rh1–P1, 2.2931(13); Rh1–P4, 2.3084(13); Rh2–P2, 2.2983(13); Rh2–P3, 2.2953(13); P1–Rh1–P4, 172.66(5); P2–Rh2–P3, 172.81(5).

The ^{11}B NMR chemical shift observed for **7** (δ = 59.0) suggests a bridging amino*borane* motif [cf. I, $\delta(^{11}B)$ 51.1].[36] However, the sharp signals observed for the hydrides in the ^1H NMR spectrum, that are unaffected by ^{11}B coupling, point to a bridging dihydrido amino*borylene* motif, which would be expected to show lower field chemical shifts in the ^{11}B NMR spectra (>90 ppm),[40,44] although examples have been observed as far upfield as 74 ppm.[45] An obvious geometric distinction between a bridging aminoborane (μ-H_2BNR_2) and a bridging aminoborylene dihydride (μ-BNR_2) structure is the orientation of the NR_2 moiety with respect to the RhBRh plane, as depicted in Figure 2. In the former case, e.g. I, a significant twist angle of 30.92° is observed between the RhBRh and HNH planes of I so as to maximise the orbital overlap between the B–H bonds and Rh centres.[36] This interaction is not present in **7** or $[\{Mn(\eta^5\text{-}C_5H_5)(CO)_2\}_2(\mu\text{-}BNMe_2)]$,[43] hence minimal twist angles are observed between the RhBRh and CNC planes of 7.25° and 8.38°, respectively. We postulate that the vacant coordination site *trans* to boron in complex **7** modifies the chemical shift to such an extent that the signal for the borylene is observed about 30 ppm to higher field than expected.

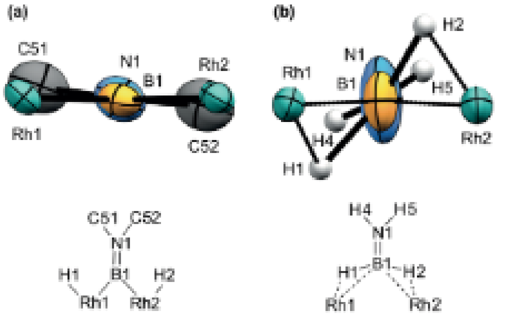

Figure 2. Solid state structures of the Rh_2BNR_2 cores of (a) μ-aminoborylene **7** (R = Me), and (b) μ-aminoborane I (R = H)[36] viewed down the B–N axis. Displacement ellipsoids are shown at the 50 % probability level. Twist angles [°]: (a) plane(Rh1B1Rh2)/plane(C51N1C52) 7.25°; (b) plane(Rh1B1Rh2)/plane(H4N1H5) 30.92°.

Density functional theory calculations[46] in conjunction with Quantum Theory of Atoms in Molecules (QTAIM) and Natural Bond Orbital (NBO) analyses have been employed to investigate the electronic structure of **7** (see Figure 3). Full geometry optimisation with the BP86 functional provided excellent agreement for the heavy atom positions and confirmed the presence of two terminal and one bridging hydride and square-pyramidal coordination around each Rh centre. Long H1···B1 and H2···B1 distances in excess of 2.9 Å preclude any direct bonding interaction and this is confirmed by the lack of a bond path between these centres (Figure 3a). In contrast, bond paths are computed between B1 and both Rh centres, as well as between Rh1/H1

(a)

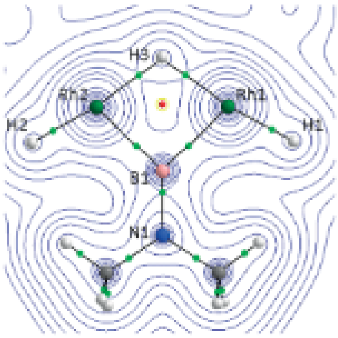

(b)

	Distance/Å	$\rho(r)$	ε	$H(r)$
Rh1–B1	2.01	0.12	0.05	-0.08
Rh1–H1	1.61	0.13	0.01	-0.06
Rh1–H3	1.80	0.08	0.02	-0.02
B1–N1	1.41	0.20	0.13	-0.16

(c)

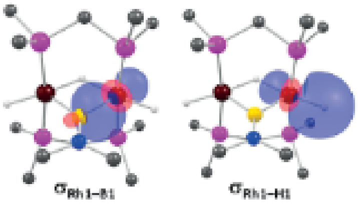

Figure 3. (a) Contour plot of the total electron density of the central part of **7** presented in the (Rh1B1Rh2) plane highlighting key bond paths and associated bond critical points (BCP, in green) and the ring critical point (RCP, in red). (b) Computed key distances and BCP metrics (a.u.) for bond paths associated with Rh1 [$\rho(r)$ = electron density; ε = bond ellipticity, $H(r)$ = total energy density; the computed structure has effective C_{2v} symmetry and so equivalent data are associated with Rh2, see Supporting Information]. (c) Natural bond orbitals highlighting Rh1–B1 and Rh1–H1 bonding (C–H hydrogens removed and Cy groups truncated at C1 for clarity).

and Rh2/H2. The associated bond critical points (BCPs) exhibit negative values of the total energy density *H(r)* and low ellipticities, *ε*, characteristics of σ-bonding that is predominantly covalent in nature. This contrasts with the μ-H_2BNH_2 motif in **I** where the BCPs associated with the Rh–H and Rh–B bond paths have large ellipticities of about 0.5 au reflecting the anisotropic *B*-agostic Rh←H–B interaction.[36] The presence of the bridging hydride in **7** means that a ring critical point is seen between the Rh centres. The computed Rh1···Rh2 distance of 2.85 Å is in good agreement with the experimental value of 2.8266(5) Å. The lack of any Rh1···Rh2 interaction is confirmed in the NBO analysis which highlights three Rh-based (d-orbital) lone pairs, as well as Rh1–H1/Rh2–H2 and Rh1–B1/Rh2–B1 bonding orbitals. In contrast NBO calculations on [{Rh(η^5-C_5H_5)(CO)}$_2${μ-BN-($SiMe_3$)$_2$}] clearly locate a Rh–Rh bonding orbital consistent with the presence of a metal–metal bond (see Supporting Information).

The formation of **7** is postulated to proceed in a similar manner to **I** and **II** (Scheme 5).[36] Displacement of the fluoroarene ligand enables initial formation of a σ-$H_3B{\cdot}NMe_2H$ complex (**A**), analogous to complex **6**. Subsequent B–H oxidative cleavage yields the intermediate aminoboryl **B**, from which elimination of the boronium salt [$H_2B(NMe_2H)_2$]$^+$ (observed at the end of the reaction) generates a neutral "{RhH(dcpm)}" fragment **C**. NMe_2H arises from $H_3B{\cdot}NMe_2H$ dissociation, consistent with the observation of $H_2B(\mu\text{-}H)NMe_2BH_2$ in the reaction. It has previously been shown that hydrogenation of [Rh($R_2PCH_2PR_2$)(η^3-CH_2Ph)] (R = Cy, *i*Pr) affords the A-frame bridging bisphosphine complex [RhH(μ-$R_2PCH_2PR_2$)(μ-H)]$_2$,[47] and an equivalent rearrangement has been noted in the reaction of [Rh(*i*Pr_2PCH_2P*i*Pr_2)(CO)(η^3-C_3H_5)] with H_2 to form [Rh(μ-*i*Pr_2PCH_2P*i*Pr_2)(CO)(μ-H)]$_2$.[39] Presumably these dimerisations are driven by ring strain. We thus propose that dimerisation of **C** first forms a neutral bridging A-frame complex, [RhH(dcpm)]$_2$ which then undergoes protonation by a half equivalent of [$H_2B(NMe_2H)_2$]$^+$ to form a bridging aminoborane **D**. Complex **7** then results from a double B–H activation of **D** to form a bridging aminoborylene dihydride. Interestingly this does not occur with the $R_2P(CH_2)_3PR_2$ ligands in **I** and **II** in which there is not an A-frame motif.[36] Similar geminal C–H activations of alkenes are effected by [{Ir(μ-$Et_2PCH_2PEt_2$)(CO)}$_2$(μ-H)(μ-CO)]$^+$[38] and [{Ir(μ-$Ph_2PCH_2PPh_2$)}$_2$(μ-CO)(CH_3)(CO)]$^+$.[48,49] Such C–H activations are proposed to proceed via a cooperative mechanism wherein π-complexation of $H_2C{=}CRR'$ to one metal enables σ-CH complexation at the other metal and consequently C–H cleavage. This bears parallels with the double B–H activation of transient $H_2B{=}NMe_2$ observed here, although aminoboranes bind end-on rather than the side-on mode adopted by alkenes.[50,51] Aminoborane to aminoborylene transformations by double B–H activation of $H_2B{=}NR_2$ (R = Cy, *i*Pr) have been observed with mononuclear iridium and ruthenium complexes,[52,53] and related transformations on boranes are also known.[54,55] However, to the best of our knowledge the complete amine–borane to aminoborylene transformation is unprecedented, and represents a new method for the preparation of bridging borylenes.

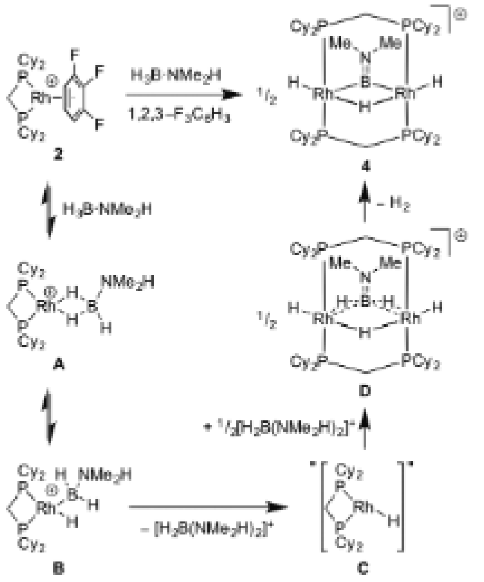

Scheme 5. Proposed mechanism of formation of **7**. [Al{OC(CF_3)$_3$}$_4$]$^-$ anion not shown.

Conclusions

The marriage of the very weakly coordinating anion [Al{OC(CF_3)$_3$}$_4$]$^-$ and fluoroarenes 1,2-$F_2C_6H_4$ and 1,2,3-$F_3C_6H_3$ enables the synthesis and isolation of a previously inaccessible σ-amine–borane complex of a small bite angle phosphine. The ring strain imposed by the dcpm ligand leads to unprecedented chemistry with amine–boranes, culminating in formation of a bimetallic aminoborylene [{RhH(μ-dcpm)}$_2$(μ-H)(μ-$BNMe_2$)]-[Al{OC(CF_3)$_3$}$_4$], the nature of which is confirmed by DFT calculations and QTAIM and NBO analyses.

Experimental Section

All manipulations, unless otherwise stated, were performed under an argon atmosphere using standard Schlenk line and glovebox techniques. Glassware was oven dried at 130 °C overnight and flame dried under vacuum prior to use. Pentane and CH_2Cl_2 were dried using a Grubbs type solvent purification system (MBraun SPS-800) and degassed by three successive freeze-pump-thaw cycles. 1,2-$F_2C_6H_4$ (purchased from Fluorochem, pretreated with alumina), 1,2,3-$F_3C_6H_3$ (purchased from Fluorochem, pretreated with alumina) and CD_2Cl_2 were dried with CaH_2, vacuum distilled and stored over 3 Å molecular sieves. $H_3B{\cdot}NMe_3$ and $H_3B{\cdot}NMe_2H$ were purchased from Sigma–Aldrich and sublimed prior to use. Li[Al{OC(CF_3)$_3$}$_4$][25] and [Rh(COD)Cl]$_2$[56] were prepared by literature methods. All other chemicals were obtained from commercial sources and used as received.

NMR spectra were recorded with a Bruker AVIIIHD 500 or Bruker AVIIIHD 400 nanobay spectrometer at room temperature, unless otherwise stated. In 1,2-$F_2C_6H_4$ and 1,2,3-$F_3C_6H_3$, ^{1}H NMR spectra were prelocked to a sample of C_6D_6 (25 %) and 1,2-$F_2C_6H_4$ (75 %)

and referenced to the centre of the downfield solvent multiplet, δ = 7.07 and 6.96 ppm, respectively. ^{31}P, ^{11}B and ^{19}F NMR spectra were referenced against 85 % H_3PO_4 (external), $BF_3{\cdot}OEt_2$ (external) and CCl_3F (external), respectively. Chemical shifts (δ) are quoted in ppm and coupling constants (J) in Hz. ESI-MS data were recorded with a Bruker MicrOTOF instrument interfaced with a glove-box. Microanalyses were performed by Stephen Boyer at London Metropolitan University.

[Rh(COD)$_2$][Al{OC(CF$_3$)$_3$}$_4$]: Prepared according to the literature procedure for [Rh(COD)$_2$][BAr$^F{}_4$].[57] An orange solution of [Rh(COD)Cl]$_2$ (0.585 g, 1.19 mmol) and 1,5-cyclooctadiene (0.2 mL) in CH_2Cl_2 (20 mL) was degassed by bubbling argon through the solution for 15 min. The solution was then added dropwise to a colourless slurry of Li[Al{OC(CF$_3$)$_3$}$_4$] (2.31 g, 2.37 mmol) in CH_2Cl_2 (60 mL) with vigorous stirring at ambient temperature. The colour of the slurry immediately changed to dark red. The reaction mixture was stirred at ambient temperature for a further 16 h and then filtered. The supernatant was then concentrated under vacuum (ca. 50 mL). Cooling to –20 °C overnight afforded a red crystalline solid which was isolated by decanting, washed with pentane (2 × 2 mL) and dried under vacuum. Further concentration followed by cooling afforded a second crop. Yield (2.53 g, 83 %). ^{1}H NMR (CD_2Cl_2, 400 MHz): δ = 5.26 (s, 8 H, COD-CH), 2.55 (s, 16 H, COD-CH_2) ppm. ^{19}F{^{1}H} NMR (CD_2Cl_2, 376 MHz): δ = –75.8 (s) ppm. ESI-MS (1,2-$F_2C_6H_4$, 60 °C, 4.5 kV): *m/z* 319.10 (calculated 319.09 for [Rh(COD)$_2$]$^+$ fragment). $C_{32}H_{24}AlF_{36}O_4Rh$ (1286.35): calcd. C 29.88, H 1.88; found C 29.93, H 1.91.

[Rh(dcpm)(COD)][Al{OC(CF$_3$)$_3$}$_4$]: Prepared according to the literature procedure for [Rh(dcpe)(COD)][BAr$^F{}_4$].[58] A solution of [Rh(COD)$_2$][Al{OC(CF$_3$)$_3$}$_4$] (400.2 mg, 0.3111 mmol) in CH_2Cl_2 (10 mL) was treated dropwise with a solution of dcpm (127.1 mg, 0.3111 mmol) in CH_2Cl_2 (70 mL) at –78 °C with vigorous stirring. Upon complete addition the colour of the reaction mixture changed from burgundy to orange. The reaction mixture was warmed to ambient temperature and stirred for 16 h. The solution was concentrated to 10 mL under vacuum and pentane (50 mL) was added to precipitate an orange solid which was isolated by filtration, washed with pentane (3 × 10 mL) and dried under vacuum. Yield 436.9 mg (0.2753 mmol, 89 %). The powder was then extracted into the minimum amount of CH_2Cl_2 and layered with pentane, which afforded large orange crystals suitable for an X-ray diffraction study. ^{1}H NMR (500 MHz, CD_2Cl_2, 298 K): δ = 5.38 (br. s, 4 H, COD-CH), 3.00 (td, $^{2}J_{PH}$ = 10, $^{3}J_{RhH}$ = 1 Hz, 2 H, PCH_2P), 2.33 (s, 8 H, COD-CH_2), 2.11–1.77 (br. m, 24 H, Cy), 1.45–1.22 (br. m, 20 H, Cy) ppm. ^{31}P{^{1}H} NMR (202 MHz, CD_2Cl_2, 298 K): δ = –27.4 (d, $^{1}J_{RhP}$ = 126 Hz) ppm. ^{19}F{^{1}H} NMR (470 MHz, CD_2Cl_2, 298 K): δ = –75.8 (s) ppm. ESI-MS (1,2-$F_2C_6H_4$, 60 °C, 4.5 kV): *m/z* 619.32 (calculated 619.31 for [Rh(dcpm)(COD)]$^+$ fragment). $C_{49}H_{58}AlF_{36}O_4P_2Rh$ (1586.76): calcd. C 37.09, H 3.68; found C 37.18, H 3.59.

[Rh(dcpm)(COD)][BAr$^F{}_4$]: Prepared according to the literature procedure for [Rh(dcpe)(COD)][BAr$^F{}_4$].[58] A solution of [Rh(COD)$_2$]-[BAr$^F{}_4$] (349 mg, 0.295 mmol) in CH_2Cl_2 (40 mL) was treated dropwise with a solution of dcpm (122 mg, 0.299 mmol) in CH_2Cl_2 (20 mL) at –78 °C with vigorous stirring. Upon complete addition the colour of the reaction mixture changed from burgundy to orange. The reaction mixture was warmed to ambient temperature and stirred for 16 h. The solution was concentrated to 5 mL under vacuum and pentane (50 mL) was added to precipitate an orange solid which was isolated by filtration, washed with pentane (3 × 10 mL) and dried under vacuum. Yield 408 mg (0.275 mmol, 93 %). The powder was then extracted into the minimum amount of CH_2Cl_2 and layered with pentane, which afforded large orange crystals suitable for an X-ray diffraction study. ^{1}H NMR (500 MHz, CD_2Cl_2, 298 K): δ = 7.72 (s, 8 H, *ortho*-BAr$^F{}_4$), 7.56 (s, 4 H, *para*-BAr$^F{}_4$), 5.37 (br. s, 4 H, COD-CH), 2.99 (t, br, $^{2}J_{PH}$ = 10 Hz, 2 H, PCH_2P), 2.31 (s, 8 H, COD-CH_2), 2.08–1.76 (br. m, 24 H, Cy), 1.43–1.20 (br. m, 20 H, Cy) ppm. ^{31}P{^{1}H} NMR (202 MHz, CD_2Cl_2, 298 K): δ = –27.5 (d, $^{1}J_{RhP}$ = 126 Hz) ppm. ^{19}F{^{1}H} NMR (470 MHz, CD_2Cl_2, 298 K): δ = –62.9 (s) ppm. ESI-MS (1,2-$F_2C_6H_4$, 60 °C, 4.5 kV): *m/z* 619.32 (calculated 619.31 for [Rh(dcpm)(COD)]$^+$ fragment). $C_{65}H_{70}BF_{24}P_2Rh$ (1482.88): calcd. C 52.65, H 4.76; found C 52.41, H 4.81.

[Rh(dcpm)(1,2-F$_2$C$_6$H$_4$)][Al{OC(CF$_3$)$_3$}$_4$] (1): [Rh(dcpm)(COD)]-[Al{OC(CF$_3$)$_3$}$_4$] (100 mg, 63.0 µmol) was dissolved in 1,2-$F_2C_6H_4$ (5 mL) in a J. Young flask. The solution was freeze-pump-thaw degassed three times and refilled with H_2 (4 atm). The reaction mixture was stirred for 16 h, over which time the colour the solution changed from orange to yellow. Volatiles and excess H_2 were removed under vacuum and the resultant solid was washed with pentane (2 × 5 mL). The solid was extracted into the minimum volume of CH_2Cl_2, filtered and layered with pentane to afford yellow crystals suitable for X-ray diffraction which were isolated by filtration and dried under vacuum. Yield: 80 mg (49 µmol, 78 %). ^{1}H NMR (400 MHz, CD_2Cl_2, 298 K): δ = 6.90 (m, 2 H, $F_2C_6H_4$), 6.17 (m, 2 H, $F_2C_6H_4$), 2.70 (td, $^{2}J_{PH}$ = 10, $^{3}J_{RhH}$ = 2 Hz, 2 H, PCH_2P), 1.94–1.63 (br. m, 24 H, Cy), 1.40–1.03 (br. m, 20 H, Cy) ppm. ^{31}P{^{1}H} NMR (162 MHz, CD_2Cl_2, 298 K): δ = –10.4 (d, $^{1}J_{RhP}$ = 168 Hz) ppm. ^{19}F{^{1}H} NMR (376 MHz, CD_2Cl_2, 298 K): δ = –75.8 (s, 36 F, CF_3), –146.3 (d, $^{2}J_{RhF}$ = 3 Hz, 2 F, $F_2C_6H_4$) ppm. ESI-MS (1,2-$F_2C_6H_4$, 60 °C, 4.5 kV): *m/z* 625.24 (calculated 625.24 for [Rh(dcpm)(1,2-$F_2C_6H_4$)]$^+$ fragment). $C_{47}H_{50}AlF_{38}O_4P_2Rh$ (1592.67): calcd. C 35.44, H 3.16; found C 35.51, H 3.19.

[Rh(dcpm)(1,2,3-F$_3$C$_6$H$_3$)][Al{OC(CF$_3$)$_3$}$_4$] (2): [Rh(dcpm)(COD)]-[Al{OC(CF$_3$)$_3$}$_4$] (107 mg, 67.4 µmol) was dissolved in 1,2,3-$F_3C_6H_3$ (0.4 mL) in a high pressure J. Young NMR tube. The solution was freeze-pump-thaw degassed three times and refilled with H_2 (4 atm). The solution was stirred for 4 h, over which time the solution changed from orange to yellow. Excess H_2 was removed by three freeze-pump-thaw cycles and the fluoroarene complex was characterised by NMR spectroscopy in situ. The solution was filtered and layered with pentane to afford yellow crystals suitable for X-ray diffraction which were isolated by filtration and dried under vacuum. Yield: 88 mg (55 µmol, 82 %). ^{1}H NMR (400 MHz, 1,2,3-$F_3C_6H_3$, 298 K): δ = 6.56 (br. s, 2 H, 1,3-$F_3C_6H_3$), 6.49 (br. m, 1 H, 2-$F_3C_6H_3$), 2.85 (t, br, $^{2}J_{PH}$ = 10 Hz, 2 H, PCH_2P), 2.00–1.67 (br. m, 24 H, Cy), 1.44–1.13 (br. m, 20 H, Cy and cyclooctane) ppm. ^{31}P{^{1}H} NMR (162 MHz, 1,2,3-$F_3C_6H_3$, 298 K): δ = –10.9 (d, $^{1}J_{RhP}$ = 167 Hz) ppm. ^{19}F{^{1}H} NMR (376 MHz, 1,2,3-$F_3C_6H_3$, 298 K): δ = –75.8 (s, 36 F, CF_3), –146.7 (br. d, $^{3}J_{FF}$ = 30 Hz, 2 F, 1,3-$F_3C_6H_3$), –167.1 (br. d, $^{3}J_{FF}$ = 30, $^{2}J_{RhF}$ = 5 Hz, 1 F, 2-$F_3C_6H_3$) ppm, [Rh(dcpm)(1,2,3-$F_3C_6H_3$)][Al{OC(CF$_3$)$_3$}$_4$] did not persist under ESI-MS conditions. $C_{47}H_{49}AlF_{39}O_4P_2Rh$ (1610.66): calcd. C 35.05, H 3.07; found C 35.19, H 3.01.

[Rh(dcpm)(1,2-F$_2$C$_6$H$_4$)][BAr$^F{}_4$] (3): [Rh(dcpm)(COD)][BAr$^F{}_4$] (50 mg, 33.7 µmol) was dissolved in 1,2-$F_2C_6H_4$ (5 mL) in a J. Young flask. The solution was freeze-pump-thaw degassed three times and refilled with H_2 (4 atm). The reaction mixture was stirred for 16 h, over which time the colour the solution changed from orange to yellow. Volatiles and excess H_2 were removed under vacuum and the resultant solid was washed with pentane (2 × 2 mL) and dried under vacuum. Crystals of **3** were obtained by layering a 1,2-$F_2C_6H_4$ solution of **3** with pentane. Yield: 41 mg (27.5 µmol, 82 %). ^{1}H NMR (400 MHz, CD_2Cl_2, 298 K): δ = 7.74 (s, 8 H, *ortho*-BAr$^F{}_4$), 7.58 (s, 4 H, *para*-BAr$^F{}_4$), 6.91 (m, 2 H, $F_2C_6H_4$), 6.15 (m, 2 H, $F_2C_6H_4$), 2.70 (td, $^{2}J_{PH}$ = 10, $^{3}J_{RhH}$ = 2 Hz, 2 H, PCH_2P), 1.94–1.63 (br. m, 24

H, Cy), 1.39–1.03 (br. m, 20 H, Cy) ppm. $^{31}P\{^1H\}$ NMR (162 MHz, CD_2Cl_2, 298 K): δ = –10.3 (d, $^1J_{RhP}$ = 169 Hz) ppm. $^{19}F\{^1H\}$ NMR (376 MHz, CD_2Cl_2, 298 K): δ = –62.9 (s, 36 F, $BAr^F{}_4$), –146.2 (br. s, 2 F, $F_2C_6H_4$) ppm. ESI-MS (1,2-$F_2C_6H_4$, 60 °C, 4.5 kV): *m/z* 625.24 (calculated 625.24 for [Rh(dcpm)(1,2-$F_2C_6H_4$)]$^+$ fragment). $C_{63}H_{62}BF_{26}P_2Rh$ (1488.79): calcd. C 50.82, H 4.20; found C 50.93, H 4.26.

In-situ Preparation of [Rh(dcpm)(1,2,3-$F_3C_6H_3$)][$BAr^F{}_4$] (4) and Isolation of [Rh(dcpm){η^6-(3,5-$(CF_3)_2C_6H_3$)$BAr^F{}_3$}] (5): [Rh(dcpm)(COD)][$BAr^F{}_4$] (54 mg, 36.4 µmol) was dissolved in 1,2,3-$F_3C_6H_3$ (0.4 mL) in a high pressure J. Young NMR tube. The solution was freeze-pump-thaw degassed three times and refilled with H_2 (4 atm). The solution was stirred for 4 h, over which time the solution changed from orange to yellow. Excess H_2 was removed by three freeze-pump-thaw cycles and the fluoroarene complex was characterised by NMR spectroscopy in situ. ^1H NMR (500 MHz, 1,2,3-$F_3C_6H_3$, 298 K): δ = 8.06 (s, 8 H, *ortho*-$BAr^F{}_4$), 7.48 (s, 4 H, *para*-$BAr^F{}_4$), 6.57 (br. s, 2 H, 1,3-$F_3C_6H_3$), 6.50 (br. m, 1 H, 2-$F_3C_6H_3$), 2.87 (t, br, $^2J_{PH}$ = 10 Hz, 2 H, PCH_2P), 2.02–1.70 (br. m, 24 H, Cy), 1.41–1.20 (br. m, 20 H, Cy and cyclooctane) ppm. $^{31}P\{^1H\}$ NMR (202 MHz, 1,2,3-$F_3C_6H_3$, 298 K): δ = –10.9 (d, $^1J_{RhP}$ = 168 Hz) ppm. $^{19}F\{^1H\}$ NMR (470 MHz, 1,2,3-$F_3C_6H_3$, 298 K): δ = –63.5 (s, 24 F, CF_3), –146.0 (br. d, $^3J_{FF}$ = 30 Hz, 2 F, 1,3-$F_3C_6H_3$), –166.0 (t, br, $^3J_{FF}$ = 30 Hz, 1 F, 2-$F_3C_6H_3$) ppm. Attempts to crystallise [Rh(dcpm)(1,2,3-$F_3C_6H_3$)][$BAr^F{}_4$] by layering with pentane afforded a yellow solution of [Rh(dcpm){η^6-(3,5-$(CF_3)_2C_6H_3$)$BAr^F{}_3$}]. The solvent was removed under vacuum and the residue was extracted into pentane. Slow cooling of the pentane solution to –20 °C afforded crystals of [Rh(dcpm){η^6-(3,5-$(CF_3)_2C_6H_3$)$BAr^F{}_3$}] (22 mg, 16 µmol, 44 %). ^1H NMR (400 MHz, F_6C_6, 298 K): δ = 7.58 (s, 6 H, *ortho*-$BAr^F{}_4$ non-coordinated rings), 7.40 (s, 3 H, *para*-$BAr^F{}_4$ non-coordinated rings), 7.21 (s, 2 H, *ortho*-$BAr^F{}_4$ Rh-coordinated ring), 6.95 (s, 1 H, *para*-$BAr^F{}_4$ Rh-coordinated ring), 2.80 (br. s, 2 H, PCH_2P), 2.04–1.67 (br. m, 24 H, Cy), 1.36–1.12 (br. m, 20 H, Cy) ppm. $^{31}P\{^1H\}$ NMR (162 MHz, F_6C_6, 298 K): δ = –12.7 (d, $^1J_{RhP}$ = 172 Hz) ppm. $^{19}F\{^1H\}$ NMR (376 MHz, F_6C_6, 298 K): δ = –61.5 (s, 1 F, $BAr^F{}_4$ Rh-coordinated ring), –64.1 (s, 3 F, $BAr^F{}_4$ non-coordinated rings) ppm. $C_{57}H_{58}BF_{24}P_2Rh$ (1374.70): calcd. C 49.80, H 4.25; found C 49.89, H 4.34.

[Rh(dcpm)(H_3B-NMe_3)][Al{$OC(CF_3)_3$}$_4$] (6): [Rh(dcpm)(1,2,3-$F_3C_6H_3$)][Al{$OC(CF_3)_3$}$_4$] (30.0 mg, 18.6 µmol) and H_3B-NMe_3 (2.8 mg, 38 µmol) were dissolved in 1,2,3-$F_3C_6H_3$ (0.3 mL) and stirred for 1 min. The solution turned red, and pentane (ca 3 mL) was added to give a red oil, which, upon sonicating, afforded a red oily solid. This was isolated by filtration, washed with pentane (3 × 3 mL) and dried under vacuum. Attempts to purify **6** resulted in isolation of an oily red solid, NMR spectroscopy of which showed no improvement in purity (ca. 80 % pure). Yield 16 mg (10 µmol, 55 %). NMR spectra were collected immediately upon dissolution in CD_2Cl_2 as extended time in solution leads to decomposition of **3**. ^1H NMR (400 MHz, CD_2Cl_2, 298 K): δ = 2.91 (br. s, 2 H, PCH_2P), 2.79 (s, 9 H, NMe_3), 2.04–1.75 (br. m, 24 H, Cy), 1.46–1.23 (br. m, 20 H, Cy), –1.75 (s, v br, 3 H, BH_3, sharpens upon ^1H-decoupling) ppm. ^{11}B (128 MHz, CD_2Cl_2, 298 K): δ = 16.3 (s, br) ppm. $^{11}B\{^1H\}$ (128 MHz, CD_2Cl_2, 298 K): δ = 16.1 (s, br) ppm. $^{31}P\{^1H\}$ (162 MHz, CD_2Cl_2, 298 K): δ –3.4 (d, $^1J_{RhP}$ = 145 Hz) ppm. [Rh(dcpm)(H_3B-NMe_3)][Al{$OC(CF_3)_3$}$_4$] did not persist under ESI-MS conditions. Satisfactory elemental analysis was not obtained.

[{RhH(µ-dcpm)}$_2$(µ-H)(µ-$BNMe_2$)][Al{$OC(CF_3)_3$}$_4$] (7): [Rh(dcpm)(1,2,3-$F_3C_6H_3$)][Al{$OC(CF_3)_3$}$_4$] (81.0 mg, 50.3 µmol) and H_3B-NMe_2H (9.3 mg, 16 µmol) were dissolved in 1,2,3-$F_3C_6H_3$ (0.4 mL) and stirred for two days. Pentane (5 mL) was added to form a yellow precipitate which was isolated by filtration and washed with pentane (3 × 3 mL). Recrystallisation from 1,2,3-$F_3C_6H_3$/pentane afforded **7** as yellow crystals suitable for X-ray diffraction (23 mg) that were contaminated with recalcitrant [$H_2B(NMe_2H)_2$][Al{$OC(CF_3)_3$}$_4$]. ^1H NMR (500 MHz, 1,2,3-$F_3C_6H_3$, 298 K): δ = 2.78 (s, 6 H, NMe_2), 2.21 (t, $^2J_{PH}$ = 5 Hz, 2 H, PCH_2P), 2.18 (t, $^2J_{PH}$ = 5 Hz, 2 H, PCH_2P), 2.66–1.24 (m, 88 H, Cy), –4.87 (br. m, 2 H, Rh-H), –7.91 (br. m, 1 H, RhHRh) ppm. ^{11}B (160 MHz, 1,2,3-$F_3C_6H_3$, 298 K): δ = 59.0 (s, v br) ppm. $^{11}B\{^1H\}$ (160 MHz, 1,2,3-$F_3C_6H_3$, 298 K): δ = 59.0 (s, v br) ppm. $^{31}P\{^1H\}$ NMR (202 MHz, 1,2,3-$F_3C_6H_3$, 298 K): δ = 55.9 (m) ppm. ESI-MS (1,2-$F_2C_6H_4$, 60 °C, 4.5 kV): *m/z* 1080.51 (calculated 1080.51 for [{RhH(µ-dcpm)}$_2$(µ-H)(µ-$BNMe_2$)]$^+$ fragment). Satisfactory elemental analysis results could not be obtained due to contamination of bulk samples with [$H_2B(NMe_2H)_2$][Al{$OC(CF_3)_3$}$_4$].

Acknowledgments

The Engineering and Physical Sciences Research Council (EPSRC) (A. S. W. and S. A. M., EP/M024210/1; N. A. B., DTP Studentship).

Keywords: Amines · Rhodium · Boranes · Fluoroarenes · Phosphines

[1] H. C. Johnson, T. N. Hooper, A. S. Weller, *Top. Organomet. Chem.* **2015**, *49*, 153–220.
[2] E. M. Leitao, T. Jurca, I. Manners, *Nat. Chem.* **2013**, *5*, 817–829.
[3] A. Rossin, M. Peruzzini, *Chem. Rev.* **2016**, *116*, 8848–8872.
[4] M. Shimoi, S. Nagai, M. Ichikawa, Y. Kawano, K. Katoh, M. Uruichi, H. Ogino, *J. Am. Chem. Soc.* **1999**, *121*, 11704–11712.
[5] Y. Kawano, M. Hashiva, M. Shimoi, *Organometallics* **2006**, *25*, 4420–4426.
[6] A. E. W. Ledger, C. E. Ellul, M. F. Mahon, J. M. J. Williams, M. K. Whittlesey, *Chem. Eur. J.* **2011**, *17*, 8704–8713.
[7] R. Dallanegra, A. P. M. Robertson, A. B. Chaplin, I. Manners, A. S. Weller, *Chem. Commun.* **2011**, *47*, 3763–3765.
[8] P. Dierkes, P. W. N. M. van Leeuwen, *J. Chem. Soc., Dalton Trans.* **1999**, 1519–1529.
[9] A. B. Chaplin, A. S. Weller, *Inorg. Chem.* **2010**, *49*, 1111–1121.
[10] A. Kumar, I. K. Priest, T. N. Hooper, A. S. Weller, *Dalton Trans.* **2016**, *45*, 6183–6195.
[11] S. D. Pike, I. Pernik, R. Theron, J. S. McIndoe, A. S. Weller, *J. Organomet. Chem.* **2015**, *784*, 75–83.
[12] S. D. Pike, T. Krämer, N. H. Rees, S. A. Macgregor, A. S. Weller, *Organometallics* **2015**, *34*, 1487–1497.
[13] I. Pernik, J. F. Hooper, A. B. Chaplin, A. S. Weller, M. C. Willis, *ACS Catal.* **2012**, *2*, 2779–2786.
[14] S. D. Pike, M. R. Crimmin, A. B. Chaplin, *Chem. Commun.* **2017**, *53*, 3615–3633.
[15] T. M. Douglas, A. B. Chaplin, A. S. Weller, X. Yang, M. B. Hall, *J. Am. Chem. Soc.* **2009**, *131*, 15440–15456.
[16] S. D. Pike, A. L. Thompson, A. G. Algarra, D. C. Apperley, S. A. Macgregor, A. S. Weller, *Science* **2012**, *337*, 1648–1651.
[17] K. Bambridge, R. M. G. Roberts, *J. Organomet. Chem.* **1991**, *401*, 125–132.
[18] J. I. Wu, F. G. Pühlhofer, P. von Ragué Schleyer, R. Puchta, B. Kiran, M. Mauksch, N. J. R. van Eikema Hommes, I. Alkorta, J. Elguero, *J. Phys. Chem. A* **2009**, *113*, 6789–6794.
[19] S. Kawahara, S. Tsuzuki, T. Uchimaru, *Chem. Eur. J.* **2005**, *11*, 4458–4464.
[20] A. R. O'Connor, P. S. White, M. Brookhart, *Organometallics* **2010**, *29*, 5382–5389.
[21] J. Powell, A. Lough, T. Saeed, *J. Chem. Soc., Dalton Trans.* **1997**, 4137–4138.
[22] A. R. O'Connor, M. Brookhart, *J. Polym. Sci., Part A Polym. Chem.* **2010**, *48*, 1901–1912.
[23] T. M. Douglas, E. Molinos, S. K. Brayshaw, A. S. Weller, *Organometallics* **2007**, *26*, 463–465.
[24] F. Eisenträger, A. Göthlich, I. Gruber, H. Heiss, C. A. Kiener, C. Krüger, J. U. Notheis, F. Rominger, G. Scherhag, M. Schultz, B. F. Straub, M. A. O. Volland, P. Hofmann, *New J. Chem.* **2003**, *27*, 540–550.

[25] I. Krossing, *Chem. Eur. J.* **2001**, *7*, 490–502.

[26] I. Krossing, I. Raabe, *Angew. Chem. Int. Ed.* **2004**, *43*, 2066–2090; *Angew. Chem.* **2004**, *116*, 2116.

[27] 1,2,3-$F_3C_6H_3$ was purchased from Fluorochem, treated with alumina, dried with CaH_2 and vacuum distilled before use. GC–MS analysis of the purified solvent identified the arenes FC_6H_5, $F_2C_6H_4$, $FCl_2C_6H_3$, $F_2ClC_6H_3$, $F_2Cl_2C_6H_2$, $F_3ClC_6H_2$ and $F_3BrC_6H_2$ as trace impurities.

[28] This reactivity profile suggests a dissociative process for substitution.

[29] V. S. Khandkarova, S. P. Gubin, B. A. Kvasov, *J. Organomet. Chem.* **1970**, *23*, 509–515.

[30] H. Ssekaalo, J. J. Lagowski, C. M. Seymour, *Inorg. Chim. Acta* **1991**, *183*, 91–95.

[31] M. J. McGlinchey, T.-S. Tan, *Can. J. Chem.* **1974**, *52*, 2439–2443.

[32] M. Roselló-Merino, J. López-Serrano, S. Conejero, *J. Am. Chem. Soc.* **2013**, *135*, 10910–10913.

[33] C. A. Jaska, K. Temple, A. J. Lough, I. Manners, *J. Am. Chem. Soc.* **2003**, *125*, 9424–9434.

[34] C. J. Stevens, R. Dallanegra, A. B. Chaplin, A. S. Weller, S. A. Macgregor, B. Ward, D. McKay, G. Alcaraz, S. Sabo-Etienne, *Chem. Eur. J.* **2011**, *17*, 3011–3020.

[35] A. Rifat, N. J. Patmore, M. F. Mahon, A. S. Weller, *Organometallics* **2002**, *21*, 2856–2865.

[36] A. Kumar, N. A. Beattie, S. D. Pike, S. A. Macgregor, A. S. Weller, *Angew. Chem. Int. Ed.* **2016**, *55*, 6651–6656; *Angew. Chem.* **2016**, *128*, 6763.

[37] C. P. Kubiak, R. Eisenberg, *J. Am. Chem. Soc.* **1977**, *99*, 6129–6131.

[38] M. E. Slaney, D. J. Anderson, M. J. Ferguson, R. McDonald, M. Cowie, *Organometallics* **2012**, *31*, 2286–2301.

[39] H. Werner, M. Manger, M. Laubender, M. Teichert, D. Stalke, *J. Organomet. Chem.* **1998**, *569*, 189–194.

[40] H. Braunschweig, M. Forster, T. Kupfer, F. Seeler, *Angew. Chem. Int. Ed.* **2008**, *47*, 5981–5983; *Angew. Chem.* **2008**, *120*, 6070.

[41] C. Y. Tang, N. Phillips, J. I. Bates, A. L. Thompson, M. J. Gutmann, S. Aldridge, *Chem. Commun.* **2012**, *48*, 8096–8098.

[42] H. C. Johnson, E. M. Leitao, G. R. Whittell, I. Manners, G. C. Lloyd-Jones, A. S. Weller, *J. Am. Chem. Soc.* **2014**, *136*, 9078–9093.

[43] H. Braunschweig, T. Wagner, *Angew. Chem. Int. Ed. Engl.* **1995**, *34*, 825–826; *Angew. Chem.* **1995**, *107*, 904.

[44] H. Braunschweig, R. D. Dewhurst, V. H. Gessner, *Chem. Soc. Rev.* **2013**, *42*, 3197–3208.

[45] H. Braunschweig, M. Forster, K. Radacki, *Angew. Chem. Int. Ed.* **2006**, *45*, 2132–2134; *Angew. Chem.* **2006**, *118*, 2187.

[46] See Supporting Information for full details and references.

[47] M. D. Fryzuk, D. H. McConville, S. J. Rettig, *J. Organomet. Chem.* **1993**, *445*, 245–256.

[48] J. Dusan Ristic-Petrovic, D. Anderson, J. R. Torkelson, M. J. Ferguson, R. McDonald, M. Cowie, *Organometallics* **2005**, *24*, 3711–3724.

[49] D. Ristic-Petrovic, J. R. Torkelson, R. W. Hilts, R. McDonald, M. Cowie, *Organometallics* **2000**, *19*, 4432–4434.

[50] C. Y. Tang, A. L. Thompson, S. Aldridge, *Angew. Chem. Int. Ed.* **2010**, *49*, 921–925; *Angew. Chem.* **2010**, *122*, 933.

[51] C. Y. Tang, A. L. Thompson, S. Aldridge, *J. Am. Chem. Soc.* **2010**, *132*, 10578–10591.

[52] D. A. Addy, J. I. Bates, M. J. Kelly, I. M. Riddlestone, S. Aldridge, *Organometallics* **2013**, *32*, 1583–1586.

[53] M. O'Neill, D. A. Addy, I. Riddlestone, M. Kelly, N. Phillips, S. Aldridge, *J. Am. Chem. Soc.* **2011**, *133*, 11500–11503.

[54] G. Alcaraz, U. Helmstedt, E. Clot, L. Vendier, S. Sabo-Etienne, *J. Am. Chem. Soc.* **2008**, *130*, 12878–12879.

[55] N. Arnold, H. Braunschweig, R. D. Dewhurst, W. C. Ewing, *J. Am. Chem. Soc.* **2016**, *138*, 76–79.

[56] B. Guzel, M. A. Omary, J. P. Fackler Jr., A. Akgerman, *Inorg. Chim. Acta* **2001**, *325*, 45–50.

[57] G. Giordano, R. H. Crabtree, *Inorg. Synth.* **1979**, *19*, 218–220.

[58] S. D. Pike, F. M. Chadwick, N. H. Rees, M. P. Scott, A. S. Weller, T. Krämer, S. A. Macgregor, *J. Am. Chem. Soc.* **2015**, *137*, 820–833.

Received: May 21, 2017

JACS JOURNAL OF THE AMERICAN CHEMICAL SOCIETY
Article
Cite This: J. Am. Chem. Soc. 2018, 140, 1481−1495
pubs.acs.org/JACS

Dehydropolymerization of $H_3B{\cdot}NMeH_2$ To Form Polyaminoboranes Using [Rh(Xantphos-alkyl)] Catalysts

Gemma M. Adams,[†,‡] Annie L. Colebatch,[†,‡] Joseph T. Skornia,[†] Alasdair I. McKay,[†] Heather C. Johnson,[†] Guy C. Lloyd−Jones,[§] Stuart A. Macgregor,[∥] Nicholas A. Beattie,[∥] and Andrew S. Weller[*,†]

[†]Chemistry Research Laboratories, Mansfield Road, Oxford OX1 3TA, United Kingdom
[§]School of Chemistry, University of Edinburgh, Edinburgh EH9 3FJ, United Kingdom
[∥]Institute of Chemical Sciences, Heriot Watt University, Edinburgh EH14 4AS, United Kingdom

Supporting Information

ABSTRACT: A systematic study of the catalyst structure and overall charge for the dehydropolymerization of $H_3B{\cdot}NMeH_2$ to form *N*-methyl polyaminoborane is reported using catalysts based upon neutral and cationic {Rh(Xantphos-R)} fragments in which PR_2 groups are selected from Et, ^{i}Pr, and ^{t}Bu. The most efficient systems are based upon {Rh(Xantphos-^{i}Pr)}, i.e., [Rh(κ^3-P,O,P-Xantphos-^{i}Pr)$(H)_2(\eta^1$-$H_3B{\cdot}NMe_3)$][BAr^F_4], **6**, and Rh(κ^3-P,O,P-Xantphos-^{i}Pr)H, **11**. While H_2 evolution kinetics show both are fast catalysts (ToF ≈ 1500 h^{-1}) and polymer growth kinetics for dehydropolymerization suggest a classical chain growth process for both, neutral **11** (M_n = 28 000 g mol^{-1}, $Đ$ = 1.9) promotes significantly higher degrees of polymerization than cationic **6** (M_n = 9000 g mol^{-1}, $Đ$ = 2.9). For **6** isotopic labeling studies suggest a rate-determining NH activation, while speciation studies, coupled with DFT calculations, show the formation of a dimetalloborylene [{Rh(κ^3-P,O,P-Xantphos-^{i}Pr)}$_2$B]$^+$ as the, likely dormant, end product of catalysis. A dual mechanism is proposed for dehydropolymerization in which neutral hydrides (formed by hydride transfer in cationic **6** to form a boronium coproduct) are the active catalysts for dehydrogenation to form aminoborane. Contemporaneous chain-growth polymer propagation is suggested to occur on a separate metal center via head-to-tail end chain B−N bond formation of the aminoborane monomer, templated by an aminoborohydride motif on the metal.

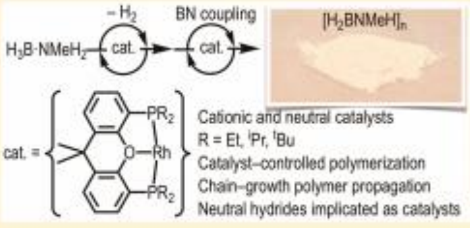

1. INTRODUCTION

The catalyzed dehydropolymerization of ammonia−borane or primary amine−boranes, such as $H_3B{\cdot}NMeH_2$, provides a potentially useful methodology for the production of new inorganic polymeric materials, polyaminoboranes (e.g., *N*-methyl polyaminoborane $(H_2BNMeH)_n$), which have alternating BN main-chain units, Scheme 1A. Although these are isoelectronic with technologically pervasive polyolefins such as polypropylene their synthesis and properties are virtually unexplored,[1] apart from a few examples that demonstrate their use as precursors for BN-based materials.[2] A variety of catalysts[1c,3] have been shown to promote the dehydropolymerization of $H_3B{\cdot}NH_3$,[4] and in particular $H_3B{\cdot}NMeH_2$,[2d,4a,b,5] for example, $Ir(POCOP)(H)_2$, **A** (POCOP = κ^3-C_6H_3-2,6-$(OP^tBu_2)_2$),[4a] (PNHP)Fe(H)(CO)(HBH_3) (PNHP = HN-$(CH_2CH_2P^iPr_2)_2$), **B**,[6] and [Rh{$Ph_2P(CH_2)_3PPh_2$}(η^6−FC_6H_5)][BAr^F_4] (Ar^F = 3,5-$(CF_3)_2C_6H_3$), **C**,[5a] Scheme 1B. These catalysts have been shown to operate under homogeneous conditions, although heterogeneous examples have also been reported,[7] and the switch between these two mechanistic extremes can be controlled by precatalyst structure.[8] However, catalyst development that originates through an understanding of the mechanism(s) that operate in dehydropolymerization is still in its infancy.[1c−e,4a,c,e,5d,6,9] Although many of the individual fundamental steps have been studied in some detail,[10] e.g.,

Scheme 1. (A) Dehydropolymerization of $H_3B{\cdot}NMeH_2$; (B) Examples of Catalysts (M_n = g mol^{-1})[a]

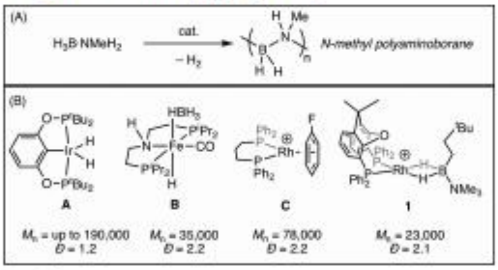

[a] $[BAr^F_4]^-$ anions are not shown.

Received: November 14, 2017
Published: December 29, 2017

DOI: 10.1021/jacs.7b11975
J. Am. Chem. Soc. 2018, 140, 1481−1495

dehydrogenation to form aminoboranes[5d,11] and the formation of oligomeric di- and triborazanes[11a,c,12] by dehydrocoupling processes, the roles of metal/ligand fragment in both promoting dehydrogenation of the precursor amine−borane and coupling (i.e., chain propagation) to form polymeric material have not been fully delineated. Valence isoelectronic primary phosphine−boranes also undergo dehydropolymerization;[13] for which mechanistic studies give complementary insight.

In contrast with olefin polymerization[14] where the monomer (e.g., propene) is stable, aminoboranes such as $H_2B{=}NH_2$ or $H_2B{=}NMeH$ are unstable toward oligomerization and can only be observed as transient species at low temperatures or trapped on metal centers.[5d,11b,13a] This presents an additional challenge for studying amine−borane dehydropolymerization as the catalyst needs to operate in a bifunctional[1c,4e] manner, dehydrogenating amine−boranes (via B−H and N−H activation) and then subsequently controlling the B−N bond-forming polymerization events (Scheme 2). Further complicating the mechanistic analysis and control of polymer chain propagation is that aminoboranes have been shown to undergo a number of different reactions when generated in situ in the absence of a catalyst. For example, dehydrocoupling to form borazines,[1e] autocatalytic roles in dehydrocoupling processes,[16] hydrogen−redistribution reactions,[17] polymerization to form product that is insoluble, e.g., $(H_2BNH_2)_n$,[4a] or low[15a]/high[15b] molecular weight $(H_2BNMeH)_n$.[15] In addition, dehydrogenation processes (on- or off-metal) have been proposed to be promoted by secondary interactions such as N−H(δ+)···(δ−)H−B dihydrogen bonds.[16a,18] As the numerous studies on the dehydrocoupling of the secondary amine−borane, $H_3B\text{-}NMe_2H$, have shown, differences in the likely mechanistic pathways can also occur by changing the catalyst.[1c]

Scheme 2. On- and Off-Metal (Dehydro)polymerization of Amine− and Aminoboranes

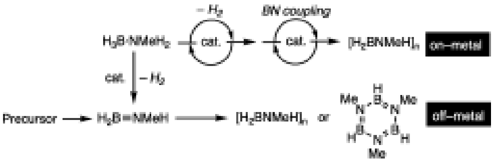

We recently reported that cationic precatalysts based upon $[Rh(\kappa^2\text{-}P,P\text{-Xantphos-Ph})(\eta^2\text{-}H_2B(CH_2CH_2{}^tBu)NMe_3)][BAr^F_4]$, **1** (Xantphos-Ph = 4,5-bis(diphenylphosphino)-9,9-dimethylxanthene), are particularly effective for the dehydropolymerization of $H_3B{\cdot}NMeH_2$, operating at 0.2 mol % in FC_6H_5 solvent to produce polyaminoborane of M_n = 23 000 g mol^{-1}, Đ = 2.1 (Scheme 1).[5b] A controlled[19] dehydrogenation/coordination/insertion[1c,4c] mechanism for chain propagation was proposed on the basis of (i) saturation kinetics being observed (and modeled) in analogous $H_3B{\cdot}NMe_2H$ dehydrocoupling, (ii) an inverse relationship between catalyst loading and polymer molecular weight, and (iii) H_2 acting as a chain termination agent to produce significantly lower molecular weight polymer (M_n = 2800 g mol^{-1}, Đ = 1.8). In such a mechanism the metal is proposed to promote dehydrogenative insertion of $H_3B{\cdot}NMeH_2$ via a transient[15,20] metal-bound $H_2B{=}NMeH$ fragment (Scheme 3A). Although the identity of the true catalyst remains unresolved, in part due to the low catalyst loadings used (0.2 mol %) and an induction period being observed before catalysis, a Rh(III) dihydride was implicated as the first formed species (Scheme 3B). This was *proposed* to evolve to a Rh(III)−amidoborane, responsible for chain propagation. Stoichiometric experiments also demonstrated hemilability[21] of the Xantphos-Ph ligand between *cis*-κ²-P,P and *mer*-κ³-P,O,P coordination motifs. The actual catalyst formed in situ could also be cationic or neutral (formed via hydride transfer from borane[5d,22]) or have a bimetallic motif as commented upon in other systems based upon kinetic studies or products characterized by single-crystal X-ray diffraction.[5c,d,23] This mechanism differs from those proposed to operate for $Fe(PhNCH_2CH_2NPh)(Cy_2PCH_2CH_2PCy_2)/H_3B{\cdot}NH_3$,[4c] catalyst **A**,[4a,24] and bifunctional $M(PNP)H(PMe_3)/H_3B{\cdot}NH_3$ (M = Fe, Ru)[4e,f] systems, for which metal-based dehydrogenation occurs but the aminoborane undergoes metal-based polymerization at a *different* metal center.

Scheme 3. (A) Proposed Coordination/Dehydrogenation/Insertion Mechanism; (B) Cationic Xantphos-Ph Precatalyst[a]

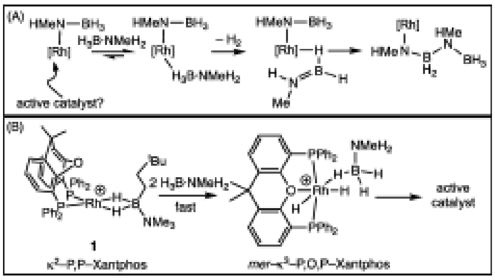

[a][BAr^F_4]⁻ anions are not shown.

While the parent Xantphos-Ph ligand is well established in organometallic catalysis,[25] the alkyl-substituted versions have only recently been explored,[26] in particular by Esteruelas.[4d,27] Scheme 4 shows examples of Rh-based complexes, both cationic and neutral. Relevant to this paper, neutral Rh−hydride **F** has been shown to be an effective catalyst for the dehydrogenation of $H_3B{\cdot}NH_3$ and $H_3B{\cdot}NMe_2H$,[28] while it also undergoes rapid C−H activation with fluoroarenes (**G**)[27a] and

Scheme 4. Examples of Alkyl-Substituted Xantphos-Based Ligands[a]

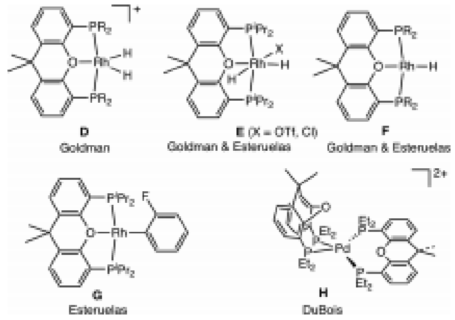

[a]Anions are not shown. R = ⁱPr, ᵗBu.

B−H activation with boranes.[27a] Interestingly for Rh-based systems, the complexes that can be observed exclusively offer the *mer*-κ^3-P,O,P binding mode in the ground state, i.e., as a pincer ligand, while *fac*-κ^3-P,O,P or *cis*-κ^2-P,P coordination modes have been observed in osmium systems.[27d] A *cis*-κ^2-P,P coordination geometry is shown by the less bulky ethyl analogue coordinated with Pd, **H**.[26c]

These reports demonstrate a rich landscape of coordination motifs and bond activations that alkyl Xantphos ligands promote when coordinated to rhodium. When coupled with our recent report using precatalyst **1**,[5b] this encourages their exploration in the dehydropolymerization of $H_3B{\cdot}NMeH_2$. We report here a systematic study of dehydropolymerization using both cationic (e.g., based upon **D**) and neutral (e.g., **F**) Rh precursors of the alkyl-substituted Xantphos motif in which the ligating PR_2 groups are also systematically varied between Xantphos-Et, Xantphos-^{i}Pr, and Xantphos-^{t}Bu.

2. RESULTS

2.1. Synthesis and Reactivity of Cationic Precursor Complexes [Rh(κ^3-P,O,P-Xantphos-R)$(H)_2$(η^1-$H_3B{\cdot}NMe_3$)]-[BAr$^F_4$], R = Et, ^{i}Pr, and [Rh(κ^3-P,O,P-Xantphos-R)$(H)_2$]-[BAr$^F_4$], R = ^{t}Bu. Catalyst precursors are ideally operationally unsaturated to allow formation of a $H_3B{\cdot}NMeH_2$ sigma complex[29] and also available as pure crystalline material. For the Xantphos-Ph system both Rh(I), **1**, and Rh(III) dihydride, [Rh(κ^3-P,O,P-Xantphos-Ph)$(H)_2$(η^1-$H_3B{\cdot}NMe_3$)][BAr$^F_4$], **2**, precursors have a weakly bound amine−borane acting as a place-holder ligand.[5b] These are conveniently prepared from a [Rh(κ^2-P,P-Xantphos-Ph)(NBD)][BAr$^F_4$] precursor (NBD = norbornadiene),[30] and we used the same route for alkyl-substituted Xantphos complexes.

Addition of Xantphos-Et to [Rh(NBD)$_2$][BAr$^F_4$] in CH_2Cl_2 solution gives [Rh(κ^2-P,P-Xantphos-Et)(NBD)][BAr$^F_4$], **3**, after recrystallization from CH_2Cl_2/pentane as an orange microcrystalline powder. In a similar manner, [Rh(κ^2-P,P-Xantphos-^{i}Pr)(NBD)][BAr$^F_4$], **4**, can be prepared. Complexes **3** and **4** were characterized by variable-temperature NMR spectroscopy (including an Eyring analysis), elemental analysis, ESI-MS (electrospray ionization-mass spectrometry), and also by single-crystal X-ray diffraction (Figure 1B shows **4**, Figure S23 for **3**), which show a *cis*-κ^2-P,P coordination geometry for the alkyl Xantphos ligands. The corresponding NBD adduct using the Xantphos-^{t}Bu ligand could not be prepared, as commented upon by Goldman and co-workers,[26b] the bulky ^{t}Bu groups disfavoring the *cis*-κ^2-P,P coordination geometry (Supporting Information).

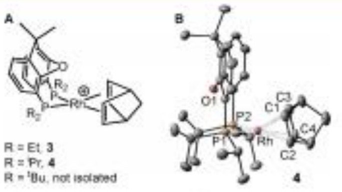

Figure 1. (A) Complexes **3** and **4**. (B) Molecular structure of the cationic portion of **4**; displacement ellipsoids at the 30% probability level; H atoms and [BAr$^F_4$]$^-$ anion are not shown. Selected bond distances (Angstroms) and angles (degrees): Rh−P1, 2.3897(8); Rh1−P2, 2.3659(8); Rh1−O1, 3.161(2); P1−Rh1−P2, 101.72(3).

Addition of H_2 to a 1,2-$F_2C_6H_4$ solution of complex **3** or **4** containing 1 equiv of $H_3B{\cdot}NMe_3$ results in the formation of [Rh(κ^3-P,O,P-Xantphos-R)$(H)_2$(η^1-$H_3B{\cdot}NMe_3$)][BAr$^F_4$] (**5**, R = Et; **6**, R = ^{i}Pr) that can be isolated as off-white solids, Figure 2A. Complex **6** was characterized by a single-crystal X-ray diffraction study (Figure 2B), which shows a *mer*-κ^3-Xantphos-^{i}Pr Rh(III) *cis*-dihydride motif with a supporting sigma-bound[29] η^1-$H_3B{\cdot}NMe_3$ ligand. The overall geometry is very similar to that measured for **2**,[31] in particular the Rh···B distance [**6**, 2.783(6) Å; **2**, 2.759(6) Å] and is also similar to [Ru(Xantphos-Ph)(PPh_3)(η^1-$H_3B{\cdot}NMeH_2$)(H)][BAr$^F_4$].[32]

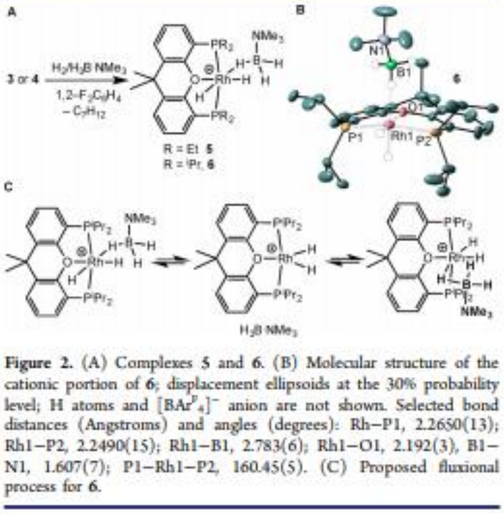

Figure 2. (A) Complexes **5** and **6**. (B) Molecular structure of the cationic portion of **6**; displacement ellipsoids at the 30% probability level; H atoms and [BAr$^F_4$]$^-$ anion are not shown. Selected bond distances (Angstroms) and angles (degrees): Rh−P1, 2.2650(13); Rh1−P2, 2.2490(15); Rh1−B1, 2.783(6); Rh1−O1, 2.192(3), B1−N1, 1.607(7); P1−Rh1−P2, 160.45(5). (C) Proposed fluxional process for **6**.

The solution NMR data show that **6** (R = ^{i}Pr) is fluxional at 298 K, while at this temperature **5** (R = Et) is not. For **6** a single hydride environment is observed at δ −19.09, of relative integral 2 H, as well as a quadrupolar broadened, 3 H relative integral, signal at δ 0.08 assigned to the Rh···H−B that is undergoing rapid site exchange between bridging and terminal B−H.[29,33] In the ^{11}B NMR spectrum a signal is observed at δ −9.9, consistent with an η^1-bound borane.[34] A single Xantphos-^{i}Pr CMe_2 environment is observed. The $^{31}P\{^1H\}$ NMR spectrum shows one environment, δ 66.5 [J(RhP) = 111 Hz]. Progressive cooling to 200 K reveals a low-temperature limiting spectrum consistent with the solid-state structure that now shows two hydride environments at δ −17.62 and −19.97 (modeled as a dtd), an upfield-shifted Rh···H−B signal (relative integral 3 H) at δ −0.58, and two Xantphos-^{i}Pr CMe_2 environments. An Eyring analysis of the hydride signals in complex **6** gives activation parameters $\Delta H^\ddagger = 59(4)$ kJ mol^{-1} and $\Delta S^\ddagger = +37(15)$ J K^{-1} mol^{-1} for this fluxional process. These data are consistent with a mechanism in which the $H_3B{\cdot}NMe_3$ ligand dissociates and recoordinates on the other side, via a (known[26b]) symmetric 16-electron intermediate [Rh(κ^3-P,O,P-Xantphos-^{i}Pr)$(H)_2$]$^+$, Figure 2C. These activation parameters are similar to those reported for a related fluxional process in [Rh(κ^3-P,O,P-Xantphos-^{i}Pr)$(H)_2$][OTf] [$\Delta H^\ddagger$ = 64(3) kJ mol^{-1} and $\Delta S^\ddagger$ = +66(8) J K^{-1} mol^{-1}].[4d] Complex **5** displays NMR data that are very similar to those measured at low temperature for **6**. We suggest these differences are driven by the steric effects of Et versus ^{i}Pr. This influence of sterics is further demonstrated in that addition of $H_3B{\cdot}NMe_3$ to $[Rh(\kappa^3\text{-}P,O,P\text{-Xantphos-}^tBu)(H)_2][BAr^F_4]$, **10**,[26b] results in no observable amine−borane adduct (eq 1), although H/D exchange experiments (vide infra) suggest such a complex is accessible. Complexes **5** and **6** do not lose H_2 when exposed to a vacuum (10^{-3} Torr). It is thus likely that during catalysis the Rh(III) oxidation state is persistent.

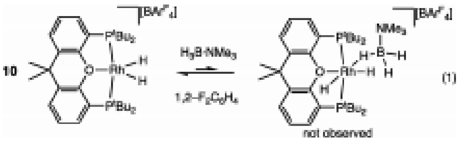

Cationic amine−borane complexes can alternatively be prepared by halide abstraction using $Na[BAr^F_4]$ from a hydrido−chloride precursor $Rh(\kappa^3\text{-}P,O,P\text{-Xantphos-}^iPr)(H)_2Cl$, **7**,[4d,26b,35] in the presence of $H_3B{\cdot}NMe_3$. Complex **6** can thus be prepared in 79% yield as a crystalline, analytically pure, solid (Scheme 5). By contrast, complex **5** cannot be prepared by this route. While addition of H_2 to dimeric $[Rh(\kappa^2\text{-}P,P\text{-Xantphos-Et})Cl]_2$ **8** (Supporting Information) gives $Rh(\kappa^3\text{-}P,O,P\text{-Xantphos-Et})(H)_2Cl$, **9**, this complex is only stable under an H_2 atmosphere regenerating **8** on its removal. For the ^tBu analogue $Rh(\kappa^3\text{-}P,O,P\text{-Xantphos-}^tBu)Cl$ Goldman has calculated that H_2 addition is favored ($\Delta G = -5$ kcal mol^{-1}).[26b] Our observations suggest that the thermodynamics of H_2 addition to **8** are more finely balanced, presumably as a consequence of the κ^2-P,P-Xantphos-Et geometry being more accessible, which promotes a dimeric structure which has two Cl bonds per metal (as noted for related Os systems[27d]).

Scheme 5. Halide Abstraction Route[a]

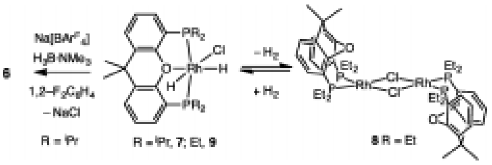

[a] $[BAr^F_4]^-$ anions are not shown.

2.2. Neutral Precursors. One of the reasons that the Xantphos-R systems are so interesting to study in amine−borane dehydropolymerization is that both cationic and neutral precursors are available with isopropyl or *tert*-butyl groups, e.g., generically **D** and **F**, Scheme 4. While $Rh(\kappa^3\text{-}P,O,P\text{-Xantphos-}^iPr)H$, **11**, can be isolated in good yield, as reported by Esteruelas,[4d] it undergoes a very fast reaction with $1,2\text{-}F_2C_6H_4$ (the current solvent of choice used in our cationic systems) on time of mixing (Scheme 6) to form C−H activated $Rh(\kappa^3\text{-}P,O,P\text{-Xantphos-}^iPr)(2,3\text{-}F_2C_6H_3)$ **12**. A single-crystal X-ray diffraction analysis confirmed the structure. C−H activation of fluoroarenes by **11** has been reported previously with FC_6H_5 and $1,3\text{-}F_2C_6H_4$.[27a] Complex **12** is thus likely the actual precatalyst when using this solvent. In contrast, $Rh(\kappa^3\text{-}P,O,P\text{-Xantphos-}^tBu)H$, **13**,[26b] is more robust and does not react with $1,2\text{-}F_2C_6H_4$. Attempts to prepare $Rh(\kappa^3\text{-}P,O,P\text{-Xantphos-Et})H$ were unsuccessful.

2.3. H/D Exchange Reactions. These observations highlight the steric constraints the P-alkyl groups place on $H_3B{\cdot}NMe_3$ coordination and related processes. As B−H activation at the metal center[1c] is a key step in dehydrogenation we were interested in probing such events, without the complication of subsequent N−H activation, by using $H_3B{\cdot}NMe_3$. Addition of excess D_2 to cationic complexes **5** or **6** resulted in H/D exchange at both the Rh−H and the BH_3 groups (**5**, 25% B−D after 5 min; **6**, 20% B−D after 5 min). Given that H_2 loss from these complexes is not observed, H/D exchange likely operates through a sigma-complex-assisted metathesis (σ-CAM) mechanism[36] (**I**, Scheme 7) in a Rh(III) manifold, similar to $[M(PCy_3)_2(H)_2(H_3B{\cdot}NMe_3)][BAr^F_4]$ (M = Rh, Ir) complexes.[33] H/D exchange also occurs in **10** when exposed to excess $D_3B{\cdot}NMe_3$ (20% RhD_2 after 5 min), showing that the borane must interact with the metal center, albeit at a low equilibrium concentration.

Scheme 6. Neutral Precatalysts

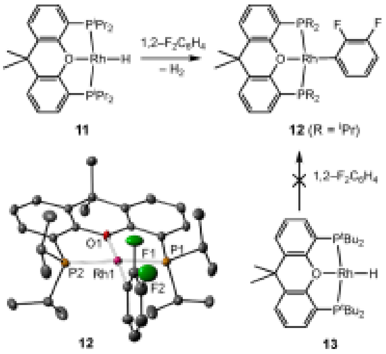

Scheme 7. H/D Exchange in Cationic and Neutral Complexes[a]

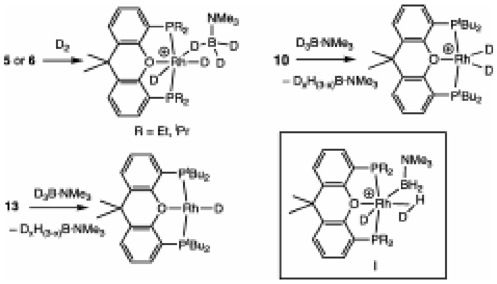

[a] $[BAr^F_4]^-$ anions are not shown.

Although neutral **13** does not form a complex with $H_3B{\cdot}NMe_3$ it does undergo H/D exchange with $D_3B{\cdot}NMe_3$ in $1,2\text{-}F_2C_6H_4$ solution to form the corresponding deuteride (10% after 10 min). Reactivity of **11** with $D_3B{\cdot}NMe_3$ in $1,2\text{-}F_2C_6H_4$ solution is frustrated by the rapid formation of **12**. These observations show that, where measurable, all cationic and neutral complexes undergo reversible B−H activation at the metal center.

2.4. Initial Catalyst Screening. Table 1 summarizes $H_3B{\cdot}NMeH_2$ dehydropolymerization screening experiments and demonstrates the influence of the sterics and charge of the

Table 1. Catalyst Screening for $H_3B{\cdot}NMeH_2$ Dehydropolymerization[a]

catalyst	conversion[b]	time/min[c]	products[d]	isolated yield[e]
5	37%	900	$(H_2BNMeH)_n$ (27%), other (10%)	8%
6	98%	20	$(H_2BNMeH)_n$ (93%), $(HBNMe)_3$ (5%)	63%
10	87%	360	$(H_2BNMeH)_n$ (76%), other (11%)	30%
11	94%	30	$(H_2BNMeH)_n$ (93%), $(HBNMe)_3$ (1%)	65%
13	90%	270	$(H_2BNMeH)_n$ (70%), $(HBNMe)_3$ (11%), other (9%)	20%

[a]Conditions: $[H_3B{\cdot}NMeH_2]$ = 0.446 M; cat. = 0.2 mol %; solvent = 1,2-$F_2C_6H_4$. Flask open to a flow of argon. [b]Conversion of $H_3B{\cdot}NMeH_2$ as measured by ^{11}B NMR spectroscopy. [c]Unoptimized. [d]As determined by ^{11}B NMR spectroscopy of the reaction solution. [e]Isolated by precipitation into hexane.

{Rh(Xantphos-R)} fragment. These experiments were performed under conditions used previously (0.2 mol % catalyst, 0.446 M $H_3B{\cdot}NMeH_2$, system open to a flow of Ar, 1,2-$F_2C_6H_4$ solvent[5b]). Notable is that both cationic (**6**) and neutral (**11**) Xantphos-^{i}Pr catalysts promote high conversions to $(H_2BNMeH)_n$ (greater than 90%) in short reaction times (less than 30 min), as signaled by a distinctive broad resonance observed at ca. δ −5.1 (1,2-$F_2C_6H_4$) in the ^{11}B NMR spectrum.[2d,4a,5b] Only small amounts of *N*-trimethylborazine $(HBNMe)_3$ [δ 33.2, d, *J*(BH) = 132 Hz][11a] were observed. Xantphos-^{t}Bu systems (**10** and **13**, respectively) are slower (hours) and produce more $(HBNMe)_3$/other dehydrocoupling side products and less isolated polymer. At 10 mol % the major product with catalysts **6** and **11** was *N*-trimethylborazine. Changing solvent to THF (which has previously been used as a solvent for **11** in dehydrogenation of $H_3B{\cdot}NH_3$[28]) resulted in low conversions and a slow reaction for cationic catalyst **6** (40% conversion after 3 h). We postulate that this is due to the formation of the cationic THF adduct $[Rh(\kappa^3\text{-}P,O,P\text{-Xantphos-}R)(H)_2(THF)][BAr^F_4]$ in which the THF binds strongly with the Rh center, thus attenuating amine–borane dehydrogenation. Complex **5** (Xantphos-Et) is a very slow catalyst, only converting 27% $H_3B{\cdot}NMeH_2$ to polymer after 15 h. Xantphos-^{i}Pr precatalysts **6** and **11** thus offered the best opportunity to study the kinetics of dehydropolymerization and catalyst control over the resulting polymer using 1,2-$F_2C_6H_4$ solvent. We concentrate on these two systems but return to Xantphos-^{t}Bu and Xantphos-Et to allow for wider comparisons.

2.5. Dehydropolymerization: Molecular Weight Determinations, Entrained Catalyst, and Polymer Growth Kinetics. Off-white polyaminoborane $(H_2BNMeH)_n$ can be isolated in yields of up to 65% (~0.7 g scale) using precatalysts **6** and **11**. The ^{11}B NMR spectra of isolated polymer produced by either catalyst are similar, showing a broad peak, centered around δ −5 (CD_2Cl_2), Figure 3. A small shoulder is also apparent at ca. 2 ppm that may be indicative of a small amount of chain branching (i.e., "BN_3" or "BN_4" in the polymer backbone).[4e,37] A signal to lower field has previously been shown to be particularly distinct in cases where chain branching is proposed.[15a] A small signal at δ −17.6 suggests some entrained $H_3B{\cdot}NMeH_2$, although this might also be masking a broader BH_3 polymer end group signal. The ^1H NMR spectra show environments assigned to NH, NMe, and BH_2 and are very similar for polymer from each catalyst. A small shoulder on the N*Me* signal is observed to low field, but this is poorly resolved. The $^{13}C\{^1H\}$ NMR spectra are also similar for both polymeric materials and show multiple environments assigned to N*Me*. In polymer derived from **6** a sharper signal is observed at δ 36.2, which resolves into two signals for polymer derived from **11** (δ 36.2, 36.1). Much broader, lower field signals are observed for both polymer samples centered at ca. δ 37.0. Very similar spectral data have been observed for *N*-methyl polyaminoborane produced using $Ir(POCOP)(H)_2$[4a] and $(PNHP)Fe(H)(CO)(HBH_3)$,[6] especially the multiple environments in the $^{13}C\{^1H\}$ NMR spectra. The $^{13}C\{^1H\}$ NMR spectrum of, related, polyphosphinoborane $(H_2BP^tBuH)_n$ formed by a thermal dehydropolymerization ($M_n \approx$ 30 000 g mol^{-1}, $Đ \approx 1.8$)[13b] also shows multiple environments for the ^{t}Bu group, not dissimilar to those observed here for the NMe groups, while in the ^{31}P NMR spectra multiple environments are also observed. The latter were interpreted as being due to the tactic environments associated with the polymer and, in particular, specific triads. A mixture of *R*,*R* and *R*,*S* diastereoisomers of the linear triborazane $H_3B\text{-}(NMeHBH_2)_2NMeH_2$ has also been synthesized, although no ^{13}C NMR data were reported.[38] We are reluctant to interpret our current data further with regard to polymer stereochemistry, especially given the possibility for additional chain branching. Nevertheless, taken together, these spectral observations could well be important in future studies of polyaminoborane tacticity.

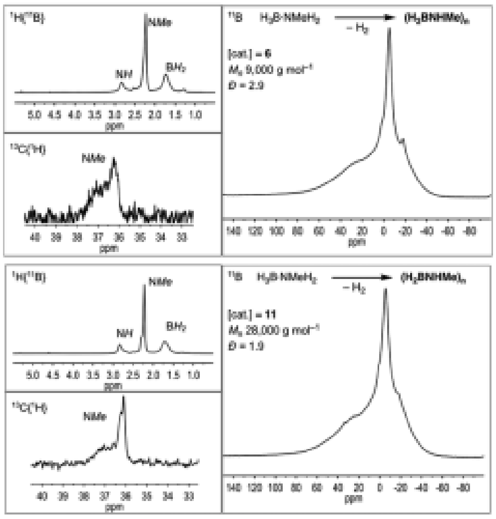

Figure 3. Selected NMR spectra (CD_2Cl_2, 298 K) for isolated polyaminoborane produced by catalyst **6** (top) and catalyst **11** (bottom): 0.2 mol %, 0.446 M $H_3B{\cdot}NMeH_2$. Broad baseline signal observed in the ^{11}B NMR spectra at ca. 20 ppm is due to background from the tube and probe (borosilicate glass).

Analysis by gel permeation chromatography (GPC, polystyrene standards, refractive index (RI) detector) of polymer produced using cationic **6** showed what appeared, at first inspection, to be a bimodal distribution of polymer molecular weights (Figure 4A, solid gray line) in which a broad low-intensity peak characteristic of $(H_2BNMeH)_n$[4a] was augmented

DOI: 10.1021/jacs.7b11975
J. Am. Chem. Soc. 2018, 140, 1481−1495

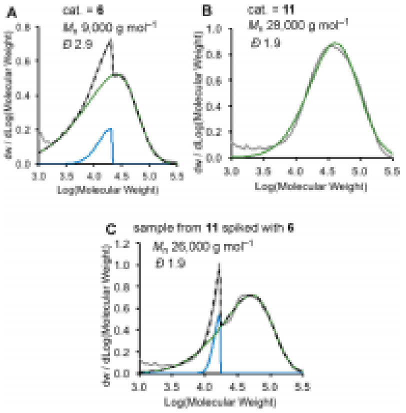

Figure 4. Experimental (gray, solid line), combined fitted (black, dashed line), and individual skewed Gaussian fits (green and blue, solid line) GPC data for polyaminoborane produced using (A) cationic catalyst **6** (0.2 mol %, 0.446 M $H_3B\text{-}NMeH_2$), (B) neutral catalyst **11** (0.2 mol %, 0.446 M $H_3B\text{-}NMeH_2$), and (C) neutral catalyst **11**, spiked post catalysis with 0.2 mol % **6** (conditions as for B).

with a sharper peak that displayed a tail to lower M_n. Significantly, this signal was absent in polymer produced using neutral catalyst **11** (Figure 4B), and we suspected it may be due to $[BAr^F_4]^-$ entrained in the polymer. Even though the catalyst is used in low concentration (0.2 mol %) the $[BAr^F_4]^-$ aryl groups would be expected to be significantly more sensitive to RI detection than polyaminoborane, a technique that has been shown to have a positive correlation to the polarizability of any functional group.[39] ^{19}F NMR spectroscopy of polymer produced using **6** showed a signal at δ −63.2 consistent with $[BAr^F_4]^-$, while for that produced using **11** this was absent. In the ^1H NMR spectrum of polymer derived from catalyst **6** signals assigned to $C_6H_3(CF_3)_2$ were observed, and when integrated with respect to the BN*Me* signal a loading of 0.18 mol % was estimated. ICP-MS analysis for Rh content from these polymer samples indicated a loading of ~450 ppm (i.e., 0.045 mol %), suggesting that the anion and cation are both entrained, albeit to differing extents. Neutral catalyst **11** showed higher levels of Rh incorporation, 1200 ppm (0.12 mol %).[40] Final evidence that this extra GPC peak comes from $[BAr^F_4]^-$ came from spiking a sample of polymer produced using catalyst **11** with 0.2 mol % **6**, which showed the characteristic skewed GPC signal (Figure 4C). These signals for $[BAr^F_4]^-$ were not reduced by reprecipitation of the polymer, suggesting that the $[BAr^F_4]^-$ anion may be associated with the polymer.[41] A similar entrainment of catalyst in phosphine−borane dehydropolymerization has recently been reported.[13c] The GPC traces were deconvoluted[42] using a skewed Gaussian bimodal distribution using a standalone program. These gave acceptable fits to the data.[43] Importantly, using these fits the molecular weight and dispersity data for the spiked samples from neutral catalyst **11** recover the unspiked data well, giving confidence in the approach.

These data show a significant difference between the polymer produced with the two catalysts under these conditions, even though the NMR data are similar for both. Cationic **6** produces polyaminoborane of low molecular weight and high dispersity (e.g., M_n = 9000 g mol^{-1}, $Đ$ = 2.9), while neutral **11** produces higher molecular weight polymer with a more uniform distribution (e.g., M_n = 28 000 g mol^{-1}, $Đ$ = 1.9). The effect of time (i.e., conversion), catalyst loading, and catalyst identity was probed in more detail using raw GPC data for **11** and modeled GPC data for **6**, as shown in Figure 5 and Table 2.

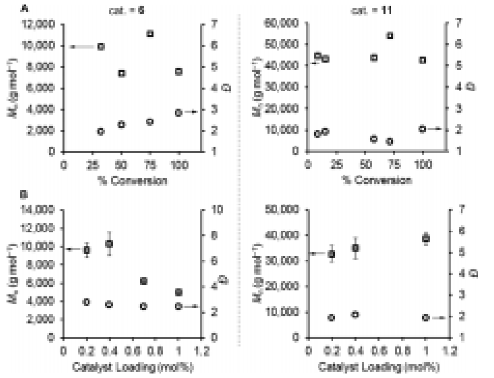

Figure 5. $(H_2BNMeH)_n$ polymer growth kinetics using catalysts **6** and **11**. M_n and dispersity ($Đ$) data derived from skewed Gaussian fits for **6**. Measured from a system open to Ar flow. $[H_3B\text{-}NMeH_2]$ = 0.446 M. (Top) M_n (g mol^{-1}) versus conversion, conversion measured by ^{11}B NMR spectroscopy, samples quenched by addition of excess (5 equiv) PPh_3. (Bottom) M_n (g mol^{-1}) versus [cat.] at 100% conversion. Errors determined by repeat polymerizations.

For cationic catalyst **6** a plot of M_n versus conversion of $H_3B\text{-}NMeH_2$ to polyaminoborane (as measured by ^{11}B NMR spectroscopy for individual samples quenched at the appropriate point by addition of excess PPh_3[44]) revealed that at low conversion polymer of appreciable molecular weight was being formed (M_n = 10 000 g mol^{-1}, $Đ$ = 2.0), and this did not change significantly over the course of dehydropolymerization, Figure 5A. At these low conversions $H_3B\text{-}NMeH_2$ is the dominant species by ^{11}B NMR spectroscopy, while the signal at ca. δ −5 assigned to polyaminoborane is broad and gives no indication that short-chain oligomers (e.g., $H_3B\text{-}NMeHBH_2\text{-}NMeH_2$) are being formed, as these would be expected to show more resolved B−H coupling.[5b,12a]

These data are broadly consistent with controlled[19] chain-growth polymer propagation in which a reactive aminoborane monomer undergoes rapid head-to-tail polymerization to give $(H_2BNMeH)_n$,[45] followed by termination. If this occurred via a coordination−dehydrogenation−insertion-type mechanism at a single metal center, reducing the catalyst loading would be expected to increase the degree of polymerization, as noted for dehydropolymerizations of $H_3B\text{-}NMeH_2$ using catalyst **1**,[5b] and $H_3B\text{-}PPhH_2$ using $Fe(\eta^5\text{-}C_5H_5)(CO)_2(OTf)$.[13d] Figure 5B shows that increasing the catalyst loading from 0.2 to 1 mol % for **6** results in a decrease in polymer molecular weight: M_n = 5000 g mol^{-1} ($Đ$ = 2.4). Within the confidence limits of polyaminoborane analysis, exacerbated by the low molecular weight polymer tailing into the intrinsic system peaks associated with GPC analysis, we consider this trend to be weak at best, and we suggest that this data does not *strongly* support a coordination−insertion mechanism. As we discuss (section 2.6), we cannot discount that this trend also reflects

Table 2. Representative Polymer Molecular Weights (g mol^{-1}) and Dispersity Data

entry	catalyst	[H_3B·$NMeH_2$], M	[cat.], M (mol %)	M_n/g mol^{-1}	Đ
1	**6**[a]	0.446	8.92×10^{-4} (0.2)	9500	2.8
2	**6**[a]	0.446	4.46×10^{-3} (1.0)	5000	2.4
3	**6**[b]	0.446	8.92×10^{-4} (0.2)	8500	2.7
4	**6**[a]	0.223	4.46×10^{-4} (0.2)	13 000	2.5
5	**6**[a]	0.1115	2.23×10^{-4} (0.2)	13 500	2.5
6	**6**[a]	0.1115	1.115×10^{-4} (1.0)	5000	2.4
7	**6**[b]	0.223	4.46×10^{-4} (0.2)	10 000	2.2
8	**6**[d]	0.223	4.46×10^{-4} (0.2)	9000	2.5
9	**6**[c]	0.223	4.46×10^{-4} (0.2)	12 000	2.4
10	**11**[a]	0.446	8.92×10^{-4} (0.2)	39 000	2.1
11	**11**[b]	0.446	8.92×10^{-4} (0.2)	33 000	2.1
12	**11**[b]	0.446	4.46×10^{-3} (1.0)	39 000	1.9
13	**11**[d]	0.446	8.92×10^{-4} (0.2)	28 000	2.1
14	**11**[c]	0.446	8.92×10^{-4} (0.2)	33 000	1.8
15	**11**[b]	0.223	4.46×10^{-4} (0.2)	17 000	2.0
16	**6**[a]	0.446 × 3	8.92×10^{-4} (0.2)	15 000	1.9
17	**11**[a]	0.446 × 3	8.92×10^{-4} (0.2)	26 000	2.3

[a] Under H_2 evolution measurement conditions connected to a gas buret. [b] Under a flow of Ar. [c] Under a flow of Ar in the presence of 2.7 equiv (relative to H_3B·$NMeH_2$) of cyclohexene. [d] A closed system allowing for H_2 build−up.

trace impurities in the solvent that might disproportionally modify catalyst concentration at low loadings. Catalyst **11** shows an opposite but still weak relationship between catalyst loading and M_n in which increased loadings lead to slightly increased degrees of polymerization: 0.2 mol % (M_n = 33 000 g mol^{-1}, Đ = 1.9) versus 1 mol % loadings (M_n = 39 000 g mol^{-1}, Đ = 1.9). An increase in the molecular weight of isolated polymer on increasing catalyst loading has been noted for Ir(POCOP)$(H)_2$, **A**,[4a] while for catalyst **B** changes in catalyst loading can induce small molecular weight changes in either direction depending on the solvent used.[6] For catalyst **11** a degree of polymerization (i.e., M_n) versus conversion plot also indicates a chain-growth-type process is in operation (Figure 5A).

Addition of two successive batches of H_3B·$NMeH_2$ to catalysis solutions post dehydropolymerization (0.2 mol % **6** or **11**, 0.446 M [H_3B·$NMeH_2$]) resulted in full consumption of H_3B·$NMeH_2$ (TON = 1500), but no significant change in the molecular weight of isolated polymer (**6**, M_n = 15 000 g mol^{-1}, Đ = 1.9; **11**, M_n = 26 000 g mol^{-1}, Đ = 2.3). This indicates that the systems are not living[19,46] but also that species present at the end of catalysis are still active for dehydropolymerization and can be recharged (section 2.7.1).

Table 2 additionally provides representative results from a study of concentration, exogenous cyclohexene and hydrogen as a potential modifier to control polymer molecular weight. For catalyst **6** concentration has no significant effect on molecular weight within the confidence limits of polymer analysis (compare entries 3 and 7). For catalyst **11** a reduction in concentration to 0.223 M results in a decrease in molecular weight, M_n = 17 000 g mol^{-1} (Đ = 1.6), entries 11 and 15. H_2 does not act to significantly modify the chain length for either catalyst when allowed to build up in a closed system or under the conditions of measuring H_2 evolution using a gas buret when compared with a system open to a flow of argon. Addition of 2.7 equiv of cyclohexene (i.e., 270 mol %) to either catalyst (**6** or **11**) at 0.2 mol % did not change the degree of polymerization significantly nor resulted in the observation of $Cy_2B{=}NMeH$ [$\delta(^{11}B)$ 44.9, br (THF)],[17a] the product of hydroboration that potentially signals free $H_2B{=}NMeH$.[1e] At 10 mol %, where $(HBNMe)_3$ becomes the major product (vide supra), trace $Cy_2B{=}NMeH$ is observed using catalyst **6** [~1%, $\delta(^{11}B)$ 45.9, 1,2-$F_2C_6H_4$] (Scheme 8). For catalyst **11** under the same conditions no hydroboration product is observed. These data suggest that any $H_2B{=}NMeH$ formed is consumed significantly faster in chain propagation/borazine formation rather than hydroboration, as has been commented upon previously.[1d,4e,47] Hydroboration of cyclohexene by transient $H_2B{=}NMeH$ has been reported in metal-free polymerizations[15] and in slower metal-promoted dehydropolymerizations.[6] We have not observed $H_2B{=}NMeH$ in any in situ NMR experiments [lit. $\delta(^{11}B)$ 37.1, t, J(BH) = 130 (Et_2O, −10 °C)].[15]

Scheme 8. Trapping Experiments

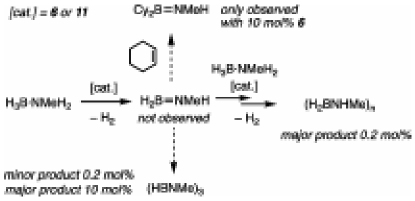

The use of H_2 as a chain-termination agent is well established in olefin polymerization and likely operates through sigma-bond metathesis of H_2 with the [M]−CH_2−R growing polymer chain to form a metal hydride and free polymer.[14,48] This lack of sensitivity to H_2 for catalysts **6** and **11** is in contrast to catalyst **1**, which shows a significant attenuation of molecular weight with H_2, but is similar to **A**[4a] and **B**[6] where no significant effects were reported. Catalyst **1** was suggested to operate via a coordination−insertion mechanism in which a nascent amino-borane, formed by dehydrogenation, inserts into a polymer chain that is propagating from the metal center via a covalent Rh−$NHMeBH_2R$ (or Rh−BH_2NMeHR) bond and is thus susceptible to hydrogenolysis, Scheme 3. The lack of H_2 sensitivity of **6** and **11** when combined with the relative insensitivity of polymer molecular weight to catalyst loading

DOI: 10.1021/jacs.7b11975
J. Am. Chem. Soc. 2018, 140, 1481−1495

suggests a polymerization process where polymer propagation follows a classical chain-growth profile rather than a coordination–insertion mechanism. An alternative mechanism is one of step growth which, characteristically, only shows higher molecular weight polymer being formed at very high conversions.[45] Such behavior has been suggested for the dehydropolymerization of $H_3B{\cdot}PRH_2$ (R = Ph) using Rh-based catalysts[13c,49] and can be explained by a facile reversible chain transfer between bound growing oligomer chains and $H_3B{\cdot}PRH_2$. Similar chain-transfer behavior has been noted for very slow amine–borane dehydrocoupling using the $[Ir(PCy_3)_2(H)_2(H_2)_2][BAr^F_4]$ catalyst.[11c,12a] We discount that such a mechanism is operating here, as at early conversions for both catalysts **6** and **11** $H_3B{\cdot}NMeH_2$ is still the major component, no short chain oligomers are observed in significant quantities (e.g., $H_3B{\cdot}NMeHBH_2{\cdot}NMeH_2$[12a]), and the molecular weight of isolated polymer remains approximately constant throughout the reaction.

2.6. H_2 Evolution Studies and the Kinetic Model. By following the evolution of H_2 during dehydropolymerization, the dehydrogenation of $H_3B{\cdot}NMeH_2$ to form transient aminoborane $H_2B{=}NMeH$[15a] can be indirectly interrogated. For catalysts **6** and **11** close to 1 equiv of H_2 is released during dehydropolymerization, consistent with the small, less than 10%, amount of $(HBNMe)_3$ formed. This means that the H_2 evolved can be used as an effective proxy for $H_2B{=}NMeH$ generation, which subsequently undergoes fast polymerization. Figure 6A shows a number of H_2 evolution experiments using catalyst **6** in which the concentration of both $H_3B{\cdot}NMeH_2$ and catalyst is varied. For all regimes a small induction period was observed (20–90 s, not shown; Supporting Information) that is variable between batches of 1,2-$F_2C_6H_4$ solvent but consistent within each batch for repeat runs, as are the temporal profiles for H_2 evolution. We, and others, recently commented upon the presence of trace impurities in fluorinated arene solvents,[50] and a GC-MS analysis of 1,2-$F_2C_6H_4$ stirred over Al_2O_3 for 1 h and vacuum distilled from CaH_2 showed trace quantities of $FClC_6H_4$ and $F(OH)C_6H_4$. We suggest that trace impurities, such as these, act to modify a small portion of catalyst in both the induction period and during productive catalysis. For this reason the data shown in Figure 6A come from using the same batch of 1,2-$F_2C_6H_4$. Notably, isolated polymer does not vary in molecular weight significantly when using different solvent batches for either catalyst. We discount the formation of a heterogeneous catalyst as the active species, as addition of excess Hg or substoichiometric PPh_3 (0.2 equiv) once turnover was established did not act to significantly modify either cationic or neutral catalysts (Figure 6B and 6C for catalyst **6** and **11**, respectively).[7b,51] H_2 release using 0.2 mol % **6** at 0.446 M $H_3B{\cdot}NMeH_2$ is fast (TOF ≈ 1700 h^{-1}). This is considerably faster than for **1** (TOF ≈ 250 h^{-1}) but similar to **A** (TOF ≈ 2400 h^{-1}, 0.5 M $H_3B{\cdot}NMeH_2$, 0.1 mol %)[4a] and comparable with the fastest catalysts reported for $H_3B{\cdot}NH_3$ or $H_3B{\cdot}NMe_2H$ dehydrocoupling.[5a,28,52]

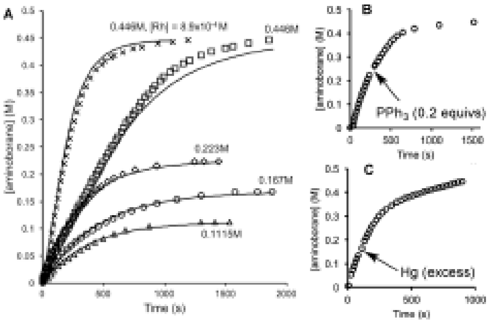

Figure 6. (A) Temporal data plots for polyaminoborane formation (as measured by H_2 evolution) and simulated fits (lines) for catalyst **6** (4.45×10^{-4} M except where stated) and $H_3B{\cdot}NMeH_2$ (Δ = 0.1115 M, ○ = 0.167 M, ◊ = 0.223 M, and □ = 0.446 M). × = **6** (8.9×10^{-4} M), $H_3B{\cdot}NMeH_2$ (0.446 M). Variable induction periods of between 20 and 90 s has been removed from the data. (B) Effect of substoichiometric PPh_3 (0.2 equiv) added at t = 250 s: [**6**] = 8.9×10^{-4} M, [$H_3B{\cdot}NMeH_2$] = 0.446 M. Note the induction period is shown. (C) Effect of excess Hg (1500 equiv) at t = 120 s: [**11**] = 8.9×10^{-4} M, [$H_3B{\cdot}NMeH_2$] = 0.446 M.

These data for catalyst **6** were simulated under a variety of scenarios. The temporal profile observed, especially at the highest concentration of $H_3B{\cdot}NMeH_2$ = 0.446 M, suggests saturation kinetics are operating, i.e., initial zero order in substrate, as we modeled previously for the dehydrocoupling of amine–boranes using catalyst **1**.[5b] However, analysis of the data did not provide a convincing solution for quasi-irreversible amine–borane coordination to the metal center. Instead, a simple first-order model in substrate that took into account the limiting solubility of $H_3B{\cdot}NMeH_2$ in 1,2-$F_2C_6H_4$ solvent (0.22 M) accounted best for all of the observed data. Experimentally this is confirmed by a visual inspection of the catalysis reaction and reflects the relatively poor solubility of $H_3B{\cdot}NMeH_2$ in 1,2-$F_2C_6H_4$. With this model in hand, overall second-order rate constants were simulated (as shown in Figure 6A) for which an averaged k = 5.9 ± 0.5 M^{-1} s^{-1} was obtained. By using $D_3B{\cdot}NMeH_2$ at 0.1115 M ([**6**] = 2.23×10^{-4} M), i.e., below the solubility limit, a KIE of 0.8 ± 0.4 for BH/BD substitution is measured, while $H_3B{\cdot}NMeD_2$ results in a KIE of 4.6 ± 0.2 for NH/ND substitution. The large KIE associated with ND suggests that N–H cleavage is involved in the turnover-limiting step. Similar KIEs have been reported for dehydrocoupling of $H_3B{\cdot}NMe_2H$ using $[TiCp_2]$ (3.6 ± 0.3)[53] or $Rh(PCy_3)_2(H)_2Cl$ (5.3 ± 1.3)[54] catalysts. For catalyst **1**, in which a coordination/dehydrogenation/insertion mechanism is proposed, the KIE associated with NH activation in $H_3B{\cdot}NMe_2H$ is smaller (2.1 ± 0.2).[5b] The small KIE associated with B–H activation in the system here may indicate an equilibrium isotope effect that arises from reversible B–H activation at the metal center,[55] occurring prior to the turnover-limiting step (section 2.3); however, within error it may also be close to unity, meaning that we are reluctant to overinterpret this value. Although the two different KIEs argue against a synchronous concerted BH/NH activation,[9c,56] they could reflect a rather asynchronous transition state in which BH activation occurs much earlier than NH activation.[17b]

The equivalent analysis of H_2 release and resulting dehydrogenation kinetics for neutral catalyst **11** is additionally complicated by the fact that, due to the sensitivity of this catalyst, even repeat runs using the same batch of solvent differed significantly (initial rates varied by 25% at 0.446 M $H_3B{\cdot}NMeH_2$ and 0.2 mol % **11**). We suggest that this is due to irreversible catalyst decomposition from trace impurities entrained in reaction vessels (O_2) even though substantial precautions for handling air-sensitive materials were taken. This means that detailed studies of catalyst loading or KIE

DOI: 10.1021/jacs.7b11975
J. Am. Chem. Soc. 2018, 140, 1481–1495

experiments were not appropriate. Nevertheless, all temporal plots of H_2 release showed a similar profile to catalyst **6**: essentially close to 1 equiv of H_2 formed and an initial pseudo-zero-order regime, although, interestingly, catalyst **11** does not display a measurable induction period. Simulating a representative example for catalyst **11** (TOF $\approx$ 1500 h^{-1}) using the model developed for catalyst **6** gave a good fit and a second-order rate constant $k = 4.1\ M^{-1}\ s^{-1}$, similar to **6**.

Thus, even though both catalyst systems operate at a similar overall rate, likely by a similar chain-growth mechanism (section 2.5), and are homogeneous, they promote very different degrees of polymerization: with neutral catalyst **11** producing significantly longer polymer than **6** (Table 2 and Figure 5).

2.7. Catalyst Speciation during and Post Catalysis.

2.7.1. [Rh(κ³-P,O,P-Xantphos-ⁱPr)(H)₂(η¹-H₃B-NMe₃)][BArᶠ₄], **6.** As dehydropolymerization is performed at low catalyst loadings, directly interrogating reaction mixtures to determine the fate of the catalyst by NMR spectroscopic techniques is difficult. However, at the end of catalysis (0.4 mol %, 6.6 mg of **6**, 20 min) concentration of the reaction mixture allowed for analysis by $^{31}P\{^1H\}$ NMR spectroscopy. Although a weak spectrum resulted, a doublet of doublets at δ 47.5 [J = 174, 6 Hz] could be resolved. Repeating catalysis at 10 mol % (e.g., 20 mg of **6**) resulted in the same major organometallic complex (ca. 85%), but now two minor components (ca. 15% combined) could also be observed. The major species was independently prepared by addition of $[NBu_4][BH_4]$ to complex **6** (as its $[BAr^{Cl}_4]^-$ salt,[57] $Ar^{Cl} = 3,5\text{-}Cl_2C_6H_3$), which allowed for NMR data and a single-crystal X-ray structure to be obtained, although the single crystals were contaminated with $[NBu_4][BAr^{Cl}_4]$ as a coproduct in the bulk. These data showed the structure to be $[\{Rh(\kappa^3\text{-}P,O,P\text{-}Xantphos\text{-}{}^iPr)\}_2B][BAr^{Cl}_4]$, **14-[BAr$^{Cl}_4$]**, Figure 7.

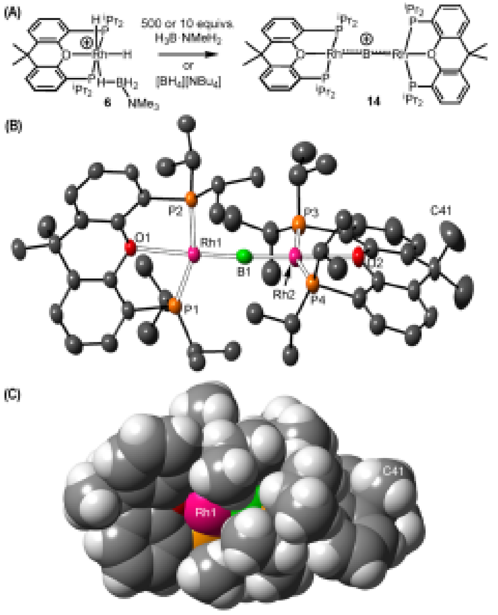

Figure 7. (A) Synthesis of complex **14-[BAr$^{Cl}_4$]**; $[BAr^{Cl}_4]^-$ anion omitted. (B) Molecular structure of the cationic portion of **14-[BAr$^{Cl}_4$]**; displacement ellipsoids are shown at the 50% probability level; H atoms and $[BAr^{Cl}_4]^-$ anion omitted. Selected bond distances (Angstroms) and angles (degrees): Rh1−B1, 1.880(8); Rh2−B1, 1.862(8); Rh1−O1, 2.343(2); Rh2−O2, 2.343(4); Rh1−B1−Rh2, 177.4(5); angle between P1/Rh1/P2/O1 and P3/Ph2/P4/O2 90.2. (C) Space filling diagram (van der Waals radii).

Due to relatively poor crystal quality and the reduction in high-angle data, the final refinement was of moderate quality (R = 7.9%), although the data collected proved adequate for confirming connectivity and bond metrics. Complex **14-[BAr$^{Cl}_4$]** has a Rh_2 dimetallic unit that is spanned by a single B atom [Rh−B−Rh 177.4(5)°]. The Xantphos-ⁱPr ligands adopt a *mer*-κ³-P,O,P geometry that places the central oxygen atom trans to the boron. As discussed later, the lack of high-field signals in the ^1H NMR spectrum, very low−field chemical shift of the ^{11}B resonance, and mass-spectral data all indicate that there are no hydrides associated with the complex. The Rh−B distances are both short [1.880(8) and 1.862(8) Å] and comparable to closely related iron[58] and ruthenium[59] dimetalloborylenes $[\{(\eta^5\text{-}C_5H_4R)(CO)_2M\}_2B]^+$ [M = Fe, R= Me; M = Ru, R = H; e.g., Ru−B 1.931(3)/1.963(3) Å; Ru−B−Ru 175.5(2)°]. The Rh−B distances are shorter than that measured in Rh(κ³-P,O,P-Xantphos-ⁱPr)(Bpin) [1.981(4) Å; pin = pinacol],[27a] which has a formal covalent Rh−B single bond, are longer than those in monometallic complexes with M=B bonds, e.g., $Ru(PCy_3)_2({=}BMes)HCl$[15a,20] [1.780(4) Å, Mes = mesityl],[60] but are similar to group 9 aminoborylenes, e.g., $[mer\text{-}Ir(PMe_3)_3HCl({=}BN^iPr_2)][B(C_6F_5)_4]$ [1.897(5) Å],[61] in which electronic unsaturation at boron can be attenuated by conjugation with the nitrogen lone pair. These comparisons suggest some partial double-bond character to the Rh−B bonding in **14**. Although the presence of dπ−pπ[58] bonding between the Rh and the B may also be suggested by the orientation of the Xantphos-ⁱPr ligands (angle between $Rh/P_2/O$ planes = 90.2°), the steric requirements of interdigitation of the ⁱPr groups likely dominate this geometry (Figure 7C).[62] The Rh−O distances [2.343(4) Å] are longer than those observed in **6** [2.192(3) Å] and Rh(κ³-P,O,P-Xantphos-ⁱPr)-(Bpin)[27a] [2.268(2) Å], suggesting that the boron atom exerts a significant trans influence.

The ^1H (and $^1H\{^{11}B\}$) NMR spectra of **14** (for both anions) showed an absence of hydride signals (between δ 0 and δ −50), while in the ^{11}B NMR spectrum a very broad resonance at δ 135 is observed, which is in the region associated with complexes in which there is a significant M···B multiple-bonding component,[63] and is considerably downfield shifted from the regions associated with amine−boranes[64] or amino-boranes[11b] interacting with metal centers. Electrospray ionization mass spectroscopy (ESI-MS) showed the dominant cationic species to be singly charged with an isotope pattern that matched very well with a formulation of $[\{Rh(\kappa^3\text{-}P,O,P\text{-}Xantphos\text{-}{}^iPr)\}_2B]^+$ (m/z = 1101.36, calculated 1101.33). The doublet of doublets observed in the $^{31}P\{^1H\}$ NMR spectrum can be rationalized by a one-bond and a three-bond $^{103}Rh-^{31}P$ coupling (i.e., an $A_2XX'A'_2$ system), the size of the former [174 Hz] being consistent with a Rh(I) center, while smaller couplings to distal Rh centers in dimeric systems have been noted before, as observed in **14**.[65] Complex **14** is particularly sensitive in solution and undergoes decomposition to unidentified species.

Complex **14** can be described by three valence extremes (Scheme 9): (a) a dimetalloborylene in which a formally

DOI: 10.1021/jacs.7b11975
J. Am. Chem. Soc. 2018, 140, 1481−1495

Scheme 9. Representation of Possible Bonding Schemes for Complex 14[a]

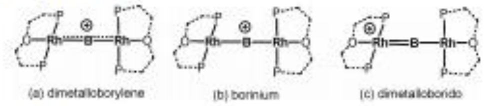

[a]Xantphos-^{i}Pr truncated.

positively charged boron engages in both σ- and π-bonding with two Rh(I) centers, (b) a cationic borinium with no multiple bonding, and (c) a dimetalloboride with a Rh(III)=B−Rh(I) core.[65] We discount (c) due to the symmetric Rh−B−Rh motif observed and NMR data that indicate equivalent Rh(I) centers and have turned to DFT calculations to discriminate between (a) and (b).[66]

The optimized structure of complex **14** showed excellent agreement with the experimentally derived metrics with computed (average) Rh−B and Rh−O distances of 1.89 and 2.37 Å, respectively. An NBO calculation on **14** provides a Lewis structure in which the B $2p_x$ and $2p_y$ appear as lone vacant (LV) orbitals with significant initial populations of ca. 0.35 (the *z* direction being coincident with the Rh−B−Rh axis). Second-order perturbation analysis indicates significant additional π-donation from Rh lone pair d orbitals into both B $2p_x$ and $2p_y$ ($\Delta E^{(2)}$ = 15.1 and 12.9 kcal mol^{-1}, respectively). A degree of multiple-bond character is also suggested by a computed Wiberg bond index of 1.11, while the computed NBO charge on B is +0.45. QTAIM bond critical point (BCP) metrics associated with the Rh−B bond paths indicate a covalent interaction with a BCP electron density, $\rho(r)$, of 0.15 au, a negative value of the Laplacian, $\nabla^2\rho(r) = -0.15$ au, and a total energy density, $H(r)$, of −0.11 au. These Rh−B BCPs also exhibit a low ellipticity (ε = 0.03), suggesting a near-spherical electron distribution at the BCP. Given the other computed evidence for a degree of multiple Rh−B bonding we interpret this result in terms of there being similar contributions to Rh−B π-bonding in both the *xz* and the *yz* planes. This multiple bonding is most readily seen in the delocalized Kohn−Sham orbital HOMO-8 (Figure 8), and a similar, orthogonal contribution is also apparent in HOMO-5 (see Figure S29). Taken together, the body of computed evidence supports formulation (a) in Scheme 9 with species **14** best described as a dimetalloborylene.

Having established that complex **14** is generated as the major organometallic species at the end of catalysis, its formation and onward reactivity were investigated as well as the identity of the other minor components observed. By following reaction progress in situ (10 mol %), the two minor components observed at the end of catalysis are shown to be initially dominant and reduce in concentration over 20 min to afford **14** as the major species. These two new species were identified spectroscopically as [Rh(κ^3-P,O,P-Xantphos-^{i}Pr)(H)$_2$(η^1-H$_3$B·NMeH$_2$)][BAr$^F_4$], **15**, and the bridging borohydride complex [{Rh(κ^3-P,O,P-Xantphos-^{i}Pr)(H)$_2$}$_2$(H$_4$B)][BAr$^F_4$], **16**. Complex **15** can be independently synthesized from **7**/Na[BAr$^F_4$]/H$_3$B·NMeH$_2$ (Supporting Information), and the NMR spectroscopic data are similar to, but distinct from, **6**.[67] Complex **15** is relatively stable in solution, but addition of 10 equiv of H$_3$B·NMeH$_2$ results in the observation of **16** and ultimately **14**. The promoting effect of additional amine−boranes toward dehydrocoupling has been noted previously.[11c,18c,d] For complex **16** a relative integral 2 H resonance at δ −2.77 is assigned to a bridging BH$_4$ group that is undergoing rapid exchange between terminal B−H and B−H···Rh, while two relative integral 1 H hydride resonances at δ −16.07 and δ −20.41, which are mutually coupled, are assigned to terminal Rh−H. The ^{31}P{^{1}H} NMR spectrum shows an environment at δ 67.2 [*J*(RhP) = 111 Hz], indicating a Rh(III) center. In the ^{11}B NMR spectrum a distinct but broad signal at δ −37.5 is observed in the region associated with a borohydride ligand. The salient NMR data for **16** are similar to those reported for [{(^{i}PrPNP)FeH(CO)}$_2$(μ^2,η^1:η^1-H$_2$BH$_2$)][BPh$_4$].[68] Complex **16** can be directly synthesized by addition of 0.5 equiv of [NBu$_4$][BH$_4$] or ~1 equiv of BH$_3$·THF to **6**. When prepared directly complex **16** evolves rapidly to give **14**, so it is never observed in pure form. These observations suggest a reaction manifold **6** → **15** → **16** → **14** (Scheme 10).

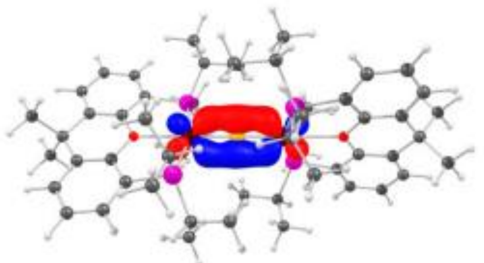

Figure 8. Kohn−Sham orbital (HOMO-8) exhibiting Rh−B π bonding in **14**.

Scheme 10. Formation of Complexes 16 and 14[a]

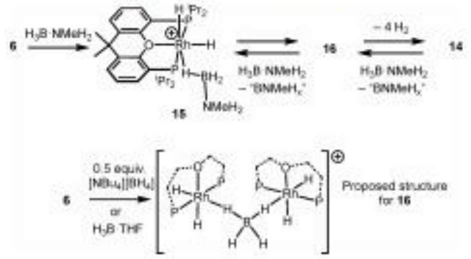

[a]Xantphos-^{i}Pr ligand shown in truncated form. [BAr$^F_4$]$^-$ anions are not shown.

Guided by previous reports of hydride transfer at cationic metal centers[22,69] and B−N bond cleavage,[4f,9c,54,70] we suggest a mechanism of formation of **16** from **6** under conditions of excess H$_3$B·NMeH$_2$, Scheme 11. This involves coproduction of

Scheme 11. Suggested Mechanism for the Formation of 16[a]

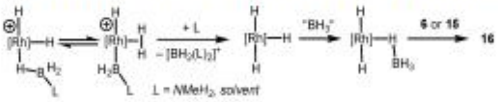

[a]Xantphos ligand and [BAr$^F_4$]$^-$ anions not shown.

a boronium cation, $[BH_2(NMeH_2)(L)]^+$ (L = $NMeH_2$ or solvent), from attack of base-stabilized boryl by, e.g., $NMeH_2$ (formed by B N bond cleavage). The resulting neutral Rh hydride is trapped by BH_3,[4f,70a] and relatively fast addition of $[Rh(\kappa^3\text{-P,O,P-Xantphos-}^{i}Pr)(H)_2]^+$ forms **16**. The formation of **16** from **6**/BH_3·THF would follow a similar route. Consistent with boronium formation a triplet at δ −8.9 [J = 108 Hz] is observed in the ^{11}B NMR spectrum (lit. δ −8.7, br, $J \approx 90$ Hz, $[BH_2(NMeH_2)_2][SC_6F_5]$[71]) when excess $H_3B\text{-}NMeH_2$ is added to, in situ formed, **15**. The subsequent formation of **14** from **16** involves the facile loss of 4 equiv of H_2 through a currently unresolved mechanism. Such an H_2 loss is well established in metalloborane chemistry.[11h,61,72]

Complex **14** forms at the end of catalysis, and catalysis restarts on addition of more substrate (section 2.5). Consistent with this, use of **14-[BAr$^{Cl}_4$]** as a catalyst (0.2 mol % Rh) afforded polymeric material (M_n = 14 000 g mol^{-1}, $Đ$ = 2.7) similar to that starting from **6**. Addition of 10 equiv of $H_3B\text{-}NMeH_2$ to **14-[BAr$^{Cl}_4$]** showed the immediate generation of a mixture of **15** and **16**, alongside $(HBNMe)_3$ and $[BH_2(NMeH_2)_2]^+$. Thus, although we cannot rule out that **14** is the actual catalyst, its temporal and reactivity profiles suggest that it is more likely to play a dormant role in the catalytic cycle, with **15** or **16** observed as resting states.

2.7.2. Rh(κ^3-P,O,P-Xantphos-^{i}Pr)H, ***11***. Although complex **12** forms on time of mixing in 1,2-$F_2C_6H_4$ with **11**, reaction with $H_3B{\cdot}NMeH_2$ (5 equiv) showed the rapid formation of the tentatively assigned pentahydride complex Rh(Xantphos-^{i}Pr)H_5 [$\delta(^{31}P)$ 87.3 (v br), 45.7 (v br), $\delta(^{1}H)$ −11.6 (v br), lit. (PhMe-d_8) ca. −13 (v br)], previously reported by Esteruelas by addition of H_2 to **11**,[28] and complete consumption of the amine−borane to form $(H_2BNMeH)_n$, $(HBNMe)_3$, and $(H_2BNMeH)_3$. No $[BH_2(NMeH_2)_2]^+$ was observed. At the end of catalysis these hydride-containing species remain active for dehydropolymerization (M_n = 26 000 g mol^{-1}, $Đ$ = 2.3).

2.7.3. [Rh(κ^3-P,O,P-Xantphos-Et)(H)$_2$(η^1-H$_3$B-NMe$_3$)][BAr$^F_4$], ***5***. Complex **5** is a very poor catalyst for dehydropolymerization (section 2.4). Addition of 2 equiv of $H_3B{\cdot}NMeH_2$ to **5** showed the formation of a new species assigned using NMR spectroscopy and ESI-MS as the monocationic-bridged aminoborane complex $[\{Rh(\kappa^3\text{-P,O,P-Xantphos-Et})\}_2(\mu\text{-}H)(\mu\text{-}H_2BNMeH)][BAr^F_4]$ **17** (Scheme 12). Complex **17** becomes the dominant species in solution after 30 min, accompanied by **5** in a 7:3 ratio, and was identified by comparison with NMR data of related complexes $[\{Rh(^{i}Pr_2P(CH_2)_3P^{i}Pr_2)\}_2(\mu\text{-}H)(\mu\text{-}H_2BNH_2)][BAr^F_4]$[5d] and $[\{Rh(\mu\text{-}Cy_2PCH_2PCy_2)H\}_2(\mu\text{-}H)(\mu\text{-}BNMe_2)][Al\{OC(CF_3)_3\}_4]$.[50a] In particular, the ^{11}B NMR spectrum contains a broad signal at δ 61.0, while in the ^{1}H NMR spectrum three broad hydride resonances at δ −5.82 (1 H, RhHB), −9.41 (1 H, RhHB), and −11.16 (1 H, RhHRh) are observed, assigned on the basis of $^{1}H\{^{11}B\}/^{1}H\{^{31}P\}$ decoupling experiments. The mechanism for formation of dimers such as **17** has been established and pivots around hydride transfer from a B−H activated amine−borane to form a boronium cation, e.g., $[BH_2(NMeH_2)(L)]^+$ (L = $NMeH_2$ or solvent), and a transient dimeric neutral hydride.[5d,22,69] Protonation of such a dimer by 0.5 equiv of the boronium leads to the observed product and loss of H_2. Consistent with this mechanism, a short-lived complex assigned to $[Rh(\kappa^3\text{-P,O,P-Xantphos-Et})(H)_2(\eta^1\text{-}H_3BNMeH_2)][BAr^F_4]$ is observed at the early stages of the reaction by ^{1}H and $^{31}P\{^{1}H\}$ NMR spectroscopy. These observations further underscore that initial hydride transfer at a cationic coordinated amine−borane complex is occurring. The formation of **17** is, presumably, driven by the ability for Xantphos-Et to adopt a *cis*-κ^2-P,P geometry on a Rh(I) center.

Scheme 12. Formation of Dimeric Complex 17[a]

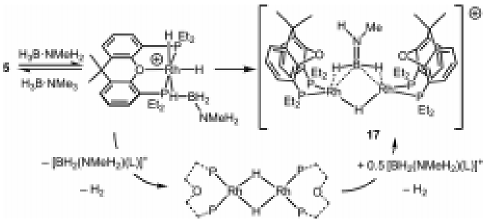

[a] $[BAr^F_4]^-$ anions are omitted for clarity. L = solvent or $NMeH_2$.

We have not been able to isolate complex **17** in pure form. When synthesized in situ and used in catalysis (0.2 mol % Rh, 0.446 M $[H_3B\text{-}NMeH_2]$) H_2 evolution is very slow, with a TOF of 0.01 s^{-1}, very similar to the rate observed for **5** (TOF = 0.01 s^{-1}), consistent with its rapid formation under catalytic conditions from **5**.

The precise role of dimeric or monomeric $\{Rh(diphosphine)\}^+$ fragments in dehydropolymerization remains to be resolved, as both are implicated in catalysis.[5c,d] However, observation of **17** and its lack of reactivity provide evidence to suggest that such dimeric hydride-bridged species are not compentent catalysts in these particular Xantphos-alkyl systems, although their ability to act as off-cycle reservoirs for actual catalysts cannot be discounted.[73] The formation of dimeric species with *cis*-κ^2-P,P geometries with Xantphos-Et but not for Xantphos-^{i}Pr or Xantphos-^{t}Bu again suggests steric effects are important in determining the course of reaction.

2.7.4. ^{t}Bu Systems — Neutral and Cationic: [Rh(κ^3-P,O,P-Xantphos-^{t}Bu)(H)$_2$][BAr$^F_4$], ***10***. Although **10** does not form a complex with $H_3B{\cdot}NMe_3$, it does promote H/D exchange (section 2.3) and was found to be capable of BH/NH activation of $H_3B{\cdot}NMeH_2$ to afford polymeric $(H_2BNMeH)_n$, albeit more slowly, in lower yield and with more side reactions than the ^{i}Pr analogue **6** (Table 1). Catalysis carried out at 10 mol % to determine the fate of the catalyst produced predominantly $(HBNMe)_3$, alongside a small quantity of $(H_2BNMeH)_n$ and a number of other side products. ^{1}H and $^{31}P\{^{1}H\}$ NMR spectroscopy indicated that **10** was the only organometallic species in solution at the end of catalysis. Interestingly, under these conditions a small amount of $[BH_2(NMeH_2)_2]^+$ was also observed, suggesting hydride transfer processes are occurring. Addition of 1 equiv of $H_3B{\cdot}NMeH_2$ to **10** did not form a σ-$H_3B{\cdot}NMeH_2$ complex $[Rh(\kappa^3\text{-P,O,P-Xantphos-}^{t}Bu)(H)_2(\eta^1\text{-}H_3B{\cdot}NMeH_2)][BAr^F_4]$, such as **15**, indicating that the bulky ^{t}Bu group inhibits $H_3B{\cdot}NMeH_2$ from binding strongly. That steric variations of the Xantphos-R ligand have significant differences in reactivity has parallels to related pincer complexes, such as Ir(R−POCOP)$(H)_2$, R = ^{i}Pr and ^{t}Bu.[74]

Rh(κ^3-P,O,P-Xantphos-^{t}Bu)H, ***13***. Complex **13** is observed as the sole organometallic species during catalysis (1 mol %), indicating that it is the likely resting state in this system. As for **10**, the ^{t}Bu groups promote slower and less selective dehydropolymerization.

2.8. Comments on the Mechanism. Use of a number of closely related rhodium-based Xantphos-alkyl systems, in which

DOI: 10.1021/jacs.7b11975
J. Am. Chem. Soc. 2018, 140, 1481−1495

Scheme 13. Suggested Mechanism for Dehydropolymerization[a]

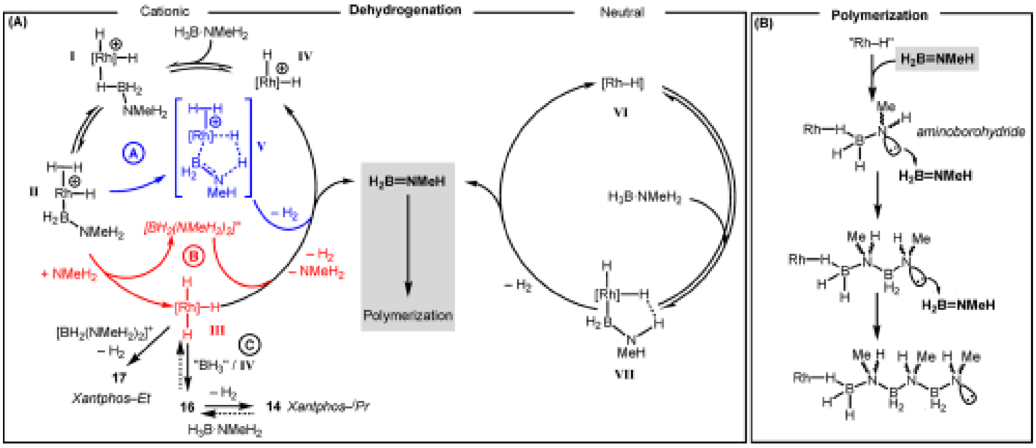

[a]Xantphos ligands and $[BAr^F_4]^-$ anions not shown.

sterics, charge, and number of hydride ligands on the precatalyst are varied, has allowed for insight into the mechanism of $H_3B{\cdot}NMeH_2$ dehydropolymerization. The studies provide the following observations:

(1) The essential chain-growth characteristics of polymerization suggest a mechanism that involves rapid addition of a reactive monomer (i.e., $H_2B{=}NMeH$) to a growing polymer chain.
(2) The catalyst remains active and is not irreversibly consumed in the polymerization process, as shown by recharging experiments.
(3) The absence of a strong effect of catalyst loading on degree of polymerization and lack of control of polymerization using H_2 suggest a single-site coordination/dehydrogenation/insertion chain-growth mechanism is likely not operating.
(4) Although complicated by solubility effects, dehydrogenation is first order in $H_3B{\cdot}NMeH_2$ for both cationic **6** and neutral **11** with broadly similar rate constants. Despite this there is a dramatic difference in the degree of polymerization observed: neutral **11** produces polymer that is considerably longer than that from cationic **6**.
(5) That different speciation is observed between cationic (Rh(III)) and neutral (Rh(I)) systems suggests that the two systems do not resolve into a common catalyst.
(6) Speciation studies all point to hydride-containing species being pervasive and hydride transfer processes in the cationic system occurring with the concomitant formation of boronium cations.

These data, however, do not allow us to definitively resolve the structure of the active catalyst. Nevertheless, based on the above speciation data we propose that neutral hydride species are involved. For the cationic system a plausible mechanistic scheme is shown in Scheme 13A. Coordination of $H_3B{\cdot}NMeH_2$ and subsequent reversible B–H activation forms boryl/hydride **II**. Pathway **A** proceeds through intramolecular NH activation via transition state **V**[28,56b] in which rate-determining N–H transfer occurs to a cationic Rh–hydride with the formation of the reactive monomer $H_2B{=}NMeH$. Alternatively, intermediate **II** can evolve via boronium formation to give neutral hydride **III**,[75] pathway **B**. Subsequently, rate-determining, intermolecular protonation by $[BH_2(NMeH_2)_2]^+$ reforms cationic dihydride **IV** and releases $H_2B{=}NMeH$. This is similar to the mechanism proposed by Conejero for $H_3B{\cdot}NMe_2H$ dehydrocoupling using cationic Pt-based catalysts.[22,76] Complex **14** forms in an off-cycle process by reaction of BH_3/**IV** with **III** (pathway **C**). For Xantphos-^{i}Pr resting states of **I** (i.e., **15**) and **16** are observed, with bulkier Xantphos-^{t}Bu it is **IV** (i.e., **10**), and with less bulky Xantphos-Et dimeric **17** forms rapidly. Boronium $[BH_2(NMeH_2)_2]^+$ thus potentially plays two different roles: as a co-intermediate (pathway **B**) or as a side product bifurcating from pathway **A** that eventually forms dormant species **14** (pathway **C**).

To probe this, polymerization was repeated at 0.1115 M $H_3B{\cdot}NMeH_2$, 0.2 mol % **6**, with and without the addition of excess, independently synthesized, $[BH_2(NMeH_2)_2][BAr^F_4]$ (2 mol %). Figure 9 details the temporal evolution plots obtained alongside the first-order rate plots for these data. Post induction period, during the first-order region of catalysis, a ~3-fold increase in k_{obs} was observed with added boronium. This is consistent with proposed mechanistic pathway **B**, which intimately involves $[BH_2(NMeH_2)_2]^+$; however we cannot discount that pathway **A** is also operating under these

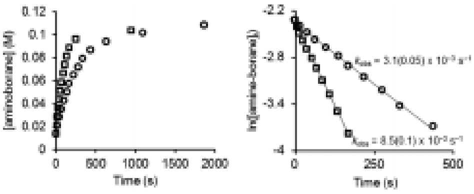

Figure 9. (Left) Temporal data plots for polyaminoborane formation (as measured by H_2 evolution) for catalyst **6** (2.23×10^{-4} M) and $H_3B{\cdot}NMeH_2$ (0.1115 M) (○ = without $[BH_2(NMeH_2)_2][BAr^F_4]$, □ = 2.23×10^{-3} M $[BH_2(NMeH_2)_2][BAr^F_4]$). Induction periods not shown. (Right) First-order rate plots showing calculated k_{obs}.

conditions. Polymer produced under the conditions of excess boronium was of low molecular weight but characteristic of catalyst **6** (M_n = 6000 g mol^{-1}, $Đ$ = 1.7).[77]

We suggest that neutral **11** and **13** operate in a similar manner to that proposed by Esteruelas for dehydrogenation of H_3B-NH_3, for which calculations indicate that B−H bond cleavage is followed by an (albeit high energy) N−H activation and elimination of $H_2B{=}NH_2$ operating via a N−H···H−Rh dihydrogen interaction, **VII.**[28] The Xantphos-^{i}Pr is proposed to change from *mer*-κ^3-P,O,P to *cis*-κ^2-P,P in this cycle.

A fast chain-growth mechanism for polymerization, but not single−site coordination/dehydrogenation/insertion, is indicated by the dehydropolymerization kinetics. We thus suggest a chain propagation process in which a low concentration of a separate, likely neutral, rhodium hydride initiator/catalyst forms a Lewis-base/acid adduct with $H_2B{=}NMeH$ which thus develops a lone pair on the nitrogen (i.e., an aminoborohydride).[78] Subsequent, fast, head−to−tail end−chain[13b] B−N bond-forming events lead to polyaminoborane (Scheme 13B). Support for this mechanism comes from Manners' experimental[4a] and Paul's computational[24] studies on the $Ir(POCOP)(H)_2$ catalyst system, **A**, the latter demonstrating a very low energy pathway (~7 kcal mol^{-1}) for this B−N bond-forming process, Scheme 14A. Given the similarities between κ^3-P,O,P-Xantphos ligands and POCOP-type pincer ligands it is not unreasonable to suggest a similar mechanism is operating here. This proposed end−chain-growth mechanism also has parallels with that suggested by Baker for dehydropolymerization of H_3B·NH_3 using $Fe(PhNCH_2CH_2NPh)(Cy_2PCH_2CH_2PCy_2)$[4c] and captures aspects of the mechanism suggested by Schneider in which the catalyst system acts in a "bifunctional" manner to dehydrogenate H_3B·NH_3 and also promote polymerization.[4e,f] It is also related to Sneddon's base-promoted anionic[57] and Aldridge's frustrated-Lewis-pair (Scheme 14B)[12c] chain-growth dehydrooligomerizations.

Scheme 14. (A) Paul's Proposed Polymerization Mechanism; (B) FLP End-Chain B−N Formation

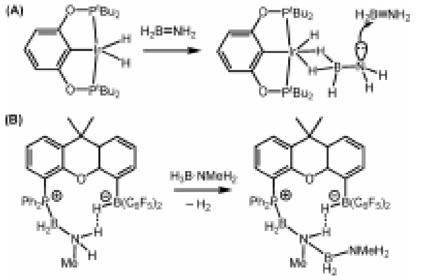

We cannot discount a process in which polymerization occurs off-metal.[15] Arguing against this, the different molecular weights of polymer produced with different catalysts, even though dehydrogenation (H_2 evolution) runs at similar rates, suggest metal involvement in the propagation step. We argue against low concentrations of $[BH_2(NMeH_2)_2]^+$ being an initiating species[79] as we previously demonstrated that closely related boronium salts do not promote dehydrocoupling at 0.5 mol % loading.[5d]

In chain-growth processes the interrelation of rates of initiation, termination, and propagation is very system dependent.[45] Adding to this potential complexity, termination events in amine−borane dehydropolymerization are currently opaque to experiment.[24] It is likely that subtle changes in dehydrogenation rate, the relative ratio of initiator sites for polymerization, and termination events (promoted by the sterics and electronics of the metal−ligand fragment and/or products of B−N bond cleavage) all combine to control the efficiency and degree of dehydropolymerization. It is, however, clear that when considering the Xantphos-^{i}Pr systems, the neutral precatalyst promotes higher degrees of polymerization, but precisely which of the above factors governs this still remains to be resolved.

3. CONCLUSIONS

The studies described here show that changes in the sterics and overall charge can have a significant effect on the course of H_3B·$NMeH_2$ dehydropolymerization when using {Rh(Xantphos-R)}-based catalysts. With Xantphos-Et the more flexible ligand allows the catalyst to access dimeric, essentially inactive, species, while the bulkier and less flexible Xantphos-^{t}Bu ligand leads to lower selectivites for polyaminoborane production and considerably slower turnovers. The optimal position comes with Xantphos-^{i}Pr, for which fast turnovers and good selectivities result. Speciation studies point toward neutral, hydride-containing, active catalysts, indicated to be formed from the cationic precatalysts by hydride transfer routes from the borane. It is interesting to note that for closely related alkane dehydrogenation catalysts based upon $Ir(pincer\text{-}R)(H)_2$ motifs ^{i}Pr-functionalized ligands often also show improved performance over ^{t}Bu.[80]

The development of such structure/activity relationships, a methodology so heavily exploited in olefin polymerization,[14] is central to harnessing metal-catalyzed dehydropolymerization for the production of polyaminoboranes "to order". In addition to resolving the fundamental details of this complex and nuanced catalytic system, future studies also need to consider more practical elements such as the development of catalysts that do not become entrained in the resulting polymer and a better understanding and control of the stereochemical aspects of these potentially exciting new materials.

■ ASSOCIATED CONTENT

Supporting Information

The Supporting Information is available free of charge on the ACS Publications website at DOI: 10.1021/jacs.7b11975.

Experimental and characterization details, including NMR spectroscopic data, and X-ray crystallographic data, and computational details (PDF)

Crystallographic information (CIF)

■ AUTHOR INFORMATION

Corresponding Author

*andrew.weller@chem.ox.ac.uk

ORCID

Annie L. Colebatch: 0000-0001-6920-3744
Guy C. Lloyd−Jones: 0000-0003-2128-6864
Stuart A. Macgregor: 0000-0003-3454-6776
Andrew S. Weller: 0000-0003-1646-8081

Author Contributions

‡G.M.A. and A.L.C.: These authors contributed equally.

Notes

The authors declare no competing financial interest.

■ ACKNOWLEDGMENTS

The EPSRC is thanked for funding (EP/M024210/1 and DTP studentships to GMA and NAB). The research leading to these results has received funding from the European Research Council under the European Union's Seventh Framework Programme (FP7/2007-2013)/ERC grant agreement no. [340163]. Joshua I. Levy is thanked for developing the GPC modelling software. Professors George Britovsek (Imperial College) and Ian Manners (University of Bristol) are thanked for helpful discussions.

■ REFERENCES

(1) (a) Staubitz, A.; Robertson, A. P. M.; Sloan, M. E.; Manners, I. *Chem. Rev.* **2010**, *110*, 4023. (b) Leitao, E. M.; Jurca, T.; Manners, I. *Nat. Chem.* **2013**, *5*, 817. (c) Johnson, H. C.; Hooper, T. N.; Weller, A. S. *Top. Organomet. Chem.* **2015**, *49*, 153. (d) Bhunya, S.; Malakar, T.; Ganguly, G.; Paul, A. *ACS Catal.* **2016**, *6*, 7907. (e) Pons, V.; Baker, R. T.; Szymczak, N. K.; Heldebrant, D. J.; Linehan, J. C.; Matus, M. H.; Grant, D. J.; Dixon, D. A. *Chem. Commun.* **2008**, 6597. (f) Priegert, A. M.; Rawe, B. W.; Serin, S. C.; Gates, D. P. *Chem. Soc. Rev.* **2016**, *45*, 922.

(2) (a) Bernard, S.; Miele, P. *Materials* **2014**, *7*, 7436. (b) Du, V.; Jurca, T.; Whittell, G.; Manners, I. *Dalton Trans.* **2016**, *45*, 1055. (c) Wang, X.; Hooper, T. N.; Kumar, A.; Priest, I. K.; Sheng, Y.; Samuels, T. O. M.; Wang, S.; Robertson, A. W.; Pacios, M.; Bhaskaran, H.; Weller, A. S.; Warner, J. H. *CrystEngComm* **2017**, *19*, 285. (d) Staubitz, A.; Presa Soto, A.; Manners, I. *Angew. Chem., Int. Ed.* **2008**, *47*, 6212.

(3) (a) Rossin, A.; Peruzzini, M. *Chem. Rev.* **2016**, *116*, 8848. (b) Dietrich, B. L.; Goldberg, K. I.; Heinekey, D. M.; Autrey, T.; Linehan, J. C. *Inorg. Chem.* **2008**, *47*, 8583.

(4) (a) Staubitz, A.; Sloan, M. E.; Robertson, A. P. M.; Friedrich, A.; Schneider, S.; Gates, P. J.; Günne, J. S. a. d.; Manners, I. *J. Am. Chem. Soc.* **2010**, *132*, 13332. (b) Vance, J. R.; Robertson, A. P. M.; Lee, K.; Manners, I. *Chem. - Eur. J.* **2011**, *17*, 4099. (c) Baker, R. T.; Gordon, J. C.; Hamilton, C. W.; Henson, N. J.; Lin, P.-H.; Maguire, S.; Murugesu, M.; Scott, B. L.; Smythe, N. C. *J. Am. Chem. Soc.* **2012**, *134*, 5598. (d) Esteruelas, M. A.; Olivan, M.; Vélez, A. *Inorg. Chem.* **2013**, *52*, 5339. (e) Marziale, A. N.; Friedrich, A.; Klopsch, I.; Drees, M.; Celinski, V. R.; Schmedt auf der Günne, J.; Schneider, S. *J. Am. Chem. Soc.* **2013**, *135*, 13342. (f) Glüer, A.; Förster, M.; Celinski, V. R.; Schmedt auf der Günne, J.; Holthausen, M. C.; Schneider, S. *ACS Catal.* **2015**, *5*, 7214. (g) Esteruelas, M. A.; López, A. M.; Mora, M.; Oñate, E. *ACS Catal.* **2015**, *5*, 187.

(5) (a) Dallanegra, R.; Robertson, A. P. M.; Chaplin, A. B.; Manners, I.; Weller, A. S. *Chem. Commun.* **2011**, *47*, 3763. (b) Johnson, H. C.; Leitao, E. M.; Whittell, G. R.; Manners, I.; Lloyd-Jones, G. C.; Weller, A. S. *J. Am. Chem. Soc.* **2014**, *136*, 9078. (c) Johnson, H. C.; Weller, A. S. *Angew. Chem., Int. Ed.* **2015**, *54*, 10173. (d) Kumar, A.; Beattie, N. A.; Pike, S. D.; Macgregor, S. A.; Weller, A. S. *Angew. Chem., Int. Ed.* **2016**, *55*, 6651. (e) St. John, A.; Goldberg, K. I.; Heinekey, D. M. *Top. Organomet. Chem.* **2013**, *40*, 271. (f) Kawano, Y.; Uruichi, M.; Shimoi, M.; Taki, S.; Kawaguchi, T.; Kakizawa, T.; Ogino, H. *J. Am. Chem. Soc.* **2009**, *131*, 14946. (g) Lichtenberg, C.; Adelhardt, M.; Gianetti, T. L.; Meyer, K.; de Bruin, B.; Grützmacher, H. *ACS Catal.* **2015**, *5*, 6230.

(6) Anke, F.; Han, D.; Klahn, M.; Spannenberg, A.; Beweries, T. *Dalton Trans.* **2017**, *46*, 6843.

(7) (a) Robertson, A.; Suter, R.; Chabanne, L.; Whittell, G.; Manners, I. *Inorg. Chem.* **2011**, *50*, 12680. (b) Sonnenberg, J. F.; Morris, R. H. *ACS Catal.* **2013**, *3*, 1092. (c) He, T.; Wang, J.; Wu, G.; Kim, H.; Proffen, T.; Wu, A.; Li, W.; Liu, T.; Xiong, Z.; Wu, C.; Chu, H.; Guo, J.; Autrey, T.; Zhang, T.; Chen, P. *Chem. - Eur. J.* **2010**, *16*, 12814.

(8) Vance, J. R.; Schäfer, A.; Robertson, A. P. M.; Lee, K.; Turner, J.; Whittell, G. R.; Manners, I. *J. Am. Chem. Soc.* **2014**, *136*, 3048.

(9) (a) Zhang, X.; Kam, L.; Trerise, R.; Williams, T. *Acc. Chem. Res.* **2017**, *50*, 86. (b) Stubbs, N. E.; Robertson, A. P. M.; Leitao, E. M.; Manners, I. *J. Organomet. Chem.* **2013**, *730*, 84. (c) Bhattacharya, P.; Krause, J. A.; Guan, H. *J. Am. Chem. Soc.* **2014**, *136*, 11153.

(10) Alcaraz, G.; Sabo-Etienne, S. *Angew. Chem., Int. Ed.* **2010**, *49*, 7170.

(11) (a) Jaska, C. A.; Temple, K.; Lough, A. J.; Manners, I. *J. Am. Chem. Soc.* **2003**, *125*, 9424. (b) Alcaraz, G.; Vendier, L.; Clot, E.; Sabo-Etienne, S. *Angew. Chem., Int. Ed.* **2010**, *49*, 918. (c) Kumar, A.; Johnson, H. C.; Hooper, T. N.; Weller, A. S.; Algarra, A. G.; Macgregor, S. A. *Chem. Sci.* **2014**, *5*, 2546. (d) Tang, C. Y.; Phillips, N.; Bates, J. I.; Thompson, A. L.; Gutmann, M. J.; Aldridge, S. *Chem. Commun.* **2012**, *48*, 8096. (e) Phillips, N.; Tang, C. Y.; Tirfoin, R.; Kelly, M. J.; Thompson, A. L.; Gutmann, M. J.; Aldridge, S. *Dalton Trans.* **2014**, *43*, 12288. (f) Friedrich, A.; Drees, M.; Schneider, S. *Chem. - Eur. J.* **2009**, *15*, 10339.

(12) (a) Johnson, H. C.; Robertson, A. P. M.; Chaplin, A. B.; Sewell, L. J.; Thompson, A. L.; Haddow, M. F.; Manners, I.; Weller, A. S. *J. Am. Chem. Soc.* **2011**, *133*, 11076. (b) Kalviri, H. A.; Gärtner, F.; Ye, E.; Korobkov, I.; Baker, R. T. *Chem. Sci.* **2015**, *6*, 618. (c) Mo, Z.; Rit, A.; Campos, J.; Kolychev, E. L.; Aldridge, S. *J. Am. Chem. Soc.* **2016**, *138*, 3306.

(13) (a) Huertos, M. A.; Weller, A. S. *Chem. Sci.* **2013**, *4*, 1881. (b) Marquardt, C.; Jurca, T.; Schwan, K.-C.; Stauber, A.; Virovets, A. V.; Whittell, G. R.; Manners, I.; Scheer, M. *Angew. Chem., Int. Ed.* **2015**, *54*, 13782. (c) Hooper, T. N.; Weller, A. S.; Beattie, N. A.; Macgregor, S. A. *Chem. Sci.* **2016**, *7*, 2414. (d) Schäfer, A.; Jurca, T.; Turner, J.; Vance, J. R.; Lee, K.; Du, V. A.; Haddow, M. F.; Whittell, G. R.; Manners, I. *Angew. Chem., Int. Ed.* **2015**, *54*, 4836. (e) Turner, J. R.; Resendiz-Lara, D. A.; Jurca, T.; Schäfer, A.; Vance, J. R.; Beckett, L.; Whittell, G. R.; Musgrave, R. A.; Sparkes, H. A.; Manners, I. *Macromol. Chem. Phys.* **2017**, *218*, 1700120.

(14) Hartwig, J. F. *Organotransition Metal Chemistry*; University Science Books: Sausalito, CA, USA, 2010.

(15) (a) Metters, O. J.; Chapman, A. M.; Robertson, A. P. M.; Woodall, C. H.; Gates, P. J.; Wass, D. F.; Manners, I. *Chem. Commun.* **2014**, *50*, 12146. (b) de Albuquerque Pinheiro, C. A.; Roiland, C.; Jehan, P.; Alcaraz, G. *Angew. Chem., Int. Ed.* **2018**, DOI: 10.1002/anie.201710293.

(16) (a) Zimmerman, P. M.; Paul, A.; Zhang, Z.; Musgrave, C. B. *Inorg. Chem.* **2009**, *48*, 1069. (b) Bhunya, S.; Zimmerman, P. M.; Paul, A. *ACS Catal.* **2015**, *5*, 3478.

(17) (a) Robertson, A. P. M.; Leitao, E. M.; Manners, I. *J. Am. Chem. Soc.* **2011**, *133*, 19322. (b) Leitao, E. M.; Stubbs, N. E.; Robertson, A. P.; Helten, H.; Cox, R. J.; Lloyd-Jones, G. C.; Manners, I. *J. Am. Chem. Soc.* **2012**, *134*, 16805.

(18) (a) Aldridge, S.; Downs, A. J.; Tang, C. Y.; Parsons, S.; Clarke, M. C.; Johnstone, R. D. L.; Robertson, H. E.; Rankin, D. W. H.; Wann, D. A. *J. Am. Chem. Soc.* **2009**, *131*, 2231. (b) Dallanegra, R.; Chaplin, A. B.; Weller, A. S. *Angew. Chem., Int. Ed.* **2009**, *48*, 6875. (c) Chen, X.; Zhao, J.-C.; Shore, S. G. *Acc. Chem. Res.* **2013**, *46*, 2666. (d) Bellham, P.; Anker, M.; Hill, M.; Kociok-Köhn, G.; Mahon, M. *Dalton Trans.* **2016**, *45*, 13969.

(19) Chen, E. *Chem. Rev.* **2009**, *109*, 5157.

(20) Johnson, H. C.; Weller, A. S. *J. Organomet. Chem.* **2012**, *721–722*, 17.

(21) Adams, G. M.; Weller, A. S. *Coord. Chem. Rev.* **2018**, *355*, 150.

(22) Roselló-Merino, M.; López-Serrano, J.; Conejero, S. *J. Am. Chem. Soc.* **2013**, *135*, 10910.

(23) (a) Lu, Z.; Conley, B. L.; Williams, T. J. *Organometallics* **2012**, *31*, 6705. (b) Lunsford, A. M.; Blank, J. H.; Moncho, S.; Haas, S. C.; Muhammad, S.; Brothers, E. N.; Darensbourg, M. Y.; Bengali, A. A. *Inorg. Chem.* **2016**, *55*, 964.

(24) Bhunya, S.; Malakar, T.; Paul, A. *Chem. Commun.* **2014**, *50*, 5919.

(25) Kranenburg, M.; van der Burgt, Y. E. M.; Kamer, P. C. J.; Van Leeuwen, P. W. N. M.; Goubitz, K.; Fraanje, J. *Organometallics* **1995**, *14*, 3081.

(26) (a) Julian, L. D.; Hartwig, J. F. *J. Am. Chem. Soc.* **2010**, *132*, 13813. (b) Haibach, M. C.; Wang, D. Y.; Emge, T. J.; Krogh-Jespersen, K.; Goldman, A. S. *Chem. Sci.* **2013**, *4*, 3683. (c) Raebiger, J.; Miedaner, A.; Curtis, C.; Miller, S.; Anderson, O.; DuBois, D. *J. Am. Chem. Soc.* **2004**, *126*, 5502.

(27) (a) Esteruelas, M.; Oliván, M.; Vélez, A. *Organometallics* **2015**, *34*, 1911. (b) Esteruelas, M. A.; Honczek, N.; Olivan, M.; Onate, E.; Valencia, M. *Organometallics* **2011**, *30*, 2468. (c) Alós, J.; Bolano, T.; Esteruelas, M. A.; Olivan, M.; Onate, E.; Valencia, M. *Inorg. Chem.* **2013**, *52*, 6199. (d) Esteruelas, M. A.; Garcia-Yebra, C.; Martin, J.; Oñate, E. *Inorg. Chem.* **2017**, *56*, 676. (e) Esteruelas, M. A.; López, A. M.; Oliván, M. *Chem. Rev.* **2016**, *116*, 8770.

(28) Esteruelas, M.; Nolis, P.; Oliván, M.; Oñate, E.; Vallribera, A.; Vélez, A. *Inorg. Chem.* **2016**, *55*, 7176.

(29) Shimoi, M.; Nagai, S.; Ichikawa, M.; Kawano, Y.; Katoh, K.; Uruichi, M.; Ogino, H. *J. Am. Chem. Soc.* **1999**, *121*, 11704.

(30) Pawley, R. J.; Moxham, G. L.; Dallanegra, R.; Chaplin, A. B.; Brayshaw, S. K.; Weller, A. S.; Willis, M. C. *Organometallics* **2010**, *29*, 1717.

(31) Johnson, H.; McMullin, C.; Pike, S.; Macgregor, S.; Weller, A. *Angew. Chem., Int. Ed.* **2013**, *52*, 9776.

(32) Ledger, A. E. W.; Ellul, C. E.; Mahon, M. F.; Williams, J. M. J.; Whittlesey, M. K. *Chem. - Eur. J.* **2011**, *17*, 8704.

(33) Algarra, A. G.; Sewell, L. J.; Johnson, H. C.; Macgregor, S. A.; Weller, A. S. *Dalton Trans.* **2014**, *43*, 11118.

(34) Merle, N.; Koicok-Köhn, G.; Mahon, M. F.; Frost, C. G.; Ruggerio, G. D.; Weller, A. S.; Willis, M. C. *Dalton Trans.* **2004**, 3883.

(35) It has been reported that complex **7** is in a slow equilbrium with an oligomeric species.[26b] We prepare **7** pure and in essentially quantitive yield, as reported by Esteruleas.[4d]

(36) Perutz, R. N.; Sabo-Etienne, S. *Angew. Chem., Int. Ed.* **2007**, *46*, 2578.

(37) Ewing, W. C.; Marchione, A.; Himmelberger, D. W.; Carroll, P. J.; Sneddon, L. G. *J. Am. Chem. Soc.* **2011**, *133*, 17093.

(38) Ewing, W. C.; Carroll, P. J.; Sneddon, L. G. *Inorg. Chem.* **2013**, *52*, 10690.

(39) Yang, C. J.; Jenekhe, S. A. *Chem. Mater.* **1994**, *6*, 196.

(40) This might be due to the greater difficulty of removing impurities from the longer polymer chains or from increased H-bonding interactions between the neutral Rh species and the polymer chains.

(41) The $[BAr^F_4]^-$ contaminant has not been previously noted in related systems.

(42) Semsarilar, M.; Jones, E. R.; Armes, S. P. *Polym. Chem.* **2014**, *5*, 195.

(43) The relatively sharp peak profile for the $[BAr^F_4]^-$ anion, coupled with its co-elution with polymer that tails into system peaks, results in the modelled fits giving similar M_n and $Đ$ to raw data.

(44) Addition of 5 equiv of PPh_3 during catalysis using **6** or **11** immediately halted the production of H_2. For complex **6** a Rh(I)−PPh_3 adduct is formed (see Supporting Information). We have not characterized the products of PPh_3 addition to **11**.

(45) Ravve, A. *Principles of Polymer Chemistry*, 3rd ed.; Springer: New York, 2012.

(46) Quirk, R.; Lee, B. *Polym. Int.* **1992**, *27*, 359.

(47) Malakar, T.; Bhunya, S.; Paul, A. *Chem. - Eur. J.* **2015**, *21*, 6340.

(48) Kim, J.; Soares, J.; Rempel, G. *Macromol. Rapid Commun.* **1998**, *19*, 197.

(49) Dorn, H.; Rodezno, J. M.; Brunnhöfer, B.; Rivard, E.; Massey, J. A.; Manners, I. *Macromolecules* **2003**, *36*, 291.

(50) (a) Colebatch, A. L.; McKay, A. I.; Beattie, N. A.; Macgregor, S. A.; Weller, A. S. *Eur. J. Inorg. Chem.* **2017**, 4533. (b) Pike, S.; Crimmin, M.; Chaplin, A. *Chem. Commun.* **2017**, *53*, 3615.

(51) Jaska, C. A.; Manners, I. *J. Am. Chem. Soc.* **2004**, *126*, 9776.

(52) Vogt, M.; De Bruin, B.; Berke, H.; Trincado, M.; Grutzmacher, H. *Chem. Sci.* **2011**, *2*, 723.

(53) Sloan, M. E.; Staubitz, A.; Clark, T. J.; Russell, C. A.; Lloyd-Jones, G. C.; Manners, I. *J. Am. Chem. Soc.* **2010**, *132*, 3831.

(54) Sewell, L. J.; Huertos, M. A.; Dickinson, M. E.; Weller, A. S.; Lloyd-Jones, G. C. *Inorg. Chem.* **2013**, *52*, 4509.

(55) (a) Jones, W. D. *Acc. Chem. Res.* **2003**, *36*, 140. (b) Simmons, E. M.; Hartwig, J. F. *Angew. Chem., Int. Ed.* **2012**, *51*, 3066.

(56) (a) Keaton, R. J.; Blacquiere, J. M.; Baker, R. T. *J. Am. Chem. Soc.* **2007**, *129*, 1844. (b) Todisco, S.; Luconi, L.; Giambastiani, G.; Rossin, A.; Peruzzini, M.; Golub, I.; Filippov, O.; Belkova, N.; Shubina, E. *Inorg. Chem.* **2017**, *56*, 4296.

(57) Chaplin, A. B.; Weller, A. S. *Eur. J. Inorg. Chem.* **2010**, *2010*, 5124.

(58) Braunschweig, H.; Kraft, K.; Kupfer, T.; Radacki, K.; Seeler, F. *Angew. Chem., Int. Ed.* **2008**, *47*, 4931.

(59) Vidovic, D.; Aldridge, S. *Angew. Chem., Int. Ed.* **2009**, *48*, 3669.

(60) Alcaraz, G.; Helmstedt, U.; Clot, E.; Vendier, L.; Sabo-Etienne, S. *J. Am. Chem. Soc.* **2008**, *130*, 12878.

(61) O'Neill, M.; A. Addy, D.; Riddlestone, I.; Kelly, M.; Phillips, N.; Aldridge, S. *J. Am. Chem. Soc.* **2011**, *133*, 11500.

(62) DFT calculations on a Xantphos-H model system also retained this geometry, suggesting that electronic effects are also relevant

(63) Braunschweig, H.; Dewhurst, R. D.; Gessner, V. H. *Chem. Soc. Rev.* **2013**, *42*, 3197.

(64) Douglas, T.; Chaplin, A.; Weller, A.; Yang, X.; Hall, M. *J. Am. Chem. Soc.* **2009**, *131*, 15440.

(65) Borrachero, M. V.; Estevan, F.; Garcia-Granda, S.; Lahuerta, P.; Latorre, J.; Peris, E.; Sanau, M. *J. Chem. Soc., Chem. Commun.* **1993**, 1864.

(66) Species **14** was fully optimized using the BP86 functional. Rh and P centers were described with SDD RECPs and associated basis sets, while 6-31g** basis sets were used for all other atoms. See Supporting Information for full details and references.

(67) We cannot rule out the identity of **15** as the linear diborazane complex $[Rh(\kappa^3\text{-}P,O,P\text{-Xantphos-}^iPr)(H)_2(H_3B\text{-}NMeHBH_2\text{-}NMeH_2)][BAr^F_4]$, as independent synthesis showed NMR data very similar to complex **15**.

(68) Koehne, I.; Schmeier, T. J.; Bielinski, E. A.; Pan, C. J.; Lagaditis, P. O.; Bernskoetter, W. H.; Takase, M. K.; Würtele, C.; Nazari, N.; Schneider, S. *Inorg. Chem.* **2014**, *53*, 2133.

(69) Kumar, R.; Jagirdar, B. *Inorg. Chem.* **2013**, *52*, 28.

(70) (a) Denney, M. C.; Pons, V.; Hebden, T. J.; Heinekey, D. M.; Goldberg, K. I. *J. Am. Chem. Soc.* **2006**, *128*, 12048. (b) Lin, T.-P.; Peters, J. C. *J. Am. Chem. Soc.* **2013**, *135*, 15310.

(71) Robertson, A. P. M.; Haddow, M. F.; Manners, I. *Inorg. Chem.* **2012**, *51*, 8254.

(72) (a) Fehlner, T. P. *Organometallics* **2000**, *19*, 2643. (b) Maekawa, M.; Daniliuc, C. G.; Jones, P. G.; Hohenberger, J.; Sutter, J.; Meyer, K.; Walter, M. D. *Eur. J. Inorg. Chem.* **2013**, *2013*, 4097.

(73) Kumar, A.; Ishibashi, J.; Hooper, T.; Mikulas, T.; Dixon, D.; Liu, S.; Weller, A. *Chem. - Eur. J.* **2016**, *22*, 310.

(74) Goldberg, J. M.; Wong, G. W.; Brastow, K. E.; Kaminsky, W.; Goldberg, K. I.; Heinekey, D. M. *Organometallics* **2015**, *34*, 753.

(75) Calculations demonstrate that Xantphos-^{t}Bu **III** is unstable with respect to H_2 loss and formation of **13** (ref 26b). Given that speciation is demonstrated to be markedly different for cationic **6** and neutral **13** precatalysts we suggest this is kinetically not relevant, and H_2 loss is relatively slow in the ^{i}Pr system.

(76) Roselló-Merino, M.; Rama, R.; Diez, J.; Conejero, S. *Chem. Commun.* **2016**, *52*, 8389.

(77) Interestingly, addition of $[BH_2(NMeH_2)_2]^+$ also led to an increase in the induction period by ~10 min.

(78) (a) Addy, D. A.; Bates, J. I.; Kelly, M. J.; Riddlestone, I. M.; Aldridge, S. *Organometallics* **2013**, *32*, 1583. (b) Drover, M.; Bowes, E.; Schafer, L.; Love, J.; Weller, A. *Chem. - Eur. J.* **2016**, *22*, 6793.

(79) Stephens, F. H.; Baker, R. T.; Matus, M. H.; Grant, D. J.; Dixon, D. A. *Angew. Chem., Int. Ed.* **2007**, *46*, 746.

(80) Choi, J.; MacArthur, A. H. R.; Brookhart, M.; Goldman, A. S. *Chem. Rev.* **2011**, *111*, 1761.

References

1. A. Staubitz, A. P. M. Robertson, M. E. Sloan and I. Manners, *Chem. Rev.*, 2010, **110**, 4023-4078.
2. Z. Huang and T. Autrey, *Energy Environ. Sci.*, 2012, **5**, 9257-9268.
3. T. Hügle, M. Hartl and D. Lentz, *Chem. Eur. J.*, 2011, **17**, 10184-10207.
4. E. Korytiakova, N. O. Thiel, F. Pape and J. F. Teichert, *Chem. Commun.*, 2017, **53**, 732-735.
5. J. K. Pagano, J. P. Stelmach and R. Waterman, *Dalton Trans*, 2015, **44**, 12074-12077.
6. G. Zeng, S. Maeda, T. Taketsugu and S. Sakaki, *J. Am. Chem. Soc.*, 2016, **138**, 13481-13484.
7. Y. Jiang, O. Blacque, T. Fox, C. M. Frech and H. Berke, *Organometallics*, 2009, **28**, 5493-5504.
8. F. Ding, Y. Zhang, R. Zhao, Y. Jiang, R. L.-Y. Bao, K. Lin and L. Shi, *Chem. Commun.*, 2017, **53**, 9262-9264.
9. S. Bhunya, T. Malakar, G. Ganguly and A. Paul, *ACS Catal.*, 2016, **6**, 7907-7934.
10. E. M. Leitao, T. Jurca and I. Manners, *Nature Chemistry*, 2013, **5**, 817-829.
11. A. M. Priegert, B. W. Rawe, S. C. Serin and D. P. Gates, *Chem. Soc. Rev.*, 2016, **45**, 922-953.
12. D. A. Resendiz-Lara, N. E. Stubbs, M. I. Arz, N. E. Pridmore, H. A. Sparkes and I. Manners, *Chem. Commun.*, 2017, **53**, 11701-11704.
13. V. A. Du, T. Jurca, G. R. Whittell and I. Manners, *Dalton Trans.*, 2016, **45**, 1055-1062.
14. A. Staubitz, A. Presa Soto and I. Manners, *Angew. Chem. Int. Ed.*, 2008, **47**, 6212-6215.
15. J. F. Hartwig, *Organotransition Metal Chemistry*, University Science Books, Sausalito, CA, USA, 2010.
16. G. M. Adams, A. L. Colebatch, J. T. Skornia, A. I. McKay, H. C. Johnson, G. C. Lloyd−Jones, S. A. Macgregor, N. A. Beattie and A. S. Weller, *J. Am. Chem. Soc.*, 2018, **140**, 1481-1495.
17. X. Zhang, L. Kam and T. J. Williams, *Dalton Trans.*, 2016, **45**, 7672-7677.
18. N. E. Stubbs, A. Schäfer, A. P. M. Robertson, E. M. Leitao, T. Jurca, H. A. Sparkes, C. H. Woodall, M. F. Haddow and I. Manners, *Inorg. Chem.*, 2015, **54**, 10878-10889.
19. C. Appelt, J. C. Slootweg, K. Lammertsma and W. Uhl, *Angew. Chem. Int. Ed.*, 2013, **52**, 4256-4259.
20. D. W. Himmelberger, L. R. Alden, M. E. Bluhm and L. G. Sneddon, *Inorg. Chem.*, 2009, **48**, 9883-9889.
21. C. A. De Albuquerque Pinheiro, C. Roiland, P. Jehan and G. Alcaraz, *Angew. Chem. Int. Ed.*, 2018, **57**, 1519-1522.

22. I. G. Green, K. M. Johnson and B. P. Roberts, *J. Chem. Soc. Perk. T. 2.*, 1989, **12**, 1963-1972

23. R. McLellan, A. R. Kennedy, R. E. Mulvey, S. A. Orr and S. D. Robertson, *Chem. Eur. J.*, 2017, **23**, 16852-16861.

24. J. Spielmann, D. F. J. Piesik and S. Harder, *Chem. Eur. J.*, 2010, **16**, 8307-8318.

25. P. Bellham, M. S. Hill, G. Kociok-Kohn and D. J. Liptrot, *Chem. Commun.*, 2013, **49**, 1960-1962.

26. P. Bellham, M. S. Hill and G. Kociok-Köhn, *Organometallics*, 2014, **33**, 5716-5721.

27. V. Butera, N. Russo and E. Sicilia, *Chem. Eur. J.*, 2014, **20**, 5967-5976.

28. K. A. Erickson and J. L. Kiplinger, *ACS Catal.*, 2017, **7**, 4276-4280.

29. D. J. Liptrot, M. S. Hill, M. F. Mahon and D. J. MacDougall, *Chem. Eur. J.*, 2010, **16**, 8508-8515.

30. M. S. Hill, G. Kociok-Kohn and T. P. Robinson, *Chem. Commun.*, 2010, **46**, 7587-7589.

31. M. S. Hill, M. Hodgson, D. J. Liptrot and M. F. Mahon, *Dalton Trans.*, 2011, **40**, 7783-7790.

32. P. Cui, T. P. Spaniol, L. Maron and J. Okuda, *Chem. Eur. J.*, 2013, **19**, 13437-13444.

33. A. J. M. Miller and J. E. Bercaw, *Chem. Commun.*, 2010, **46**, 1709-1711.

34. Z. Mo, A. Rit, J. Campos, E. L. Kolychev and S. Aldridge, *J. Am. Chem. Soc.*, 2016, **138**, 3306-3309.

35. H. C. Johnson, T. N. Hooper and A. S. Weller, *Top. Organomet. Chem.* , 2015, **49**, 153.

36. A. Rossin and M. Peruzzini, *Chem. Rev.*, 2016, **116**, 8848-8872.

37. J. F. Sonnenberg and R. H. Morris, *ACS Catal.*, 2013, **3**, 1092-1102.

38. A. P. M. Robertson, R. Suter, L. Chabanne, G. R. Whittell and I. Manners, *Inorg. Chem.*, 2011, **50**, 12680-12691.

39. J. R. Vance, A. P. M. Robertson, K. Lee and I. Manners, *Chem. Eur. J.*, 2011, **17**, 4099-4103.

40. W. Luo, P. G. Campbell, L. N. Zakharov and S. Y. Liu, *J. Am. Chem. Soc.*, 2011, **133**, 19326-19329.

41. S. Akbayrak, P. Erdek and S. Ozkar, *Appl. Catal., B.*, 2013, **142**, 187-195.

42. S. Akbayrak, Y. Tonbul and S. Ozkar, *Dalton Trans.*, 2016, **45**, 10969-10978.

43. S. Caliskan, M. Zahmakiran, F. Durap and S. Ozkar, *Dalton Trans.*, 2012, **41**, 4976-4984.

44. S. Duman and S. Ozkar, *Int. J. Hydrog. Energy*, 2013, **38**, 10000-10011.

45. O. Metin, S. Duman, M. Dinc and S. Ozkar, *J. Phys. Chem., C.*, 2011, **115**, 10736-10743.

46. M. Zahmakiran and S. Ozkar, *Inorg. Chem.*, 2009, **48**, 8955-8964.

47. M. Zahmakiran, K. Philippot, S. Ozkar and B. Chaudret, *Dalton Trans.*, 2012, **41**, 590-598.

48. K. Mori, K. Miyawaki and H. Yamashita, *ACS Catal.*, 2016, **6**, 3128-3135.

49. H. R. Sharpe, A. M. Geer, T. J. Blundell, F. R. Hastings, M. W. Fay, G. A. Rance, W. Lewis, A. J. Blake and D. L. Kays, *Catal Sci Technol*, 2018, **8**, 229-235.
50. L. Wang, H. Li, W. Zhang, X. Zhao, J. Qiu, A. Li, X. Zheng, Z. Hu, R. Si and J. Zeng, *Angew. Chem. Int. Ed.*, 2017, **56**, 4712-4718.
51. W.-W. Zhan, Q.-L. Zhu and Q. Xu, *ACS Catal.*, 2016, **6**, 6892-6905.
52. M. E. Bluhm, M. G. Bradley, R. Butterick, U. Kusari and L. G. Sneddon, *J. Am. Chem. Soc.*, 2006, **128**, 7748-7749.
53. W. R. H. Wright, E. R. Berkeley, L. R. Alden, R. T. Baker and L. G. Sneddon, *Chem. Commun.*, 2011, **47**, 3177-3179.
54. S. S. Mal, F. H. Stephens and R. T. Baker, *Chem. Commun.*, 2011, **47**, 2922-2924.
55. A. Kumar, H. C. Johnson, T. N. Hooper, A. S. Weller, A. G. Algarra and S. A. Macgregor, *Chem. Sci.*, 2014, **5**, 2546-2553.
56. D. Pun, E. Lobkovsky and P. J. Chirik, *Chem. Commun.*, 2007, **31**, 3297-3299.
57. A. Rossin, M. Caporali, L. Gonsalvi, A. Guerri, A. Lledós, M. Peruzzini and F. Zanobini, *Eur. J. Inorg. Chem.*, 2009, **2009**, 3055-3059.
58. T. J. Clark, C. A. Russell and I. Manners, *J. Am. Chem. Soc.*, 2006, **128**, 9582-9583.
59. M. E. Sloan, A. Staubitz, T. J. Clark, C. A. Russell, G. C. Lloyd-Jones and I. Manners, *J. Am. Chem. Soc.*, 2010, **132**, 3831-3841.
60. D. J. Wolstenholme, K. T. Traboulsee, A. Decken and G. S. McGrady, *Organometallics*, 2010, **29**, 5769-5772.
61. T. D. Forster, H. M. Tuononen, M. Parvez and R. Roesler, *J. Am. Chem. Soc.*, 2009, **131**, 6689-6691.
62. T. Beweries, S. Hansen, M. Kessler, M. Klahn and U. Rosenthal, *Dalton Trans.*, 2011, **40**, 7689-7692.
63. T. Beweries, J. Thomas, M. Klahn, A. Schulz, D. Heller and U. Rosenthal, *ChemCatChem*, 2011, **3**, 1865-1868.
64. N. T. Coles, M. F. Mahon and R. L. Webster, *Organometallics*, 2017, **36**, 2262-2268.
65. T. Miyazaki, Y. Tanabe, M. Yuki, Y. Miyake and Y. Nishibayashi, *Organometallics*, 2011, **30**, 2394-2404.
66. Y. Kawano and M. Shimoi, *Dalton Trans.*, 2017, **46**, 11950-11955.
67. Y. Kawano, M. Uruichi, M. Shimoi, S. Taki, T. Kawaguchi, T. Kakizawa and H. Ogino, *J. Am. Chem. Soc.*, 2009, **131**, 14946-14957.
68. J. A. Buss, G. A. Edouard, C. Cheng, J. D. Shi and T. Agapie, *J. Am. Chem. Soc.*, 2014, **136**, 11272-11275.
69. A. Rossin, G. Bottari, A. M. Lozano-Vila, M. Paneque, M. Peruzzini, A. Rossi and F. Zanobini, *Dalton Trans.*, 2013, **42**, 3533-3541.

70. R. J. Keaton, J. M. Blacquiere and R. T. Baker, *J. Am. Chem. Soc.*, 2007, **129**, 1844-1845.

71. D. Ai, Y. Guo, W. Liu and Y. Wang, *J. Phys. Org. Chem.*, 2014, **27**, 597-603.

72. X. Z. Yang and M. B. Hall, *J. Am. Chem. Soc.*, 2008, **130**, 1798-1799.

73. X. Z. Yang and M. B. Hall, *J. Organomet. Chem.*, 2009, **694**, 2831-2838.

74. P. M. Zimmerman, A. Paul and C. B. Musgrave, *Inorg. Chem.*, 2009, **48**, 5418-5433.

75. P. M. Zimmerman, A. Paul, Z. Zhang and C. B. Musgrave, *Angew. Chem. Int. Ed.*, 2009, **48**, 2201-2205.

76. A. M. Chapman, M. F. Haddow and D. F. Wass, *J. Am. Chem. Soc.*, 2011, **133**, 8826-8829.

77. O. J. Metters, S. R. Flynn, C. K. Dowds, H. A. Sparkes, I. Manners and D. F. Wass, *ACS Catal.*, 2016, **6**, 6601-6611.

78. R. T. Baker, J. C. Gordon, C. W. Hamilton, N. J. Henson, P. H. Lin, S. Maguire, M. Murugesu, B. L. Scott and N. C. Smythe, *J. Am. Chem. Soc.*, 2012, **134**, 5598-5609.

79. N. Blaquiere, S. Diallo-Garcia, S. I. Gorelsky, D. A. Black and K. Fagnou, *J. Am. Chem. Soc.*, 2008, **130**, 14034-14035.

80. T. P. Lin and J. C. Peters, *J. Am. Chem. Soc.*, 2013, **135**, 15310-15313.

81. G. Ganguly, T. Malakar and A. Paul, *ACS Catalysis*, 2015, **5**, 2754-2769.

82. M. A. Esteruelas, I. Fernandez, A. M. Lopez, M. Mora and E. Onate, *Organometallics*, 2014, **33**, 1104-1107.

83. M. A. Esteruelas, A. M. López, M. Mora and E. Oñate, *ACS Catal.*, 2015, **5**, 187-191.

84. I. Göttker-Schnetmann, D. M. Heinekey and M. Brookhart, *J. Am. Chem. Soc.*, 2006, **128**, 17114-17119.

85. A. Paul and C. B. Musgrave, *Angew. Chem. Int. Ed.*, 2007, **46**, 8153-8156.

86. E. M. Titova, E. S. Osipova, A. A. Pavlov, O. A. Filippov, S. V. Safronov, E. S. Shubina and N. V. Belkova, *ACS Catal.*, 2017, **7**, 2325-2333.

87. A. Rossin, A. Rossi, M. Peruzzini and F. Zanobini, *ChemPlusChem*, 2014, **79**, 1316-1325.

88. S. Todisco, L. Luconi, G. Giambastiani, A. Rossin, M. Peruzzini, I. E. Golub, O. A. Filippov, N. V. Belkova and E. S. Shubina, *Inorg. Chem.*, 2017, **56**, 4296-4307.

89. M. Käß, A. Friedrich, M. Drees and S. Schneider, *Angew. Chem. Int. Ed.*, 2009, **48**, 905-907.

90. A. N. Marziale, A. Friedrich, I. Klopsch, M. Drees, V. R. Celinski, J. Guenne and S. Schneider, *J. Am. Chem. Soc.*, 2013, **135**, 13342-13355.

91. A. Glüer, M. Förster, V. R. Celinski, J. Schmedt auf der Günne, M. C. Holthausen and S. Schneider, *ACS Catal.*, 2015, **5**, 7214-7217.

92. D. F. Schreiber, C. O'Connor, C. Grave, Y. Ortin, H. Muller-Bunz and A. D. Phillips, *ACS Catal.*, 2012, **2**, 2505-2511.

93. S. Bandaru, N. J. English, A. D. Phillips and J. M. D. MacElroy, *J. Comput. Chem.*, 2014, **35**, 891-903.

94. B. L. Conley and T. J. Williams, *Chem. Commun.*, 2010, **46**, 4815-4817.

95. F. Anke, D. Han, M. Klahn, A. Spannenberg and T. Beweries, *Dalton Trans.*, 2017, **46**, 6843-6847.

96. S. Bhunya, L. Roy and A. Paul, *ACS Catal.*, 2016, **6**, 4068-4080.

97. B. L. Conley, D. Guess and T. J. Williams, *J. Am. Chem. Soc.*, 2011, **133**, 14212-14215.

98. M. Roselló-Merino, J. López-Serrano and S. Conejero, *J. Am. Chem. Soc.*, 2013, **135**, 10910-10913.

99. A. Telleria, C. Vicent, V. San Nacianceno, M. A. Garralda and Z. Freixa, *ACS Catal.*, 2017, **7**, 8394-8405.

100. R. Kumar and B. R. Jagirdar, *Inorg. Chem.*, 2013, **52**, 28-36.

101. A. Ravve, *Principles of Polymer Chemistry, 3rd ed,*, Springer, New York, 2012.

102. S. Bhunya, T. Malakar and A. Paul, *Chem. Commun.*, 2014, **50**, 5919-5922.

103. A. Staubitz, A. P. Soto and I. Manners, *Angew. Chem. Int. Ed.*, 2008, **47**, 6212-6215.

104. T. Malakar, L. Roy and A. Paul, *Chem. Eur. J.*, 2013, **19**, 5812-5817.

105. L. J. Sewell, M. A. Huertos, M. E. Dickinson, A. S. Weller and G. C. Lloyd-Jones, *Inorg. Chem.*, 2013, **52**, 4509-4516.

106. T. M. Douglas, A. B. Chaplin, A. S. Weller, X. Z. Yang and M. B. Hall, *J. Am. Chem. Soc.*, 2009, **131**, 15440-15456.

107. L. J. Sewell, G. C. Lloyd-Jones and A. S. Weller, *J. Am. Chem. Soc.*, 2012, **134**, 3598-3610.

108. R. Dallanegra, A. P. M. Robertson, A. B. Chaplin, I. Manners and A. S. Weller, *Chem. Commun.*, 2011, **47**, 3763-3765.

109. V. Butera, N. Russo and E. Sicilia, *ACS Catal.*, 2014, **4**, 1104-1113.

110. H. C. Johnson, E. M. Leitao, G. R. Whittell, I. Manners, G. C. Lloyd-Jones and A. S. Weller, *J. Am. Chem. Soc.*, 2014, **136**, 9078-9093.

111. M. A. Esteruelas, P. Nolis, M. Oliván, E. Oñate, A. Vallribera and A. Vélez, *Inorg. Chem.*, 2016, **55**, 7176-7181.

112. H. Cavaye, F. Clegg, P. J. Gould, M. K. Ladyman, T. Temple and E. Dossi, *Macromolecules*, 2017, **50**, 9239-9248.

113. T. J. Clark, K. Lee and I. Manners, *Chem. Eur. J.*, 2006, **12**, 8634-8648.

114. A. B. Burg and R. I. Wagner, *J. Am. Chem. Soc.*, 1953, **75**, 3872-3877.

115. A. B. Burg, *J. Inorg. Nucl. Chem.*, 1959, **11**, 258.

116. C. Marquardt, T. Jurca, K.-C. Schwan, A. Stauber, A. V. Virovets, G. R. Whittell, I. Manners and M. Scheer, *Angew. Chem. Int. Ed.*, 2015, **54**, 13782-13786.

117. J.-M. Denis, H. Forintos, H. Szelke, L. Toupet, T.-N. Pham, P.-J. Madec and A.-C. Gaumont, *Chem. Commun.*, 2003, DOI: 10.1039/B206559B, 54-55.
118. U. S. D. Paul, H. Braunschweig and U. Radius, *Chem. Commun.*, 2016, **52**, 8573-8576.
119. S. Pandey, P. Lönnecke and E. Hey-Hawkins, *Inorg. Chem.*, 2014, **53**, 8242-8249.
120. C. A. Jaska, A. J. Lough and I. Manners, *Dalton Trans*, 2005, **2**, 326-331
121. H. Dorn, E. Vejzovic, A. J. Lough and I. Manners, *Inorg. Chem.*, 2001, **40**, 4327-4331.
122. C. A. Jaska and I. Manners, *J. Am. Chem. Soc.*, 2004, **126**, 1334-1335.
123. T. J. Clark, J. M. Rodezno, S. B. Clendenning, S. Aouba, P. M. Brodersen, A. J. Lough, H. E. Ruda and I. Manners, *Chem. Eur. J.*, 2005, **11**, 4526-4534.
124. A. Schäfer, T. Jurca, J. Turner, J. R. Vance, K. Lee, V. A. Du, M. F. Haddow, G. R. Whittell and I. Manners, *Angew. Chem. Int. Ed.*, 2015, **54**, 4836-4841.
125. M. A. Huertos and A. S. Weller, *Chem. Commun.*, 2012, **48**, 7185-7187.
126. M. A. Huertos and A. S. Weller, *Chem. Sci.*, 2013, **4**, 1881-1888.
127. T. N. Hooper, M. A. Huertos, T. Jurca, S. D. Pike, A. S. Weller and I. Manners, *Inorg. Chem.*, 2014, **53**, 3716-3729.
128. T. N. Hooper, A. S. Weller, N. A. Beattie and S. A. Macgregor, *Chem. Sci.*, 2016, **7**, 2414-2426.
129. N. A. Szabo, Ostlund *Modern Quantum Chemistry*, McGraw-Hill Publishing Company, 1989.
130. C. Cramer, *Essentials of Computational Chemistry, 2nd Ed.,* , John Wiley & Sons Ltd. , 2004.
131. M. H. W. Koch, *A Chemist's Guide to Density Functional Theory, 2nd Ed.,* , Wiley VCH, 2011.
132. E. Schrödinger, *Phys. Rev.*, 1926, **28**, 1049-1070.
133. R. Krishnan, H. B. Schlegel and J. A. Pople, *J. Chem. Phys.*, 1980, **72**, 4654-4655.
134. J. A. Pople, R. Krishnan, H. B. Schlegel and J. S. Binkley, *Int. J. Quantum Chem*, 1978, **14**, 545-560.
135. D. A. Matthews and J. F. Stanton, *J. Chem. Phys.*, 2015, **142**, 064108.
136. D. Hegarty and M. A. Robb, *Mol. Phys.*, 1979, **38**, 1795-1812.
137. A. E. F. J. B. Foresman, *Exploring Chemistry with Electronic Structure Methods, 3rd ed.*, Gaussian, Inc., Wallingford, CT, 2015.
138. C. Møller and M. S. Plesset, *Phys. Rev.*, 1934, **46**, 618-622.
139. M. Head-Gordon, J. A. Pople and M. J. Frisch, *Chem. Phys. Lett.*, 1988, **153**, 503-506.
140. R. Krishnan and J. A. Pople, *Int. J. Quantum Chem*, 1978, **14**, 91-100.
141. P. Hohenberg and W. Kohn, *Phys. Rev.*, 1964, **136**, B864-B871.
142. S. H. Vosko, L. Wilk and M. Nusair, *Can. J. Phys.*, 1980, **58**, 1200-1211.

143. A. D. Becke, *Phys. Rev. A.*, 1988, **38**, 3098-3100.

144. J. P. Perdew, *Phys. Rev. B.*, 1986, **33**, 8822-8824.

145. C. Lee, W. Yang and R. G. Parr, *Phys. Rev. B.*, 1988, **37**, 785-789.

146. J. P. Perdew, K. Burke and M. Ernzerhof, *Phys. Rev. Lett.*, 1996, **77**, 3865-3868.

147. A. D. Becke, *J. Chem. Phys.*, 1993, **98**, 5648-5652.

148. S. F. Sousa, P. A. Fernandes and M. J. Ramos, *J. Phys. Chem., A.* , 2007, **111**, 10439-10452.

149. C. Adamo and V. Barone, *J. Chem. Phys.*, 1999, **110**, 6158-6170.

150. A. D. Becke, *J. Chem. Phys.*, 1997, **107**, 8554-8560.

151. J. Tao, J. P. Perdew, V. N. Staroverov and G. E. Scuseria, *Phys. Rev. Lett.*, 2003, **91**, 146401.

152. J.-D. Chai and M. Head-Gordon, *PCCP*, 2008, **10**, 6615-6620.

153. W. J. Hehre, R. F. Stewart and J. A. Pople, *J. Chem. Phys.*, 1969, **51**, 2657-2664.

154. M. S. Gordon, *Chem. Phys. Lett.*, 1980, **76**, 163-168.

155. M. S. Gordon, J. S. Binkley, J. A. Pople, W. J. Pietro and W. J. Hehre, *J. Am. Chem. Soc.*, 1982, **104**, 2797-2803.

156. P. C. Hariharan and J. A. Pople, *Theor. Chem. Acc.*, 1973, **28**, 213-222.

157. W. J. Hehre, R. Ditchfield and J. A. Pople, *J. Chem. Phys.*, 1972, **56**, 2257-2261.

158. D. Andrae, U. Häußermann, M. Dolg, H. Stoll and H. Preuß, *Theor. Chem. Acc.*, 1990, **77**, 123-141.

159. G. Kovács, A. Stirling, A. Lledós and G. Ujaque, *Chem. Eur. J.*, 2012, **18**, 5612-5619.

160. A. Comas-Vives, A. Stirling, A. Lledós and G. Ujaque, *Chem. Eur. J.*, 2010, **16**, 8738-8747.

161. G. Scalmani and M. J. Frisch, *J. Chem. Phys.*, 2010, **132**, 114110.

162. A. V. Marenich, C. J. Cramer and D. G. Truhlar, *J. Phys. Chem., B.*, 2009, **113**, 6378-6396.

163. J. E. Jones, *Proc. Royal Soc. A.*, 1924, **106**, 463.

164. S. Grimme, J. Antony, S. Ehrlich and H. Krieg, *J. Chem. Phys.*, 2010, **132**, 154104.

165. S. Grimme, S. Ehrlich and L. Goerigk, *J. Comput. Chem.*, 2011, **32**, 1456-1465.

166. Y. Zhao and D. G. Truhlar, *Theor. Chem. Acc.*, 2008, **120**, 215-241.

167. S. Grimme, *J. Comput. Chem.*, 2006, **27**, 1787-1799.

168. AIMAll (Version 13.02.26, Professional), T. A. Keith, TK Gristmill Software,Overland Park KS, USA, 2015 (aim.tkgristmill.com)

169. R. F. W. Bader, *Atoms in Molecules: A Quantum Theory*, Oxford University Press, Oxford, 1990.

170. R. J. B. C. F. Matta, *The Quantum Theory of Atoms in Molecules: From Solid State to DNA and Drug Design*, Wiley-VCH, Weinheim, 2007.

171. D. Cremer and E. Kraka, *Angew. Chem. Int. Ed.*, 1984, **23**, 627-628.

172. NBO 6.0. E. D. Glendening, J. K. Badenhoop, A. E. Reed, J. E. Carpenter, J. A. Bohmann, C. M. Morales, C. R. Landis and F. Weinhold (Theoretical Chemistry Institute, University of Wisconsin, Madison, WI, 2013); http://nbo6.chem.wisc.edu/

173. M. J. Frisch, G. W. Trucks, H. B. Schlegel, G. E. Scuseria, M. A. Rob, J. R. Cheeseman, J. A. Montgomery Jr., T. Vreven, K. N. Kudin, J. C. Burant, J. M. Millam, S. S. Iyengar, J. Tomasi, V. Barone, B. Mennucci, M. Cossi, G. Scalmani, N. Rega, G. A. Petersson, H. Nakatsuji, M. Hada, M. Ehara, K. Toyota, R. Fukuda, J. Hasegawa, M. Ishida, T. Nakajima, Y. Honda, O. Kitao, H. Nakai, M. Klene, X. Li, J. E. Knox, H. P. Hratchian, J. B. Cross, V. Bakken, C. Adamo, J. Jaramillo, R. Gomperts, R. E. Stratmann, O. Yazyev, A. J. Austin, R. Cammi, C. Pomelli, J. W. Ochterski, P. Y. Ayala, K. Morokuma, G. A. Voth, P. Salvador, J. J. Dannenberg, V. G. Zakrzewski, S. Dapprich, A. D. Daniels, M. C. Strain, O. Farkas, D. K. Malick, A. D. Rabuck, K. Raghavachari, J. B. Foresman, J. V. Ortiz, Q. Cui, A. G. Baboul, S. Clifford, J. Cioslowski, B. B. Stefanov, G. Liu, A. Liashenko, P. Piskorz, I. Komaromi, R. L. Martin, D. J. Fox, T. Keith, M. A. Al-Laham, C. Y. Peng, A. Nanayakkara, M. Challacombe, P. M. W. Gill, B. Johnson, W. Chen, M. W. Wong, C. Gonzalez, and J. A. Pople, Gaussian 03 (Gaussian, Inc., Wallingford, CT, 2003)

174. A. Höllwarth, M. Böhme, S. Dapprich, A. W. Ehlers, A. Gobbi, V. Jonas, K. F. Köhler, R. Stegmann, A. Veldkamp and G. Frenking, *Chem. Phys. Lett.*, 1993, **208**, 237-240.

175. M. J. Frisch, G. W. Trucks, H. B. Schlegel, G. E. Scuseria, M. A. Robb, J. R. Cheeseman, G. Scalmani, V. Barone, B. Mennucci, G. A. Petersson, H. Nakatsuji, M. Caricato, X. Li, H. P. Hratchian, A. F. Izmaylov, J. Bloino, G. Zheng, J. L. Sonnenberg, M. Hada, M. Ehara, K. Toyota, R. Fukuda, J. Hasegawa, M. Ishida, T. Nakajima, Y. Honda, O. Kitao, H. Nakai, T. Vreven, J. A. Montgomery, Jr., J. E. Peralta, F. Ogliaro, M. Bearpark, J. J. Heyd, E. Brothers, K. N. Kudin, V. N. Staroverov, R. Kobayashi, J. Normand, K. Raghavachari, A. Rendell, J. C. Burant, S. S. Iyengar, J. Tomasi, M. Cossi, N. Rega, J. M. Millam, M. Klene, J. E. Knox, J. B. Cross, V. Bakken, C. Adamo, J. Jaramillo, R. Gomperts, R. E. Stratmann, O. Yazyev, A. J. Austin, R. Cammi, C. Pomelli, J. W. Ochterski, R. L. Martin, K. Morokuma, V. G. Zakrzewski, G. A. Voth, P. Salvador, J. J. Dannenberg, S. Dapprich, A. D. Daniels, Ö. Farkas, J. B. Foresman, J. V. Ortiz, J. Cioslowski, and D. J. Fox, Gaussian 09 (Gaussian, Inc., Wallingford CT, 2009).

176. H. Helten, B. Dutta, J. R. Vance, M. E. Sloan, M. F. Haddow, S. Sproules, D. Collison, G. R. Whittell, G. C. Lloyd-Jones and I. Manners, *Angew. Chem. Int. Ed.*, 2013, **52**, 437-440.

177. R. N. Perutz and S. Sabo-Etienne, *Angew. Chem. Int. Ed.*, 2007, **46**, 2578-2592.

178. R. Krishnan, J. S. Binkley, R. Seeger and J. A. Pople, *J. Chem. Phys.*, 1980, **72**, 650-654.

179. A. D. McLean and G. S. Chandler, *J. Chem. Phys.*, 1980, **72**, 5639-5648.

180. F. Weigend and R. Ahlrichs, *Phys. Chem. Chem. Phys.*, 2005, **7**, 3297-3305.

181. F. Weigend, *Phys. Chem. Chem. Phys.*, 2006, **8**, 1057-1065.

182. G. Bénac-Lestrille, U. Helmstedt, L. Vendier, G. Alcaraz, E. Clot and S. Sabo-Etienne, *Inorg. Chem.*, 2011, **50**, 11039-11045.

183. C. Y. Tang, A. L. Thompson and S. Aldridge, *J. Am. Chem. Soc.*, 2010, **132**, 10578-10591.

184. A. B. Chaplin and A. S. Weller, *Angew. Chem. Int. Ed.*, 2010, **49**, 581-584.

185. M. Bühl, M. Kaupp, O. L. Malkina and V. G. Malkin, *J. Comput. Chem.*, 1999, **20**, 91-105.

186. W. H. Bernskoetter, C. K. Schauer, K. I. Goldberg and M. Brookhart, *Science*, 2009, **326**, 553-556.

187. G. Bouhadir and D. Bourissou, *Chem. Soc. Rev.*, 2016, **45**, 1065-1079.

188. A. Amgoune, S. Ladeira, K. Miqueu and D. Bourissou, *J. Am. Chem. Soc.*, 2012, **134**, 6560-6563.

189. A. B. Burg, *Inorg. Chem.*, 1978, **17**, 593-599.

190. K.-C. Schwan, A. Y. Timoskin, M. Zabel and M. Scheer, *Chem. Eur. J.*, 2006, **12**, 4900-4908.

191. U. Vogel, P. Hoemensch, K.-C. Schwan, A. Y. Timoshkin and M. Scheer, *Chem. Eur. J.*, 2003, **9**, 515-519.

192. C. A. Tolman, *J. Am. Chem. Soc.*, 1970, **92**, 2956-2965.

193. H. C. Johnson, E. M. Leitao, G. R. Whitten, I. Manners, G. C. Lloyd-Jones and A. S. Weller, *J. Am. Chem. Soc.*, 2014, **136**, 9078-9093.

194. M. T. Nguyen, V. S. Nguyen, M. H. Matus, G. Gopakumar and D. A. Dixon, *J. Phys. Chem., A.*, 2007, **111**, 679-690.

195. W. R. Nutt and M. L. McKee, *Inorg. Chem.*, 2007, **46**, 7633-7645.

196. A. L. Colebatch, A. I. McKay, N. A. Beattie, S. A. Macgregor and A. S. Weller, *Eur. J. Inorg. Chem.*, 2017, **2017**, 4533-4540.

197. A. L. Colebatch, A. I. McKay, N. A. Beattie, S. A. Macgregor and A. S. Weller, *Eur. J. Inorg. Chem.*, 2017, **38**, 4533-4540

198. A. Kumar, N. A. Beattie, S. D. Pike, S. A. Macgregor and A. S. Weller, *Angew. Chem. Int. Ed.*, 2016, **55**, 6651-6656.

199. G. Alcaraz, L. Vendier, E. Clot and S. Sabo-Etienne, *Angew. Chem. Int. Ed.*, 2010, **49**, 918-920.

200. M. C. MacInnis, R. McDonald, M. J. Ferguson, S. Tobisch and L. Turculet, *J. Am. Chem. Soc.*, 2011, **133**, 13622-13633.

201. H. Braunschweig, B. Christ, M. Colling-Hendelkens, M. Forster, K. Götz, M. Kaupp, K. Radacki and F. Seeler, *Chem. Eur. J.*, 2009, **15**, 7150-7155.

202. H. Braunschweig, M. Forster and F. Seeler, *Chem. Eur. J.*, 2009, **15**, 469-473.

203. H. Braunschweig, C. Kollann and U. Englert, *Eur. J. Inorg. Chem.*, 1998, **1998**, 465-468.

204. A. Rifat, N. J. Patmore, M. F. Mahon and A. S. Weller, *Organometallics*, 2002, **21**, 2856-2865.

205. R. T. Baker, D. W. Ovenall, R. L. Harlow, S. A. Westcott, N. J. Taylor and T. B. Marder, *Organometallics*, 1990, **9**, 3028-3030.

206. H. Braunschweig, M. Forster, T. Kupfer and F. Seeler, *Angew. Chem. Int. Ed.*, 2008, **47**, 5981-5983.

207. L. J. Farrugia and H. M. Senn, *J. Phys. Chem., A.*, 2010, **114**, 13418-13433.

208. P. Macchi, L. Garlaschelli, S. Martinengo and A. Sironi, *J. Am. Chem. Soc.*, 1999, **121**, 10428-10429.

209. H. Braunschweig and M. Müller, *Chem. Ber.*, 1997, **130**, 1295-1298.

210. K. B. Wiberg, *Tetrahedron*, 1968, **24**, 1083-1096.

211. H. Braunschweig, R. D. Dewhurst, K. Kraft and K. Radacki, *Chem. Commun.*, 2011, **47**, 9900-9902.

212. H. Braunschweig, M. Burzler, R. D. Dewhurst and K. Radacki, *Angew. Chem. Int. Ed.*, 2008, **47**, 5650-5653.

213. D. Vidovic and S. Aldridge, *Angew. Chem. Int. Ed.*, 2009, **48**, 3669-3672.

214. C. Fonseca Guerra, J. G. Snijders, G. te Velde and E. J. Baerends, *Theor. Chem. Acc.*, 1998, **99**, 391-403.

215. E. J. Baerends, T. Ziegler, A. J. Atkins, J. Autschbach, D. Bashford, O. Baseggio, A. Brces, F. M. Bickelhaupt, C. Bo, P. M. Boerritger, L. Cavallo, C. Daul, D. P. Chong, D. V. Chulhai, L. Deng, R. M. Dickson, J. M. Dieterich, D. E. Ellis, M. van Faassen, A. Ghysels, A. Giammona, S. J. A. van Gisbergen, A. Goez, A. W. Gtz, S. Gusarov, F. E. Harris, P. van den Hoek, Z. Hu, C. R. Jacob, H. Jacobsen, L. Jensen, L. Joubert, J. W. Kaminski, G. van Kessel, C. Knig, F. Kootstra, A. Kovalenko, M. Krykunov, E. van Lenthe, D. A. McCormack, A. Michalak, M. Mitoraj, S. M. Morton, J. Neugebauer, V. P. Nicu, L. Noodleman, V. P. Osinga, S. Patchkovskii, M. Pavanello, C. A. Peeples, P. H. T. Philipsen, D. Post, C. C. Pye, H. Ramanantoanina, P. Ramos, W. Ravenek, J. I. Rodrguez, P. Ros, R. Rger, P. R. T. Schipper, D. Schlns, H. van Schoot, G. Schreckenbach, J. S. Seldenthuis, M. Seth, J. G. Snijders and Sol, *Journal*.

216. G. te Velde, F. M. Bickelhaupt, E. J. Baerends, C. Fonseca Guerra, S. J. A. van Gisbergen, J. G. Snijders and T. Ziegler, *J. Comput. Chem.*, 2001, **22**, 931-967.

217. E. Van Lenthe and E. J. Baerends, *J. Comput. Chem.*, 2003, **24**, 1142-1156.

218. E. v. Lenthe, E. J. Baerends and J. G. Snijders, *J. Chem. Phys.*, 1993, **99**, 4597-4610.

219. F. Jensen, *J. Chem. Theory Comput.*, 2014, **10**, 1074-1085.

220. L. J. L. Haller, E. Mas-Marza, M. K. Cybulski, R. A. Sanguramath, S. A. Macgregor, M. F. Mahon, C. Raynaud, C. A. Russell and M. K. Whittlesey, *Dalton Trans.*, 2017, **46**, 2861-2873.

221. C. J. Stevens, R. Dallanegra, A. B. Chaplin, A. S. Weller, S. A. Macgregor, B. Ward, D. McKay, G. Alcaraz and S. Sabo-Etienne, *Chem. Eur. J.*, 2011, **17**, 3011-3020.

222. A. B. Chaplin and A. S. Weller, *Inorg. Chem.*, 2010, **49**, 1111-1121.